NASA SP–259

AIRCRAFT PROPULSION

14

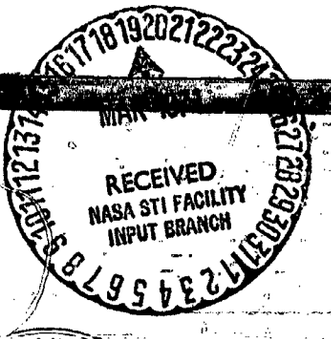

A conference held at
LEWIS RESEARCH CENTER
CLEVELAND, OHIO
November 18–19, 1970

NATIONAL AERONAUTICS AND SPACE ADMINISTRATION

NASA SP-259

AIRCRAFT PROPULSION

The proceedings of a conference held at
NASA Lewis Research Center, Cleveland, Ohio
November 18–19, 1970

Prepared by Lewis Research Center

Scientific and Technical Information Office 1971
NATIONAL AERONAUTICS AND SPACE ADMINISTRATION
Washington, D.C.

FOREWORD

The Lewis Research Center is the National Aeronautics and Space Administration's principal field installation for research and development of advanced aerospace-propulsion and power-generating systems. More specifically, a substantial part of the Center's activities is devoted to progress in the technology of aircraft propulsion. Work includes such diverse areas as components, controls and other aspects of installation, V/STOL and low-cost engine designs, and noise reduction.

The results of this work are published as NASA reports and as articles in the technical journals. In addition, an occasional technical conference assists us in communicating more directly with others in the engineering fraternity. Accordingly, this conference - in which the NASA Ames, Flight, and Langley Research Centers are represented where they are working in related areas - is held to present the results of our recent and current work.

Bruce T. Lundin
Director

CONTENTS

I. FAN AND COMPRESSOR TECHNOLOGY

Melvin J. Hartmann, William A. Benser, Cavour H. Hauser, and Robert S. Ruggeri

Advanced airbreathing engines are required for a wide variety of aircraft. These engines must be capable of operating at a low specific fuel consumption. They must be light weight, dependable, relatively quiet, and low in cost. Most advanced engines must operate over a wide range of flight conditions. Sketches of advanced aircraft and the related engines are presented in figure I-1. A supersonic transport, for example, may require light-weight, augmented turbojet engines. Advanced military aircraft operate over a number of mission profiles and must be capable of severe maneuvers at both subsonic and supersonic flight speeds. These types of aircraft may use a low bypass ratio turbofan engine. Both of these applications require supersonic inlets. The engine components may be subjected to flow distortions due to the inlet or to the flow field established by the forward portions of the aircraft. Advanced subsonic commercial transports require high bypass ratio turbofan engines for low specific fuel consumption and low noise. VTOL or STOL aircraft may use even higher bypass ratio fan systems. A VTOL aircraft may require a large number of lift fans, so that weight, noise, and low cost are particularly important.

Fans and compressors for advanced engines may take a variety of forms. The compressor of a turbojet engine requires a number of high pressure ratio stages as shown in figure I-2. A low bypass ratio turbofan engine may require two or three stages in the fan. For high bypass ratio engines, the fan pressure ratio is low and single-stage fans may be adequate.

Some of the general requirements of fans and compressors are listed in figure I-2. As usual, high component efficiency is essential for low specific fuel consumption. Light weight is generally desirable for all applications. Light weight may be achieved by using high pressure stages so that fewer stages are required to achieve the required pressure. Light weight materials and advanced construction techniques must also be used. Fans and compressors must operate over a wide range of flows and must tolerate inlet flow distortions that may occur during some portions of the flight. Low noise limits may require the selection of specific rotational speeds and blade loadings. Even with suitable selection of these parameters, considerable noise suppression may be required.

The NASA Fan and Compressor Technology Program has been set up to provide machines which meet the general requirements listed in figure I-2. This paper discusses the performance of a number of high pressure ratio stages, and the technology used to make these useful for fans and multistage compressors. The rotor blade requirements and blade selection to achieve good performance will be discussed first. Stator blades for these high pressure stages will then be covered. Next, stall margins and distortion tolerance of high pressure ratio stages will be considered. Then casing treatment methods to improve the stall margin and distortion tolerance of these stages will be covered. Finally, NASA multistage compressor investigations applying high pressure ratio stages will be discussed.

HIGH PRESSURE RATIO ROTORS

In the NASA program, the goals in rotor aerodynamics are to obtain increased pressure ratio per stage, while maintaining acceptable efficiency and operating range. If higher pressure ratio per stage can be achieved, the number of stages required for a given application can be reduced. This results in lighter and more compact fans and compressors.

The major factors affecting rotor pressure ratio are shown in figure I-3; where calculated values of rotor pressure ratio are plotted as a function of rotor blade tip speed for three levels of rotor aerodynamic blade loading. An increase in blade loading corresponds to an increase in lift, or energy addition, for the rotor blades. The curves indicate that higher rotor pressure ratios can be obtained by either increased tip speed or increased blade loading. Of course, the highest rotor pressure ratios are obtained when both high loading and high tip speed are used.

Attainment of gains in pressure ratio are complicated by the requirements of maintaining high efficiency and broad range of operation. As loading is increased, losses also increase, and the potential of flow separation and blade-row stall are much greater. As blade tip speed is increased, the Mach numbers relative to the blades are also increased. For the range of blade speeds shown in figure I-3, the tip relative Mach numbers are supersonic, and increases in these supersonic Mach numbers can result in severe shock losses and corresponding decreases in efficiency. Current fans and compressors operate over the range of blade tip speeds from about 1000 to 1600 feet per second depending on the application. Fans usually operate at the high speed end of the range, and compressors operate at the lower speeds. Current fans and compressors are designed for blade loadings of the order of 0.35.

An extensive NASA program is aimed at determining the blade shapes and de-

sign controls necessary to extend loading levels to the range of 0.45 to 0.50 and thereby to achieve higher values of rotor pressure ratio as indicated by the calculated curves of figure I-3. Tip speeds for actual engine applications may be dictated by factors such as turbine stresses or rotor noise rather than rotor aerodynamics. Therefore, the NASA program covers a broad range of speeds.

The fan and compressor program includes research conducted entirely within the NASA as well as NASA contract studies conducted by various engine companies. The overall NASA program covers a wide range of design parameters and test conditions. A photograph of the NASA-Lewis single-stage test facility, and some of the rotors that have been tested in the facility are presented in figure I-4. The rotors all have a 20-inch tip diameter. The facility includes extensive instrumentation and automatic data processing equipment to aid in the complete and rapid evaluation of either rotor or complete stage performance. Some highly loaded research rotors built and tested under NASA contracts are shown in figure I-5. The rotor shown at the upper left incorporates part-span shrouds (vibration dampers), and the rotor shown at the upper right does not although it had a higher design blade tip speed (1600 ft/sec). Research rotors of the NASA program are subjected to very severe conditions during stall and distortion testing, and occasionally a rotor experiences catastrophic failure as shown by the photograph at the lower left of figure I-5. This failure was due to metal fatigue. A front view of a research rotor installed in its test casing is shown at the lower right of figure I-5.

The experimental performance for several highly loaded rotors is presented in figure I-6. The rotor pressure ratio at the maximum polytropic efficiency, the maximum polytropic efficiency, and the approximate range of blade tip relative Mach numbers are shown plotted as functions of design blade tip speed. The data are for rotors only, and each point represents design speed performance for a different rotor. Blade loading levels varied from 0.4 to 0.5. Rotor pressure ratios ranged from 1.4 to 2.0 and are appreciably higher than current levels for similar speeds. As indicated by the shaded band, the maximum polytropic efficiencies were quite good; ranging from greater than 0.9 at the lower blade tip speeds to slightly less than 0.9 at the higher speeds. The blade tip inlet relative Mach numbers varied from somewhat over 1.0 to about 1.6.

The data presented in figure I-6 show that highly loaded stages can provide good efficiencies, even at high blade tip speeds. These results are sufficiently encouraging that the NASA program has been extended to include even higher blade speeds. At present, a stage with a design rotor blade tip speed of 1800 feet per second is in the design phase, and plans have been made for a 2200-foot-per-second stage. The rotor blades for the 1800-foot-per-second stage will be fabricated from titanium

alloy, and those for the 2200-foot-per-second stage will be made of a fibre-resin composite material.

ROTOR BLADE SHAPE CONSIDERATIONS

To achieve the high levels of rotor pressure ratio shown in figure I-6 while maintaining high rotor efficiencies as well, it is apparent that the blade profile for supersonic relative flows must be carefully designed. Before we can discuss the proper selection of rotor blade shapes and the associated factors that affect efficiency, it is first necessary to consider the flow through a rotating blade row. The flow condition in a stream surface in the blade tip region (see fig. I-7) is considered first.

Measurements of static pressure on the outer casing wall of an experimental compressor were made using high-response instrumentation (ref. 1). Static-pressure contours relative to the rotating blades are presented in figure I-8, which shows a view of two rotor blades looking in from the rotor casing. For the data shown, the inlet relative Mach number was 1.4. The inlet relative flow is supersonic, a strong shock is formed within the blade passage, and the outlet flow is subsonic. Thus, conditions associated with a mixed supersonic and subsonic flow field must be considered. Three important points are discussed, namely, shock loss, the throat area (which is the minimum passage area behind the shock), and the subsonic diffusion of the flow downstream of the shock. The pressures on the contours are given in psia. The inlet and outlet pressures are 12 and 20 psia, respectively.

With the inlet Mach number of 1.4 a weak bow shock exists at the blade leading edge which causes the pressure to rise to 14 psia. However, the flow is still supersonic on this forward portion of the blade, and this supersonic flow accelerates on the convex suction surface. A change in flow angle of only a few degrees along this surface causes appreciable supersonic acceleration. For the case shown in figure I-8, this acceleration causes a drop in pressure to 10 psia in the region where the pressure contours become closely grouped at the entrance to the blade passage. This close grouping of pressure contours denotes the presence of a shock wave that extends across the passage. As noted, a small region exists downstream of the shock where the pressure is 18 psia, but otherwise the static pressure rises from 10 to 16 psia across the shock. The Mach number ahead of the shock is higher near the blade suction surface as noted by the lower pressure in this region. Losses in the shock are a significant part of the total measured loss. Because shock losses increase rapidly with Mach number, it is important to minimize the supersonic acceleration upstream of the shock.

The minimum passage flow area, or throat area, is a critical factor with respect to the flow capacity of the blade row. For the blades shown in figure I-8, the throat is a short distance downstream of the shock. Throat area is geometrically related to the degree of turning or curvature of the suction surface of the blade from the leading edge to the shock. Thus greater throat area is obtained by increased turning of the flow from the leading edge. However, as previously mentioned, such turning increases the Mach number ahead of the shock and thereby increases the shock losses. Therefore the throat area should be no larger than that necessary to pass the mass flow.

There is another reason to limit the size of the throat. Because of shock wave boundary-layer interaction, there is inevitably some separation of the flow from the suction surface of the blade just downstream of the shock. The loops in the two contours noted downstream of the shock in figure I-8 are probably caused by this separation. When the throat area is optimum, the degree of this separation is limited, which is conducive to good subsonic diffusion downstream of the throat.

The design of the blade suction surface downstream of the throat is important because appreciable subsonic diffusion, or flow deceleration, must take place in this region. In figure I-8, this subsonic diffusion is noted by the rise in static pressure from 16 to 20 psia over the rear portion of the blade suction surface. If the diffusion is too abrupt, severe separation and high losses will result. Thus, the blade shape downstream of the throat must be selected to properly control diffusion rate.

The preceding discussion does not specify particular blade shapes used in fan and compressor rotors. However, a series of circular arcs can generally be used to define blade profiles that meet the aforementioned principal requirements of low suction surface Mach number, minimum allowable throat area, and good subsonic diffusion.

EFFECT OF DESIGN PRINCIPLES ON ROTOR PERFORMANCE

The effect of shock loss and throat area on the performance of two experimental compressor rotors is presented in figure I-9. Both rotors had the same blade speed and inlet relative Mach number but the throat sizes differed for the two rotors. Throat size is defined as the ratio of the actual throat area A_t to the critical flow area A^* (the area which would just pass the required mass flow at sonic velocity without viscous, or boundary layer, losses). To compensate for boundary-layer losses, the actual throat area must be somewhat greater than the critical area. The ratio of the actual throat area to the critical area, A_t/A^*, was 1.11 for one

rotor and 1.20 for the other. As previously discussed, the larger throat area causes a higher Mach number upstream of the shock. This Mach number, M_s', was 1.79 for the rotor with the larger throat and 1.61 for the other. The rotor with more moderate M_s' has a peak efficiency about two points greater than the other rotor because of lower shock and diffusion losses.

The minimum flow shown for each rotor represents the point of initiation of rotating stall. There is a small difference in the maximum flow for these rotors, but the significant difference in these two designs is the larger flow range obtained for the rotor with the smaller throat area. This range effect is probably related to the reduction in the flow separation that occurs downstream of the shock.

The data of figure I-9 show that the combination of reduced throat area and reduced suction surface Mach number can provide gains in both efficiency and flow range. Although the smallest area ratio used in this comparison was 1.11, other data indicate that throat area ratios of about 1.05 are preferable. The data of figure I-9 are reported in reference 2.

The effect of changes in the subsonic diffusion portion of the blade passage on rotor performance is illustrated in figure I-10. Two rotor blades are shown as dashed and solid contours. The forward or supersonic portion of both blades were the same but the subsonic diffusion rate was changed by altering the extent of the rearward or subsonic portion of the blade. This resulted in a change of blade row solidity which is defined as the ratio of chord length to the spacing between the blades. The solidity was 1.1 for one design and 1.5 for the other. For both rotor designs, the tip speed was 1375 feet per second and the design pressure ratio was 1.65.

The performance plots show that the higher solidity design provided higher peak pressure ratio and a four-point increase in efficiency. Apparently the 1.1 solidity blade was too short for effective subsonic diffusion.

Existing data were reviewed to further evaluate the influence of solidity on rotor blade tip losses. Data for a large number of rotors are presented in figure I-11 where rotor tip loss is plotted as a function of rotor blade loading. Blade rows with solidities greater than 1.2 are shown as solid symbols while those with solidities less than 1.2 are denoted by open symbols. Although appreciable data scatter exists, as expected for this type of data, there is a definite trend for the higher solidity rotors to have lower tip loss at blade loadings greater than about 0.4. Thus, the data give a strong indication that there is an advantage in the use of relatively high solidities for highly loaded transonic rotors.

The data presented in figures I-6, I-9, and I-10 have shown that good single-stage rotor performance can be achieved when the three previously discussed blade design principles are applied. These important design principles are (1) the suc-

tion surface Mach number ahead of the shock should be a minimum, (2) the throat area should be just sufficient to pass the required mass flow, and (3) the downstream portion of the blade should be shaped to provide good subsonic diffusion.

STATOR REQUIREMENTS AND STAGE EXPERIENCE

The previous discussions concerned the design of highly loaded rotor blades which achieved good performance. However, in order to fully evaluate the usefulness of highly loaded rotors, it is necessary to study the problems associated with adding a stationary blade row, or stator, behind these rotors to form a complete stage. A schematic of a typical rotor-stator combination is presented in figure I-12. The purpose of stators is to convert the rotor exit whirl velocity to static pressure rise.

A number of the rotors discussed have been tested with stators, and the results are presented in figure I-13. All the data shown are for the design speed, and each symbol represents a separate stage. The open symbols denote measured rotor performance, and the solid symbols represent the performance of the rotor and stator (i.e., the complete stage). The decrease in pressure ratio and efficiency from the open symbols to the solid symbols is a measure of the losses across the stator blade row. Reductions in pressure ratio are not severe, but these losses in pressure ratio result in losses in efficiency that vary from three to five percentage points. The data of figure I-13 are all for highly loaded stages, and the stage efficiencies are considered to be good. The efficiencies vary from about 0.89 to 0.85 even with the indicated high stator losses.

STATOR LOSS CONSIDERATIONS

Conditions that contribute to high stator losses are illustrated by the calculated curves presented in figure I-14. Calculated stator hub aerodynamic loading and stator hub Mach number are plotted as a function of rotor blade tip speed for two levels of rotor blade loading. Stator hub conditions were selected because these are the most critical. These calculations are for a stage with an inlet hub-to-tip radius ratio of 0.5.

The curves of figure I-14 show that increases in rotor blade loading result in high stator hub loadings and in high stator hub Mach numbers at all rotor blade tip speeds. On the other hand, increased rotor blade tip speed has little effect on the stator hub loading and Mach number. Most of the stage data shown in figure I-13

are for rotor blade loadings in excess of 0.45. Thus, the stator loadings and stator Mach numbers were both relatively high, and this led to the high stator losses indicated by the stage performance data (fig. I-13).

To determine the level and distribution of losses for a highly loaded, high Mach number stator blade row, total pressure surveys were made in a plane just downstream of a stator blade row. These surveys covered the entire blade passage as represented by the shaded area shown in figure I-15. Some typical survey results are presented in figure I-16. In order to normalize the results, stator loss data are presented in terms of loss coefficients. A contour plot of local values of loss coefficient measured over a complete stator blade passage is shown on the left side of the figure. At midspan, there is little or no loss over at least one half the width of a blade passage as represented by the zero-loss contour. In the blade wake region, the loss coefficient increases to values of 0.1 to 0.2. These values correspond to a total pressure loss equal to 10 to 20 percent of the dynamic head of the flow entering the stator blade row. Thus, the stator losses at midspan are relatively small. At the stator tip, the losses increase somewhat and reach local values of loss coefficient of 0.3. The area of this higher loss is still quite small. Far greater losses are observed at the stator hub. Not only is the level of the loss quite high (reaching a loss coefficient value of 0.5), but also the region of high losses cover a much larger area. In general, stator end-wall losses stem from flow separation and secondary flows that occur in the corners formed by the blade suction surface and the adjacent walls.

A mass-average integration of the local loss coefficients across the flow passage at various blade spans yields an average loss coefficient as a function of the blade span, as shown in the plot of figure I-16.

As expected, the minimum losses occur in the midspan region; these increase to about twice the minimum value in the tip region but the greatest losses by far occur in the stator hub region. Thus, it is apparent that the efforts to reduce stator losses should be concentrated in the hub region because it is in this area that the greatest benefits are likely to be realized.

One method for reducing stator end-wall losses is shown in figure I-17. Suction is applied by means of a narrow slit at the intersection of the blade suction surface and the hub wall (ref. 3). By use of a narrow slit, air is removed from a discrete region of high loss which should tend to maximize the benefits for a given amount of slit suction. The effectiveness of slit suction is illustrated by the two curves of loss coefficient shown. Use of a slit suction flow rate of only 0.2 percent of the total through-flow of the stage (dashed curve) reduced losses in the stator hub region by as much as 20 percent, and some improvement was noted out to about one-third of the blade span. For this particular fan stage, use of stator hub slit

suction improved overall stage efficiency by about 1.5 percentage points. For suction flow rates greater than the 0.2 percent used, it is expected that even greater improvements in overall stage efficiency would have been realized. Flow rates for this study, however, were limited to the values shown. The NASA programs include several other concepts for reducing stator losses; four of which are shown schematically in figure I-18. With wall suction, air is removed through a continuous ring of porous material at the hub or tip of the stators. Although this method did reduce stator losses, the suction flow rate was excessive; amounting to 2.0 to 2.5 percent of the total through-flow for each wall treated. This is about 10 times the flow rate used in the hub slit suction studies described previously.

Use of blade surface suction, in combination with wall suction, gave only a slight improvement in stator performance over that obtained using wall suction alone. As previously discussed, stator losses in the midspan portion of the stator blade are quite low (figs. I-16 and I-17). Consequently, blade surface suction in this midspan region can not be expected to have a large effect on overall losses. This indicates that, in general, corner flows and wall boundary layer are more important factors than is blade surface boundary layer when considering stator losses.

The concept of corner blowing is based simply on the use of properly directed high-energy jets to energize the lower energy flow in the end-wall regions near the suction surface. As yet, this concept has not been tested.

The tandem blade is designed primarily to operate satisfactorily over a wider range of stator incidence angles before encountering flow separation and stall. The energizing effect on the flow through the space between blade segments may delay flow separation, particularly in the end-wall regions. If this occurs, then stator losses in the end-wall region should decrease accordingly. The tandem stator design is currently in test, but no loss data are presently available.

The NASA program has demonstrated that it is possible to design good fan and compressor stages with high blade tip speeds and rotor blade loadings. However, as blade loadings and pressure ratios continue to increase, it is evident that the stator problem is becoming increasingly more important, and more study should be directed toward reducing stator end-wall losses, particularly in the hub region.

STALL MARGIN AND EFFECTS OF INLET FLOW DISTORTION

To be useful, high pressure ratio fan and compressor stages, even with good performance, must be capable of stable operation over a range of flow conditions. For purposes of illustration, a stage performance map is shown in figure I-19.

With the fan or compressor stage operated at constant speed, the pressure ratio is increased until unstable flow conditions are observed. The locus of these unstable, or stall, points at various rotational speeds forms the stall limit line. Peak efficiency usually occurs at flows slightly greater than the stall limit point. Fan and compressor stages are designed to place the operating line at a flow rate near the peak efficiency but at a sufficient distance from the stall limit line to avoid stall. The required margin between the operating line and the stall limit line depends on the particular application.

Some of the factors that determine the required stall margin include the rematching of components for operation over a range of flight conditions; transient operating conditions during engine acceleration; expected performance variations from one assembly to another; or any deterioration of component performance that may occur during the life of the engine such as errosion, wear, or foreign object damage. However, in many applications, the most critical factor contributing to stall margin requirement is the necessity to avoid stall under conditions of inlet flow distortion.

An infinite variety of inlet flow distortion patterns may be encountered during flight maneuvers or other flight conditions. Inlet flow distortions produce a nonuniformity of total pressures at the fan or compressor inlet as illustrated in figure I-20. The constant-pressure contours indicate that both radial and circumferential gradients of total pressure occur. (Other chapters of these proceedings will discuss in detail various aspects of inlet flow distortions and their effect on engine performance.) To obtain comparative performance for research fan and compressor stages, test distortion patterns are generated by means of circumferential and radial screen configurations such as those included in figure I-20. The effect of these screen-induced flow distortions on the performance of a high pressure ratio stage (ref. 4) is shown in figure I-21. The solid lines represent the stage performance obtained with uniform inlet flow at 100 and 70 percent of design speed.

For the results of figure I-21, circumferential distortion was produced by a screen which covered 90° of the inlet annulus; the screen used for the radial distortion tests covered 40 percent of the outer annulus area (see fig. I-20). A substantial reduction in stall margin occurred with both circumferential and radial distortion; as indicated by the fact that the stall limit lines with distortion lie well below that for uniform flow. Reasons for the loss in performance can be examined by comparing the radial distribution of pertinent parameters for the two near-stall points shown by the symbols on the performance curves obtained with uniform flow and with radial distortion. Radial distributions of inlet total pressure, pressure ratio, and total temperature ratio at near-stall conditions (ref. 4) are presented in figure I-22. The radial distortion screen produced a decrease in inlet total pres-

sure that was about 18 percent less than the maximum pressure. The inlet total pressures shown were all corrected to standard conditions; consequently, the average inlet total pressure for both test conditions has the same value of 14.7 psia. The total pressure ratio generated by the stage for both test conditions is about 1.8 in the tip region. For the case of radially distorted inlet flow, the pressure ratio in the unscreened area is substantially lower than that measured when the inlet flow was uniform. This resulted from a redistribution of the inlet flow in toward the hub. The hub portion of the blading operated at a high flow and a low pressure ratio condition whereas the tip portion operated at a low flow and high pressure ratio condition.

The temperature ratio of the stage indicates that the energy addition to the air was also lower in the unscreened region than it was for the uniform flow case. The temperature ratio measured in the tip region was the same for both test conditions. This indicates that, for this stage, the limiting energy addition in the blade tip region at stall with tip radial distortion was the same as that obtained with uniform inlet flow.

The overall performance data previously presented in figure I-21 shows that the stage total pressure ratio at stall is appreciably less than that for uniform flow. This lower overall pressure ratio with distortion results from the lower pressure ratios experienced in the unscreened portion of the inlet passage due to redistribution of the flow, as already noted in figure I-22. As a further consequence of this flow shift with distortion, the blade tip reached its limiting loading condition at a higher flow rate. Thus the change in stall limit line with distorted inlet flow depends on the resulting flow redistribution and the location of the critical loading region on the blade.

In order to compare stall margins and inlet flow distortion effects for a number of different stages, it is first necessary to establish some criterion upon which to base these comparisons. The criterion used is illustrated in figure I-23. The first requirement in establishing a stall margin is the selection of a reference operating point. To obtain a good compromise of stall margin and operating point efficiency, the operating point is generally selected at a flow rate which is slightly greater than that for maximum efficiency. For comparison purposes, an operating condition which was 1 percentage point below peak efficiency was arbitrarily chosen. This establishes the operating point on the design speed curve of the performance map (see fig. I-23). Comparisons presented herein are all for design speed; consequently, the discussions will not be concerned with the shape of the operating line, but only with its intersection with the design speed curve.

The stall margin parameter SM used in this paper is defined as

$$SM = \left\{ \left[\frac{(PR)_{ST}}{(PR)_{OL}} \times \frac{(W)_{OL}}{(W)_{ST}} \right] - 1.0 \right\} \times 100$$

where PR is the pressure ratio, W is the weight flow, and the subscripts ST and OL indicate conditions at stall and on the operating line, respectively. The factor of 100 is used simply to express stall margin in terms of a percentage. The stall margin, as defined, is a commonly used parameter, and, in brief, it is essentially a measure of the distance between the operating point and the stall point at a fixed speed.

The stall margins for several experimental stages, with and without inlet flow distortion, are compared in figure I-24. The design blade tip speeds for the various stages ranged from 1000 to 1600 feet per second. With uniform inlet flow, the stall margins varied from about 8 percent to a little over 30 percent. For the 1000-foot-per-second stage, the limiting loading occurred at the stator hub. For the remaining stages, limiting loading occurred in the rotor blade tip region. From consideration of the uniform flow data for blade tip speeds of 1140 feet per second and above, it might be concluded that stall margin decreases with increased speed. The different stages represent many variations in design details; and because experience with high speed stages is limited, these stages may not be optimum from the standpoint of range. Consequently, any implication that blade tip speed is the predominant factor affecting stall margin is not intended.

In general, blade loading might be considered as the prime factor affecting stall margin, but at present the data available for complete stages are not sufficient to determine the pertinent parameters that most affect stall margin with uniform inlet flow.

When severe tip radial distortion was imposed on the stages, all stages lost an appreciable amount of stall margin except the 1000-foot-per-second stage. As previously stated, this stage normally stalled at the stator hub with uniform flow. Tip radial distortion unloaded this critical region, and, for this distortion case, stall was initiated by the rotor tip. This stage would probably have responded very adversely to a hub radial distortion, but no data were taken with this type of distortion. The 1140-foot-per-second stage suffered extensively from tip radial distortion. This particular stage had a large stall margin with uniform inlet flow because it had an extremely large flow range at essentially constant pressure ratio. Stages with this flat type of pressure ratio characteristic appear to be very susceptible to inlet flow distortions.

The data obtained with tip radial inlet flow distortions show no general trend

with regard to decreases in stall margins. Stall for each stage can be traced to some critical region such as the rotor tip or the stator hub. The data of figure I-24 are all for tip radial distortion; however, the results obtained with circumferential distortion were quite similar. Seemingly, one factor which should influence stall margin under distorted flow conditions is that of rotor blade loading. To determine the effect of blade loading, two rotors of very similar design were studied both with and without tip radial distortion. The results are compared in figure I-25. The data (from ref. 2) are for isolated rotors operated at design speed and with uniform inlet flow. Both rotors had a design blade tip speed of 1400 feet per second and used the same type of blading. The pressure ratios on the operating lines shown were 1.72 and 1.6.

As shown by the small bar chart, lower blade loading provided the greater stall margin with uniform flows: about 20 percent for the lower blade loading and about 15 percent for the more highly loaded rotor. However, when the same degree and extent of tip radial distortion was imposed on the rotors, the stall margin for both rotors dropped to about the same value of 3 to 4 percent. Thus the stall margin available with uniform flow can be a rather poor criterion for estimating stall margin with tip radial distortion. The 1140-foot-per-second stage shown in figure I-24 is another example where a large stall margin with uniform flow did not insure an adequate stall margin with tip radial distortion. Although reduced blade loadings will, in general, provide greater stall margin with uniform flow, reduced loadings do not necessarily provide greater stall margin with distortion.

CASING TREATMENT CONCEPTS

From previous discussions, it is obvious that stall margins for fans and compressors must be increased. However, before discussing remedial measures that can be used to increase the useful flow range of a compressor stage, it appears desirable to briefly describe the mechanism of rotor stall. A simple illustration of flow through a rotor at stall conditions, together with a view looking into the inlet annulus, is presented in figure I-26. For the flow condition illustrated, stall exists at the rotor tip as indicated by the flow reversal of the outer streamline. For normal operating conditions no reverse flow exists, and the outer streamline would follow the casing contour. At some low flow rate, the blades reach a limiting loading condition and cells of instability (rotating stall cells) and flow reversal occur (fig. I-26). Stall generally occurs in one or more of these isolated stall cells which rotate in the same direction as the rotor but at a lower speed. To increase the

useful range of the compressor, it is necessary to delay the formation of these rotating stall cells.

One means for delaying the onset of tip stall is to bleed air from the rotor tip region. With the system shown in figure I-27, air may be bled from the blade tip region by means of a honeycomb grid. Design speed performance curves and stall limit lines with tip distortion (ref. 5) are shown for three test conditions. Before testing the honeycomb casing treatment, the compressor was tested with a conventional solid casing for performance comparisons. Design speed performance and the stall limit line are shown as the solid line curves. With 4 percent bleed through the honeycomb, a marked improvement in range was obtained, as indicated by the large shift in the stall limit line. The third condition of operation retained the honeycomb bleed system, but the exhaust valve was closed. Surprisingly, even with zero bleed flow, the honeycomb caused a marked increase in flow range. This suggested that simpler casing treatments, without bleed flow, might provide appreciable improvements in the stall range. To further explore this phenomenon, a program was initiated to evaluate the effect of various casing treatment configurations on stall margin and compressor performance.

Some of the casing treatments which have been studied are illustrated in figure I-28. One treatment consisted of circumferential grooves which covered the whole axial chord of the blading. Both the axial extent and the depth of the grooves were varied. Various depths of honeycomb were tried. Slots were cut in the casing in the direction of the mean blade angle; both long slots, somewhat greater than the blade chord, and short slots were evaluated. For the skewed slot casing, the slots were alined nearly axially but were cut at an angle of 60° from the radial direction. The casing treatments shown in figure I-28 all delayed rotating stall, but to varying degrees.

The flow mechanisms involved with casing treatment are not fully understood as yet. However, the following emperically determined parameters were found to be significant in controlling the effectiveness of various casing treatments:

(1) Axial extent
(2) Open area
(3) Depth or volume
(4) Limited recirculation

It was generally desirable to limit the axial extent of treatment to a dimension less than the axial projection of the blade chord. The percentage of open area in the area of treatment must be appreciable. For the more successful casing treatments studied, the open area was at least two-thirds of the total area treated. The depth or total volume of the treatment also has an effect. Shallow treatments were not as effective in extending useful range.

It was desirable to limit the amount of recirculation from the downstream high pressure regions to the upstream low pressure regions. Although recirculation can be effective in delaying rotating stall, excess recirculation causes an undue loss in efficiency. For the blade angle slots (fig. I-28), recirculation was limited by shortening the slots.

When the empirical parameters were taken into account, a number of the casing treatments were found to be quite effective in extending the range of compressor rotors with both uniform and with distorted inlet flow. The list of parameters is not complete nor have the values associated with these parameters been optimized. Casing treatment studies are continuing, so this discussion covers only the results obtained thus far.

EFFECT OF CASING TREATMENT ON STAGE PERFORMANCE

Casing treatment was applied to several single stages. The reference performance of one of these stages with a conventional solid casing is shown in figure I-29. The two curves show the design speed performance obtained with uniform flow and with tip radial distortion. The overall stage performance with uniform flow was good. The maximum efficiency was about 86 percent at a pressure ratio of 1.61; and the stage also had a good initial stall margin as indicated by the large range in flow between the operating line and the stall limit line. When the stage was subjected to a rather severe tip radial distortion, the stall margin was severely limited as indicated by the lower curve. If this stage had required a stall margin with distortion that was greater than the limited amount shown, it would have been necessary to move the operating line further down on the speed line. Matching this stage in this manner would result in a large penalty in efficiency due to the rapid fall-off in efficiency at weight flows greater than that for the operating point shown.

The results obtained with the application of casing treatment to this stage are shown in figure I-30. The solid curve represents stage performance at design speed with tip radial distortion and no casing treatment. This curve is the same as the curve shown for flow distortion in figure I-29.

With casing treatment and for the same distortion, the stall margin was greatly improved over that obtained with a solid casing as indicated by the large shift in the stall limit line. In fact, the measured stall margin using casing treatment with flow distortion approached that obtained with an untreated casing and uniform flow. Casing treatment also provided large improvements in stall margin at lower speeds as well. In fact, at lower speeds, the stall margin obtained with casing treatment and distorted flow were actually greater than those measured for

uniform flow. The casing treatment used on this stage consisted of skewed slots over the center portion of the rotor blades with a partition added to limit recirculation in the axial direction (see fig. I-28).

Casing treatment has been successfully applied to several other fan and compressor stages. The results are presented in figure I-31. The solid casing results shown for uniform and radially distorted flow were presented previously in figure I-24. The additional cross-hatched bars represent the casing treatment results with tip radial distortion. By use of casing treatment, the stall margins with distortion were greatly improved for all stages studied. In fact, the stall margins with distortion practically equalled and in some cases, even exceeded the initial stall margins obtained with uniform flow.

The results presented in figure I-31 were obtained using various types of casing treatment, such as those previously discussed. Although not discussed herein, casing treatment provides good improvements in stall margin with circumferential distortion as well. Also, casing treatment works quite well over a full range of speeds. Thus casing treatment is an effective and relatively simple means for combating the distortion problem.

CASING TREATMENT EFFECTS ON STAGE EFFICIENCY

An important factor to consider with use of casing treatment is its effect on overall stage efficiency with uniform flow such as exists at cruise flight conditions where efficient operation is essential.

The data previously presented in figure I-30 show that this stage responded favorably to casing treatment with distortion of the inlet flow. The performance of this same stage with casing treatment but with uniform inlet flow is shown in figure I-32. With uniform flow, casing treatment caused about a one point loss in peak efficiency and a small gain in the stable flow range. Although the use of casing treatment did cause a small drop in efficiency, this penalty is more acceptable than the alternatives that are available. Because this stage has a very limited stall margin with distortion, it would probably be necessary to move the operating line to a lower pressure ratio. This would cause a drop in efficiency much greater than that caused by the casing treatment. With treatment, the desirable operating line can be preserved.

For the various casing treatments that have been tested, some have given greater improvement in range but with significant losses in efficiency, and others with smaller efficiency losses have not been as effective in improving range. The casing treatment applied to the stage for which data are presented in figures I-30

and I-32 represents a good compromise; that is, an appreciable increase in range under distorted flow conditions with only a small loss in peak efficiency.

In stages which are tip critical, casing treatment is a very promising method for extending both the operating range and the distortion tolerance with little or no loss in efficiency.

STATOR HUB CASING TREATMENT

As methods are developed for delaying the occurrence of stall in the rotor tip region, it is apparent that some other portion of the compressor will become the critical problem area. This critical area is likely to be the stator hub region, particularly for highly loaded stages. Some method of treatment the stator hub will eventually be required if continued increases in range and stall margin are to be realized. As an example, for the 1000-foot-per-second stage previously discussed, the use of stator hub slit suction alone provided improvements in stall margin with uniform flow. Also, since no-bleed casing treatments worked so well in delaying rotor stall, the use of similar treatments for stators may help alleviate stator hub problems. The first such stator hub casing treatment to be studied at NASA-Lewis is shown in figure I-33. The treatment consists of a series of circumferential grooves in the hub beneath cantilevered stator blades. To fully evaluate this stator hub treatment, tests will use casing treatments for the rotor as well (see fig. I-33). Several other methods of stator hub casing treatment are also being considered.

If even greater stall margins can be obtained through the use of casing treatment on both the rotor and the stator, then the use of such stages can lead to improved performance of multistage compressors.

MULTISTAGE COMPRESSORS

The data presented thus far have all been for either single rotor blade rows or for single stages. A further step in NASA research on high pressure ratio blading and casing treatment is to apply these research findings to multistage fans and compressors. This step in the research program is to uncover any stage interactions that may limit the application of single stage results to multistage fans and compressors.

At present, the NASA program at Lewis includes two multistage compressors. Both units have highly loaded stages and incorporate the design principles developed

in our single-stage research. The first compressor has seven stages and is designed for a first stage-blade tip speed of 1200 feet per second and overall pressure ratio of 9.0. The second compressor has five stages and is designed for a blade tip speed of 1400 feet per second. It also has a pressure ratio of 9.0. Both units meet the general requirements of compressors for turbojet or turbofan engines.

A photograph of the seven-stage compressor, with half the casing removed, is presented in figure I-34. This machine is currently being tested. Very complete overall and blade row performance measurements will be made, and casing treatment will be applied to several of the inlet and exit stages. Because of an unusual number of aerodynamic and mechanical problems, satisfactory data are not yet available.

The five-stage compressor is currently being fabricated. In addition, a two-stage fan is being designed. This fan will be designed, built, and tested on NASA contract. The design tip speed for this fan is 1450 feet per second and the pressure ratio is 2.8. Casing treatment will be applied to both the five-stage compressor and the two-stage fan.

SUMMARY

Test results of rotors for high pressure fan or compressor stages showed rotor efficiencies that ranged from slightly above 90 percent at a blade tip speed of 1000 feet per second to slightly less than 90 percent at 1600 feet per second. The blade design principles that must be used to obtain these high levels of efficiency were discussed. Studies have shown that a relatively high level of losses are encountered in stator blade rows for high pressure ratio stages. These losses are particularly high in the end-wall regions. Several approaches to reduce end-wall losses have been, or are being, investigated. However, even with these high stator losses, a stage efficiency greater than 85 percent at a pressure ratio approaching 2.0 has been achieved. The flow range or stall margin of high pressure ratio stages may or may not be adequate, depending on the severity of inlet flow distortion that must be tolerated. Casing treatment was discussed as an effective approach to delaying stall when the rotor blade tip is critical; that is, when the blade stalls at the tip first. Casing treatment is particularly effective with inlet flow distortions. Although the data presented were all for tip radial distortion, casing treatment was also quite beneficial with circumferential distortion. Empirical principles identified in the NASA research program were used to design casing treatments that provided substantial improvement in stall margin and distortion tolerance with little or no loss

in component efficiency. Results from the single-stage programs are being incorporated in multistage research fans and compressors.

REFERENCES

1. Miller, G. R.; and Bailey, E. E.: Static Pressure Contours in Tip Passage of Several High Mach Number Rotors. NASA TM X-2170, 1970.

2. Gostelow, J. P.; Krabacher, K. W.; and Smith, L. H., Jr.; Performance Comparisons of High Mach Number Compressor Rotor Blading. NASA CR-1256, 1968.

3. Harley, K. G.; and Burdsall, E. A.: High-Loading Low-Speed Fan Study. Part II - Data and Performance, Unslotted Blades and Vanes. Rep. PWA-3653, Pratt & Whitney Aircraft. (NASA CR-72667), 1969.

4. Doyle, V. L.; and Koch, C. C.: Evaluation of Range and Distortion Tolerance for High Mach Number Transonic Stages, Task 1 Stage Final Report. NASA CR-72806, 1971.

5. Koch, C. C.: Experimental Evaluation of Outer Case Blowing or Bleeding of Single Stage Axial Flow Compressor. Part VI. Rep. R69AEG256, General Electric Co. (NASA CR-54592), Jan. 30, 1970.

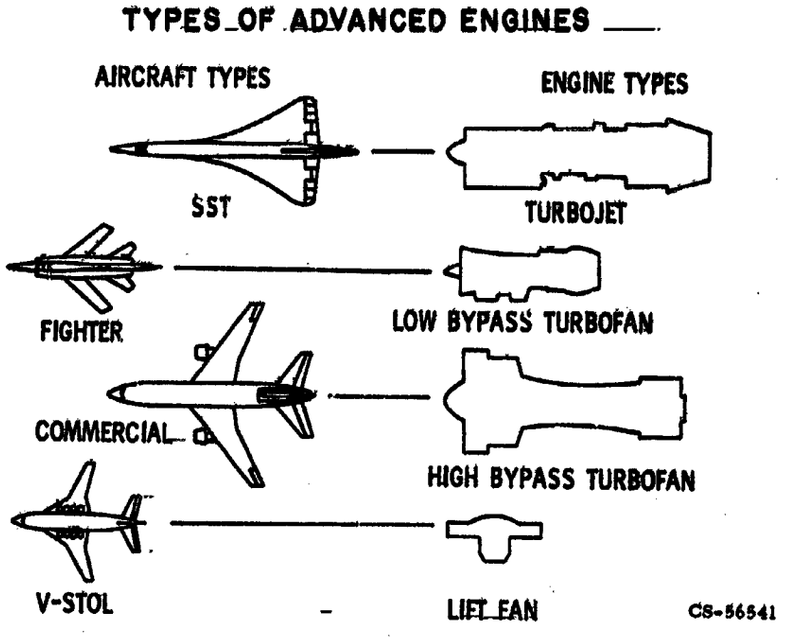

Figure I-1

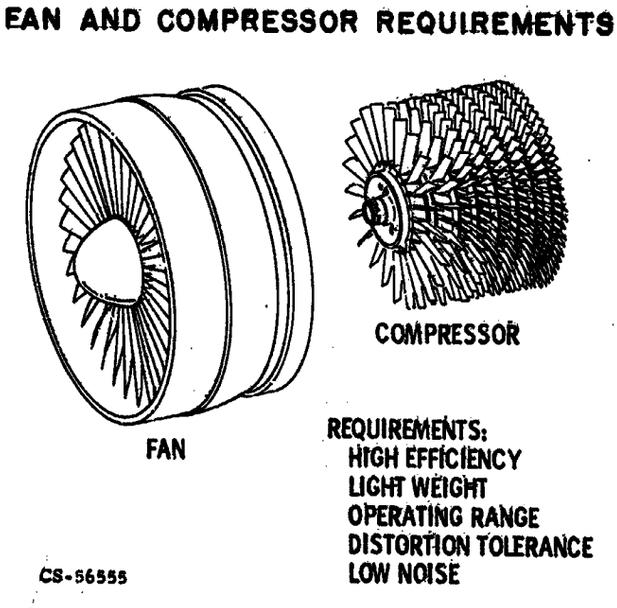

Figure I-2

CALCULATED ROTOR PRESSURE RATIO TRENDS

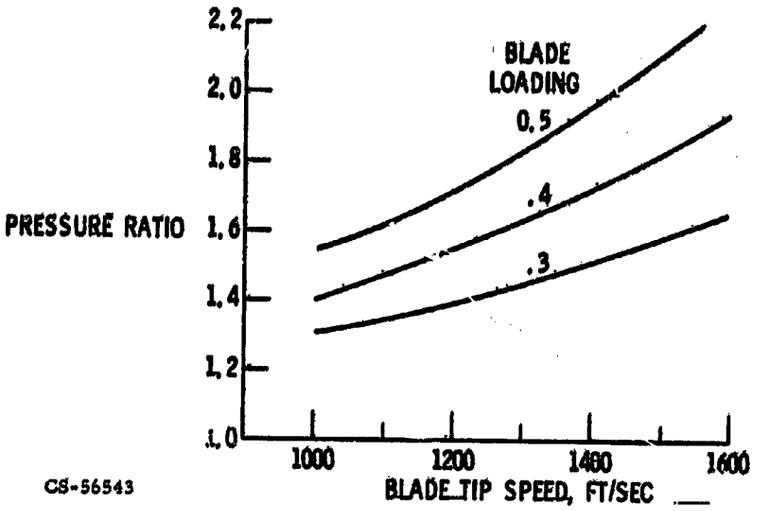

Figure 1-3

NASA COMPRESSOR TEST FACILITY

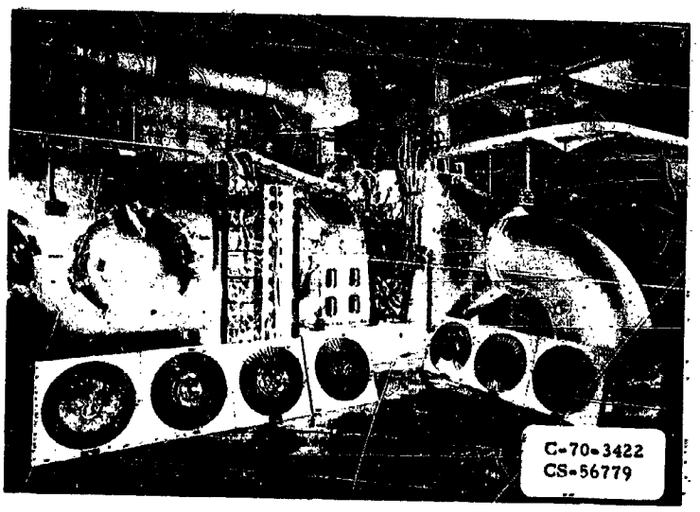

Figure 1-4

VARIOUS ROTORS TESTED UNDER NASA CONTRACTS

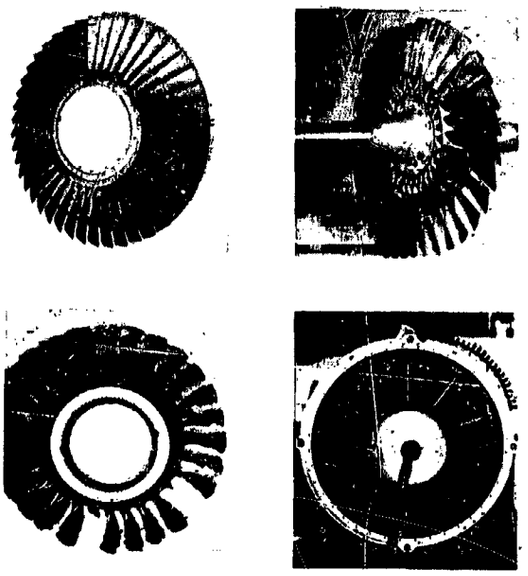

CS-56771

Figure I-5

EXPERIMENTAL TRANSONIC ROTOR PERFORMANCE

DESIGN SPEED

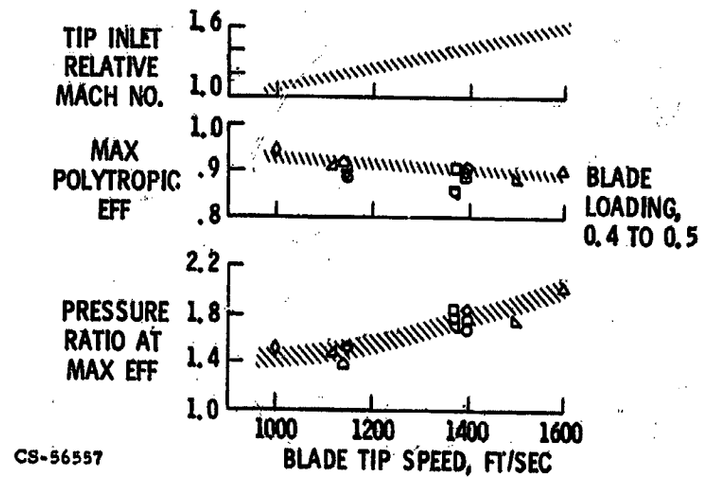

CS-56557

Figure I-6

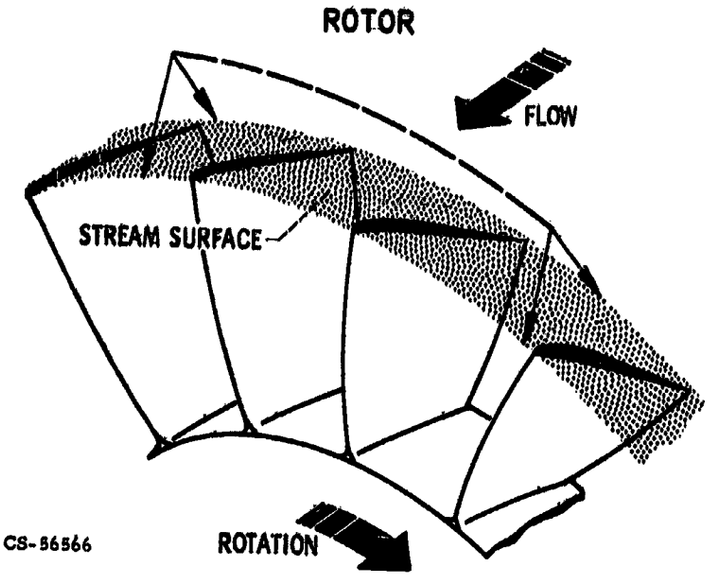

Figure I-7

STATIC PRESSURE CONTOURS AT ROTOR TIP

INLET RELATIVE MACH NO., 1.4

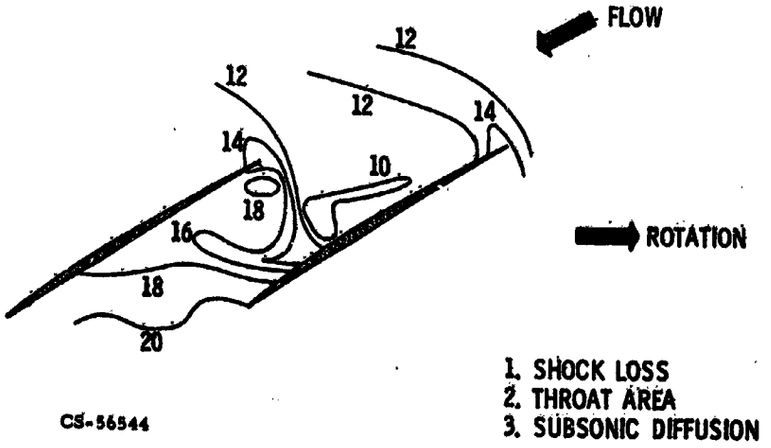

Figure I-8

EFFECT OF SHOCK LOSS AND THROAT AREA ON ROTOR PERFORMANCE

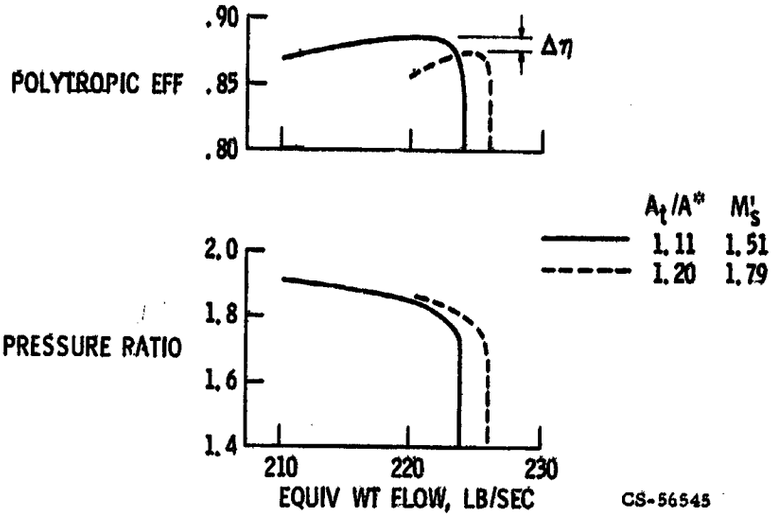

Figure I-9

EFFECT OF SUBSONIC DIFFUSION ON ROTOR PERFORMANCE

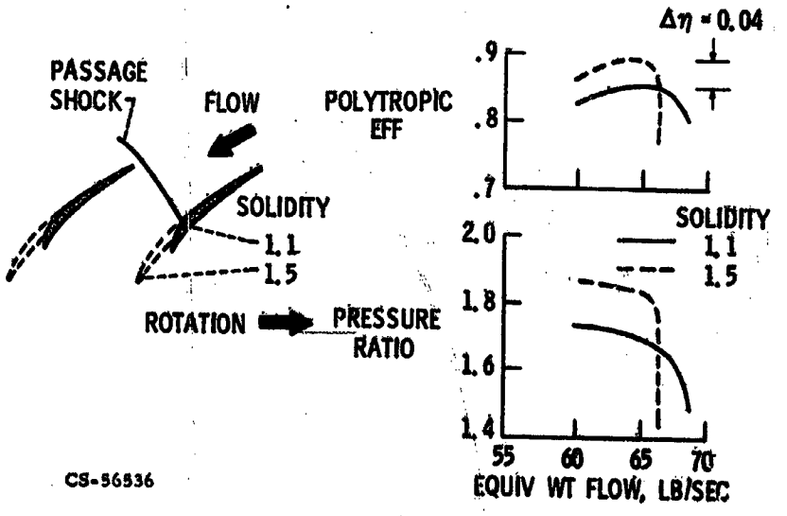

Figure I-10

EFFECT OF SOLIDITY ON ROTOR TIP LOSS

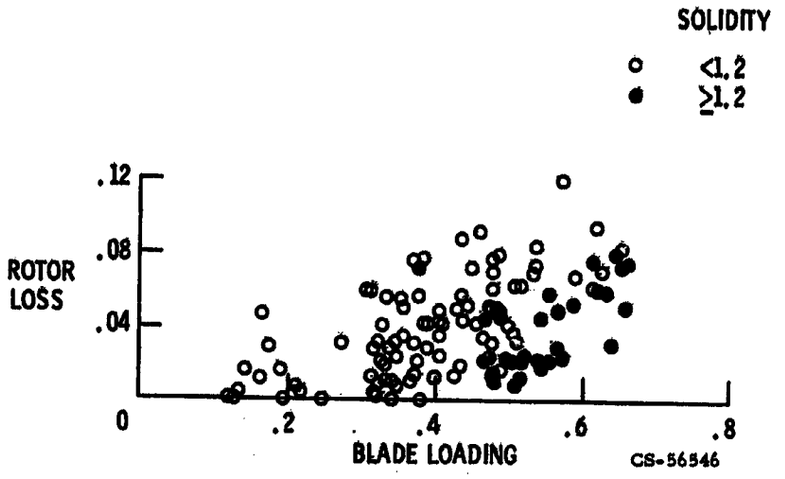

Figure I-11

COMPRESSOR STAGE

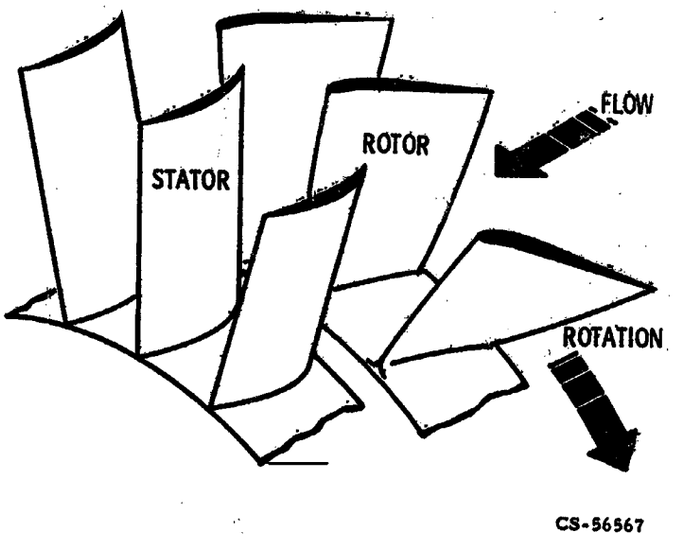

Figure I-12

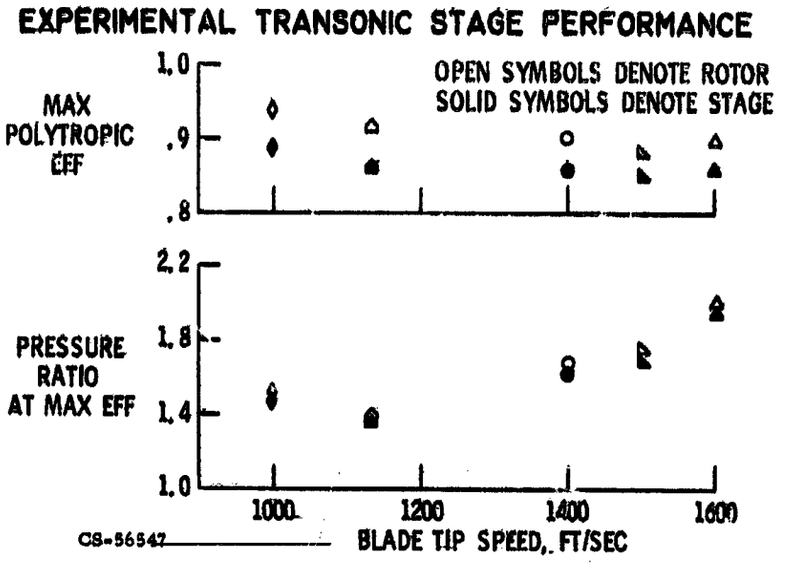

Figure I-13

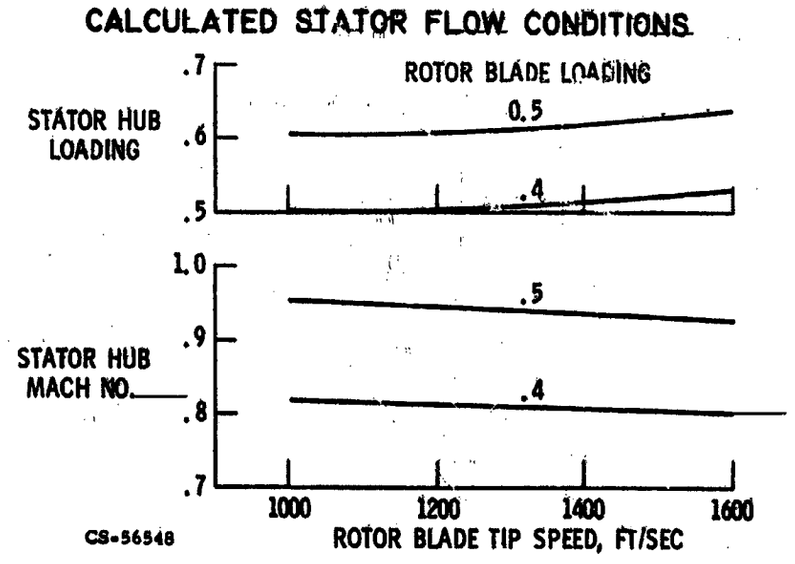

Figure I-14

AREA OF TOTAL PRESSURE SURVEYS
DOWNSTREAM OF STATORS

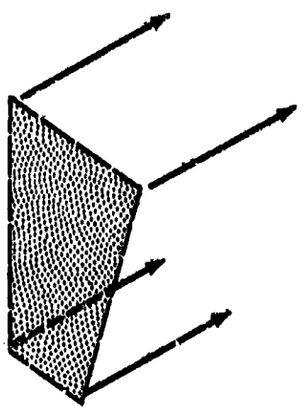

CS-96593

Figure I-15

DISTRIBUTION OF STATOR LOSS

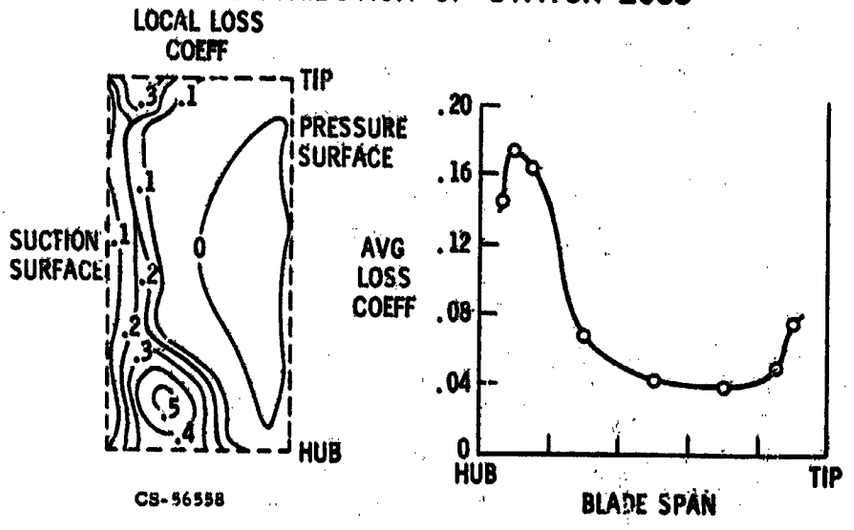

CS-96588

Figure I-16

EFFECT OF SLIT SUCTION ON STATOR LOSS

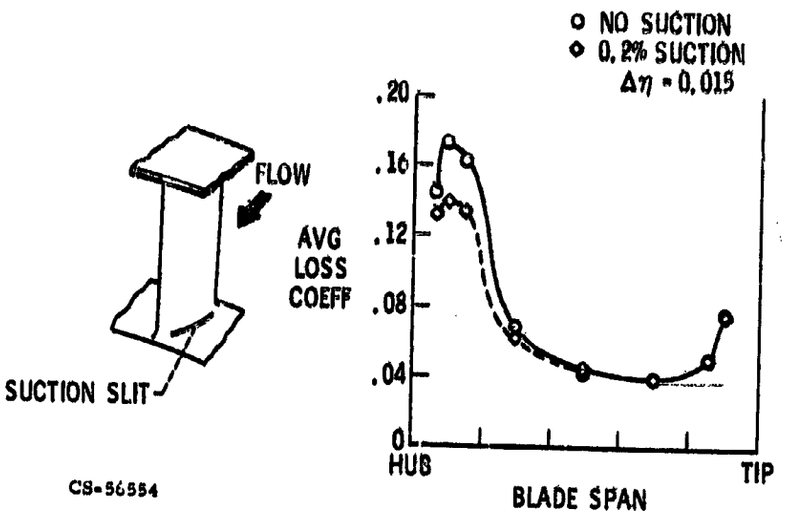

Figure I-17

CONCEPTS FOR REDUCING STATOR LOSSES

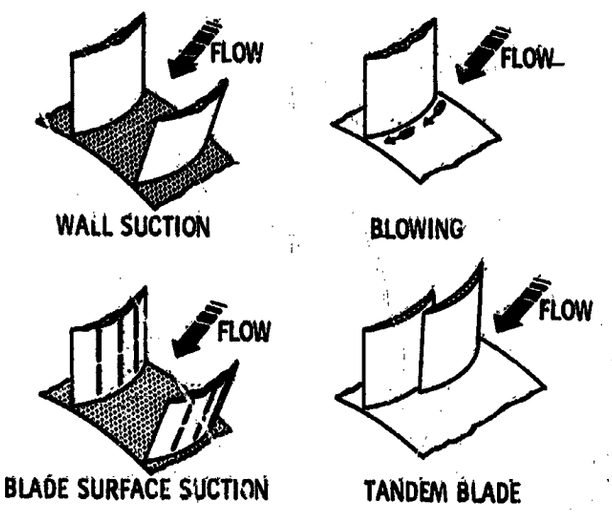

Figure I-18

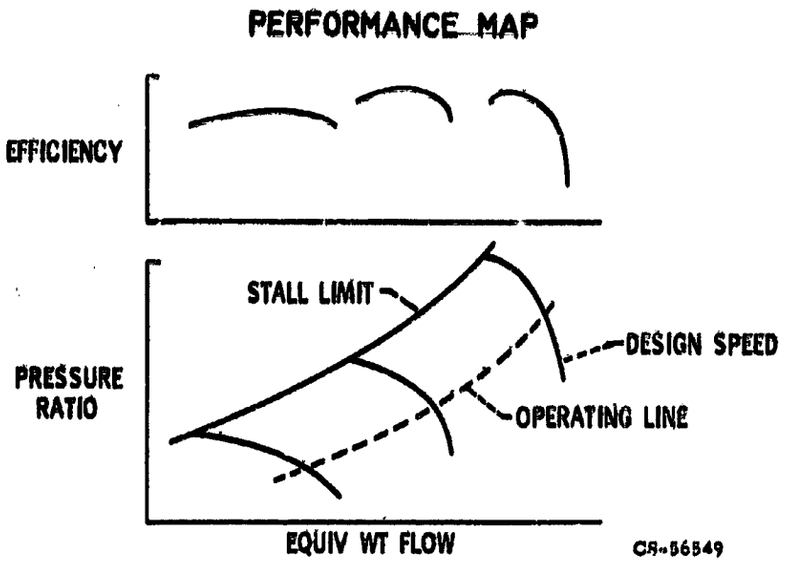

Figure I-19

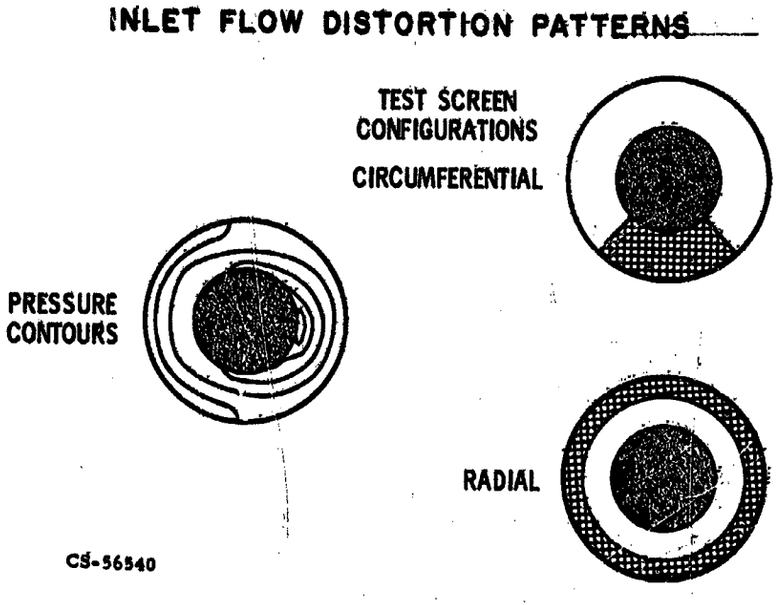

Figure I-20

EFFECT OF INLET FLOW DISTORTION ON STAGE PERFORMANCE

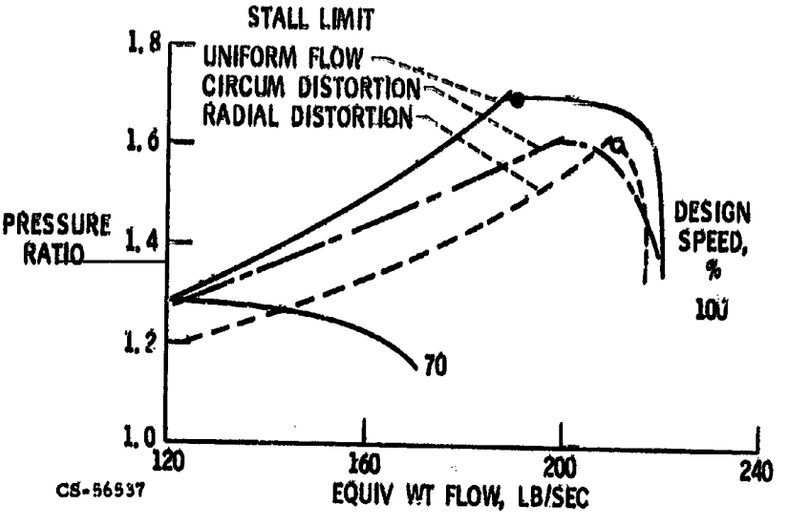

Figure I-21

RADIAL DISTRIBUTIONS OF VARIOUS PARAMETERS AT NEAR-STALL CONDITIONS

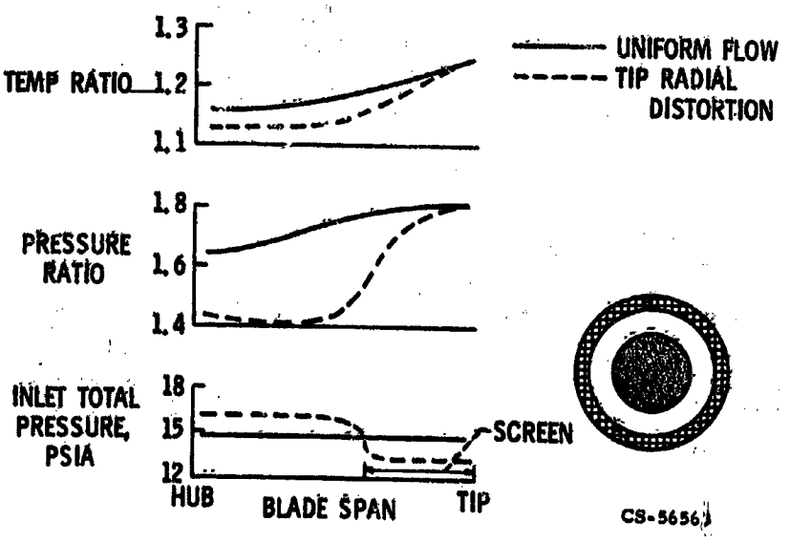

Figure I-22

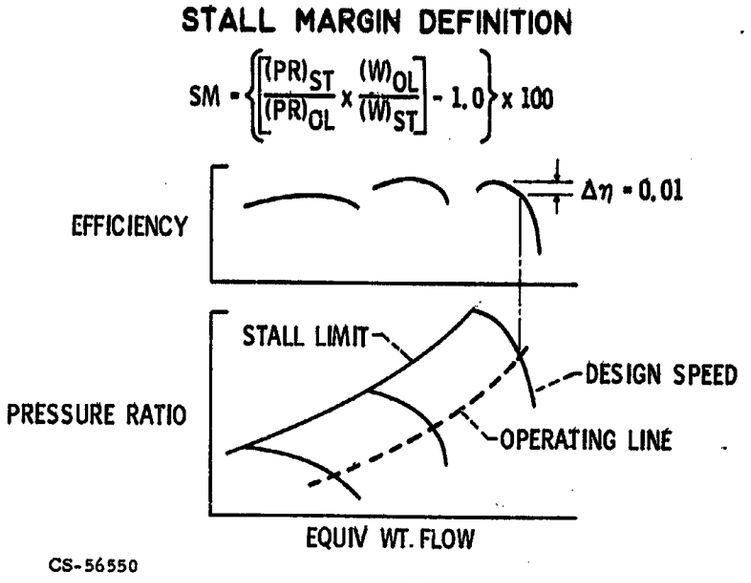

Figure I-23

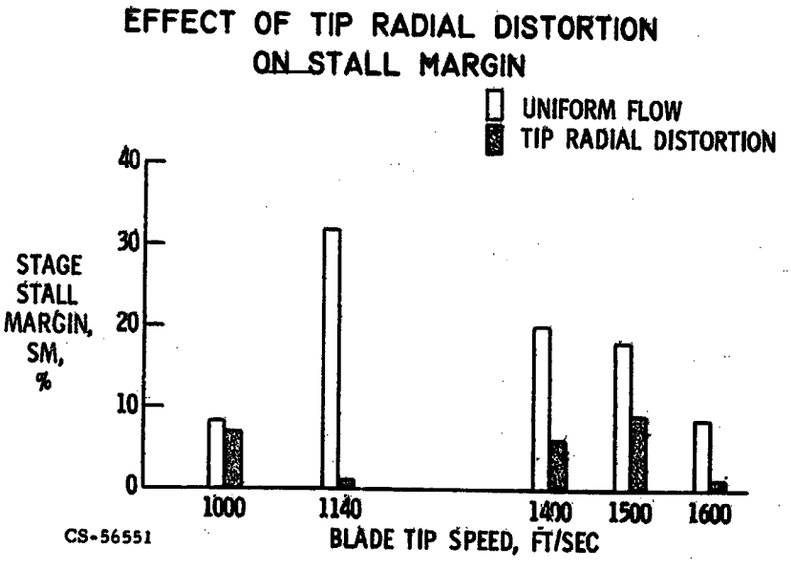

Figure I-24

EFFECT OF BLADE LOADING ON STALL MARGIN

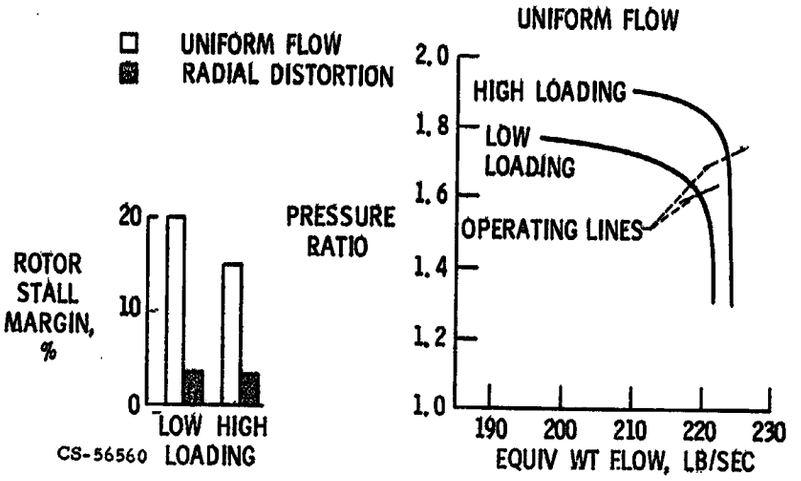

Figure I-25

MODEL OF ROTOR TIP STALL

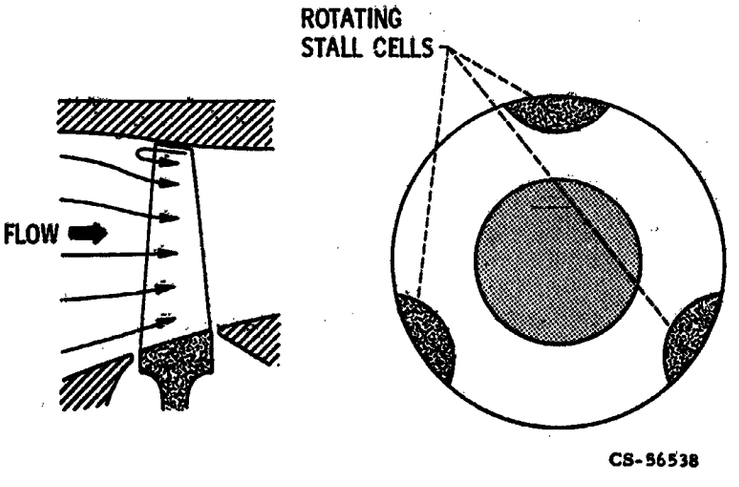

Figure I-26

HONEYCOMB CASING TREATMENT

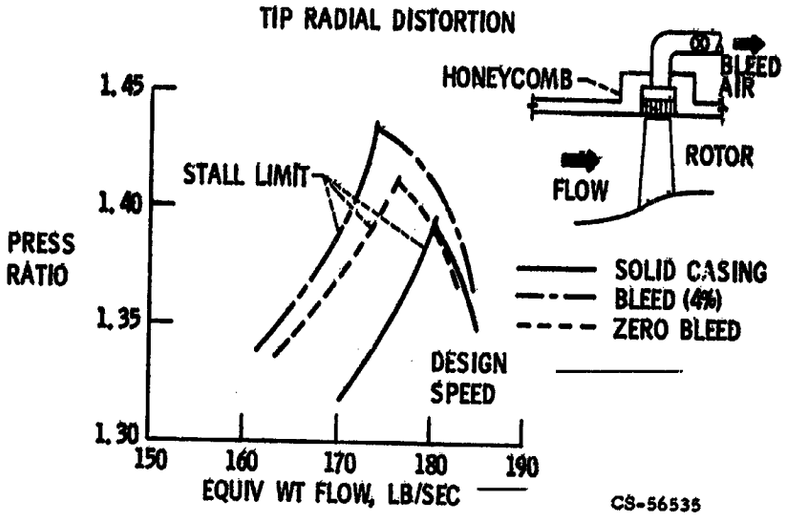

Figure I-27

VARIOUS TYPES OF CASING TREATMENT

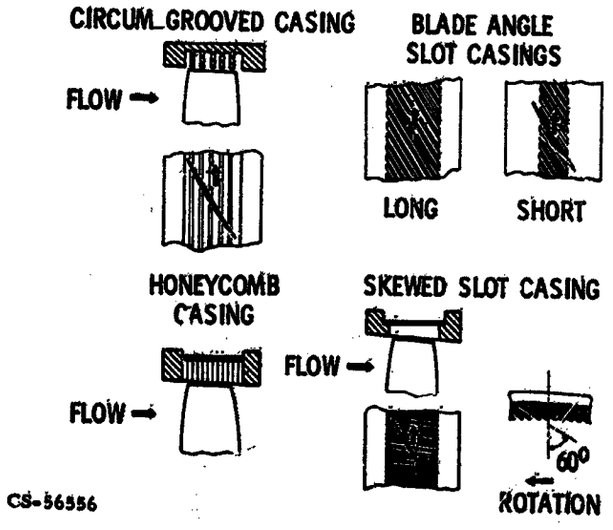

Figure I-28

STAGE PERFORMANCE WITH SOLID CASING

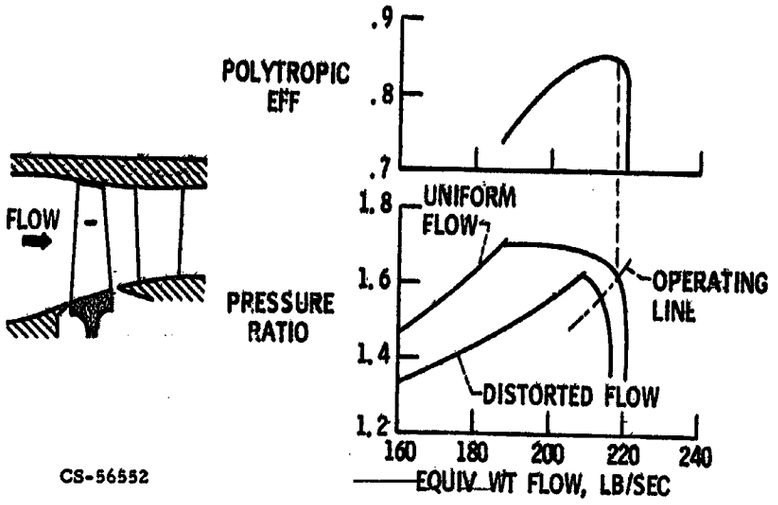

Figure I-29

STAGE PERFORMANCE WITH CASING TREATMENT AND TIP RADIAL INLET FLOW DISTORTION

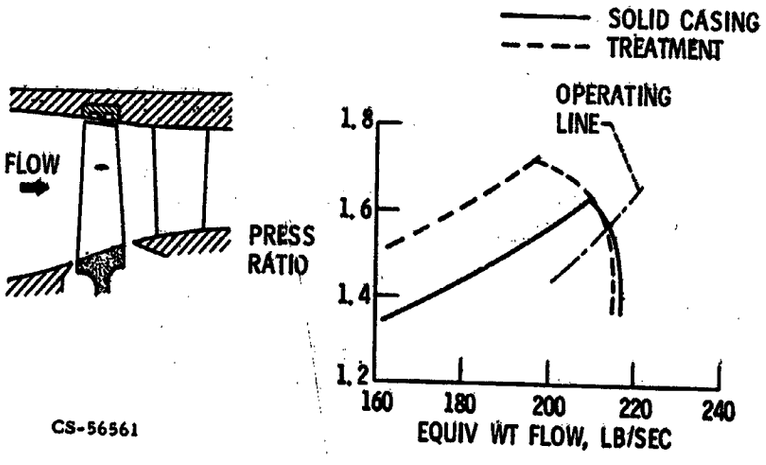

Figure I-30

EFFECT OF CASING TREATMENT ON STALL MARGIN

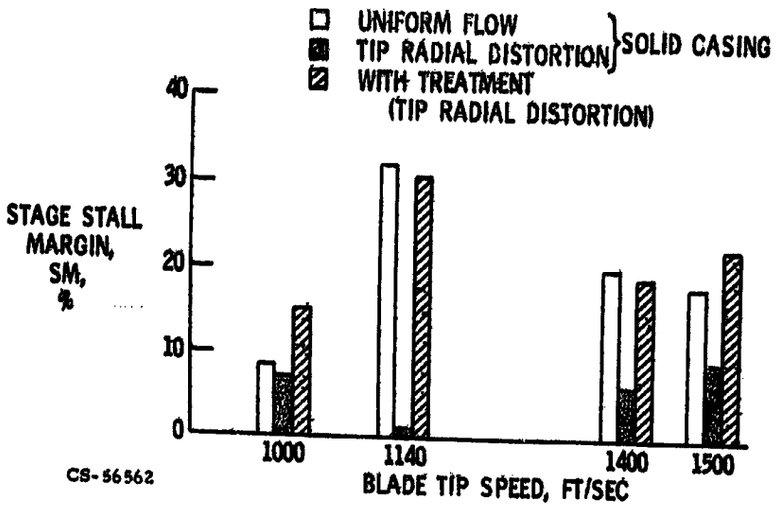

Figure I-31

STAGE PERFORMANCE WITH CASING TREATMENT AND UNIFORM FLOW

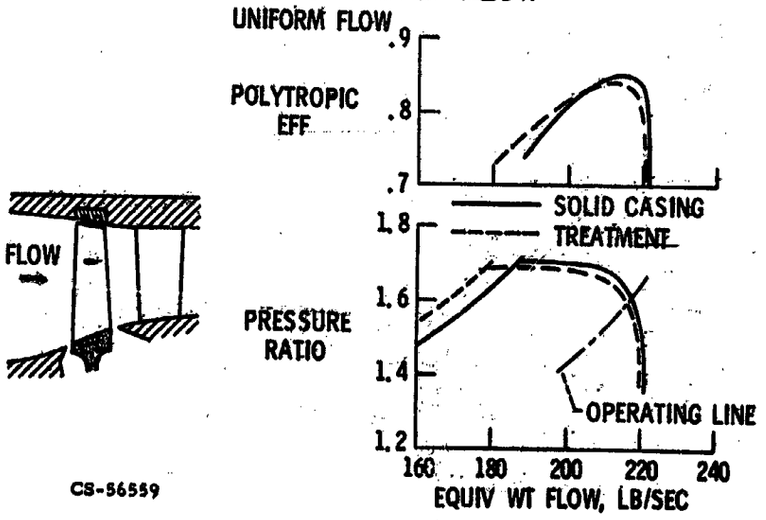

Figure I-32

ROTOR AND STATOR CASING TREATMENT

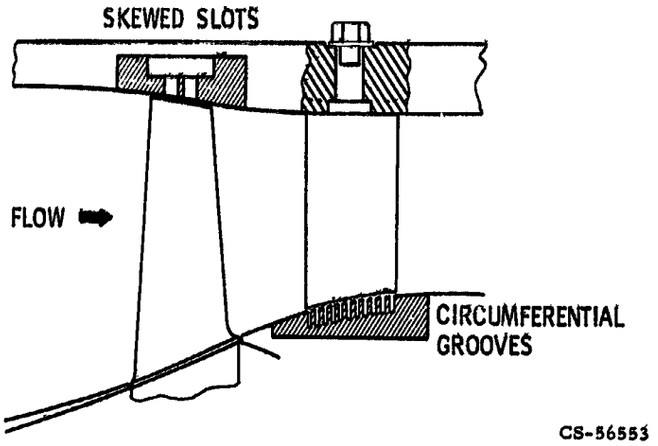

Figure I-33

MULTISTAGE COMPRESSOR

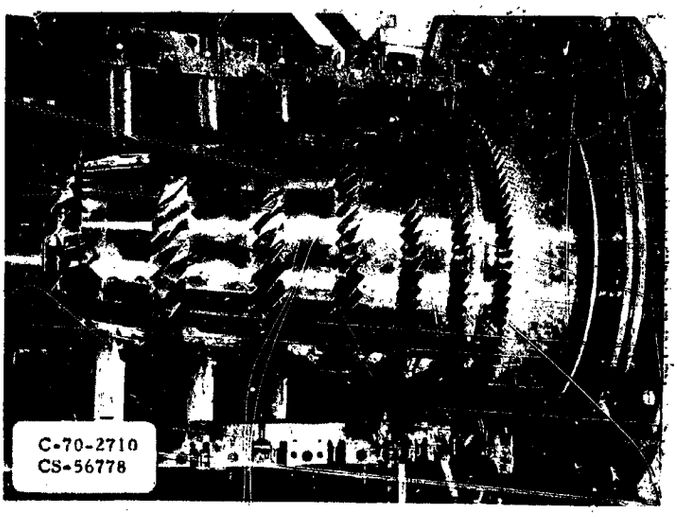

Figure I-34

II. TURBINE AERODYNAMIC CONSIDERATIONS FOR ADVANCED TURBINES

Thomas P. Moffitt, Stanley M. Nosek, and Richard J. Roelke

Advanced engines offer many interesting challenges to the turbine designer. For example, the continuing trend to higher temperature complicates the problem of effectively cooling the turbine. Another example is the trend in fan engines toward higher bypass ratios. These trends create special problems for the turbines that drive these fans. This paper briefly describes some of the turbine aerodynamic work currently under way at Lewis to study two of these problem areas.

TURBINE BLADE LOADING

The first problem area is related primarily to fan type engines and deals with turbine loading requirements. High blade loadings may be required for the following reasons:

(1) As bypass ratios increase, the diameter of the turbine to drive the fan becomes smaller. This decrease in diameter tends to increase the number of turbine stages required to extract energy from the gas, which, of course, is undesirable.

(2) Decreasing the number of stages is desirable in order to keep down the length and weight of the turbine.

(3) Reducing the number of blades per stage could also be desirable from a weight or turbine cooling consideration.

Figure II-1 shows how blade loading is related to the velocity distribution along the suction and pressure surfaces of a typical blade. As indicated, the loading is proportional to the area bounded by the two velocity distributions. One obvious way to increase the area and loading is to increase the maximum velocity on the suction surface. This increases the amount of diffusion, or flow deceleration, required on the aft portion of the suction surface from the maximum velocity to the required outlet velocity. If this diffusion is too large for a given boundary-layer condition, the flow can separate and cause high blade loss. The effect of this flow separation on blade efficiency is demonstrated in figure II-2. The blade on the left had attached

flow with a reasonably low blade loading and high efficiency. As blade loading was increased to higher values, the flow separated from the blade on the right and resulted in high losses, or low efficiency, as indicated. What is desired, then, are techniques to increase blade loading to higher values while still maintaining high efficiency.

Advanced Loading Concepts

Several blade types were screened to increase blade loading and included plain blades, tandem blades, jet-flap blades, tangential slots, and blades with vortex generators (refs. 1 to 5). Of those investigated, two that appeared promising and were pursued were the tandem and the jet-flap blades (fig. II-3).

As indicated, the tandem blade requires only one gas stream, whereas the jet-flap blade requires a secondary source of gas that might already be required for turbine cooling. The use of this type for both cooling and high loading depends largely on whether or not the coolant would have enough momentum left after internal cooling to be effective as a jet flap. The descriptions, test procedures, and results for both the tandem and jet-flap blades are found in the references. However, this paper concerns only the tandem blade, since the general results are typical of those obtained from the jet-flap blade also. The concept of the tandem blade is this. The flow initially accelerates on the forward foil, with a corresponding boundary-layer growth. Before the large diffusion to the outlet condition, the blade is cut off and the diffusion is allowed to take place on a second, or rear, foil which starts with a clean boundary layer. The concept, then, is to have the diffusion take place on a relatively thin boundary layer in an attempt to cause the flow to remain attached. The effectiveness of this concept is demonstrated in figure II-4. This figure shows wake traces of total pressure taken behind a tandem and a plain blade in cascade tests for the same test conditions. As shown for the tandem blade on the left, the wake from the forward foil persisted to the exit of the blade. The deficit in area as shown by the depth and width of these traces is a measurement of the losses on the blade, and as can be seen from the figure, the deficit in area for the plain blade appears to be larger than the combined wakes from the tandem blade. As a matter of fact, the losses from the tandem blade were determined to be about one-half those of the plain blade.

Initial Tandem Rotor

The initial tandem rotor tested is shown in figure II-5. This turbine stage had a tip diameter of 30 inches. The number of blades in this rotor is comparable to that in a typical plain blade turbine. It is labeled as a "high solidity" rotor to distinguish it from a rotor that is shown later with a low solidity. A large amount of diffusion was imposed across the hub of this blade by requiring that the outlet velocity at the hub be less than the inlet velocity. This reduction in velocity across the blade row is called "negative reaction" and is discussed later. The performance of this rotor in terms of turbine efficiency is shown in figure II-6. As indicated, the efficiency of the turbine remained at a relatively high level over the range of pressure ratios tested. The design pressure ratio was 2.1, and the corresponding efficiency was about 90 percent.

Low Solidity Tandem Rotor

With the concept of the tandem blade demonstrated by the initial cascade and rotor tests, a second tandem rotor was designed with considerably higher blade loading. A photograph of this rotor compared to the rotor just described is shown in figure II-7. It can be seen that the mechanism used to increase blade loading was solidity. That is, there are both fewer blades and shorter chord lengths for the low solidity rotor compared to the high solidity rotor. Both rotors were designed to produce the same power for the same weight flow and imposed pressure drop across the turbine. The performance of this rotor compared to the high solidity rotor is shown in figure II-8.

It is apparent from this comparison that the efficiency dropped considerably for the low solidity rotor, especially at the higher pressure ratios. At the low pressure ratio tested, 1.6, the efficiencies of the two turbines were about equal. However, at the design pressure ratio of 2.1 there was a decrease in efficiency of about 4 points. This decrease became larger as pressure ratios increased. It appears from these results, then, that there is a Mach number effect on performance of this turbine. That is, as pressure ratio and Mach number increased to higher values, the losses became considerably higher. This can be partially explained by going back to the blade loading description of figure II-1. Because of the low solidity and high loading, the maximum velocity on the suction surface was above sonic. Apparently the interaction of the local shocks with the diffusing condition resulted in high local losses and possibly flow separation.

Application of Tandem Blades

The evidence indicates, then, that the tandem blade may be a useful device to control large amounts of diffusion efficiently provided that the maximum surface velocity is subsonic. This would be especially true in the case of a negative reaction blade row, where the outlet velocity would be lower than the inlet velocity, which then would require even more diffusion. This is shown in figure II-9. This theoretical velocity distribution shows an imposed outlet velocity less than the inlet velocity, or a condition of negative reaction. Also, the maximum velocity is less than sonic. This could be an application, then, where a tandem blade could be considered as a useful device to control large amounts of diffusion efficiently.

Such an application could be made to a high bypass-ratio fan drive turbine. Figure II-10 is a schematic of a three-stage turbine designed for a fan drive that is characterized by low blade speeds, low Mach numbers, and negative reaction conditions across the hub region of the last stage. This is an example, then, where a tandem blade design could be applied.

TURBINE COOLING AERODYNAMICS

The second area to be discussed deals with the aerodynamics of turbine cooling. To design cooled turbines properly, it is necessary to account for the effect that the proposed coolant will have on turbine efficiency. It was felt that the effect of the coolant is mostly a function of the location and direction of the coolant ejection and the energy level of the coolant flow.

Blade Types Tested

In view of this, two extreme cases were investigated with respect to coolant ejection types. The blade types tested are shown in figure II-11. They are the slotted trailing edge on the left and two types of porous skin blades on the right. They all have the same blade profile as the solid uncooled stator blade shown at the top of the figure. The detailed description and test results can be found in references 6 to 14.

The trailing edge slot blades ejected all the coolant through a slot in the trailing edge in a direction generally the same as the adjacent primary air. The two types of porous skin blades tested, the discrete holes and the wire mesh, ejected air

around the entire periphery of the blading and in a direction generally normal to the adjacent airstream. A number of qualifying statements ought to be made now. First, the relative performance of the blades was determined by measuring and comparing the total-pressure losses at the exit of the blades. It was felt that temperature ratio would have only a small effect on these measurements. Therefore, all tests were conducted with cold air, with no attempt to match any temperature ratio between the coolant and primary air. Second, the blades were made as simple as possible, with no internal pressure drop devices installed to simulate that which might be encountered in an actual cooled blade. For example, in the blade on the left, the trailing edge slot, required very little pressure drop to eject the coolant out the trailing edge. On the other hand, the porous skin types on the right required a considerable pressure drop on the coolant side to eject the coolant through the porous skin. The effect of some of these differences is discussed later.

A photograph of the three blades tested is shown as figure II-12. The blade on the left had a slot extending along the entire length of the trailing edge. The discrete hole blade was self-supporting and the variation in flow around the blade was controlled by varying the porosity of the holes around the surface. The wire mesh blade was made by wrapping and welding a wire mesh around internal struts. The electron beam welds between the mesh and the internal strut can be seen in the figure. The distribution of the coolant around the periphery of this blade was controlled by the size of the metering holes in the orifice plate that can be seen at the top of the blade.

Stator Surveys

Figure II-13 shows one type of blade (the wire mesh blade) installed in a complete stator assembly. Annular surveys of total-pressure loss were made behind each of the stator blade rows. A comparison of the wake traces made at the mean section behind the various blades is shown in figure II-14. The wake traces are shown as a drop in total pressure as a percent of inlet total pressure for coolant flows up to 7 percent. Again, the deficit in area shown by the wake is an indication of blade losses. The blip for 7 percent coolant on the left (negative value of pressure drop) means that the total pressure of the ejected coolant was higher than the inlet total pressure of the primary air. It was higher because the only way to vary the coolant flow rate for a fixed slot size was to vary the cavity pressure of the coolant within the blade.

Both wakes show a 0 percent coolant trace taken when the coolant was turned off. Of particular interest is a comparison of what happens to the width of this wake as

coolant is added. As can be noted on the left for the trailing edge slot, the coolant filled in the wake from the trailing edge of the blade. However, its effect did not extend outward into the region of the primary flow. This was not the case for the porous skin type. As flow was added, there was a large buildup of boundary layer on the suction side that extended this boundary layer considerably into the free stream area. A comparison of the efficiencies determined by the full annular surveys taken behind the various blades is shown in figure II-15. The stator efficiency indicated is a measurement of the total kinetic energies of both flows involved, compared to the total ideal energies of both flows involved. An obvious difference exists in the level of efficiencies experienced by both the porous skin blades when compared to the trailing edge slot. The efficiency of the trailing edge slot varied very little from its value at zero flow and is close to the 97-percent efficiency of the solid blades tested. The porous skin types, on the other hand, decreased in efficiency continuously as coolant flow was added. As an example, at 6 percent coolant flow the efficiency of the porous skin blades decreased about 10 points. The reason that the efficiencies of the porous skin blades were lower at zero flow is that a small amount of primary air "leaked through" the blades when the coolant was turned off and caused a small drop in efficiency. This leaking condition did not exist at coolant flow rates above 2 percent.

Stage Performance Tests

The solid rotor used to determine stage performance of all three stator configurations is 30 inches in diameter and the blades are 4 inches long (fig. II-16). A comparison of the resulting stage efficiencies for the various turbines is shown in figure II-17. As expected, this comparison of stage efficiency is similar in trend to the comparison of the stator efficiencies shown previously. The thermodynamic efficiency of the turbine with trailing edge slots remained very close to that of the uncooled turbine with solid blades, which had an efficiency of 92 percent. The porous skin turbines had efficiencies of about 90 percent at zero coolant flow and decreased to about 86 percent at 4 percent coolant flow and about 81 percent at 7 percent coolant flow.

Partially Blocked Porous Skin

It should be restated that the results presented have been for blades purposely selected to represent two extremes in terms of location and direction of coolant

ejection. Returning to the sketch of the blades tested (fig. II-11) it is recognized that literally hundreds of various cooling schemes could fall somewhere between these two extremes. For example, the trailing edge slot blade tested on the left had a relatively small pressure drop required to eject the coolant. For an actual blade, of course, the particular internal flow passages would decrease the energy level of the coolant as it is ejected from the slot. Also, practical considerations should be made for porous skin blades. For example, it may be desirable selectively to block off various portions of the blade. To demonstrate this blocking, the wire mesh blades were retested with the back two-thirds portion of the suction surface sealed. All the coolant, then, was ejected from the forward one-third of the suction surface and the entire length of the pressure surface.

A comparison of the total-pressure wake traces for this test is made in figure II-18. A considerable difference in the pattern of the wake traces can be noted. For the full ejection case on the left, there was the large buildup of boundary layer on the suction side referred to earlier. For the partially blocked blade on the right, the thickness of the boundary layer on the suction surface became substantially less, and, of course, because a larger portion of the air was ejected out the pressure surface, the boundary layer on the pressure side became substantially greater. Therefore, if the general width and depth of the two boundary layers are compared, the partially blocked blade on the right should have a higher performance. This is true as shown in figure II-19, where stator efficiency is presented as a function of coolant flow for the two blades. To calculate efficiency, both blades were charged with the same coolant pressure drop to eject a given amount of coolant flow. As indicated, a small improvement in efficiency resulted.

SUMMARY

In summary, concepts to increase blade loading may be useful tools to control large amounts of diffusion efficiently, provided that the maximum local surface velocities are subsonic. One indicated area of application could be high bypass ratio fan drive turbines, where the required low blade speed results in a generally low level of Mach number throughout the turbine.

For turbine cooling, the effect of the coolant on turbine efficiency has been shown to be a function of the location and direction of the coolant ejection and the energy level of the coolant. Although the blades tested were not designed for actual cooling, the results indicate that the aerodynamic penalty can be significant and should be considered when evaluating a given cooling application. Some of the actual turbine coolant considerations are discussed in the paper by Ellerbrock and Cochran.

REFERENCES

1. Lueders, H. G.; and Roelke, R. J.: Some Experimental Results of Two Concepts Designed to Increase Turbine Blade Loading. Paper 69-WA/GT-1, ASME, Nov. 1969.

2. Bettner, James L.; and Nosek, Stanley M.: Summary of Tests on Two Highly Loaded Turbine Blade Concepts in Three-Dimensional Cascade Sector. Paper 69-WA/GT-5, ASME, Nov. 1969.

3. Nosek, Stanley M.; and Kline, John F.: Two-Dimensional Cascade Investigation of a Turbine Tandem Blade Design. NASA TM X-1836, 1969.

4. Lueders, H. G.: Experimental Investigation of Advanced Concepts to Increase Turbine Blade Loading. VI - Performance Evaluation of Modified Tandem Rotor Blade. NASA CR-1616, 1970.

5. Lueders, H. G.: Experimental Investigation of Advanced Concepts to Increase Turbine Blade Loading. VII - Performance Evaluation of Modified Jet-Flap Rotor Blade. NASA CR-1759, 1971.

6. Whitney, Warren J.; Szanca, Edward M.; Moffitt, Thomas P.; and Monroe, Daniel E.: Cold-Air Investigation of a Turbine for High-Temperature - Engine Application. I - Turbine Design and Overall Stator Performance. NASA TN D-3751, 1967.

7. Prust, Herman W., Jr.; Schum, Harold J.; and Behning, Frank P.: Cold-Air Investigation of a Turbine for High-Temperature Engine Application. II - Detailed Analytical and Experimental Investigation of Stator Performance. NASA TN D-4418, 1968.

8. Whitney, Warren J.; Szanca, Edward M.; Bider, Bernard; and Monroe, Daniel E.: Cold-Air Investigation of a Turbine for High-Temperature-Engine Application. III - Overall Stage Performance. NASA TN D-4389, 1968.

9. Whitney, Warren J.; Szanca, Edward M.; and Behning, Frank P.: Cold-Air Investigation of a Turbine With Stator-Blade Trailing-Edge Coolant Ejection. I - Overall Stator Performance. NASA TM X-1901, 1969.

10. Prust, Herman W., Jr.; Behning, Frank P.; and Bider, Bernard: Cold-Air Investigation of a Turbine With Stator-Blade Trailing-Edge Coolant Ejection. II - Detailed Stator Performance. NASA TM X-1963, 1970.

11. Szanca, Edward M.; Schum, Harold J.; and Prust, Herman W., Jr.: Cold-Air Investigation of a Turbine With Stator-Blade Trailing-Edge Coolant Ejection. III - Overall Stage Performance. NASA TM X-1974, 1970.

12. Prust, Herman W., Jr.; Schum, Harold J.; and Szanca, Edward M.: Cold-Air Investigation of a Turbine With Transpiration-Cooled Stator Blades. I - Performance of Stator With Discrete Hole Blading. NASA TM X-2094, 1970.

13. Szanca, Edward M.; Schum, Harold J.; and Behning, Frank P.: Cold-Air Investigation of a Turbine With Transpiration-Cooled Stator Blades. II - Stage Performance With Discrete Hole Stator Blades. NASA TM X-2133, 1970.

14. Behning, Frank P.; Prust, Herman W., Jr.; and Moffitt, Thomas P.: Cold-Air Investigation of a Turbine With Transpiration-Cooled Stator Blades. III - Performance of Stator With Wire-Mesh Shell Blading. NASA TM X-2166, 1971.

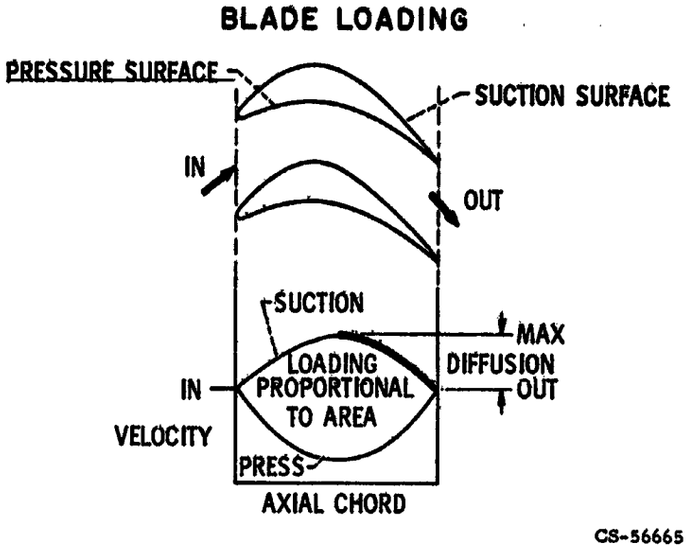

Figure II-1

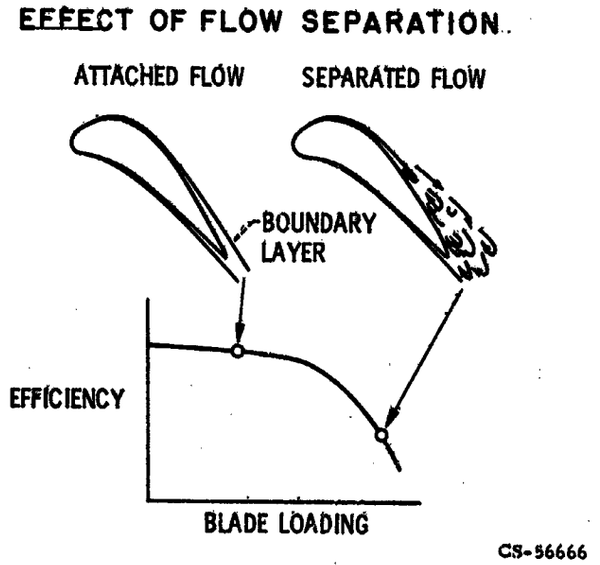

Figure II-2

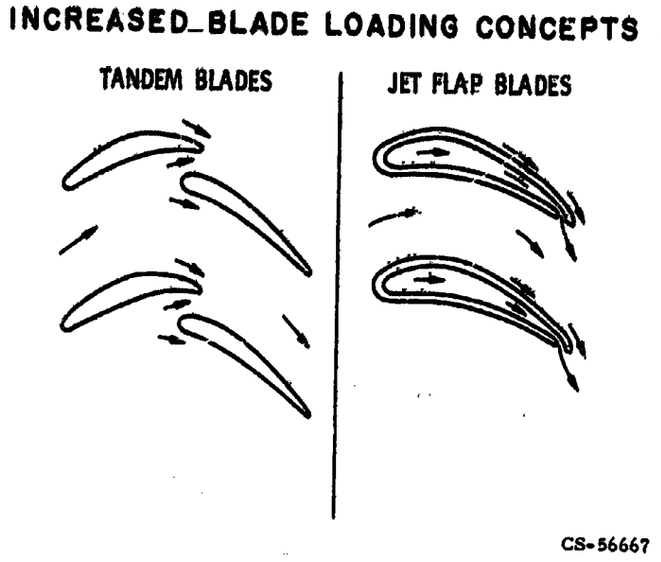

Figure II-3

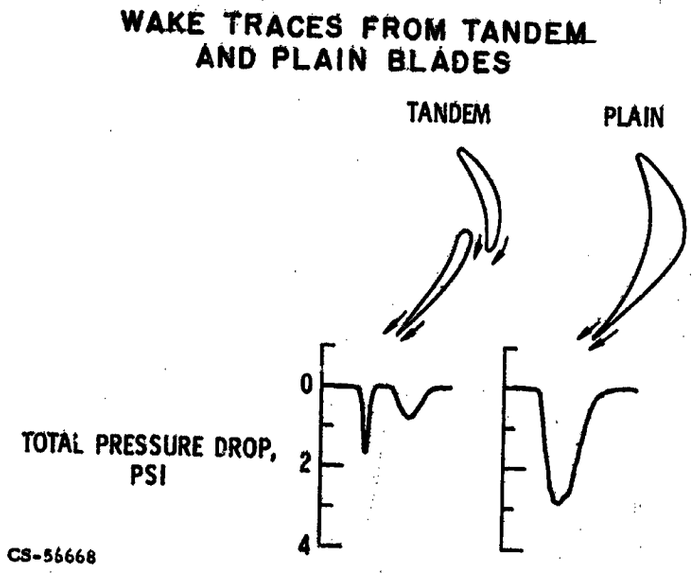

Figure II-4

TANDEM ROTOR
HIGH SOLIDITY

Figure II-5

TANDEM ROTOR TURBINE EFFICIENCY

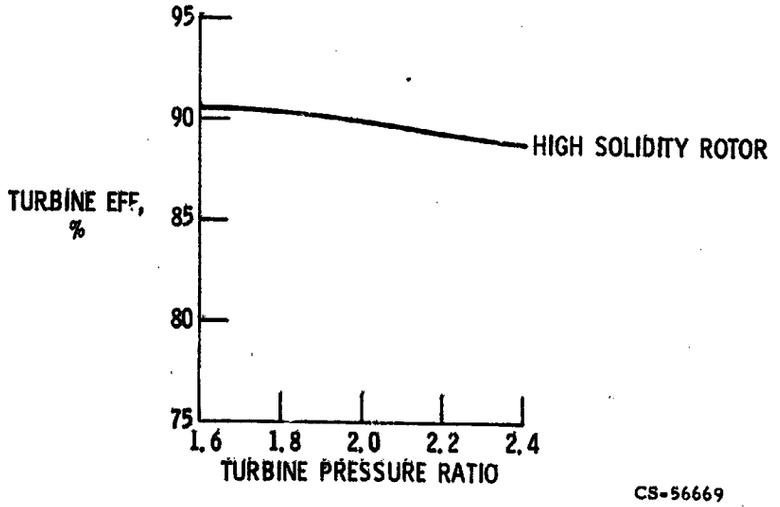

Figure II-6

TANDEM ROTORS

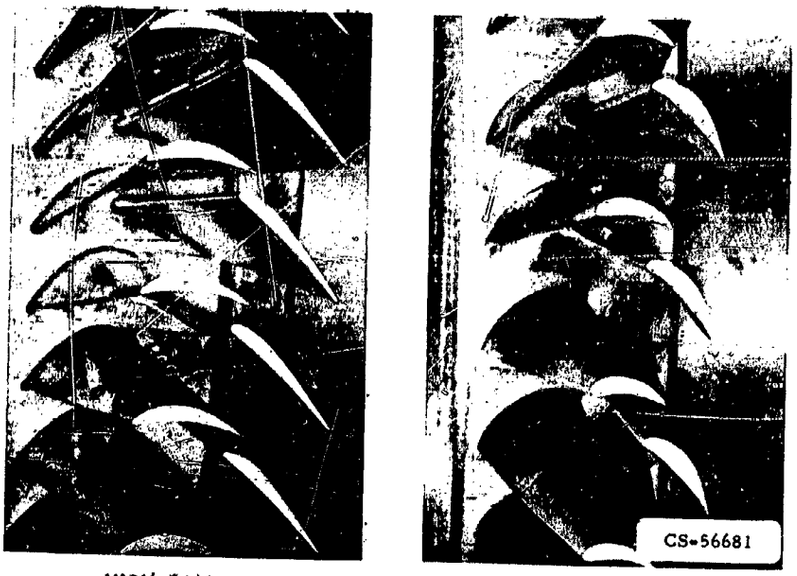

HIGH SOLIDITY

LOW SOLIDITY

Figure II-7

TANDEM ROTOR TURBINE EFFICIENCY

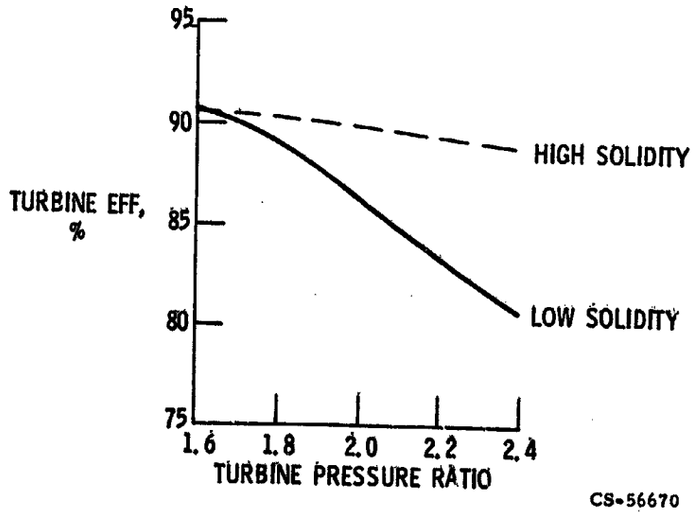

Figure II-8

SURFACE DIFFUSION FOR NEGATIVE REACTION BLADES

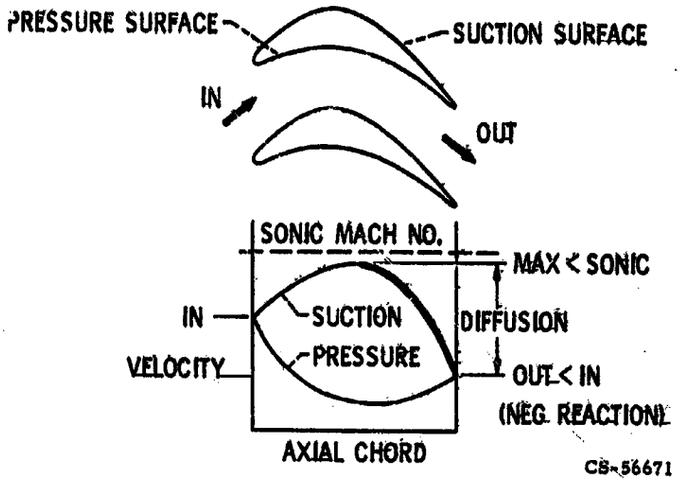

Figure II-9

APPLICATION OF TANDEM ROTOR BLADES

THREE-STAGE FAN DRIVE RESEARCH TURBINE

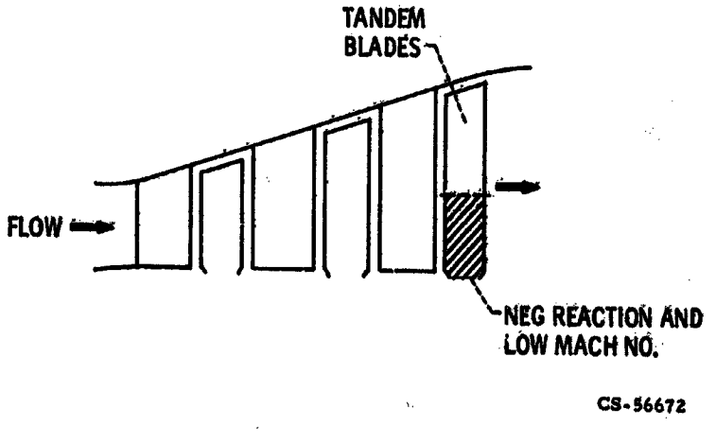

Figure II-10

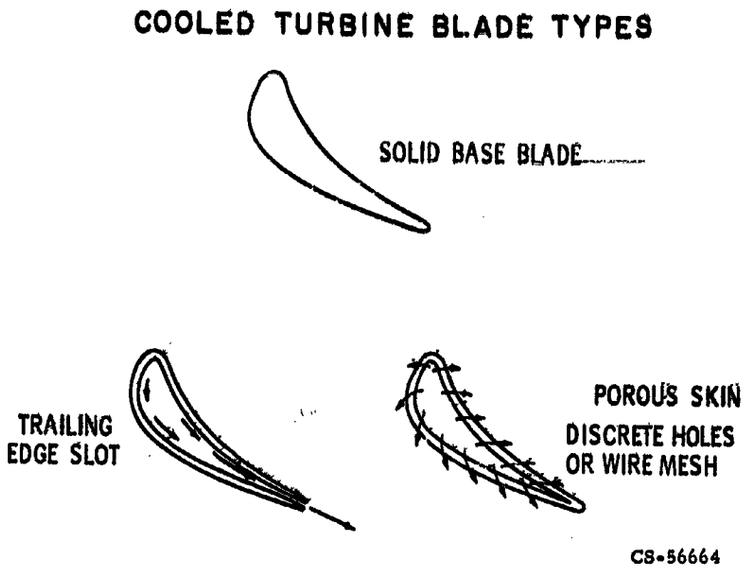

Figure II-11

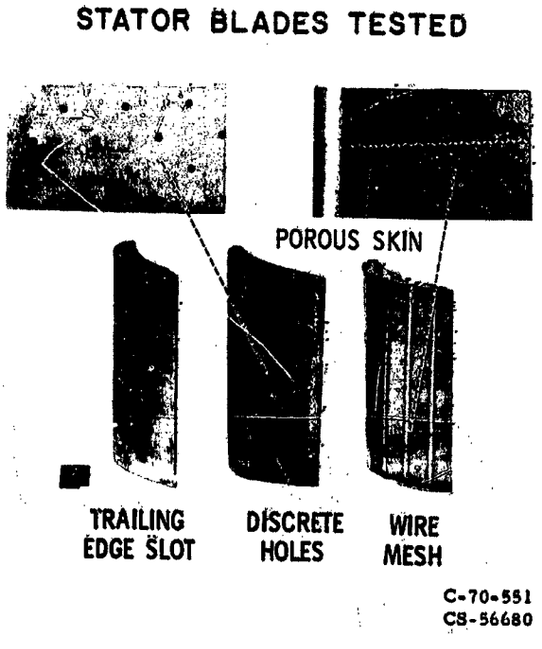

Figure II-12

ASSEMBLED WIRE MESH STATORS

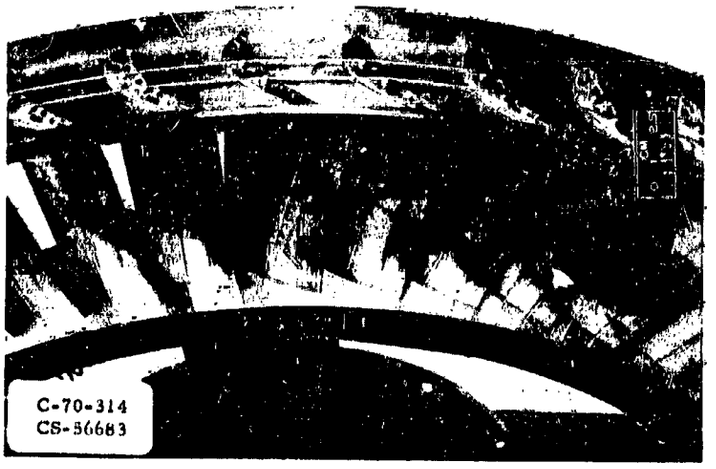

Figure II-13

STATOR WAKE TRACES

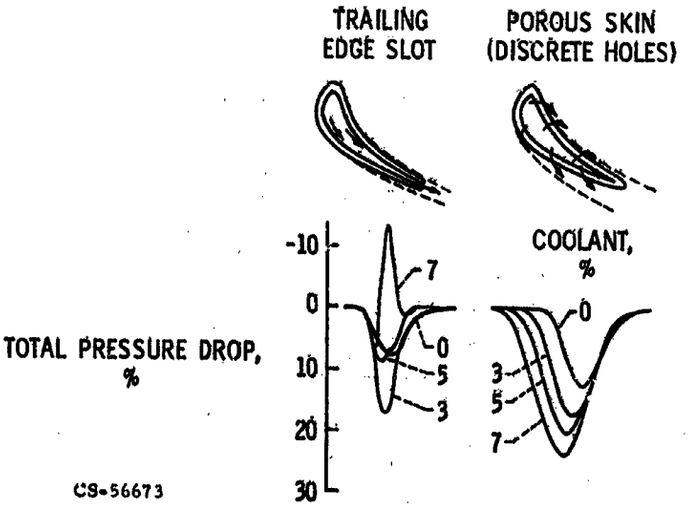

Figure II-14

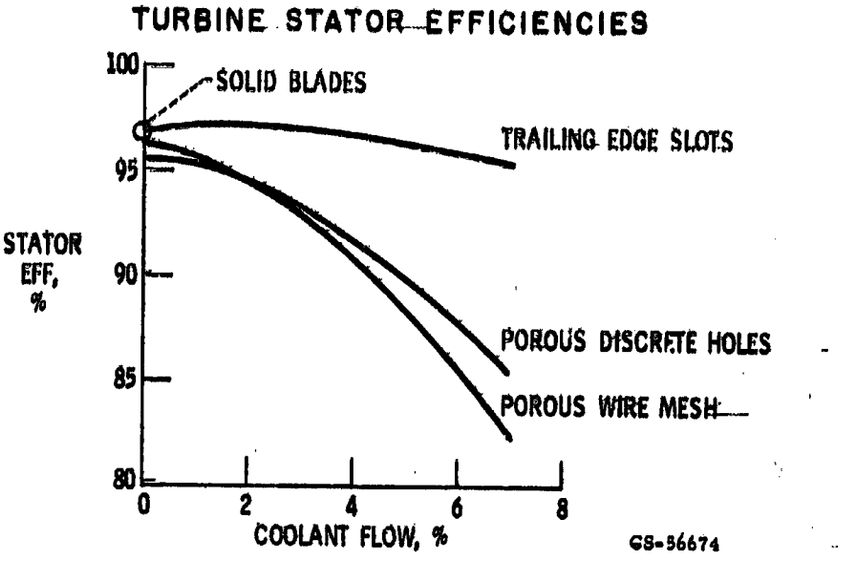

Figure II-15

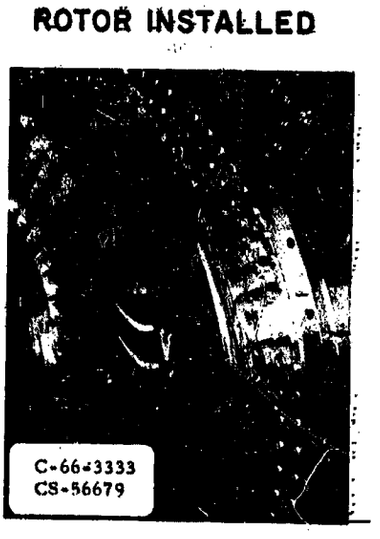

Figure II-16

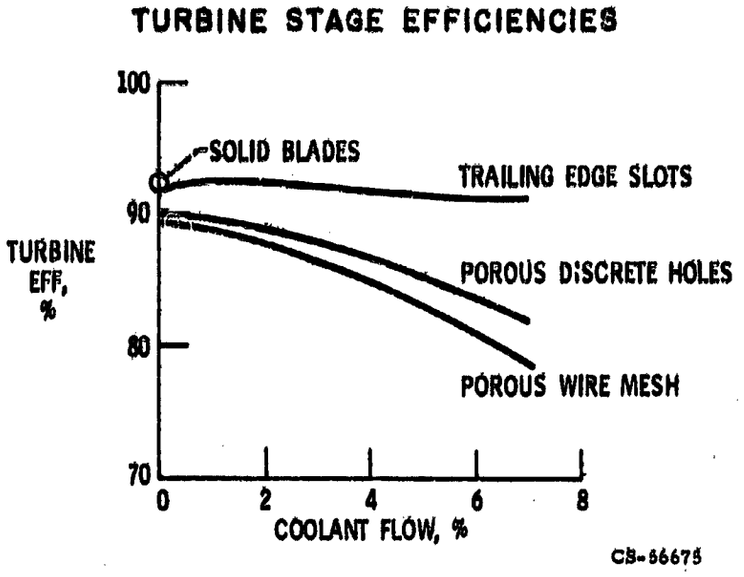

Figure II-17

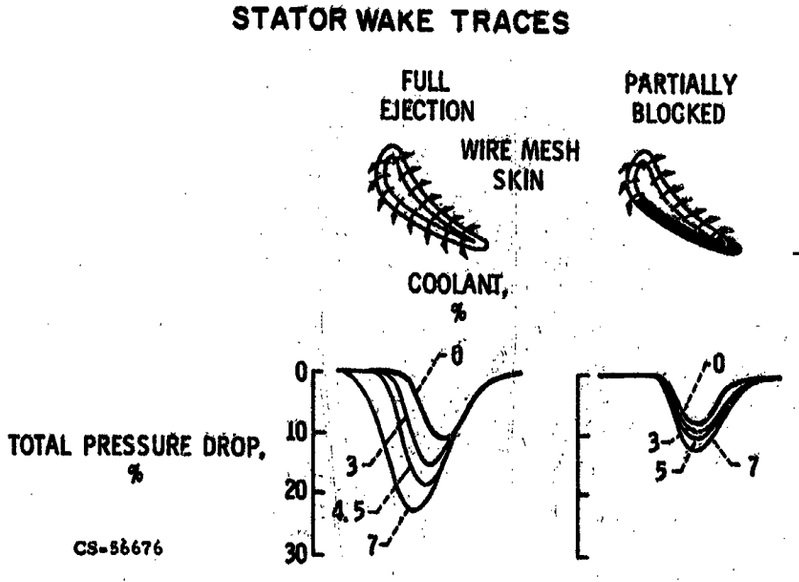

Figure II-18

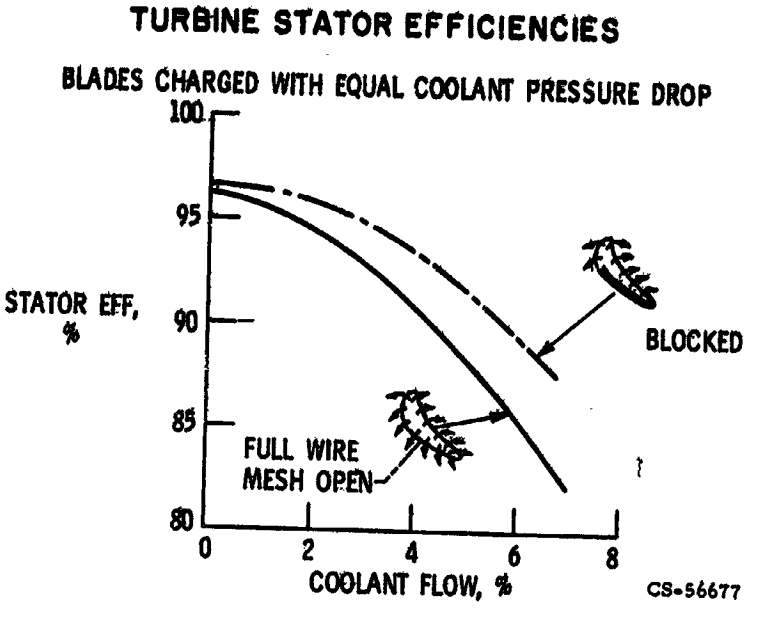
TURBINE STATOR EFFICIENCIES
BLADES CHARGED WITH EQUAL COOLANT PRESSURE DROP
100
95
90
85
80
STATOR EFF, %
BLOCKED
FULL WIRE MESH OPEN
0
2
4
6
8
COOLANT FLOW, %
CS-56677

Figure II-19

III. TURBINE COOLING RESEARCH

Herman H. Ellerbrock and Reeves P. Cochran

The trend in both military and commercial aircraft gas turbine engines is toward turbofan engines having a compact, high-temperature, high-pressure gas generator or "core." As the turbine inlet temperature is increased, it is necessary to increase the compressor pressure ratio to obtain minimum specific fuel consumption; therefore, increases in turbine inlet temperature will generally be accompanied by increases in the compressor pressure ratio. With present-day technology, plus the expected development of improved turbine cooling processes, advances in turbine materials, and advances in vane and blade fabrication techniques, it seems probable that turbine inlet temperatures equivalent to those achieved by stoichiometric combustion will be employed in future gas turbine engines. For JP type fuels burning at stoichiometric fuel-air ratios, the resulting combustion gas temperature will be of the order of 3500° to 4000° F, or higher, depending on the flight speed and altitude of the airplane in which the engine is installed. For these very high gas temperatures, the associated compressor pressure ratio may be of the order of 30 or 40 to 1. It appears, therefore, that future gas turbine aircraft engines may operate at turbine inlet temperatures of the order of 4000° F and gas pressures as high as 600 psia.

The NASA Lewis Research Center is currently engaged in investigating turbine cooling for application to aircraft gas turbine engines at gas temperatures up to about 4000° F and gas pressures up to about 600 psia. Present facilities permit experimental research at gas temperature and pressure of about 2500° F and 125 psia, respectively. Proposed facilities will extend the range of experimental environments to the higher levels.

The purposes of this paper are threefold, namely, (1) to discuss the objectives of the Lewis turbine cooling program, (2) to indicate how and with what facilities the research is conducted, and (3) to present some results that have been obtained to date. In brief, the turbine cooling research goals are

(1) To develop improved methods and to modify existing theories for predicting vane and blade local temperatures for all types of cooling processes

(2) To develop methods for predicting vane and blade life

(3) To investigate cooling concepts for future high-temperature, high-pressure engines

(4) To investigate advanced metal joining techniques that can be employed to fabricate vanes and blades having high cooling effectiveness

Up to the present time convection cooling with air has been the primary means of cooling the vanes and blades of aircraft gas turbines. In some instances augmentation of the convection cooling has been achieved by the use of film cooling from holes or slots located in certain critical regions of the vane or blade airfoil. For the severe cooling conditions anticipated for future high-temperature, high-pressure engines, it is unlikely that convection cooling will be adequate; therefore, more effective cooling processes such as full-coverage film cooling and transpiration cooling will be required. Reference 1 discusses these various cooling methods, analyzes their limitations, and indicates their future potential in terms of turbine inlet temperature, gas pressure, coolant temperature, and relative coolant flow requirements. Reference 2 discusses the cooling potential of convection-cooled turbines, including the effects of reduced cooling air temperature, for Mach 3 flight conditions. References 3 to 11 report research that has been conducted on film and transpiration cooling; references 12 and 13 discuss impingement cooling.

Presently most convection-cooled turbine vanes and blades are made from one-piece castings of nickel-base high-temperature alloys. For some cooling applications, sheet metal inserts are placed within the finished castings to provide impingement cooling. In order to utilize some of the most effective advanced convection cooling concepts, the vanes and blades may have to be fabricated in separate subassemblies and then joined together. For practical application, such fabricated vanes and blades must employ metal joining processes that result in highly efficient joints. Two promising joining processes that might be used to bond vane and blade subcomponents together with resulting high joint efficiencies are activated diffusion brazing and gas pressure welding. Both of these processes are discussed in reference 14.

The turbine cooling research program at the Lewis Research Center includes both in-house work and contractual efforts by universities and industry. The in-house research is being conducted on both an experimental and analytical basis. The major Lewis Research Center experimental research facilities for turbine cooling consist of a static cascade facility, a modified J-75 research engine, and a flow apparatus for studies of airflow within vanes, blades, and turbine disk components, all of which will be discussed in this paper. Some of the initial results obtained from these facilities are presented in this paper, as well as results obtained from contractual research.

Experimental results from the static cascade and engine facilities cover combustion gas temperatures ranging from about 1045° to 2564° F, gas pressures from about 18 to 45 psia, and coolant temperatures from 75° to 900° F.

METHODS FOR TURBINE COOLING

Description of Cooling Methods

Four methods of turbine cooling are illustrated in figure III-1. The least complicated method is convection cooling (fig. III-1(a)). In this cooling method, the heat that is picked up by the blades from the hot gas is conducted through the blade wall to cooling air that is flowing through internal passages in the blade. Generally fins are used on the inside (coolant side) wall to increase the surface area exposed to the cooling airflow. The heat transferred by convection from the inside blade wall to the cooling air is a function of the exposed surface area, the wall-to-cooling-air temperature difference, and the convective heat-transfer coefficient.

A variation of convection cooling that can be used in certain areas on the blade is impingement cooling, which is illustrated in figure III-1(b). In impingement cooling, jets of cooling air are directed against the inner surface of the blade wall to transfer heat from the metal to the coolant in a more efficient way than can be done with normal convection cooling. The heat transfer in impingement cooling is higher than that of normal convection cooling because of the very high stagnation point heat-transfer coefficients that can be obtained at the points of jet impingement.

Even more efficient use of the cooling air can be made by combining film cooling with convection cooling as shown in figure III-1(c). In this method, cooling air is passed through holes or slots in the blade wall to establish a film of relatively cool air on the outer surface of the blade. The cooling air picks up heat convectively in the holes through the blade walls and thus reduces the metal temperature. Then, the film of cooling air that is formed on the outer wall further reduces the blade temperature by reducing the quantity of heat that is transferred from the gas stream through the film to the blade. The cooling effect of this film dissipates quickly in the presence of the gas stream and must be renewed with additional downstream holes if more than local film cooling is desired.

The most efficient use of cooling air can be attained by passing the air through a porous wall to establish a complete and continuous blanket of cool air on the outer surface of the blade as shown in figure III-1(d). The air that transpires through the porous wall picks up heat very effectively from the wall by convection. The uniform

film established on the outer wall results in an even greater reduction of gas-to-wall heat-transfer coefficient than was accomplished in film cooling.

Examples of Cooled Configurations

Two typical blade configurations incorporating the various cooling methods are shown in figure III-2. In the upper configuration (fig. III-2(a)), three of the four cooling methods are combined. Cooling air enters the blade in several parallel radial flow paths. Air in the forwardmost flow path impinges on the inner surface of the leading edge of the blade through a radial array of holes. This air then flows chordwise toward the rear along the inside wall on both sides of the blade to convectively cool the forward portion of the blade immediately behind the leading edge. Slots in the blade wall transfer the air to the outer surface of the blade to establish a film-cooling layer. Air in the midchord region flows radially outward in channels adjacent to the blade outer wall. This airflow makes a 180° turn at the blade tip to enter the central midchord cavity. The air then flows radially inward and discharges from the central cavity through trailing edge slots over the blade span.

The lower configuration (fig. III-2(b)) is a transpiration-cooled blade. A fluted support strut is the structural part of the blade. The porous material which forms the blade wall is attached to this fluted strut. The channels formed by the flutes act as radial coolant flow passages. From these channels, the coolant passes through the porous wall and forms a protective film on the outer surface of the blade.

Potentials of Cooling Methods

Simplified comparison of cooling methods. - Convection cooling (including impingement cooling) is currently being used on operational gas turbine engines, with some augmentation from film cooling in critical regions. At the severe cooling conditions expected in future engines, it is likely that convection cooling will be inadequate, and more advanced cooling schemes such as film and transpiration cooling will have to be used. The potentials of the various cooling methods as applied to a blade can be determined in a relatively simple manner by considering the blades as heat exchangers and evaluating the cooling requirements on a basis of the heat capacity of the cooling air flowing through the blades. An example of such an evaluation is given in reference 1 and is repeated in figure III-3. This example shows relative coolant flow ratio required as a function of turbine inlet temperature. For this evaluation, a convection efficiently of 0.7 was assumed. Convection efficiency is

defined as the ratio of the rise in cooling air temperature to the maximum potential rise in cooling air temperature. Mathematically this can be expressed as

$$\eta_{conv} = \frac{T_{C,o} - T_{C,i}}{T_{M,i} - T_{C,i}} \qquad (1)$$

(All symbols are defined in the appendix.) It is further assumed that the outside metal temperature $T_{M,o}$ is 1800° F, the coolant temperature $T_{C,i}$ is 1000° F, the gas stream pressure is 20 atmospheres, and the blade wall thickness is 0.05 inch. As a basis of comparison, the coolant flow ratio required to cool the blade convectively at a turbine inlet temperature of 2500° F was assigned the value of unity. All other coolant flow ratios were referenced to this base. As can be seen in figure III-3, the required convection coolant flow rises very rapidly over the range of turbine inlet temperatures considered. At 3000° F, the required coolant flow ratio is three times that required at 2500° F.

Also shown in figure III-3 are curves for full-coverage film- and transpiration-cooled blades. The same conditions were used to develop these curves as were used for the convection curve except that the efficiency of film cooling was assumed to be 0.6 and the efficiency of transpiration cooling was assumed to be 0.8. The definitions of these efficiencies are the same as those for the convection efficiency except that the blade outside surface temperature is substituted for the blade inside surface temperature. From figure III-3 it can be seen that the required coolant flow ratios at 2500° F are 62 and 42 percent of the required convection coolant for full-coverage and transpiration cooling, respectively. When turbine inlet temperature is increased to 3000° F, the required coolant flow ratio increases by 53 percent for full-coverage film and by 43 percent for transpiration cooling. Even at 3500° F, the required coolant flow ratios for these two cooling methods compare favorably with the required coolant flow ratio for convection cooling at a turbine inlet temperature of 2500° F.

Possible improvements in convection cooling. - At temperature levels where convection cooling can provide adequate protection, this method does have several advantages over film and transpiration cooling. The holes or slots in the blade wall that are required for film cooling and the porous wall that is required for transpiration cooling result in structures that are inherently weaker than the solid wall of a convection-cooled blade. Also, these openings in the blade walls are susceptible to vibration and fatigue failures. Foreign object damage and clogging of the very small coolant passages by surface oxidation or dirty cooling air can be serious problems in film- or transpiration-cooled blades. Fabrication techniques for film-

and transpiration-cooled blades are usually more complicated and more unconventional than the fabrication techniques for convection-cooled blades. As pointed out in the paper on turbine aerodynamics by Moffitt, Nosek, and Roelke, the entry of low-energy cooling air into the gas stream along the blade surface in film and transpiration cooling can have a detrimental effect on turbine performance. Therefore, ways of inproving convection cooling should be investigated.

Some possible improvements in convection cooling at a gas temperature level of 2750° F are shown in figure III-4. This temperature level is also shown as the square symbol in figure III-3. The other assumptions that were made in this comparison are indicated by the values at the tops of the bars in figure III-4. First, consider the possible improvement with increased convective efficiency. If a vane cooling configuration with an ideal, but unobtainable, 100 percent convection efficiency could be produced, the relative coolant flow ratio could be reduced as shown by the bar on the left in figure III-4. The same magnitude of coolant flow reduction can be obtained by reducing the vane wall thickness to 0.03 inch as shown by the bar on the right in figure III-4. Thinner walls result in a smaller temperature drop through the walls. For a constant outside wall surface temperature, which may be determined by oxidation limitations, a smaller temperature drop through the wall results in a larger temperature difference between the inside wall temperature and the cooling air temperature. This larger temperature difference permits better utilization of the cooling air by allowing higher cooling air temperature rises. It can be concluded from this that the wall should be made as thin as possible consistent with structural considerations such as foreign object damage, gas pressure forces, and oxidation effects.

Even greater improvements in convection cooling can be obtained by reducing the coolant temperature or increasing the allowable vane metal temperature. The bars in figure III-4 show that the effects of a 400° F reduction in cooling air temperature or a 200° F increase in the allowable vane wall temperature to 2000° F reduce the coolant flow required to about half the original value. This comparison shows that reductions in cooling air temperature or increases in allowable metal temperature are far more effective in permitting either higher turbine inlet temperature or lower coolant flow ratios than will ever be possible by improving the cooling effectiveness of convection-cooled turbine vanes.

EFFECT OF CHORD SIZE ON COOLANT REQUIREMENTS

Trend in Blade Size

The trend in future engine design is toward the "core" type engine which has higher gas temperatures and compressor pressure ratios than engines currently in use. The turbine vanes and blades of these core engines are much smaller than those used in most present-day engines. These advanced engines will operate at temperatures up to 4000° F and pressures as high as 600 psia with blade spans of about $1\frac{1}{2}$ inches. Future helicopter and lift engines will operate at less severe conditions with turbine inlet temperatures reaching 2500° F at pressures of approximately 150 psia. However, these latter engines will have blades with spans of about 0.75 inch.

Effect of Chord Size

Because of these trends toward small-sized turbine hardware, a study of the effect of blade size on the coolant requirement has been initiated within the NASA Lewis program. This study is being done under NASA contract NAS 3-13205 by AiResearch Manufacturing Company. In this contract study, an analysis is being made to determine the effect on cooling performance of scaling down given turbine blade cooling configurations within fabrication constraints. Any attempt to determine the effect of chord size on cooling performance in a wide variety of engine applications would be prohibitively complex. As a consequence, for the analysis simplifying assumptions were used. Some of the more important assumptions were (1) a fixed external aerodynamic shape, (2) constant solidity and constant corrected velocity triangles, (3) chords of 0.75, 1, and 1.5 inches, (4) a constant turbine blade span which was consistent with the radius ratio and aspect ratio for the 1-inch-chord blade, (5) turbine inlet and cooling air inlet pressures and temperatures that would be expected in advanced engines, and (6) a creep life of 1000 hours for the blade material.

For a specific engine design when blade solidity is held constant, a reduction in chord length (i.e., larger aspect ratio) will result in higher aerodynamic efficiency and a lighter weight turbine. However, fabrication limitations can make the cooling of short-chord blades difficult. Usually proportional reductions of the already-small dimensions of the internal passages and wall thicknesses of the blades are not practical. Therefore, the ratio of internal to external heat-transfer areas and the ratio

of cooling airflow to gas flow areas decrease as chord size decreases. These factors can result in higher coolant flow requirements at a given turbine inlet temperature or in reduced allowable turbine inlet temperatures where cooling air pressure drop is a limitation.

The results of the analysis of one of the convection-cooled blade configurations considered in the study are shown in figure III-5. The blade is of cast construction with transverse cast-in fins at the leading edge and cast-pin fins on a triangular spacing in the remainder of the blade. At the leading edge, air flows radially outward to exit at the tip. In the remainder of the blade, air flows both radially outward to exit at the tip and horizontally (chordwise) to exit through holes in the trailing edge. The results with this blade design are shown for a turbine inlet gas temperature of 2100° F. This gas temperature was the maximum allowable gas temperature for a 1000-hour life for the 0.75-inch chord blade. This figure shows an increase in cooling flow requirement as chord size decreases. This trend held true for cooling air supply temperatures of both 900° and 1200° F. It can be concluded from this study that convection cooling of short-chord blades will be difficult.

The analytical study showed that for blades cooled by a combination of convection and film cooling, a consistent trend with chord size did not necessarily result. In some of these designs, local thermal stresses induced by the film cooling resulted in the 0.75- and 1-inch-chord blades having allowable temperatures higher than the 1.5-inch-chord blade. Additional information on the effect of chord size on weight and cooling is contained in reference 15.

EXPERIMENTAL APPROACH FOR EVALUATION OF COOLED CONFIGURATIONS

Experimental evaluations are required on air-cooled configurations to verify that the criteria used in the design of these configurations are valid. These design criteria are based on the best available knowledge of the heat-transfer processes in and around the configuration. To provide accurate inputs for checking the design calculations, the temperature, pressure, and flow rate of both the gas stream and the cooling air are measured in the experimental testing. The design criteria can then be modified and refined on the basis of comparison between analytical and experimental results. The improved design criteria can then be used to produce better configurations. Ideally, these well-designed configurations will not have to be subjected to expensive developmental testing to determine unknown effects that were not accounted for in the design. Typical procedures for determining cooling air,

gas stream, and metal temperature conditions experimentally are illustrated in this section.

Cooling Airflow Distribution Studies

On the cooling air side, the distribution of the cooling air in the various passages within the configuration is very important. This flow distribution can be determined from airflow studies on the actual configuration. Such a study on a typical air-cooled vane configuration is described in the following paragraph.

Description of typical air-cooled vane. - A typical air-cooled vane is shown in figure III-6. This vane was designed for operation in a gas environment of 2500° F temperature and 150 psia pressure with a flow of 750° F cooling air equal to about $3\frac{1}{2}$ percent of the total engine flow. The airfoil portion of the vane is a single-piece casting with a slotted tubular insert at the leading edge and a perforated sheet metal insert in the midchord section. A cast cap is used on the vane tip to enclose an integral tip cooling air chamber and provide a cooling air inlet tube. Cooling air enters the vane through the short radial tube on the tip platform. Inside this hollow platform, the cooling flow divides into two paths. Some of the cooling flows radially inward inside the slotted tube in the leading edge section. The air then passes through a linear array of radial slots to impinge on the inside surface of the vane leading edge. After impingement, the air flows chordwise to the rear on both sides of the blade to convectively cool the section immediately behind the leading edge. This air then flows radially inward behind the leading edge supply tube to be discharged at the vane hub (see arrow).

The remainder of the cooling air entering the vane flows into a central midchord cavity formed by the perforated sheet metal insert. This air impinges on the inside walls in the midchord section and then flows chordwise to the rear to further convectively cool this region. At the trailing edge, the airflow separates into three flows. One flow exits through a radial row of slots to film cool the suction surface. A second flow exits through similar slots on the pressure surface for film cooling. The remaining flow passes through a series of staggered pin-fins in the split trailing edge to convectively cool this part of the blade.

Airflow distribution test apparatus. - To determine the distribution of cooling airflow within the complicated vane passages, static flow tests were made as illustrated in figure III-7. On the left in this figure is a cross-sectional sketch showing pressure tap locations for measuring cooling air pressure losses in the midchord section. The cooling air discharging from the single exit path at the leading edge and from the three exit paths at the trailing edge flows into separate collectors as

shown on the right in figure III-7. The cooling air pressures in these collectors are set at levels representative of gas stream conditions during engine operation. Thus, the quantity of cooling air discharging from each exit path can be measured. In this way the apportionment of air to the various parts of the vane can be determined over a range of flow or pressure conditions. A detailed description of a cooling airflow distribution study on this vane and the apparatus is given in reference 16.

Static Cascade Testing

The next step is to determine the effect of this flow distribution on vane temperatures in a hot-gas environment. To do this, four vanes were installed in the static cascade shown schematically in figure III-8. This static cascade was designed for continuous operation at an average gas stream temperature of 2500° F and a gas stream pressure of 150 psia. Short-time operation at 3000° F gas stream temperature is also permissible. Gas stream pressure and temperature are measured by probes at the inlet to the cascade test section. Static pressure is also measured downstream of the vane row by a line of wall taps. A picture of the cascade is shown in figure III-9.

The two central vanes in the cascade are used as the test specimens. The two outside vanes are used as guard vanes to complete the flow channels and partially shield the test vanes from view of the water-cooled walls. Cooling air is supplied to the two test vanes from a metered and temperature-controlled source. Conditions of cooling air temperature, pressure, and weight flow are measured in the supply line. A separate cooling airflow is supplied to each of the guard vanes. A detailed description of the static cascade is given in reference 17.

Vane metal temperatures are measured at local positions with thermocouples embedded in the vane wall. In addition, observation ports in the cascade walls (as shown in fig. III-8) can be used to obtain thermal radiation measurements by various methods. One method is infrared photography. An image of the hot vane is recorded by a camera containing infrared photographic film, and the changes in density on the film image are resolved by calibration into an isotherm map of the vane surface. An example of this method is shown in figure III-10. On the left in figure III-10 is a thermal image of a hot vane as recorded on 35-millimeter infrared film. A reference thermocouple is located in the field of view of the camera to establish a base temperature for evaluated density changes. The image is scanned by an optical instrument which automatically converts the continuous tone film image into isodensity contours as shown on the right in figure III-10. By using the temperature of the reference thermocouple and calibration curves for film characteris-

tics, temperature levels can be assigned to the isodensity contours to make this plot into an isothermal map. This method of temperature measurement gives the detailed local metal temperatures that are essential to a thorough evaluation of the heat transfer taking place on the cooled vanes. A detailed description of this method is given in reference 18.

Research Engine Testing

Promising vane cooling configurations are installed in a test bed turbojet research engine for testing under actual engine environment. A schematic view of the turbine section of this engine is shown in figure III-11. This engine can be operated continuously at an average turbine inlet temperature of 2500° F; the gas stream pressure is 45 psia. An extensive description of the research engine is presented in reference 17.

A cascade of five test vanes is installed in the vane row of this engine. This cascade is cooled by an airflow that is controlled in temperature and flow rate separately from the cooling airflow for the remaining vanes in the engine. The cooling air for the five test vanes is ducted directly to the inlet air tube on each vane to minimize leakage and thus maintain accuracy in the measurement of cooling air to the vanes. The remaining vanes in the row can be continuously cooled with a conservative coolant flow and temperature while the test vanes are being evaluated over ranges of coolant flow rates and temperatures. This engine is also used to test air-cooled blade configurations.

A five-blade test cascade is installed in the blade row of the engine as shown in the inset sketch in figure III-11. This test cascade is also cooled by an airflow that is metered separately from the cooling air for the remaining blades in the row. The test blade cooling air is ducted through a balanced pressure labyrinth seal assembly and radially outward along the rear face of the turbine disk to the test blades. This seal assembly minimizes the leakage of cooling air at the transfer point between the stationary and rotating parts of the engine. An experimental study of this type of seal is presented in reference 19. A combination experimental and analytical study of the entire test blade cooling airflow path from the engine centerline through the blades is presented in reference 20. A photograph of the rear face of the turbine rotor is shown in figure III-12.

Gas stream conditions in the engine are determined from pressure and temperature measurements ahead on the turbine and weight flow measurements at the engine inlet. Cooling air conditions are measured in the cooling air supply lines. Metal temperatures on the blades and vanes are measured with thermocouples. Currently,

the thermocouple signals from the rotating blades are transferred to stationary readout equipment through a slipring assembly. Because of the inherent maintenance and electric noise problems of sliprings, development work is now in progress on a rotating shaft-mounted microelectronics data system which will accomplish this signal transfer more efficiently with a rotary transformer. This latter data system is discussed in reference 21. A rotating assembly with ten pressure transducers is also being developed to make rotating pressure measurements on the blades. Signals from the pressure transducer outputs also will be transferred through the shaft data system.

COMPARISONS OF EXPERIMENTAL AND ANALYTICAL RESULTS

The ultimate objective of the heat-transfer investigations described herein is to develop correlations that can be applied generally to the design of cooled vanes and blades. When properly developed, such correlations could result in better designs that would not require so much developmental testing to qualify as flight hardware. To accomplish this objective, the analytically predicted cooling performance of vanes and blades designed from currently available correlations is compared with experimental performance determined under actual or simulated engine environments. Modifications or refinements are made in the current correlations to obtain good agreement between analytical and experimental results.

Vane and blades of various cooling configurations have been tested in the static cascade and the research engine just described. The cooling characteristics of these cooling configurations have been evaluated also by two analytical methods. The first of these methods is a simple extrapolation of experimental vane temperature data obtained at low values of gas and coolant temperatures to predict vane temperatures that would occur at higher gas and coolant temperatures. The second method is a thorough analysis of the heat-transfer processes in and around the vanes using the best available heat-transfer correlations. The analysis is made on a high-speed digital computer. Comparisons of the results from both analytical methods with experimental results are given in this section.

Extrapolation of Low-Temperature Results to High-Temperature Conditions

Experimental heat-transfer investigations of cooled vanes and blades at high gas stream temperatures are costly and time-consuming because of the deteriorating effects of the test environment on the test apparatus and the associated instrumenta-

tion. For example, thermocouple wires that can be used on thin-walled vanes and blades are necessarily small (approximately 3 mils diam). These small-diameter wires are highly susceptible to failure when subjected to the effects of hot gas streams. To conserve the service life of test apparatus and instrumentation, a method was developed for extrapolating experimental vane temperature data obtained at low gas and coolant temperature levels to predict vane temperatures that would occur at higher levels of gas and coolant temperatures.

A comparison of extrapolated and experimental data for the vane shown in figure III-6 is presented in figure III-13. The experimental data points (circles) shown in the lower part of this figure were obtained during low-temperature cascade operations. The operating conditions were a gas temperature of 1030° F, a gas pressure of 18 psia, and a cooling air temperature of 70° F. The solid line was drawn through these experimental data. The average vane temperature under these environmental conditions was 580° F. Prediction of the vane temperatures at higher gas and cooling air temperature levels was based on the assumptions that the gas Reynolds number, the gas Mach number, the coolant Reynolds number, the coolant Mach number, the coolant flow ratio (W_C/W_G), and the ratios of coolant to gas temperatures ($T_{C,i}/\overline{T}_G$) were constant for both high- and low-temperature cases. A gas temperature of 2564° F was selected for the high-temperature case. From the ratio of coolant to gas temperature at the low-temperature level, the corresponding value of the coolant temperature was determined to be 605° F. Then, by assuming a constant ratio of the difference between gas and average metal temperatures to the difference between the gas and inlet coolant temperatures (i.e., $(\overline{T}_G - \overline{T}_M)/(\overline{T}_G - T_{C,i})$ = constant), the extrapolated value of the average vane temperature was determined to be 1580° F. Finally, by determining ratios of local to average vane temperatures ($T_M/\overline{T}_M$) for the low-temperature data and applying these ratios to the average vane temperature for the high-temperature case, a chordwise distribution of local vane temperatures was obtained. This extrapolated distribution of local vane temperatures is shown by the dashed line at the top of figure III-13. The validity of this data extrapolation was checked by experimentally testing the vane at the gas and coolant conditions that were assumed for the extrapolation. The experimental local vane temperatures are shown by the square symbols in figure III-13. The agreement between experimental and extrapolated temperatures is very good. This agreement shows that, for the levels at gas temperatures and wall temperature gradients considered, this extrapolation method can be used for preliminary experimental evaluation of the cooling performance of vanes and blades designed for high-temperature application without testing experimentally in the high-temperature environment.

Prediction of Vane Temperatures by Analytical Method

The objective of good design criteria is the accurate prediction of the temperature of an air-cooled vane knowing the vane geometry and the gas and cooling air environment in which the vane will operate. To establish a calculation procedure that can be used for this purpose, detailed knowledge of the coolant flow distribution within the vane, the internal heat-transfer coefficients, the cooling air temperature and pressure, the gas stream temperature and pressure, and the external heat-transfer coefficients is required. The more accurately these factors are known, the more reliable are the predicted vane temperatures. For the vane shown in figure III-6, the cooling flow distribution was determined as described previously. The appropriate heat-transfer coefficients were determined from the best available correlations, and the inputs of gas and coolant conditions were determined by measurements in the test facilities (the static cascade (fig. III-9) and the research engine (fig. III-12)). These measurements included the gas temperature, the local gas pressure distribution around the vane, the gas flow rate, the cooling air temperature, and the cooling air pressure. Fundamental heat-transfer investigations of transpiration and film cooling are being done under NASA sponsorship by Professor Kays of Stanford University (NASA grant NGR-05-02-134) and Professor Eckert of the University of Minnesota (NASA contract NAS 3-13200), respectively. Detailed methods of obtaining local cooling airflow rates and discharge coefficients for thick plate orifices with approach flow perpendicular and inclined to the orifice axis are reported in references 16 and 22, respectively. Additional detailed flow studies are in progress at General Electric under NASA contract NAS 3-13499 for large-scale models simulating portions of turbine vanes. Studies are also in progress concerning the amount of heat picked up by the cooling air under an impingement cooling contract (NASA contract NAS 3-11175) by Professor Hrycak of the Newark College of Engineering.

By employing the best available heat-transfer and flow information, metal temperatures were calculated on a digital computer for the vane of figure III-6. The digital computer program combines an internal airflow analysis with a three-dimensional heat conduction analysis; iterations between the two phases are performed until a final converged answer is obtained. The vane is divided into a nodal network which varies for each vane profile and internal cooling configuration.

The internal friction factor law (for both turbulent and laminar flow) is of the following form:

$$f = C_1 Re^{C_2} \qquad (2)$$

The constants in this law and the entrance and exit loss coefficients are established by forcing the predicted flow distribution to match one of the experimental static flow distributions. When these distributions agree, the program is ready to predict flow distributions for any other set of test conditions.

Cooling air temperature and metal-to-coolant heat-transfer coefficients are calculated in the program from existing correlations. A stagnation impingement correlation is modified for use in the leading edge, while an average impingement correlation for an array of circular jets is used in the midchord region.

An experimental correlation of stagnation Nusselt numbers for a linear array of circular jets is presented in reference 23. To make use of this correlation in the present application, each slot jet on the vane was treated as a circular jet having equal area. The center-to-center nozzle spacing of the slot jets was retained as the center-to-center nozzle spacing of the equivalent circular jets. The resulting correlation for the heat-transfer coefficient, after having been evaluated at the equivalent geometry, appears as follows:

$$h_C = 0.06549\, Re_b^{0.7} \frac{k}{b} \tag{3}$$

The average impingement correlation used in the midchord region is given in reference 24. In the terms of this paper, this correlation is expressed as

$$h_C = 0.286\, Re^{0.625} \left(6.63 \frac{c}{Z}\right)^{0.625} \frac{k}{C} \tag{4}$$

Other inputs to the program consist of the cooling air temperature, flow rate, and inlet and exit pressures as well as nodal values for the effective gas temperature and the gas-to-wall heat-transfer coefficient. The gas pressure profile from which the cooling air exit pressures are obtained can either be calculated or measured. This pressure profile and an isentropic, perfect gas relation are then used to determine nodal values of velocity over the entire surface of the vane, from which follows the nodal values of both the effective gas temperature and the gas-to-wall heat-transfer coefficient. The equations which are used for these final determinations are as follows:

$$T_{G,e} = T_T - (1 - \Lambda) \frac{V^2}{2gJc_p} \tag{5}$$

where $\Lambda = Pr^{1/3}$ for turbulent flow,

$$h_G = 1.14\,Re^{0.5}Pr^{0.4}\left[1 - \left(\frac{\theta}{90}\right)^3\right]\frac{k}{D_{le}} \tag{6}$$

for flow around a cylinder, and

$$h_G = 0.0296\,Re^{0.8}Pr^{1/3}\frac{k}{x} \tag{7}$$

for turbulent flow over a flat plate.

On the film-cooled trailing edge regions, correlations for the film cooling effectiveness from reference 25 are used and appear as follows:

$$\eta_{fc} = -0.00001\left(\frac{X}{M \cdot s}\right)^{1.952} + 0.5 \tag{8}$$

for the suction surface, and

$$\eta_{fc} = -0.026\left(\frac{X}{M \cdot s}\right)^{0.498} + 0.5 \tag{9}$$

for the pressure surface.

This film cooling effectiveness is used to evaluate the adiabatic wall temperature, which in turn is used with the convection heat-transfer coefficient to determine the heat input to the vane. It is generally recognized that this type of film cooling analysis does not apply immediately downstream of the slot. However, this analysis is being used in the present investigations while better methods of analysis are being perfected.

The vane in figure III-6 has a staggered pin-fin configuration in the split trailing edge with the trailing edge slot width varying between 0.070 and 0.037 inch. However, the heat-transfer correlation was chosen more for the slot width than for the pin-fin configuration. The metal-to-coolant heat-transfer coefficient in the split trailing edge region is obtained from a curve fit of experimental data for square-spaced, circular pin fins from reference 26:

$$h = 0.248\,Re^{0.594}Pr^{0.333}\frac{k}{D_h} \tag{10}$$

In the preceding equations, the form of the correlation is part of the program. The constants in the correlation are part of the program input so that a different correlation for the metal-to-coolant heat-transfer coefficient may be used merely by changing the constants in the program input.

The predicted chordwise temperature distribution was determined for the midspan portion of the vane when operating in the static cascade (fig. III-9) at the following conditions: $\overline{T}_G = 1050^\circ$ F, $T_C = 87^\circ$ F, coolant flow rate = 0.024 pound per second, and static-pressure distribution around the vane surface corresponding to a gas flow of 0.454 pound per second per channel ($W_G/W_G = 0.053$). This predicted temperature distribution is shown as the dashed curve in figure III-14. Experimental vane temperature data for the same operating conditions in the static cascade are shown by the circled points in figure III-14. These temperatures were measured by thermocouples imbedded in the vane wall. A comparison of experimental and predicted temperature for the cascade tests shows good agreement over most of the vane. The greatest divergence between these data occurred in the midchord region that was cooled by impingement.

A similar predicted temperature distribution was determined for the vane midspan when the research engine (fig. III-11) was operated at the following conditions: $\overline{T}_G = 2250^\circ$ F, $T_C = 78^\circ$ F, coolant flow rate = 0.027 pound per second, and a static-pressure distribution around the vane surface corresponding to a gas flow of 0.762 pound per second per channel ($W_C/W_G = 0.035$). The predicted temperature distribution for the engine tests is the dashed curve in figure III-15. The experimental data points in figure III-15 were obtained from operation of the vane in the engine at the quoted conditions. The experimental and predicted temperatures for the engine test agree well in all parts of the vane except in the midchord impingement cooled area, as was the case in the cascade tests.

The data comparison in figures III-14 and III-15 show that current temperature prediction methods yield good agreement between analytical and experimental vane temperatures. However, more work must be done to improve temperature predictions for use in vane and blade life calculations. Predicted temperatures are used as input data into a computer program for this life determination. A description of the calculation procedure is given in references 27 and 28.

SOME RESULTS FROM STUDIES OF EXPERIMENTAL COOLING CONCEPTS

To date, the investigations being pursued under the NASA Lewis turbine cooling research program have covered (1) design studies of advanced cooling concepts for engines for Mach 3 flight operation, (2) flow model studies of small internal flow

passages, (3) analytical studies of small blade configurations and the effects of chord size, (4) basic impingement cooling studies, (5) heat-transfer investigations on advanced cooling concepts, (6) developmental work on joining techniques for assembling air-cooled vanes and blades, and (7) oxidation studies on film- and transpiration-cooled material. Representative results from some of these investigations are discussed in this section.

Examples of Experimental Cooling Concepts

Present-day production-type air-cooled blades and vanes are usually made of one-piece castings. To obtain better cooling performance for the higher temperature environments of future engines, more sophisticated internal configurations will be required. This sophistication will probably mean more finning of smaller thickness and closer spacing for convection-cooled configurations, perforated inserts to direct the jets to the proper places for impingement-cooled configurations, and new ideas for supporting the walls of full-coverage film- and transpiration-cooled configurations. These requirements will necessitate studies of blade and vane configurations for both heat-transfer and structural characteristics. Some examples of such experimental concepts for vanes are shown in figure III-16.

Film- and convection-cooled vane configuration. - The vane shown in figure III-16(a) is cooled by a combination of film and convection flows with impingement augmentation in the leading edge. Cooling air enters the midchord cavity of this vane as radial flow from the inlet air tube. Some of this air passes through a radial array of holes to impinge on the inside surface of the leading edge. This air then flows along the inside surface on both sides of the vane to be discharged into the gas stream through film-cooling holes. The remainder of the cooling air in the midchord cavity enters chordwise finned passages on both sides of the blade and flows to the rear. Thin sheets at the tops of the fins confine this airflow to do convective cooling in the chordwise passages. All the air exits through a split trailing edge to convectively cool this part of the vane. Fabrication of a complicated configuration such as this on a production basis will be difficult. Prototype specimens have been made in the NASA Lewis shops for experimental test purposes. The fabrication procedures used were satisfactory for the short operating times required for research investigations; however, the joining technique used resulted in joints that had neither durability nor resistance to low-cycle fatigue. More reliable fabrication methods will be required for production-type vanes.

To investigate and develop joining techniques that can be used to assemble engine-worthy cooled vane and blade configurations, NASA Lewis is currently spon-

soring two contractual efforts. One contract (NAS 3-12433) will cover work on activated diffusion brazing by the General Electric Company; the other contract (NAS 3-10941) will cover work on gas pressure welding by the Battelle Memorial Institute. These joining techniques were selected because of apparent potentials for attaining stronger, more reliable joints than would be possible with other techniques such as convetional brazing, fusion welding, explosive welding, or hot pressure welding with dies. It is not within the scope of this paper to discuss the details of these investigations. In general, the results showed that joints of suitable strength levels for application to cooled vanes and blades could be obtained from both techniques. Where applicable, activated diffusion brazing is preferable to gas pressure welding from the standpoint of cost. The welding process is inherently expensive. A special high-pressure autoclave, careful preparation of the components to be joined, and internal cooling to support portions of the components during the bonding process are some of the major factors affecting the cost of the welding technique. Details of the work on both techniques and results of strength tests are presented in reference 14.

Film- and impingement-cooled vane configuration. - The vane shown in figure III-16(b) is film-cooled in the trailing edge section and impingement-cooled in the leading edge and midchord sections. This cooling is augmented by convection cooling in the split trailing edge and in the midchord region, where the air from the impingement jets exits toward the trailing edge. This is the same vane that is shown in figure III-6 and has been discussed previously. The vane was designed and fabricated by Pratt and Whitney Aircraft Division, United Aircraft Corporation. This vane is made from a one-piece casting with a slotted tube in the leading edge and a perforated insert in the midchord region to provide impingement cooling in these two areas. Pin-fins are cast in the split trailing edge to improve the convection cooling from air exiting by that route. The film-cooling slots were made by electrical discharge machining (EDM).

Full-coverage film-cooled vane configurations. -

Porous sheet metal vane: The vane shown in figure III-16(c) is a full-coverage film-cooled vane made of porous sheet metal. The size and spacing of the holes can be varied to distribute the cooling airflow on the vane surface as required. This laminated sheet material and vanes made from this material have been and are being investigated under contracts with the Detroit Diesel Allison Division of the General Motors Corporation (NASA contracts NAS 3-7913 and NAS 3-12431). Most of this work is under a security classification. These investigations have covered studies of the internal flow, oxidation, and strength characteristics of the material. On the basis of the results of these studies, a vane configuration was designed, fabricated, and tested for cooling performance in a hot static cascade. Results of

these investigations are given in references 29 and 30. Additional testing is planned to determine the low-cycle fatigue and oxidation characteristics of this vane configuration.

Laminated platelet vane: In figure III-16(d) is another type of full-coverage film-cooled vane. This vane is made from a large number of 0.010-inch-thick metal platelets. The outer periphery of each platelet is shaped to the contour of the airfoil profile. The center of each platelet is cut out to provide a central cooling air cavity. One of the flat surfaces of each platelet is photoetched to provide cooling passages from the central cavity to the outer wall of the vane. These coolant passages are of two types and mating passages from two adjacent platelets are required to complete the flow path from the central cavity to the outside of the vane (see insert in fig. III-16(d)). Each photoetched coolant passage in the lower platelet shown in the inset consists of a flow control nozzle and a plenum chamber in series. Each photoetched coolant passage in the upper platelet consists of a radial slot through the platelet (in line with the plenum chamber in the lower platelet) and a relatively wide duct connecting this slot to the outer surface of the vane. Cooling air flows through the combination of coolant passages in the two adjacent platelets and film cools the outer wall of the vane. The multiplicity of passages provides for full-coverage film cooling. Convection cooling of the vane wall also occurs along the flow path through the platelets. In the vane illustrated in figure III-16(d), all of the vane outer surface except the extreme trailing edge region is cooled by full-coverage film cooling. The trailing edge is convectively cooled by air that is ducted through photoetched passages in the platelets that connect the central cavity with the trailing edge.

Local control of coolant flow can be achieved at any point on the vane by adjusting the size of the flow nozzles. Because the coolant passages are relatively large compared to those in transpiration-cooled materials (minimum dimension about 0.002 inch), the material should be less sensitive to the effects of oxidation than the porous materials. An investigation of this material is being made under contract to NASA Lewis by Aerojet Liquid Rocket Company (NAS 3-10495). The results of this investigation are summarized in reference 31. The investigation covered a study of flow characteristics through the small photoetched passages, the effects of oxidation on the coolant flow for platelets made of TD nickel-chromium, and the strength of a diffusion-bonded TD nickel-chromium platelet assembly at a metal temperature of 1800° F. From data obtained in this investigation, a full-coverage film-cooled vane was designed for fabrication from laminated TD nickel-chromium platelets. This vane has a span of 4 inches and a chord of about 2.5 inches. The design operating conditions were a gas temperature of 2500° F, a coolant temperature of 1200° F, and a maximum vane metal temperature of 1800° F.

Five vanes of this design have been fabricated for experimental testing in the NASA Lewis 2500° F static cascade (fig. III-9).

Transpiration-cooled vane configuration. - A transpiration-cooled vane fabricated at the NASA Lewis Research Center is shown in figure III-16(e). The outer wall of this vane is made of wire-wound cloth (Poroloy). The Poroloy cloth was formed around a fluted strut (see fig. III-16(e)) and attached to the strut by electron beam welding to form the vane airfoil contour. This strut supports the porous vane wall and also compartmentalizes the central part of the vane into separate cooling air chambers. Cooling airflow into each of these chambers or compartments is controlled by a properly sized orifice. The cooling air flows from the compartments through the porous wall to transpiration cool the vane. Research on the transpiration-cooled vane shown in figure III-16(e) is being carried on at the Lewis Research Center, and other research on similar vanes and blades is reported in references 32 to 34.

Experimental Heat-Transfer Results

Experimental heat-transfer results from the investigation of some of the experimental vanes are shown in figure III-17. The data in this figure are taken from cascade testing of the film- and impingement-cooled vane shown in figure III-16(b) and from engine testing of the film- and convection-cooled vanes shown in figure III-16(a). The ordinate of this plot, the temperature difference ratio (φ), is a measure of the heat exchanger effectiveness of the cooling configurations. In this ratio $\overline{T}_G$ is the average midspan total gas temperature, $\overline{T}_M$ is the average midspan vane metal temperature, and $T_{C,i}$ is the coolant temperature at the inlet to the vane. The higher the value of this ratio, the more effective the cooling configuration. (Effective gas temperature $T_{G,e}$ rather than the average gas temperature is usually used in the temperature difference ratio. Because the numerical difference in value between these two quantities was very small, T_G was used in this case.)

It can be seen from the plot that the film-impingement vane (configuration B) has a higher cooling effectiveness than the film- and convection-cooled vane (configuration A). This comparison shows that impingement cooling is a more efficient cooling method than the usual convection cooling illustrated in figure III-1.

This correlation is based on four independent variables ($\overline{T}_G$, T_M, $\overline{T}_{C,i}$, and W_C/W_G) that affect heat transfer on the vane. By assuming values for any three of the four variables, the remaining one can be determined. For example, for conditions of $W_C/W_G = 0.05$, $\overline{T}_G = 2500^\circ$ F, and $T_{C,i} = 1000^\circ$ F, the vane metal temperatures would be 1820° F for the film- and convection-cooled vane, 1710° F for

the film- and impingement-cooled vane, and 1488° F for the full-coverage film-cooled vane.

Another way of showing the relative cooling performance of these vanes is to replot the information in figure III-17 for fixed values of average vane metal temperature $\overline{T}_M$ and coolant inlet temperature T_C to show allowable gas temperature as a function of coolant flow ratio. Such a replot is shown in figure III-18 as allowable gas temperature $\overline{T}_G$ as a function of coolant flow ratio W_C/W_G. The value of $\overline{T}_M$ in this cross plot was 1800° F; the value of $T_{C,i}$ was 1000° F. This comparison shows that at a coolant flow rate of 0.05, the allowable gas temperature is about 2400° F for the film- and convection-cooled vane (vane A) and about 2650° F for the film- and impingement-cooled vane (vane B). Peak metal temperatures on the vane can reduce the allowable operating temperature below that indicated by the plot. For vanes with large metal temperature gradients, this reduction in allowable operating temperature can be significant. A comparison such as this also does not account for any deterioration of aerodynamic performance due to entry of the low-energy cooling air into the gas stream. In the overall evaluation of the full-coverage film-cooled vanes, this factor must be investigated. Such investigations are in progress within the overall NASA Lewis program, as was discussed in the paper by Moffitt, Nosek, and Roelke.

Oxidation Problems With Transpiration-Cooled Materials

A major problem in using transpiration-cooled and full-coverage film-cooled materials for turbine blades and vanes has been the susceptibility of these materials to flow restrictions due to oxidation of the metal surfaces in the coolant passages. The pores in the wire-wound porous material (fig. III-16(e)) are of the order of 0.0002 to 0.0015 inch. (The internal structure of the wire-wound cloth is described in ref. 35.) The minimum dimension of the coolant passage in the laminated platelet vane is about 0.002 inch. Formation of even thin oxide coatings will represent significant dimension changes in these cooling passages. Once significant oxidation occurs in these materials, the metal temperature rises because of coolant flow restrictions and thus further accelerates the oxidation and flow restriction process.

A comparison of the oxidation characteristics of specimens of wire-wound cloth having the same permeabilities but fabricated from two different materials (Hastelloy X and GE 1541) is shown in figure III-19. The wire-wound cloth specimens made of Hastelloy showed complete flow obstruction after 350 hours of exposure in air at 1800° F. The GE 1541 specimens showed no flow reduction after 600 hours exposure at 1800° F. This represents a significant advance in the state of the art of

transpiration cooling at elevated temperature. From these results it can be seen that the choice of materials for transpiration- (and film-) cooled applications should probably be dictated by oxidation characteristics.

The GE 1541 wire-wound porous materials were developed by the Filter Division of the Bendix Corporation under NASA contract NAS 3-10477. The main fabrication problem involved sintering of the GE 1541 wires. The wires have an extremely adherent oxide which protects them against further oxidation but makes sintering very difficult. However, Bendix was able to develop a process for producing good sinter bonds in porous material made from GE 1541 wire. The main features of this process are (1) winding the wire over a stainless steel mandrel and then overwrapping it with molybdenum or tungsten wire and (2) sintering the assembly in a vacuum furnace for 4 hours at 2200° F. Pressure is applied to the GE 1541 wires during sintering by the differential thermal expansion between the overwrap and the mandrel. A parting compound is used to prevent the GE 1541 from being bonded to the overwrap or the mandrel.

Twelve oxidation-resistant alloys for turbine blade transpiration cooling have been screened in investigations conducted under the NASA Lewis program. The results of these investigations are reported in references 36 and 37. In reference 38, a method is presented for analytically determining the flow reduction from oxidation of wire-form sheets over a wide range of permeabilities using only oxidation data from wire specimens such as were obtained in reference 37.

SUMMARY

This discussion can be summarized as follows:

1. Analytical methods that have been developed for predicting metal temperatures in cooled turbines give good agreement with experimentally determined temperature. More investigation is required to determine correlations that take full account of the complicated heat-transfer processes that occur within the small coolant passages of the vanes and blades.

2. Advanced concepts of cooling configurations that incorporate film and/or transpiration cooling will be required at very high gas temperatures. However, some tradeoffs will have to be made to match gains in operating temperature with losses in turbine performance and airfoil life when using these cooling methods.

3. To make these advanced cooling concepts feasible, improvements must be made in fabrication techniques and material properties, particularly in resistance to oxidation.

4. Oxidation and the resultant blockage of coolant passages will probably dictate the choice of materials to be used for film and transpiration cooling.

5. For a convection-cooled turbine, more significant reductions in required coolant flow can be obtained by reducing coolant temperature or increasing allowable metal temperature than can be obtained by improving convection efficiency of the configuration.

6. Convection cooling becomes more difficult as chord size decreases.

APPENDIX - SYMBOLS

b	equivalent slot width
C_1, C_2	constants
c	distance between centers of adjacent impingement nozzles
c_p	specific heat at constant pressure
D	diameter
f	friction factor
g	gravitational constant
h	heat-transfer coefficient
J	mechanical equivalent of heat
k	thermal conductivity
L	surface length from leading edge to trailing edge
LE	leading edge
M	$(\rho V)_C/(\rho V)_G$
P	pressure
Pr	Prandtl number
Re	Reynolds number
s	slot width
T	temperature
$\bar{T}$	average temperature
TE	trailing edge
t	wall thickness
V	velocity
W	weight flow
X	distance from downstream edge of film cooling slot
x	distance along surface from stagnation point
Z	impingement nozzle to plate spacing
η	thermal effectiveness

θ	angular displacement from stagnation point on leading edge
Λ	recovery factor
ρ	density
φ	temperature difference ratio, $\frac{\bar{T}_G - \bar{T}_M}{\bar{T}_G - T_{C,i}}$

Subscripts:

b	equivalent slot width
C	cooling air
conv	convection
e	effective
fc	film cooling
G	gas
h	hydraulic
i	in or inside
le	leading edge
M	metal
o	out or outside
T	total

REFERENCES

1. Esgar, Jack B.; Colladay, Raymond S.; and Kaufman, Albert: An Analysis of the Capabilities and Limitations of Turbine Air Cooling Methods. NASA TN D-5992, 1970.

2. Stepka, Francis, S.: Considerations of Turbine Cooling Systems for Mach 3 Flight. NASA TN D-4491, 1968.

3. Goldstein, R. J.; Eckert, E. R. G.; and Ramsey, J. W.: Film Cooling with Injection Through a Circular Hole. Rep. HTL-TR-82, Minnesota Univ. (NASA CR-54604), May 14, 1968.

4. Metzger, D. E.; Carper, H. J.; and Swank, L. R.: Heat Transfer with Film Cooling Near Nontangential Injection Slots. J. Eng. Power, vol. 90, no. 2, Apr. 1968, pp. 157-163.

5. Metzger, D. E.; and Fletcher, D. D.: Surface Heat Transfer Immediately Downstream of Flush, Non-Tangential Injection Holes and Slots. Paper 69-523, AIAA, June 1969.

6. Goldstein, R. J.; Eckert, E. R. G.; Eriksen, V. L.; and Ramsey, J. W.: Film Cooling Following Injection Through Inclined Circular Tube. Rep. HTL-TR-91, Minnesota Univ. (NASA CR-72612), Nov. 1969.

7. Moffat, R. J.; and Kays, W. M.: The Turbulent Boundary Layer on a Porous Plate: Experimental Heat Transfer with Uniform Blowing and Suction. Rep. HMT-1, Stanford Univ., Aug. 1967.

8. Simpson, R. L.; Kays, W. M.; and Moffat, R. J.: The Turbulent Boundary Layer on a Porous Plate: An Experimental Study of the Fluid Dynamics With Injection and Suction. Rep. HMT-2, Stanford Univ., Dec. 1967.

9. Whittan, D. G.; Kays, W. M.; and Moffat, R. J.: The Turbulent Boundary Layer on a Porous Plate: Experimental Heat Transfer with Variable Suction, Blowing, and Surface Temperature. Rep. HMT-3, Stanford Univ., Dec. 1967.

10. Julien, H. L.; Kays, W. M.; and Moffat, R. J.: The Turbulent Boundary Layer on a Porous Plate: An Experimental Study of the Effects of a Favorable Pressure Gradient. Rep. HMT-4, Stanford Univ. (NASA CR-104140), Apr. 1969.

11. Thielbahr, W. H.; Kays, W. M.; and Moffat, R. J.: The Turbulent Boundary Layer on a Porous Plate: Experimental Heat Transfer with Blowing, Suction, and Favorable Pressure Gradient. Rep. HMT-5, Stanford Univ. (NASA CR-104141), Apr. 1969.

12. Hrycak, Peter; Lee, David T.; Gaunter, James W.; and Livingood, John N. B.: Experimental Flow Characteristics of a Single Turbulent Jet Impinging on a Flat Plate. NASA TN D-5690, 1970.

13. Gaunter, James W.; Livingood, John N. B.; and Hrycak, Peter: Survey of Literature on Flow Characteristics of a Single Turbulent Jet Impinging on a Flat Plate. NASA TN D-5652, 1970.

14. Kaufman, A.; Berry, T. F.; and Meiners, K. E.: Joining Techniques for Fabrication of Composite Air-Cooled Turbine Blades and Vanes. To be presented at the ASME Gas Turbine Conference and Products Show, Houston, Texas, Mar. 28-Apr. 1, 1971.

15. Esgar, Jack B.; Schum, Eugene F.; and Curren, Arthur N.: Effect of Chord Size on Weight and Cooling Characteristics of Air-Cooled Turbine Blades. NACA TR 1354, 1958.

16. Clark, John S.; Richards, Hadley T.; Poferl, David J.; and Livingood, John N. B.: Cooling Pressure and Flow Distribution Through an Air-Cooled Vane for a High-Temperature Gas Turbine. NASA TM X-2028, 1970.

17. Calvert, Howard F.; Cochran, Reeves P.; Dengler, Robert P.; Hickel, Robert O.; and Norris, James W.: Turbine Cooling Research Facility. NASA TM X-1927, 1970.

18. Pollack, Frank G.; and Hickel, Robert O.: Surface Temperature Mapping With Infrared Photographic Pyrometry for Turbine Cooling Investigations. NASA TN D-5179, 1969.

19. Yeh, Frederick C.; and Cochran, Reeves P.: Comparison of Experimental and Ideal Leakage Flows Through Labyrinth Seals for Very Small Pressure Differences. NASA TM X-1958, 1970.

20. Yeh, Frederick C.; Poferl, David J.; Cochran, Reeves P.; and Richards, Hadley T.: Airflow Study on Air Cooled Disk and Blade. NASA TM X-2171, 1971.

21. Lesco, Daniel J.; Sturman, John C.; and Nieberding, William C.: Rotating Shaft-Mounted Microelectronic Data System. NASA TN D-5678, 1970.

22. Rohde, John E.; Richards, Hadley T.; and Metger, George W.: Discharge Coefficients for Thick Plate Orifices With Approach Flow Perpendicular and Inclined to the Orifice Axis. NASA TN D-5467, 1969.

23. Chupp, Raymond E.; Helms, Harold E.; McFadden, Peter W ; and Brown, T. R.: Evaluation of Internal Heat-Transfer Coefficients for Impingement-Cooled Turbine Airfoils. J. Aircraft, vol. 6, no. 3, May-June 1969, pp. 203-208.

24. Gardon, Robert; and Cobonpue, John: Heat Transfer Between a Flat Plate and Jets of Air Impinging on It. International Developments in Heat Transfer. ASME, 1963, pp. 454-460.

25. Burggraf, F.; Murtaugh, J. P.; and Wiltson, M. E.: Design and Analysis of Cooled Turbine Blades. Part I. Leading and Trailing Edge Configurations. Rep. R68AEG101, General Electric Co. (NASA CR-54513), Jan. 1, 1968.

26. Theoclitus, G.: Heat-Transfer and Flow-Friction Characteristics of Nine Pin-Fin Surfaces. J. Heat Transfer, vol. 88, no. 4, Nov. 1966, pp. 383-390.

27. Kaufman, Albert: Steady-State Stress Relaxation Analysis of Turbine Blade Cooling Designs. NASA TN D-5282, 1969.

28. Kaufman, Albert: Analytical Study of Cooled Turbine Blades Considering Combined Steady-State and Transient Conditions. NASA TM X-1951, 1970.

29. Anderson, R. D.; and Nealy, D. A.: Evaluation of Laminated Porous Material for High-Temperature Air-Cooled Turbine Blades. Rep. EDR-4968, General Motors Corp. (NASA CR-72281), Jan. 16, 1967.

30. Nealy, D. A.; Anderson, R. D.; and Hufford, A. A.: Design and Experimental Evaluation of a Turbine Vane Fabricated From Laminated Porous Material. Rep. EDR-6296, General Motors Corp. (NASA CR-72649), July 31, 1969.

31. Klessig, C. E.: Investigation of Laminated Convection-Film Cooled Turbine Stator Vanes. Rep. AGC-2100-1, Aerojet Liquid Rocket Co. (NASA CR-72506), July 31, 1970.

32. Lombardo, S.; Moskowitz, S. L.; and Schnure, S. A.: Experimental Results of a Transpiration-Cooled Turbine Operated in an Engine for 150 Hours at 2500° F Turbine Inlet Temperature. Paper 67-GT-29, ASME, Mar. 1967.

33. Moskowitz, S. L.; and Schober, T. E.: Design and Test of a Small Turbine at 2500° F With Transpiration Cooled Blading. Paper 690035, SAE, Jan. 1969.

34. Mindrala, Joseph; Wysocki, Dennis A.; and Hollenbeck, Brian L.: J65-W-18 Engine Evaluation of Curtiss-Wright Transpiration-Cooled Turbine Blades and Variable-Geometry Turbine Concepts. Rep. NAPTC-ATD-129, Naval Air Propulsion Test Center, Nov. 1967.

35. Wheeler, H. L., Jr.: Transpiration Cooling in the High Temperature Gas Turbine. Bendix Filter Div., Bendix Corp., Mar. 1964.

36. Cole, Fred W.; Padden, James B.; and Spencer, Andrew R.: Oxidation Resistant Materials for Transpiration Cooled Gas Turbine Blades. I. Sheet Specimen Screening Tests. NASA CR-930, 1968.

37. Cole, Fred W.; Padden, James B.; and Spencer, Andrew R.: Oxidation Resistant Materials for Transpiration Cooled Gas Turbine Blades. II. Wire Specimen Tests. NASA CR-1184, 1968.

38. Kaufman, Albert: Analytical Study of Flow Reduction Due to Oxidation of Wire-Form Porous Sheet for Transpiration Cooled Turbine Blades. NASA TN D-5001, 1969.

METHODS FOR TURBINE COOLING

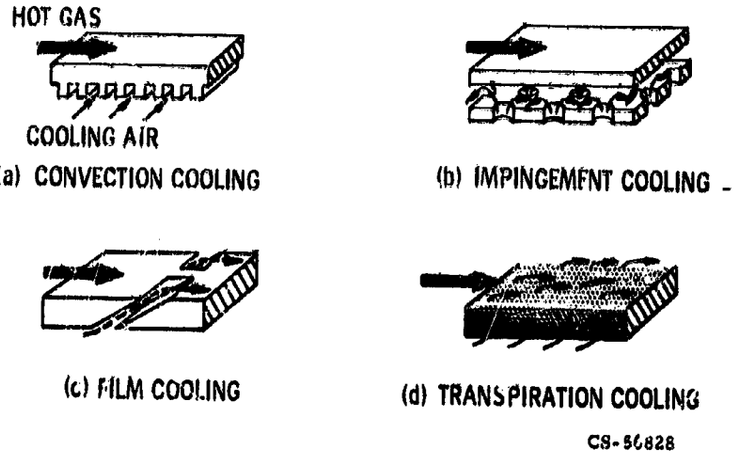

Figure III-1

TYPICAL AIR-COOLED VANE CONFIGURATIONS

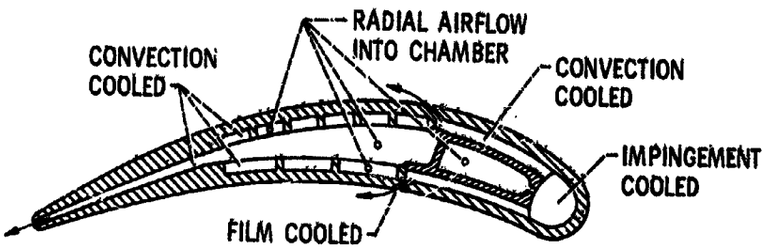

(a) CONVECTION-, IMPINGEMENT-, AND FILM-COOLED BLADE CONFIGURATION.

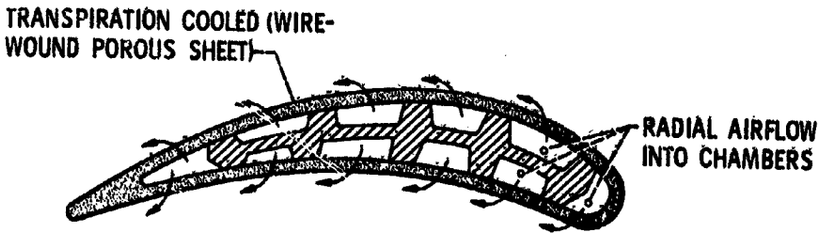

(b) TRANSPIRATION-COOLED BLADE CONFIGURATION.

Figure III-2

POTENTIALS OF COOLING METHODS

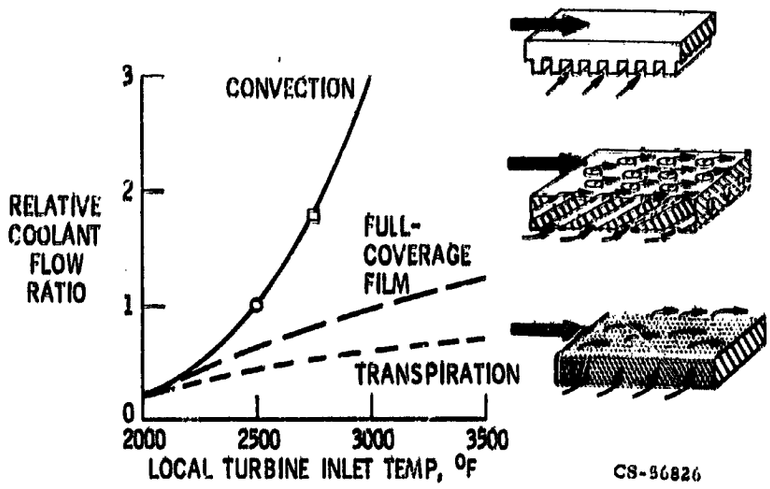

Figure III-3

IMPROVING CONVECTION COOLING

$\bar{T}_G = 2750^0$ F

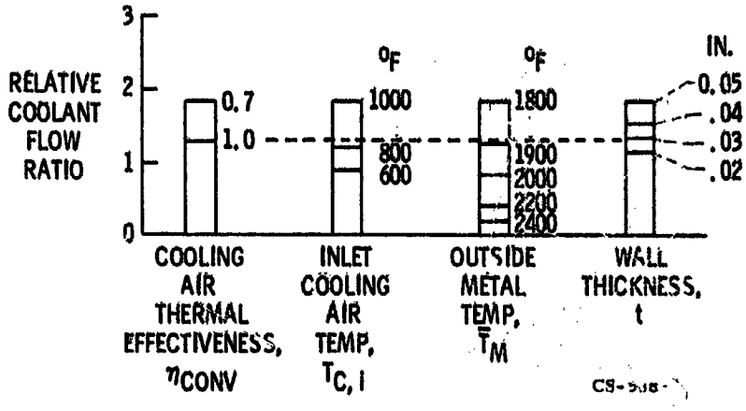

Figure III-4

CHORD SIZE AS FUNCTION OF COOLANT REQUIRED FOR CONVECTION-COOLED BLADE

$\bar{T}_G$ = 2100° F; P_G = 150 PSIA

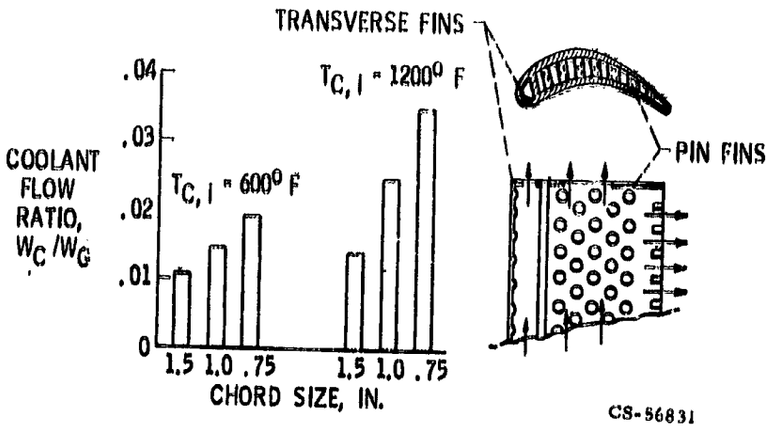

Figure III-5

AIR-COOLED TURBINE VANE

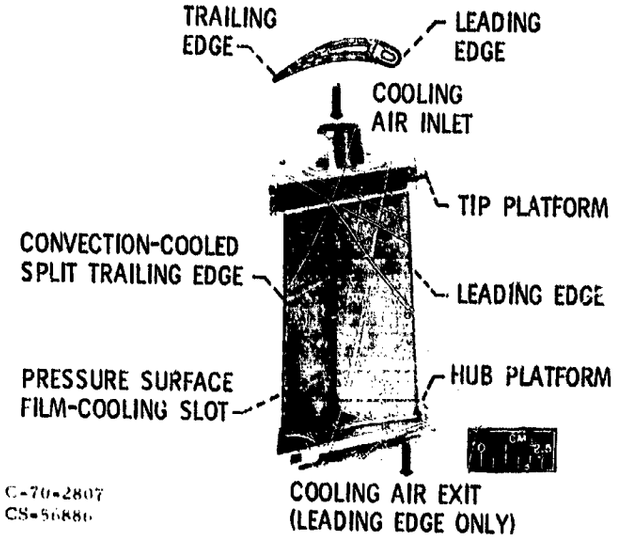

Figure III-6

AIRFLOW DISTRIBUTION TEST APPARATUS

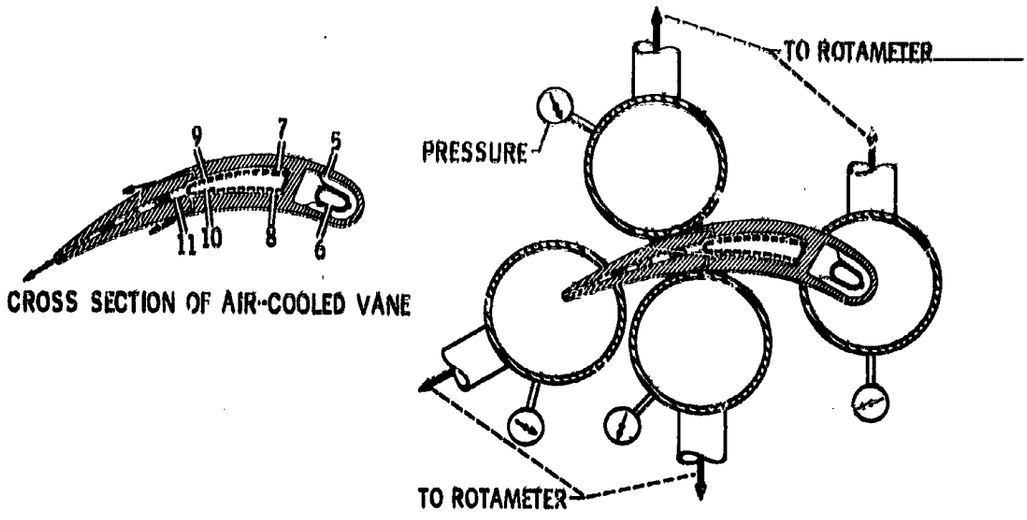

Figure III-7

2500°F STATIC CASCADE

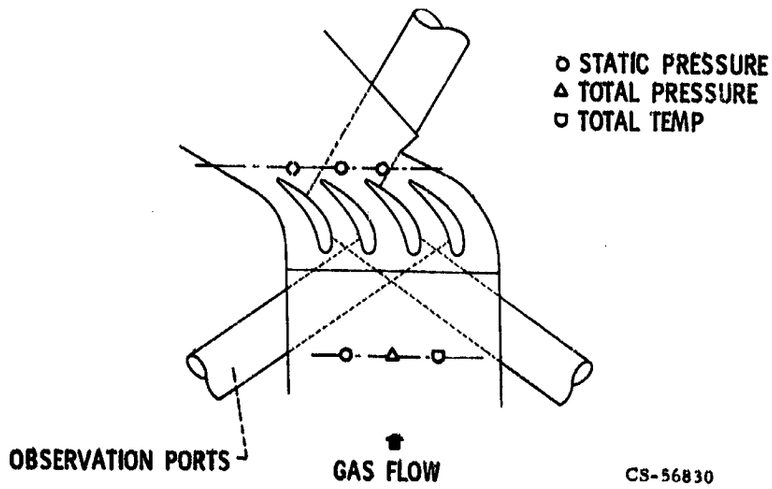

Figure III-8

CASCADE TEST SECTION WITH COVER REMOVED

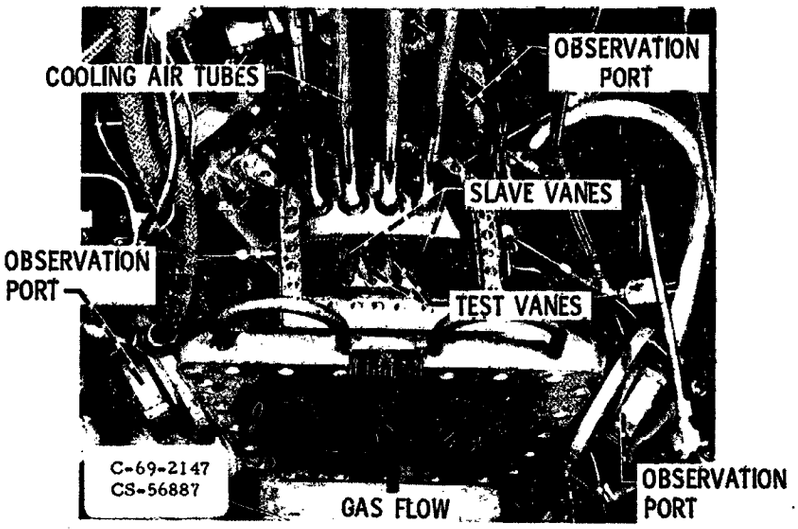

Figure III-9

TEMPERATURE MEASUREMENT BY INFRARED PHOTOGRAPHY

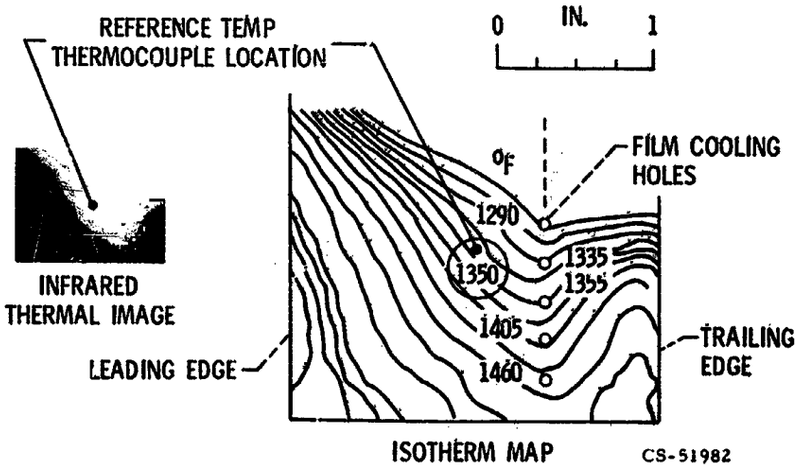

Figure III-10

TURBINE COOLING RESEARCH ENGINE

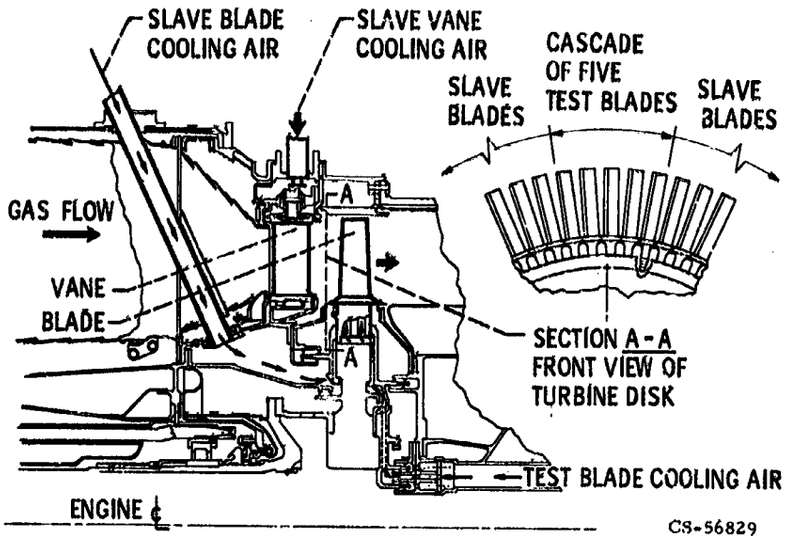

Figure III-11

VIEW OF REAR FACE OF TURBINE

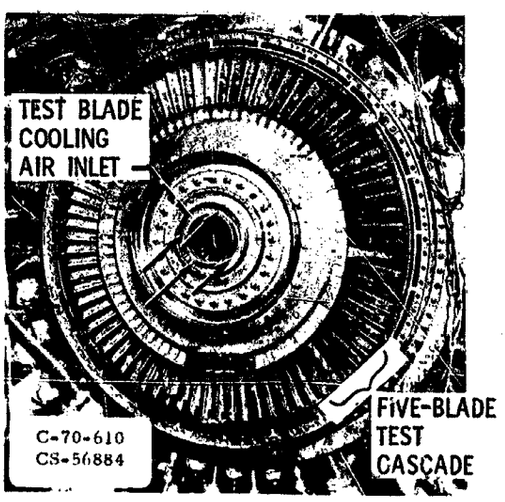

Figure III-12

COMPARISON OF EXPERIMENTAL AND EXTRAPOLATED VANE TEMPERATURES FOR CASCADE TESTS

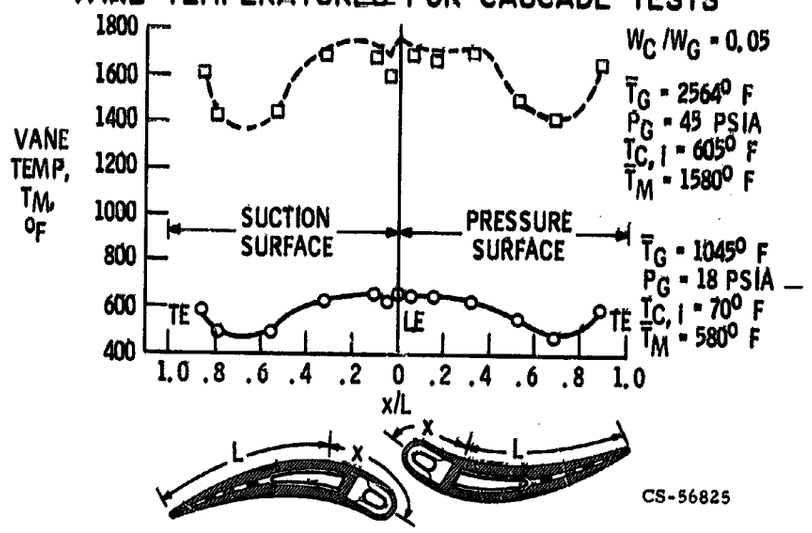

Figure III-13

COMPARISON OF EXPERIMENTAL AND ANALYTICAL VANE TEMPERATURES FOR CASCADE TESTS

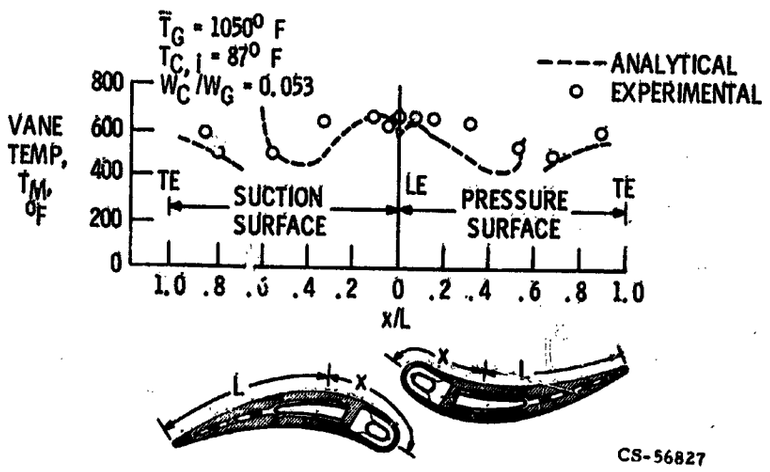

Figure III-14

COMPARISON OF EXPERIMENTAL AND ANALYTICAL VANE TEMPERATURES FOR ENGINE TESTS

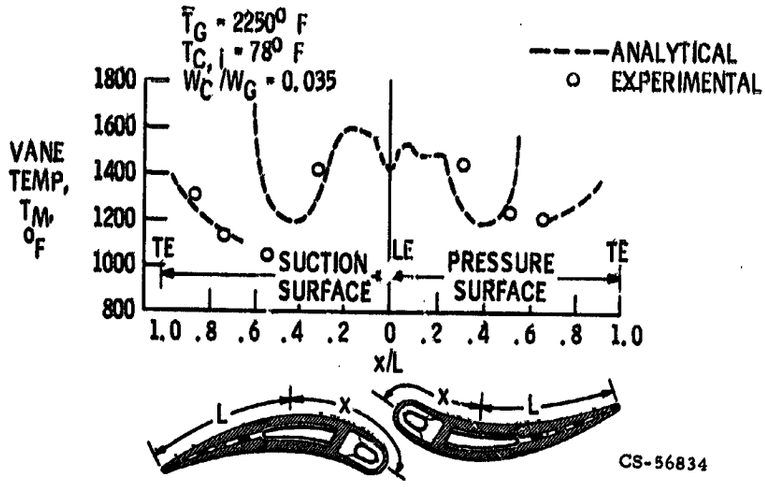

Figure III-15

EXPERIMENTAL COOLING CONCEPTS

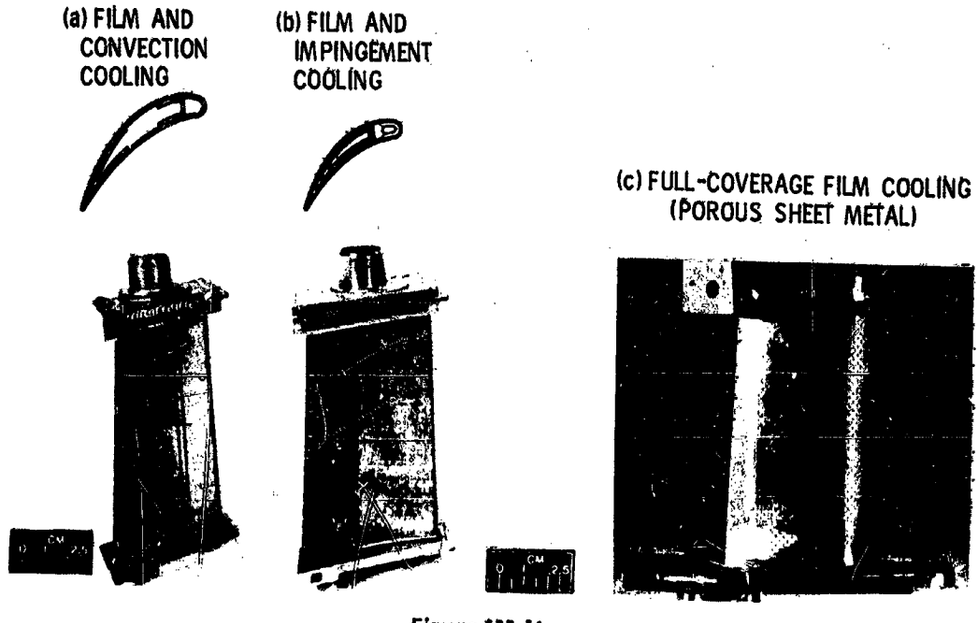

Figure III-16

CS-56883

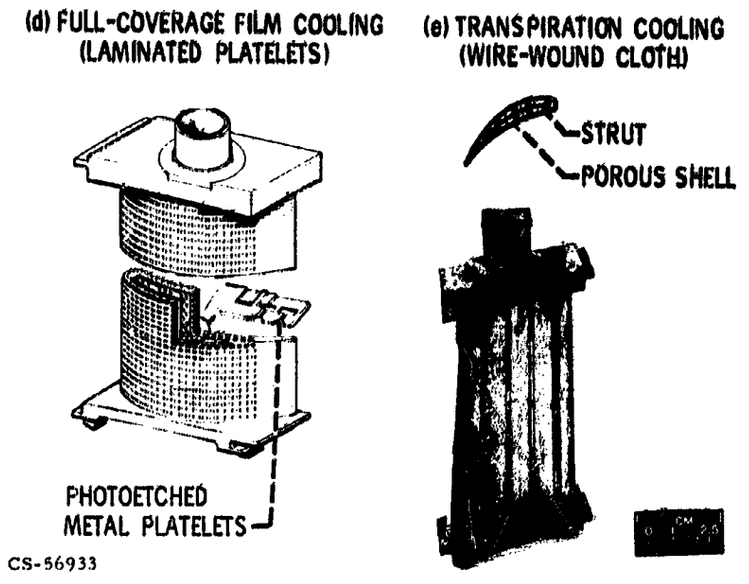

Figure III-16. - Concluded.

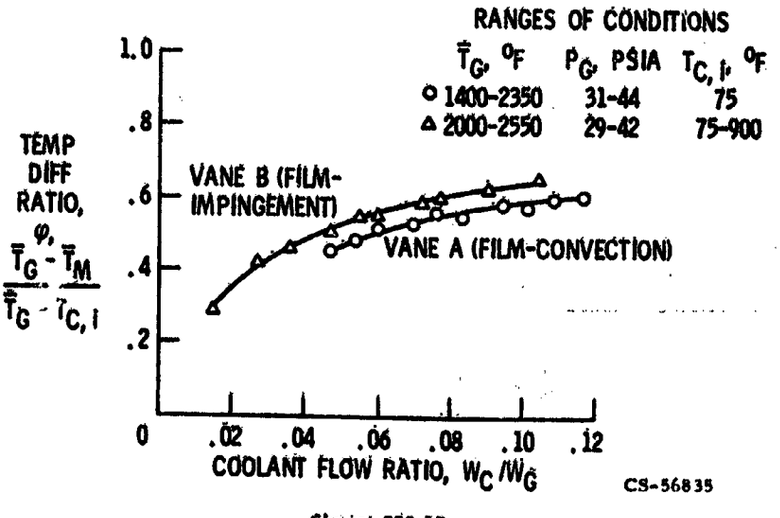

Figure III-17

ALLOWABLE GAS TEMPERATURE AS FUNCTION OF COOLANT FLOW RATIO

$\bar{T}_M = 1800^0$ F; $T_{C,I} = 1000^0$ F

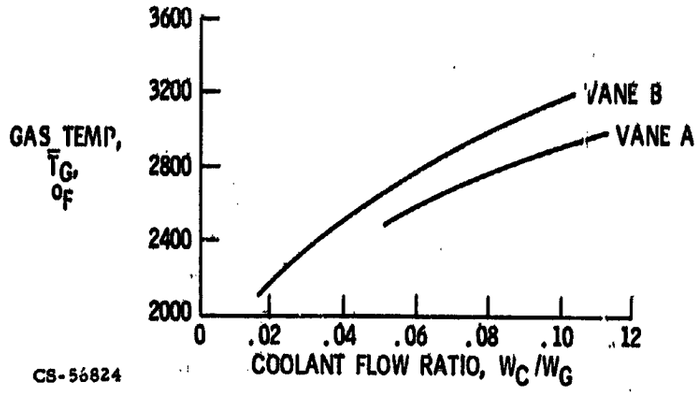

Figure III-18

EFFECT OF OXIDATION ON COOLANT FLOW

WIRE-WOUND TRANSPIRATION COOLING MATERIAL

$T_M = 1800^0$ F

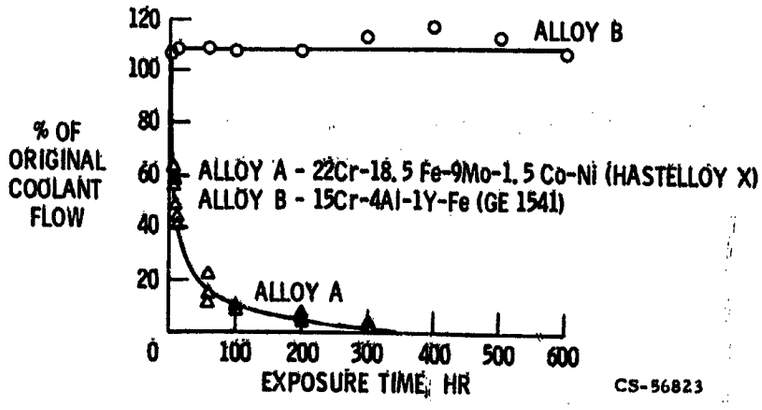

Figure III-19

IV. - COMBUSTION

Jack Grobman, Robert E. Jones, Cecil J. Marek,
and Richard W. Niedzwiecki

The trend toward higher temperatures and pressures in primary combustors has necessitated research on liner cooling and development of shorter combustors to reduce the cooling-air requirements. One experimental short-length combustor has demonstrated efficiency, pressure loss, and pattern factor equal to those of a conventional combustor which is 50 percent longer; further work is needed to improve its altitude relight performance. Another experimental combustor has been operated to an outlet temperature of 3616° F with 100 percent efficiency, low pressure loss, and a pattern factor of 0.11. The experimental short-length combustors produce very little exhaust smoke. Recent tests reveal that one of these combustors emits only one-sixth as much nitric oxide as a conventional combustor; this improvement is attributed to the reduced dwell time in the combustor.

This report reviews some of the present-day requirements for gas turbine combustors and shows how the latest engine operating conditions are affecting the problems in combustor design. The research approaches being used to solve these problems are discussed. By way of review, the various criteria that are used in the design of gas turbine combustors are considered. Combustion efficiency, total-pressure loss, durability, exit temperature profile, and altitude relight are important for obvious reasons. Combustor size and weight are important because they influence the overall weight of the engine. Combustor length affects the turbine shaft length and the bearing requirements. Reducing combustor length also reduces the amount of air required to cool the combustion liner by reducing liner surface area (ref. 1). Minimizing exhaust emissions such as smoke and gaseous pollutants is a relatively new requirement. All these criteria are used as yardsticks as the results of recent NASA Lewis combustor research are discussed.

Figure IV-1 illustrates the trends in combustor operating conditions with time. These data are representative of engines that are either operational or in development. The date indicated for each engine was taken to be at the time of its military qualification test or other qualifying acceptance test. The dates beyond 1970 are dates estimated for engines in the development stage. All data shown are for

sea-level takeoff conditions. It is apparent from this figure that there has been a steady increase in both inlet pressure and inlet temperature in the combustion chamber. The effect is due, of course, to increasing compressor pressure ratios. Also there has been a steady increase in combustor exit temperatures from about 1500° F during the early 1950's to projected values of exit temperature in excess of 2500° F for engines currently in development. The trend to higher combustor exit temperature has, of course, followed the use of turbine cooling and has increased as improvements have been made in turbine materials and cooling methods. Figure IV-1 also shows that there has been no significant increase in reference velocity with time. This is probably due to the fact that combustor pressure drop is a function of reference velocity squared and, in order to maintain good specific fuel consumptions and cycle efficiencies, pressure drop has not been permitted to increase.

Figure IV-2 shows the combustion efficiency of a typical annular combustor. Combustion efficiency is plotted against a correlating parameter made up of inlet pressure, inlet temperature, and reference velocity. The figure shows that combustion efficiency increases as pressure and temperature increase and decreases as combustor velocity increases. It has been mentioned that the use of higher compressor pressure ratios has resulted in increases in both inlet pressure and inlet temperature for the combustor. The use of higher cruise speeds also leads to an increase in combustor inlet pressure and inlet temperature. Typical values of the correlating parameter for sea-level takeoff and cruise of present-day annular combustors fall far to the right of the bend in the curve. Therefore, there are not any significant problems in obtaining good combustion efficiency for takeoff and cruise with present-day combustor designs. This is quite a different situation than 15 years ago, when there was concern about high-altitude subsonic flight using low-compressor-pressure-ratio engines in which low values of combustor inlet temperature and pressure created a problem in obtaining good combustion efficiency.

This paper discusses four main topics of combustor research that have been influenced by recent trends in engine operating conditions and performance requirements. The first section describes the effect of higher pressures and temperatures on liner surface temperatures and the problem of cooling the combustor liner. The second section reviews the results of recent NASA Lewis research on short-length combustors. The third section describes the performance of a short modular combustor designed to operate at near-stoichiometric exit temperatures. The final section discusses the jet aircraft exhaust emissions problem.

LINER COOLING

With the trend towards higher pressures along with higher inlet and exit temperatures, liner temperatures are increasing, thus affecting the durability and life of the liner. The liner temperatures were measured within a combustor to determine the severity of the problem. Shown in the inset of figure IV-3 is a sketch of the combustor. The measurement point was in the primary zone, 1 inch downstream of a cooling slot. The flame temperatures in this zone ranged from 3440° to 3940° F, as measured with a radiometer.

The liner temperature rises proportionately with increases in inlet air temperature, as shown in figure IV-3. The direct dependence on inlet air temperature is caused by both the heat-sink capacity of the air decreasing and the primary zone temperatures increasing. The calculated temperatures show the same trend as the experimental data. The calculated values were adjusted based on the 600° F inlet temperature data to correct for conduction in the wall and for the entrance lengths for the convective coefficients.

Liner cooling is a problem at high inlet air temperatures. When the inlet air temperature reached 1200° F, the liner temperature at the 1-inch-downstream location was 1470° F. Since this is only 1 inch from the film-cooling slot exit, the wall will have approached 1600° F before the next cooling slot at 4 inches downstream. This is the maximum wall temperature that should be used in order to avoid oxidation and loss of strength.

The effect of increasing pressure on radiant output from a flame was obtained within the same combustor and is shown in figure IV-4. The data for combustor A show that the radiation from a flame increases rapidly with pressure. Doubling the pressure doubles the measured radiant output. It might be expected that the liner wall temperatures would increase significantly with pressure due to this increased radiation.

Figure IV-5 shows the liner wall temperature data plotted against increasing pressure for combustor A. The rise in liner temperature is not as great as might be expected from observing the increases in radiation. Doubling the pressure did not double the liner temperatures for the same percentage cooling airflows. This is a result of the increases in convection. The convective rate increases as the density increases at a fixed reference velocity. The calculated values agree well with the experimental data.

From the radiation output curves shown in figure IV-4, it is apparent that there can be a wide variation in radiant output at the same pressure for two simi-

lar combustors. Combustor A has a low smoke output that is well below the visible threshold and that at low pressures approaches the nonluminous values of radiation output. Combustor B is of the same geometry but has a rich primary zone which produces a high carbon-particulate concentration. The radiation level of a smoky combustor at low pressure can be as high as that of a low smoker operating at a 30 to 1 pressure ratio. The effect of this high radiant output is shown in figure IV-6. The calculated results for combustor B show that the increase in radiation due to the carbon particulates in the primary zone produces significant increases in liner temperatures. The only way to remove this added heat is by increases in convection. Note the unusual trend that the liner temperature decreases with increasing pressure. This is due to the fact that at high wall temperatures increases in convection are more effective in lowering liner temperatures. In summary, the cooling problem is not as severe at high pressures as might be expected for clean-burning combustors because the radiation increase with pressure is compensated for by the increases in convection.

With the trend towards higher exit temperatures, cooling-air requirements will increase. This increase in cooling-air temperature will limit the maximum average exit temperature that can be reached, as shown in figure IV-7. With 600° F inlet air the maximum temperature that can be achieved at a stoichiometric fuel-air ratio for ASTM-A1 fuel is 3950° F. If the cooling-air requirement to maintain the wall below 1600° F is as little as 10 percent, the maximum temperature which can be obtained is 3800° F. When the cooling-air requirements are still greater, the maximum average exit temperature will be less. In combustors operating at 2200° F exit temperatures, over 50 percent of the air could be available for cooling. However, if these large amounts were used, poor exit temperature profiles would be obtained. Therefore, the cooling-air requirements should be reduced to a minimum.

The data which have been presented were for one type of slot geometry. In order to optimize the cooling-air requirements, it is important to consider the effect of geometry. Four typical geometries are shown in figure IV-8. In the first configuration, continuous slots of various heights are used, with some small spacers to maintain slot height. A second configuration is slots with metering holes. With this configuration the cooling-air flow is relatively unaffected by warpage of the plate. Another important feature of this slot is that the injection angle is such that the jets impinge on the upper lip and spread to form a continuous film of air. A third configuration uses a wiggle strip, which is placed in the slot to maintain slot height. This also gives the slot rigidity for accurate metering of the air. Of current interest is the use of a channeled wall with extended

surfaces, designed to increase the convective heat transfer. The channeling runs the complete length of the plate, which prevents mixing between the convectively heated air and the annular air.

The first three configurations with various slot heights and hole sizes were studied within a combustor, using film cooling only. All the data are plotted as cooling effectiveness against x/Ms in figure IV-9. The cooling effectiveness is the temperature difference between the hot gas and the wall divided by the maximum temperature difference (the hot gas temperature minus the inlet cooling-air temperature). The conventional film-cooling parameter used is x/Ms, where x is the distance downstream of the slot, s is the slot height, and M is the mass flux ratio of cold gas to hot gas. All the data for 10 different geometries fall on a single curve. Within a combustor there was no significant difference between slot geometries at the same value of x/Ms. Therefore, slot geometry does not seem to be a major parameter which affects film-cooling effectiveness.

There is, however, a large difference between the combustor data and film-cooling correlations published in the literature. When a relatively simple mixing model was used, the difference between the combustor data and literature correlations was a result of the increased turbulence in the combustor. Literature correlations are based on data taken in ducted flows, where the turbulence is low and varies from 1 to 3 percent. The combustor turbulence level was approximately 15 percent. Curves from references 2 to 4 shown in figure IV-9 are typical results of literature correlations.

The solid line passing through the data in figure IV-9 is the predicted curve given for the higher turbulence level. The equation which was used to predict film-cooling effectiveness η is given by

$$\eta = \frac{1}{1 + C_m \frac{x}{Ms}}$$

where C_m is the mixing coefficient and has been set equal to the turbulence level. The increase in turbulence resulted in the literature correlations overpredicting the film-cooling effectiveness by a factor of 5 or more. Other combustors may have a different level of turbulence, which would produce either a higher or lower film-cooling effectiveness. In fact, even within the same combustor, the turbulence level might be expected to vary.

Thus, turbulence is an important parameter in determining the film-cooling effectiveness. One way of reducing the cooling-air requirements would be to

lower the turbulence level in the neighborhood of the wall. Other means are being investigated to increase the effectiveness of the cooling air. For example, the use of reverse cooling flow on the annulus side of the wall would introduce the air further upstream so that it could be used for combustion. A rather simple way to significantly reduce cooling-air requirements is to reduce the surface area which must be cooled by shortening the combustors.

SHORT COMBUSTORS

We are presently studying many ways of shortening the combustor. The following discussion relates the several different approaches being used to obtain a high-performance short combustor and how these approaches differ from the conventional turbojet combustor design.

Figure IV-10 shows how the length of turbojet engine combustors has been dependent on the engine size, as exemplified here by the engine sea-level takeoff airflow rate. Three different types of combustor are compared: the can, the can-annular, and the annular. Annular combustors are becoming the conventional practice, as this design uses the engine volume available for the combustor more efficiently than the other types. The short-combustor program at NASA Lewis assumes a fairly large engine having a takeoff airflow of 280 pounds per second. All the NASA combustors are 20 inches long. By comparison a typical present-day annular combustor of a similar-size engine would be about 30 inches long, or 50 percent longer than the short combustors.

A typical combustor is shown in figure IV-11. This annular combustor has all the features that are common in present-day combustors. A relatively long diffuser is used to diffuse the compressor exit airflow to a high static pressure. Often a snout or flow splitter is used to assist in dividing the diffuser airflow properly. Fuel is injected by a pressure atomizing nozzle and combustion is initiated and stabilized in the primary zone. The remaining airflow is injected into the combustor secondary zone through holes or slots and mixes with the hot gases of the primary zone to complete the combustion reaction and achieve the desired exit temperature profile. The differences between the conventional combustor and the short combustors are noted in the following discussion.

The first short combustor is called the double-annular ram-induction combustor. A cross-sectional sketch of the combustor is shown in figure IV-12. This combustor consists of two concentric combustor annuli; the exhaust of each

annulus blending together in the exit transition region. This combustor has a very short diffuser since the ram-induction concept requires that a high dynamic pressure be maintained at the diffuser exit. Therefore, the diffuser is shorter than those conventionally designed. The airflow is captured by shrouds and ducted into the combustor primary and secondary zones through rows of scoops. Each scoop has turning vanes to minimize the losses in turning a high-velocity airstream. Each annulus of this combustor is conservatively designed in terms of its own length-to-annulus-height ratio. The combustor is effectively shortened by using a double-annulus geometry and the ram-induction concept, which requires high-velocity airstreams and hence a short diffuser. Further details regarding the construction and performance of the double-annular ram-induction combustor can be found in references 5 to 7. Figure IV-13 is a view of the double-annular combustor looking upstream toward the headplate. The scoops are clearly shown, those furthest upstream being the primary zone scoops and those downstream being in the secondary zone. The turning vane in each scoop can also be seen.

Another short combustor presently being investigated is called the one-side-entry combustor. Figure IV-14 is a cross-sectional sketch of this combustor. This combustor is different from the conventional combustor in that all the primary and secondary air is ducted into the combustor from only one side; in this case, the outer-diameter side. This is also a ram-induction combustor, as scoops are used to turn the high-velocity air into the combustor. The requirement to maintain a high dynamic pressure in the airstream (ram-induction approach) shortens the diffuser. The diffuser has also been shortened by being radially extended and overlapping the combustor. A small portion of the air, approximately 10 to 15 percent, is captured by chutes regularly spaced around the diffuser inlet. This air is passed through the swirler around the fuel nozzle in the headplate and is also used to cool the lower liner. This combustor is of particular interest because its exit temperature profile is extremely insensitive to radial airflow profile distortions coming from the compressor. This insensitivity results from all the flow being ducted into the combustor from only one side and that flow being captured by scoops that extend to the full height of the airflow passage. Therefore, regardless of the shape of the radial airflow profile leaving the compressor, the same amount of air is captured by each scoop and turned into the combustor. Thus, the mixing patterns inside the combustor are not changed and the exit radial temperature profile is unchanged. Figure IV-15 is a view of a portion of the side-entry combustor. The slots for the admission of the primary and secondary air can be seen on the outer wall. The segment tests of this combustor are described in reference 8.

The third short combustor being investigated is still more unconventional in design approach. This combustor is the modular swirl-can combustor, which is shown in cross section in figure IV-16. The combustor consists of 120 individual swirl-can modules arranged in three concentric annular rows. The modular combustor has no well-defined primary or secondary zones as in the conventional combustor. Nearly all the airflow, except for that required to cool the liner, passes directly through or around the modules. Each module combines the functions of fuel injection, vaporization, and combustion stabilization. The combustor can be shortened because of the rapid burning and mixing that occurs downstream of each module. The modular approach tends to maximize the area between the hot gases leaving each module and the air flowing around each module. Only a small fraction of the total airflow is required to cool transition liners as they are physically displaced from contact with the hottest combustion gases. Figure IV-17 is a view of this combustor. The inner transition liner has been removed so that the modules can be seen more clearly. The three rows of swirl-can modules can be seen. The inset in the figure is a closeup view of the combustion modules. The combustor is very simple and a minimum of metal is exposed to the flame so that combustor durability should be good. The modules themselves are very simple. Figure IV-18 shows the detailed construction of a typical combustor module. Each module consists of three basic parts: a carburetor, where air and JP fuel are introduced - the air coming through the inlet and the fuel being injected tangentially on the outer wall; a swirler, where the fuel and air are further mixed and a swirl imparted to this mixture; and finally, a flame stabilizer, where the combustion is initiated and maintained. The air flowing around the outside of the module mixes with the hot combustion gases in the wake of each module. There the combustion reaction is completed and mixing of the gases to the desired exit temperature is achieved. Segment tests of this combustor are described in references 9 to 12. The modular concept is not new at Lewis. The swirl can was originally developed in 1956. At that time there was a great deal of interest in buring hydrogen in turbojet combustors and the swirl can was developed as a new combustor concept for that fuel. References 13 to 15 document that work. Figure IV-19 shows one of these early swirl-can combustors. This was a quarter-sector of a combustor used to simulate the performance of a full-annular design. This particular combustor is of interest because it was tested with vaporized JP fuel and demonstrated performance nearly as good as that achieved with hydrogen fuel (ref. 15). That result gave impetus to the belief that a small-diameter combustor module could give good performance using liquid fuel.

Performance tests have been conducted with all three short combustors. The following discussion compares their performance with the performance of a typical annular combustor of this size, which would be about 50 percent longer. The first combustor criterion mentioned in the introductory paragraphs of this section was combustion efficiency. Since these combustors are designed for a modern engine, the combustor operating conditions, at takeoff and cruise for instance, are extremely favorable for efficient combustion. The combustion efficiency of all three short combustors is 100 percent at these conditions. Thus, reducing the combustor length by 33 percent had no effect on combustion efficiency. Figure IV-20 compares the pressure loss of the three short combustors with that of the longer annular combustor. The side-entry and swirl-can combustors have total-pressure losses similar to that of the conventional annular combustor. The double-annular combustor has a much higher pressure loss. This combustor has been redesigned by increasing its open flow area and the pressure losses have been reduced to 4 percent at a diffuser inlet Mach number of 0.25, as shown by the solid square. These test results are for a quarter-sector. Reducing the total-pressure loss caused no change in the other combustor performance parameters. Thus, it appears that short-length combustors can have low pressure losses similar to those of longer length combustors.

Figure IV-21 compares the exit temperature pattern factor of the short combustors. The pattern factor is a measure of the quality of the exit temperature distribution. It is defined as the difference between the maximum local combustor exit temperature and the average combustor exit temperature divided by the average combustor temperature rise. Low values of the pattern factor indicate more uniform temperature distribution. The pattern factor for the typical annular combustor varies between 0.2 and 0.3. The double-annular combustor has demonstrated a pattern factor variation of 0.2 to 0.25. Pattern factor values as low as 0.15 have been achieved in sector tests. The swirl-can combustor and the one-side-entry combustor have pattern factors somewhat higher, indicating that more work needs to be done to improve them. But as is indicated here by the open portions of the bars, both combustors have demonstrated very low pattern factors in previous segment tests. Good pattern factors should also be achievable for these combustors in their annular form.

Another important combustor criterion is that of altitude relight. We are also concerned with combustor blowout, as the combustor blowout limit is the minimum point where relight could ever be achieved. The best relight performis the result of optimizing many variables, such as spark plug position, fuel-air

ratio, and nozzle spray angle. While not ignoring the relight problem, we are devoting more effort to measuring and improving the combustor blowout limits. Figure IV-22 compares the blowout performance of the short combustors with that of the more conventional annular combustor. This is the one area where some of the short combustors have not yet achieved performance similar to that of longer combustors. At a reference Mach number of 0.1, both the double-annular and the swirl-can combustor blow out at pressures considerably higher than the longer annular combustor. The blowout limits of the side-entry combustor are, however, practically identical to those of a longer combustor. The blowout performance of the double-annular and swirl-can combustors should be improved. Many ways of improving the combustor blowout limits are being investigated - for instance, a reduction in combustor reference velocity. Figure IV-23 shows the magnitude of improvement that can be made by reducing the reference Mach number from 0.1 to 0.05 for the double-annular combustor. A reduction in reference Mach number means a reduction in combustor airflow rate. This air might be bled from the engine or bypassed around the combustor. Some form of variable-geometry combustor might also be used. Any such approach would only be needed during an actual in-flight relighting process. Once the combustor was relit, the bleed or bypass flow would be reduced until the combustor was again operating at the proper throughflow condition.

Attempts to improve the blowout limits of the swirl-can combustor are focused on improving the overall combustion stability range of the individual module. In the past, special start fuel nozzles have been used with the prevaporizing type of combustor. These fuel nozzles have also been tested with swirl-can module combustors; they do extend the ground start capability and presumably will also improve altitude relight limits. Because altitude relight is an important combustor design criterion, continuing efforts will be made to improve the relight limits of short combustors.

Another component whose length affects the overall combustor length is the diffuser. In order to realize the full benefit of short-combustor technology, the diffuser length must be kept to a minimum while the same inlet- to exit-area ratio is maintained. The resulting wide-angle diffusers will have flow-separation problems unless special techniques are used to keep the flow attached to the walls. One such technique is the use of boundary-layer bleed.

This air can be drawn out through the walls of the combustor diffuser. The effect this could have on shortening the diffuser is illustrated in figure IV-24. The top sketch is the swirl-can combustor with wedge-shaped inserts to maintain

the proper flow splits. The bottom sketch illustrated how the diffuser might be shortened by using boundary-layer bleed on both walls. In this way, the compressor bleed can be doubly useful by improving diffuser performance as well as by cooling the turbine. As was pointed out in the previous sections of this report, large quantities of compressor bleed may be needed to cool the turbine.

Figure IV-25 shows how small an amount of bleed flow is required to improve the performance of a large-area-ratio short diffuser. Here are results of tests on a two-dimensional diffuser that had an area ratio of 4 to 1. When there was no suction applied to either surface, the diffuser was in jet flow. With only 4.3 percent of the total airflow bled away, there is a very marked lowering of the center velocity and a corresponding increase in flow at the upper and lower walls. Surprisingly, increasing the bleed rate to 7 percent did not produce much more of an improvement. Therefore, some bleed is very beneficial; but the rate, once above some minimum value, is not critical to diffuser performance.

Figure IV-26 shows how the diffuser pressure losses are affected by boundary-layer bleed. Note that the diffuser total-pressure loss decreases as the percent of bleed flow increases. As before, increasing the quantity of bleed flow above some minimum value has a diminishing improvement on diffuser performance. So a small amount of bleed flow is very beneficial and large quantities of bleed air are not required - though the use of large bleed flows is in no way detrimental.

HIGH-EXIT-TEMPERATURE COMBUSTOR

An interesting application of short-combustor technology is the high-exit-temperature combustor research program. The program aim is to evolve full-annular combustors capable of performing with fuel-air ratios approaching stoichiometric values. Initial results have been most encouraging. A swirl-can modular combustor was used to extend good combustor performance to exit temperatures over 3600° F.

A modular combustor design has always appeared to be desirable for engines requiring very high turbine inlet temperatures. However, before undertaking the operation of a combustor at high temperatures, it was first necessary to obtain satisfactory performance levels at lower temperatures. Swirl-can combustors have been investigated for many years at NASA Lewis. The initial work in 1956, (refs. 13 and 14) was conducted with hydrogen fuel. Later work (ref. 15) used vaporized hydrocarbon fuel. The more recent work described in references 9

to 12 was conducted with liquid jet fuel and was devoted to improving the design of swirl-can combustors and extending their operating range to conditions typical of modern engines. Thus, it was only after completing sufficient background work that combustor operation at near-stoichiometric temperatures was attempted.

Figure IV-27 is a schematic of the high-temperature test combustor. It is a modular design quite similar to the swirl-can combustor shown earlier. A modular configuration was selected because of several apparent advantages that modular combustors have for high-exit-temperature applications. These advantages include a near-homogeneous mixture of fuel and air, minimal liner coolant-air flow requirements, and high attainable heat-release rates.

The combustor utilized 120 fuel inlets to produce good mixing of fuel and air. A homogeneous fuel-air mixture is important since stoichiometric burning requires the reaction of all the air with the fuel. For comparison, a conventional combustor design would contain about 30 fuel nozzles.

A minimum amount of air was used for cooling the combustor liners since this air is generally not available for combustion. Film-cooled liner designs were used. The total coolant flow under the liners was set at 6 percent of the total airflow for a combustor exit temperature of 1600° F. Due to increased momentum burning loss, this flow increased to about 8 percent at an exit temperature of 3600° F.

Such relatively small coolant flows could be utilized because of the following combustor features:

(1) The combustor is short, being only 11.4 inches long from the fuel entry plane to the combustor exit. Thus, there was less liner to cool. Also, simple liner designs with minimal surface area were used, since scoops or slots were not required to supply diluent air.

(2) The coolant film was utilized to maximum advantage by reducing the turbulence level at the liners. This occurred since recirculation zones of hot gases were confined in the module wakes and could not wash along the combustor liners. Liners were also extended radially away from the flame streamlines of these wake zones.

(3) Additional coolant air was supplied between the array and the hot-gas side of the liners. Since this air was supplied far upstream, it had ample opportunity to enter into combustion reactions.

Modular combustors are also capable of high-intensity burning, which results in high heat-release rates. The combustor is essentially a pre-mix system, with mixing of fuel and air occurring upstream of the burning zone in the carburetors. And, since nearly all the airflow passes through the array, there

is abundant air available during all stages of the combustion process.

Combustor performance was monitored by over 400 pressure and temperature readings. Average combustor exit temperatures up to 2300° F were measured by a circumferential traverse, five-point probe. Higher exit temperatures were calculated by using a choked nozzle. An iterative calculation using the following equation was employed:

$$\frac{\dot{W}(T)^{1/2}}{PACd(1+da)} = \left(\frac{Kg}{R}\right)^{1/2}\left(\frac{2}{K+1}\right)^{(K+1)/2(K-1)}$$

where

K	specific heat ratio
g	32.174 ft/sec^2
R	53.35 ft-lb/(lb)(°R)
W	total mass flow rate
P	total pressure at nozzle throat
T	total temperature
A	nozzle throat area, 132.50 in.^{2}
Cd(1 + da)	nozzle growth function

The choked nozzle was calibrated with the traversing probe, and a nozzle growth function of $0.985\left[1 + (T_{exit} - T_{ambient})\,(0.018/2500)\right]$ was determined, which produced an area growth of 0.72 percent per 1000° F temperature rise. Effects of the nozzle on test conditions and performance are discussed later in this section.

Figure IV-28 is a view looking upstream into the combustor after a 3600° F run. The inner liner was removed to better illustrate the module array. Modules were clustered in groups of three and held in place by fuel struts. These struts can be seen protruding through the outer combustor housing. Instrumentation leads can also be observed extending from the centerbody and the outer combustor housing.

Combustor module details are shown on figure IV-29. The swirl-can design was modified for these high-temperature tests. The basic components of carburetor and swirler were retained. However the cone flame stabilizers described previously, and shown by the dashed lines on the figure, were replaced by flat

plates. Plates were used to eliminate metal from the burning zone. The circumference of the flame stabilizers was also increased to maximize interfacial mixing area between the hot gases in the module wakes and the air flowing through the array. Sharp edges were retained to induce further turbulence. This hexagonal-plate flame stabilizer is one of several designs that are currently being investigated.

Combustion efficiency is indicated in figure IV-30 by a plot of combustor exit temperature against fuel-air ratio. These data were generated in a single test run of $6\frac{1}{2}$ hours duration. The combustor inlet air temperature was 600° F. Inlet pressure was varied between 3 and 6 atmospheres and airflows were between 49 and 63 pounds per second. A fuel-air ratio span of 0.017 to 0.06 produced an exit temperature span of 1630° to 3616° F. The highest average exit temperature achieved, 3616° F, is only 337 degrees F below the maximum theoretical temperature, which is 3953° F at these conditions. Nearly all the data are within a 2.5-percent span of 100-percent combustion efficiency. The source of the 2.5-percent variation is the choked nozzle calculation. A 1-percent variation in the choked nozzle parameters produces approximately a 2.5-percent deviation in combustion efficiency. The fixed-area choked nozzle also restricted the flow conditions which could be investigated. The reference velocity with 600° F inlet air was 132 feet per second for isothermal conditions, 98 feet per second at 1600° F exit temperature, and 67 feet per second at 3600° F.

Figure IV-31 shows the combustor total-pressure loss as a function of diffuser inlet Mach number for isothermal and burning conditions. Acceptable levels of pressure loss were obtained. A comparison of isothermal pressure loss of this combustor (open circles) with the typical annular combustor described previously (open square) shows comparable pressure loss values. Also presented are burning pressure losses (solid circles) for three combustor exit temperatures corresponding to combustor-exit to -inlet temperature ratios of 2, 3, and 3.85.

The following discussion covers additional results obtained in the high-exit-temperature tests:

(1) Pattern factor: Combustor exit pattern factors were 0.32 at a combustor exit temperature of 2280° F. The traversing probe was not used for higher temperatures. However, pattern factors at higher exit temperatures can be inferred. For example, the pattern factor at 3616° F was 0.112 or less, since the maximum theoretical temperature was only 337 degrees F higher.

(2) Heat release rate: A maximum heat release rate of 13.3×10^{6} Btu per hour per cubic foot of combustor volume per atmosphere was obtained.

(3) Smoke formation: Smoke concentrations at the combustor exit were measured using a stained-filter-paper method. No smoke could be detected for exit temperatures below 3050° F. At 3600° F the smoke level was below the visible threshold.

(4) Resonance: Acoustic resonance or combustion instability was not encountered. Resonance is often a problem in high-temperature combustion systems.

(5) Liner temperature: The maximum liner temperature was 1680° F. This temperature occurred on the inner liner about $1\frac{1}{2}$ inches downstream of the modular array and prevented further increases in combustor exit temperature.

(6) Damage: Some damage occurred to the combustor during the high-temperature run. The damage was minimal and was restricted to five vanes from five different swirlers and to a warped spacer ring between the outer housing and the outer film-cooled liner.

(7) Run times: The sum total of high-temperature run times to date are 4 hours and 50 minutes at exit temperatures over 3000° F and, 1 hour and 26 minutes at average exit temperatures over 3500° F.

A more complete description of these tests is given in reference 16.

The initial results with this combustor have been very encouraging. High exit temperatures have been attained for a full-annular, large-diameter combustor without sacrificing good combustor performance. Reasonable run times were obtained with minimal damage to the combustor. Future work with this combustor will emphasize durability, particularly at higher inlet air temperatures; endurance runs; exhaust emission data; and altitude relight performance.

EXHAUST EMISSIONS

Lately, the concern over air pollution has drawn the attention of the combustor design engineer to the quantities of exhaust emissions contributed by the gas turbine engine. Pollutant emissions may be classified as either particulate matter (i.e., smoke) or as gaseous emissions such as carbon monoxide, partially burned hydrocarbons, and nitric oxide. The first pollutant to come under attack has been exhaust smoke because the smoke trails that are left by jet aircraft on takeoff and landing are an obvious annoyance to the general public. In general, exhaust smoke becomes a problem when combustors operate at pressures greater than 10 atmospheres and when local fuel-air ratios in the primary zone of the

combustor are in excess of an equivalence ratio of 1 (i.e., stoichiometric). These conditions occur during takeoff and approach for landing.

Figure IV-32 illustrates the effect of combustor pressure on smoke number. Smoke number is a parameter related to the density of the exhaust smoke. As the smoke density increases, the smoke number increases. In general, the smoke becomes visible as the smoke number exceeds a value of about 25. The threshold of visible smoke may vary, however, depending on such things as atmospheric conditions, the engine exhaust diameter, and the position from which the smoke is being viewed. The data shown for a J-57 combustor are typical of earlier combustors, which were purposely designed with rich primary zones to enhance the altitude relight characteristics of the engine. Smoke number is shown to increase rapidly with increasing pressure. These data were obtained from a single J-57 combustor operating at an inlet temperature of 600° F, a fuel-air ratio of 0.013, and a reference velocity of 54 feet per second.

More recently, Pratt & Whitney Aircraft has been able to reduce the smoke number for the JT8D engine from a value of about 60 to a value below the visible threshold of smoke. This was done by altering the primary zone design for this combustor. Similarly, more recent engines, such as the CF6 and JT9D, have been designed with smoke numbers that are well below the visible threshold of smoke.

The short-length, double-annulus combustor and swirl-can combustor which were described previously were shown to have an extremely low smoke number at a pressure of about 6 atmospheres. Data at higher pressures are not available for these two configurations; however, we expect that their smoke number at higher pressures will remain below the threshold of visible smoke. Combustors A and B are two experimental segment combustors that were designed to have increased primary zone airflow and increased mixing intensity. The difference in smoke number between combustors A and B is due to a difference in primary zone airflow. Combustor A, which has an extremely low smoke number in relation to the other combustors shown on the curve, does not have a satisfactory altitude relight capability, and further work would be required to improve its relight capability.

A recent survey (ref. 17) has indicated that the contribution to the overall urban air pollution problem by jet aircraft amounts to less than 1 percent compared to other contributors, such as the automobile and stationary power sources. However, its contribution to the local pollution in the vicinity of the airport can be significant. The gaseous emission level for a typical turbofan engine is compared to that of an automobile engine in the following table:

Engine	Operating mode	Emission index, lb/1000 lb of fuel		
		CO	Hydrocarbon	NO
Turbofan	Idle	50 to 174	10 to 75	2.0
	Approach	7 to 9	1 to 16	2.7
	Takeoff	0.7 to 1.2	0.1 to 0.6	4.3
Automobile	Overall average	104	10	18

The data shown for the turbofan were obtained from reference 17 and are representative of engines such as the JT3D and JT8D. The data presented for the automobile are representative of an automobile that meets the 1970 Federal standard for hydrocarbons and carbon monoxide emissions and the 1971 standard for nitrogen oxide emission. The automobile data were calculated from the Federal standards, which are expressed in grams per vehicle mile, by assuming an average mileage of 12 miles per gallon. Three different operating modes are listed for the turbofan engine: idle, approach, and takeoff. An overall average mode is shown for the automobile. The exhaust emission level is expressed in terms of pounds of pollutant per thousand pounds of fuel burned.

The table indicates that the greatest quantity of carbon monoxide and unburned hydrocarbons produced by the turbofan occur during idle conditions, while the quantity of carbon monoxide and unburned hydrocarbon emissions at approach and takeoff conditions are relatively small. The nitric oxide emission level produced by the turbofan is largest at takeoff, but even here the maximum value is approximately one-quarter of that for the automobile. For the present, the most significant pollution from jet aircraft occurs in the vicinity of the airport due to the large emissions of carbon monoxide and unburned hydrocarbons during operation at idle. In the future, the relative contribution by jet aircraft to the overall urban pollution problem may become more significant as air traffic increases and as emission controls are applied to the automobile and to industry.

Figure IV-33 illustrates the effect of combustor operating conditions on the exhaust emission level for a typical gas turbine combustor. The data shown were obtained from a single J-57 combustion liner. The exhaust emission level in ppm is plotted against a correlating parameter (described previously) which contains

inlet pressure, inlet temperature, and reference velocity. Data were obtained for a range of inlet pressure of 1 to 20 atmospheres, a range of inlet temperatures of 80° to 600° F, and a range of reference velocities of 25 to 150 feet per second. The values shown for the partially burned hydrocarbons are expressed as the total amount of organic carbon in ppm carbon. The exhaust emissions for the unburned hydrocarbons and carbon monoxide are shown to increase as the value for the correlating parameter is reduced. Plotted on the same figure is a curve for combustion efficiency against the correlating parameter. As shown in figure IV-2, as the value of the correlating parameter decreased, the combustion efficiency decreased. The increase in the carbon monoxide and unburned hydrocarbon emission level is directly proportional to the decrease in combustion efficiency. The data shown are for a fixed fuel-air ratio of 0.013. At lower fuel-air ratios, the drop in combustion efficiency and the increase in carbon monoxide and hydrocarbon emissions become even greater. At idle conditions, the value of PT/V is low. This factor, combined with a value of fuel-air ratio lower than that shown in the figure leads to lower combustion efficiency and causes even higher hydrocarbon and carbon monoxide emission levels. At high values of the correlating parameter such as occur at takeoff and cruise, combustion efficiency is high and the emission of hydrocarbon and carbon monoxide levels off and is at a minimum.

Nitric oxide is formed during any combustion process involving air. The amount of nitric oxide formed is a function of flame temperature and dwell time. The flame temperature increases as the combustor inlet temperature increases and as the primary zone fuel-air ratio approaches a stoichiometric value. Dwell time is affected by combustor length and velocity. For the range of data shown, the nitric oxide emission level gradually increases and levels off as the correlating parameter is increased. The variation in nitric oxide level that is shown is mainly attributed to increasing inlet temperatures and to reductions in reference velocity, which lead to increased residence time.

Nitric oxide emission levels have recently been measured in the high-temperature modular combustor that was described in the previous section. These data are shown in figure IV-34. The nitric oxide concentration plotted on the ordinate is expressed in ppm on the left ordinate and in terms of an emission index in pounds of nitric oxide per thousand pounds of fuel on the right ordinate. Data were obtained for an inlet temperature of 600° F and a range of combustor exit temperatures from about 1600° to 3600° F. The emission level is 10 ppm at an exit temperature of 1600° F. The concentration increases and levels off to a value of about 100 ppm at 3600° F. Similarly, the nitric oxide emission index increases from a value of about 0.5 pound per thousand pounds of fuel burned at

1600° F to a peak value of about 2.9 pounds per thousand pounds of fuel at 2400° F and then decreases and approaches a value of about 1.9 pounds per thousand pounds of fuel at 3600° F. The curve for the emission index is different than that for the emission expressed in ppm since it is affected by the increasing fuel-air ratio, which approaches stoichiometric as temperature increases. A reference data point shown for a conventional J-57 combustor on the same figure has a value of about 60 ppm at about 1600° F compared to the value of 10 ppm for the modular combustor. The lower nitric oxide emission level for the modular combustor is attributed to reduced residence time.

The approaches to reducing jet aircraft exhaust emissions may be summarized as follows:

(1) The elimination of visible smoke is obtained by improving primary zone fuel-air mixing and avoiding fuel-rich regions in the primary zone. However, smoke number has been shown to increase with pressure and the trend to higher operating pressures makes the problem more difficult. Furthermore, methods used to reduce smoke must not sacrifice the altitude relight capability of the aircraft.

(2) Carbon monoxide and unburned hydrocarbon emissions appear to be mainly a problem in the vicinity of the airport during idle operation. As has been shown, the emission level for carbon monoxide and unburned hydrocarbons can be reduced by improving combustion efficiency. One way of doing this is to reduce the number of fuel entry points during idle operation in order to improve fuel atomization and to optimize the local fuel-air ratio in the primary zone.

(3) The trend to higher inlet and exit temperatures tends to increase the amount of nitric oxide formed. It appears, however, that nitric oxide emission can be reduced by minimizing combustion residence time, as has been done in the high-temperature modular combustor.

Work on the emissions problem is just beginning. These approaches are not necessarily final solutions, but merely indicate possible directions to take in eliminating the problem.

CONCLUDING REMARKS

There are four major achievements of the short-combustor-technology programs. We have shown that combustors for aircraft turbine engines can be built that should have the same performance as combustors that are 50 percent longer. The short combustors have performance similar to the longer combustors in

nearly all respects except for altitude relight. This program is continuing with increased emphasis on improving the altitude relight performance of these combustors.

One of the short combustors, the modular swirl-can combustor, was operated to give turbine inlet temperatures as high as 3600° F. Performance of this combustor was very good; however, much additional work will be required to obtain satisfactory durability at high inlet air temperatures.

The lack of visible smoke has been one of the outstanding characteristics of the short combustors. This is due in part to the relatively lean fuel-air ratio and the very high intensity of turbulence in the primary zones of these combustors. Finally, we have shown that a reduced level of nitric oxide emissions may be obtained by reducing the residence time in the combustor. While these results must still be considered preliminary, control of nitric oxide emissions even at very high turbine inlet temperatures should not be difficult to obtain.

REFERENCES

1. Roudebush, William H.: State of the Art in Short Combustors. Presented at the Sixth Congress of the International Council of the Aeronautical Sciences, Munich, Germany, Sept. 9-13, 1968.

2. Eckert, E. R. G.; and Birkebak, R. C.: The Effects of Slot Geometry on Film Cooling. Heat Transfer Thermodynamics and Education. H. A. Johnson, ed., McGraw-Hill Book Co., Inc., 1964, pp. 150-163.

3. Stollery, J. L.; and El-Ehwany, A. A. M.: A Note on the Use of a Boundary-Layer Model for Correlating Film-Cooling Data. Int. J. Heat Mass Transfer, vol. 8, no. 1, Jan. 1965, pp. 55-65.

4. Hatch, James E.; and Papell, S. Stephen: Use of A Theoretical Flow Model to Correlate Data for Film Cooling or Heating an Adiabatic Wall by Tangential Injection of Gases of Different Fluid Properties. NASA TN D-130, 1959.

5. Perkins, Porter J.: Comparison of Test Results form a 90° Sector and a Full Annulus Advanced Turbojet Combustor. NASA TM X-52707, 1969.

6. Kitts, D. L.: Development of a Short-Length Turbojet Combustor. Rep. PWA-FR-2433, Pratt & Whitney Aircraft (NASA CR-54560), Mar. 18, 1968.

7. Clements, T. R.: A 90-Degree Sector Development of a Short Length Combustor for a Supersonic Cruise Turbofan Engine. Rep. PWA-FR-3790, Pratt & Whitney Aircraft (NASA CR-72734), Aug. 6, 1970.

8. Humenik, Francis M.: Performance of a Short Length Turbojet Combustor Insensitive to Radial Distortion of Inlet Airflow. NASA TN D-5570, 1970.

9. Butze, Helmut F.; Trout, Arthur M.; and Moyer, Harry M.: Performance of Swirl-Can Turbojet Combustors at Simulated Supersonic Combustor-Inlet Conditions. NASA TN D-4996, 1969.

10. Niedzwiecki, Richard W.; and Jones, Robert E.: Combustion Stability of Single Swirl-Can Combustor Modules Using ASTM-A1 Liquid Fuel. NASA TN D-5436, 1969.

11. Niedzwiecki, Richard W.; and Moyer, Harry M.: Performance of a 48-Module, Swirl-Can Turbojet Combustor Segment at High Temperatures Using ASTM-A1 Fuel. NASA TN D-5597, 1969.

12. Niedzwiecki, Richard W.: Preliminary Tests of a Simplified Modular Turbojet Combustor. NASA TN D-5688, 1970.

13. Rayle, Warren D.; Jones, Robert E.; and Friedman, Robert F.: Experimental Evaluation of "Swirl-Can" Elements for Hydrogen-Fuel Combustors. NACA RM E57C18, 1957.

14. Jones, Robert E.; and Rayle, Warren D.: Performance of Five Short Multielement Turbojet Combustors for Hydrogen Fuel in Quarter-Annulus Duct. NACA RM E58D15, 1958.

15. Jones, Robert E.; and Pawlik, Eugene V.: A Preliminary Investigation of the Performance of a Short-Length Turbojet Combustor Using Vaporized Hydrocarbon Fuels. NACA RM E57J03, 1958.

16. Niedzwiecki, Richard W.; Juhasz, Albert J.; and Anderson, David N.: Performance of a Swirl-Can Primary Combustor to Outlet Temperatures of 3600° F (2256 K). NASA TM X-52902, 1970.

17. Anon.: Nature and Control of Aircraft Engine Exhaust Emissions. Rep. No. 1134-1, Northern Res. and Eng. Corp., Nov. 1968.

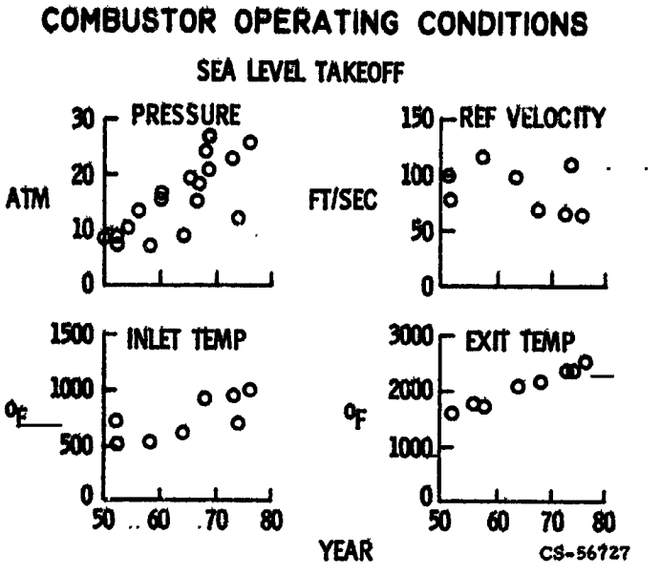

Figure IV-1

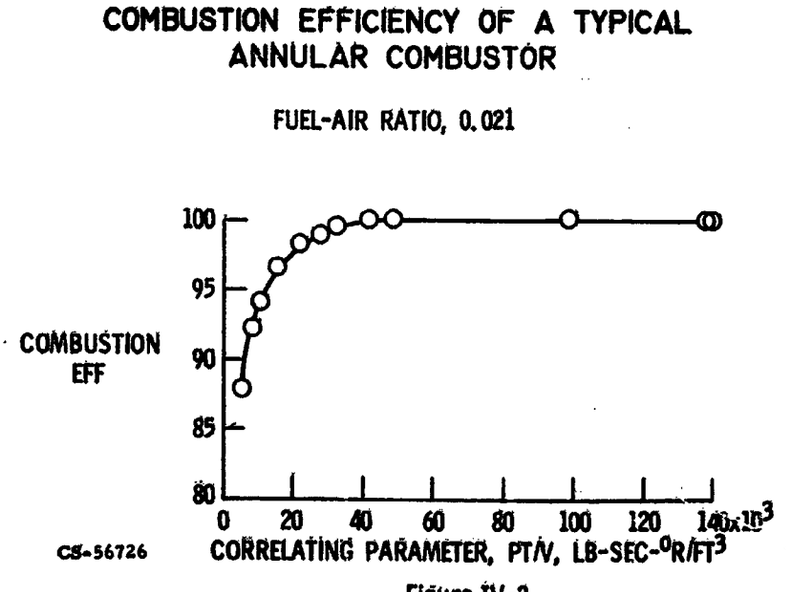

Figure IV-2

EFFECT OF COMBUSTOR INLET AIR TEMPERATURE ON LINER TEMPERATURE

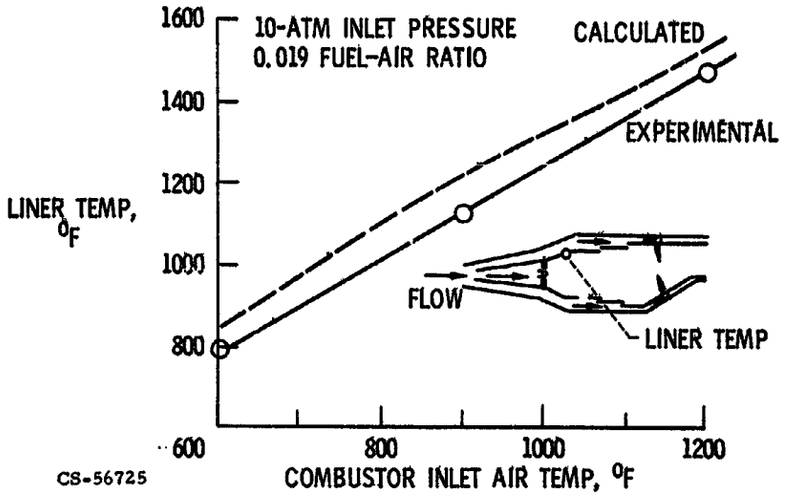

Figure IV-3

EFFECT OF PRESSURE ON TOTAL RADIATION

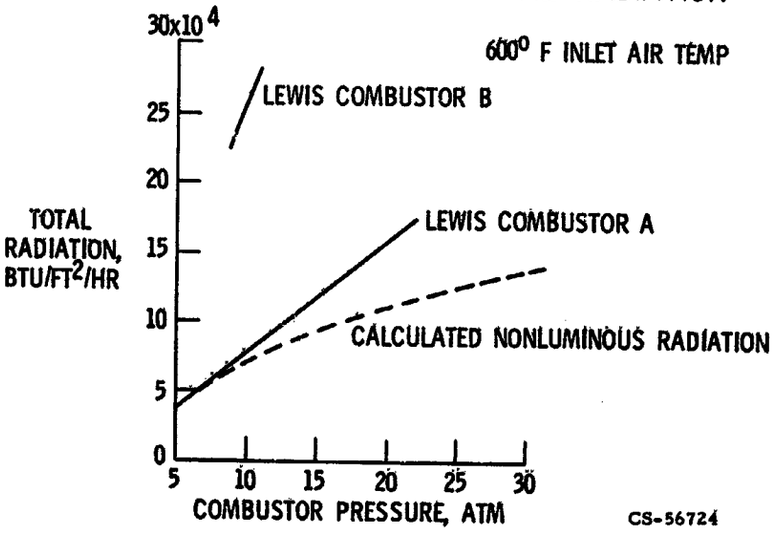

Figure IV-4

EFFECT OF COMBUSTOR PRESSURE ON LINER TEMPERATURE

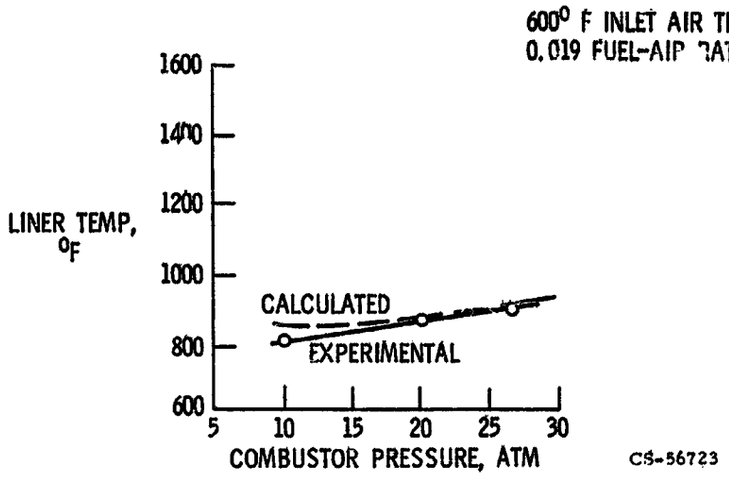

Figure IV-5

EFFECT OF COMBUSTOR PRESSURE ON LINER TEMPERATURE

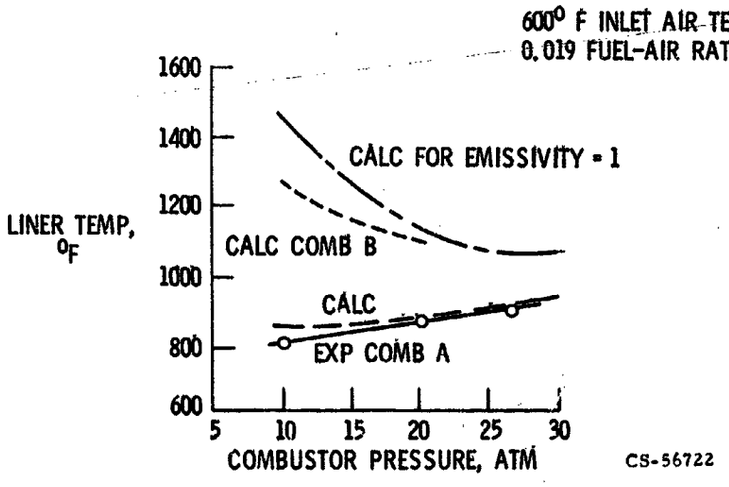

Figure IV-6

EFFECT OF COOLING AIR ON EXIT TEMPERATURE

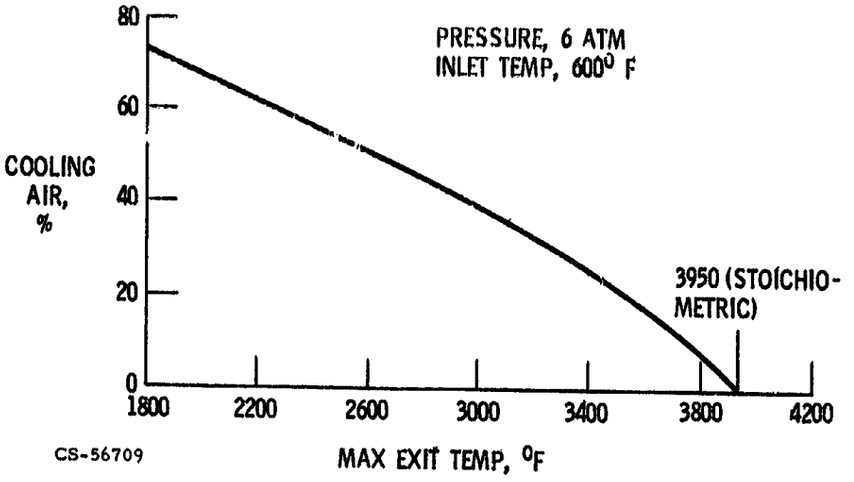

Figure IV-7

COOLING SLOT GEOMETRIES

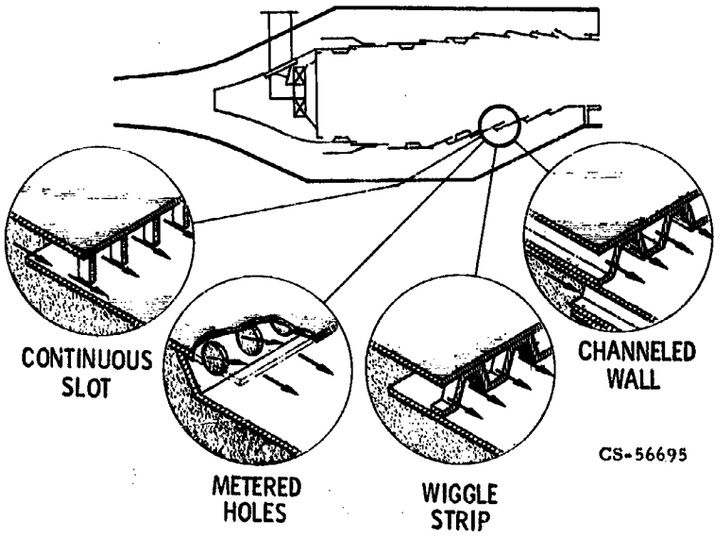

Figure IV-8

COOLING EFFECTIVENESS IN COMBUSTORS

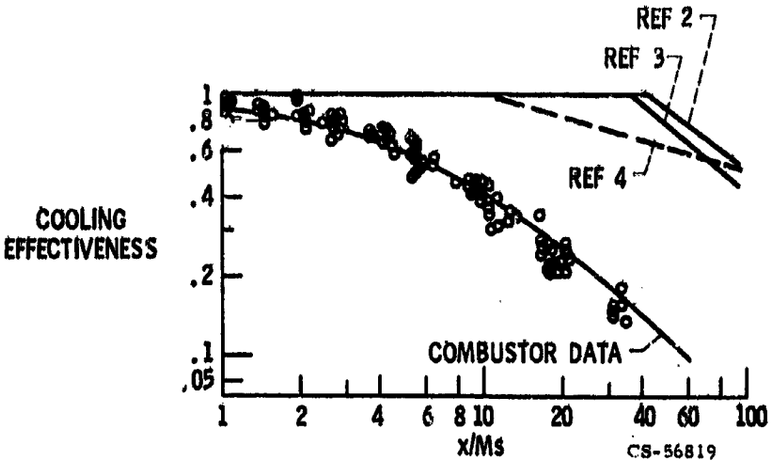

Figure IV-9

COMBUSTOR LENGTH AS FUNCTION OF AIRFLOW

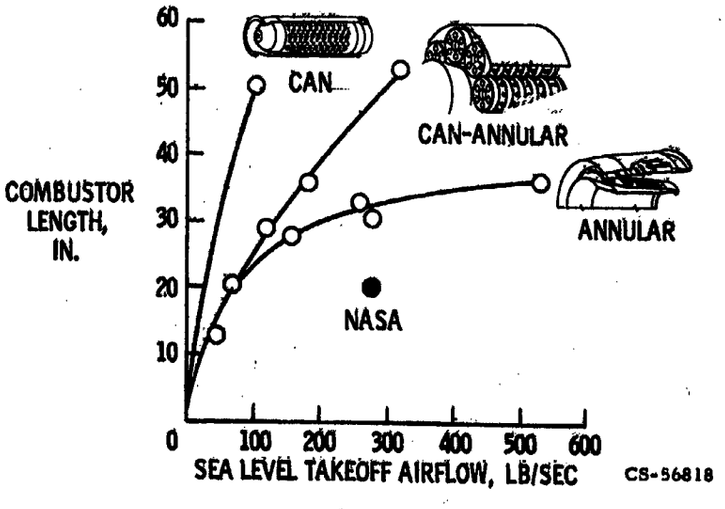

Figure IV-10

CONVENTIONAL ANNULAR COMBUSTOR

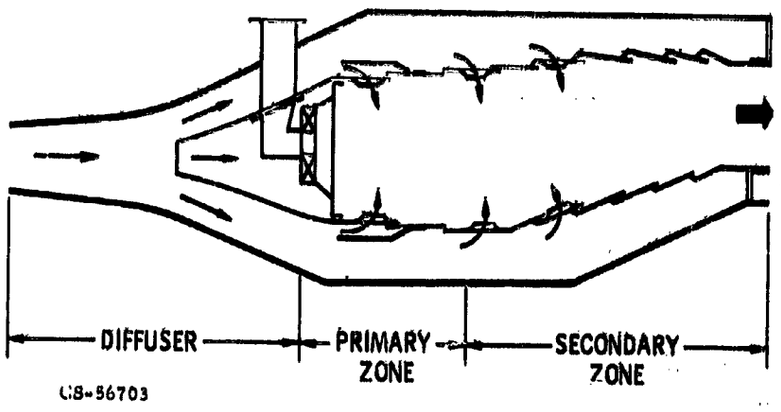

Figure IV-11

CROSS-SECTIONAL SKETCH OF DOUBLE-ANNULAR COMBUSTOR

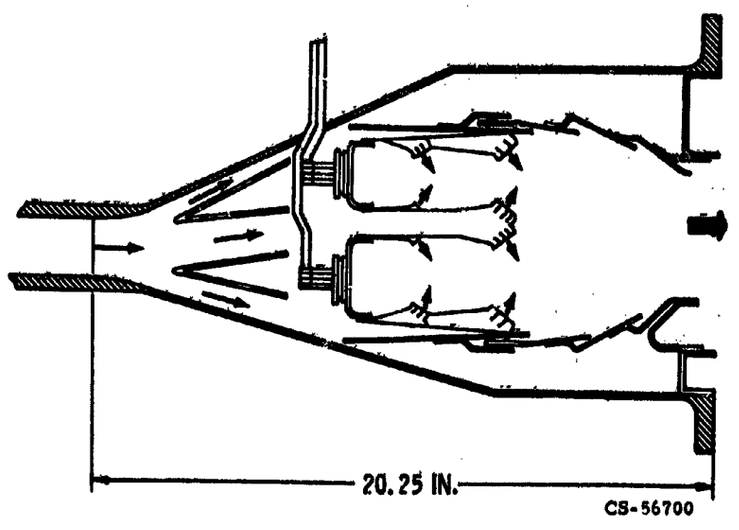

Figure IV-12

DOUBLE-ANNULAR COMBUSTOR,
VIEW LOOKING UPSTREAM

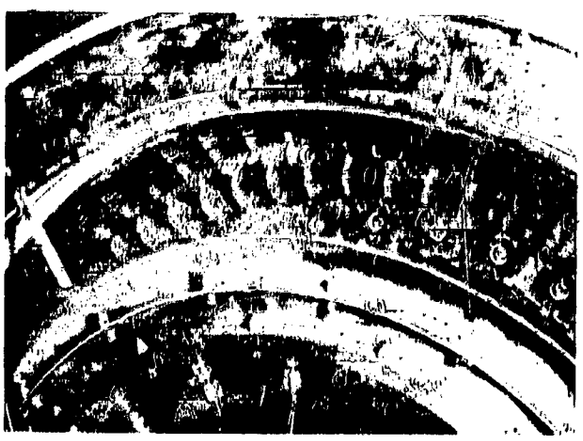

C-68-4334
CS-56730

Figure IV-13

CROSS-SECTIONAL SKETCH OF
ONE-SIDE-ENTRY COMBUSTOR

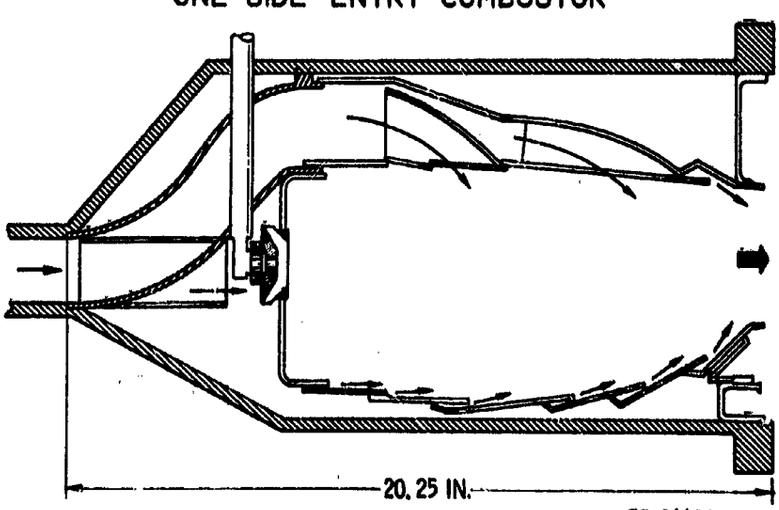

CS-56699

Figure IV-14

ONE-SIDE-ENTRY COMBUSTOR,
VIEW LOOKING UPSTREAM

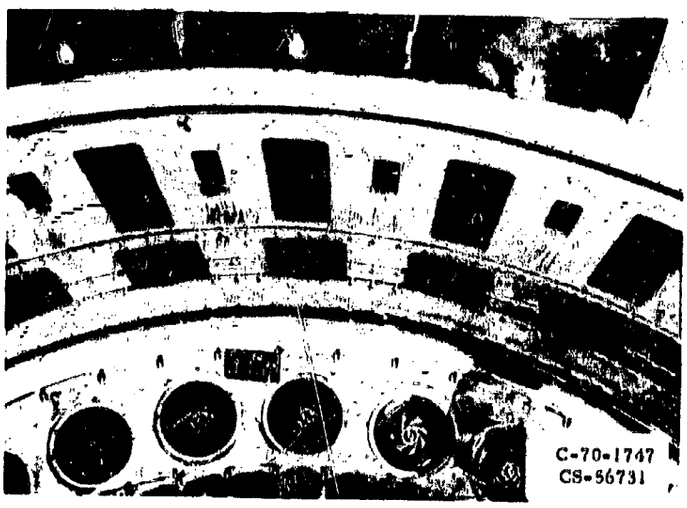

Figure IV-15

CROSS-SECTIONAL SKETCH OF
SWIRL-CAN COMBUSTOR

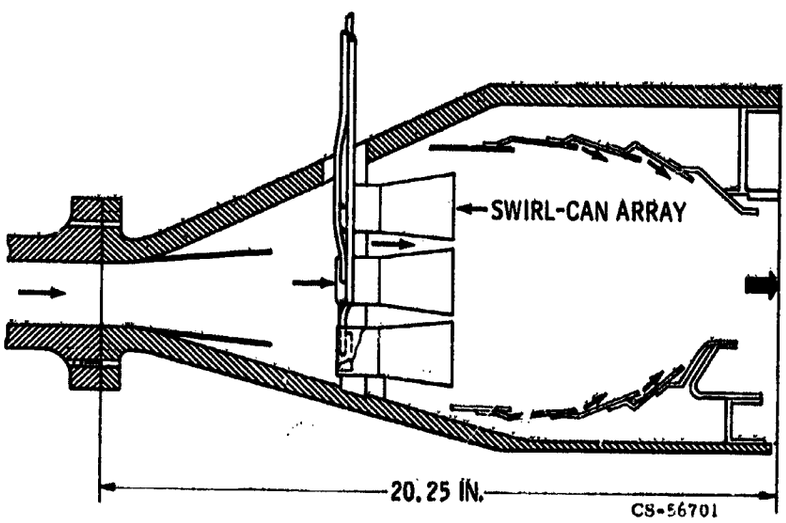

Figure IV-16

SWIRL-CAN COMBUSTOR,
VIEW LOOKING UPSTREAM

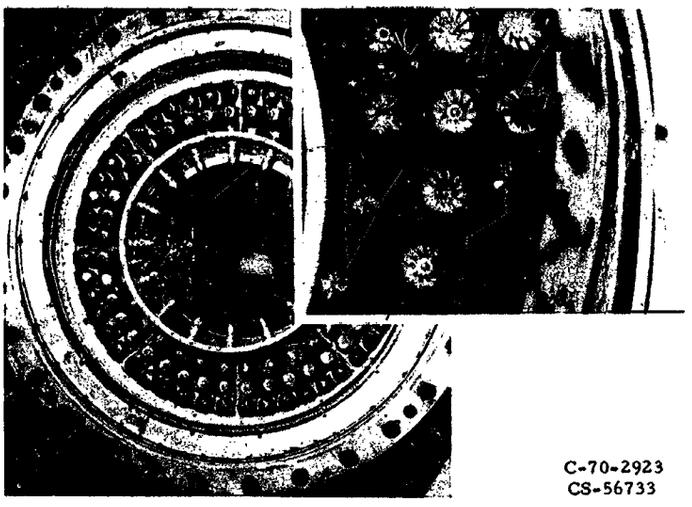

C-70-2923
CS-56733

Figure IV-17

SWIRL-CAN MODULE

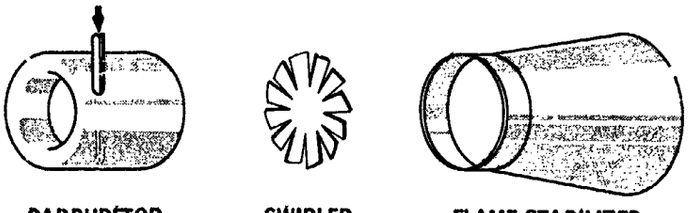

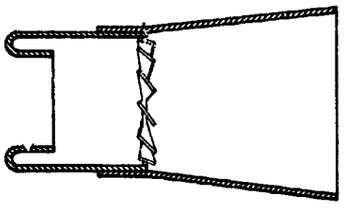

CS-56697

Figure IV-18

1956 SWIRL-CAN COMBUSTOR

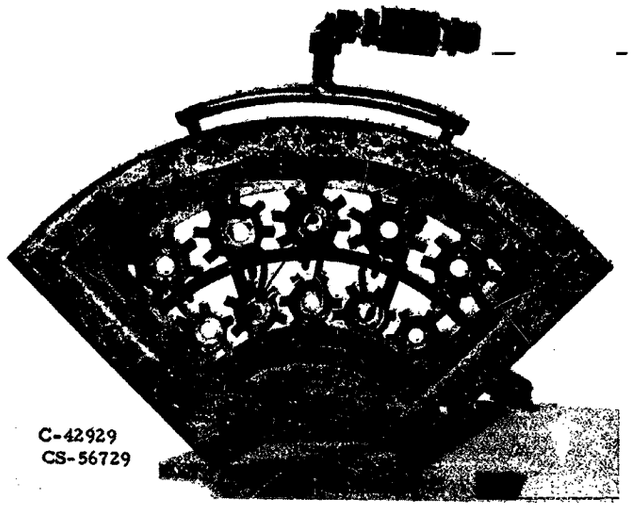

Figure IV-19

TOTAL PRESSURE LOSS COMPARISON

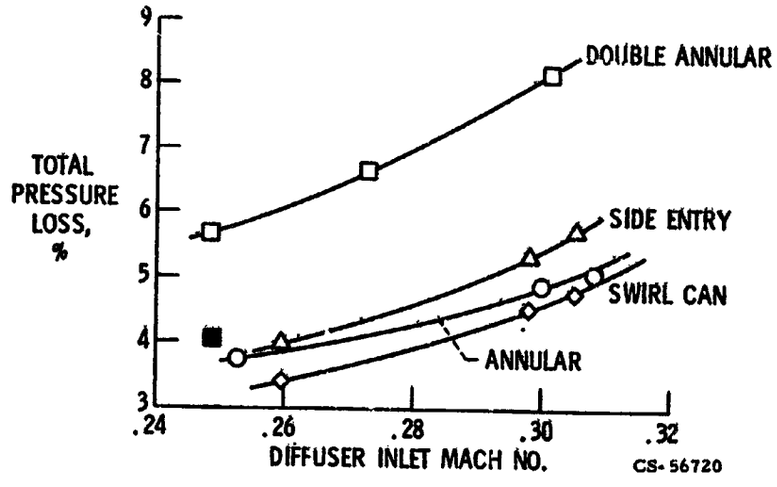

Figure IV-20

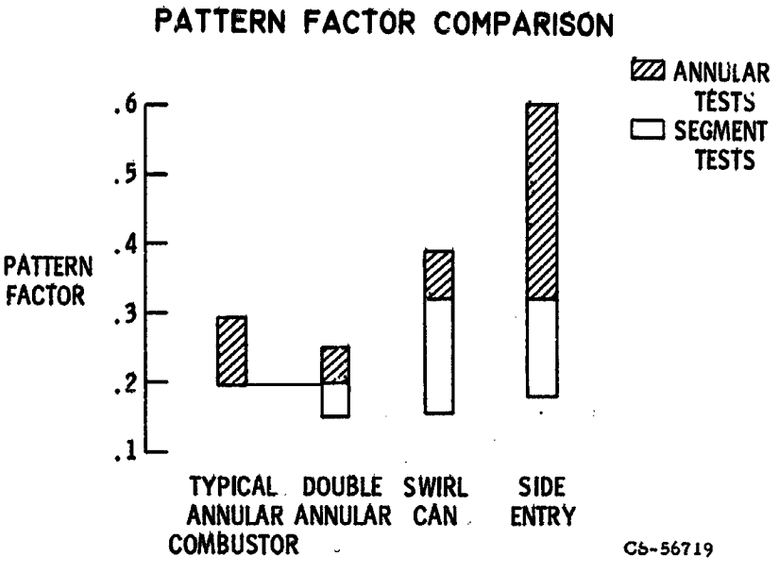

Figure IV-21

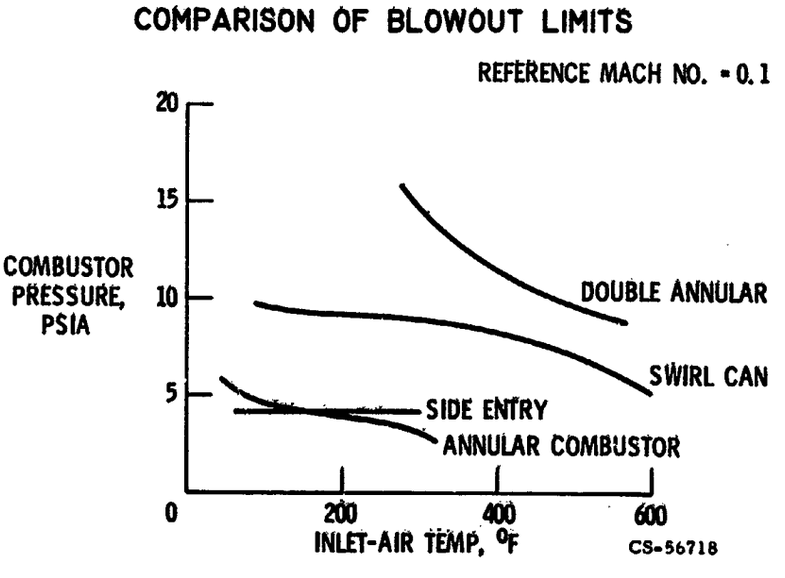

Figure IV-22

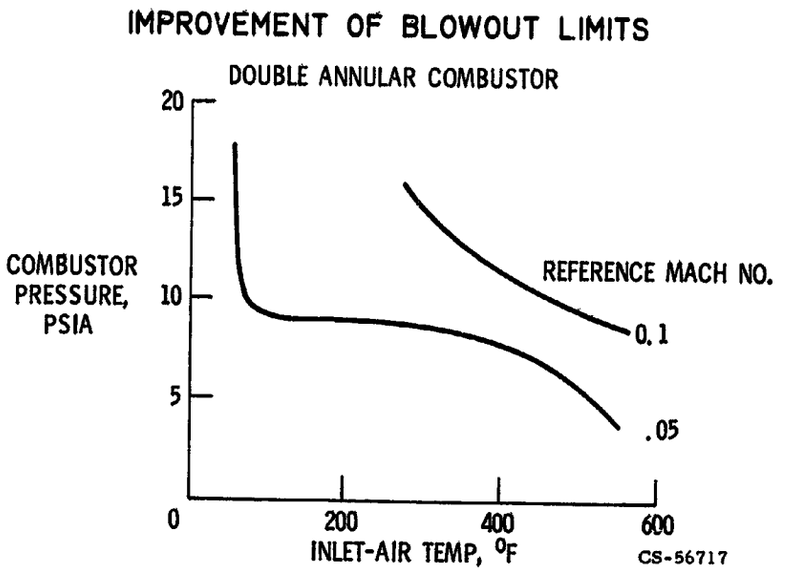

Figure IV-23

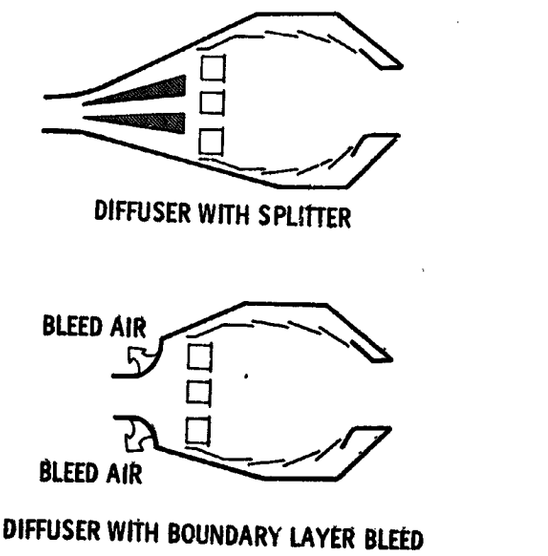

Figure IV-24

SHORT DIFFUSER VELOCITY PROFILES

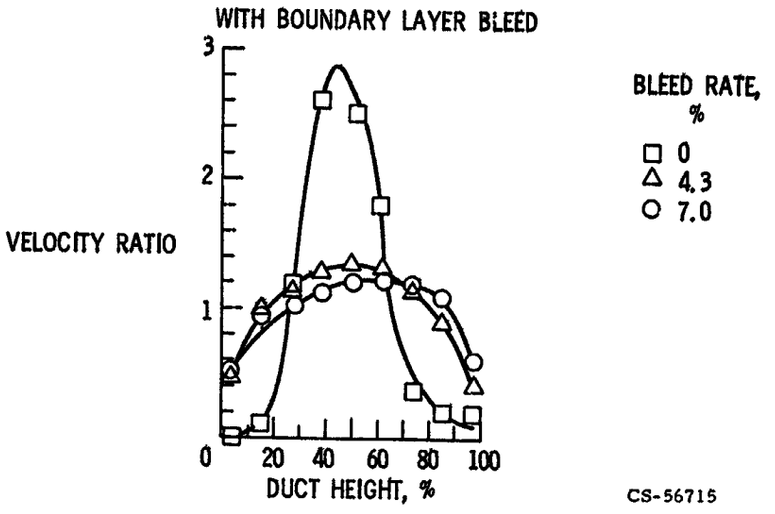

Figure IV-25

DIFFUSER TOTAL PRESSURE LOSS

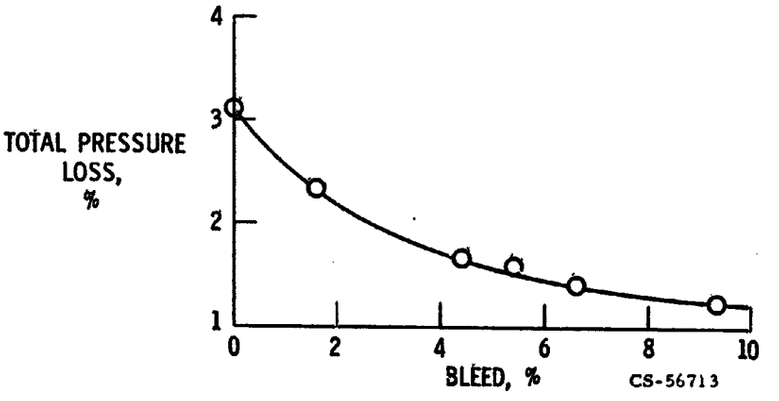

Figure IV-26

HIGH TEMPERATURE COMBUSTOR

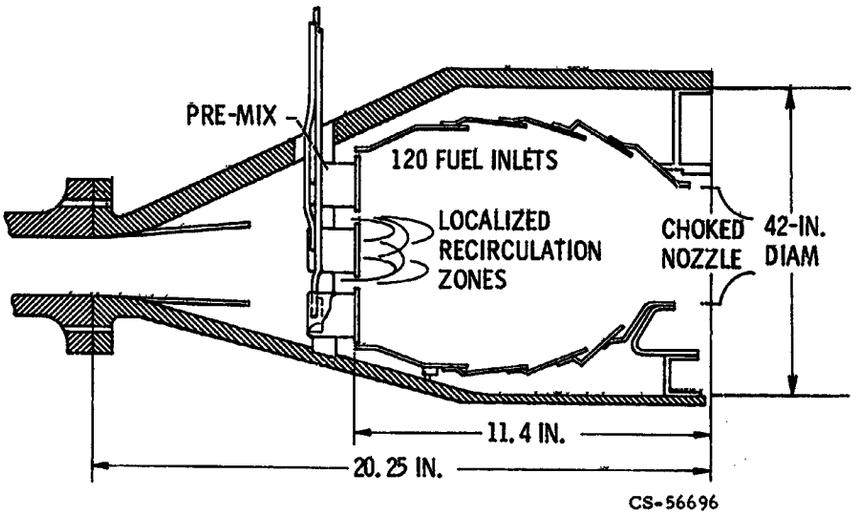

Figure IV-27

HIGH TEMPERATURE COMBUSTOR
AFTER 3600° F TEST

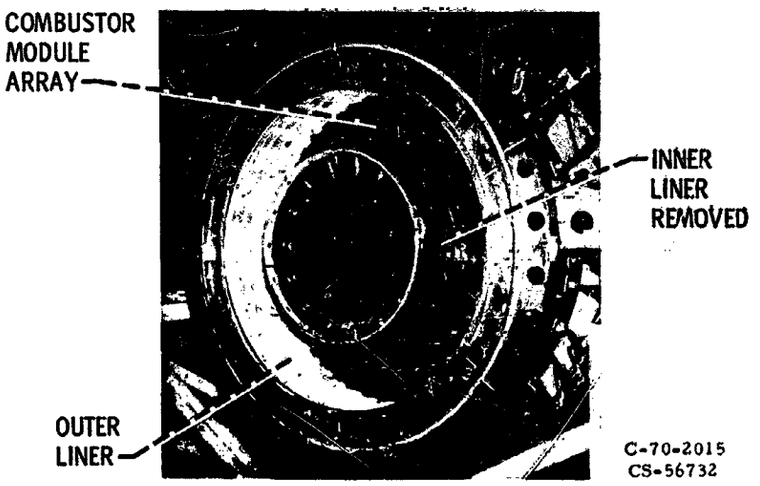

Figure IV-28

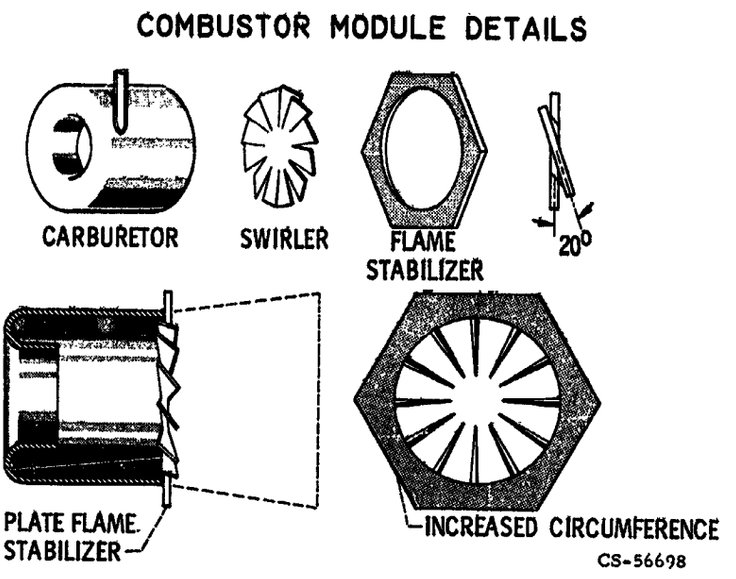

Figure IV-29

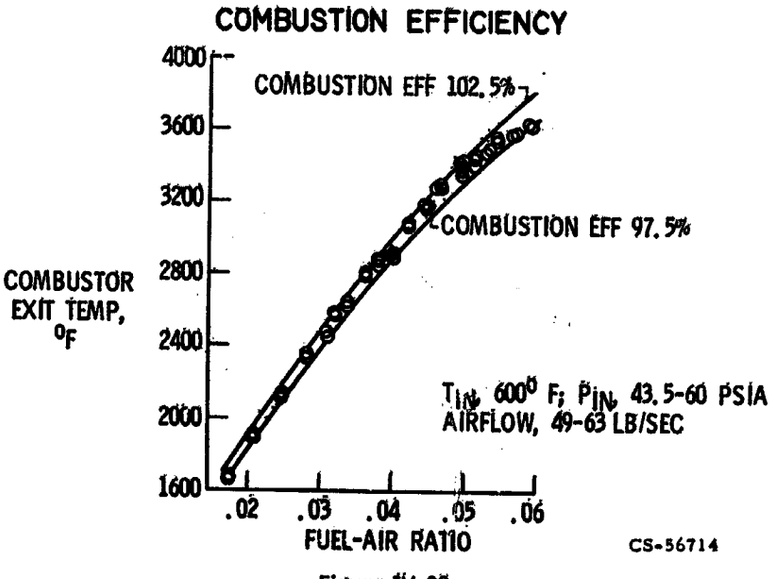

Figure IV-30

COMBUSTOR PRESSURE LOSS

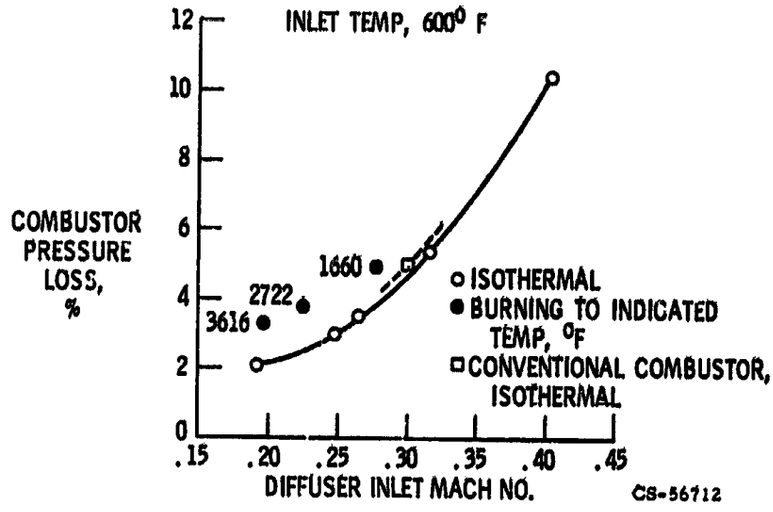

Figure IV-31

EFFECT OF COMBUSTOR PRESSURE ON SMOKE

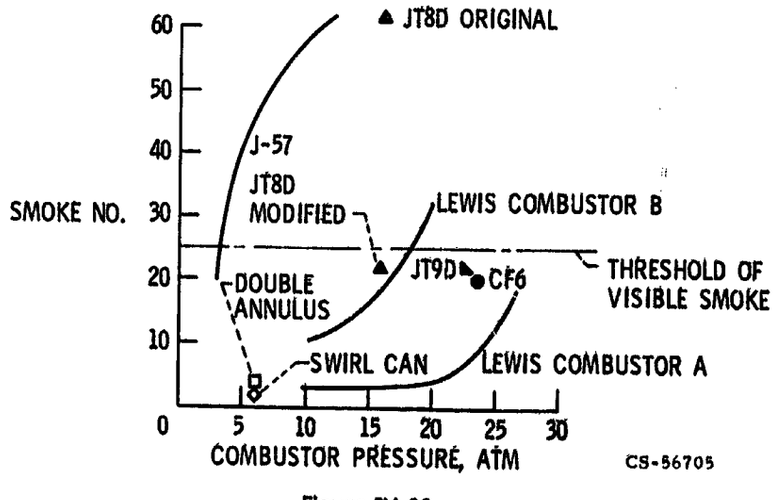

Figure IV-32

EXHAUST EMISSIONS OF A J-57 COMBUSTOR

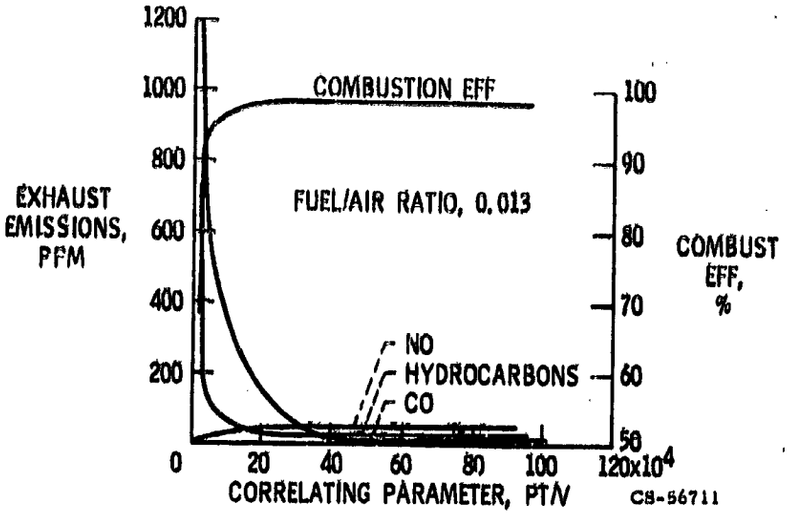

Figure IV-33

NITRIC OXIDE EMISSION

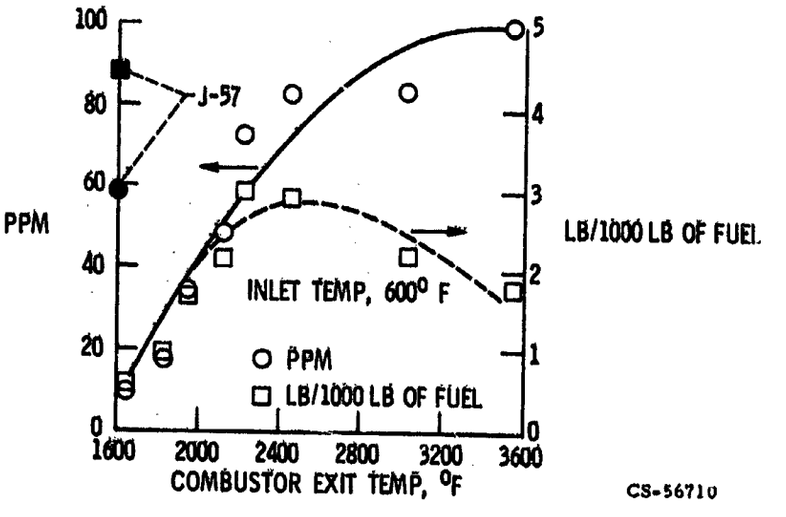

Figure IV-34

V. V/STOL PROPULSION

Newell D. Sanders, James H. Diedrich, James L. Hassell, Jr.,*
David H. Hickey,** Roger W. Luidens, and Warner L. Stewart

This paper describes the propulsion technology for commercial airplanes designed for short takeoff and landing (STOL) or for vertical takeoff and landing (VTOL). Some differences between those airplanes and conventional takeoff and landing (CTOL) airplanes are illustrated by the trajectories in figure V-1.

The CTOL airplane uses the lift of wings caused by forward speed to get off the ground. A relatively long runway is necessary for acceleration to flying speed. In the STOL aircraft, wing lift is augmented by the engine power. Engine power can be used to increase the lifting effectiveness of the wings or the engine can produce direct lift to aid the takeoff. In both cases, the takeoff speed is lowered, and acceleration distance is reduced. The VTOL airplane lifts off at zero airspeed, and the wings do not provide lift at all; engines provide the lift directly. In forward flight, the wings do provide lift.

We recognize immediately a greater demand for engine thrust, or lift, as we proceed from CTOL to STOL and to VTOL airplanes. Values of engine thrust to airplane gross weight might be as follows:

CTOL airplanes, 0.3
STOL airplanes, 0.6
VTOL airplanes, 1.2

The desired thrust of the STOL airplane is double the thrust of the CTOL airplane. The VTOL airplane requires another doubling of the thrust. These values are generalizations; they are intended to convey a sense of magnitude only. Substantial deviations from these values will be evident in this paper.

Increasing thrusts mean increasing engine weights. Unless the thrust to engine weight ratio is improved, the engine weights can become too large for economical operation. Today's CTOL airplanes have engine thrust to weight ratios near 5. For STOL aircraft an improvement in the engine thrust to weight ratio is necessary to offset an otherwise 2 to 1 increase in engine size. A value of 7 is suggested, but we

*NASA-Langley Research Center.
**NASA-Ames Research Center.

would be happy with 20 for all these engines. For the VTOL, a large improvement in engine thrust to weight ratio is needed to offset an otherwise 4 to 1 increase in engine size. An engine thrust to weight ratio of 10 would cut the potential weight penalty in half.

As we all know, today's conventional airplanes are criticized because of the noise they create. The noise problem with STOL and the VTOL airplanes will be more severe because these airplanes will be used at airports in highly populated urban areas. A noise limit of 95 equivalent perceived noise decibels (EPNdB) at an altitude of 500 feet has been suggested. This limit is 10 to 20 decibels more stringent than the present federal regulation for certifying new CTOL airplanes. This stringent noise limit has a first order effect on the selection of propulsion arrangement and the engine cycle.

The next item is safety, particularly with respect to engine failure. The CTOL has an engine-out safety problem, also, but, because lift at takeoff and landing is critically dependent on the engines in STOL and VTOL airplanes, engine failure becomes even more serious and has a much greater effect on propulsion system design.

High cruising speeds, approaching the speeds of CTOL airplanes, are demanded by potential operators of STOL and VTOL aircraft. These last two items, speed and economy of operation, favor the turbofan and the airpump types of engines. Our discussion will be limited to these two engines.

In the immediately succeeding portions of this paper, STOL airplane propulsion is discussed, and, in the final sections, VTOL airplane propulsion is discussed.

STOL AIRPLANE PRINCIPLES

There are, at present, proposals for a wide variety of designs for STOL airplanes. One of the main reasons for this is that the STOL airplane designs are sensitive to the requirements placed on the airplane in terms of field length and ride quality, and these requirements are, at present, not firmly defined. We can illustrate this sensitivity first with the factors that determine the thrust required in the airplane. In figure V-2 the ratio of the sea level static thrust to the airplane gross weight is plotted as a function of FAA field length for two wing loadings, 70 and 100 pounds per square foot. Some airlines have asked for airplanes with a field length of 1500 feet, or about two times a city block. Conventional airplanes require field lengths four and five times this value. The short, 1500-foot field would, of course, reduce airport land costs in populated areas.

High wing loadings like those mentioned are desirable for good ride and for economic high speed cruise. Even for a very efficient lifting system, specifying a 1500-

foot field length and a 100-pound-per-square-foot wing loading requires a thrust to gross weight ratio of 0.6, or about twice that of CTOL airplanes. If the required field length is increased only 300 feet to 1800 feet and the wing loading is decreased from 100 to 70 pounds per square foot, a thrust to gross weight ratio of 0.36 can suffice. This is a significant difference.

The specific values of thrust to gross weight ratio depend on the airplane design as indicated by the wide shaded area. For example, the required thrust to gross weight ratio would exceed 0.6 for a 1500-foot field length. The important point is that STOL airplanes require high thrust to gross weight ratios whose value depends on field length, wing loading, and airplane design.

If the STOL airplane can take off from a short field, it should also be able to land in the same field length. Whether it will be able to do so depends largely on the lift coefficient that the wing can develop. This is illustrated in figure V-3 where the required lift coefficient is plotted as a function of field length for the same two wing loadings. To achieve a 1500-foot landing field length with a 100 pound per square foot wing loading requires a lift coefficient of 7.0. If the field length is increased to 1800 feet and the wing loading is reduced to 70, the required C_L is reduced to about 4.0, a large difference. In general, STOL airplanes require high lift coefficients, which, as was the case with the installed thrust, are sensitive to field length and wing loading.

In considering how the required high lift coefficients can be achieved, keep in mind the high thrusts installed in the airplane. A powerful aerodynamic principle for achieving high lift coefficient has been known for many years and is shown in figure V-4; it is the jet flap wing concept. Some of the propulsive force of the engine is exhausted downward along the trailing edge of the wing. In its effect on wing lift, this jet sheet acts like an extensive mechanical flap. Also, the deflected jet itself contributes to the lift.

Implementating this concept gives rise to a number of problems:

(1) How is a spanwise jet sheet achieved?

(2) How is flow attachment on the wing upper surface maintained at high lift coefficients?

(3) How is the failure of one of the engines that produces the jet sheet dealt with?

The airplane designers have devised many designs in attempts to solve these problems. Also, as discussed earlier, the exact requirements for a STOL airplane are not firmly established and these have a strong effect on the airplane design. It is for these reasons that there is at present many STOL airplane designs under consideration.

Three types of STOL airplane designs will be discussed, namely, the externally blown flap, the augmentor wing, and the multiple fan airplane. For each design, the

concept and propulsion system will be described, and some of its advantages and problems will be discussed.

EXTERNALLY BLOWN-FLAP AIRPLANE

The externally blown-flap concept is illustrated in figure V-5. The exhaust flow from the underslung turbofan engines is directed onto the highly deflected flaps so that the flow is turned downward. Lift is generated not only as a result of the redirected thrust but also as a result of the jet flap effect which comes from the spreading of the flow outward to cover most of the flap span and the resulting extension of the physical flap by the jet sheet so formed. Flow separation on the upper surface is prevented because some of the engine exhaust passes through the slots in the flaps to energize the boundary layer. Moderate wing sweep, like that of conventional jet transports, is required for good spreading of the flow. Also, the high bypass ratio fan engines currently being developed are ideally suited for the externally blown flap concept because of the high mass flow at relatively low velocity and the relatively low temperature of their exhaust.

A photograph of an externally blown-flap model being tested in the Langley full scale tunnel at a very low tunnel speed is presented in figure V-6. The stream of smoke passing over the wing and then sharply downward is clearly visible. This flow deflection is an indication of lift coefficients two or three times greater than for the wing alone.

An obvious problem with the externally blown-flap concept is engine failure because of the asymmetric loss of lift and the resulting rolling moment. This problem can be minimized by locating the engines close inboard, but this placement does not eliminate the problem. Correction of engine-out rolling moments has been investigated very thoroughly at the Langley Research Center. In figure V-7, the rolling-moment coefficient is shown plotted against lift coefficient. For the case shown here, the airplane has four engines and a thrust-to-gross weight ratio of 0.6. The maximum lift coefficient is 9, and, of course, there is no rolling moment asymmetry. The solid curve illustrates the asymmetric rolling moment from failure of the left outboard engine and also shows that for this case with three engines operating at maximum thrust, the maximum lift coefficient has dropped off to about 7. The real challenge has been to devise an aerodynamic control that provides sufficient roll control power to trim out the asymmetry of the failed engine without incurring additional loss of lift. The rolling moment can be balanced by decreasing the flap deflection behind the two active engines and increasing the flap deflection on the side with the failed engine. This technique is called differential flap control. Results of

tests using this technique are shown by the dashed curve which indicates that the rolling moment has been trimmed without further reduction of maximum lift coefficient below 7.

Safety considerations dictate that the airplane operate at some margin above stall speed. For a 20 percent speed margin, the safe usable approach lift coefficient is about 4.7. This lift coefficient permits operation into a 1500-foot field with a wing loading of 70 pounds per square foot.

Although they would not be used to trim the engine failure asymmetry because of the lift penalty that would occur, spoilers do provide a very healthy roll control increment for normal maneuvering control as is indicated by the curve at the top.

In an alternate method also tested at Langley, high pressure air is bled from the engines and is cross ducted to the opposite ailerons to provide boundary-layer control. When engine failure occurs, twice as much bleed air is directed to the drooped aileron on the side with the failed engine as is to the aileron on the side with the two active engines. This boundary-layer control system is quite powerful and provides rolling moment trim very similar to that shown with the differential flap control technique. In addition, such a system has the distinct advantage of operating passively in that most of the rolling moment asymmetry would be trimmed without action on the part of the pilot. Engines capable of supplying sufficient bleed air to power the boundary-layer control would be required or provision for auxiliary power from another source would be necessary.

A candidate engine for the blown-flap STOL airplane is shown in figure V-8. The trend in engines for conventional transports has been to higher bypass ratio and lower fan pressure ratios. Conventional twin-spool engines of today can meet all requirements for this service except a noise limit of 95 EPNDB at an altitude of 500 feet. Acoustical treatment of existing turbofan engines with bypass ratios of 6 could put us within 6 PNdB of this limit. The next section will show that still lower core jet velocities, low fan pressure ratios, and sound absorbing treatment are required to meet the 95 EPNdB noise limit goal. New fan technology employing propeller techniques might be applied to these new engines.

In summary, wind-tunnel experiments show that the desired lift coefficients and control of engine-out rolling moments can be achieved with an airplane thrust to gross weight ratio of 0.6. Further development of the trend to lower fan pressure ratio engines is required to meet the noise limits.

AUGMENTOR WING AIRPLANE

The propulsion requirements for an augmentor wing airplane will be considered now. The question of installed thrust required, core thrust - fan thrust split, and

fan and core pressure ratios will be examined.

Like the externally blown flap concept, the augmentor wing concept is a derivative of the jet flap principle. Figure V-9 shows a cross section of an augmentor wing. The augmentor is a two-dimensional ejector formed by the biplane flap system and the pressurized duct containing the primary nozzle. The augmentor increases the thrust of the primary jet by about 30 percent. The secondary inlets for the ejector are shown in the cross section. The inlets on the top flap remove the boundary layer so that the external flow follows the highly deflected flap. The discharge from the augmentor forms a jet sheet and generates high lift coefficients by the jet flap effect. As shown on the plan view, the augmentor typically covers from the fuselage to 70 percent of the span. For additional lift, the ailerons (typically covering the outboard 30 percent of the wing) would be drooped and have boundary layer control.

The engine-out characteristics of this concept are one of its strong points. The interconnected ducting as shown in the figure minimizes upset moments due to engine failure by providing uniform distribution of air into the flap system despite the failure of any one of the engines supplying the pressurized air. This feature, along with the high lifting efficiency, makes a two-engine commercial STOL aircraft feasible.

Figure V-10 shows a conceptual installation of a two-spool, two-stream engine (i.e., the core stream and bypass stream) in a nacelle. At takeoff and landing, all the bypass air passes up through the pylon into the wing ducts and out the duct nozzle. If braking on the ground is required, the forward valve might be opened, eliminating the augmentor lift and providing a retarding force. During cruise, the valves to the wing ducts are closed, the flaps are retracted to a streamline position, and the valve at the rear of the pylon is opened to augment the forward cruise thrust provided by the core jet.

The Canadian government, deHavilland of Canada, and NASA have been working on the augmentor wing concept for several years. Figure V-11 shows a large-scale model mounted in the Ames Research Center 40- by 80-foot wind tunnel. The model span is approximately 40 feet. The augmentor inlet is shown along the trailing edge of the wing. Ailerons were drooped and had boundary-layer control applied at the knee. Boundary-layer control was also applied at the slot across the top of the fuselage. A special pump for the augmentor air was mounted in the fuselage. The pump consisted of a J-85 engine driving two Viper compressors; hence, the three inlets on the fuselage visible in the photograph. An augmentor wing airplane would not have these fuselage inlets.

Data from this model are shown in figure V-12. Lift coefficient is plotted as a function of drag coefficient. This curve is for an augmentor and boundary-layer control thrust to gross weight ratio of 0.21 and a flap deflection of 70°. Even for this low thrust, the maximum lift coefficient is above 7, which should be sufficient for a

1500-foot field length airplane.

These data define an engine specifically for an augmentor wing aircraft, but first a landing approach design point must be selected. Figure V-13 is the same as the previous figure, but more information has been added. An airplane descends at an angle determined by the ratio of drag-to-lift. Lines of constant descent angles of 3°, 6°, and 9° are shown, and of course the vertical axis corresponds to level flight. A design point at a 5° angle of attack and 20 percent above stall speed was chosen. This design point provides a 15° angle of attack and a 13-knot stall margin, which exceeds the margin recommended by some authorities. At the lift coefficient of 5.1, an airplane with a wing loading of 77 pounds per square foot could land in a 1500-foot field. At this design point, the descent angle of 5° and the 5° angle of attack gives a horizontal fuselage altitude.

One of the requirements of commercial aircraft is that they be able to arrest the rate of landing descent with a minimum loss of altitude after the pilot's decision is made to go around. This is done conventionally by rotating the airplane, increasing power, and in some cases reducing flap deflection. However, as attempts are made to lower weather minimums, these techniques become less acceptable. With the augmentor wing, this characteristic can be improved by designing the engine so that the core thrust will be sufficient to arrest the rate of sink (corresponding to 0.09 thrust to gross weight ratio) and make the thrust immediately available for emergencies. To provide this capability, a fast-acting thrust modulator for the core is necessary. By including a thrust reverser in the modulator, the airplane can have a descent angle between 0° and 8° at fixed power. With the provision of the thrust modulator, handling qualities have probably been improved because the modulator provides a descent control independent of lift or airplane airspeed.

The figure contains enough information to define important characteristics of the augmentor wing engine. With a duct loss of 20 percent, an augmentor augmentation of 30 percent, and a flight speed of 65 knots, the required installed gross thrust to gross weight ratio required is 0.3. Commercial transport regulations will require this performance with one engine failed, thus the installed thrust for a four-engine airplane is 0.4. The information also establishes that the ratio of the core thrust to the total engine thrust is 30 percent. The remaining 70 percent of the thrust is delivered by the fan to the augmentor. Of course, other core thrust ratios can be obtained with different airplane variables or matching philosophies, but the case derived here is representative.

Thus far two questions have been ignored. One is the limitations on duct sizes imposed by the wing cross-sectional area, and the other is the practicality of the engine cycle and its adaptability to noise reduction technology. These questions will now be considered.

Enough air can be passed through the wing by resorting to high pressure ratios, but pressure must be minimized because of cruise specific fuel consumption and noise from the augmentor. The relative duct areas required to pass the augmentor flow at Mach 0.3 in the most critical wing section is shown in figure V-14 as a function of fan pressure ratio. A duct loss of 20 percent thrust is included. The capacity of the ducting system shown in the sketch was estimated for a wing loading of 77 pounds per square foot and a 12 percent thick wing with spars at 15 and 50 percent chord. The relative duct areas available are shown for wing aspect ratios of 6, 8, and 10. At an aspect ratio of 8, a pressure ratio of 2.3 is required. However, the curves indicate a wide range of possible compromises between the engine, aerodynamics, and noise. For example, with a wing aspect ratio 6, the data indicate that a 1.6 pressure ratio fan may pump the required amount of air. This, as a single-stage fan, will reduce compressor and augmentor noise significantly but would increase the required airplane thrust to gross weight ratio by about 10 percent. Studies to evaluate these compromises are required.

As defined here, the engine should have 30 percent of the thrust from the core and 70 percent from the fan. Furthermore, the jet exhaust velocity should be low to minimize core jet noise. Figure V-15 shows the core thrust fraction as a function of the core jet velocity for an 1800° F turbine inlet temperature. Fan pressure ratio is 2.5. The core jet velocity must be around 800 feet per second to keep the core jet noise down. The desired core thrust fraction is obtained at the moderate turbine inlet temperature of 1800° F. These figures represent one solution to the engine-airplane matching problem. As with the blown flap, conventional engines could have been used, but the core jet noise is prohibitive; thus, a new engine is required for noise reduction. This engine will probably be well within the state of the art; however, no engines like this are being built today. A new or highly modified engine will probably be developed specifically for the augmentor wing airplane.

This has been a review of the augmentor wing state-of-art. The augmentor wing is an efficient high lift system. It is possible to get the required duct sizes into the aircraft wing. A two-spool engine of special design can generate the required wing duct flows and pressures with a low jet core exhaust noise. Considerable work is still required to optimize the matching between the engine, airframe, and noise.

MULTIFAN AIRPLANE

The major factors affecting STOL airplane design are noise, engine-out, and a lateral spreading of the jet sheet to achieve high lift coefficients efficiently. Given

these factors, the use of multiple, low-pressure-ratio fans is an approach to a STOL airplane that may have some advantages. One possible airplane layout is shown in figure V-16. On the airplane, 16 fans are spread along the wing trailing edge. These fans have a pressure ratio of 1.25 so that the propulsion can be quiet, and the same fans provide both the takeoff and the cruise thrust. The large number of fans gives a good spanwise extent of the jet sheet. The fans are mounted on a hinged flap to achieve a downward deflected jet for high lift. The fan inlets create a massive suction to maintain flow attachment on the wing upper surface. The effect of one fan-out is small because the thrust of each fan is only a small fraction of the total thrust.

The fans are driven by high-pressure air from four air pumps that deliver air at a pressure ratio of about 7. This pressure ratio allows the duct sizes in the wing to be small compared with the wing cross sectional area.

To help determine if this arrangement has merit, the model shown in figure V-17 was built. It is a semispan model, and, hence, has eight fans. They are driven by high pressure air, and the whole system is mounted on a force balance. The tests were run in the Lewis 9- by 15-foot V/STOL test section. A typical set of results is shown in figure V-18.

Lift coefficient is plotted as a function angle of attack for two conditions: a 30° flap deflection corresponding to takeoff and a 60° flap deflection corresponding to landing. The data extend to a 30° angle of attack, and the wing has not stalled for either flap deflection. These data have been interpreted in terms of a STOL airplane with a 100-pound-per-square-foot wing loading, a 1500-foot field length, and an installed thrust-to-weight ratio of 0.57. Takeoff would occur at a lift coefficient of about 4.0 at about a 10° angle of attack. At this flight condition, the wing can easily tolerate a 30-foot-per-second vertical gust.

The landing approach would occur at a lift coefficient of 7.0 with the engines partly throttled and a thrust to gross weight ratio of 0.44 (the installed value is 0.57). Again, at this flight condition, the wing has a 30-foot-per-second vertical gust tolerance. This performance together with the fact that it is achieved with potentially low-noise fans makes this a configuration of interest.

The propulsion system is described in more detail next. A drawing of one of the fans is shown in figure V-19. It has a single-stage rotor with a pressure ratio of 1.25. Turbine drive air enters an annular scroll, passes through the turbine nozzles and turbine blades mounted on the tip of the fan to drive the fan, and then exits to provide part of the thrust. The drive air temperatures are low enough so the ducting, scroll, and turbine materials can be titanium.

High pressure drive air is provided by the air pump shown in figure V-20. It is a two-spool engine. The first spool generates a pressure ratio of about 7.0. Half

of this air is ducted off to drive the fans; the remainder is routed through the second spool, is burned, and is used to drive the turbines for both spools.

The consequence of an airpump failure depends on the ducting system. It is proposed that the ducting be arranged so that each fan receives one-quarter of its drive air from each airpump. The loss of one airpump causes a one-quarter loss of power, but all the fans continue to run uniformly so no roll or yawing moments are developed. Also, because this is a power interconnected system, the one-quarter power loss ideally causes only a one-eighth loss in thrust. Thus, this concept is tolerant of either a fan or airpump loss.

Studies and tests to date indicate that a multiple low-pressure-ratio fan configuration has the potential for low noise, good engine failure tolerance, and has very high usable lift coefficients. As a consequence of the high usable lift coefficients, the multifan concept can yield airplanes with a wing loading of about 100 pounds per square foot for a 1500-foot field. What is it worth to increase the wing loading from 70 to 100? The decrease in wing weight corresponds to an increase of about 20 percent in payload weight. The cruise lift-drag ratio at Mach 0.75 and at an altitude of 25 000 feet is improved about 10 percent, and there is qualitative improvement in ride quality.

In brief, the multiple fan airplane appears to have a number of significant advantages, but there are also problems that require further study such as cruise drag, aeroelastic stability, and system weight.

VTOL AIRPLANE PRINCIPLES

VTOL airplanes employ engines for lift as shown in figure V-21. This drawing is purely schematic and is not proposed as a favored configuration. A multiplicity of engines are required to provide the enormous lift and to provide safety in case of engine failure. The engines also must perform new control functions. At zero lift-off speed, there are no aerodynamic forces acting on the control surfaces. The power system must provide the control. The lift engines shown in the wing tips are for roll control, and fore and aft engines shown are for pitch control. In addition, engines must provide cruise thrust for forward flight. Separate engines are shown for each of these functions; it is probable that some of these functions can be combined into fewer engines.

The remainder of this section is limited to a discussion of lift fans. Although the lift engines are required only at takeoff and landing, we must drag them along for the entire flight. To avoid the drag penalty of these inactive engines as much as possible, the airplane designer tries to bury the engines in the wing, in small pods, in extensions of the fuselage, or in the fuselage itself. Consequently, the engine designer

is required to make the engine as short and as small as possible.

Another problem concerns an unusual flow situation around the engines. After liftoff, the engines must operate while the airplane is in forward flight until complete wing lift is established. The flow of external air across the inlet causes severe distortions of flow at the engine face. The engine and engine installation must be designed to withstand these flow distortions.

The minimum engine thrust, or lift, must be at least as great as the gross weight of the airplane. Additional lift is required for acceleration and maneuvering. To allow for engine failure, the installed thrust must be great enough to provide lift and maneuvering acceleration with an engine out. The failure of an engine causes upsetting moments; correction of these moments requires still more installed lift. When all of these factors are considered, the installed thrust to gross weight ratio will range between 1.2 and 1.6.

The importance of engine thrust-to-weight ratio is shown by the result of a parametric study of VTOL airplanes (fig. V-22). The plane in this figure can carry 100 passengers 500 miles, and its engine thrust to weight ratio is 1.3. Aircraft gross weight is plotted as a function of the ratio of engine thrust-to-engine weight as installed in the airplane. Curves corresponding to lifting times of 5 and 10 minutes are shown. You may recall that the engine thrust to weight ratios of today's airplane engines are near 5; such engines are totally unsuitable of this service. A thrust to weight ratio of 10 gives an airplane gross weight close to 100 000 pounds for a lifting time of 10 minutes. DC9's and 737's are approximately this size and carry approximately the same number of passengers. We would like, therefore, to have engines with thrust to weight ratios of 10 or better. New engine designs and new technology will be required to produce these engines.

The figure also shows the effect of varying specific fuel consumption (SFC) on airplane gross weight. Increasing the specific fuel consumption from 0.4 to 0.5 has minor effect of airplane gross weight because these fan engines are already very efficient and the fuel consumed in the 5 or 10 minutes of operation is not great.

The noise limitation drives us to very high-bypass-ratio, low-pressure-ratio, and low-tip-speed fans.

In summary, the installed lift must be 1.2 to 1.6 times the gross weight of the airplane. The engine thrust to weight ratio must be high, probably above 10; the engine must be compact, have low noise, and be tolerant to the external flow across the inlet.

EFFECT OF EXTERNAL FLOW ON VTOL FAN PERFORMANCE

A picture of a fan installed in the 9- by 15-foot V/STOL wind-tunnel test section is shown in figure V-23. The model lift fan has a diameter of 15 inches and is mounted in a wing which spans the tunnel test section. The wing was mounted vertically to facilitate the measurement of forces. The fan is driven by a compact, high-pressure air turbine which is mounted in the hub of the fan. The fan has a design pressure ratio of about 1.3 at a tip speed of approximately 1000 feet per second.

The axis of the fan is perpendicular to the direction of the tunnel airflow. Consequently, the air is forced to turn 90° to enter the fan. This is termed the crossflow environment.

The oncoming airstream is forced to turn sharply to enter the fan on the upstream edge of the fan inlet. At high crossflow velocities, the flow separated and blocked a portion of the inlet area. This is potentially a severe problem; but in this particular case, the maximum inlet area blockage amounted only to about 6 percent. Blockages like these can be tolerated by the lift fan and aircraft as will be shown later.

Another problem caused by crossflow is more serious: the change of rotor incidence angle (see fig. V-24). The inset is a planform of the fan in crossflow. The rotation of the fan is indicated by the long arrow. Each fan blade advances and retreats relative to the crossflow as the fan rotates. This causes positive and negative relative incidence angles of the flow, as shown in the inset. In the figure the theoretical change in incidence angle is plotted as a function of the circumferential position. There is a cyclic pattern which is aggravated as the crossflow velocity increases from 0 to 160 mph. When rotor incidence angle changes, rotor pressure ratio changes. Confirming experimental data are shown in figure V-25.

The rotor total pressure ratio is shown as a function of circumferential position. Static conditions resulted in a uniform pressure ratio. As crossflow increased to 100 and 160 mph, the predicted cyclic behavior was observed. However, the curves were not symmetrical in the advancing portion of the cycle. The data reached a limiting value which was independent of the crossflow velocity. This effect produces a net reduction of the mean rotor total pressure ratio as the crossflow velocity increases. Consequently, we would expect the fan thrust to fall off with increases in crossflow velocity.

Figure V-26 shows model lift fan total thrust per unit frontal area as a function of the tunnel air velocity. Data are shown for a tip speed of 980 feet per second (or design conditions). Two additional curves are superimposed for comparison purposes. The top curve is an ideal fan performance curve, which assumes recovery of all the momentum of the tunnel airstream. The lower curve is the lift fan thrust

requirement of a VTOL aircraft converting to wing-supported flight at 140 mph. We have referenced the two curves to the static thrust of the model lift fan at design speed.

For the design condition, the experimental fan thrust falls off with increasing crossflow velocities. The performance of this fan is far from ideal. The crossflow environment degrades the fan performance by a considerable amount, but there is sufficient margin to provide the required thrust for the example shown.

This is just one case, and further tests are being planned with low-pressure ratio, low-tip speed, low-noise fans to see if these trends are maintained.

VTOL FAN PROPULSION SYSTEMS

As has been pointed out before, noise constraints have resulted in the requirement of rather low pressure ratios, 1.25 or less, for lift fans. These fans in themselves, then become rather well-defined and are flat and light weight. The reasons we get into various fan systems lies in the question of how the fans are driven.

In general, the drive systems can be put in two categories, as shown in figure V-27. The integral drive fan engine is self-contained with a hub drive turbine and its own inner spool. It is, in principle, a conventional two-spool, high bypass ratio turbofan engine. The lower part of the figure shows examples of the remote drive systems. In such systems the power source is in a location remote from the fan itself, with pneumatic energy transmitted to the power turbine through ducts or pipes. These ducts can be configured in such a way that fans and power sources can be interconnected to reduce the engine failure and control problems. The fan modules are rather short in depth. This, and the ability to orient the power source along a different axis results in a potential reduction in installation problems as compared to the integral drive system.

Two remote systems are shown. One is a gas generator system, in which a conventional turbojet engine is employed. The hot pressurized gas, rather than being used for thrust, is diverted through appropriate ducting to the fan-drive turbine inlet. This fan system has been used in some of the direct lift research aircraft that have been examined in recent years, notably the XV5. The other system uses an airpump. This airpump would be a very low bypass ratio, high-pressure ratio turbofan engine. The pressurized air, which is considerably cooler than the gas generator exhaust, is routed through ducts to the lift fan. An auxiliary combustor heats the air just before it goes into the fan turbine drive.

The ultimate choice of the fan drive system is a function of many factors, some related to the engine itself, such as weight, system fuel consumption, volume, and

depth and others related to aircraft operation, such as control and engine-out. The discussion here will be confined to the engines themselves and their features.

INTEGRAL DRIVE FAN

Some of the features of the integral drive fan are shown in figure V-28, which presents a cross-sectional view of one fan currently being considered. This is a single-stage, relatively low-speed fan (due to the required low pressure ratio). It has the potential of being very light weight because of the possible use of advanced composite structures. The fan is shown with the flow to the compressor split off from that of the bypassed flow. Such a fan geometry is attractive because it permits the pressure rise at the hub section to be lower than that of the main fan, thereby permitting a lower fan inner radius and, therefore, a smaller diameter engine. The inner spool includes a multistage compressor driven by a single-stage turbine. The combustor shown is a reverse-flow type. Such a combustor geometry is considered to be attractive because it shortens the length of the engine, thereby minimizing its depth and volume.

The inner spool must be rather simple and compact for this application. Fortunately, the engine cycle parameters, namely, pressure ratio and turbine inlet temperature, are such that this is possible. The results of engine cycle calculations made to find the optimum cycle pressure ratio and turbine inlet temperature are shown in figure V-29. The engine weight plus 5 minutes fuel is shown on a relative scale as a function of the turbine inlet temperature at three compression ratios. The optimum temperature is 1800° F, which is surprisingly low and a conservative value by today's standards. The optimum pressure ratio is also surprisingly low, being about 8. Low optimum temperature and pressure ratio are obtained because the short operating time of the engine minimizes the importance of specific fuel consumption. These modest cycle temperatures and pressures greatly simplify the gas generator.

From figure V-28, it can be seen that the fan is driven by a multistage turbine. Because of speed restrictions on the fan and because the turbine diameter is substantially less than that of the fan, the turbine blade speeds and associated stresses of this turbine are quite low. Therefore, the turbine is potentially light in weight through the generous use of thin sheet metal in its construction.

From an aerodynamic standpoint, this turbine has requirements that are considered to be beyond that of conventional practice. The reason for this is indicated in figure V-30, where stage efficiency is plotted as a function of turbine stage work factor. (Stage work factor relates the work being extracted per pound of air per

stage to the kinetic energy of the rotating blades.) Increasing the work factor results in decreasing the turbine efficiency. Current cruise engines usually operate at work factors of 1 to 2 because of the desire to have high turbine efficiency and, thus, low specific fuel consumption. Studies of the integral engine have shown that, when considering both turbine weight and efficiency, work factors in the range from 4 to 6 become necessary. Such high work factors are encountered because the blade speed is low, as previously mentioned, and the work per pound is high because of the low flow through the gas generator. Shown is a broad band of uncertainty in the expected efficiency at these high work factors, thus indicating that there are major questions regarding the ultimate efficiency in this range. Programs are currently under way to attempt to answer these questions.

TIP TURBINE FAN SYSTEM

The low blade speed encountered in the turbine for the integral engine is one of the reasons why other approaches permitting increased blade speeds are desirable. Introducing a gear system would be one way of accomplishing this. To date, however, the added complexity and weight has not resulted in this approach being shown to have a net advantage.

Another idea to increase the turbine blade speed - also considered to be unpractical for the integral engine - is the use of a turbine located at the tip of the fan. These tip turbines are located where the blade speed is greatest, thereby resulting in more modest values of stage work factor, about 2. Tip turbines are used in the remote drive systems described previously. Because of the location of the turbine, rather large scrolls are required to direct the high pressure gas to the turbine entrance. Also, turbine inlet temperatures on the order of 1400° F are being considered for the drive systems, resulting in the whole outer section being at high temperatures. These outer elements, of course, require insulation and major attention to maintain the structural integrity and life of the hot parts.

A cross sectional view of one of these fans is shown in figure V-31 for the gas generator system. The fan rotor, its stator, the scroll, and the single stage tip turbine are shown. Although the gas generator and air pump drive systems appear to be similar (fig. V-27), there are substantial differences. These differences occur principally because of the difference in the available pressure ratio across the turbine. Since the gas generator is basically a turbojet engine, the pressure available to the tip turbine is modest - perhaps on the order of 3 atmospheres. The air pump system, on the other hand, can deliver pressures considerably greater than that. We have been examining delivery pressures as high as 8 atmospheres in order

to allow the pump to operate with a single spool and to minimize the size and weight of the associated ducts. These ducts could be at a sufficiently low temperature to permit titanium to be used.

A substantial impact of these differences in pressure ratio is felt on the scroll and turbine. Figure V-32 illustrates these differences. Shown is the volume flow to the hot scroll as a function of turbine pressure ratio. The flow for the gas generator system is seen to be over four times that for the air pump system, and this results in a larger and heavier scroll for the gas generator system. On the other hand, the low pressure ratio across the tip turbine for the gas generator system permits a single-stage turbine to be used. The high pressure ratio across the tip turbine for the air pump case has forced us to consider a two-stage tip turbine for this system.

Cross sectional views of the tip regions for these two cases are shown in figure V-33. The difference in the scroll size and the number of turbine stages can be seen. Some other factors that affect the turbine and fan performance can also be seen. First, generous axial clearances must be provided to accommodate large motions of the fan tip. Second, the very short blading, particularly for the airpump turbine, has an adverse effect on the efficiency. Third, leakage at the front face of the fan, which occurs due to the pressure differential between the turbine stator outlet and fan tip inlet, reduces efficiency. This leakage penalizes the turbine by diverting the flow and penalizes the fan by the introduction of hot gas into the fan at the tip. This is a rather serious problem since these seals are in a region that is 5 feet in diameter. More investigation is needed to determine the best seal geometry for this application.

This discussion has pointed up some of the features and problem areas internal to the lift fans themselves. Little was discussed about weight comparisons since considerable design improvements must be made before practical values can be obtained. The discussion has shown, however, that the efficiency of high work factor turbines must be determined for the integral engine. On the other hand for the remote drive fans, major questions arise regarding the tip turbine performance, particularly as related to the clearances and leakages. There is also the question of acceptability of all the hot components that are located outside the fan. These and other questions must be answered to determine which configuration is best for the VTOL transports.

CONCLUDING REMARKS

For the blown-flap airplane, the engine thrust must be close to 0.6 of the gross weight. The problem of engine-out rolling moments has been investigated with

models in a wind-tunnel, and the results encourage us to believe that these moments can be managed by differential flaps or boundary-layer control and proper airplane proportioning. Engines similar to existing CTOL engines can meet all propulsion requirements except low noise. A special engine having a high bypass ratio, low fan pressure ratio, and sound treatment will be required to stay within the noise goals.

The example augmentor wing airplane required an installed thrust-to-weight ratio near 0.4. The airplane has good engine-out characteristics. However, a special engine design is required to give a thrust split of approximately 70 percent to the augmentor and 30 percent to the core jet. In addition to achieving the noise goals, the core velocity must be held to a low value near 800 feet per second. A major problem with this airplane is the control of the noise from the augmentor.

The novel multifan system is promising, but further research is required for evaluation of its potential.

For the VTOL airplane, we have shown some of the features and problems of the integral drive fan, the tip-turbine fan driven by a gas generator, and a tip-turbine fan driven by a compressed air generator. In all cases, advanced technology will be required to produce useful engines.

TYPICAL TAKEOFF AND LANDING TRAJECTORIES
FOR CTOL, STOL AND VTOL AIRPLANES

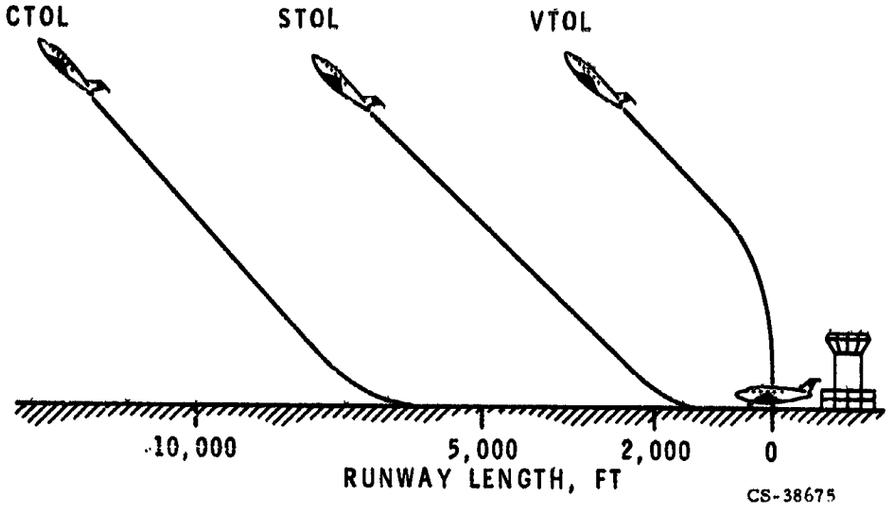

Figure V-1

STOL AIRPLANE TAKEOFF THRUST REQUIREMENTS

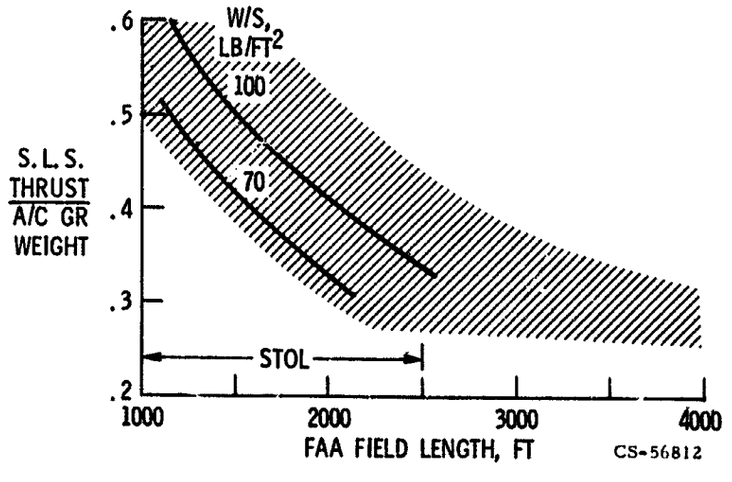

Figure V-2

STOL AIRPLANE LANDING LIFT REQUIREMENTS

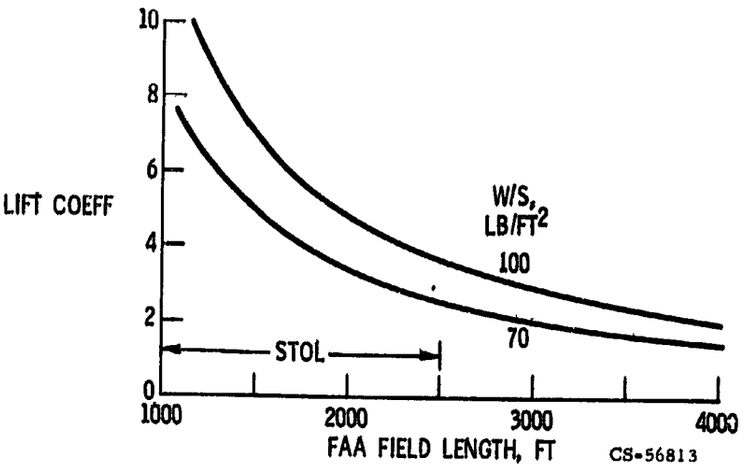

Figure V-3

HIGH LIFT COEFFICIENTS AND THEIR PROBLEMS

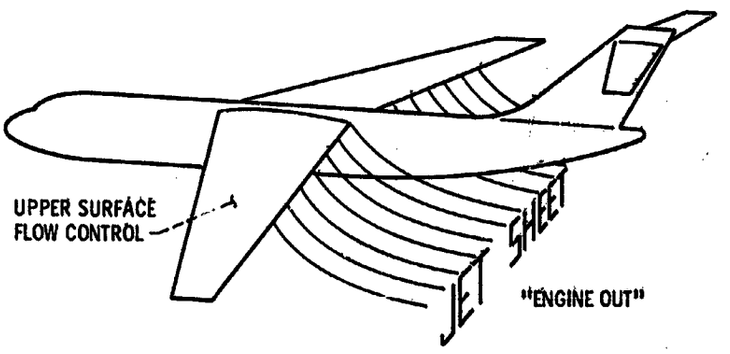

Figure V-4

CS-56814

EXTERNALLY BLOWN-FLAP STOL AIRPLANE

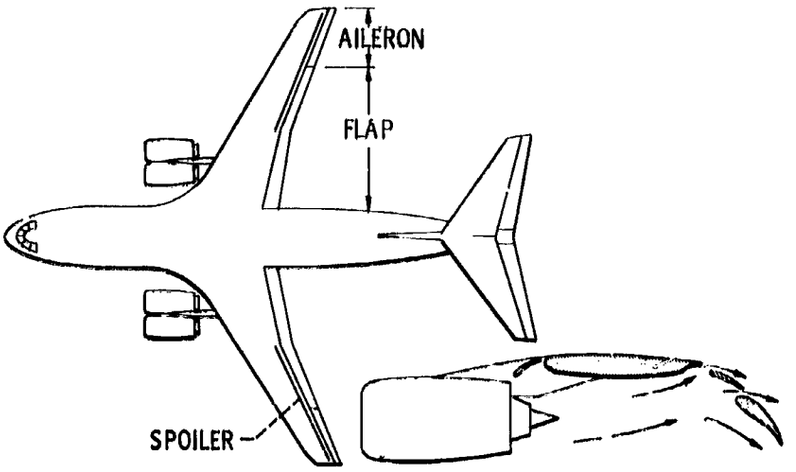

Figure V-5

BLOWN-FLAP MODEL IN WIND TUNNEL

Figure V-6

BLOWN FLAP ENGINE-OUT CONTROL

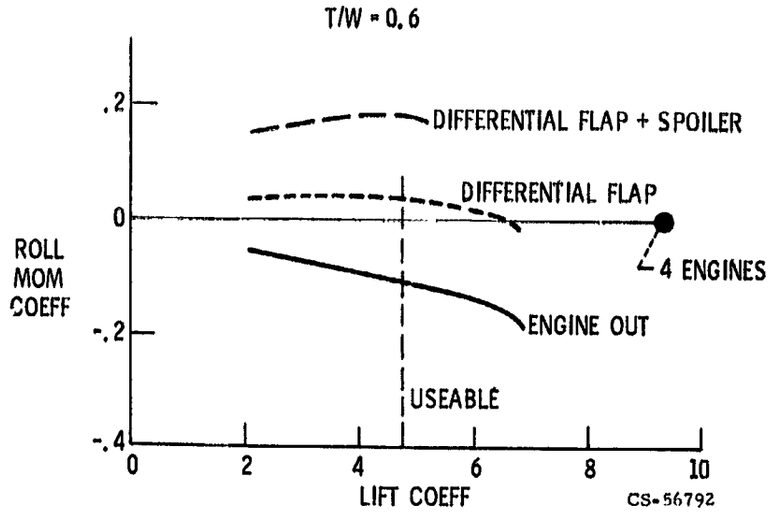

Figure V-7

ENGINE FOR BLOWN—FLAP AIRPLANE

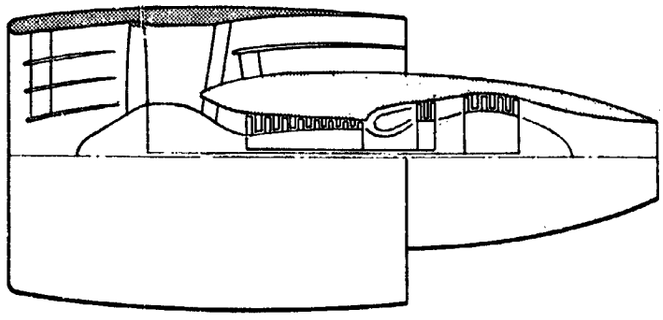

Figure V-8 CS-56802

AUGMENTOR WING STOL AIRPLANE

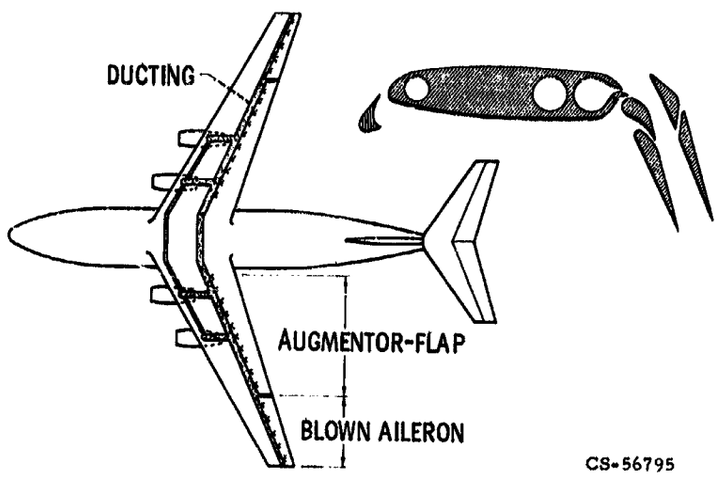

Figure V-9

ENGINE FOR AUGMENTOR WING AIRPLANE

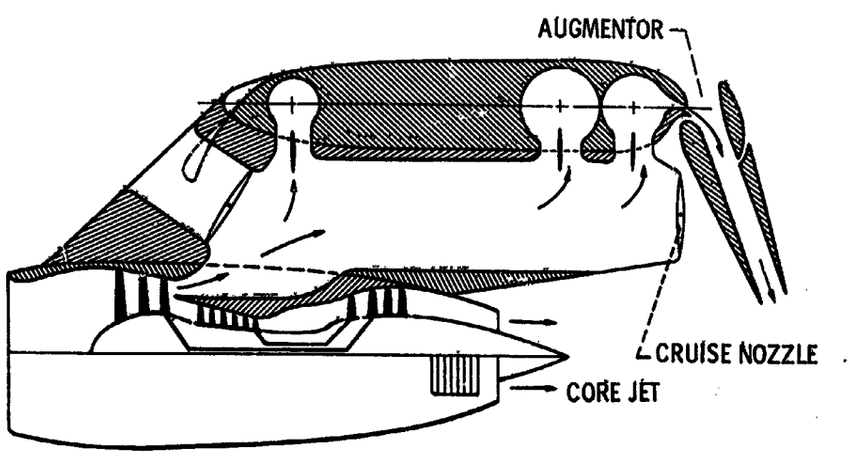

Figure V-10

AUGMENTOR WING AIRPLANE MODEL IN WIND TUNNEL

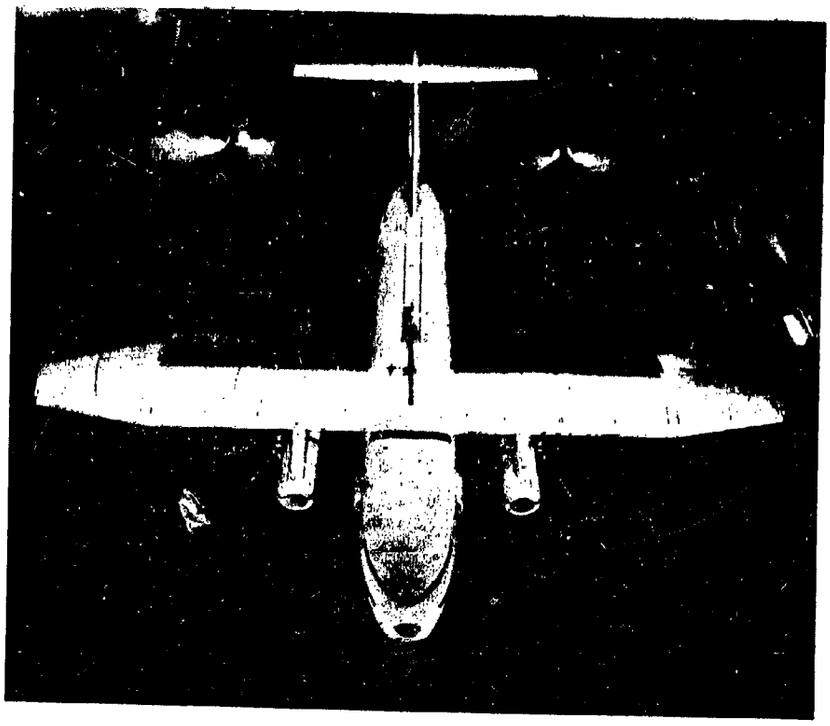

Figure V-11

EXPERIMENTAL AUGMENTOR WING DATA

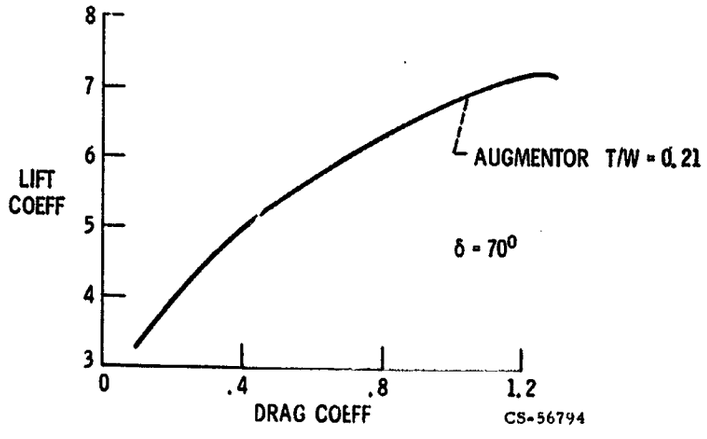

Figure V-12

AUGMENTOR WING DESCENT PERFORMANCE

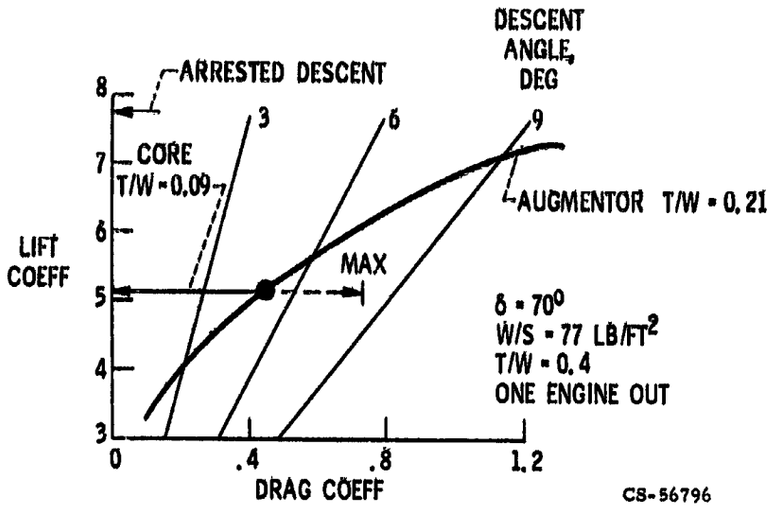

Figure V-13

AUGMENTOR WING DUCT REQUIREMENTS

T/W = 0.40, W/S = 77 LB/FT², t/c = 0.12

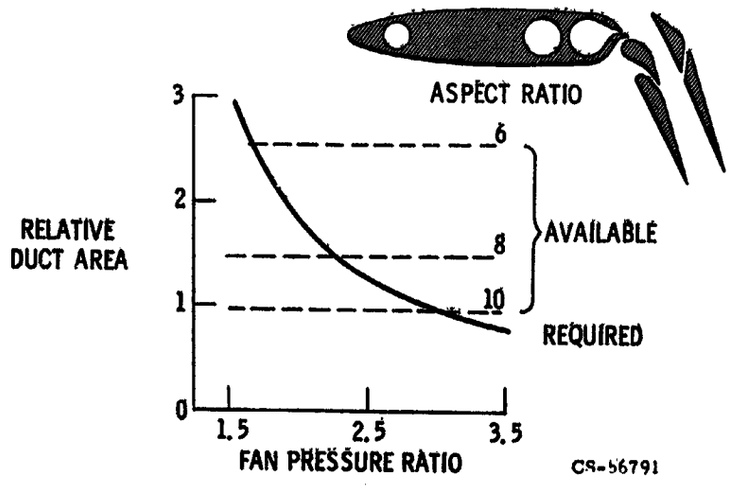

Figure V-14

AUGMENTOR ENGINE THRUST DIVISION

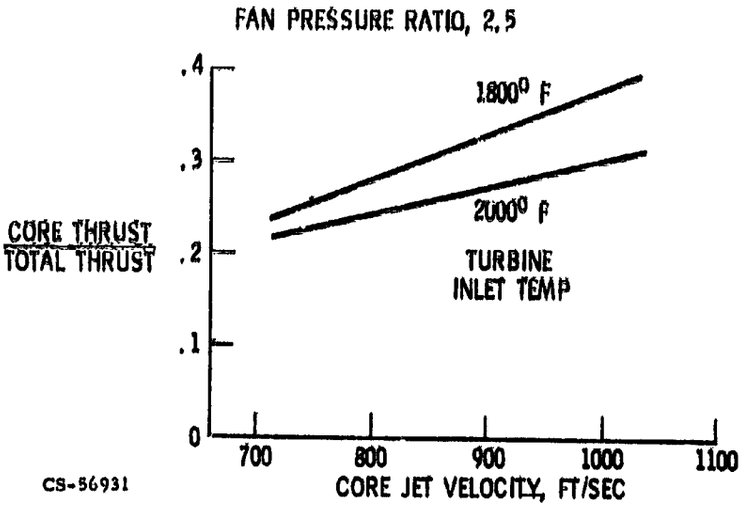

Figure V-15

MULTIFAN ON FLAP STOL AIRPLANE

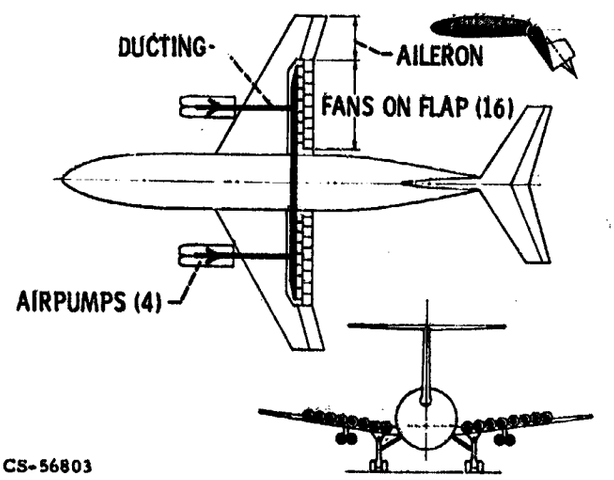

Figure V-16

MULTIFAN ON FLAP WIND TUNNEL MODEL

ASPECT RATIO, 5 (MODEL + IMAGE)

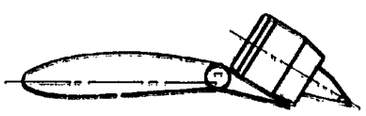

30^0 JET ANGLE

CS-56807

Figure V-17

EXPERIMENTAL MULTIFAN ON FLAP DATA

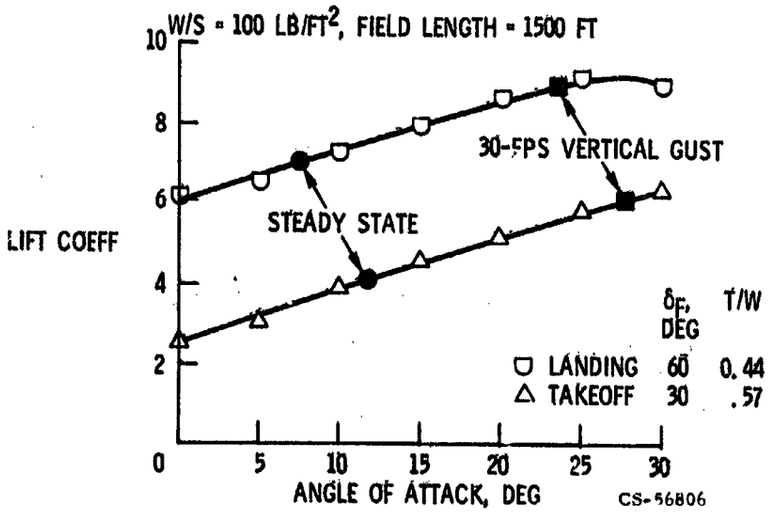

Figure V-18

TIP TURBINE FAN

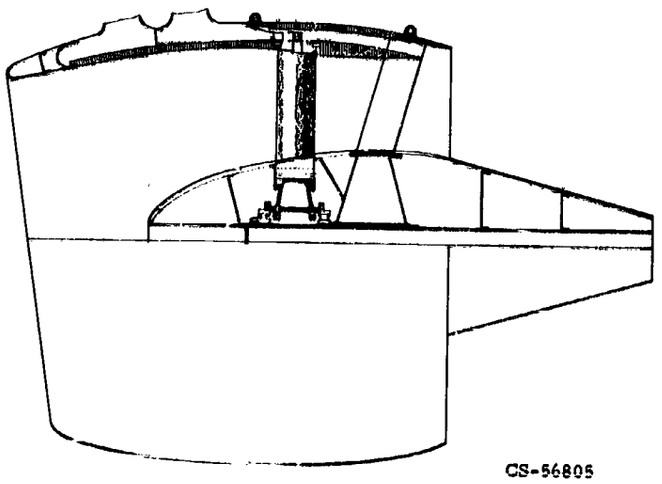

CS-56805

Figure V-19

AIR PUMP

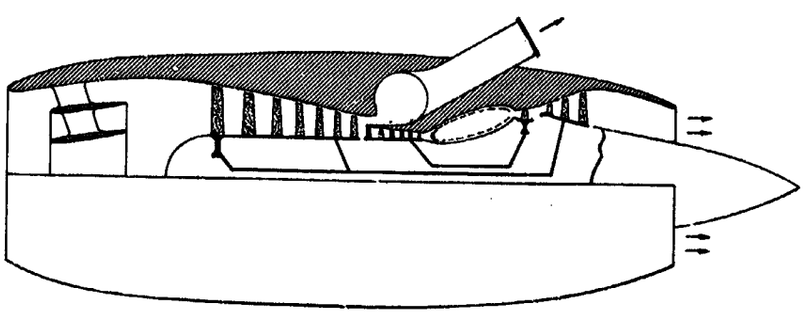

Figure V-20

CS-56804

VTOL PROPULSION FUNCTIONS

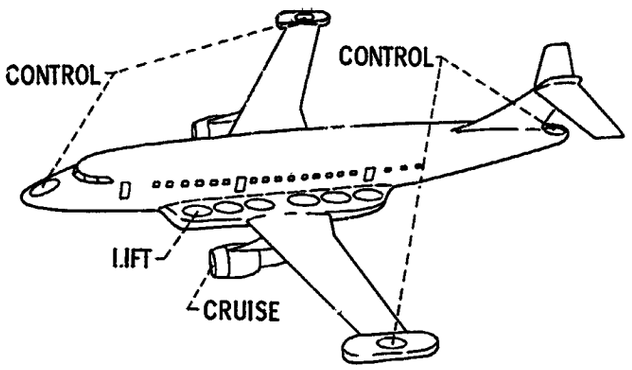

Figure V-21

CS-56798

LIFT FAN VTOL TRANSPORT GROSS WEIGHT

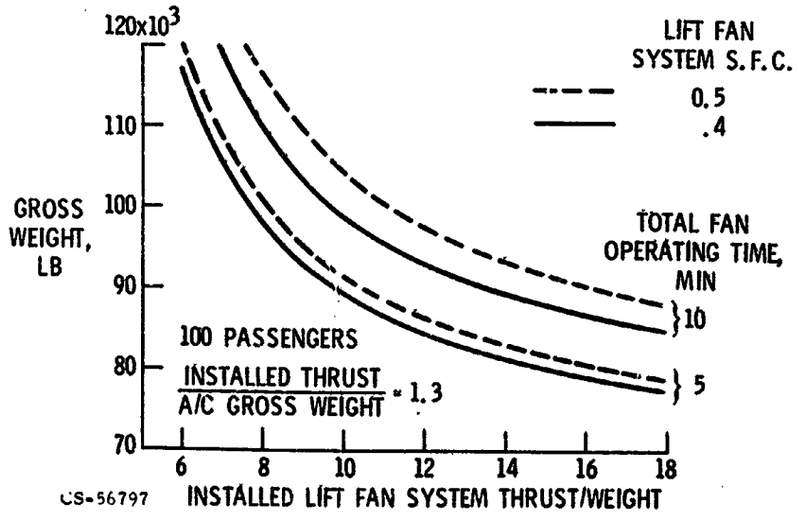

CS-56797

Figure V-22

MODEL LIFT FAN-IN-WING

C-69-3531
CS-56789

Figure V-23

CHANGE OF ROTOR INCIDENCE ANGLE IN CROSSFLOW

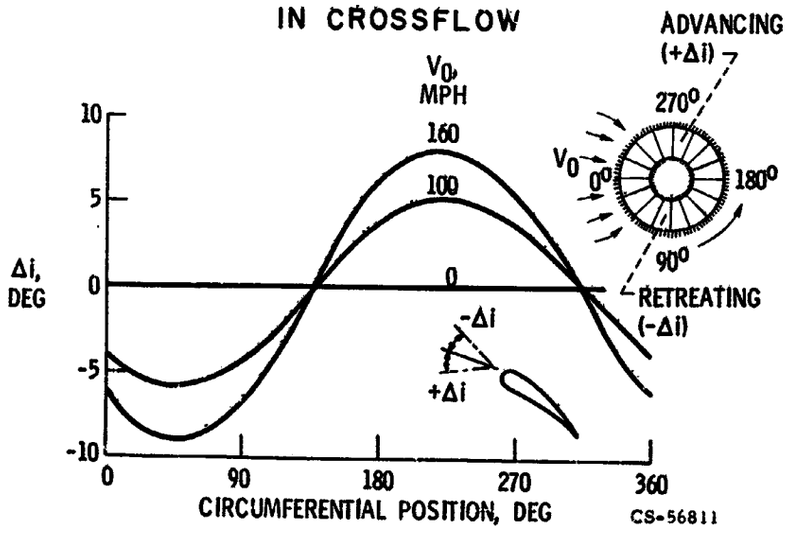

Figure V-24

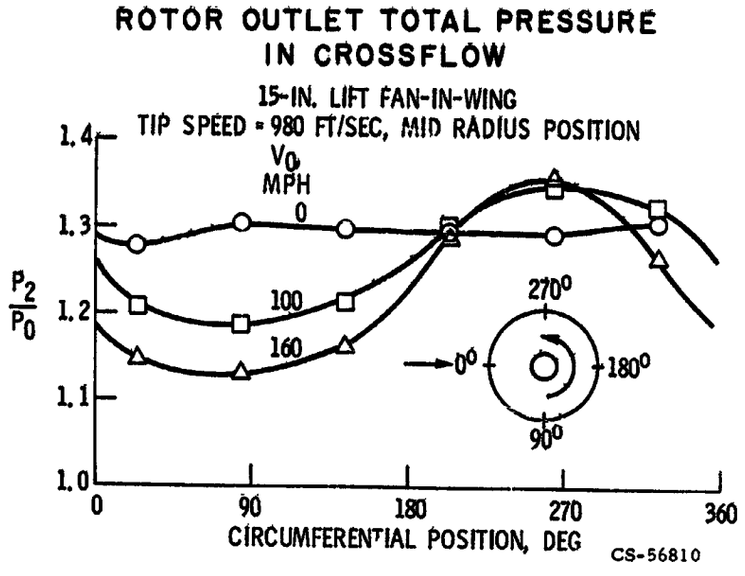

Figure V-25

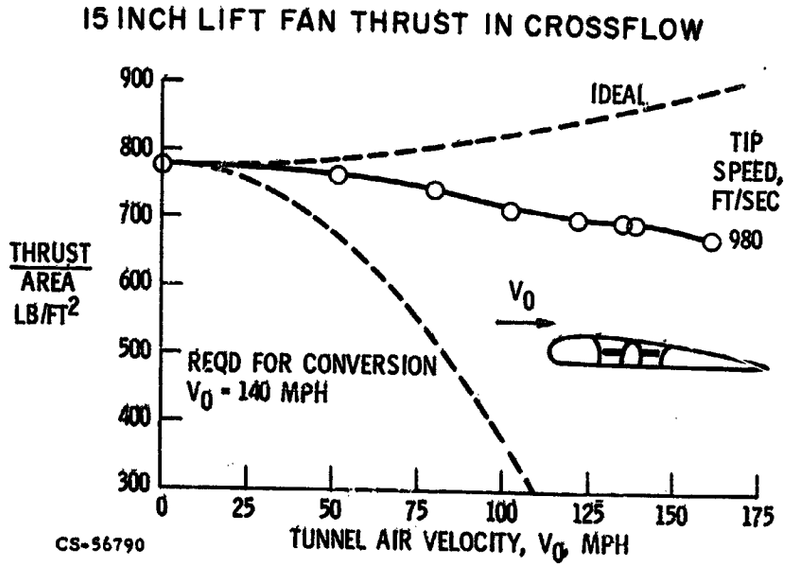

Figure V-26

FAN DRIVE DESIGNS

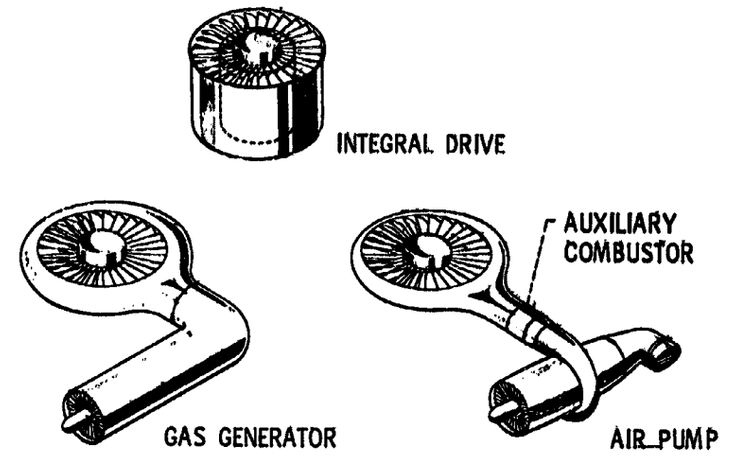

CS-56577

REMOTE DRIVE

Figure V-27

INTEGRAL DRIVE LIFT FAN

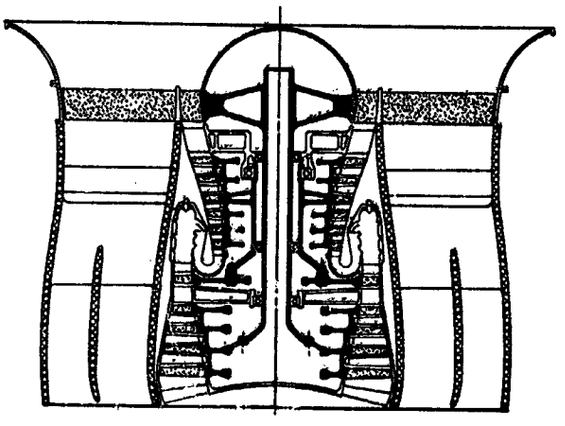

Figure V-28

CS-56578

INTEGRAL ENGINE CYCLE SELECTION

FAN PRESSURE RATIO ≈ 1.2
WEIGHT INCLUDES ENGINE PLUS FUEL

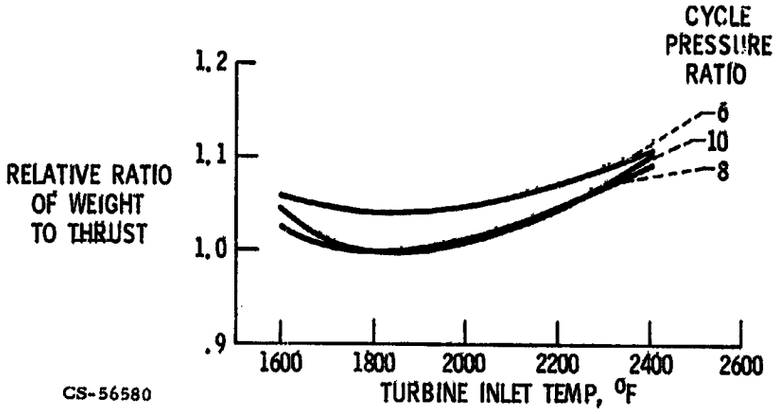

Figure V-29

EFFECT OF TURBINE STAGE WORK ON EFFICIENCY

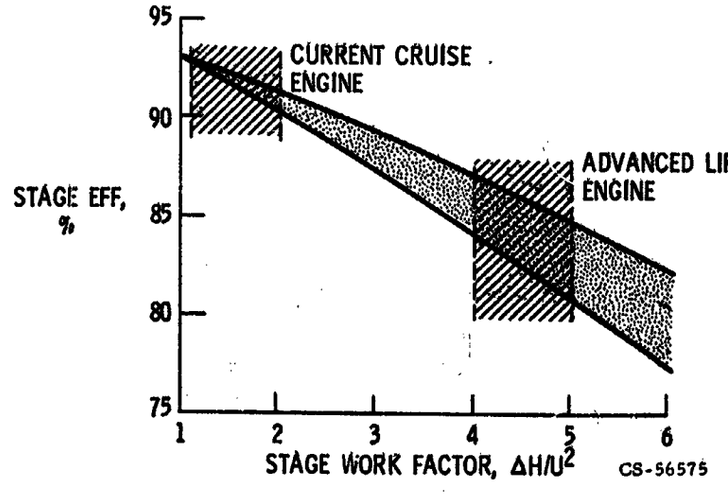

Figure V-30

REMOTE DRIVE LIFT FAN

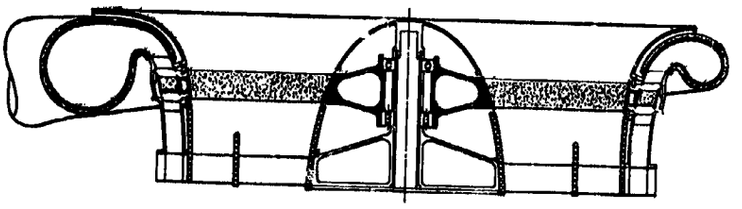

Figure V-31

CS-56574

FAN DRIVE SYSTEM VOLUME FLOW

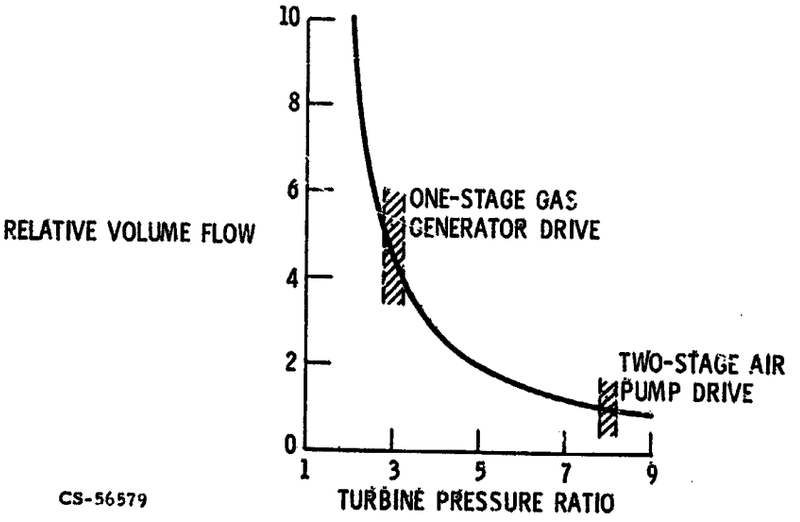

CS-56579

Figure V-32

TIP TURBINE DRIVES

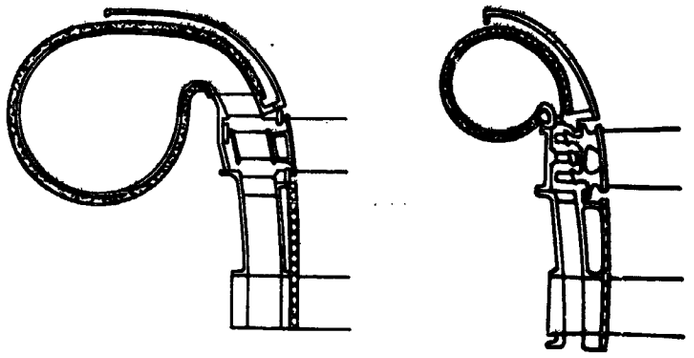

GAS GENERATOR

AIR PUMP

Figure V-33

CS-56576

VI. NOISE REDUCTION

James J. Kramer, David Chestnutt, Eugene A. Krejsa,
James G. Lucas, and Edward J. Rice

Increased use of jet transports along with a growing concern for the quality of the environment has resulted in considerable emphasis on noise reduction efforts in the past 5 years. In order to discuss the noise an aircraft engine makes, it is necessary to define several items: where the observer is with respect to the plane, the engine power setting, and the units of noise measurement. Noise energy levels are measured on a logarithmic scale in decibels. What we are really interested in, however, is not how much energy is in a certain sound but how angry it makes the person who hears it. We want to measure the human response. A new unit, the perceived noise decibel, was developed to reflect the varying human response to the different kinds of sound, distinguished by their frequency spectra. Sounds which have high energy content in the frequencies to which humans are most sensitive are weighted so as to have high PNdB or perceived noise decibel values. These frequencies of high annoyance are in the range of 1000 to 5000 cycles per second or hertz. Other factors are known to affect human response - most importantly the duration of exposure and the presence of discrete tones in the spectrum. Correction factors have been developed and when these are applied, the resultant levels are in effective perceived noise decibels or EPNdB.

Both conventional takeoff and landing (CTOL) and vertical/short takeoff and landing (V/STOL) aircraft noise is discussed. The subsonic aircraft flight profile is considered first. Noise is a factor for subsonic aircraft when they are landing and taking off. These aircraft land on a 3° glide slope, so that their altitude above the community is fairly well defined as a function of distance from touchdown. The engine power setting varies as the pilot maneuvers down the glide slope, but generally the engines are at about 25 percent of takeoff thrust. During takeoff the altitude above the community depends on the operating weight of the aircraft and the power setting. It is possible for the pilot to reduce power after he has achieved some safe altitude. This power reduction results in less noise.

*NASA-Langley Research Center.

CTOL AIRCRAFT

Recently, the FAA issued an aircraft certification standard for noise. The FAA-selected measuring stations for conventional takeoff and landing (CTOL) aircraft are below the aircraft 1 nautical mile from touchdown on approach and 3.5 nautical miles from brake release on takeoff (fig. VI-1). Power cutback is permitted during takeoff if other safety requirements are met. For approach on a 3° glide slope, the aircraft is 370 feet above the ground at 1 nautical mile from touchdown; and at 3.5 nautical miles from brake release, the aircraft is anywhere from 600 to 1200 feet in altitude, or higher. The sideline station is at 0.35 nautical mile for four-engine aircraft and 0.25 nautical mile for two- and three-engine aircraft. The maximum permitted noise levels at these stations are shown in figure VI-2.

Consider a 707/DC-8-class long-range transport. It produces about 118 PNdB of noise at 1000 feet altitude at full takeoff power. If a replacement aircraft were to be built, it could make no more than 103 EPNdB according to this FAA standard. The actual permitted noise levels are a function of aircraft size, with the variation in effective perceived noise level (EPNL) a function of aircraft gross weight as shown in figure VI-2. Generally, the levels required now are about 10 to 15 PNdB lower than previous levels.

At Lewis we have been working for several years on a low-noise engine suitable for use on a CTOL airplane. The engine will incorporate all available sound reduction features in an effort to consolidate and advance the technology of noise reduction. The engine is called the Quiet Engine. This engine in conjunction with an acoustically treated nacelle should permit the attainment of noise levels about 10 PNdB below the current FAA certification levels. Currently being built under contract with General Electric is a high-bypass-ratio engine developing 22 000 pounds of takeoff thrust. A cross-sectional view of the engine is shown in figure VI-3. In this program, several fans and turbines for the engine are being built, linings for the cold and hot ducts are being investigated, and some potential noise reduction devices are being tested on a half-scale model fan. We expect to be testing the engine at General Electric in about 6 months and to take delivery here at Lewis in late 1972. This engine serves as the basis for the following discussion of our noise research.

Noise Sources

Gas turbine engine noise can be divided into two general categories: internally generated noise, usually associated with the rotating machinery; and externally generated noise, or jet noise. Any noise reduction program must consider all sources

and bring them all down to an acceptable level.

The cutaway view of the Quiet Engine shown in figure VI-4 reveals the sources of internally generated noise. These primary sources are the fan, the compressor, and the turbine. In this engine, as in most high-bypass-ratio engines, the fan is the dominant source of the internally generated noise. The fan noise propagates out both the engine inlet and the fan discharge duct, the compressor noise propagates out the engine inlet, and the turbine noise propagates out the jet exhaust nozzle.

There are two sources of externally generated noise in a turbofan engine. In figure VI-5 the mixing regions which produce the jet noise are shown. One is located downstream of the fan exhaust duct and the other at the nozzle exhaust.

There is an important distinction between the internally generated and externally generated noises. The internal noise can be suppressed in the engine passages, whereas the external noise obviously can not. The most effective control of externally generated noise is to keep the jet velocities as low as possible. Figure VI-6 shows how acoustic treatment might be applied to the engine passages for the reduction of internal noise. The fan noise is reduced by inlet and fan exhaust suppressors. The compressor noise is mostly absorbed in the core engine inlet, while the turbine noise is suppressed inside the core exhaust nozzle area.

The relative magnitude of the different noise sources can vary from engine to engine, and even for a given engine they can vary with operating conditions. This is illustrated in the figures VI-7 and VI-8. All noise sources have to be lowered since overall sound pressure level is determined by the highest level source. Figure VI-7 shows the perceived noise level for a Boeing 707 or DC-8 aircraft at takeoff and landing approach. The Pratt & Whitney JT-3D engines for these aircraft have a bypass ratio of 1.43. At takeoff the jet noise is greater than the engine inlet noise and nearly as loud as the fan exhaust duct noise. Therefore, internal noise suppression would provide very little noise reduction. At landing approach, however, the jet noise is much less than the noise radiated from the engine inlet and fan exhaust duct. In this case, internal accustic suppression would result in substantial reduction in perceived noise level.

In figure VI-8 the same type of plot is shown for the Quiet Engine. With a bypass ratio of 5.5 to 1, the noise relation has changed considerably. For both takeoff and approach the jet noise is considerably below the noise radiated from both the inlet and the fan exhaust duct. This is due to the high-bypass feature, which extracts significant propulsive energy from the main jet. This feature has been incorporated in some of the newest engines now in production. Thus, internal noise suppression results in substantial perceived noise level reductions at both approach and takeoff.

Jet noise. - There are two external noise sources in a turbofan engine such as the Quiet Engine. These are shown schematically in figure VI-9. One source of external noise is the turbulent mixing region produced when the fan jet mixes with ambient air. The other source of external noise is the mixing region produced when the core jet mixes with the fan jet and ambient air.

When two airstreams at different velocities mix, considerable turbulence is generated and some of this turbulent energy is radiated as sound. As the difference in velocity increases, the intensity of the turbulence increases and, hence, the noise increases.

Figure VI-10 shows the relation of the sound power generated by jet mixing to the jet velocity. The data points shown were obtained from noise studies on jet engines and on nozzles supplied with hot and cold air. These data points were taken in the velocity range which is typical of turbojet and turbofan engines. The slope of this line on the log plot indicates that the noise is proportional to the jet velocity to the eighth power. Due to this strong dependence, a moderate reduction in jet velocity will produce a considerable reduction in noise. For example, a reduction from 2000 feet per second, which is a typical jet velocity for a turbojet at takeoff, to 1500 feet per second, which is a typical jet velocity for a low-bypass-ratio turbofan at takeoff, produces about a 10-dB reduction in noise. Further reduction in the jet velocity to that of the Quiet Engine would result in further reduction in the noise.

The Quiet Engine operates with a core jet velocity of about 1150 feet per second and a fan jet velocity of about 900 feet per second. These jet velocities are at static conditions. The takeoff community noise measurement point is at 3.5 nautical miles from brake release. At this point the airplane will have a forward velocity of about 250 feet per second. Since the noise produced depends on the relative jet velocity, the jet noise will be determined by exhaust velocities which are about 250 feet per second lower than those shown.

Data have been taken on jet engines in this lower velocity range and are shown in figure VI-11. These data, shown as circular points in the lower velocity range, fall above the eighth-power curve. The reason that the data fall above the eighth-power curve is that in this velocity range the noise is dominated by the internal machinery noise.

Recent work here at the Lewis fan noise facility has demonstrated that, if the jet noise is extracted from the total noise, the jet noise does follow the eighth-power curve. These points are the square points in this figure. They fall slightly below the curve but generally follow the eighth-power law.

Figure VI-12 shows the jet noise produced by a 300 000-pound-gross-weight airplane having a thrust of 90 000 pounds. The core jet produces a noise indicated by the upper band. The noise produced by the fan jet is indicated by the lower band.

The Quiet Engine will operate at a pressure ratio of 1.5. At this pressure ratio the jet noise will be about 90 or 95 PNdB.

Fan noise. - One of the major noise problems of the high-bypass-ratio turbofan engine is internal noise associated with turbomachinery. For the purpose of discussion we will consider the propulsion system for a 300 000-pound subsonic airplane of the DC-8 or 707 class. A new airplane of this size would have a thrust-weight ratio of about 0.3 and, hence, would require 90 000 pounds of thrust. If four engines are used, as they are in these airplanes, they will each have about 22 000 pounds of thrust, which is the size of the Quiet Engine shown in figure VI-3. An engine of this type is normally found to produce most of its internal noise in the fan component and this is quite understandable for several reasons. First, noise essentially is generated by the moving of air, and the fan has a higher airflow than any other engine component, in fact six times higher in an engine of this type. In addition, the fan is the component most exposed to the observers view and, hence, its noise has the easiest path to the observer. Also, the fan is physically the largest component, and it has quite high velocities relative to the air. All this adds up to make the fan a potentially large generator of noise.

The fan produces noise of three types: broadband, discrete tones, and multiple pure tones. Broadband noise is essentially the noise from turbulence in the air and scrubbing of the air across hard fan surfaces. It can be seen from figure VI-13 that the spectral plot of broadband noise shows essentially a straight line at a constant decibel level. Discrete tones are those at the frequency of rotor blade passage and its harmonics, and they are influenced greatly by the flow conditions over the rotor blades and by impingement of rotor wakes on the stators. Multiple pure tones, shown on the figure as a small field of fine spikes at a low frequency, are most probably generated by shock patterns on the rotor blades caused by supersonic local relative Mach numbers. They can occur anywhere in the spectrum and at any level. Broadband noise is associated with any flow process and, hence, will always be present in the spectrum of a fan noise. The discrete tones or multiple pure tones may or may not be prominent in a particular spectrum, depending on the fan design and the operating conditions. The extent to which they are present in the spectrum can affect the characteristics of the fan-generated noise greatly. On the typical spectrum shown in figure VI-13 the noise with the highest decibel level is the discrete tone and this tone would dominate the noise that the observer hears. This, in fact, is the whine that is so characteristic of the noise heard from current jet airplanes having turbofan engines. Sounds dominated by multiple pure tones tend to have a raspy, buzzing quality to them.

Before details of our fan research program and some of the results of the program are presented, mention must be made of the other internal noises, those from

the core engine and the fan turbine. Normally, these produce a level of noise which is low enough that it is insignificant in the total engine noise. However, if the fan component were quieted sufficiently either by design or by suppression treatment, the noise levels of the core engine and the turbine could possibly become dominant. Indeed this can happen, and for this reason the Quiet Engine has some acoustic suppression treatment in the turbine exhaust duct.

The facility shown in figure VI-14 was built to acoustically evaluate a series of full-size fans. Drive is by an electric motor of 37 000 horsepower through the shaft to the inlet of the fan rotor. Far-field noise is measured by microphones on poles, some of which are shown in the figure. A cutaway view of the fan nacelle (fig. VI-15) shows such internal details as the drive shaft, rotor blading, stator blades, cowling, and exhaust nozzle. The basic aerodynamic design of the fan, such as its thrust and bypass ratio, is very closely determined by the performance requirements of the engine itself. The fan designer then would like to select an optimum combination of tip speed, pressure ratio, weight flow, and mechanical arrangement to yield the lowest possible noise output. To do this he must know the relations between these various design parameters and the types and amounts of noise produced. These relations are not known at present, but they should become evident as the result of a test program with a series of full-size fans of varying design. These designs are shown in figure VI-16, where they are defined in terms of tip speed and pressure ratio. Tip speed is used because it is an important noise parameter which indicates the expected level of relative Mach numbers on the blading. Thus, it affects the generation of all three types of noise. Pressure ratio is used in this figure simply as an indicator of blade loading at a given speed, or how much turning the blading has to do on the air passing by it. These fans are all about 72 inches in tip diameter; they are all single-stage fans; and most of them were designed for about 22 000 pounds of thrust. A pressure ratio range of about 1.4 to 1.6 is of interest for the CTOL airplane and most of the fan designs are concentrated in this area. In the aerodynamic design of a fan a trade-off can be made between tip speed and loading. Among other things, the designer must know how to balance these two parameters to yield the lowest possible noise output. This can be determined by systematically varying each parameter separately and studying the noise generated. Testing a series of fans designed at the same tip speed, for example, will indicate how the blade loading affects the noise output. Similarly, tests on a series of fans designed at a particular pressure ratio will show how tip speed affects the noise generation. As a result of these tests, the interrelations among blade loading, rotor tip speed, and noise generation should become apparent. One fan, designed at low tip speed and low pressure ratio, represents the type of design which may be required for a high-bypass STOL engine, or for a VTOL engine. In

designing these fans, generous advantage was taken of some of the previously known techniques for reducing noise generation. For example, these fans were designed with a wide spacing between the rotor and stator blade rows to allow the rotor blade wakes to dissipate before hitting the stators, thus lowering the generation of discrete tones. In addition, in most of the fans the number of rotor and stator blades was chosen to minimize the propagation of discrete tones.

One fan, that designed at 1100-feet-per-second tip speed and a pressure ratio of 1.5, has already been tested. It was found that the maximum forward-projected fan noise occurred about 40° off the fan inlet axis. Figure VI-17 presents a spectrum of sound pressure level taken by a microphone at that location. This spectrum was obtained with the fan operating at takeoff speed with the standard exhaust nozzle. The base level on the spectrum at about 75 to 80 dB is the broadband part of the overall noise. The tall spike is the discrete tone which occurs at rotor blade passage frequency (in this case about 2700 Hz), and the two spikes at higher frequencies are its harmonics. At about 400 and 1500 hertz there are small contributions of multiple pure tones. Obviously, the loudest sound in this particular spectrum is the discrete tone and the observer below the airplane would hear the whine previously described. When the fan is run at the same speed but with the exhaust nozzle area increased about 10 percent, thus increasing the level of relative Mach number on the blading, the spectrum (shown in fig. VI-18) is considerably different. It still has about the same broadband base level but now the discrete tone has dropped considerably, as have its harmonics. The most striking difference between these two spectra is the presence now between 1000 and 1500 hertz of a band of very loud multiple pure tones. In this case the observer would hear the raspy sound of a noise dominated by multiple pure tones. The interesting feature of this comparison is that the increasing presence of multiple pure tones is accompanied by a considerable lowering of the discrete tone which is in the high-annoyance frequency range. The result is that the calculated perceived noise level of the fan is somewhat lowered. These two spectra were obtained at rotor inlet relative Mach numbers of 0.97 and 0.99, respectively, which indicates a very sensitive relation of the multiple pure tones with Mach number.

Calculations were made to estimate, on the basis of the best available data, the fan machinery noise to be expected from turbofan engines of varying design, all sized to provide a total of 90 000 pounds of thrust from four engines. Figure VI-19 presents the calculated perceived noise level of single-stage fans at takeoff operation as a function of the fan pressure ratio. The curve is shown as a band of several dB width, which reflects the uncertainty in the calculation. Data points for the fan just discussed and for a half-scale model of one of the Quiet Engine fans are shown to verify the level of the curve. The Quiet Engine fan, which operates at a

pressure ratio of 1.4 during takeoff, is shown to produce about 105 PNdB of noise, which will nearly satisfy the current FAA regulations for new airplanes. An upper limit to the pressure ratio that can be obtained from a conservative single-stage fan is shown on the figure at around 1.7 or 1.8. This means that if a higher pressure ratio is needed for some particular engine cycle a two-stage fan would be required. Some thought has also been given to using a two-stage fan, even at lower pressure ratio, to decrease blade loading. For these two reasons, figure VI-20 presents the same curve as figure VI-19, with the addition of an equivalent noise prediction curve for the two-stage fan. The level of the two-stage-fan curve is supported by data points from the JT3D engine and from a modified TF-39 engine. The two-stage fan is shown to typically produce about 7 or 8 PNdB more noise than the single-stage fan. This is the result of interaction effects caused by the additional blading. Some propulsion schemes do require high pressure ratio and, of course, must accept the noise penalty of the two-stage fan. In the lower pressure ratio range, however, the single-stage fan is clearly the better. It has been shown that the single-stage-fan engine by itself will nearly meet the FAA regulations; moreover, its noise can be lowered still further by acoustic suppression treatment, which is the subject of the following section.

Suppressors

Large noise reductions can be achieved by the use of acoustic suppression in the internal passages of an engine. This discussion stresses the use and results of a typical suppression configuration in the Quiet Engine.

The cutaway view in figure VI-6 reveals the acoustic liners of the Quiet Engine. The forward-radiated noise of the fan is partially absorbed by the inlet suppressor consisting of the treated cowl and splitter rings. The long fan exhaust duct is treated on the inner and outer walls to provide suppression of the aft-radiated fan noise. The internal passage leading to the compressor is also lined. The acoustic lining in the core nozzle will remove turbine noise.

The mechanisms behind the operation of the acoustic liners can be shown by observing the ducts in a little more detail. A small section of the acoustic liner is shown enlarged in figure VI-21. A perforated plate over a honeycomb backing cavity is further magnified in the inset. When the acoustic pressure is high on the duct side of the plate, a jet will be formed flowing into the back cavity. The jet will flow out of the orifice when the acoustic pressure drops below ambient. The absorption of acoustic power is accomplished through the turbulent dissipation of the kinetic energy of these jets. The resonant properties of the liner can be adjusted to provide

maximum acoustic power dissipation at a given frequency, such as the frequency of noise providing the greatest annoyance. This is done by adjustment of the back cavity depth and the sheet thickness and porosity. Adjusting these parameters allows us to obtain the proper wall acoustic impedance to optimize the coupling between the liner and the duct.

Other wall constructions could also be used. The face plate could be made of very fine wires or screens. The back cavity could be packed with a bulk absorber such as fiber glass. In these constructions the main dissipation mechanism would be the viscous shearing effect in the very small passages of the material.

In the fan and compressor passages, common materials, such as aluminum, are sufficient for the absorber. In the core engine exhaust, moderately high-temperature materials must be used.

A 6-foot-diameter turbofan similar to that of the Quiet Engine has been tested here at Lewis. Figure VI-22 shows the inlet suppressor used with this fan. The suppressor is made up of a lined outer cowl and three splitter rings lined on both sides. The outer ring has a lined length of about 3 feet. All liners are constructed of aluminum perforated plate bonded to an aluminum honeycomb backing. The inlet is shown with a bellmouth which is used for static testing only.

Figure VI-23 shows the effect of the inlet suppressor on the narrow-band noise spectrum at the position of maximum front-end noise. This occurs at 40° off the inlet axis. The fan was operated at takeoff speed for this data. The upper curve represents the noise for the hard-cowl configuration. The lower is for the acoustically lined configuration. The liner absorbs noise over a very wide frequency range, with substantial reductions between 400 and 10 000 hertz. The maximum absorption is near the blade passage frequency. The harmonics of the discrete tone are also reduced. The multiple pure tones near 500 and 1500 hertz have been completely removed.

The suppressors provided perceived noise level reductions of 12 PNdB at simulated takeoff conditions and 13 PNdB at approach. It is felt that a 15-PNdB reduction could be realized with proper suppressor design and balance. This is reflected in figure VI-24. The predicted PNL versus fan pressure ratio is shown. The upper curves represent the turbomachinery noise for one- and two-stage engines without suppression. The lower curves indicate the results with the expected 15-PNdB reductions.

Choking

Aerodynamic choking is defined as the acceleration of airflow to sonic velocity

by reducing the flow area to a critical value. The concept of choking for noise reduction is shown diagrammatically in figure VI-25. The noise being generated propagates to the left against the airflow until it reaches the choked region, where the air velocity is equal to the speed of sound. The sound waves begin to reflect but are believed to lose their phase identity due to the irregularity of the shock wave. This condition is termed "hard" acoustic choking; that is, none of the noise generated downstream can propagate upstream beyond the choked region. If this phenomenon is going to be used in an aircraft engine inlet, it must be variable since the engine requires varying airflows for its operation. Figure VI-26 shows a variety of mechanisms that can be used to accomplish this. The first type of mechanism indicates variable geometry vanes, some of these vanes may be translated, rotated, or expanded; the second type indicates that the cowl may be contracted; the third type includes variation of the centerbody by either expanding it or translating it.

In figures VI-27 and VI-28 are typical results obtained by rotating the inlet guide vanes to cause choking. The outer curve in figure VI-27 shows the unchoked noise level at all azimuthal locations in a forward quadrant. The inner curve shows the corresponding choked noise level. Figure VI-28 shows spectra taken at the point of maximum sound pressure level (SPL), which was at the 30° azimuth from the compressor centerline. These measurements were made using a model compressor operating at high rotational speeds, hence, the high frequency noise. The upper curve shows a typical unchoked spectrum. The maximum peak is that associated with the fundamental blade passing frequency. The lower curve shows the choked spectrum taken at the same azimuth. Not only have the fundamental frequency and its harmonics been drastically reduced, but the broadband level has been significantly reduced also.

Since the choking concept is so promising acoustically, we will now examine the design requirements associated with using a choked mechanism in a production engine for commercial flight operations. Of particular concern is operational safety. Whatever mechanism is chosen for choking must be fail-safe. It is most desirable to use a device that is mechanically simple. A certain amount of effort is being directed toward this goal. In addition, there are design considerations to minimize the effects of inlet pressure recovery, inlet distortion at the fan rotor, cowl drag, and weight.

CTOL Summary

Based on the preceding discussion of the two types of noise (jet and fan) and noise estimates for CTOL aircraft, we can estimate the total propulsion system noise. Unsuppressed fan noise follows trends like those shown in figure VI-29. A single-stage fan should be used if at all possible. Noise reduction can be achieved by passive linings or choked inlets. These techniques can give reduced machinery noise, as shown in the figure VI-29. The jet noise from the core and bypass streams follows the trend shown. Suppressed fan and jet noise sources are pretty well balanced around a fan pressure ratio of 1.5, the ratio for which we designed our Quiet Engine. Noise is even lower at lower fan pressure ratios, but engine diameter increases and drag losses rise. All levels in figure VI-29 are for 90 000 pounds of thrust at 1000 feet altitude at full takeoff power. The levels that appear to be achievable are in the range of 90 to 95 PNdB. These values are about 10 PNdB below current FAA regulations for new CTOL aircraft.

STOL AIRCRAFT

The air transportation system of the 1980's will include not only CTOL aircraft but will also probably include substantial numbers of STOL and VTOL aircraft. An advantage of short-takeoff-and-landing (STOL) aircraft is that the airport can be closer to the center of town. But noise levels must therefore be lower than for CTOL aircraft. Short-takeoff-and-landing field requirements result in considerably increased installed thrust levels compared to conventional aircraft. And this increased engine power produces more noise than with CTOL aircraft. The reason for the high thrust is that part of the propulsion is used to augment the lift. There are several lift augmentation schemes, and these may themselves be noise sources. Two of these lift augmentation systems - the blown flap and the augmentor wing - are examined.

Blown-Flap Noise

In considering the blown-flap geometry, the emphasis is on noise production when the flap is lowered into the engine exhaust.

A four-engine STOL aircraft using blown flaps for lift augmentation is shown in figure VI-30. It looks very similar to conventional aircraft, except that the flap is

much larger in comparison to the main wing section. This can be seen in the wing cross section at the lower right corner of the figure.

Two important questions about blown-flap noise need to be answered:

(1) Can the flow interacting with the flap become a significant external noise source?

(2) Can the flap redirect internally generated fan noise?

In order to get some preliminary answers to these questions, noise measurements were made on the blown-flap model that was used in the STOL wind tunnel tests.

In figure VI-31 a cross section of the blown-flap model is shown. The maximum flap angle of 60°, to simulate approach, is shown. Noise measurements were also made for takeoff conditions with 30° flap deflection and for cruise conditions with no flap deflection.

This model is shown in figure VI-32. The model is roughly 1/10 scale based on a 100 000-pound-gross-weight aircraft. Only one 6-inch-diameter fan was used. A 60° flap deflection corresponding to the approach condition is shown. Noise was measured in the plane perpendicular to the wing looking at the underside, and in the plane of the wing looking at the end.

A typical noise spectrum produced by the model is shown in figure VI-33. Sound pressure levels versus frequency are shown for no flap deflection. Of course, all the frequencies are high because of the small scale of the model As might be expected, when there is no flap interaction with the flow, the spectrum is typical of any fan. At the higher frequencies there are internally generated fan noise spikes at blade passage frequency and its harmonics, along with some broadband fan noise. In the experiments no significant changes in fan noise strength or directivity were found as the flap was lowered into the flow.

At lower frequencies there is some evidence of externally generated jet noise. The slight bulging of the curve is associated with this jet noise. The change in this low-frequency hump which occurs when the flap is fully lowered into the exhaust flow is shown in figure VI-34. While fan noise remained about the same, the low-frequency hump was substantially increased as the flap was lowered to the 60° approach condition. This increase is due to the fan flow interacting with the flap. The band indicates differences associated with different measurement angles. Results for a 30° flap deflection at takeoff conditions fell between the 0° and 60° flap cases, as would be expected.

If the model fan had been acoustically treated or designed with quieting features, the high-frequency fan noise would be lowered and the lower-frequency flap interaction noise could become the dominant source.

The experimental interaction noise data were scaled to full scale, and perceived noise levels were calculated. Such scaling involves shifting the data to lower fre-

quencies, so that some uncertainty results. However, scaling does allow the use of the model results to make estimates of how the interaction noise contributes to the total noise of the blown-flap propulsion system.

First, consider the noise produced by the turbofans alone, as shown in figure VI-35. A 500-foot distance is used here since the STOL aircraft will operate very close to densely populated areas. The jet noise becomes the dominate source above pressure ratios of about 1.4.

In figure VI-36 a third band is added, which is the flap interaction noise that was obtained by scaling the model results. It includes both the noise of the redirected jet and the noise produced in the process of redirecting it. The interaction noise becomes the dominant noise source at a pressure ratio of about 1.3, whereas jet noise alone dominated at 1.4.

The two questions posed earlier have now been given at least preliminary answers. First, a significant interaction noise can be generated in the process of turning the engine exhaust flow. Second, no significant redirection of the internal engine noise was observed.

Augmentor-Wing Noise

Shown in figure VI-37 is a schematic of the augmentor-wing propulsion system. High-pressure air is ducted to the wing during takeoff and landing. This air exhausts through a slot in the wing and flows through an ejector made up of flaps on the wing trailing edge. This arrangement provides the high lift coefficients needed for short takeoff and landing.

Since the pressure ratio across the wing slot is high, about 2.5, considerable noise could be generated when this air mixes with ambient air. However, since most of the mixing occurs between the flaps, some beneficial shielding may help reduce this noise. To study this noise source, an augmentor-wing noise test facility was built at Lewis. This facility is shown in figure VI-38. Pressurized air is fed to the wing through the pipe shown. The wing is a 6-foot span of an approximately 1/2-scale wing for a 100 000-pound-gross-weight airplane. The air flows out of the slot and flows between the two flaps. Noise measurements were made over a range of pressure ratios for several slot heights.

Figure VI-39 shows a typical directivity pattern of the noise produced by this wing. These data were taken with a slot height of 0.7 inch and a pressure ratio of 2. The two-lobed pattern centered about the jet exhaust is typical of jet noise. Due to the angle of the flaps, the lower lobe is almost directly below the wing. During flyover, sound in this lobe is radiated straight downward toward the ground. Sound

from the other lobe travels farther before hitting the ground. Thus, even though the noise power of the two lobes is nearly equal, the noise represented by the lower lobe appears louder to an observer on the ground.

Figure VI-40 shows the spectrum of the noise in this lower lobe. The noise is broadband, which is typical of jet noise. There are no spikes in the spectrum, as there were in the spectrums of machinery noise. These data were also taken with a slot height of 0.7 inch and a pressure ratio of 2. The location of the microphone relative to the wing is shown in the schematic in the upper right corner of the figure. The spectrum peaks at about 3000 hertz. The frequency of this peak is predictable from the slot height. Since the slot height is small, about 1.5 inches for the full-scale plane, the noise generated by the wing will be in the frequency range that the ear is most sensitive to.

In order to study ways of reducing the noise produced by the wing, the flaps were lined with acoustic absorbing material, as shown in figure VI-41. The material is similar to that used in the fan tests. It is made of a perforated sheet bonded to a honeycomb backing. The material was placed on the flaps as shown in the figure.

The effect of this material on the noise spectrum is shown in figure VI-42. Data for the unlined flaps are shown as circular points, and the square points are the data obtained with the lined flaps. About an 8-dB reduction was obtained at 5000 hertz. Even though this lining produced only 2 PNdB reduction in the overall noise, the test did indicate that the noise produced by the wing can be attenuated by lining the flap surfaces.

The results of these tests were scaled to a 100 000-pound-gross-weight airplane and are shown in figure VI-43. For a plane of this size, about 30 000 pounds of thrust would be obtained from the wing. The estimates indicate that a plane of this size would produce about 105 to 115 PNdB with no lining on the flap surfaces. If the flaps are lined, the noise may be reduced to about 100 to 110 PNdB.

Conventional aircraft noise technology and experimental work has been applied to STOL aircraft noise prediction and has led to the prediction of engine inlet noise as the dominant noise source, as shown in figure VI-44. These predictions are scaled to the anticipated size of the augmentor-wing prototype aircraft. In addition, the engines are assumed to be designed for low jet exhaust velocities and, hence, low jet noise. In order to obtain a high pressure ratio for small ducts in the wing, the unsuppressed fan inlet noise is estimated to be in the range of 120 PNdB, as shown. This is for two or three stages of compression. If larger ducting with lower pressure ratios could be tolerated, a distinct noise advantage (about 10 PNdB) could be realized. This is shown by the lower band for fan inlet noise at low

pressure ratios. This decrease in noise is associated with the use of a single-stage fan. This inlet noise could be further reduced by either inlet choking or inlet suppressors. The inlet suppressor system is shown in figure VI-45. The suppressors shown in this figure are estimated to be capable of noise reduction of the order of 10 PNdB. If a wing slot pressure ratio of 1.4 were acceptable, the 95-PNdB goal might be reached. If a higher wing slot pressure ratio is required, a choking mechanism in the inlet is indicated. A candidate choking mechanism is shown in figure VI-46. This choking device is called a grid inlet. It is made of a series of airfoils arranged across the inlet like a venetian blind. In the cruise mode these vanes are in several rows. When choking is required, all the rows are brought together to reduce the inlet area. This technique has been tested successfully on a cascade rig and on 6-inch- and 12-inch-diameter model fans. Choking should reduce the fan inlet noise by 25 to 30 dB, which is within the 95 PNdB goal. However, the noise created at the wing slot will now dominate, and some method must be found to further reduce this level before 95 PNdB can be realized.

STOL Summary

The limited amount of blown-flap data available indicate that this augmentation system may have a noise problem. Small-scale model tests have indicated no redirection of the fan discrete frequency noise, but have shown an amplification of the jet noise. The amount of amplification is estimated at about 5 PNdB for the wing configuration at takeoff. At approach, the amplification is larger because of the larger flap immersion in the jet. However, the jet velocities are lower at approach. The jet noise becomes a dominant source above a fan pressure ratio of about 1.3. Acoustic results on one model of an augmentor wing show rather high noise levels and point to the need for further work in developing a wing configuration with acceptable acoustic and aerodynamic characteristics.

For both the augmentor wing and the blown flap it is clear that considerable effort is required to produce systems with low noise output.

VTOL Aircraft

Several characteristics of the VTOL airplane and its propulsion system stand out. First, of course, the very reason for existence of the VTOL airplane is to allow it to operate from population centers, which means that people will be very close to the airplane during its takeoff and landing operations. In addition, during

these operations, the aircraft velocity will be quite low, and hence the relative jet velocity will be about equal to the absolute jet velocity. This implies an increase in jet noise generation over the CTOL or STOL airplanes. Also, lift fans will be used to generate the low-pressure-ratio jets for vertical thrust, and they will tend to be installed very compactly to permit good cruise performance. As a result, it will be difficult to surround them with a generous amount of acoustic suppression. Finally, an enormous amount of thrust will be installed on the VTOL airplane so that its thrust-to-gross-weight ratio will exceed unity, and the added thrust will represent an increased source of noise. These characteristics combine to make the VTOL noise problem difficult. Because there is only a limited amount of data available on VTOL lifting systems, machinery noise data and jet noise data have been used to estimate the noise performance of some VTOL propulsion systems.

In a similar format as was used for the CTOL and STOL systems, figure VI-47 presents calculated perceived noise levels at 500 feet from the takeoff point of a VTOL aircraft. The propulsion systems have been generalized so they can operate at different pressure ratios. The calculations assume a 100 000-pound-gross-weight airplane having twelve 10 000-pound-thrust units. The fan machinery noise of these 12 engines unsuppressed follows the trend shown. As discussed earlier, if space were available, this fan machinery noise could be suppressed by 15 PNdB. Acoustically there is no reason why such suppression would not be possible. However, there may be a severe mechanical problem in just finding sufficient area to treat in the small engine nacelle. Because of this, the overall feasibility of 15-PNdB suppression is problematic at this point and needs further study. The jet mixing noise of the VTOL lift fans will produce the trend shown, obviously falling off rapidly as the pressure ratio of the fans decreases. The overall implication of these curves is that VTOL lift fans must operate at a fairly low pressure ratio if they are to produce low noise levels. In addition, a serious effort must be made to introduce sufficient acoustic suppression into the housing around these lift fans to reduce the machinery noise.

SUMMARY

For conventional aircraft there is a potential for substantial further noise reductions below present FAA certification limits. Complete system work is underway within NASA in the Quiet Engine Program.

STOL aircraft require even lower noise levels, while at the same time adding another noise producer in the lift augmentation system. Both externally-blown-flap and augmentor-wing concepts need considerably more research effort in order

to define accurately the severity of their noise and to devise noise reduction schemes. To achieve noise levels as low as 95 PNdB at 500 feet will require technology beyond that currently available. This technology, however, may well be developed if serious attention is given the problem, as has been done in the case of CTOL aircraft.

VTOL aircraft using lift fans have two noise problems: Installation of enough acoustic treatment to suppress the fan machinery noise is difficult in the typical compact installation. Low-velocity jet noise appears to follow the eighth-power law; but in order to have a low-jet-noise signature these lift fans will have to operate at low pressure ratios.

FAA CTOL NOISE REFERENCE LOCATIONS

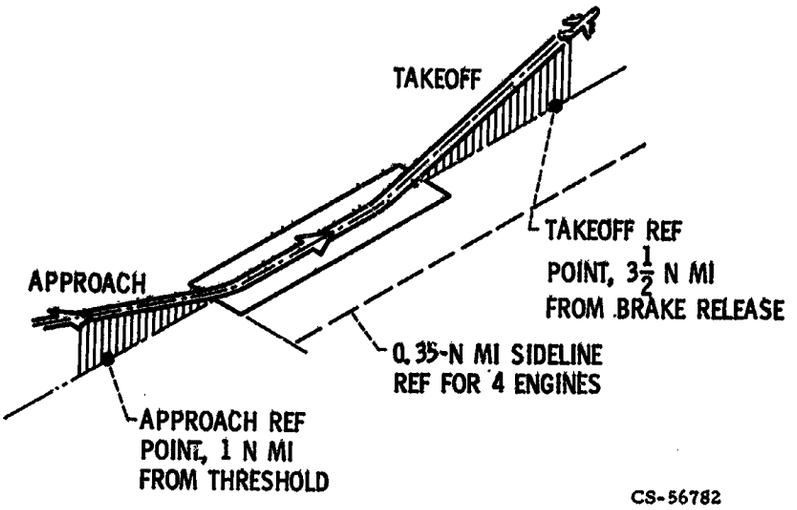

Figure VI-1

CTOL NOISE RESTRICTIONS

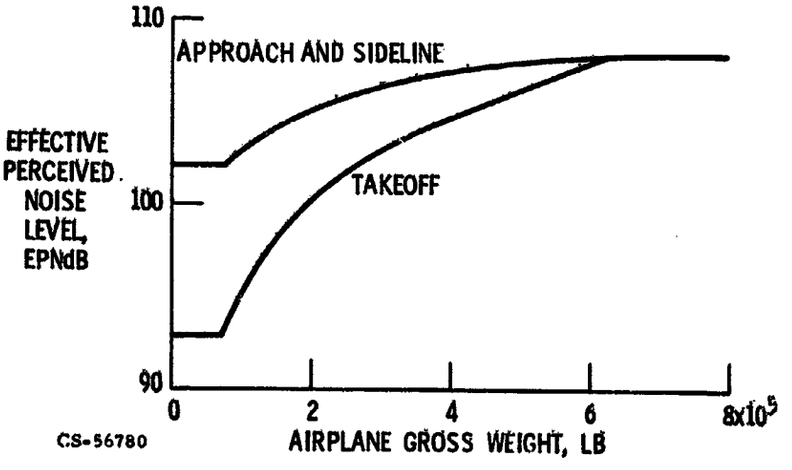

Figure VI-2

QUIET ENGINE

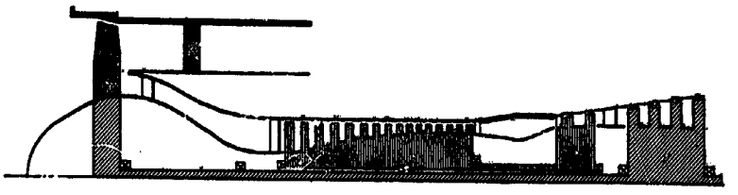

CS-56783

Figure VI-3

INTERNAL NOISE SOURCES – QUIET ENGINE

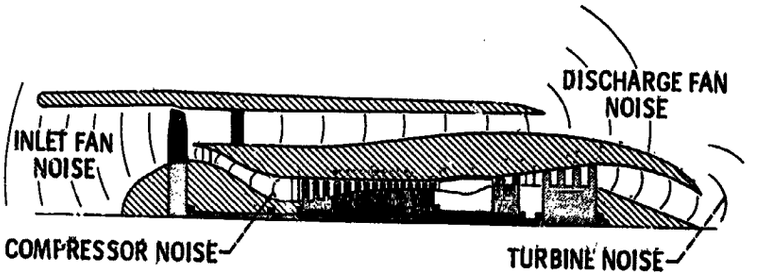

CS-56623

Figure VI-4

EXTERNAL NOISE SOURCES

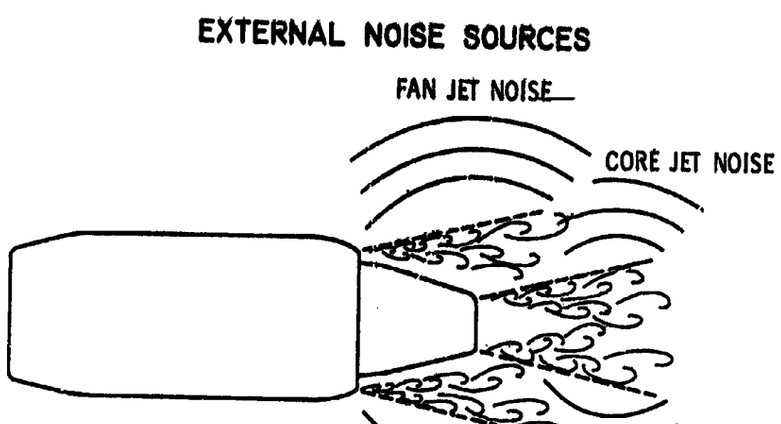

Figure VI-5

QUIET ENGINE: WITH SUPPRESSION

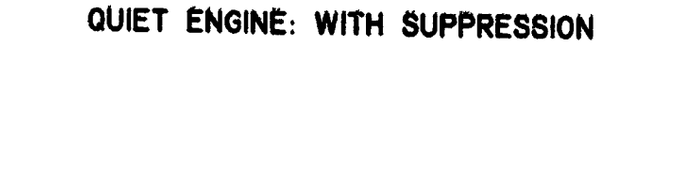

Figure VI-6

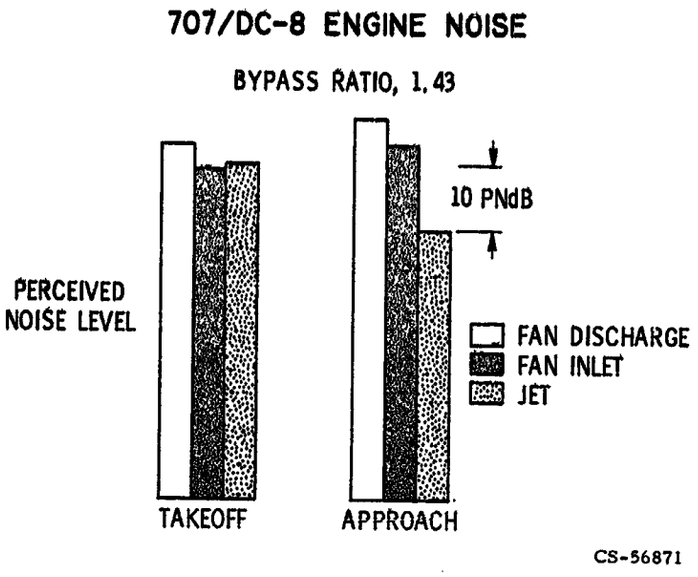

Figure VI-7

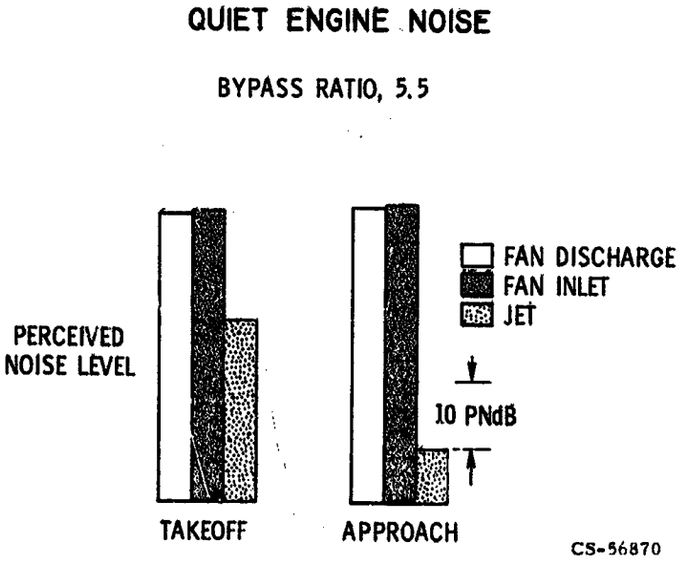

Figure VI-8

EXTERNAL NOISE SOURCES

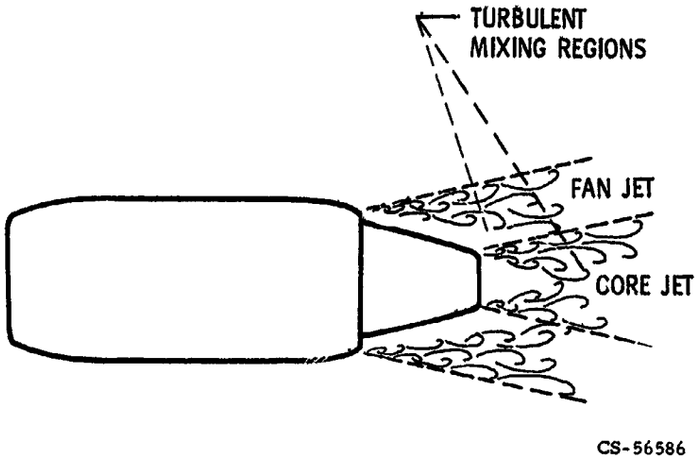

Figure VI-9

JET NOISE CORRELATION FOR VELOCITIES OF 1000 TO 2000 FT/SEC

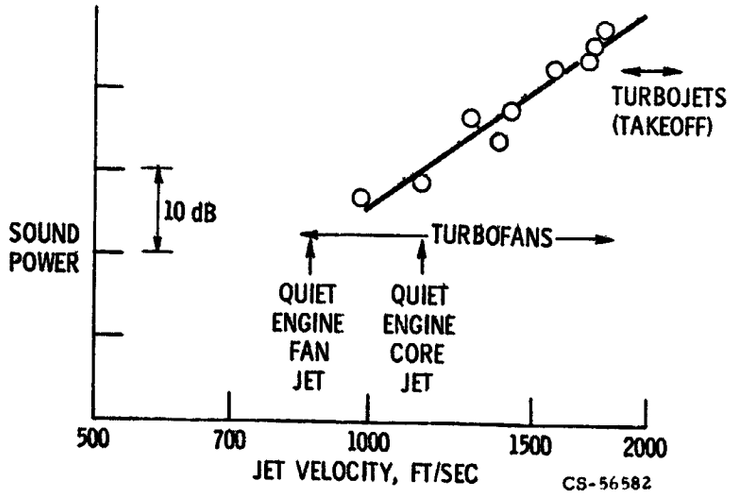

Figure VI-10

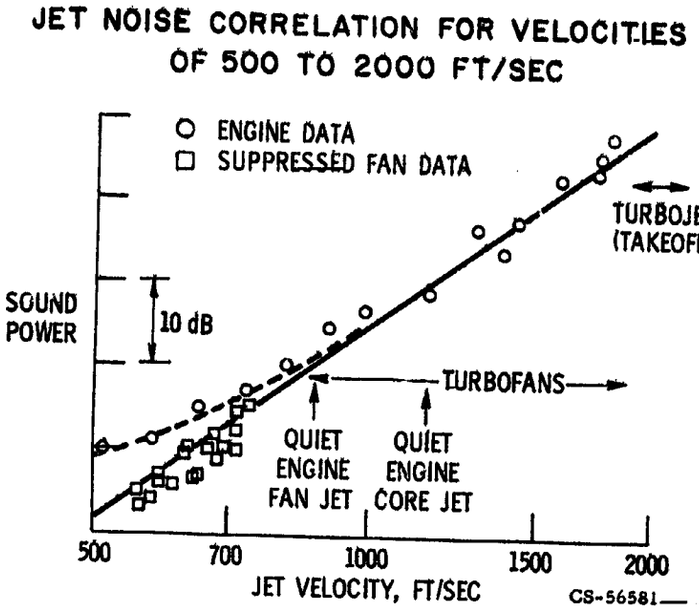

Figure VI-11

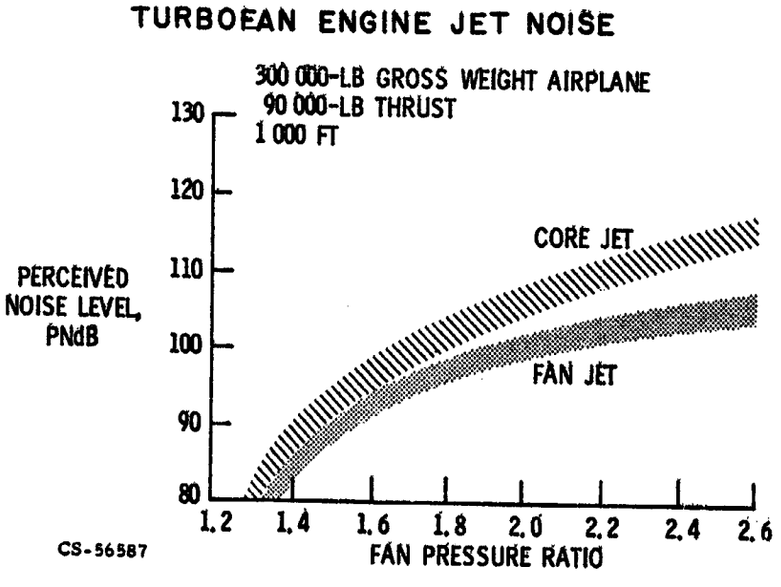

Figure VI-12

FAN NOISE COMPONENTS

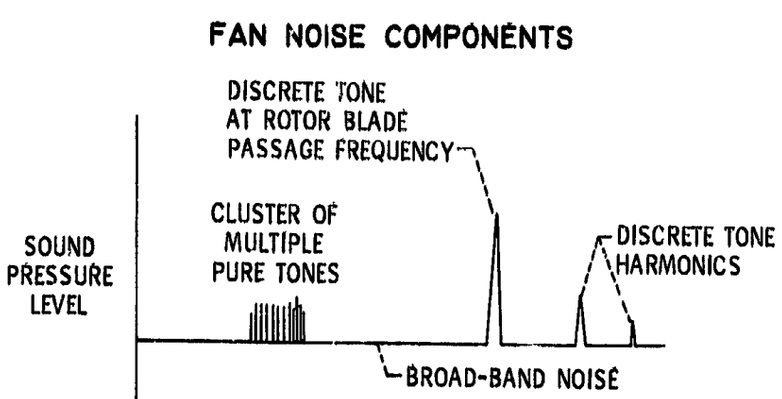

Figure VI-13

CS-56507

FAN NOISE FACILITY

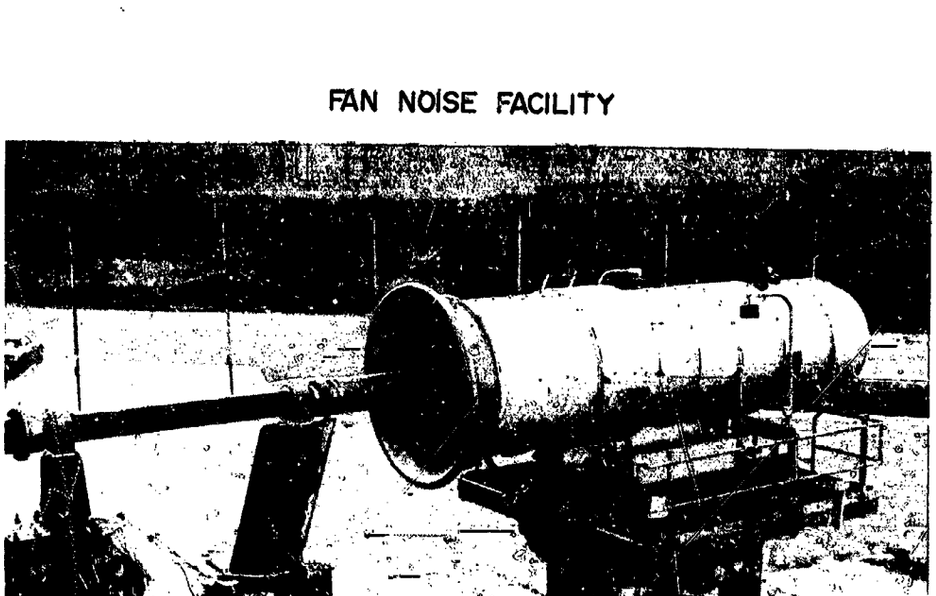

Figure VI-14

FAN NACELLE

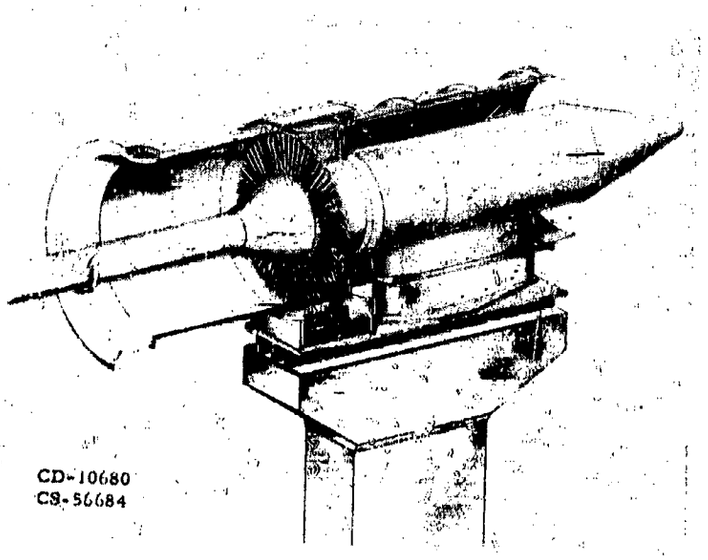

Figure VI-15

FULL–SCALE RESEARCH FANS

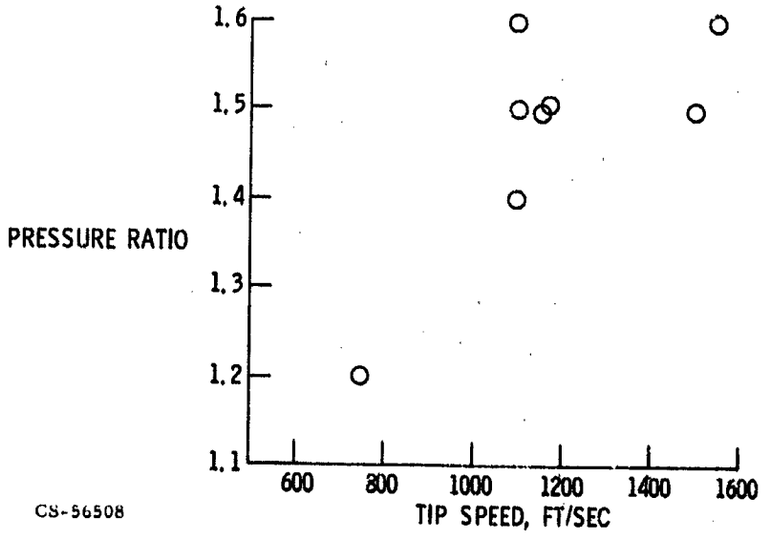

Figure VI-16

FAN INLET NOISE – STANDARD NOZZLE

TAKEOFF SPEED

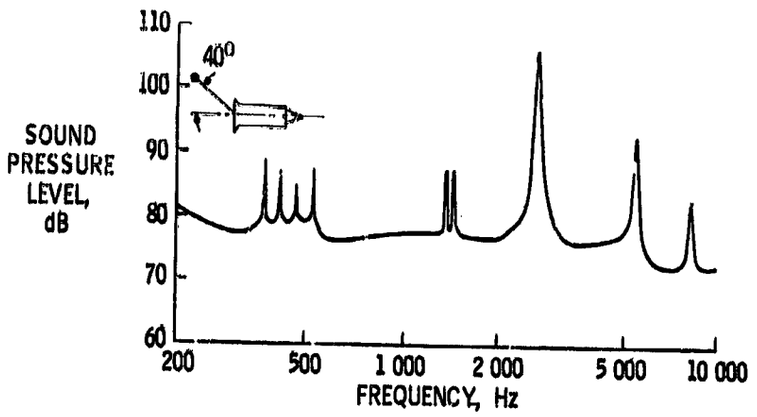

CS-56506

Figure VI-17

FAN INLET NOISE – OPEN NOZZLE

TAKEOFF SPEED

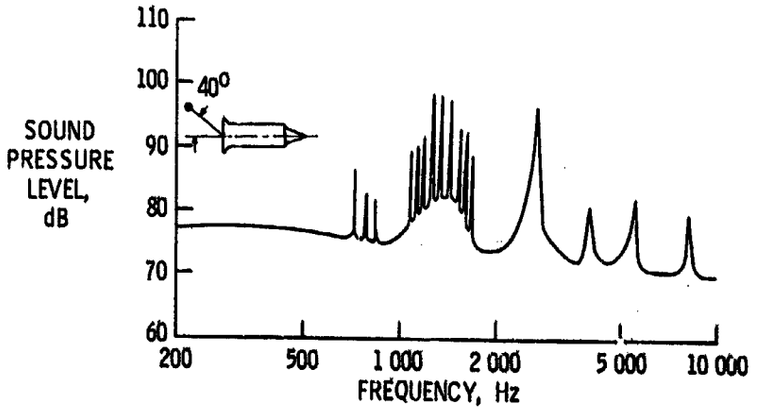

CS-56505

Figure VI-18

FAN MACHINERY NOISE ESTIMATES — SINGLE-STAGE FANS

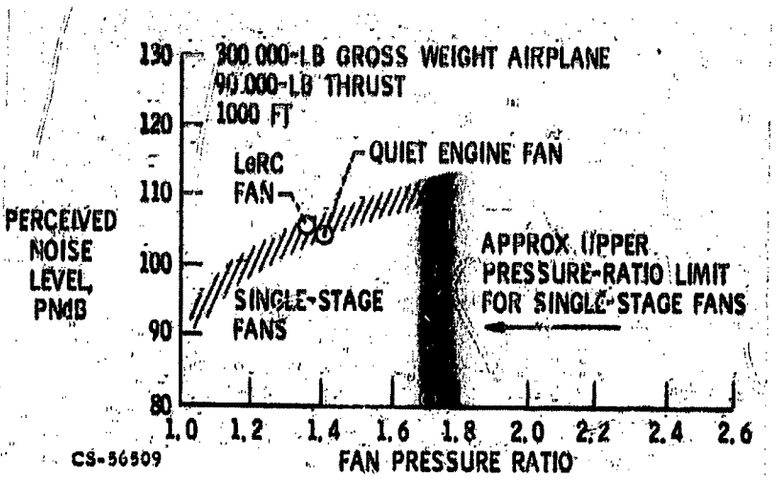

Figure VI-19

FAN MACHINERY NOISE ESTIMATES — SINGLE-STAGE AND TWO-STAGE FANS

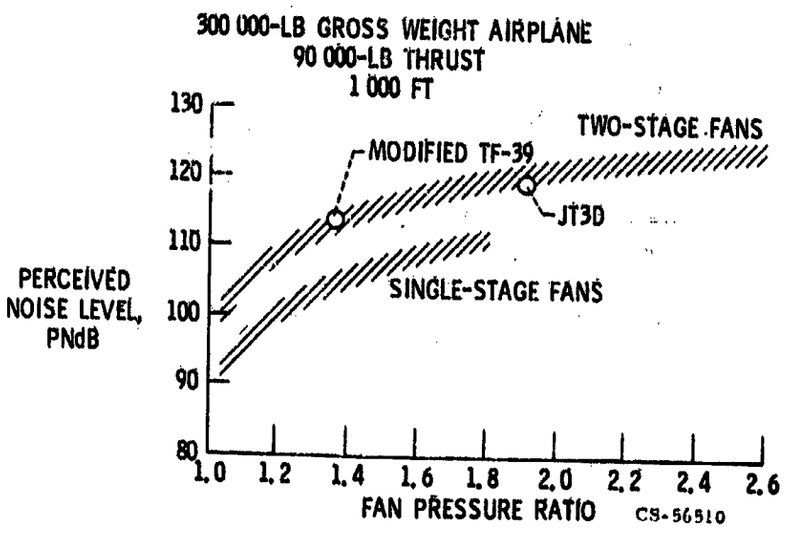

Figure VI-20

FAN EXHAUST DUCT
WITH WALL DETAIL

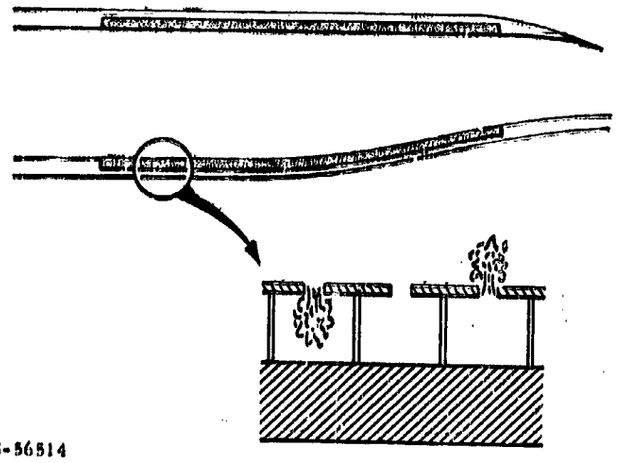

CS-56514

Figure VI-21

INLET DUCT WITH ACOUSTIC TREATMENT

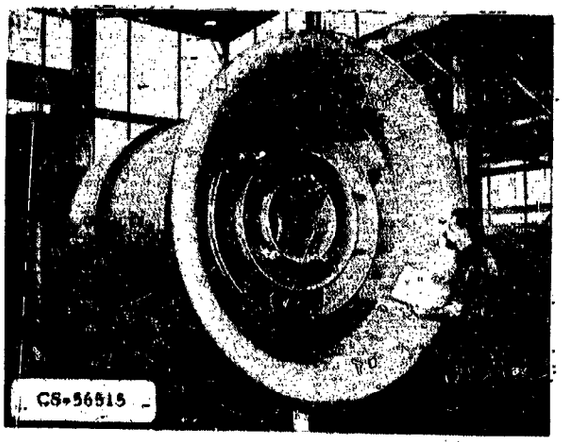

Figure VI-22

FAN INLET NOISE – WITH AND WITHOUT SUPPRESSION

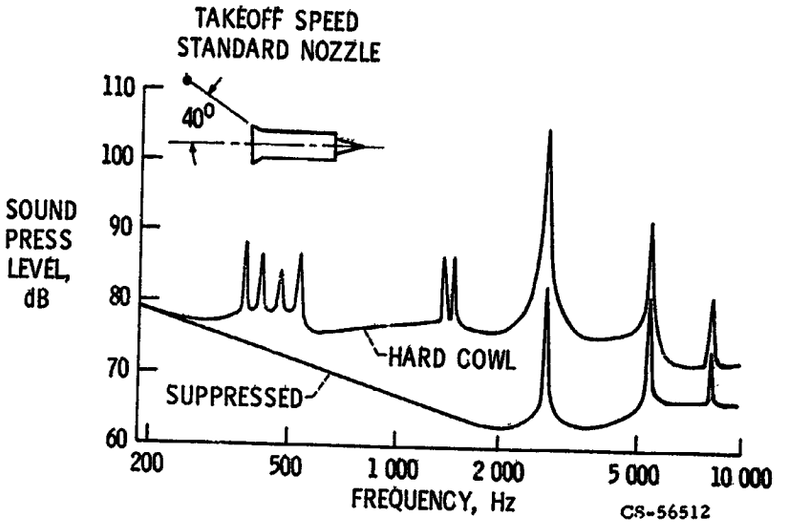

Figure VI-23

FAN MACHINERY NOISE ESTIMATES– WITH AND WITHOUT SUPPRESSION

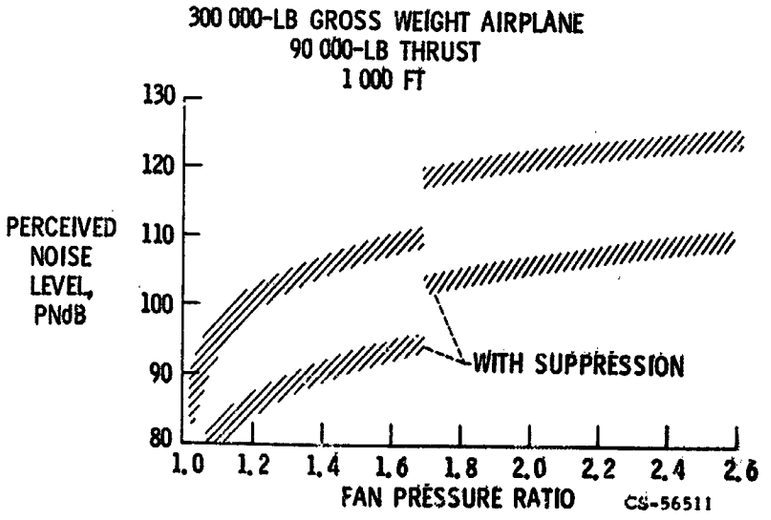

Figure VI-24

CHOKING CONCEPT

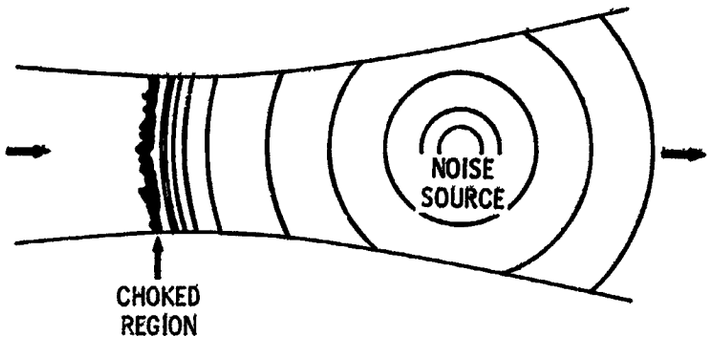

Figure VI-25 CS-56572

INLET CHOKING MECHANISMS

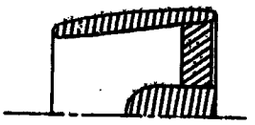

VARIABLE GEOMETRY BLADES OR VANES

VARIABLE COWL

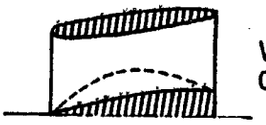

VARIABLE CENTERBODY EXPANDING
OR TRANSLATING

Figure VI-26 CS-56571

SOUND PRESSURE LEVEL –
WITH AND WITHOUT CHOKING

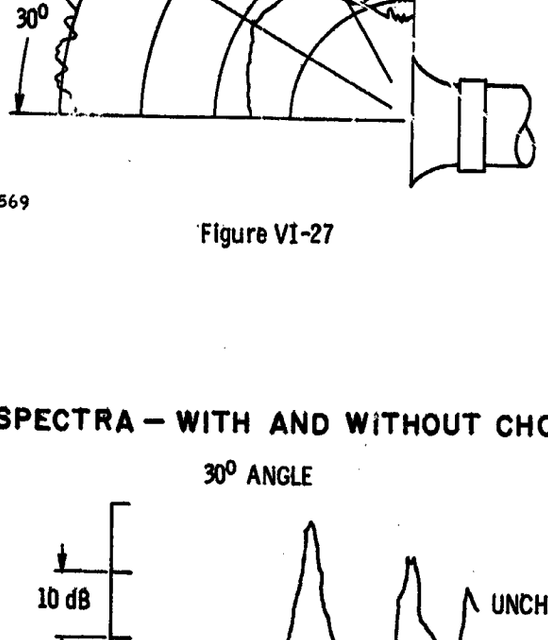

CS-56569

Figure VI-27

INLET SPECTRA – WITH AND WITHOUT CHOKING

CS-56570

Figure VI-28

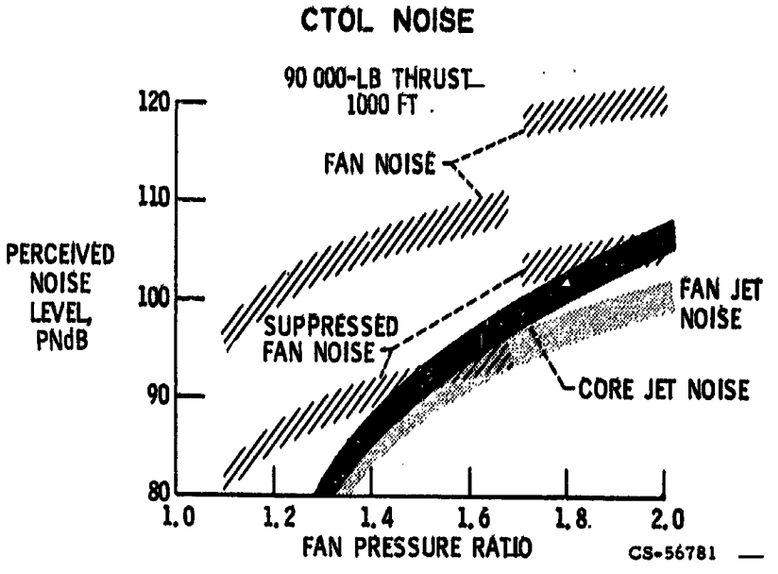

Figure VI-29

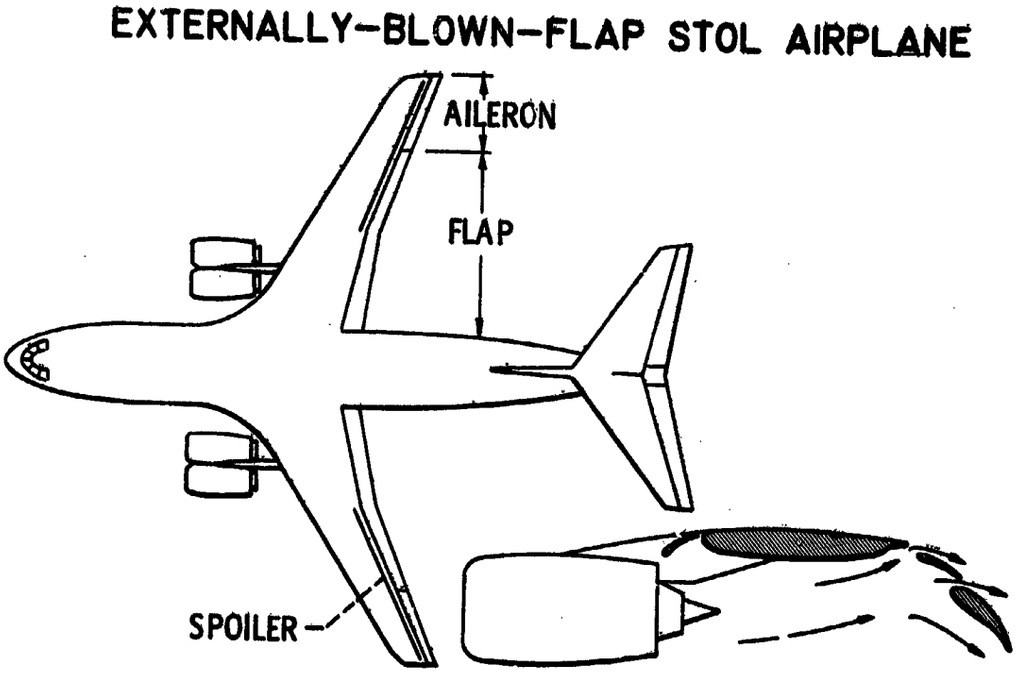

Figure VI-30

CS-56800

BLOWN-FLAP GEOMETRY

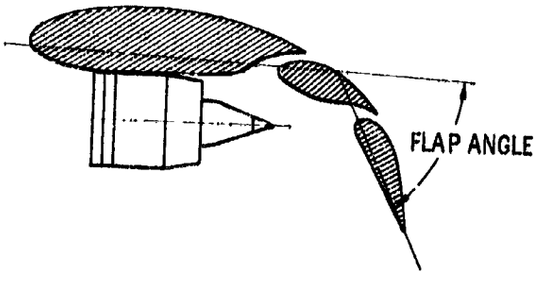

60^{0} FLAP APPROACH

CS-56820

Figure VI-31

BLOWN-FLAP MODEL

Figure VI-32

BLOWN-FLAP MODEL NOISE SPECTRUM

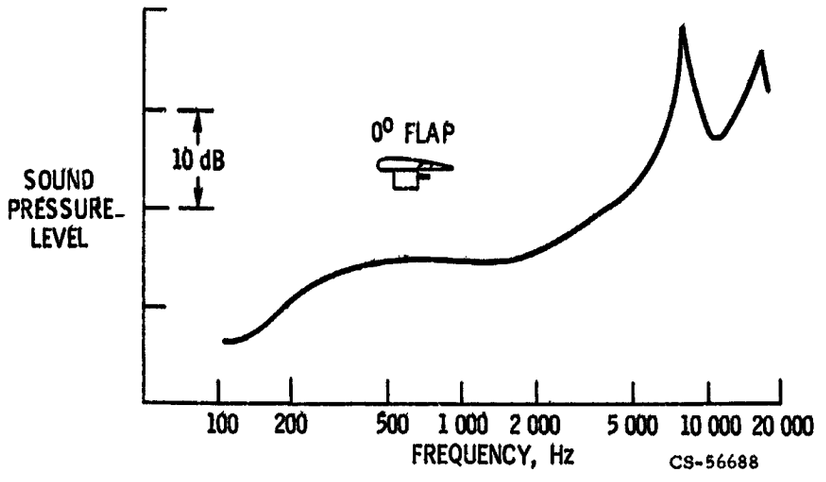

Figure VI-33

FLAP INTERACTION NOISE

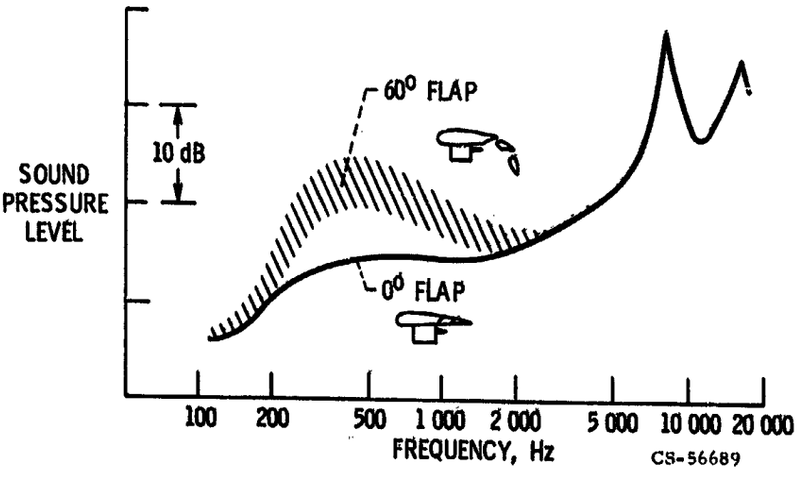

Figure VI-34

NOISE ESTIMATES FOR BLOWN-FLAP ENGINES – WITHOUT FLAP INTERACTION

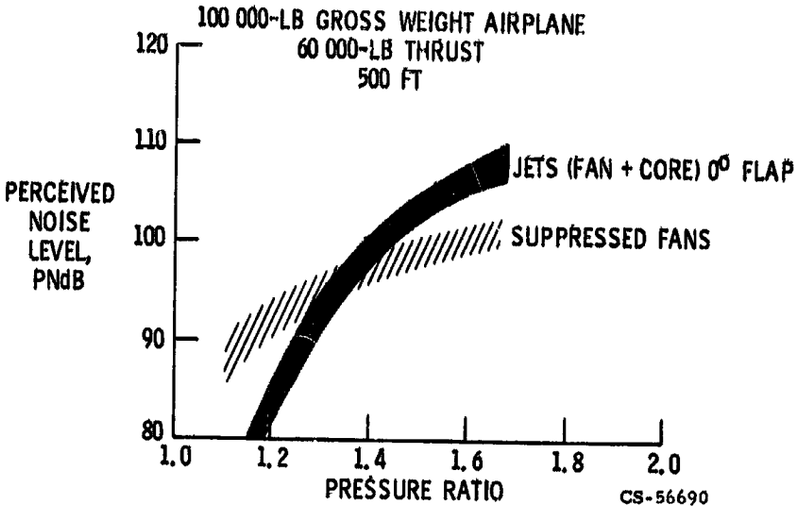

Figure VI-35

NOISE ESTIMATES FOR BLOWN-FLAP SYSTEM – INCLUDING FLAP INTERACTION

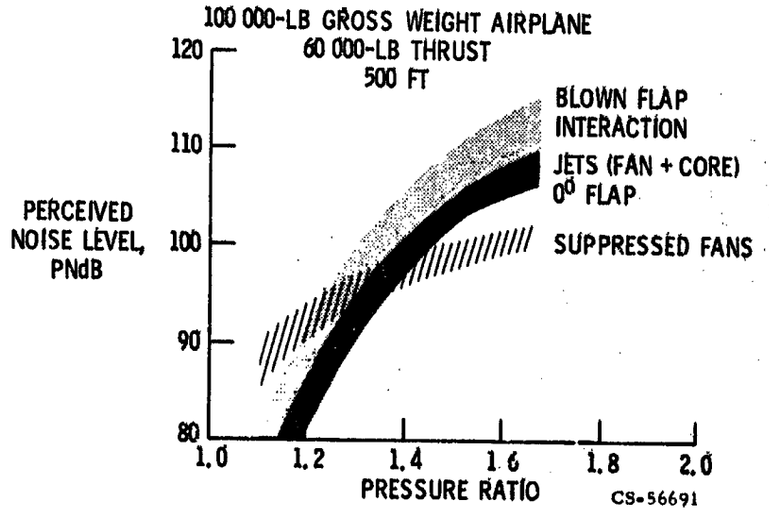

Figure VI-36

AUGMENTOR-WING PROPULSION SYSTEM

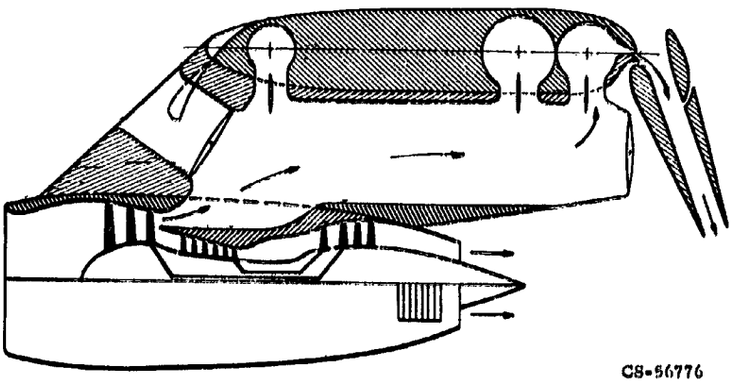

Figure VI-37

AUGMENTOR-WING NOISE TEST FACILITY

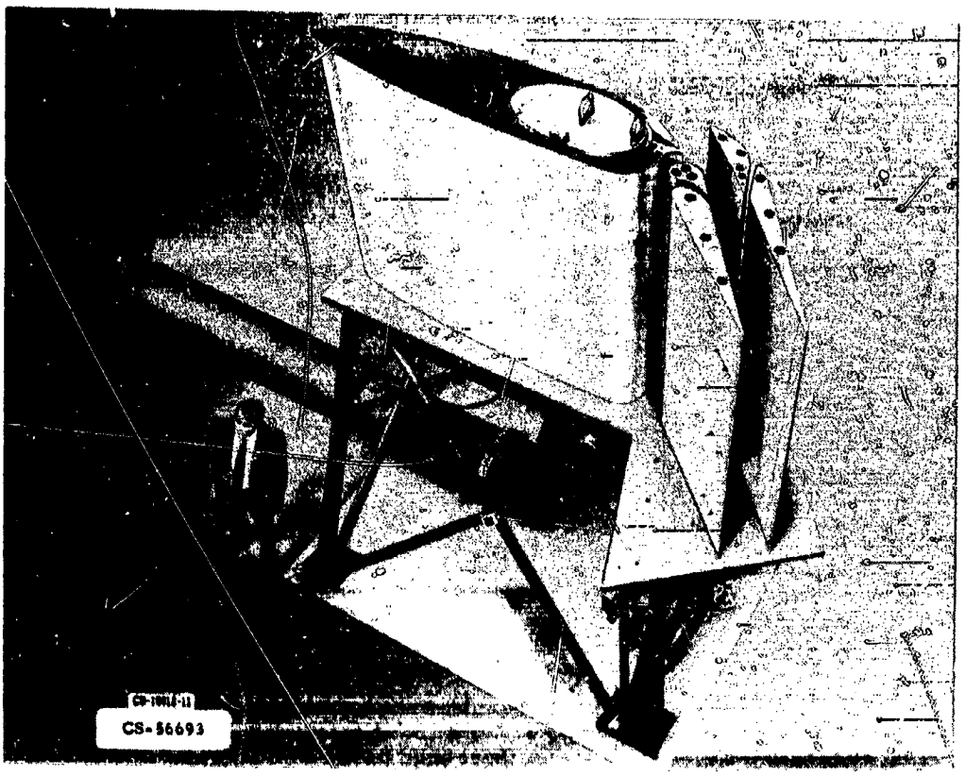

Figure VI-38

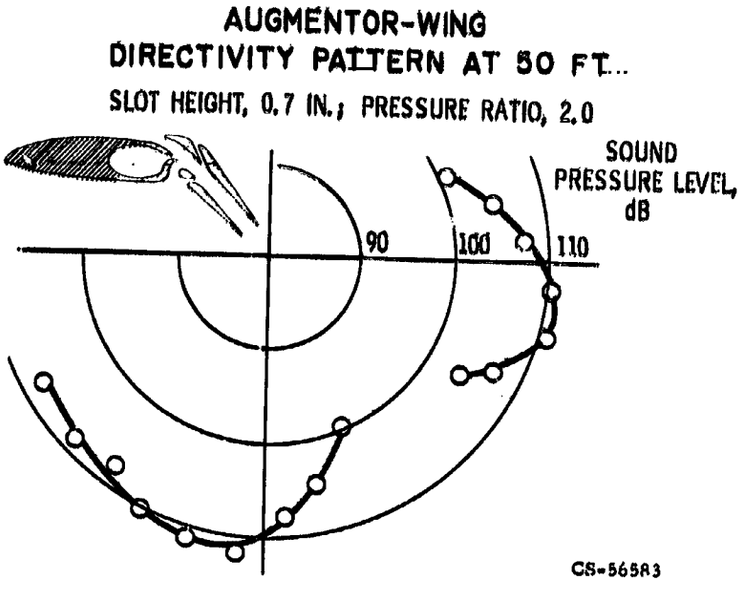

Figure VI-39

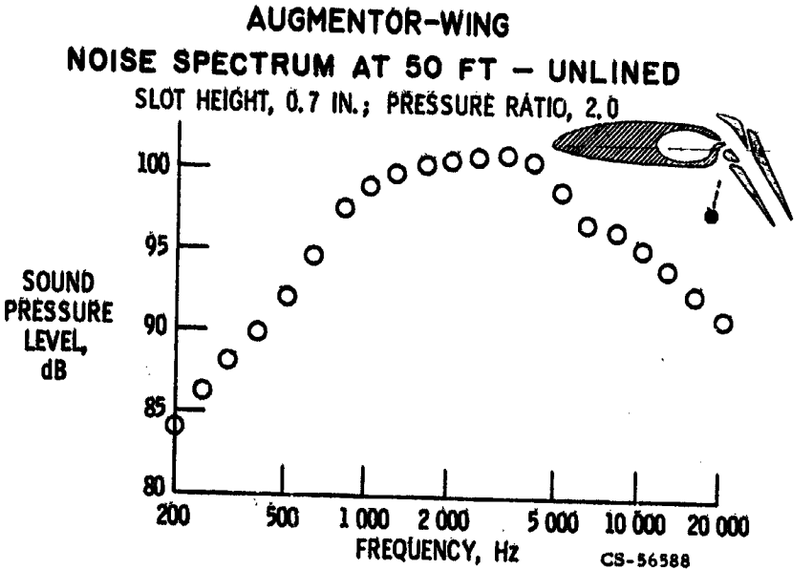

Figure VI-40

FLAP ACOUSTIC LINER

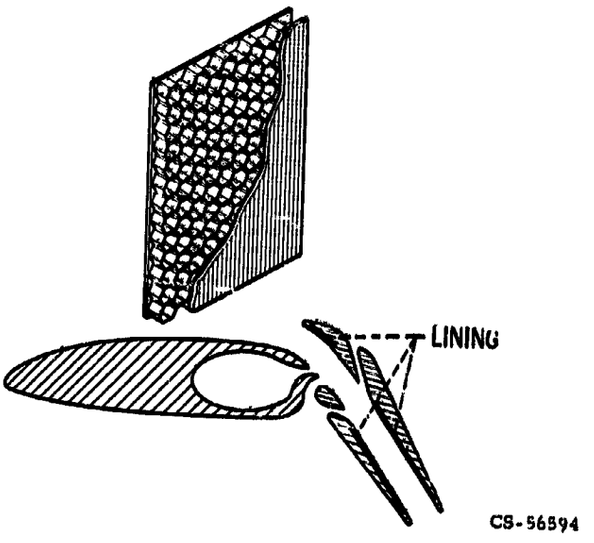

Figure VI-41

AUGMENTOR-WING NOISE SPECTRUM AT 50 FT – LINED AND UNLINED

SLOT HEIGHT, 0.7 IN.; PRESSURE RATIO, 2.0

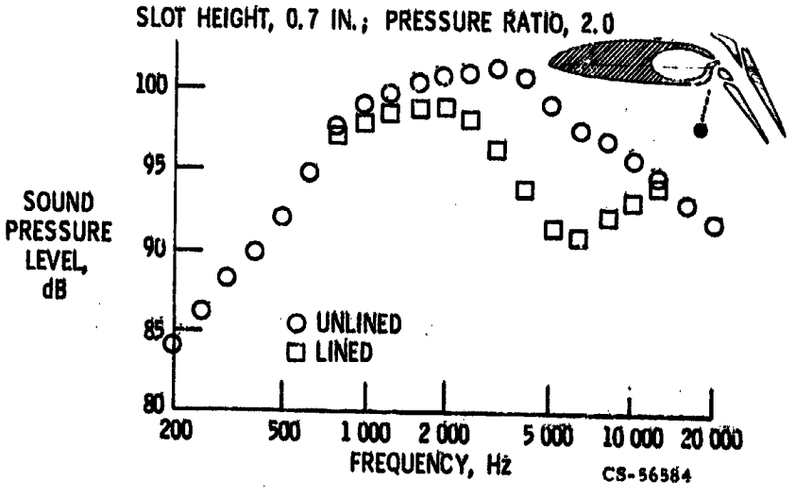

Figure VI-42

NOISE ESTIMATES FOR AUGMENTOR-WING – PREDICTED FROM AUGMENTOR-WING MODEL STUDIES

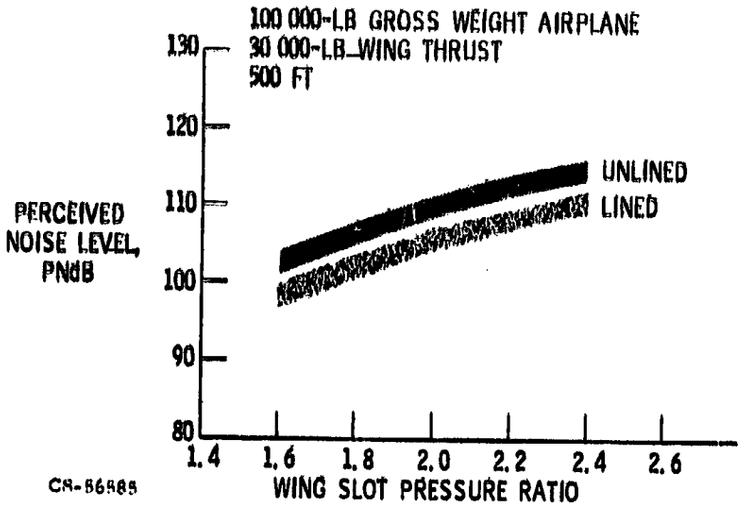

Figure VI-43

NOISE ESTIMATES FOR AUGMENTOR-WING – PREDICTED FROM CTOL TECHNOLOGY

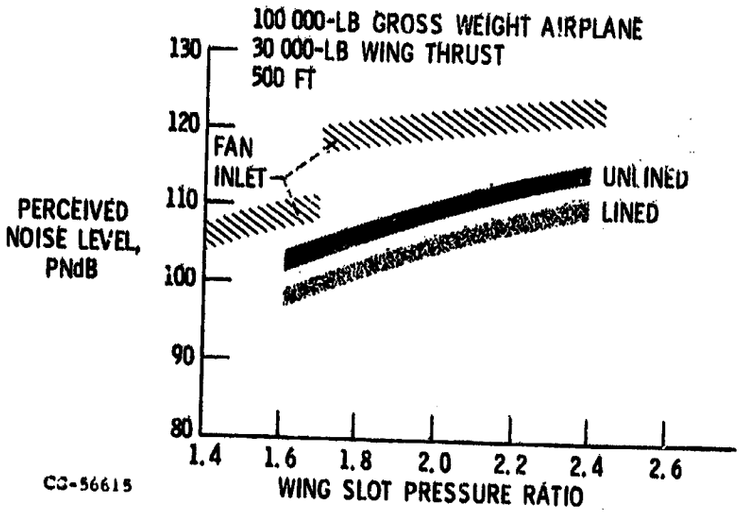

Figure VI-44

AUGMENTOR-WING PROPULSION SYSTEM WITH
INLET SUPPRESSOR

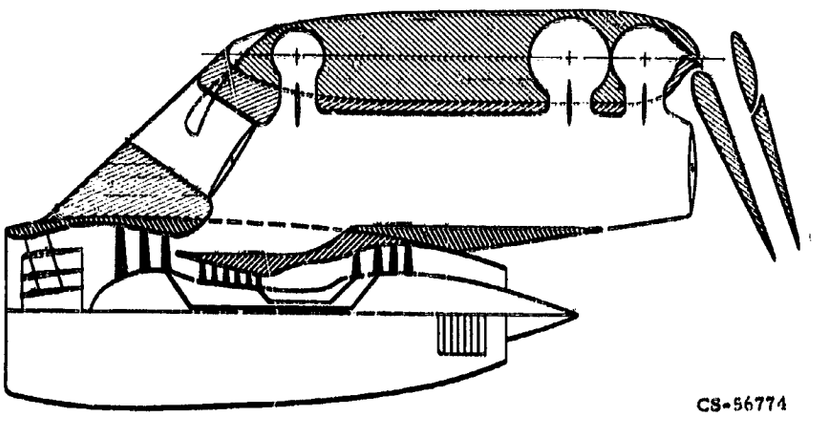

CS-56774

Figure VI-45

AUGMENTOR-WING PROPULSION SYSTEM WITH
CHOKED INLET

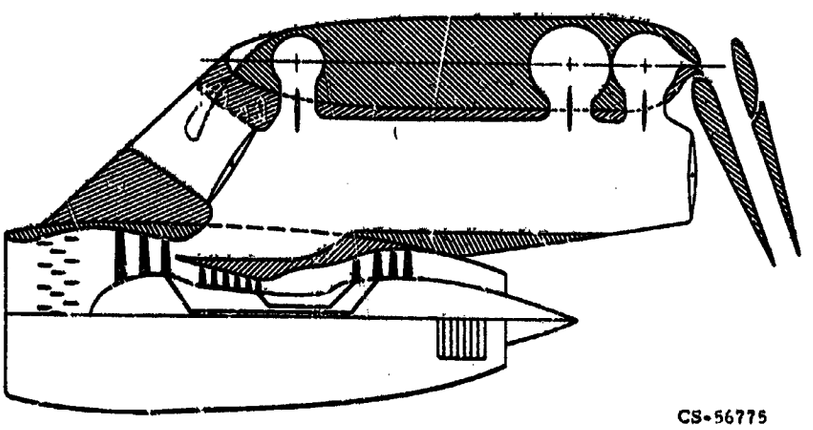

CS-56775

Figure VI-46

NOISE ESTIMATES FOR VTOL PROPULSION

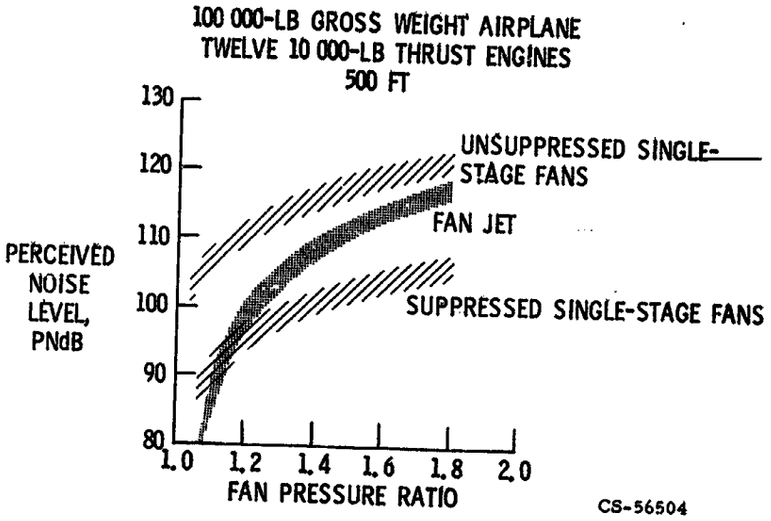

Figure VI-47

VII. LOW-COST ENGINES FOR AIRCRAFT

Robert L. Cummings and Harold Gold

Gas turbine engines have now almost completely taken over the field of large aircraft propulsion. Their small size and weight also make them very attractive for light aircraft. A major obstacle, not technical but economic, is the very high cost of current gas turbine engines which substantially restricts their use. The approximate cost of several current general aviation engines are shown in the following table:

Turbocharged piston engines and prop	
Direct-drive 285-hp engine	$10 200
Direct-drive 290-hp engine	11 300
Geared 425-hp engine	17 400
Turbine engines:	
Low pressure ratio 1025-lbf thrust turbojet	22 200
Turboshaft 605-shp engine	35 300
Turbojet 2850-lbf thrust engine	65 500
Fanjet 200-lbf thrust engine	65 000

It should be kept in mind that the general aviation light plane must be suitable for a retail sales price of around $30 000 for a single-engine aircraft and $45 000 for a light twin-engine aircraft. The turbocharged piston engines are themselves quite costly. For the high flight speeds that we will consider, a 425-horsepower engine would be required, but the price of over $17 000 is already too high. The currently available turbojet, turboshaft, and fanjet engines are much too costly, with prices ranging from $22 000 to over $65 000.

Looking at these prices, we can now understand the competitive impact of a really low-cost gas turbine engine with a 1000-pound static sea level thrust having a total manufacturing price of $5000, or $5 per pound of thrust. Such an engine would provide important performance gains for light aircraft and also have a very important price advantage over either current piston engines or current jet engines. In order to sell at 1/5 the price per pound of thrust of current jet engines, however, this engine would require really major design simplifications and manufacturing cost reduction.

This paper discusses the major results of a program which is concerned with such low-cost engines. This small Lewis program has had only limited assistance from contractors. It has been essentially exploratory, covering a number of problem areas: The main areas covered in this paper are (1) engine cycle analysis and airplane performance studies relating to the cost-performance tradeoff question, (2) engine configurations which are being emphasized, (3) new compressor and turbine rotor construction methods and results from spin tests, (4) construction and test results on a low-cost annular combustor, (5) results on a new type of hydromechanical fuel control, (6) work on low-cost accessories, and (7) current plans for construction and test of complete turbojet and fanjet engines.

ENGINE DESIGN

To achieve low cost on a device as complex and critical as a gas turbine engine, we must be willing to give up some performance to limit the design temperature to a level low enough to obtain reliable machinery, requiring only low cost materials, and to limit the pressure ratio to reduce the tip speeds, the stress levels, and the number of expensive stages. The decisions as to just how far to go with this approach are a matter of judgment involving a tradeoff of engine performance against its initial cost.

The performance tradeoffs on fuel consumption and thrust are shown in figures VII-1 and VII-2, where we have the specific fuel consumption and specific thrust of turbojet and fanjet engines plotted against pressure ratio. These results are for a flight speed of 450 mph at an altitude of 25 000 feet, which are being used as a typical advanced general aviation aircraft design point and for a turbine inlet temperature of 1300° F. This choice of a low turbine temperature was made to promote economy and reliability in the design.

From figure VII-1 we can see that choice of a low pressure ratio of 4.0 does indeed cause about a 25 percent higher fuel consumption than if 12.0 were chosen. The pressure ratio of 4.0 can be achieved with about half the number of stages required for a pressure ratio 12.0, however, and this is the type of tradeoff we must make if we are to achieve low cost. For the turbojet, it is our expectation that the main application would be for missile and drone engines. The design point for the turbojet has therefore been chosen, as shown on the figure, at the lowest pressure ratio that is consistent with moderate performance.

The fanjet engine design point takes advantage of the added fan stage to operate at a higher overall pressure ratio. The fan stage also provides additional propulsive mass flow. Both of these factors improve the engine performance. Note in fig-

ure VII-2 that the fanjet design point uses a moderate bypass ratio of 2.5 and a fan pressure ratio of 1.3 and thereby achieves a significant performance improvement, compared to a simple turbojet. At the design point a specific fuel consumption of 0.90 pounds per hour per pound of thrust is achieved with only one additional stage. The fanjet engine, thus, has moderately good fuel consumption and should be the most attractive for aircraft propulsion.

Both the turbojet and the fanjet engines in figure VII-2 have very useful specific thrust levels, in the range of from 45 to 55 pounds per pound per second of core engine airflow. Here the core engine airflow is considered as the relevant parameter, since the core engine contains the expensive components. This specific thrust level means that 1000 pounds static sea level thrust can be obtained with either a turbojet or a fanjet engine with an inlet diameter of less than 10 inches. The gas turbine engine is, thus, much smaller than the piston engine it would replace. A further factor, which should be noticed in figure VII-2, is the specific thrust advantage of the fanjet. For the same thrust level, the fanjet has a size advantage that would tend to offset the cost penalty due to the added complexity of the fan stage.

With design points chosen, as shown, the performance obtained for both the turbojet and the turbofan is substantially lower than most modern jet engines of the type described elsewhere in this publication. The critical question, however, is whether these performance levels are good enough to provide useful range and operating cost for a light aircraft. The performance figures for a light twin-engine airplane, which is designed to cruise at 450 miles per hour at an altitude of 25 000 feet are as follows:

Design cruise at 25 000 ft, mph	450
Airplane characteristics:	
Twin engine gross weight, lbm	6000
Fuel weight including 3/4 hr reserve, lbm	2000
Takeoff thrust, lbf/engine	1050
Cruise thrust, lbf/engine	350
Takeoff wing loading at $C_L = 2.5$, lbf/ft^2	40
Approximate takeoff and landing speed, mph	80
Performance at cruise:	
Specific fuel consumption	0.90
Takeoff distance, ft	1050
Useful range, mi	1070
Comparative fuel cost (reciprocating engine = 1.0)	0.81

It has a typical fuel-to-gross-weight ratio and fuel reserve and a wing loading low enough to provide the low takeoff and landing speed of 80 miles per hour. For this airplane the two 1000-pound takeoff thrust engines are capable of achieving a low takeoff distance of only 1060 feet. The very useful range of over 1000 miles is also obtained at an operating fuel cost level less than piston engines of equivalent thrust. These cost estimates, of course, take into account the lower cost of jet fuel compared with aviation gasoline.

This airplane must be stressed to operate at flight speeds at least twice as great as current light airplanes and be capable of cabin pressurization. To achieve these qualities at reasonable cost, work will be necessary on the airplane frame as well as the engine. For the present, however, the discussion will be limited to the engine.

During the course of this program, numerous turbojet and fanjet designs have been considered and compared. For application to light aircraft, the improved range and the lower noise levels of the fanjet caused major interest to be centered on this type engine. The objective of the fanjet design study was to obtain the economy of its smaller size core engine without adding costs because of undue complexity.

A configuration being studied for the fan engine is shown in figure VII-3. This figure shows a geared fanjet engine, which is not only a low noise, low tip speed fan but also a single-shaft, two-bearing design, for the core engine. The 1000-pound thrust engine uses a 15-inch-diameter fan, a 10-inch-diameter, five-stage compressor, and a two-stage axial turbine. It also uses a 650-horsepower gear box with a speed reduction ratio of 2 to 1. This gear box allows the turbine stages to operate at high speed and to share the work and, therefore, minimizes the diameter and the number of stages required.

The design of this gear box has been studied by the Allison Division of General Motors under a NASA contract, and their results indicate that a conservative, 650-horsepower, coaxial gearing system can be produced at a total cost of approximately $600. Using such a gear box avoids the complexity of coaxial shafting with its additional high DN bearing and seals. The sheet metal compressor and turbine shown in the figure will be described later. This geared fan engine configuration has a number of advantages. However, other fan engine designs are adaptable to the low-cost fabrication techniques and are also still under consideration.

In addition to general aviation applications, Lewis has been working in cooperation with the U. S. Navy to determine the applicability of the low-cost designs and fabrication techniques to engines for missiles and drones. Such expendable engines are referred to as ordnance engines. A typical current requirement for such an

engine is given in the following table and the resulting four-stage compressor engine design is shown in figure VII-4:

Cruise thrust required, lbf	350
Sea level static thrust, lbf	650
Engine weight limit, lb	100
Engine diameter limit, in.	12
Specific fuel consumption	<1.8
Flight duration, min	15

The requirement is for 350 pounds of thrust at the design point of Mach 0.8 at an altitude of 20 000 feet and a sea level thrust of 650 pounds. The weight limit is 100 pounds, the diameter limit is 12 inches, and the specific fuel consumption must be below 1.8. Both windmill start under ram conditions (cruise) and impingement start at sea level are required. The design flight duration is only 15 minutes.

The turbojet engine designed to meet these conditions uses a four-stage cast axial-flow compressor and a single-stage investment cast turbine. Figure VII-4 also shows the simple shaft and bearing design. The engine outside diameter is only $11\frac{1}{2}$ inches, and it is estimated to weigh less than 100 pounds and to have a specific fuel consumption of 1.3. With these size and performance figures, it will provide overall range and payload much better than can be achieved by a rocket engine. It is also attractive in its promise for low production cost.

FABRICATION DEVELOPMENT

In addition to this engine design work, investigation has been made of techniques for the fabrication of low-cost axial-flow rotor stages. The main approaches being considered are (1) casting and (2) sheet metal stampings. The casting approach is already known in the industry and will not be further discussed in this paper. It also appears that the stamping approach, using coined blade profiles, may have a better potential for low cost and reliability. This construction has therefore been emphasized in a fabrication and test program; its main features are illustrated in figure VII-5. An axial-flow compressor is composed of two sheet-metal disks, with blades formed on tabs on the edge of the disks. A pair of such disks is placed together to give the solidity required for good transonic axial-compressor performance, and fitted into a pair of rings. The rings are slotted to receive the blades, or a filler material is used between the blades. A complete sheet-metal compressor rotor is shown in figure VII-6. There a 10-inch diameter sheet metal

compressor is installed in an end plate assembly as required for spin testing. A coining or cold forging process has been used to form the blades. This produces accurate reproducible contours with small leading- and trailing-edge radii. There is, consequently, no known aerodynamic performance penalty imposed by use of this type of construction.

A number of these sheet-metal compressor rotors having slightly differing construction have been built and tested in a Lewis spin test rig. Strain measurement data, taken during spin testing of the slotted hub version of this compressor, are shown in figure VII-7 where the calculated strain at two points on the rotor is plotted against the rotational speed. Also, plotted in the figure are the measurements taken from strain gages attached to the rotor at the same two points. The measured values correspond very well with the calculated ones and the measured strain is linear. The rotor has been tested to 25 percent above its design speed, indicating a good strength margin and safety factor at the operating speeds of our fanjet and turbojet engines.

The sheet-metal construction technique is also being evaluated for application to axial-flow turbine rotors. A model of this is shown in figure VII-8. Here, the problem is somewhat more complicated because of the additional camber of the turbine blades, but stress calculations show the designs to be attractive with respect to both centrifugal stress and thermal stress. As shown in the figure, the turbine rotor would consist of two sheet-metal plates formed with coined blades on their rim, fitted together and placed into rings in a manner similar to that of the compressor. A test rotor of the type shown is now being constructed.

In addition to this sheet-metal approach, both cast and welded turbine designs are also being investigated.

The fan requires an axial stage, as shown in figure VII-9 which is larger than the core engine and which has substantially longer blades. This stage is also the one which would be the most adversely affected by damage from foreign objects. Therefore, for this rotor we have investigated the use of hollow, stamped sheet-metal blades that are removable. These blades are stamped from two pieces of stainless-steel sheet metal and are joined together by welding or brazing. They have a stamped or cast base to provide a low-cost, freely pivoting attachment to the hub. Because of their hollow construction, they have the advantage of a high resonant vibration frequency and low root stresses and can operate without requiring midspan vibration dampers. The hollow construction also favors a lightweight, low-cost rotor disk. These blades have been vibration tested to verify the high bending frequencies, and the complete rotor shown has been spin tested to a speed 40 percent above the fan rotor design speed.

A low-cost annular combustor has been constructed from perforated sheet metal (fig. VII-10). This combustor uses a cooling airflow layer obtained from special orientation of the pattern of holes in commercial perforated sheet, along with a simple pattern of punched holes. It also uses a very simple air-atomizing fuel nozzle. This combustor has been tested, and results on combustion efficiency over a range of fuel-air ratio are shown in figure VII-11. Good design point combustion efficiency was obtained and ignition and blowout characteristics were very satisfactory. In addition, the combustor exhibited a good temperature variation pattern factor of about 0.20 and a design pressure drop of 6 percent at a relatively high design point Mach number.

Accessories are also very important to the overall cost and size of small jet engines since they tend to be large and expensive. The most critical accessory is the engine speed and fuel control, which must provide capability for rapid thrust response without surging the compressor or exceeding the allowable turbine temperature. The control is, therefore, a key to the safety and reliability of the entire engine. It is, furthermore, critical to the cost and may add up to 20 percent of the cost of the engine. The fuel control has, therefore, been extensively investigated, using a hydromechanical control based on use of a zero gradient pump speed sensing technique. The principles on which the work is based are shown in figure VII-12 wherein a parameter, consisting of fuel flow divided by speed and by the ambient pressure correction factor, is plotted as a function of the compressor pressure ratio.

The values plotted in figure VII-12 are for a current typical turbojet engine, and it will be noted that the steady-state operating line, the surge temperature limit, and the combustion blowout limit can all be approximated by the linear relation between the fuel-flow speed parameter and the pressure ratio. A control that schedules fuel flow, following a linear relation will, therefore, approximately provide the correct steady-state fuel flow to the engine over the complete range of rotational speed, altitude, and flight Mach number. Such a fuel-flow schedule can then be modulated by a speed error signal from a speed governor to control the speed of the engine. The engine may be kept below the surge line during an acceleration and avoid blowout during a deceleration by keeping the fuel-speed parameter between the limits shown.

Plotted in figure VII-13 is a typical acceleration fuel-flow schedule of a current jet engine. Here the uncorrected quantity, fuel flow divided by pressure, is used. The limiting fuel flow is, therefore, a function of three variables: speed, temperature, and pressure. From the complexity of this limit schedule, it may be appreciated that the simple linear limit of the hydromechanical fuel control should offer some important simplifications in construction.

The techniques which were used to incorporate these principles into a functional fuel control device are shown in figure VII-14. As may be seen, a small speed sensing positive displacement gear pump is driven by the engine. The pressure difference across this pump is kept at zero by a pressure regulating valve which bypasses flow from the main fuel pump. Since no pressure rise occurs across the small pump, its output flow rate is directly proportional to the engine speed. This flow quantity is then passed through a fixed-area orifice to generate a pressure signal, which is directly proportional to the square of engine speed. The actual speed may then be compared with the pilot's speed command setting to generate a speed error signal. The area of an orifice that bypasses the speed sensing pump is then controlled by the compressor inlet and discharge pressures. With this circuit the total fuel flow delivered to the engine at any speed and pressure is then a linear function of speed and pressure ratio as required for the fuel flow schedules previously discussed. This orifice area may also be modulated by the speed error signal to control or govern the engine speed. Thus, when the throttle is advanced, the control provides additional fuel flow to increase the engine speed. During such speed transients, however, the changes in fuel flow are limited by the acceleration and deceleration schedules previously discussed. In an actual control, the variable area orifice would be provided by spool valves.

This simple hydraulic circuit provides all the required functions of the jet engine control. The working parts required to construct such a control are shown in figure VII-15: In the figure are shown the small gear pump which provides the speed signal, the fuel bypass valve which controls the zero pressure gradient, and the valve which adjusts the flow according to the speed error signal. In addition, there are two valves operated by compressor inlet and discharge pressures which provide the controlled area orifice for the fuel schedule.

For comparison, briefly look at figure VII-16 which shows the parts required for the fuel and speed controller of a current turbojet engine. The zero gradient pump control has a substantially smaller number of working parts. It is also simpler for assembly and adjustment, and it is direct acting (i.e., it does not require servo-actuators).

This control has been extensively analyzed, and its operation has been simulated on the analog computer. It has been built and has performed successfully in actual operation on a J85 engine. A typical operating sequence during a throttle burst from 50 to 95 percent is shown in figure VII-17. Here, the sequence is initiated by a sudden change in throttle position. The initial fuel flow increases as the governor calls for more fuel. Then there is a further increase following the surge limit schedule. This produces a smooth acceleration of the engine in a very short response time. Finally, the governor cuts back the fuel flow as the speed set point

is approached and the speed levels out at the set point with no overshoot or oscillation.

In addition to the work on the fuel control, a number of other accessory areas have been considered. They are

(1) Electric starter generators
(2) Hydraulic motor-pumps
(3) Fan drive gearing design
(4) Fan blockage thrust control
(5) Engine mounts and accessory installation

The more important results are summarized in the following paragraphs.

The startup technique for the engine has been extensively considered. After evaluation of numerous possible startup techniques, it has been concluded that, since a generator and a battery will be needed for flight, the overall best economy will be achieved by using these same components for engine cranking. Since the cost of starter-generators rises very rapidly with power output, cranking must be achieved with the smallest unit possible. This type of starter-generator has, therefore, been tested to verify its capabilities in both modes of operation and to investigate possible mechanical simplifications that may permit cost reduction. The conclusion was reached that the 150-ampere starter-generator, operating at 24 volts, should be adequate to crank the 1000-pound-thrust engine.

The frontal area of accessories has proven to be a substantial penalty for the 8- to 10-inch-diameter engines here considered. The accessory power takeoff shafting and gearing is also expensive and limits the allowable design configurations. A hydraulic drive system using positive displacement gear pumps and motors has, therefore, been designed and is currently being tested. This system would allow remote placement of accessories.

A design study has also been undertaken on the fan drive speed gearing. The result of this study was favorable on both a technical and a cost basis. This fan drive system was shown in figure VII-3 and previously discussed. The gearing system selected consisted of three parallel reduction gear shafts each having two meshes, giving an overall speed ratio range of 28 to 15. This gearing system has the advantage of a coaxial output shaft and of fitting a small space. It also has low gear tooth loads and bearing loads such that very good life can be obtained with small, low-cost bearings and gears. Both a low fabrication cost and a long life, therefore, appear possible for this design.

The geared-fan engine requires that a means be incorporated for reducing the fan torque at idle speeds to prevent excessively high turbine inlet temperatures.

Such torque reduction can be accomplished by blocking the fan flow duct. This technique has the additional advantage of reducing the engine thrust to a low level at a relatively high idle speed and could, therefore, provide rapid thrust response as well as other advantages. Preliminary tests have been performed on this system, and the necessary torque and flow reduction was obtained without causing surge.

Additional low-cost accessories and auxiliaries which have been designed and investigated include engine mounting struts and vibration dampers, an accessory drive gearbox, and lubrication and scavenge pumps. These accessories are all being designed to fit within the engine mounting pylon in order to preserve the low frontal area of the basic fan jet engine.

CONCLUDING COMMENTS

The foregoing has briefly summarized and described the major aspects of this low-cost-engine program. At this time, major results and conclusions cannot be made because the program is at an intermediate point.

For the future, it is planned to continue the fabrication development program on sheet-metal axial stages and the control development and its application to the turbojet and the fanjet engines. Design work on the fanjet engine will continue and also the final design will be completed on the Navy Ordnance engine. Fabrication of prototype Ordnance engines will then begin. This engine will be built so as to simulate a production engine fully, and it will be tested at its full design operating conditions.

In connection with our overall interest in low-cost aircraft engines, it is instructive to examine the estimates that have been made on the production prices of the components of this engine. These are shown in table VII-1 and are based on production rates of 2000 units per year where the tooling writeoff costs may be neglected.

It is not the purpose of this paper to discuss these prices completely. The total cost of just over $3000 for the 650-pound-thrust engine, clearly indicates, however, that we can expect to provide the advantages of turbojet propulsion to missiles and drones at a price that is competitive with any other form of propulsion. Similar price estimates were previously made for the 1000-pound-thrust level turbojets, which indicated that manufacturing costs of about $5000 to $6000 should be attained for production quantities of 2000 per year. The production cost level of $5.00 per pound of thrust has, therefore, been indicated for both thrust levels. We are not concluding that $5.00 per pound of thrust would be a final manufacturer's selling price since there are a number of indirect costs which would affect the selling price. For example, the costs for calibration runs, the writeoff of qualification expenses, sales, and

TABLE VII-I. - PRELIMINARY COST ESTIMATES

OF NAVY ORDNANCE ENGINE

Item	Cost dollars
Axial compressor and stator	630
Turbine rotor and stator	220
Front and rear bearing supports	165
Compressor housing assembly	55
Combustor and housing assembly	185
Compressor shaft	40
Fuel manifold and nozzles	55
Bearings, springs, bolts, etc.	50
Fuel control, pump, filter, etc.	385
Ignition system and igniters	175
Subtotal purchased parts	1960
Cost of assembly and inspection	250
Material handling burden	200
Manufacturer's general and administrative expense and profit	755
Total cost assembled	3165

field engineering, and the distributor's markup. It is possible that these items could actually double the price at which the engines would be finally sold to the user.

From the estimates made in the program, however, it is evident that gas turbine engines of the type here considered will be attractive and cost competitive for general aviation, for missiles and drones, for additional services uses (such as reconnaisance airplanes), and possibly for the smaller business category aircraft. If the obstacle of high cost can be eliminated, gas turbine engines will make major performance improvements available for these purposes.

LOW COST ENGINE SPECIFIC FUEL CONSUMPTION

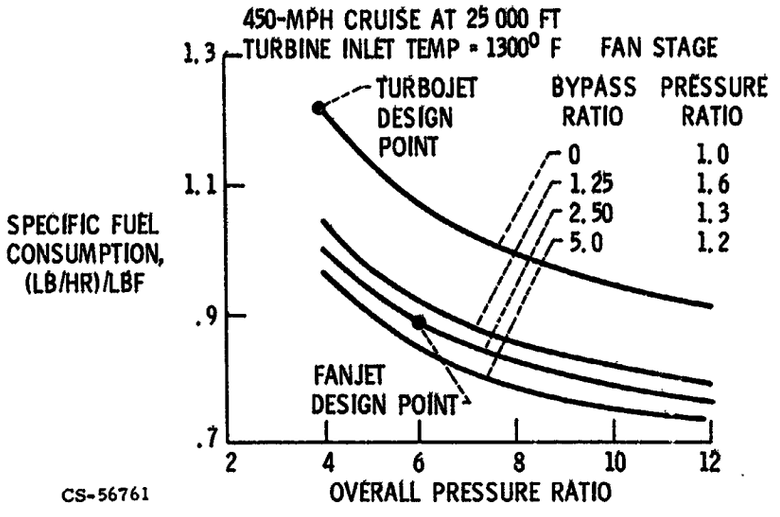

Figure VII-1

LOW COST ENGINE SPECIFIC THRUST

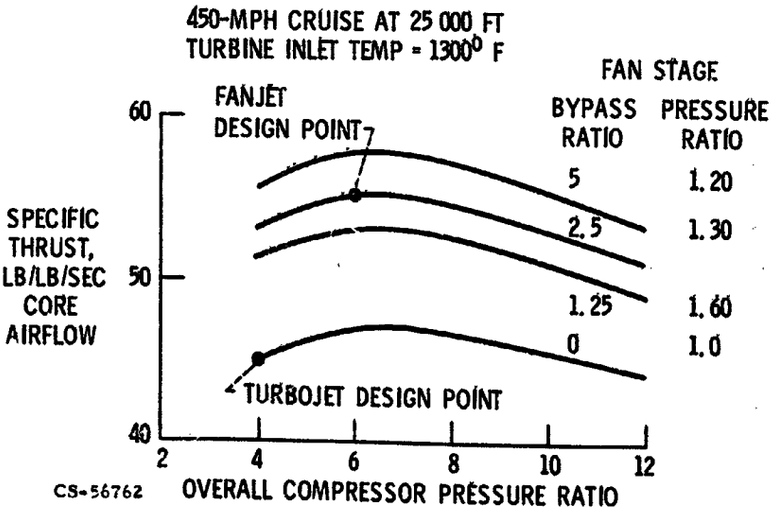

Figure VII-2

GEARED FAN JET CONFIGURATION

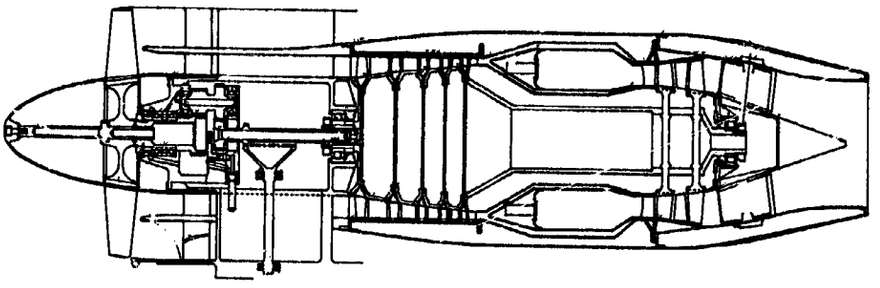

Figure VII-3 CS-53727

650 LB STATIC SEA LEVEL THRUST

NAVY ORDNANCE ENGINE

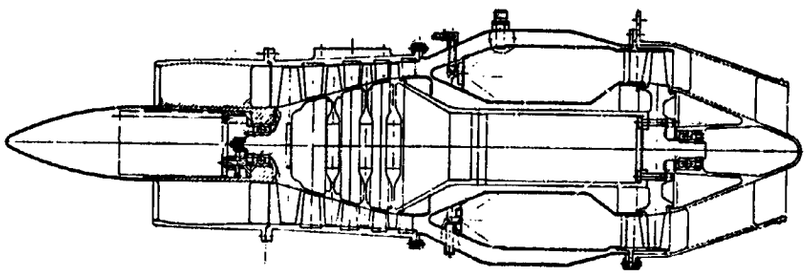

Figure VII-4 CS-56759

SHEET METAL COMPRESSOR
ROTOR COMPONENTS

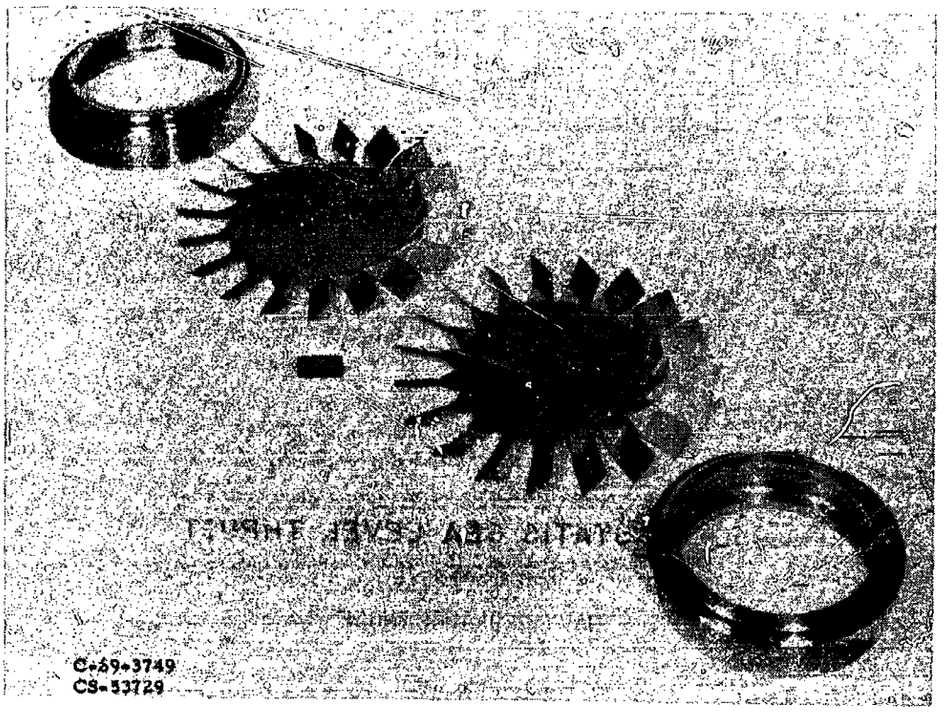

Figure VII-5

ASSEMBLED SHEET METAL COMPRESSOR ROTOR

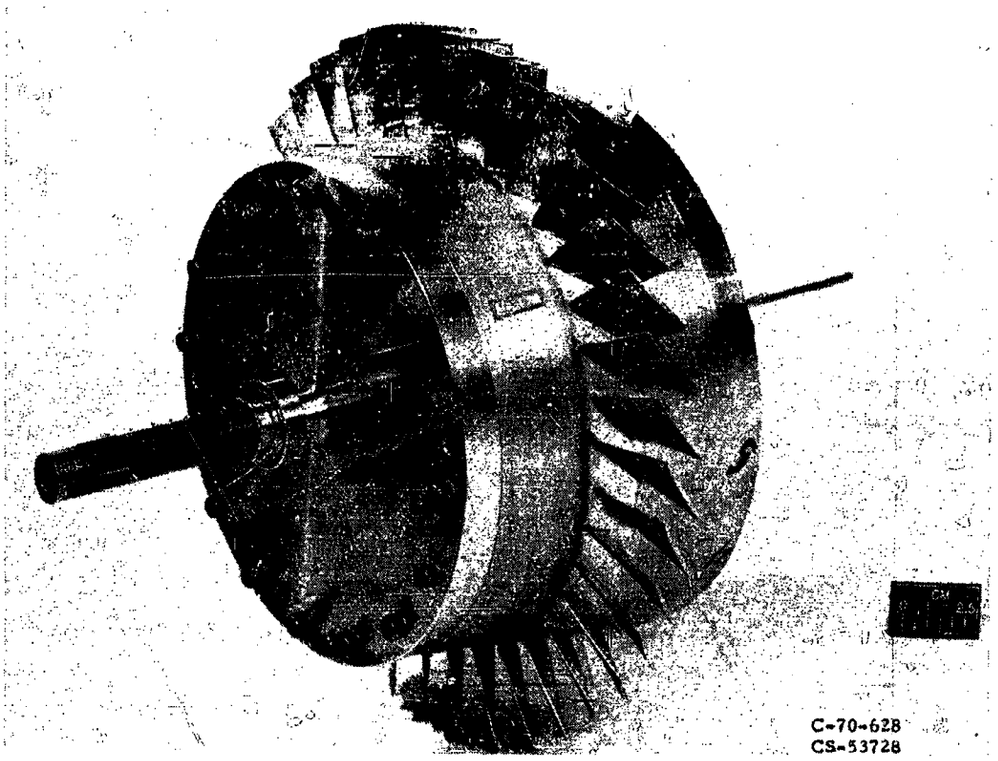

Figure VII-6

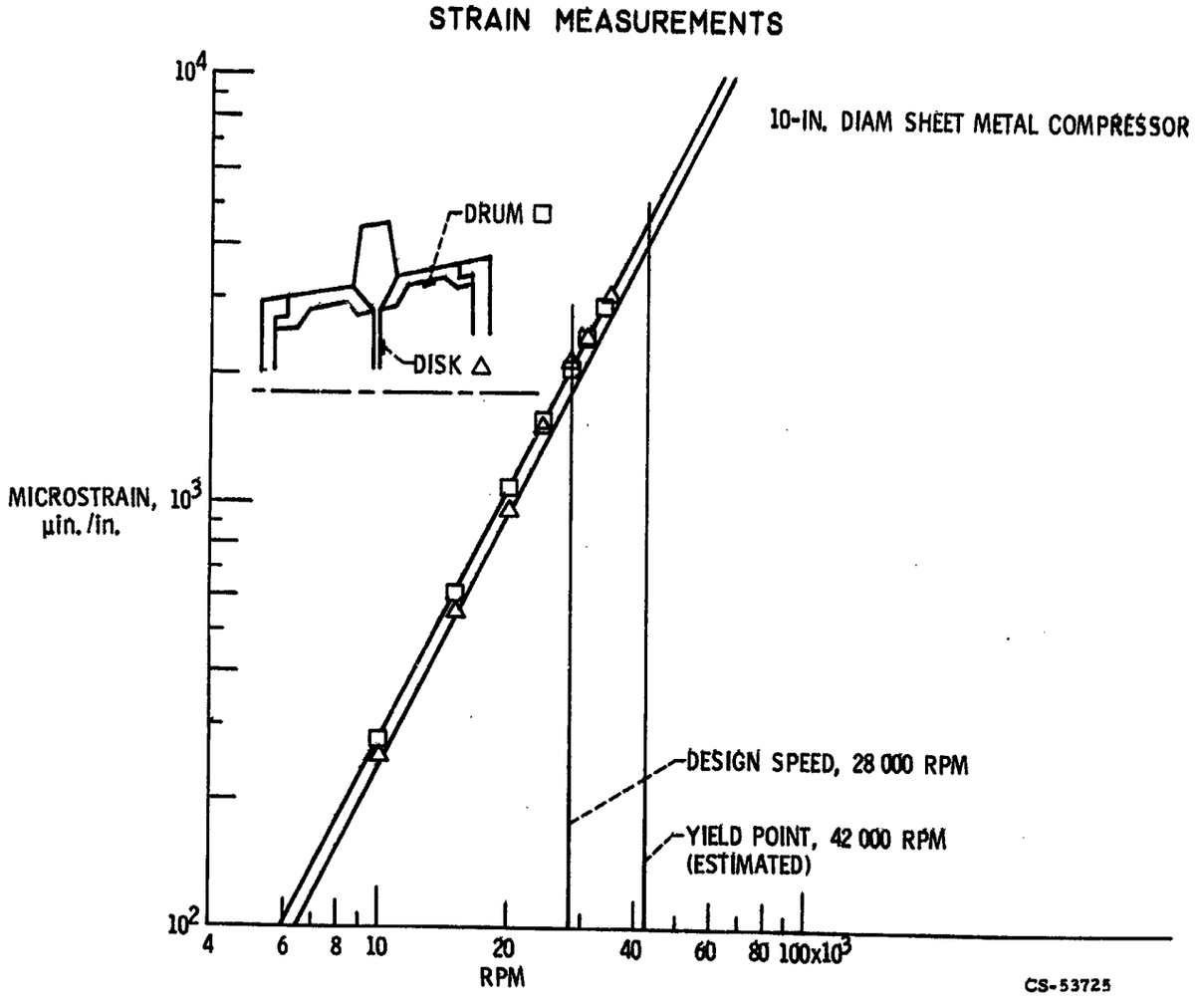
STRAIN MEASUREMENTS
10-IN. DIAM SHEET METAL COMPRESSOR
DRUM □
DISK △
MICROSTRAIN, 10³ µin./in.
10⁴
10²
4
6
8
10
20
40
60
80
100x10³
RPM
DESIGN SPEED, 28 000 RPM
YIELD POINT, 42 000 RPM (ESTIMATED)
CS-53725

Figure VII-7

SHEET METAL TURBINE CONSTRUCTION

C-70-3474
CS-56821

Figure VII-8

SHEET METAL BLADED FAN ROTOR

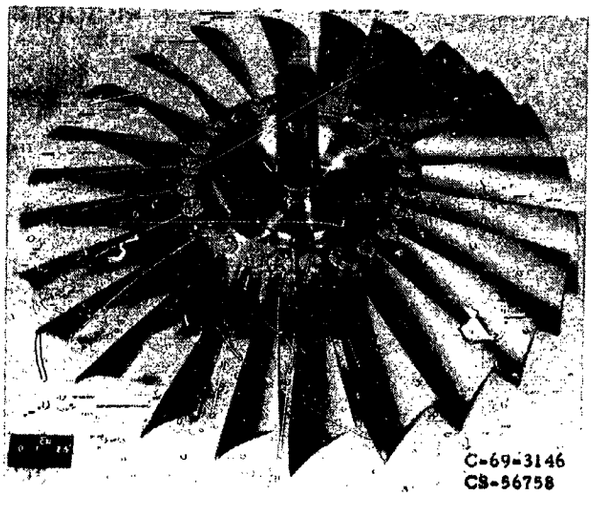

C-69-3146
CS-56758

Figure VII-9

LOW COST ENGINE COMBUSTOR

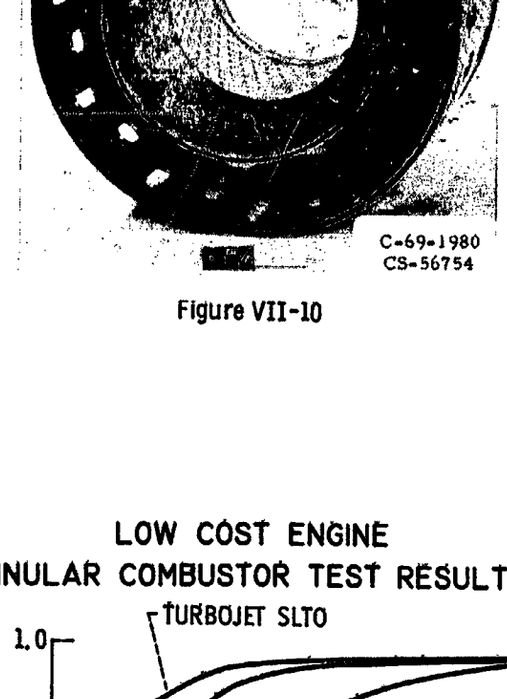

Figure VII-10

Figure VII-11

FUEL CONTROL ACCELERATION LIMITS

TYPICAL TURBOJET ENGINE

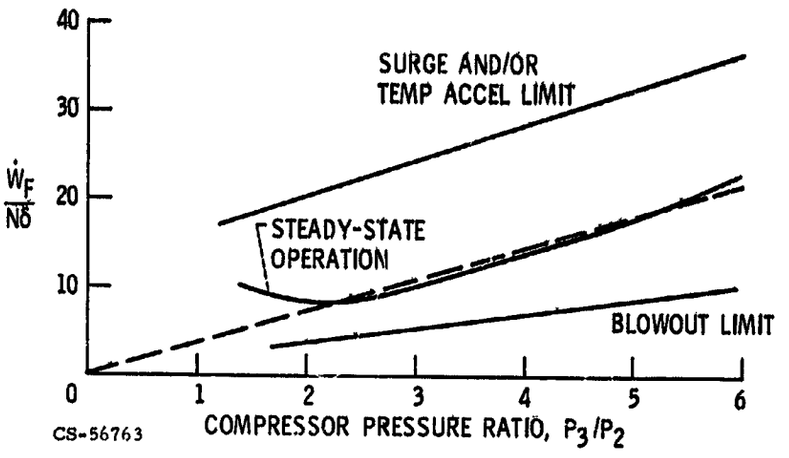

Figure VII-12

CURRENT JET ENGINE ACCELERATION SCHEDULE

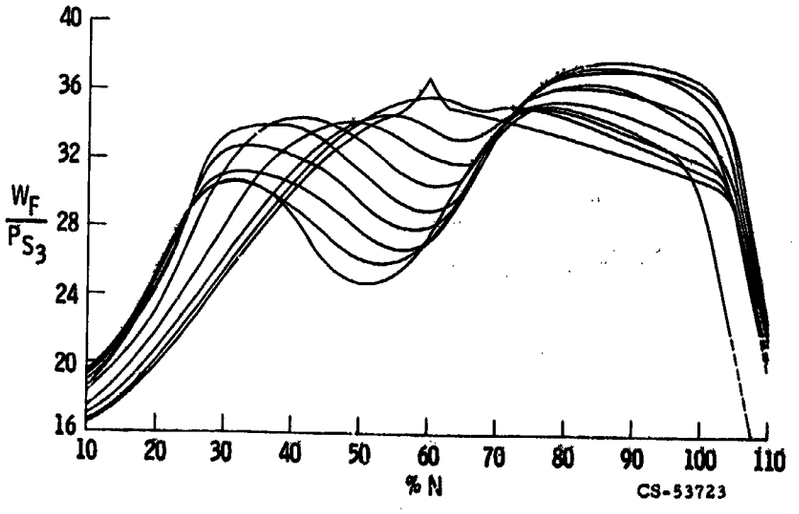

Figure VII-13

ZERO GRADIENT PUMP FUEL CONTROL

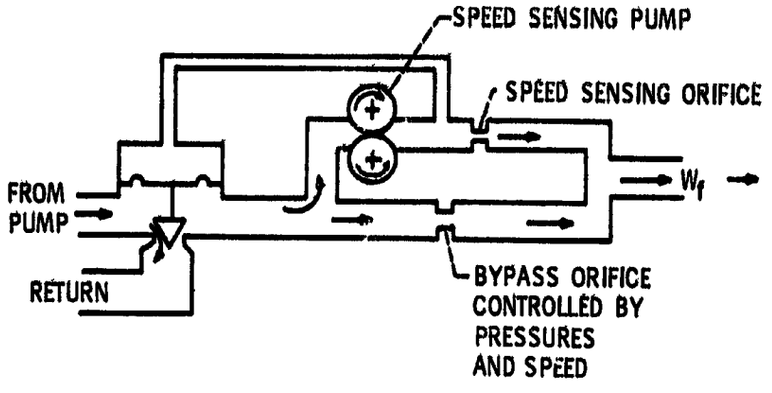

Figure VII-14

FUEL CONTROL COMPONENT PARTS

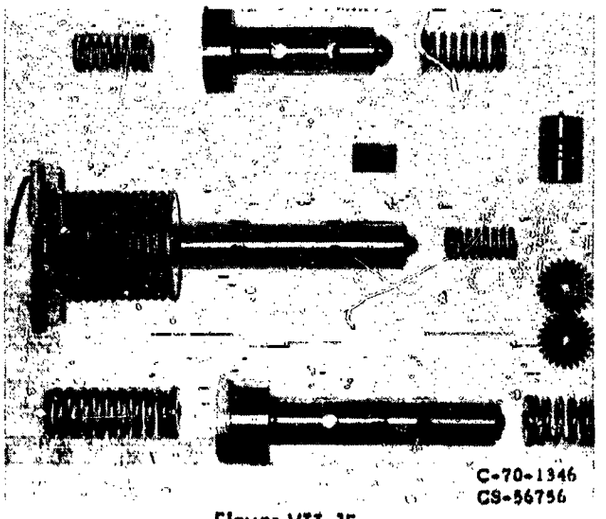

Figure VII-15

EXPLODED VIEWS
CURRENT TURBOJET FUEL CONTROL

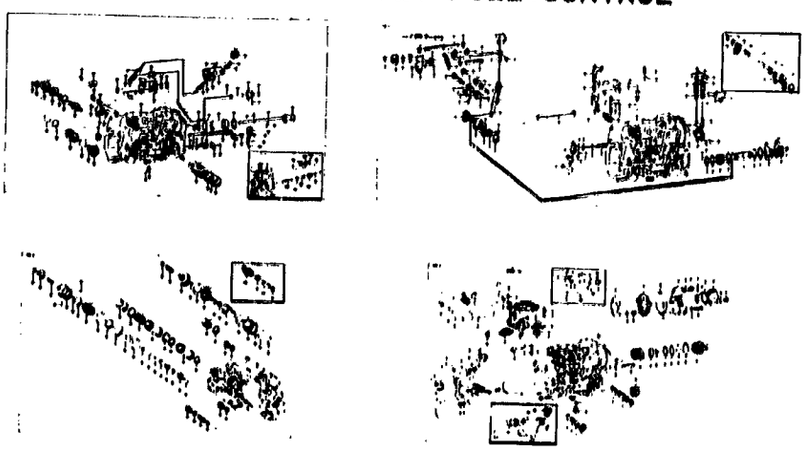

Figure VII-16 CS-56757

J85 ENGINE ACCELERATION 50 TO 95%

EXPERIMENTAL FUEL CONTROL

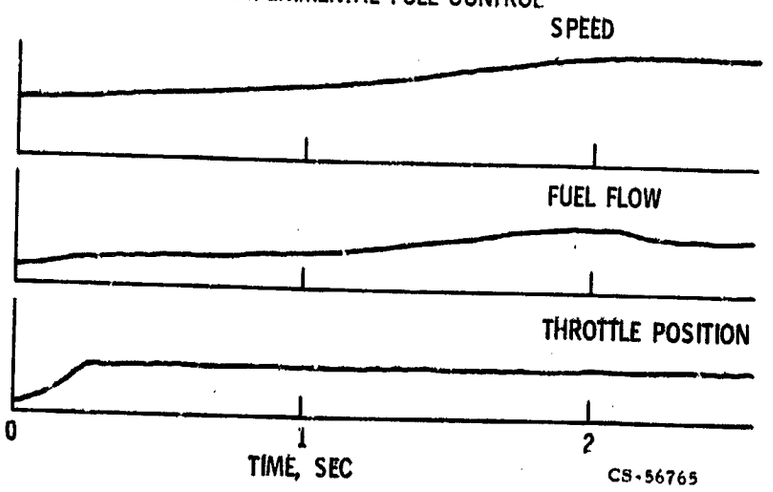

Figure VII-17

VIII. SUPERSONIC EXHAUST NOZZLES

Milton A. Beheim, Bernhard H. Anderson, John S. Clark, Blake W. Corson, Jr.,* Leonard E. Stitt, and Fred A. Wilcox

A major problem in the design of an exhaust system for a supersonic airplane is that its geometrical shape should change as flight conditions are changed. The sonic area and expansion ratio must be variable, and it might also be required to reverse thrust and to suppress jet noise or infrared radiation. The mechanisms that are needed to do this can be complicated and heavy. Therefore, there is a trade between weight and performance that depends on the mission.

The missions for supersonic aircraft can be divided into the following types:

(1) Supersonic cruise, such as the B-70, SR-71, and the supersonic transport

(2) Supersonic dash, such as the B-58, F-4, F-111, B-1, F-14, and F-15 (some of which are aircraft of the future)

The supersonic dash aircraft fly long distances subsonically but are also able to go supersonic for relatively short distances. Exhaust nozzle concepts for both types of aircraft are considered in this section. Supersonic cruise nozzles are discussed first, and then some of the supersonic dash problems are described.

SUPERSONIC CRUISE AIRCRAFT

The first step in analyzing the exhaust system is to get some indication of the sensitivity of a mission to its design. Some results of an analysis for a supersonic cruise airplane are shown in figure VIII-1. The airplane is assumed to have a takeoff gross weight of 750 000 pounds and a payload $6\frac{1}{2}$ percent of the takeoff weight. On the left side of the figure, the changes in range for a 1-percent change in nozzle gross thrust coefficient at cruise and loiter are compared to a 1-percent change in nozzle weight, for a cruise speed of Mach 2.7 for 3930 nautical miles. Getting enough range out of a supersonic cruise airplane has always been a fundamental problem, and it is even more critical for commercial operations. Since cities are fixed distances apart and since runways will never be more than 2 miles long, range increments have to be watched closely. For this mission, the cruise nozzle effi-

*NASA-Langley Research Center.

ciency affects range by $3\frac{1}{2}$ percent and is quite important. In fact, a 1-percent gain here is at least three times as effective as a 1-percent gain in performance of any other component of the propulsion system. On the right side of figure VIII-1 it is presumed that this same airplane flys an all-subsonic mission at a cruise speed of Mach 0.9 for 3280 nautical miles. A 1-percent change in subsonic cruise thrust coefficient affects range by about 2 percent, and the sensitivity to loiter thrust is the same as it was before. For these assumptions, then, it can be worth a lot of nozzle weight to keep performance high at all speeds.

Some exhaust nozzles which could be used on this airplane are shown in figure VIII-2. On the left is a variable flap ejector, which is the type used on the J-93 engine. For a turbojet engine the sonic area is varied by about 40 percent for afterburner operation, and some kind of iris mechanism is required. For flight at Mach numbers near 2.7 the expansion ratio from the sonic area to the exit area is about 3.6, but at subsonic speeds it must be decreased to a value near 1. Therefore, the divergent shroud is made up of several overlapping flaps and seals so that it can be closed down at subsonic speeds. The second nozzle is like that used on the J-58 and TF-30 engines. At high speeds its appearance is similar to that of the variable flap ejector and secondary flow is still used to cool the hot parts. For low-speed operation the divergent shroud also uses multiple flaps, but it does not close as far in order to simplify the flap mechanism. Auxiliary inlets are then opened up in the secondary flow passage at these low speeds to bring in additional air to help fill up the exit area. The dashed lines indicate the position of the doors when the inlets are opened. The minimum diameter inside the shroud is larger than it is on the variable flap ejector so that this inlet air can get through. The conical plug shown on the right is a more recent idea than the divergent ejectors and it has not yet been used on a production engine. The sonic area could be varied either with an iris primary flap or by an axial translation of the flap relative to the plug. At high speeds the internal expansion occurs in the annular flow passage between the plug and the cylindrical shroud. For low-speed operation, the exit area could be decreased by translating the cylindrical shroud upstream. For subsonic flight, then, the shroud would be completely retracted so that the primary flap is exposed to the external flow. This kind of nozzle is harder to cool than the divergent ejectors, but if that problem can be solved, it has some advantages. For one thing, it would not leak as much since the length of seal between the movable surfaces could be decreased from about 300 feet to 30 feet. In addition, the mechanisms appear simpler and might be more durable. Some jet-noise tests also indicate that it is inherently a little quieter than the other nozzles (ref. 1).

Supersonic Cruise Performance

Since the performance of a high-speed nozzle is so important, small differences affect the optimization of its design. In its development, a lot of configurations must be tested but it is hard to measure the experimental performance with enough accuracy. Fortunately, some methods of analysis have been improved so that they are becoming quite helpful.

The ejector flow model is based on the inviscid and viscid interaction between a high-energy stream (primary flow) and a low-energy stream (secondary flow) (fig. VIII-3). These two streams begin to interact at the primary nozzle lip. For the ejector operating in the supersonic regime, the secondary flow is effectively "sealed off" from ambient conditions. When this occurs, the ejector mass-flow characteristics become independent of the ambient static pressure. It is this ejector operating condition that is considered in the theoretical analysis. The flow regimes occurring within the ejector system can be categorized on the basis of the predominant flow mechanisms.

When the amount of secondary flow supplied to the ejector is small, the primary flow plumes out and impinges on the shroud wall (bottom of fig. VIII-3). This causes an oblique shock to form which effectively "seals off" the secondary flow from ambient conditions. The secondary flow is "dragged" through the oblique shock by its mixing with the higher velocity primary jet flow. If the secondary flow is increased, the secondary pressure increases and this "pushes" the primary jet away from the shroud wall. The oblique shock can no longer be sustained at the shroud wall, and thus the secondary flow accelerates and chokes within the shroud (top of fig. VIII-3).

The aerodynamic phenomena that determine equilibrium conditions at "low" secondary ejector flows are the same as those that determine the base pressure behind a backward-facing step. For "zero" secondary flow, the mass flow entrained by the mixing process must be equal to the mass flow reversed by the pressure rise through the recompression zone (oblique shock). This condition is satisfied when the total pressure on the dividing streamline in the mixing zone equals the recompression static-pressure rise. Within this base flow concept, the flow which "leaks out" past the recompression zone is that amount of fluid which has a total pressure greater than the pressure rise through the recompression zone. Equilibrium conditions are thus established in the "low" ejector flow regime when the amount of secondary flow supplied to the ejector is equal to the fluid which "leaks" past the recompression zone associated with the oblique shock.

For "high" ejector flows, the interaction between the two streams is such that the secondary flow accelerates to a critical condition somewhere downstream of the primary nozzle lip. The viscous interaction between the two streams occurs along

the interface (dashed line in fig. VIII-3). The effect of mixing results (1) in a transfer of energy (shear work) from the primary jet flow to the secondary stream, and (2) in a modification of the pumping characteristics due to the displacement thickness of the mixing zone.

In figure VIII-4, the two effects due to mixing are evaluated for an ejector with a large secondary shoulder diameter compared to the primary nozzle exit diameter. The inviscid solution (solid curve) is obtained if mixing between the two streams is neglected. The primary flow field is determined by the method of characteristics, whereas the secondary flow is assumed to be one dimensional and reversible adiabatic. Two conditions were applied along the interface boundary: (1) the local static pressure must be equal for both streams at their boundary, and (2) continuity between the streams must be preserved. The effects of mixing along the interface boundary have been evaluated by locally superimposing the mixing region on the established inviscid flow field solution (solid curve) at the critical secondary flow area. The assumption is that mixing takes place as though the interface were a constant pressure boundary (ref. 2). The results of such a mixing correction are represented by the upper dashed-line solution in figure VIII-4. Inherent in this type of mixing correction is the assumption that the displacement effects due to mixing have a negligible effect on pumping characteristics. When this kind of correction is used, the effects of mixing are viewed as an increase in the secondary corrected weight-flow ratio over that given by the inviscid solution. Continuity is thus preserved by increasing the initial secondary weight-flow ratio by the amount that was entrained as a result of mixing, and by assuming the two flow fields are not appreciably changed by mixing.

In order to account for the change in shape of the primary jet boundary due to mixing, the mixing correction must be applied at each point along the interface boundary. The results of this type of mixing solution are shown as the lower dashed line for low flow rates and dash-dot line for the high-flow-rate solution. For these solutions, continuity was applied along the interface boundary by requiring that the sum of the inviscid weight-flow ratio plus the mixing component be the same as the secondary weight-flow ratio supplied to the ejector. This resulted in a much larger effect due to mixing than was originally calculated. In general, these solutions agree quite well with the data indicated by the circular symbols.

This analysis is particularly useful in trying to find the best shape of the divergent shroud. For the auxiliary inlet ejector the minimum diameter at the shoulder must be relatively large to accommodate the auxiliary air at off-design speeds. The position of this shoulder downstream of the primary exit must then be picked to ensure high nozzle performance.

Figure VIII-5 shows calculations which help in making this choice. The nozzle

thrust coefficient is shown as a function of the spacing ratio, which is defined as the distance between the shoulder and the primary exit divided by the primary exit diameter. With a relatively sharp contour at the shoulder, an abrupt loss in thrust occurs if the spacing is too low, as shown by the lower curve. If the shoulder is more rounded, the ejector is less sensitive to spacing; and higher performance results, as indicated by the upper curve. In most designs the position of this shoulder is fixed but the flaps must be moved to vary the divergent shroud exit area. The shape of these flaps is another design variable. For the sharp-shoulder performance curve, it was assumed that the flaps had an isentropic contour. If the flaps were changed to a conic shape, the dash-dot curve resulted, and it may be a better choice. Some data points are shown on the figure to indicate that the theoretical trends actually occur. The circle is for an isentropic contoured shroud, while the square is for a conic flap configuration.

These curves are shown for the auxiliary inlet ejector. A similar study has been made for the variable flap ejector and the results show an even greater sensitivity to shroud geometry than is shown here.

All these curves are shown for a 2-percent corrected secondary flow ratio. However, these results may be sensitive to this flow rate. In figure VIII-6, the secondary flow is varied. Theoretical results are shown for the geometry with a sharp shoulder and contoured flaps. The 2-percent flow curve is repeated from the previous figure. However, for this particular figure, the ram drag of the secondary flow has been subtracted from the gross thrust. Curves for secondary flows of 4- and 8-percent are also shown. Although higher performance is reached at 4-percent corrected weight-flow ratio, it requires a study of the overall design of the propulsion system to decide whether these higher flows should be used. The experimental data points again show good correlation with the theory.

A summary of supersonic cruise nozzle performance is shown in figure VIII-7. The gross thrust coefficient is shown for each of the three nozzles at 2-percent corrected secondary flow. The top of the bar is the theoretical maximum performance which could be obtained with an optimized design. The performance of the variable flap and the auxiliary inlet ejectors were taken from curves similar to those of figure VIII-5. Preliminary calculation on the plug nozzle indicate that its performance could be as high as that shown for the variable flap ejector. The auxiliary inlet ejector is less because of its requirement for a larger secondary diameter. The best experimental results obtained to data are indicated by the dashed lines and are quite close to theory.

Subsonic Cruise Performance

The off-design performance of a nozzle is harder to analyze because of the interactions between the internal and external flows. Therefore, we have to depend more on experimental data. The isolated nozzle model shown in figure VIII-6 is used for wind tunnel tests at this Center. A 21.6-centimeter-diameter cylinder is supported by a strut, and high-pressure air is ducted to the test nozzle to simulate the engine exhaust. In the 8- by 6-Foot Supersonic Wind Tunnel, tests are made from Mach 0 to 2. However, the transonic performance of a nozzle is particularly hard to get because of tunnel wall interference. At transonic speeds the most important airframe installation effects occur. These effects result because the external flow is distorted by the airframe, and it varies depending on the engine location. So the transonic testing problem is made even more difficult since a big piece of the airframe must be tested along with the exhaust nozzle. As a result, the nozzle model ends up being a lot smaller than we would like when working within the size limits of our present wind tunnels. One approach to this problem that would help is to have a coordinated flight and wind tunnel model program that uses the best features of each test technique. An effort like this is in progress at the Lewis Research Center using a modified F-106 as illustrated in figure VIII-8. A new engine nacelle has been added under each wing so that the nozzle sticks out behind the wing. This kind of engine installation has not been used before, but it has an important advantage since the wing can be used to shield the inlet from angle-of-attack effects. An afterburning J-85 turbojet engine was used in each pod. These pods were 60.8 centimeters in diameter and were designed to accept any of the nozzles which gave good results in the isolated tests. For each nozzle design the airplane is also flown at low altitudes for fly-by noise measurements.

In parallel to the flight tests, a wind tunnel model program is being conducted in an effort to get more flexibility in the nacelle shape and its location. An example is the 1/20-scale model F-106 shown in figure VIII-8. It was small enough to avoid the transonic wall interference problems but the nacelle diameter was only about 3.18 centimeters, and the wing structure was so thin that we could not get pressurized air to the nacelle to simulate jet effects. Therefore, only the simplest exhaust nozzles could be tested with this model.

Flights have been made with the F-106 at Mach 0.4 for noise fly-by measurements and at Mach numbers from 0.6 to 1.3 for exhaust nozzle evaluation. Mach number 0.9 is used in the ensuing figures for discussion of subsonic cruise. The flight test program is described in references 3 to 5.

The installation of the nacelles is shown in figure VIII-9. The nacelles were tangent to the wing lower surface at the trailing edge of the wing and they were at-

tached by two links. Axial forces were measured by a load cell. A simple normal shock inlet was adequate for the Mach number range used. A movable rotating valve was located at the engine face to control flow of secondary air to the nozzle.

With an exhaust nozzle located in the combined flow fields of the wing and nacelle, flow conditions differ from those around the model of figure VIII-8 that was used to evaluate isolated exhaust nozzles. These flow field differences are first pointed out and then the effect of installing various nozzles in an underwing flow field is described. Flow field effects are reported in references 6 to 10.

Installed flow fields. - The variation of static-pressure coefficient under the wing at a spanwise location near the nacelle location is presented in figure VIII-10. Data are shown with and without the nacelle. Without the nacelle the value of pressure coefficient drops along the wing chord and then rises to zero at the wing trailing edge. When the nacelle is added to the wing, the effect of the combined flow field is to raise the pressure in the region of the inlet. The flow then overexpands around the juncture of the inlet and nacelle; the pressure coefficient drops to a lower value than with the clean wing and then it rises back to zero. High pressure near the inlet increases inlet drag. Some of this drag may be cancelled, however, by pressure forces acting on the surfaces of the nozzle if pressure coefficient downstream of the wing trailing edge reaches a value above zero. Some nozzles may be more effective than others in this drag cancellation. There is a compression shock present in the pressure rise near the wing trailing edge. The position of this shock varies with flight Mach number.

The movement of the compression shock with flight Mach number is shown on figure VIII-11. At Mach 0.8 there is a small amount of overexpansion and a gradual rise in pressure coefficient back to zero near the wing trailing edge and above zero on the boattail of the nozzle. At Mach 0.9 there is more overexpansion, followed by a sharp rise in pressure. The compression shock is located in this steeply rising pressure region. At Mach 0.95 the shock has moved rearward near the trailing edge of the wing and at Mach 1 it has moved off the end of the nozzle. Pressure remains low along the entire length of the nacelle and nozzle. Low pressure on the nozzle boattail for this condition results in high nozzle drag.

The external static-pressure coefficient was uniform along the isolated nozzle test model at a value of about zero for all subsonic conditions. There was no circumferential variation in pressure around the isolated model. This was also the case in flight about one nozzle diameter ahead of the boattail juncture and at the rear of the boattail. In the region just downstream of the wing trailing edge, however, the external pressure was higher around the top of the nozzle than at the bottom.

There were differences in external boundary layer measured upstream of the nozzle. In flight the boundary layer was generally thinner than on the isolated model,

except in the corners between the nacelle and wing and over the top of the wing. There were regions of low energy within the boundary layer all around the nacelle as a result of the more complex flow field and presence of shocks. The various exhaust nozzles shown in figure VIII-2 have been tested in this flow field. Isolated nozzle tests were made prior to the flight tests.

Variable flap ejector. - The variable flap ejector nozzle is shown in figure VIII-12 in the subsonic cruise configuration. The nozzle flaps are closed down and provide a low internal area ratio ($A_9/A_8 = 1.40$) and good internal performance at this flight speed (ref. 11). The boattail drag can be a problem since the projected area of the boattail is 60 percent of the nacelle area and the boattail angle is 15°. Boattail drag depends on the static-pressure distribution, which is affected by the shape of the boattail. It would be desirable from a drag standpoint to radius the corner between the cylindrical nacelle and the 15° boattail angle. However, it is impractical to provide much of a radius at this external hinge point and still be able to maintain a cylindrical boattail shape at supersonic cruise when the trailing-edge flaps are fully open.

Typical static-pressure distributions for both a sharp- and a rounded-corner boattail are shown in figure VIII-13 at a Mach number of 0.90. The flow overexpands considerably downstream of a sharp corner (R/D = 0) and results in a high drag. Rounding the corner can reduce both the initial overexpansion and the drag, as discussed in reference 12. The boattail static-pressure distribution can also be affected by the jet boundary that is located at the trailing edge of the boattail. This jet boundary varies with nozzle pressure ratio and, therefore, jet effects must be duplicated when measuring the boattail drag (ref. 13).

The isolated pressure drag of a 15° boattail is shown in figure VIII-14 at a Mach number of 0.90 as a function of nozzle pressure ratio, defined as the total pressure of the primary jet divided by the ambient static pressure. The boattail pressure drag is ratioed to the ideal gross thrust of the primary flow. The highest drag was obtained with a sharp-cornered boattail (R/D = 0) and a thin boundary layer, typical of a nacelle installation. For the example shown, the boundary-layer thickness was 7 percent of the nacelle diameter. At a nozzle pressure ratio of 3.75, typical for a turbojet engine at subsonic cruise, the pressure drag of this conical boattail was about 6 percent of the ideal gross thrust of the nozzle. At this flight speed the net thrust of the engine is about one-half of the gross thrust, so that the boattail drag would be about 12 percent of the airplane drag. A thicker boundary layer, typical of a fuselage installation, reduces the drag of the sharp-cornered boattail to 5 percent of the ideal gross thrust. For this example the boundary-layer thickness was 18 percent of the fuselage diameter. It is interesting that the effect of a thick boundary layer is to make a sharp corner appear rounded. It reduces the initial over-

expansion and raises the general level of pressures over the boattail, as shown in reference 12. The effect of boundary-layer thickness on the pressure drag of a series of boattails over a range of Mach number is presented in reference 14.

A small radius at the corner of the boattail with the thicker boundary layer (fig. VIII-14) reduced the pressure drag to 4 percent of the ideal gross thrust. This radius ratio, R/D = 0.5, appears to be a reasonable value for the type of flap and seal arrangement shown on the model in figure VIII-12. A more generous radius can reduce the pressure drag even more, as shown in figure VIII-14. It is evident that the isolated boattail drag for a variable flap ejector nozzle can be significant at subsonic cruise. How this external drag is modified when the nacelle is installed on the F-106 aircraft is now examined.

Figure VIII-15 shows a variable flap ejector nozzle mounted on the F-106. Flight performance for this nozzle type is reported in reference 15. A section of the elevon was cut out and rigidly attached to the wing. To simplify its fabrication, the boattail part of the nozzle was solid rather than made of individual flaps and seals and the area ratio was fixed at the appropriate value for subsonic cruise.

Installation effect on boattail drag is shown in figure VIII-16 for a sharp-junctured variable flap ejector nozzle. The installation effect is to greatly reduce boattail drag at the higher subsonic speeds. Drag is about zero at Mach numbers from 0.8 to 0.9, where the compression shock is ahead of the nozzle. At Mach 0.95, where the shock is near the nozzle, the drag goes negative. The drag rises sharply when the compression shock moves off the end of the nozzle at higher speeds.

In the isolated case, rounding the boattail juncture was effective in reducing drag. The effect of doing this in flight is shown on figure VIII-17. Data are shown for R/D = 0 and R/D = 2.5 nozzles. Little decrease in drag below the already low subsonic values was obtained. There was some reduction in drag above Mach 1.0, however.

Auxiliary inlet ejector. - An auxiliary inlet ejector nozzle is shown in figure VIII-18. At subsonic cruise the auxiliary inlet doors are open and external air enters the secondary shroud to prevent overexpansion of the primary jet at low values of nozzle pressure ratio. Since this air fills part of the shroud there is a reduced requirement for exit-area variation with the trailing-edge flaps. If this boattail is compared with the variable flap ejector (fig. VIII-12), we find that the projected area has been reduced from 60 percent to 45 percent of the nacelle area. For an equal trailing-edge-flap length, the boattail angle can be reduced from 15° to 10°. The internal expansion ratio A_9/A_8 for the auxiliary inlet ejector at this flight speed is about 2.0 (ref. 16), compared to a value of 1.4 for the variable flap ejector.

The isolated performance of auxiliary inlet ejector nozzles is shown in figure VIII-19 at a Mach number of 0.90. The gross thrust coefficient is used as a measure

of nozzle performance and is defined as thrust minus drag divided by the ideal gross thrust of the primary flow. The optimum performance was obtained when the inlet doors were fixed open and the trailing-edge flaps were held closed (ref. 16), as shown by the upper curve. It would be desirable to minimize the actuation requirements and the mechanical complexity of this nozzle type by allowing some of its components to be positioned by the air loads. At a subsonic cruise pressure ratio of 3.76 the nozzle performance was reduced by 4 percent when the inlet doors were allowed to float and ended up being closed over half way (ref. 17). An additional loss of $2\frac{1}{2}$ percent in performance resulted when the trailing-edge flaps floated slightly open from the closed position (ref. 18). At this flight speed, then, the use of floating components resulted in a nozzle that was operating well overexpanded at a low value of performance.

The geometry of the floating doors and flaps would have to be carefully selected to avoid the problems of instability. There is a lot of energy in the primary flow. If the hinge locations and flap lengths are not picked with care, oscillations of the floating components might result. Several configurations with floating components have been tested in the wind tunnels at the Lewis Research Center. Some of these designs proved to be stable (refs. 11 and 18). Some examples of trailing-edge flap and auxiliary inlet door instability are discussed in reference 19.

The auxiliary inlet ejector nozzle is shown installed on the F-106 in figure VIII-20. Results for this nozzle are reported in reference 20. This nozzle had 16 auxiliary inlet doors which were either fixed in place or free floating. The top three opened into the trough built into the wing. The boattail part of this nozzle was again fixed at the subsonic cruise area ratio.

Performance of the auxiliary inlet ejector nozzle isolated and in flight is shown in figure VIII-21. Nozzle gross thrust coefficient and boattail drag ratioed to ideal thrust are presented as a function of door position. The isolated gross thrust coefficient fell along the dashed curve and it continued to rise as the doors were opened. The flight thrust coefficient was somewhat higher and it also rose as the doors were opened but it leveled off and was the same as isolated for full-open doors. The upper part of the figure shows that boattail drag was lower in flight. The lower boattail drag accounts for the higher nozzle gross thrust with the doors closed and part way open. The benefit of the lower drag was lost, however, when the doors were full open.

As indicated in figure VIII-21, the performance of floating doors in flight was nearly the optimum. The doors floated to an average position somewhat over mid-open. In the isolated case, floating door performance was considerably lower. When the trailing flaps were allowed to float in addition, performance was even lower. In flight the trailing flaps probably would have floated to a lower-area-ratio position

than they did in isolated tests because boattail pressures were higher due to the presence of the shock. This would have resulted in a higher gross thrust coefficient.

Positions of the floating inlet doors are shown in figure VIII-22 for flight at Mach 0.9. The trailing edges of the doors are viewed from the rear. The higher external pressure around the top of the nozzle held the doors open around the top and the outboard side. These doors admitted air from the lowest energy regions of the flow field. The lower external pressure on the bottom and the inboard side closed the remaining doors. In the case where all the doors were fixed open, little air appeared to be entering the doors on the bottom. The performance shown on the previous figure for this condition was about the same as for floating doors. Higher performance was not achieved with full-open doors because very little of the higher energy air around the bottom entered the nozzle.

Plug. - The low-angle conical plug nozzle is shown in figure VIII-23 in the subsonic cruise position. The outer shroud is retracted upstream for operation at this flight speed. Both the primary flap and the plug surface are now exposed to the external flow. This nozzle concept utilizes secondary flow to cool some of the engine parts and the primary flap. This cooling air is discharged in the annulus between the primary flap and the outer shroud. The major difference between the two configurations shown is in the shape of the surfaces upstream of the primary throat. The configuration on the left has a cylindrical outer shroud and a conical primary flap, while the other has a boattailed outer shroud and a rounded primary flap shape.

It was shown earlier in this discussion that floating components of nozzles can be unstable. In the plug concepts shown, the plug is immersed in the high-energy primary stream and can be unstable if not supported properly (refs. 21 and 22). From a stability standpoint it would be desirable to support the plug from the outer shroud with struts. However these struts are now immersed in the afterburner flow and present a difficult cooling problem. Support struts also act as flameholders for unburned fuel in the afterburner. Another support concept of interest is to cantilever the plug from the turbine frame with a sting through the center of the afterburner. Afterburner temperature profiles can be tailored to maintain cooler temperatures along the sting to minimize the cooling requirements. However, the sting must be stiff enough to prevent oscillations of the plug.

The isolated performance of these two plug configurations is shown in figure VIII-24. Data are presented both at static conditions and at a Mach number of 0.90. At a subsonic cruise pressure ratio of 3.75, there is a sizeable effect of external flow on the performance of these two configurations. The loss of about 5 percent in performance resulted from the combined drag on the primary flap and on the annular base where the secondary flow is discharged. Rounding the surfaces upstream of the primary throat did improve the performance, as expected. A further discussion

of the isolated performance of a series of conical plug nozzles over a wide range of flight speeds is presented in references 23 to 27.

The plug nozzle is shown installed on the aircraft in figure VIII-25. This nozzle was uncooled and was operated with the primary throat in the fixed position shown with the engine in the nonafterburning mode. The installed performance of this nozzle is compared to isolated data in figure VIII-26. The effect of the movement of the compression shock can be seen on this figure. It is ahead of the nozzle at Mach numbers below 0.9. At Mach number 0.95 it is near the primary flap, and the highest nozzle gross thrust coefficient is obtained. The thrust coefficient drops sharply near Mach 1.0, where the compression shock moves off the end of the nozzle and low external pressure is obtained - primarily on the plug surface. Flight performance data for this nozzle are presented in reference 20.

Nozzle performance comparison. - Figure VIII-27 shows gross thrust coefficient both isolated and in flight. The variable flap ejector was the poorest when isolated because of its boattail drag, but the best when installed. The plug had very high performance when isolated and improved in flight, so that it was second best. Isolated performance of the auxiliary inlet ejector was good if the doors and flaps were actuated; but flight performance stayed about the same.

Nozzle Cooling

In the discussion so far, aerodynamic performance has been stressed. Nozzle cooling is another problem, particularly with the plug nozzle. Experimental heat-transfer studies have been made at Lewis on both ejector-type nozzles and plug-type nozzles. A brief discussion of these experimental results is presented in the following paragraphs.

Film cooling. - Figure VIII-28 shows some typical results from the ejector cooling study. A cylindrical ejector was tested on a J-85 afterburning turbojet engine in an altitude facility. Ejector cooling was accomplished by film cooling and radiation. Film cooling is a means of insulating the ejector wall from the hot primary jet with a layer of the cooler secondary air. Ejector wall temperatures are shown as a function of distance from the primary exit for a case with maximum afterburning (approximately 3100° F) and high secondary flow rate. The predicted temperatures were obtained from a heat-balance calculation for the wall (ref. 28). The insulating effect of the secondary stream was calculated by using a modified Hatch-Papell film-cooling correlation. This correlation was empirically developed for a flat plate, subsonic flow, and no pressure gradient. It was modified for annular flow with vary-

ing pressures. The predicted temperatures agree reasonably well with the measured values.

A comparison of the various calculated heating and cooling mechanisms is shown in figure VIII-29. The upper part of the figure shows the parameters that heat the wall and the lower part shows the cooling terms as a function of distance from the primary exit. Radiation from the hot gas to the wall is approximately uniform over the entire ejector. The secondary airstream film cools the wall for about two-thirds of the ejector length. At this point, the secondary stream has become hotter than the wall and, thereafter, adds heat to the wall. Radiation from the wall to the surroundings is the only cooling mechanism over the last third of the nozzle. Similar results were obtained for other pressure ratios and secondary flow rates. Thus, the prediction techniques developed can be used with confidence to design ejector-type nozzles.

Figure VIII-30 shows some typical results from the plug film-cooling study. A 21.6-centimeter-diameter model was tested in an altitude facility. Cooling air entered the plug through a sting mount. Three separate plug models were tested. The first had a film-cooling slot at the 50-percent point (i.e., halfway between the primary throat and the end of the plug). The second had a slot at the 10-percent point and the third plug had a slot upstream of the nozzle throat at the -10-percent point. Tests were made at primary temperatures to 540° F. A typical plug static-pressure distribution is shown for a high nozzle pressure ratio. Typically, the pressure distributions downstream of the 50-percent slot are about constant, while pressure gradients following the other two slots are first favorable and then adverse.

In figure VIII-31, measured cooling efficiencies are compared with the Hatch-Papell film-cooling correlation. Cooling efficiency is simply a ratio of primary recovery temperature minus wall temperature to the primary recovery temperature minus the coolant inlet static temperature. When the wall temperature is equal to the coolant temperature, this ratio is equal to 1.0; as the wall temperature increases, the ratio decreases. The Hatch-Papell parameter includes about 10 different terms, including distance from slot exit and coolant flow rate (see ref. 28). The curve on the figure represents the correlation. The circular symbols on the figure, for the 50-percent slot, correlated well for all pressure ratios, coolant flow rates, and appropriate secondary shroud positions. The triangular symbols, for the 10-percent slot, generally fell above the correlation line. The "knee" in the data was found to correspond to the point where the pressure gradient turns from favorable to adverse. The favorable pressure gradient retards mixing of the primary and coolant streams, keeping the wall temperatures low. The adverse pressure gradient accelerates the mixing, causing a sharp increase in wall temperature. For the -10-percent slot, similar results were obtained. All the data of interest fell on or above

the correlation line, however. This means the measured wall temperatures were lower than would be predicted using the correlation. Therefore, the use of the correlation should result in the conservative prediction of plug wall temperatures.

Convectively cooled plug nozzle. - Heat-transfer tests were also made on a convectively cooled plug nozzle system (ref. 29). The plug was strut supported for easy attachment to the J-85 engine (see fig. VIII-32). Cooling air was obtained from the compressor discharge ports of the engine. Cooling channels (shown in section A-A, fig. VIII-32) were formed along the surface of the plug and struts by attaching nickel fins to the high-strength outer wall. Nickel was used because of its high thermal conductivity and the resulting high effective heat transfer from the outer wall to the coolant. A conical extension was attached to the 60-percent point on the plug and was film cooled with the cooling air discharging from the plug cooling channels. The nozzle during a high-temperature test in the altitude facility is shown in figure VIII-33. The primary gas temperature was 2900° F - slightly less than maximum afterburning. The nozzle pressure ratio was about 3.0. The plug and struts were cooled with $3\frac{1}{2}$ percent of the primary airflow.

The plug was designed for wall temperatures of 1740° F with this cooling flow rate, but the maximum temperature on the plug was only 1500° F. The highest temperature on the extension was only 1300° F and the hottest temperature on the primary was about 1700° F. The plug wall temperatures were lower than expected because of the gas temperature profile that existed in the engine. A typical profile is shown on the bottom left in figure VIII-32. A radius ratio of zero is on the centerline, and a radius ratio of 1.0 is on the primary wall. This profile results from the particular afterburner fuel nozzle design for this engine. Temperatures were found to be as much as 500° F cooler at the plug surface than the maximum gas temperature. Since this profile eases the plug cooling problem, it should be designed into any advanced plug nozzle system.

The experimental heat-transfer tests are summarized as follows:

(1) First, for ejector-type nozzles, the Hatch-Papell film-cooling correlation appears to yield a reasonable prediction of wall temperature when combined with radiation terms.

(2) Second, for the film-cooled plug, the Hatch-Papell correlation resulted in a conservative prediction of plug wall temperatures.

(3) Finally, it was demonstrated that an air-cooled plug could be cooled in an afterburning turbojet with a reasonable amount of compressor bleed air.

The purpose of these experimental tests was to develop the prediction methods necessary to evaluate advanced systems.

Supersonic cruise aircraft studies. - The next logical step is to use the prediction methods developed and to extrapolate the small-scale plug nozzle data to a full-

size supersonic cruise engine. The following is a brief summary of two theoretical studies that are underway at the Lewis Research Center. In the first, engine fuel is used to regeneratively cool the plug. In the second, compressor air is the coolant.

In each case, a sting-supported plug was selected, to eliminate the struts that are immersed in the hottest region of the hot gas. The fuel-cooled nozzle appears feasible, from a heat-transfer standpoint, to cool the plug and sting support. Therefore, no engine cycle air would be required to cool the plug. Also, plug wall temperatures could be kept below 1000° F when using fuel cooling.

The theoretical study using air cooling indicates that for maximum afterburning, $2\frac{1}{2}$ percent of the engine cycle air would be required to cool the plug below 1740° F. Also, the afterburner is presumed to be on during supersonic cruise, resulting in primary temperatures of about 1900° F. The plug would not have a very long life at this temperature unless it were cooled. The calculations show that 1/2 percent of the engine cycle air is needed to ensure reasonable plug temperatures during supersonic cruise.

Summary

The effect of nozzle type on the range of a supersonic cruise aircraft, if the cooling requirements are included along with the aerodynamic performance characteristics, is shown in figure VIII-34. The airplane and the two missions illustrated are the same as those presented in figure VIII-1. The auxiliary inlet ejector nozzle is used as a baseline configuration and it provides 3930 nautical miles of range for a typical Mach 2.70 mission. Both analytical calculations and experimental data (fig. VIII-7) have shown that the variable flap ejector has about 1/2-percent higher gross thrust during cruise and, therefore, provides an additional 68 nautical miles of range. The plug nozzle is competitive with the variable flap ejector if the plug surface is cooled with the engine fuel at no loss in cycle efficiency. However, a plug cooled with compressor discharge air shows little gain in range over the baseline nozzle. The range of the air-cooled plug could be improved if an interstage bleed could be used as the source for the cooling flow. The plug nozzle has some other features that make it an attractive nozzle concept. As mentioned previously, it may be easier to seal, has less mechanical complexity, and may be inherently quieter. The range comparison shown does not account for any of these factors.

The variable flap ejector and the plug nozzle also provide more range for an all-subsonic (Mach 0.90) mission (fig. VIII-34). These two nozzle concepts had the highest installed performance at subsonic cruise, based on in-flight thrust measurements using the F-106 aircraft (fig. VIII-27).

SUPERSONIC DASH AIRCRAFT

The exhaust systems for the second type of aircraft - the supersonic dash airplanes that cruise primarily at subsonic speeds - are examined briefly in this section. For this kind of mission, afterburning turbofan engines would be used rather than turbojets. Subsonic performance is most important, but it is acceptable to compromise supersonic performance if it helps to minimize the nozzle weight. Some examples of these nozzles are shown on figure VIII-35. On the left is a variable convergent-divergent nozzle which is shown in the subsonic cruise position. The tufts sticking out of the top of the nozzle were used in flight tests to detect flow separation. In concept, it is similar to the variable flap ejector except that for use on a turbofan engine the secondary airflow could be eliminated. In addition, the sonic area variation is larger. In fact, during full afterburning the sonic area could be twice as large as that shown. Some amount of internal expansion is needed again for high-speed operation, but it would be less than that of the variable flap ejector. By constructing the boattail with overlapping flaps and seals and by using enough actuators, these variations could be provided. But to minimize the mechanical problems, these flaps should be short. Therefore, at subsonic cruise speeds, the boattail on this type of nozzle is even larger and has steeper angles than the variable flap ejector. For the nozzle shown, the projected area is about 75 percent of the nacelle area and the maximum angle is 24°. Putting a plug in the nozzle, as shown on the right, would decrease both the boattail area and angle. If the plug had adequate cooling, it could also be used to suppress infrared radiation from the hot engine parts. However, its structural weight would probably be higher than that of the other nozzle.

Isolated Performance

The isolated performance of the two supersonic dash configurations is shown in figure VIII-36. For reference, the internal performance of an ideal convergent nozzle without any external drag is presented. The dropoff in performance of this nozzle with increasing pressure ratio is an indication of its underexpansion losses. The plug nozzle has the same performance characteristics as the ideal convergent nozzle. The small decrease in performance with external flow resulted from the drag on the 9° circular-arc boattail. At a typical subsonic cruise pressure ratio of 2.8 for a turbofan engine, the plug nozzle provides a high gross thrust coefficient of better than 97 percent. At the same nozzle pressure ratio the variable convergent-divergent nozzle had a slightly lower performance, about 96 percent. The difference

in performance was due to the higher drag associated with the 24° boattail. Some additional discussion of the isolated performance of plug and convergent-divergent nozzles for application to a supersonic dash aircraft are presented in references 30 and 31.

The high-angle boattail shown for the variable convergent-divergent nozzle (fig. VIII-35) is operating near the limit for maintaining attached flow. Typical pressure distributions for this 24° boattail shape are shown in figure VIII-37. If the flow remains attached the distribution is as shown by the solid curve. If the flow separates locally, a distribution as shown by the dashed curve results, with an increase in boattail drag. It is important, then, to define the separation characteristics of these high-angle boattails and to determine their sensitivity to Reynolds number and to installation effects. The Lewis Research Center has recently flight tested a series of these high-angle boattails and data are now available that show some of these effects on boattail drag.

Nacelle Installation

The convergent-divergent nozzles that were test flown are shown in figure VIII-38. These three nozzles all had the same projected boattail area and a 24° angle at the end of the nozzle. The two on top were the same, except that the Case 1 nozzle was moved downstream relative to the Case 2 nozzle by about one-half nozzle diameter. The boattail juncture for these two was fairly sharp. The Case 3 nozzle had a full circular-arc boattail.

Boattail drag divided by ideal primary thrust for these nozzles is shown in figure VIII-39 as a function of Reynolds number. Reynolds number was varied by flying the F-106 at different altitudes. Angle of attack was held constant at 6° by flying in coordinated turns at the higher Reynolds number. The lowest Reynolds numbers were obtained by flying straight at an altitude of 45 000 feet. The highest Reynolds numbers were obtained by flying in 3-g turns at an altitude of 15 000 feet. Reynolds number was based on the length from the inlet cowl lip to the nozzle attachment point. The case number on the lines of data correspond to the nozzle designations of figure VIII-38. With the Case 1 nozzle at the lowest Reynolds number the boattail drag was as much as 10 percent of the ideal primary gross thrust. The drag was lowered considerably when this nozzle was moved forward, giving Case 2. This was a result of the more favorable flow field closer to the wing. The Case 3 circular-arc contour provided the lowest drag.

Separation of the type described in figure VIII-37 was encountered with these nozzles. Separation was detected by pressure measurements and tufts. Areas of separation are shown on figure VIII-39 by the shaded regions. Separation was en-

countered with all the nozzles except the circular arc at the highest Reynolds number. As the Reynolds number was increased, drag was reduced for all these nozzles because this reduced the tendency of the external flow to separate.

Two frames from a motion picture of tufts for the Case 2 nozzle are shown in figure VIII-40. This motion picture was taken by a camera mounted low in the tail. The angle of view is such that the tufts that appear to be on the top are actually on the upper inboard side. The two frames show extreme positions taken by the inboard tufts, which were in a region of separated flow. Flow on the outboard side and over the top of the wing is seen to be steady.

Fuselage Installation

n many fighter designs the engines are packed into the fuselage as shown in figure VIII-41. The nozzles become more buried, then, within the airframe. The Langley Research Center has been studying these problems and in one series of tests they made some parametric variations in the region of the nozzles (shown by the solid lines). Some of the results of these tests are presented in references 32 to 36. A portion are repeated herein since exhaust nozzle installation in the aft fuselage of twin-engine aircraft is currently pertinent to the development of military aircraft.

The results presented herein were obtained with the twin-engine-fuselage afterbody-nozzle dynamometer shown in figure VIII-42, described in reference 37. The maximum diameter of nozzles was 10.2 centimeters, which represented approximately a 1/12-scale model. The engine exhaust jets were simulated with compressed air, and were operated over a wide range of pressure ratio. The data presented herein were analyzed at values of pressure ratio representative of those for a turbofan engine. The circumferential line at the mid-body is a transverse cut closed with a flexible seal. The nonmetric forebody served as a support for the afterbody. All forces on the afterbody and nozzles were measured with two six-component balances arranged to yield a breakdown of the forces into nozzle thrust minus drag, and afterbody drag. These investigations were conducted in the 16-foot transonic tunnel at the Langley Research Center. This presentation deals with the effects of model configuration changes in the vicinity of the exhaust nozzles.

Jet-exit axial location. - Results of a brief study of the effect of jet-exit axial location on afterbody drag, extracted from reference 38, are presented in figure VIII-43. The afterbody drag coefficient is based on nacelle maximum cross-sectional area, and drag variation with Mach number is shown.

The afterbodies were all the same length and were shaped for minimum wave drag at Mach 1.001, using the procedures of reference 39. The lower sketch indi-

Installation effect on nozzle performance. - To this point, interest has been centered on afterbody drag. Figure VIII-45, prepared from material in references 33 and 40, is concerned with installation effect on exhaust nozzle performance. The performance coefficient used for making comparisons is $\Delta[(F - D_n)/F_i]$, the sum of nozzle gross thrust minus nozzle boattail drag, taken as a ratio to ideal gross thrust. The drag term in this expression is drag on only the nozzle boattails indicated by the shaded regions in the sketches on the right. This figure shows increments in the coefficient using the nozzle static performance as the reference. Results are presented for convergent and convergent-divergent nozzles.

The lower sketch on the right represents a model in which the nozzles were installed in an aerodynamically clean aft-fuselage, for which the afterbody contours faired smoothly into those of the nozzle. With this installation at subsonic speeds, good pressure recovery in the external flow exerted a thrust on the nozzle boattail. The vertically hatched bars show that in the clean installation, at Mach 0.8, the nozzle performance exceeded the static value by 5 or 6 percent of the ideal gross thrust, for both types of exhaust nozzles.

Another type of installation is represented in the upper sketch, in which the afterbody incorporated extended fairings outboard of the nozzles and a fuselage extension between the nozzles. The presence of these extensions tended to disturb the streamline flow over the nozzles, and to prevent good pressure recovery in the external flow. The result was a severe drag on the nozzle boattail. The shaded bars on the lower side of the plot at the left show that for Mach 0.8 the increased drag on the nozzles resulted in a large loss of performance. The difference in performance between these two installations of 10 or 12 percent of ideal gross thrust at high subsonic speed represents approximately 20 percent difference in net thrust. The installation effects are important. At Mach 1.2, both types of nozzles suffered a small loss. These comparisons show that the nozzle operating environment has a critical influence on nozzle performance at high subsonic speeds, but relatively less effect at supersonic speeds.

Afterbody boattail angle. - Another factor to be considered in the design of an exhaust nozzle installation, namely the boattail angle of the afterbody just upstream of the nozzle attachment, is treated in figure VIII-46. Again the basic configuration was the clean twin-engine afterbody with closely spaced convergent nozzles. The data present increments in the performance parameter as a function of afterbody boattail angle.

At a Mach number of 0.8, with the nozzle in the military power setting, good pressure recovery in the external flow was realized; the nozzle installed performance exceeded the static performance in all cases, and improved with increasing boattail angle.

cates a configuration with the jet exits at the downstream end of the fuselage, for which the afterbody drag is shown by the circular points. From this downstream position the jet exits were moved forward on the fuselage by one-half body width as shown in the middle sketch, and then by one full body width as shown in the top sketch. For these latter two afterbodies to have the same area progression as that in the lower sketch, the cross-sectional area of cylindrical jets is included. While the direct thrust of the nozzles is excluded from these measurements, the results do include the effects of jet interference on afterbody drag.

At low supersonic speeds, the dashed curve shows calculated drag for an axisymmetric afterbody having an area progression equal to that of the models, the values being the sum of wave drag and skin friction. The good agreement between the calculated drag and that measured on the afterbody with downstream exits improves confidence both in the theory (ref. 39) and in the experimental techniques used.

At all speeds up to Mach 1.3, the afterbody with jet exits at the extreme aft end shows the lowest values of drag. At subsonic speeds, jet interference on the extended wedge interfairings increases the afterbody drag. At the higher speeds, however, the afterbodies with wedge-shaped extensions begin to show increasing benefit of favorable jet interference.

Interfairing shape. - The effect of interfairing shape on the combined drag of the afterbody and nozzles is illustrated in figure VIII-44. The sketch on the upper right is a rear view of the nozzle installation, and the shaded area shows the region in which the interfairing shapes were modified. The sketch on the upper left shows the basic afterbody, which had closely spaced nozzles located in the downstream position. The dashed line in the sketch indicates the contour in the plane of symmetry of the elliptical interfairing shape. Other shapes were circular arc, blunt, and blunt extended. The blunt interfairing had a flat base at the nozzle-fuselage juncture. The blunt-extended interfairing terminated in a flat base approximately flush with the nozzle exits.

The results presented in the plots show relative drag as a function of Mach number, where the highest value of drag is given a value of unity. At subsonic speeds the afterbody with the elliptical interfairing showed the least drag for operation either at military power or with maximum afterburner. There is little choice between the elliptical and circular-arc shapes. The use of a flat base was consistently detrimental at subsonic speeds. The data points at the upper right show all the interfairing shapes to have approximately the same drag at low supersonic speeds, though the flat-base interfairings did show slightly lower values in this speed range.

The plot on the right shows that at low supersonic speed, Mach 1.2, pressure recovery in the external flow is relatively poor, and that the nozzle performance is not significantly better than for static operation. In this speed range, afterbody boattail angle has little effect on the installed nozzle performance.

Nozzle lateral spacing. - The effect of nozzle lateral spacing on nozzle performance and on afterbody drag is illustrated in figure VIII-47. The sketch on the upper left represents the basic twin-engine afterbody with convergent nozzles. In the middle sketch, which is a rear view of the nozzle installation, the spacing ratio is defined as the ratio of the distance between the nozzle centerlines s to the nozzle diameter d_n at the nozzle-fuselage juncture.

The left side of figure VIII-47 shows the effect of lateral spacing on exhaust nozzle performance. The small rate of increase in performance with increased spacing at both subsonic and low supersonic speeds indicates that the mutual interference drag of the nozzles decreases with increasing distance between the nozzles. The effect of increased spacing on nozzle performance, then, is beneficial but small.

The right side of this figure shows the effect of lateral spacing on the drag of the complete afterbody and nozzles. Values of relative drag are shown as a function of the spacing ratio. The afterbodies having spacing ratios of 1.59 and 2.31 had lower values of fineness ratio than the basic afterbody, which had a spacing ratio of 1.32. At Mach 1.2 the basic data indicate a much more rapid increase in afterbody drag with increasing lateral spacing than is shown here, because the drag was influenced by afterbody fineness ratio as well as by lateral spacing. The values of relative drag presented for Mach 1.2 were obtained by applying a correction for fineness ratio to the wave drag of the two afterbodies having the larger values of spacing ratio. The values presented on the plot for Mach 1.2 presumably show only the effect of lateral spacing on afterbody relative drag. The fineness ratio correction is based on information contained in reference 41, and is outlined in reference 33.

The drag tends to increase slightly as space between the nozzles increases at both subsonic and low supersonic speeds. The net result, then, is that lateral spacing of the exhaust nozzles appears not to be a critical factor in the aerodynamic design of an afterbody-nozzle installation.

Tail interference. - The effect on exhaust nozzle performance of adding tail surfaces to the afterbody in the vicinity of the nozzle installation is shown in figure VIII-48. The basic model was the aerodynamically smooth twin-engine afterbody with convergent-divergent nozzles. The plot presents the variation with Mach number of the change in nozzle performance which occurred when horizontal and vertical tail surfaces were added to the basic configuration. The direct drag of the tail surfaces does not enter these measurements; the change in exhaust nozzle performance reflects only the change in nozzle drag caused by proximity of the tail surfaces.

As shown in the lower curve in figure VIII-48, with the engines operating at military power adding the tail surfaces caused a loss in nozzle performance at subsonic speeds, which at Mach 0.95 amounted to 4 percent of the ideal gross thrust. The upper curve shows results obtained with the nozzle in the maximum afterburner setting. At this condition, adding the tail surfaces to the afterbody had a small favorable effect on nozzle performance at all speeds below Mach 1.3.

Summary

The installation problems encountered in these tests are summarized as follows: For underwing engine nacelles with high-angle boattails, increasing Reynolds number tends to decrease the extent of flow separation and, therefore, decrease drag. For the F-106 nacelle installation a more forward location of the boattail tends to reduce drag. And a pure circular-arc boattail had the least drag. For engines mounted in the fuselage, a disturbance to streamline flow near the nozzle boattail is detrimental. A shallow boattail angle is required for supersonic speed but not for subsonic. The best performance is obtained with the nozzles downstream of the terminus of the airframe, and finally the lateral spacing does not appear to be critical.

REFERENCES

1. Darchuk, George V.; and Balombin, Joseph R.: Noise Evaluation of Four Exhaust Nozzles for Afterburning Turbojet Engine. NASA TM X-2014, 1970.

2. Chow, W. L.; and Addy, A. L.: Interaction Between Primary and Secondary Streams of Supersonic Ejector Systems and Their Performance Characteristics. AIAA J., vol. 2, no. 4, Apr. 1964, pp. 686-695.

3. Crabs, Clifford C.; Boyer, Earle O.; and Mikkelson, Daniel C.: Engineering Aspects and First Flight Results of the NASA F-106 Transonic Propulsion Research Aircraft. NASA TM X-52559, 1969.

4. Wilcox, Fred A.; Samanich, Nick E.; and Blaha, Bernard J.: Flight and Wind Tunnel Investigation of Installation Effects on Supersonic Cruise Exhaust Nozzles at Transonic Speeds. Paper 69-427, AIAA, June 1969.

5. Crabs, Clifford C.; Mikkelson, Daniel C.; and Boyer, Earle O.: An Inflight Investigation of Airframe Effects on Propulsion System Performance at Transonic Speeds. Soc. Exper. Test Pilots, Tech. Rev., vol. 9, no. 4, 1969, pp. 51-66.

6. Blaha, Bernard J.; and Mikkelsen, Daniel C.: Wind Tunnel Investigation of Airframe Installation Effects on Underwing Engine Nacelles at Mach Numbers from 0.56 to 1.43. NASA TM X-1683, 1968.

7. Blaha, Bernard J.; Mikkelsen, Daniel C.; and Harrington, Douglas E.: Wind Tunnel Investigation of Installation Effects on Underwing Supersonic Cruise Exhaust Nozzles at Transonic Speeds. NASA TM X-52604, 1969.

8. Blaha, Bernard J.: Effect of Underwing Engine Nacelle Shape and Location on Boattail Drag and Wing Pressures at Mach Numbers from 0.56 to 1.46. NASA TM X-1979, 1970.

9. Mikkelsen, Daniel C.; and Blaha, Bernard J.: Flight and Wind Tunnel Investigation of Installation Effects on Underwing Supersonic Cruise Exhaust Nozzles at Transonic Speeds. Presented at AGARD 1970 Aerodynamic Interference Specialists Meeting, Silver Spring, Md., Sept. 28-30, 1970.

10. Blaha, Bernard J.: Wind Tunnel Investigation of the Flow Field Under a 60 Degree Swept Wing at Mach Numbers From 0.6 to 2.6. NASA TM X-52585, 1969.

11. Steffen, Fred W.; and Jones, John R.: Performance of a Wind Tunnel Model of an Aerodynamically Positioned Variable Flap Ejector at Mach Numbers From 0 to 2.0. NASA TM X-1639, 1968.

12. Shrewsbury, George D.: Effect of Boattail Juncture Shape on Pressure Drag Coefficients of Isolated Afterbodies. NASA TM X-1517, 1968.

13. Harrington, Douglas E.: Jet Effects on Boattail Pressure Drag of Isolated Ejector Nozzles at Mach Numbers From 0.60 to 1.47. NASA TM X-1785, 1969.

14. Blaha, Bernard J.; and Bresnahan, Donald L.: Wind Tunnel Installation Effects on Isolated Afterbodies at Mach Numbers From 0.56 to 1.5. NASA TM X-52581, 1969.

15. Mikkelsen, Daniel C.; and Head, Verlon L.: Flight Investigation of Airframe Installation Effects on a Variable Flap Ejector Nozzle of an Underwing Engine Nacelle at Mach Numbers From 0.5 to 1.3. NASA TM X-2010, 1970.

16. Johns, Albert L.; and Steffen, Fred W.: Performance of an Auxiliary Inlet Ejector Nozzle With Fixed Doors and Single-Hinge Trailing-Edge Flap. NASA TM X-2027, 1970.

17. Johns, Albert L.; and Steffen, Fred W.: Performance of an Auxiliary Inlet Ejector Nozzle With Fixed Inlet Doors and Triple-Hinge Trailing-Edge Flap. NASA TM X-2034, 1970.

18. Bresnahan, Donald L.: Performance of an Aerodynamically Positioned Auxiliary Inlet Ejector Nozzle at Mach Numbers From 0 to 2.0. NASA TM X-2023, 1970.

19. Johns, Albert L.: Performance of Auxiliary Inlet Ejector Nozzle With Floating Inlet Doors and Floating Single-Hinge Trailing-Edge Flaps. NASA TM X-2169, 1970.

20. Samanich, Nick E.; and Burley, Richard R.: Flight Performance of Auxiliary Inlet Ejector and Plug Nozzle at Transonic Speeds. Paper 70-701, AIAA, June 1970.

21. Wasko, Robert A.: Stability Characteristics of a Sting-Supported Collapsible Plug Nozzle at Mach Numbers From 0 to 2.0. NASA TM X-1704, 1968.

22. Blaha, Bernard J.: Effect of Nozzle Total Pressure and Base Bleed on the Stability Characteristics of a Sting-Supported Truncated Plug Nozzle. NASA TM X-1775, 1969.

23. Bresnahan, Donald L.; and Johns, Albert L.: Cold Flow Investigation of a Low Angle Turbojet Plug Nozzle With Fixed Throat and Translating Shroud at Mach Numbers From 0 to 2.0. NASA TM X-1619, 1968.

24. Bresnahan, Donald L.: Experimental Investigation of a 10° Conical Turbojet Plug Nozzle With Iris Primary and Translating Shroud at Mach Numbers From 0 to 2.0. NASA TM X-1709, 1968.

25. Bresnahan, Donald L.: Experimental Investigation of a 10° Conical Turbojet Plug Nozzle With Translating Primary and Secondary Shrouds at Mach Numbers From 0 to 2.0. NASA TM X-1777, 1969.

26. Johns, Albert L.: Quiescent-Air Performance of a Truncated Turbojet Plug Nozzle With Shroud and Plug Base Flows From a Common Source. NASA TM X-1807, 1969.

27. Steffen, Fred W.: Performance of a 10° Conical Plug Nozzle With a Stowed Thrust Reverser at Mach Numbers From 0 to 2.0. NASA TM X-2116, 1970.

28. Chenoweth, Francis C.; and Lieberman, Arthur: Prediction of Heat-Transfer Characteristics for Ejector Exhaust Nozzles. Analytic Methods in Aircraft Aerodynamics. NASA SP-228, 1970, pp. 623-638.

29. Clark, John S.; Graber, Edwin J.; and Straight, David M.: Experimental Heat Transfer and Flow Results From an Air-Cooled Plug Nozzle System. NASA TM X-52897, 1970.

30. Wasko, Robert A.; and Harrington, Douglas E.: Performance of a Collapsible Plug Nozzle Having Either Two-Position Cylindrical or Variable Angle Floating Shrouds at Mach Numbers From 0 to 2.0. NASA TM X-1657, 1968.

31. Harrington, Douglas E.: Performance of Convergent and Plug Nozzles at Mach Numbers From 0 to 1.97. NASA TM X-2112, 1970.

32. Runckel, Jack F.: Aerodynamic Interference Between Exhaust System and Airframe. Presented at the AGARD Specialists Meeting on Aerodynamic Interference, Silver Spring, Md., Sept. 28-30, 1970.

33. Corson, Blake W., Jr.; and Runckel, Jack F.: Exploratory Studies of Aircraft Afterbody and Exhaust-Nozzle Interaction. NASA TM X-1925, 1969.

34. Greathouse, William K.: Blending Propulsion with Airframe. Space/Aeronaut., vol. 50, no. 6, Nov. 1968, pp. 59-68.

35. Migdal, D.; Miller, E. H.; and Schnell, W. C.: An Experimental Evaluation of Exhaust Nozzle/Airframe Interference. Paper 69-430, AIAA, June 1969.

36. Throndson, L. W.: Close-Spaced Nozzles Twin Jet Configuration. Paper 70-934, AIAA, July 1970.

37. Maiden, Donald L.; and Runckel, Jack F.: Effect of Nozzle Lateral Spacing on Afterbody Drag and Performance of Twin-Jet Afterbody Models with Convergent Nozzles at Mach Numbers up to 2.2. NASA TM X-2099, 1970.

38. Berrier, Bobby Lee; and Wood, Frederick H., Jr.: Effect of Jet Velocity and Axial Location of Nozzle Exit on the Performance of a Twin-Jet Afterbody Model at Mach Numbers up to 2.2. NASA TN D-5393, 1969.

39. Harris, Roy V., Jr.: An Analysis and Correlation of Aircraft Wave Drag. NASA TM X-947, 1964.

40. Mercer, Charles E.; and Berrier, Bobby L.: Effect of Afterbody Shape, Nozzle Type, and Engine Lateral Spacing on the Installed Performance of a Twin-Jet Afterbody Model. NASA TM X-1853, 1969.

41. Morris, Deane M.: A Summary of the Supersonic Pressure Drag of Bodies of Revolution. J. Aerospace Sci., vol. 28, no. 7, July 1961, pp. 563-572.

MISSION SENSITIVITY FOR EXHAUST NOZZLES

SUPERSONIC CRUISE AIRCRAFT; TAKEOFF GROSS WEIGHT = 750 000 LB;
PAYLOAD = 49 000 LB

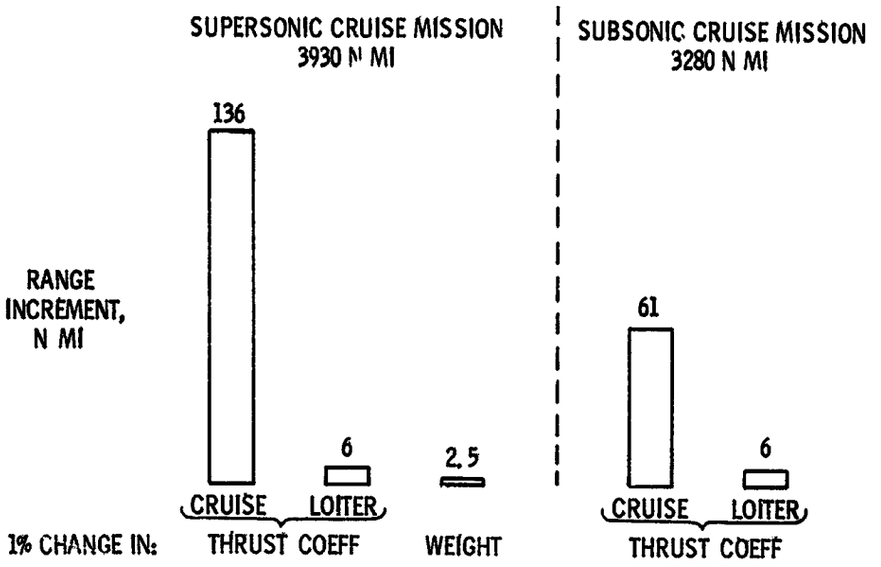

CS-56952

Figure VIII-1

EXHAUST NOZZLE CONCEPTS

SUPERSONIC CRUISE AIRCRAFT

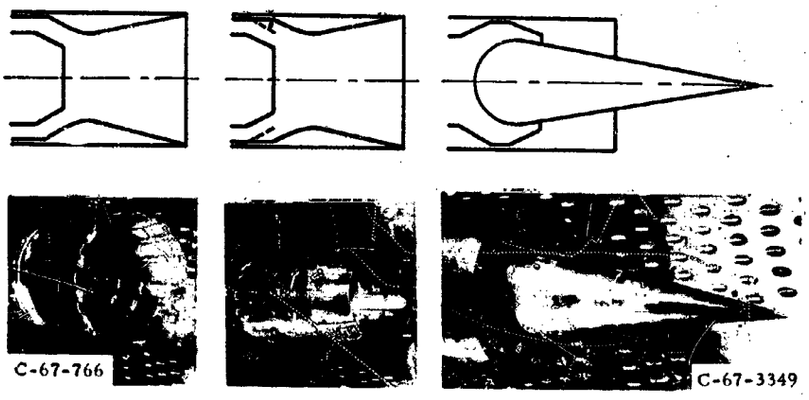

VARIABLE FLAP EJECTOR

AUXILIARY INLET EJECTOR

PLUG

CS-56942

Figure VIII-2

DIVERGENT EJECTOR FLOW FIELD

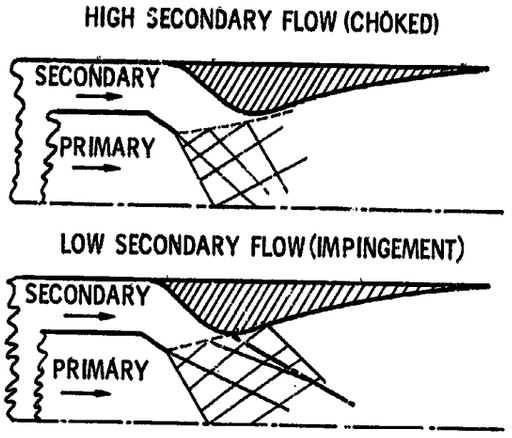

CS-56937

Figure VIII-3

COMPARISON OF EXPERIMENTAL AND THEORETICAL EJECTOR CHARACTERISTICS

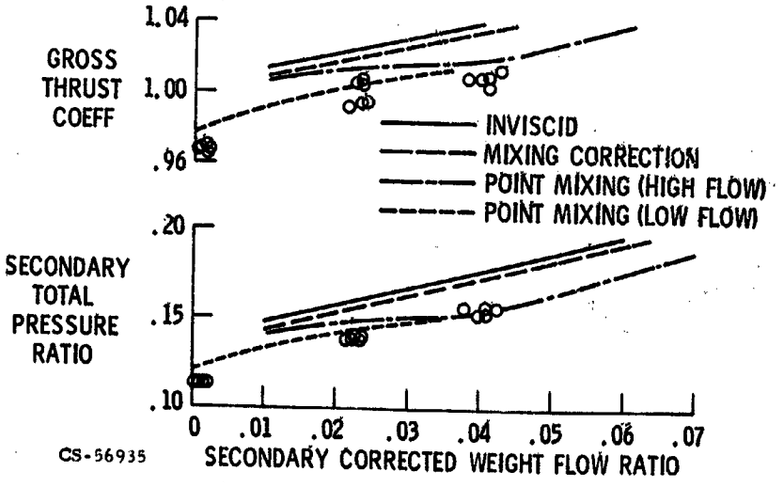

CS-56935

Figure VIII-4

SHROUD CONTOUR SENSITIVITY AUXILIARY INLET EJECTOR

2% CORRECTED SECONDARY FLOW RATIO

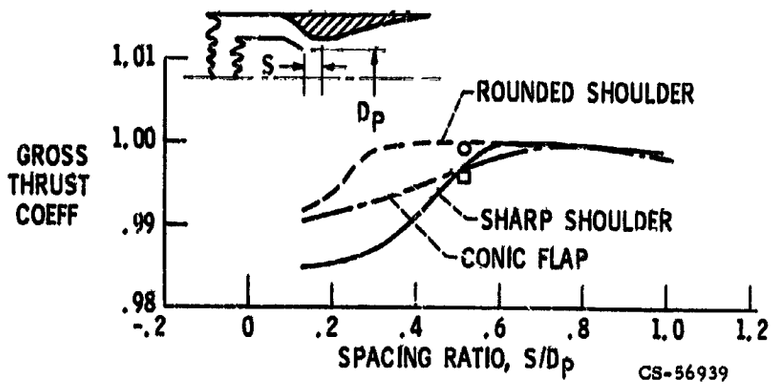

Figure VIII-5

WEIGHT FLOW SENSITIVITY AUXILIARY INLET EJECTOR

SHARP SHOULDER, CONTOURED FLAP

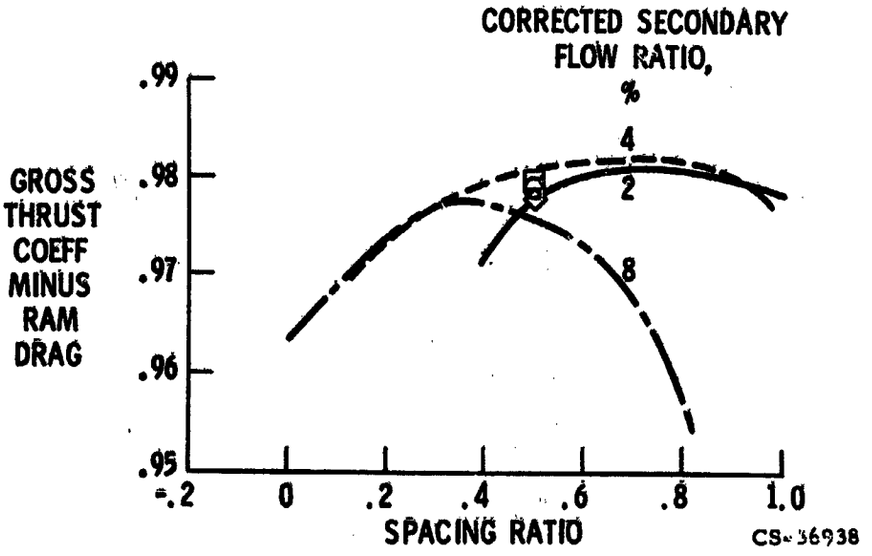

Figure VIII-6

NOZZLE PERFORMANCE AT SUPERSONIC CRUISE

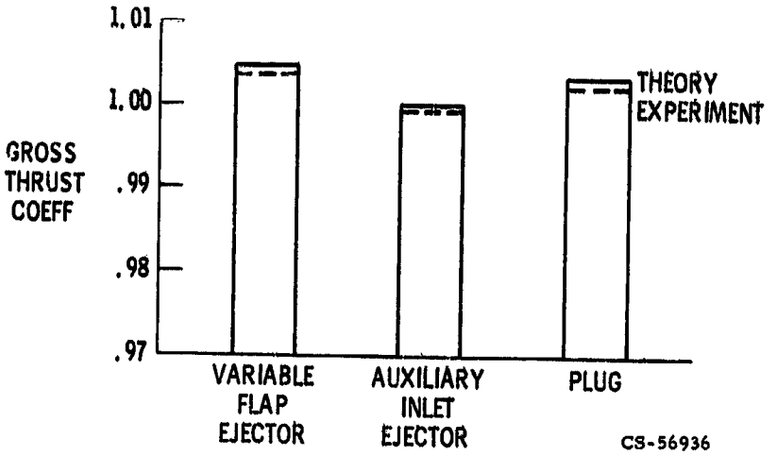

Figure VIII-7

EXHAUST NOZZLE TEST PROGRAMS

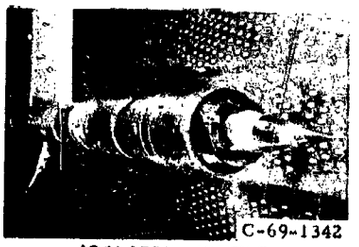

ISOLATED NOZZLE

1/20 SCALE F-106

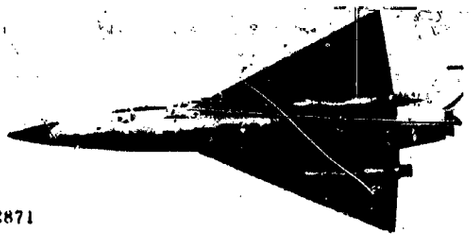

C-69-2871

F-106 FLIGHT

CS-57005

Figure VIII-8

NACELLE-ENGINE INSTALLATION

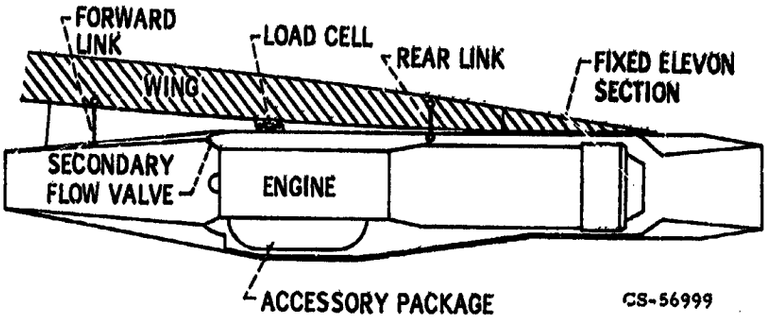

Figure VIII-9

INSTALLATION EFFECT ON WING PRESSURES

$M_0 = 0.90$

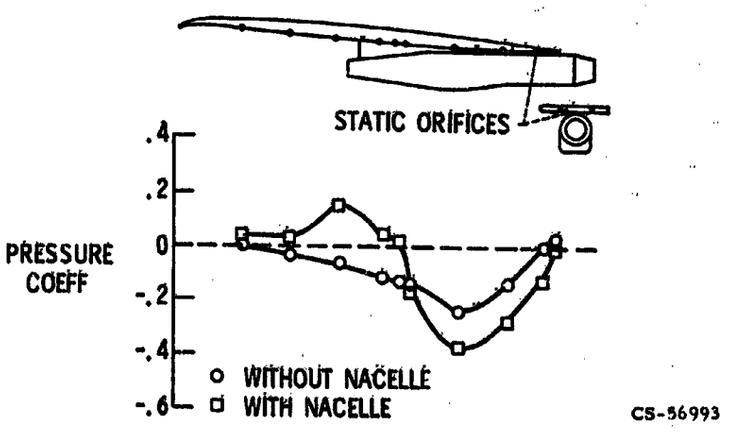

Figure VIII-10

INSTALLATION EFFECT ON NACELLE PRESSURES

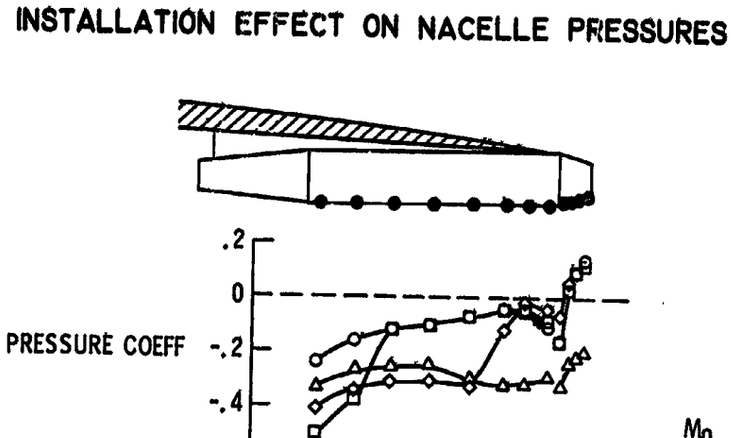

Figure VIII-11

VARIABLE FLAP EJECTOR

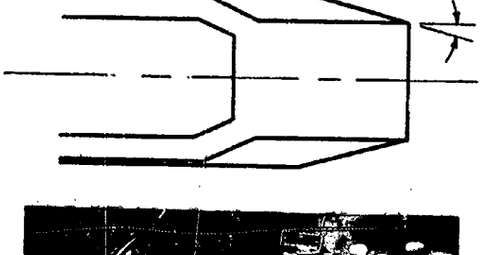

C-69-1585
CS-56943

Figure VIII-12

BOATTAIL PRESSURE DISTRIBUTION

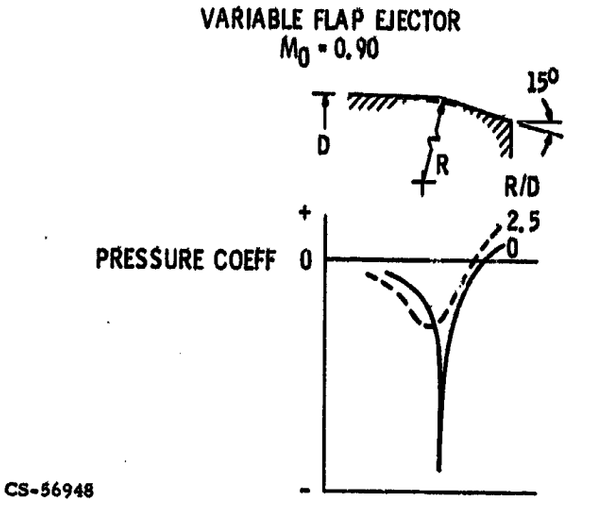

Figure VIII-13

ISOLATED BOATTAIL DRAG

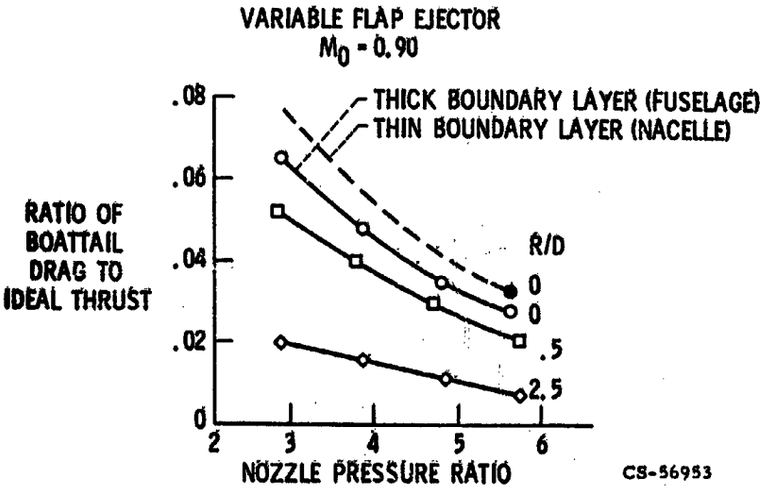

Figure VIII-14

VARIABLE FLAP EJECTOR NOZZLE INSTALLATION

R/D = 2.5

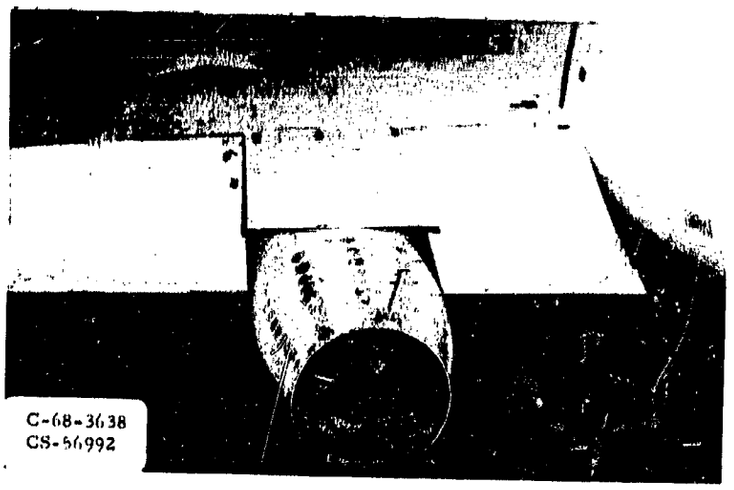

Figure VIII-15

INSTALLATION EFFECT ON BOATTAIL DRAG

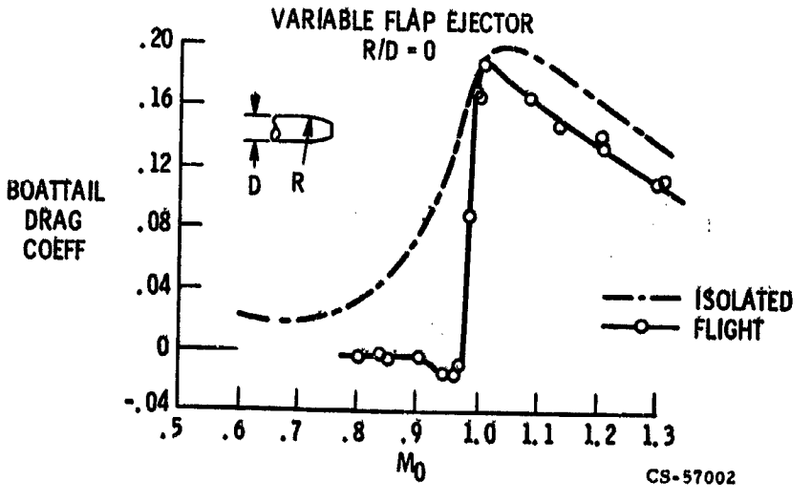

Figure VIII-16

EFFECT OF ROUNDED JUNCTURE ON BOATTAIL DRAG

FLIGHT DATA

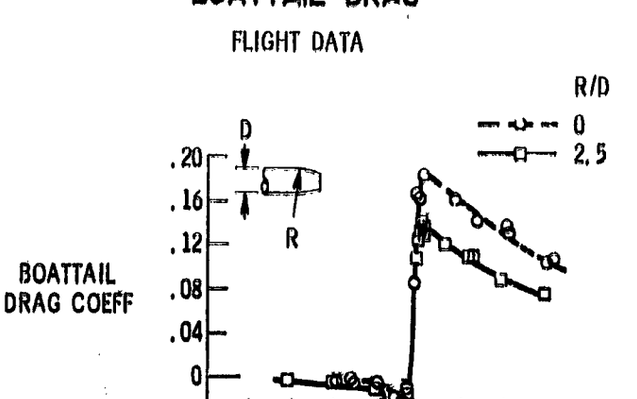

Figure VIII-17

AUXILIARY INLET EJECTOR

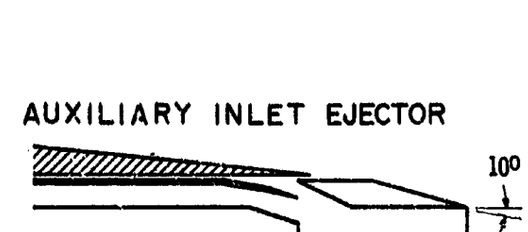

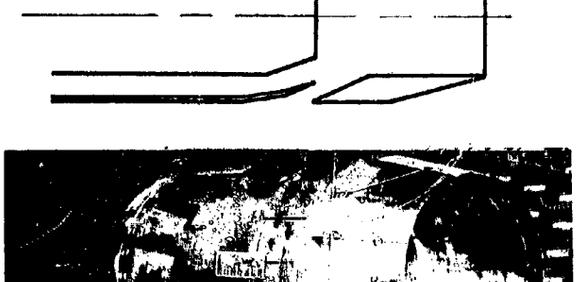

C-69-1581
CS-56940

Figure VIII-18

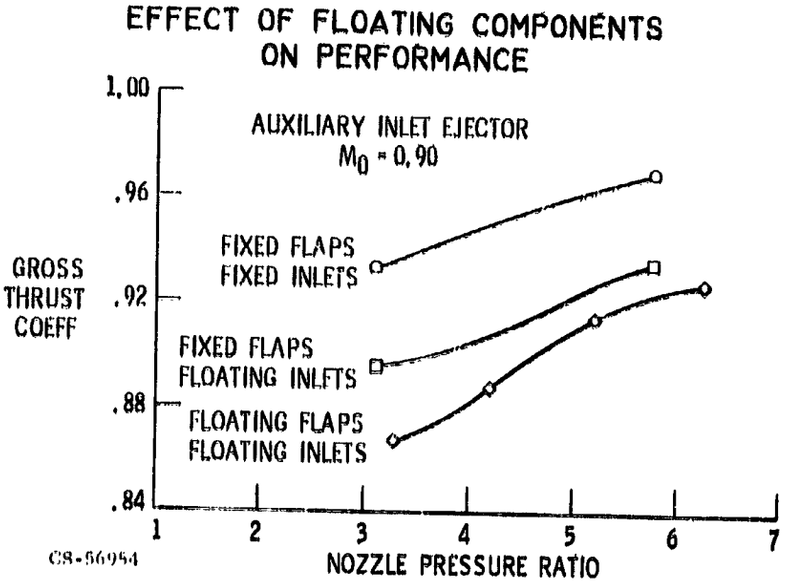

Figure VIII-19

AUXILIARY INLET EJECTOR NOZZLE AND ELEVON TROUGH

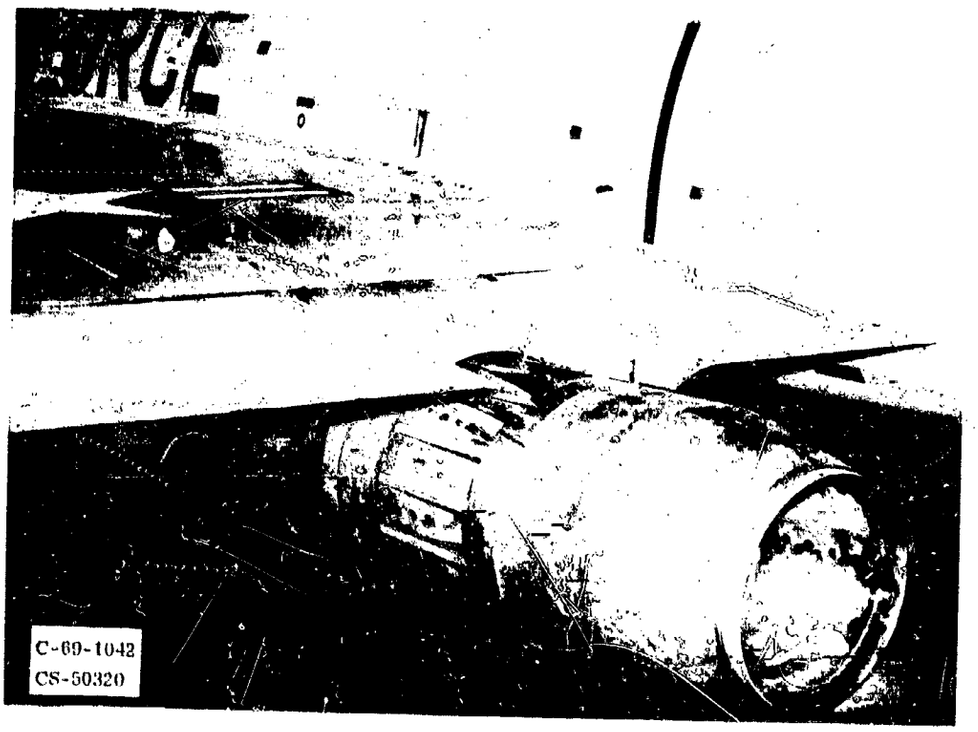

Figure VIII-20

INSTALLATION EFFECT ON AUXILIARY INLET EJECTOR PERFORMANCE

$M_0 = 0.90$

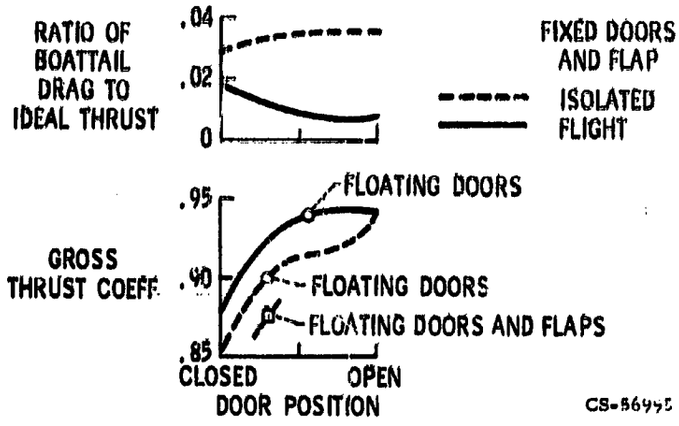

Figure VIII-21

POSITION OF FLOATING DOORS

$M_0 = 0.9$

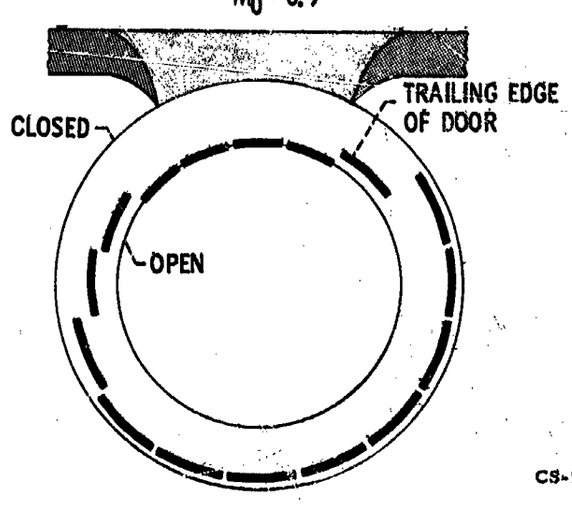

Figure VIII-22

PLUG NOZZLE

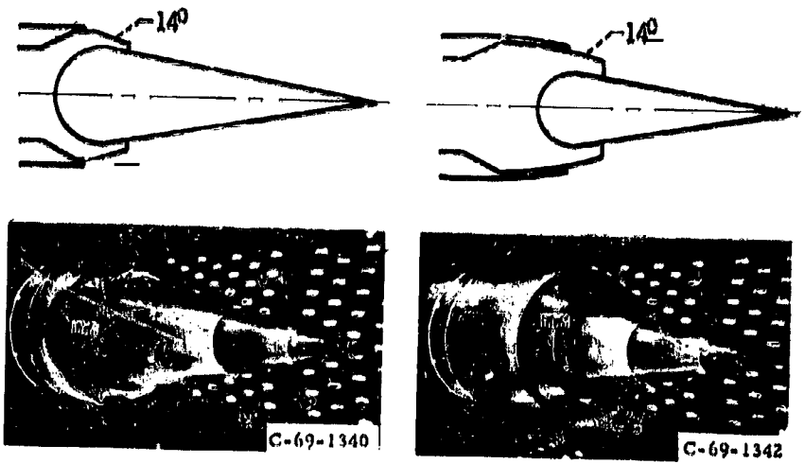

CONICAL PRIMARY ROUNDED PRIMARY

CS-56944

Figure VIII-23

EFFECT OF EXTERNAL FLOW ON PLUG NOZZLE PERFORMANCE

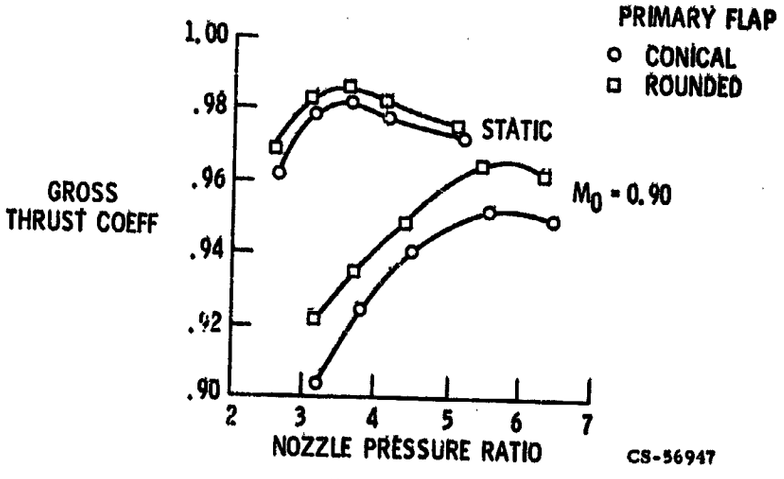

CS-56947

Figure VIII-24

PLUG NOZZLE INSTALLATION

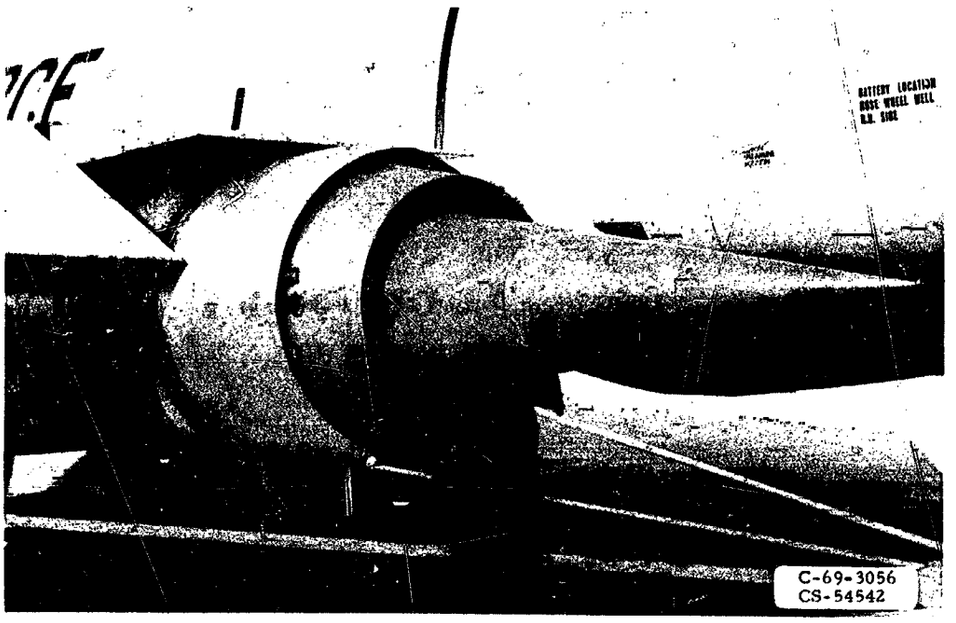

Figure VIII-25

INSTALLATION EFFECT ON PLUG NOZZLE PERFORMANCE

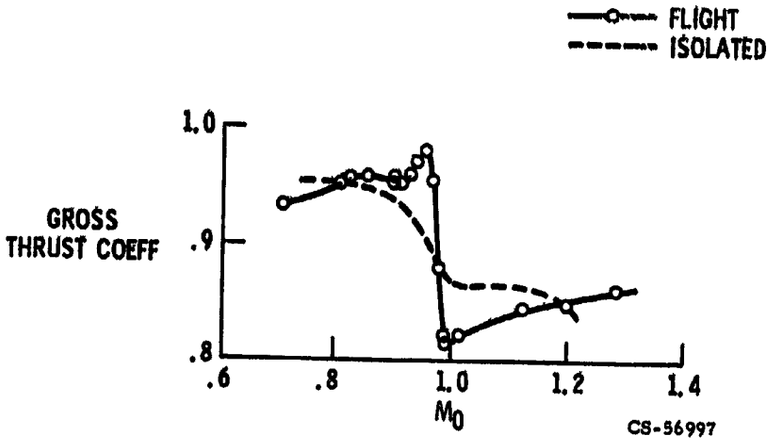

Figure VIII-26

COMPARISON OF NOZZLE PERFORMANCE

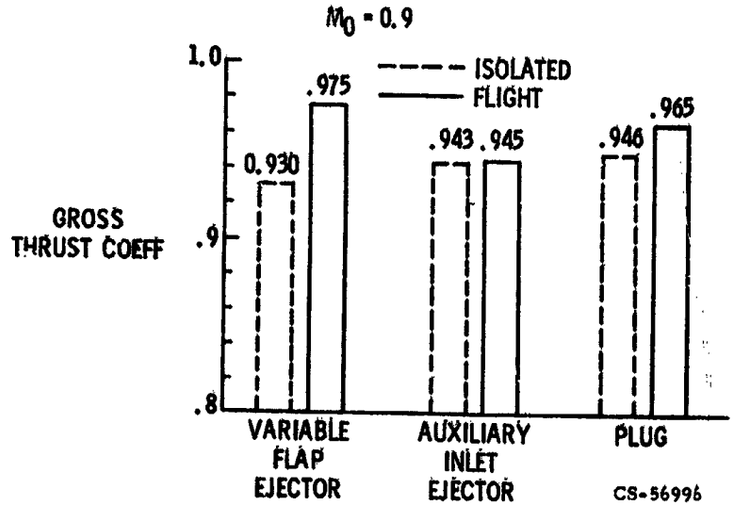

Figure VIII-27

EJECTOR SHROUD COOLING

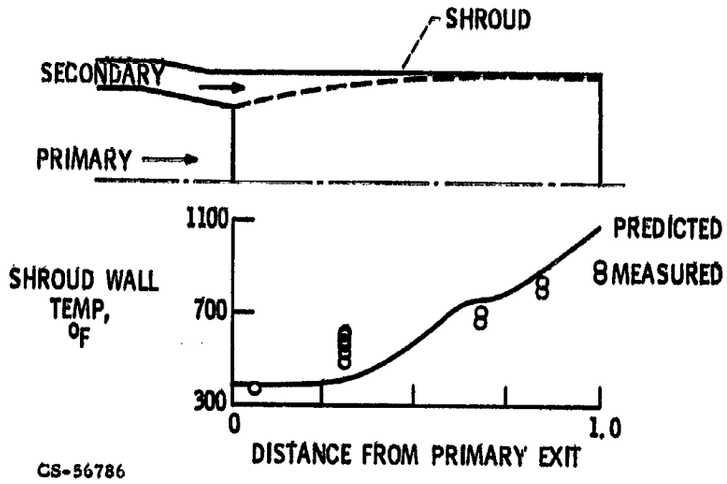

Figure VIII-28

HEAT DISTRIBUTION

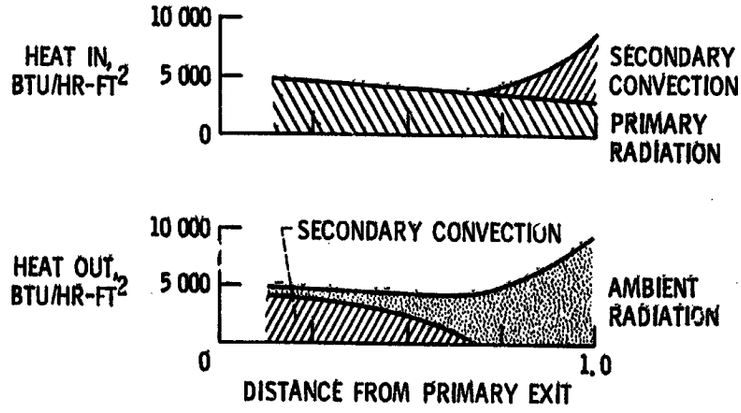

Figure VIII-29

CS-56787

FILM-COOLED PLUG NOZZLE

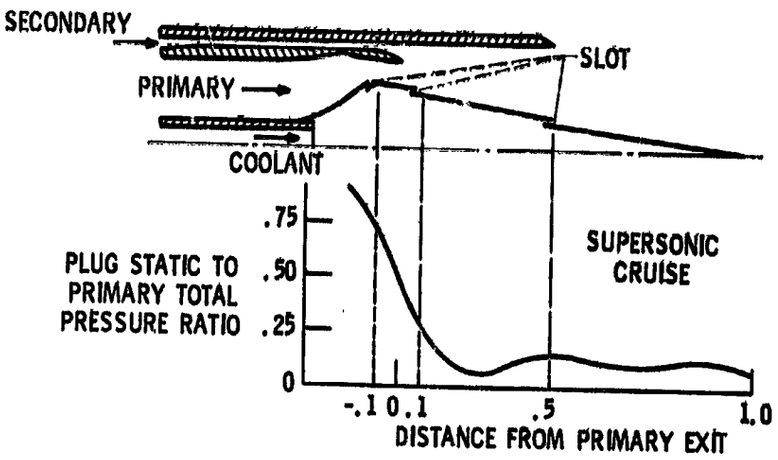

Figure VIII-30 CS-56788

PLUG SURFACE FILM-COOLING CORRELATION

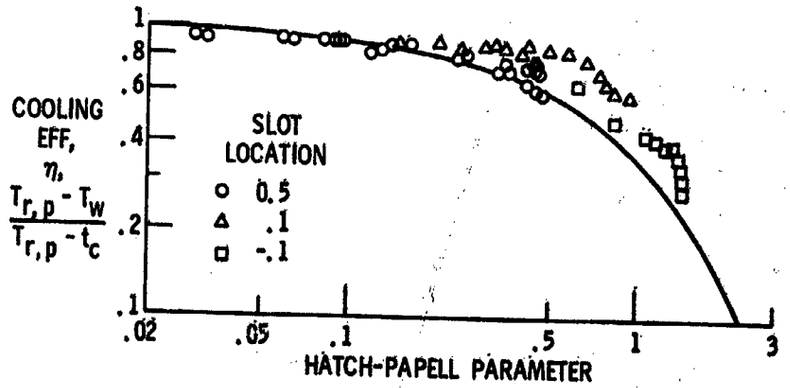

Figure VIII-31 CS-56784

CONVECTIVELY COOLED PLUG NOZZLE

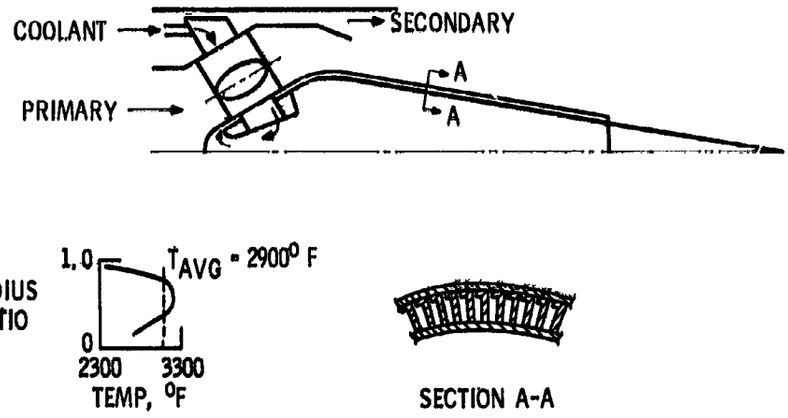

Figure VIII-32

CS-56785

CONVECTIVELY COOLED PLUG NOZZLE AT AFTERBURNING TEMPERATURE OF 2900° F

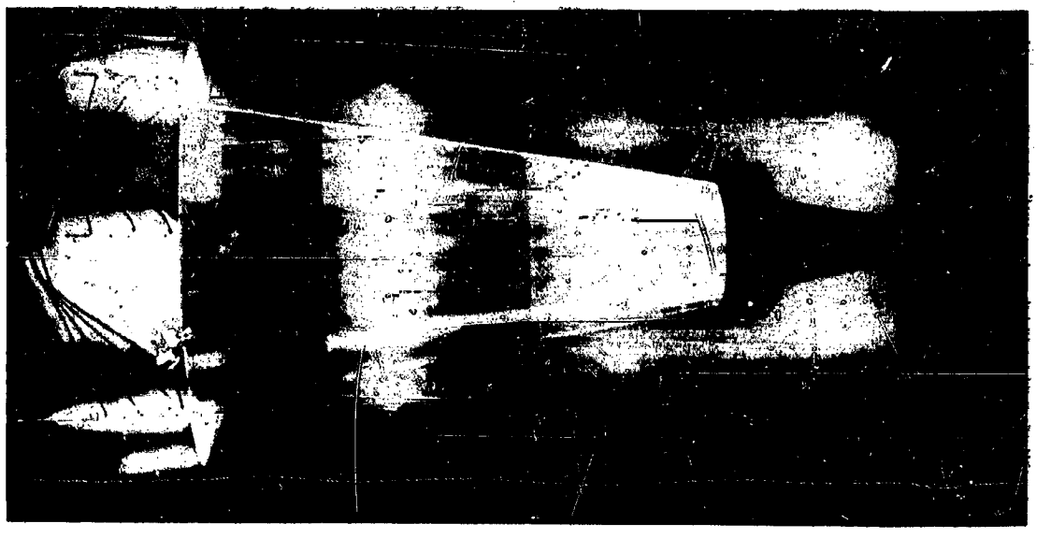

Figure VIII-33

EFFECT OF NOZZLE TYPE ON RANGE

SUPERSONIC CRUISE AIRCRAFT; TAKEOFF GROSS WEIGHT = 750 000 LB; PAYLOAD = 49 000 LB

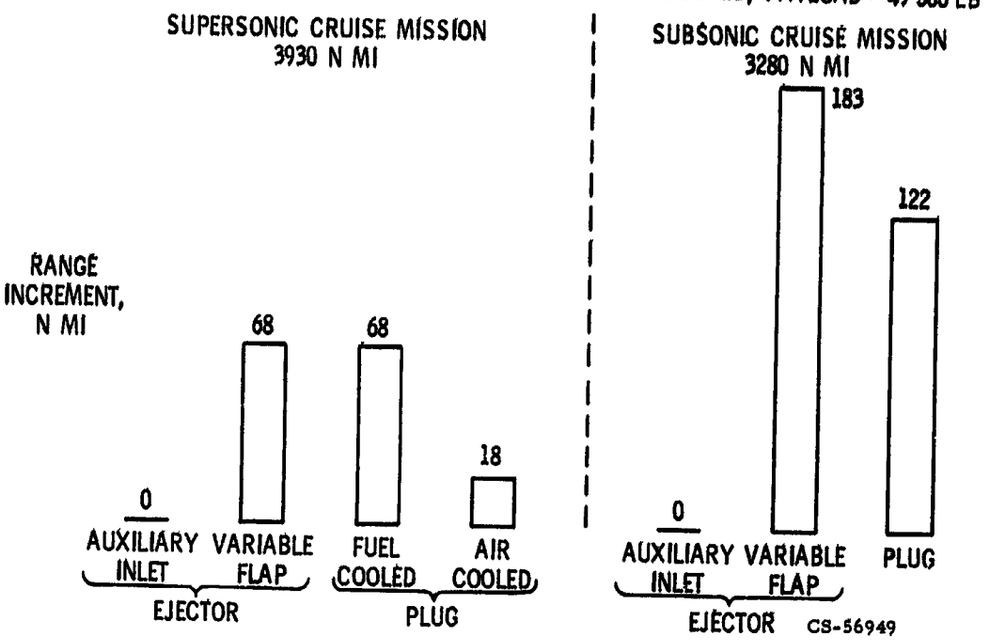

Figure VIII-34

EXHAUST NOZZLE CONCEPTS FOR SUPERSONIC DASH AIRCRAFT

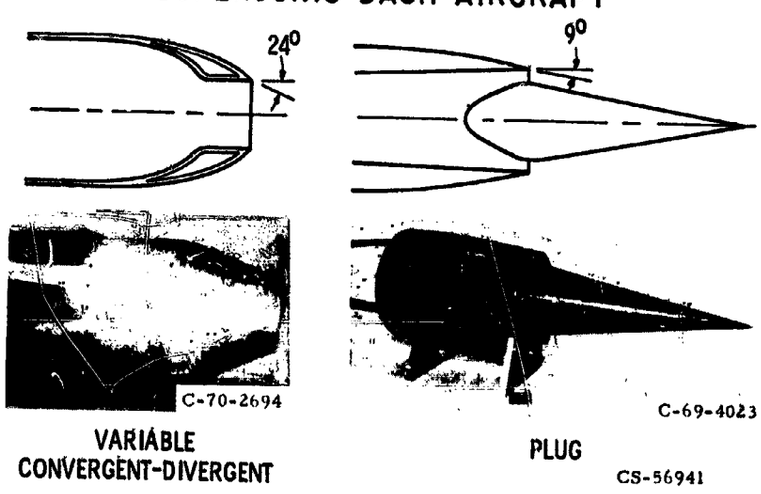

Figure VIII-35

EFFECT OF EXTERNAL FLOW ON SUPERSONIC DASH NOZZLE PERFORMANCE

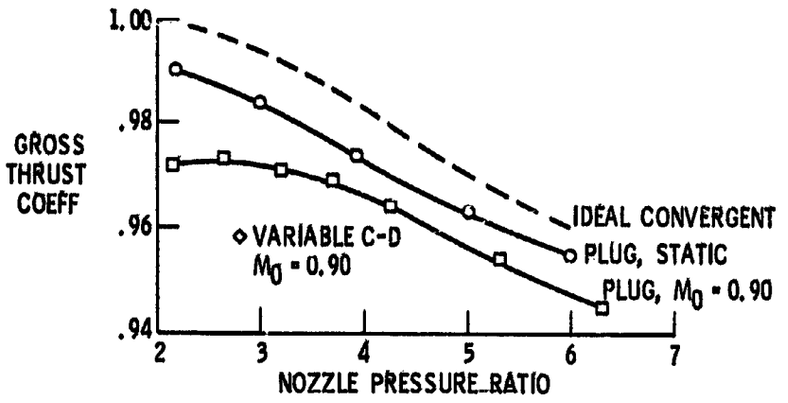

Figure VIII-36

BOATTAIL PRESSURE DISTRIBUTION

VARIABLE CONVERGENT-DIVERGENT
M_0 = 0.90

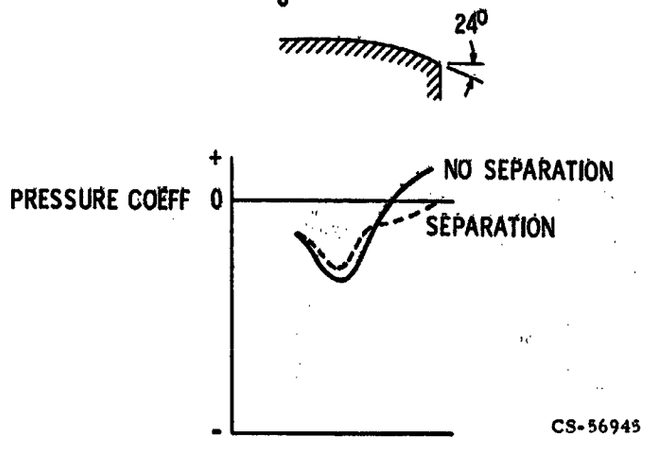

Figure VIII-37

VARIABLE CONVERGENT-DIVERGENT NOZZLES

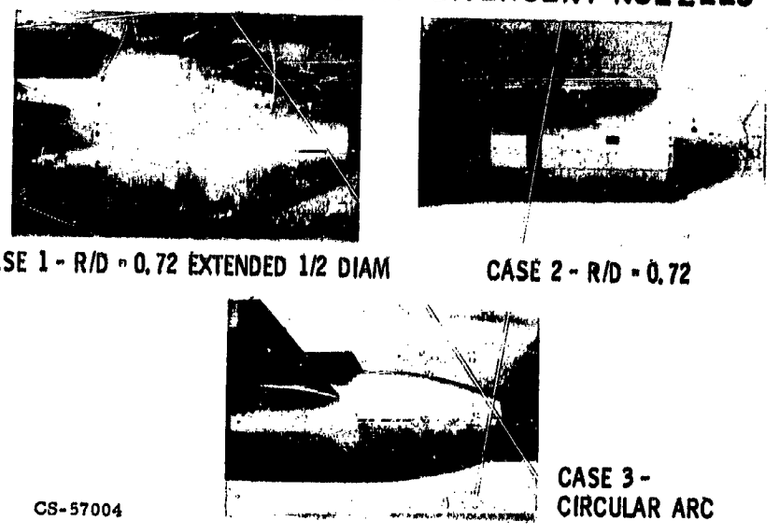

Figure VIII-38

REYNOLDS NUMBER EFFECT ON BOATTAIL DRAG

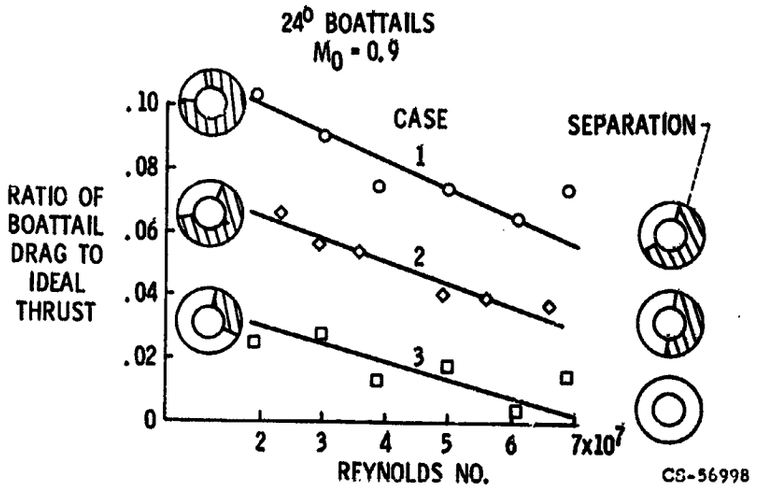

Figure VIII-39

FRAME FROM MOTION PICTURE OF
TUFTS FOR CASE 2 NOZZLE

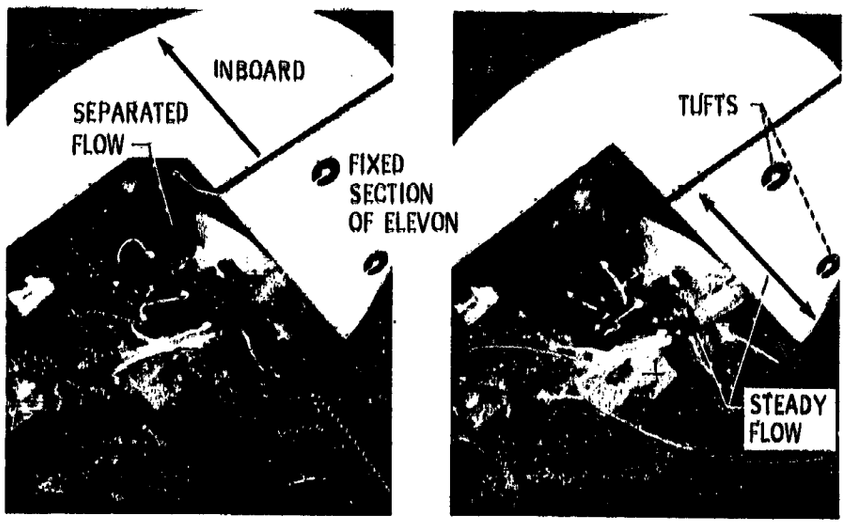

Figure VIII-40

SUPERSONIC DASH AIRCRAFT

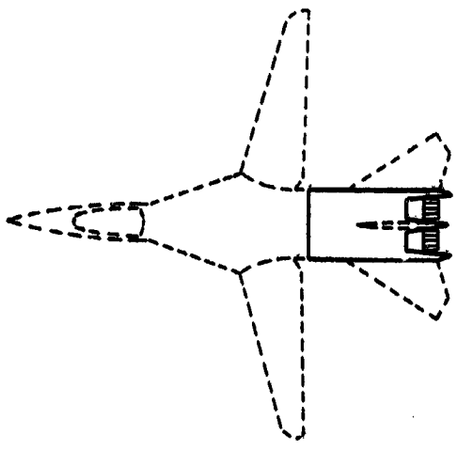

CS-56950

Figure VIII-41

TWIN-ENGINE AFTERBODY-NOZZLE DYNAMOMETER

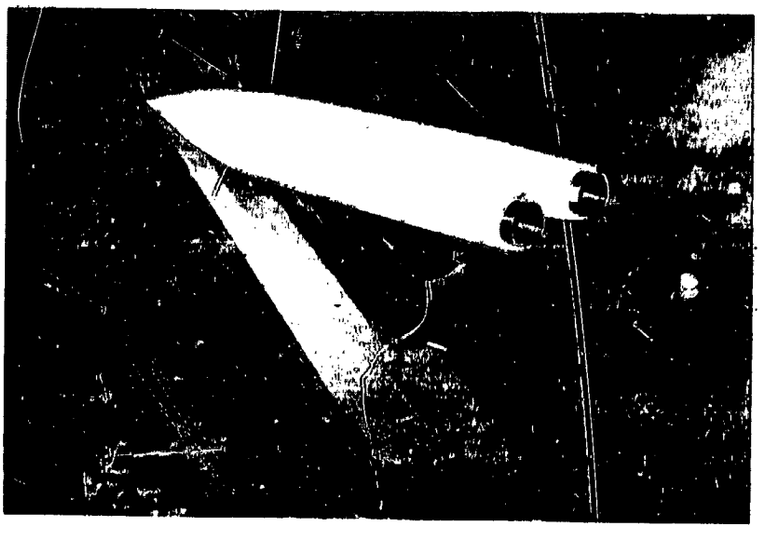

Figure VIII-42

JET-EXIT AXIAL LOCATION — EFFECT ON AFTERBODY DRAG

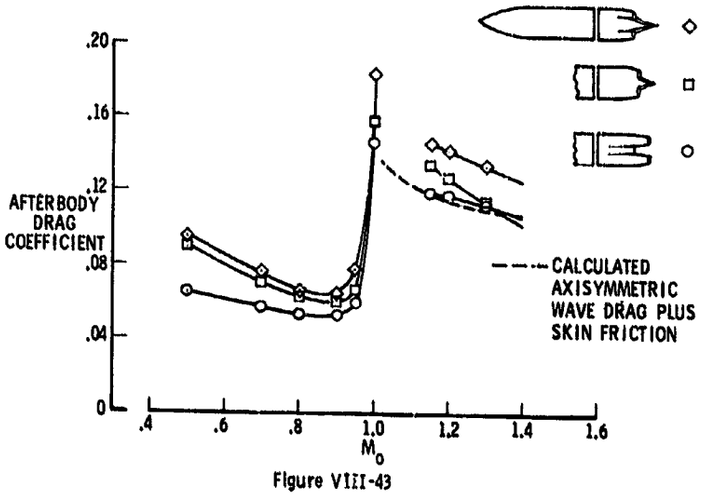

Figure VIII-43

INTERFAIRING SHAPE EFFECT ON AFTERBODY PLUS NOZZLE DRAG

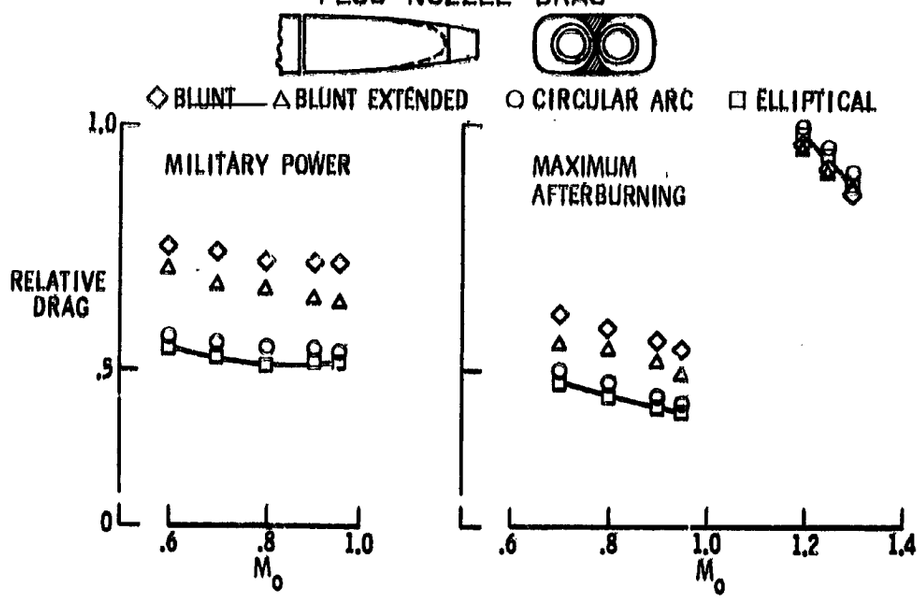

Figure VIII-44

INSTALLATION EFFECT ON EXHAUST NOZZLE PERFORMANCE

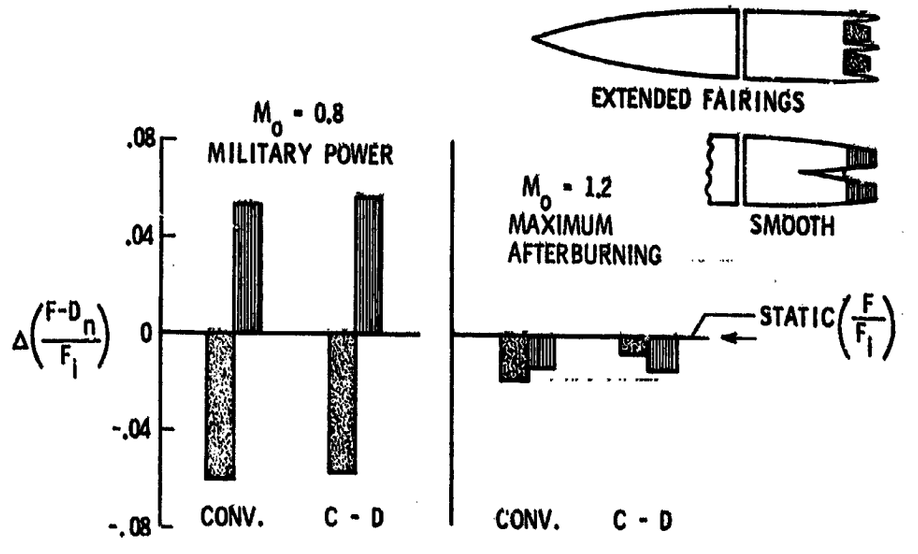

Figure VIII-45

EFFECT OF AFTERBODY APPROACH ANGLE ON NOZZLE PERFORMANCE

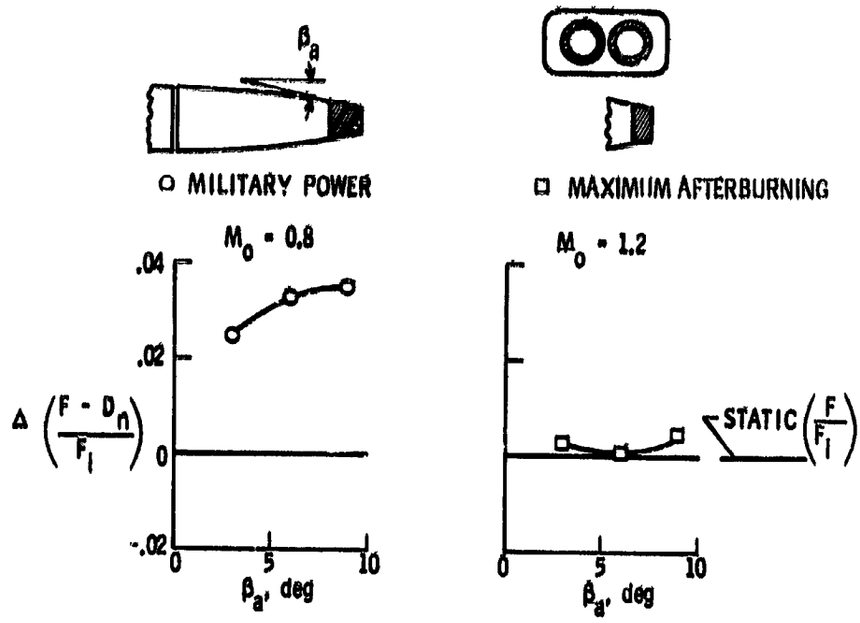

Figure VIII-46

EFFECT OF NOZZLE LATERAL SPACING

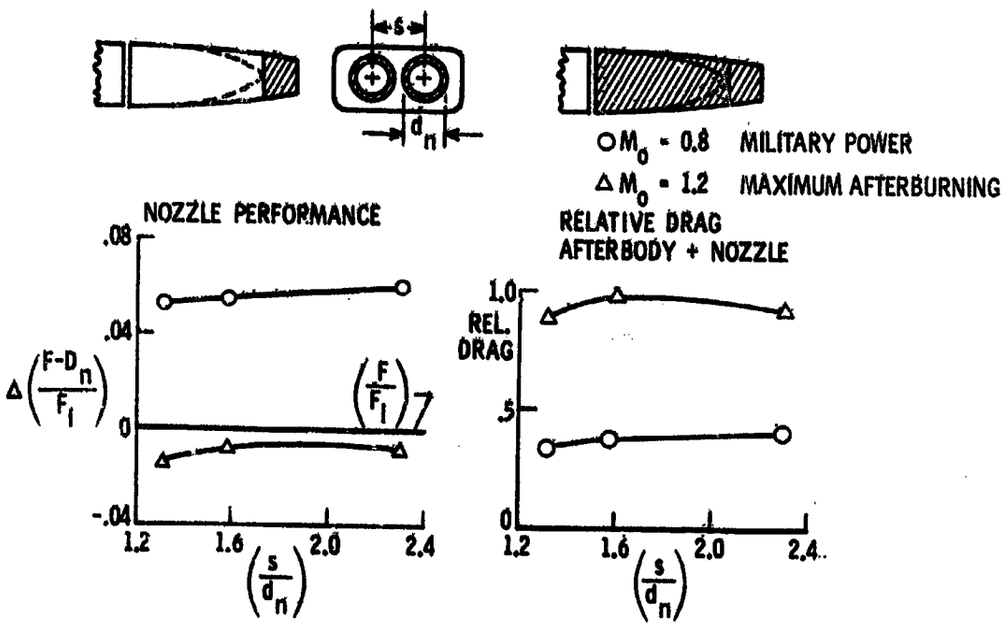

Figure VIII-47

TAIL INTERFERENCE ON NOZZLE PERFORMANCE

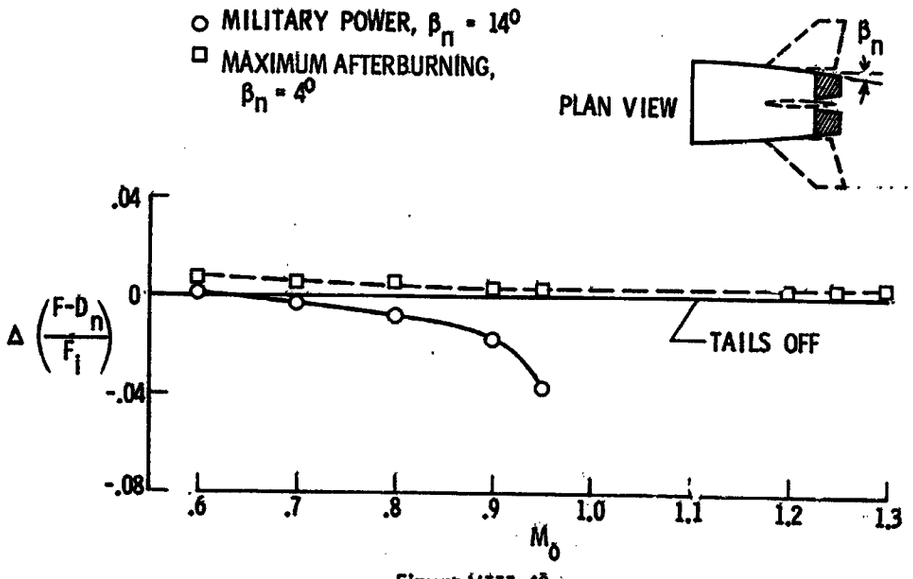

Figure VIII-48

IX. SUPERSONIC CRUISE INLETS

David N. Bowditch, Robert E. Coltrin, Bobby W. Sanders, Norman E. Sorensen,* and Joseph F. Wasserbauer

The design of a supersonic cruise inlet is dependent on its application. The best inlet for a mission incorporates an optimum combination of inlet characteristics such as total-pressure recovery, cowl drag, bleed flow, and weight. To determine the best inlet, it is necessary to define the sensitivity of the aircraft range to each inlet characteristic. This sensitivity is shown in figure IX-1 for a supersonic transport powered by afterburning turbojet engines and with a nominal range of a little over 3900 nautical miles. The sensitivity is shown as a range decrement, or decrease in range, in nautical miles, for the indicated changes in each of the inlet characteristics. Reducing the total-pressure recovery from 91 percent to 90 percent of the free-stream total pressure causes a 32-mile range decrement. Increasing the nacelle drag coefficient, based on the inlet capture area, from 0.08 to 0.09 reduces range 41 miles. This drag increase corresponds to increasing the external cowl lip angle from 3° to 7°. Increasing bleed flow 1 percent of the capture mass flow decreases range 23 miles, while a 10-percent increase in weight decreases range 17 miles. Therefore, the supersonic transport inlet tends to favor high recovery, low drag, and low bleed at the expense of inlet weight, a less important characteristic.

For supersonic cruise at Mach numbers greater than 2, one of the inlet parameters that affects these important inlet characteristics is the internal contraction of the supersonic diffuser. This paper compares the performance of several inlets to show how the amount of internal contraction affects their characteristics. Not only those inlet characteristics that can be measured in terms of range are considered, but also inlet characteristics such as angle-of-attack tolerance which are more difficult to evaluate. In addition, methods to improve the stability of the internal contraction inlets and some typical distortions that have been measured during wind tunnel testing are discussed.

*NASA-Ames Research Center.

EFFECT OF AMOUNT OF INTERNAL CONTRACTION ON INLET CHARACTERISTICS

Performance Characteristics

To show the effect of internal contraction, the performance of the inlets shown in figures IX-2 and IX-3 is discussed. (Some of these inlets (as well as others) were designed by using a computer program which incorporates the method of characteristics, as described in refs. 1 to 3.) The cowl lip diameters of the inlets shown in those figures range from 14 inches for the all-external-compression inlet to about 18 inches for the three inlets with internal contraction. All the inlets are axisymmetric; however, some results of the comparison also apply to two-dimensional inlets. The designations such as 100-0 and 60-40 indicate the amount of supersonic flow area contraction that occurs upstream and downstream of the cowl lip. Therefore, the 100-0 inlet has all its supersonic flow area contraction ahead of the cowl lip; while the 20-80 inlet has only 20 percent of the flow area contraction occurring ahead of the cowl lip, with 80 percent of the contraction occurring internally.

The job of the supersonic inlet is to diffuse the high Mach number, free-stream air to a near-sonic value at the throat, where a normal shock can efficiently transfer the flow from low supersonic to high supersonic speeds. Downstream of the throat, the flow is further diffused to the low Mach number required by the engine at cruise. All the supersonic diffusion must be accomplished by turning the flow. Therefore, for the all-external-compression inlet, or 100-0 inlet, all the flow turning must be away from the inlet axis, leaving the flow at a high angle at the cowl lip. A high cowl lip angle of 22° is required to capture all the flow and turn it back toward the engine. This high cowl angle produces high drag (ref. 4).

With 40 percent of the supersonic area contraction downstream of the cowl lip, as in the 60-40 inlet, it is possible to reduce the internal cowl angle from 22° to 5°, thus reducing the cowl drag. This cowl angle produces a moderately strong oblique shock in turning the flow back toward the engine, but total-pressure recovery is still high.

If the internal contraction is further increased to 60 or 80 percent, by using the 40-60 inlet (refs. 5 and 6) or the 20-80 inlet, a 0° internal cowl angle will produce a weak, highly efficient, internal oblique shock system and will provide a low-drag cowl.

During transonic acceleration, the required engine flow is twice the flow required at supersonic cruise. Therefore, the inlet throat area must be doubled dur-

ing this acceleration. For the inlets with 60-percent internal contraction or less, the centerbody must be collapsed to double the throat area, as indicated by the dashed lines in figure IX-3. However, by using 80-percent internal contraction, the centerbody can be made small enough, so that when it is translated forward, the annular area between the centerbody and the cowl lip will provide the transonic engine flow. This provides a mechanically simpler centerbody with a potential weight advantage.

Another effect of increasing the internal contraction from 40 percent to 80 percent is that the length of the internal supersonic diffuser increases. As will be seen later, this affects the inlet operating characteristics.

The performance of these inlets is compared in figure IX-4. This figure presents the total-pressure recovery as a function of the diffuser mass-flow ratio. The diffuser mass-flow ratio includes both bypass and engine flows. A value of 1.0 corresponds to the inlet capture mass flow, and the difference between any curve and 1.0 is the boundary-layer bleed flow. Inlet operation with the terminal shock at a downstream supercritical position corresponds to the vertical low-recovery portion of each curve. As the terminal shock is moved upstream into the throat region, where the boundary-layer bleed is located, both the total-pressure recovery and the bleed flow increase. If the terminal shock is moved too far into the supersonic diffuser, it becomes unstable and will pop out in front of the cowl lip, drastically reducing pressure recovery. This transient is called inlet unstart. Therefore, the left limit of each curve for inlets with internal contraction corresponds to the unstart limit. The all-external-compression inlet has no unstart, but encounters an inlet instability called buzz that determines the low mass-flow limit of its curve.

It is difficult to obtain an exact comparison of inlets because their performance can change with different bleed systems (ref. 7). However, the bleed system for each inlet presented herein provided reasonable flow distortion at the engine face and reasonable gust tolerance. From figure IX-4 it can be seen that, in general, as internal contraction is increased from the all-external-compression 100-0 to the 20-80, bleed flow increases and maximum total-pressure recovery increases. To obtain a better comparison of the inlet performance, a comparison was made for the inlets operating at the conditions indicated by the slash marks on the curves. These conditions were chosen as far from the unstart or buzz limit as possible without sacrificing a significant amount of aircraft range. This comparison is shown in figure IX-5.

The range decrement in nautical miles is based on the sensitivity values presented in figure IX-1 for a supersonic transport, and the differences in cowl drag, boundary-layer bleed, and pressure recovery obtained for each inlet. The 40-60 inlet obtained the longest range and is used as a reference. The 60-40 inlet had a higher cowl lip angle, and the resulting drag reduced the range 53 miles. The other

significant range loss of 53 miles is due to reduced total-pressure recovery. The total range decrement is 125 miles. The high cowl drag of the all-external-compression inlet produces such a large range penalty that this inlet is not even competitive. The highest internal contraction inlet, the 20-80, has slightly less total-pressure recovery and slightly more bleed flow, for a penalty of 63 miles. However, the reduced range tends to be offset by its simpler translating centerbody and its design Mach number of 2.65, which is slightly higher than the 2.5 value for the 40-60 inlet. Therefore, the general trend is that the inlets with higher internal contraction have lower range decrements. A range comparison clearly favors inlets with high internal contraction.

Unstart Characteristics

As shown in figure IX-4, all these mixed-compression inlets which afford efficient diffusion and minimum cowl drag also have an undesirable transient characteristic known as inlet unstart. This unstart causes a sharp reduction in mass flow and pressure recovery and a large increase in drag. An unstart can result from an internal disturbance such as a reduction in the engine airflow requirement or from an external disturbance such as a gust.

An inlet unstart for the model installation shown in figure IX-6 was recorded on high-speed schlieren film. Selected frames from this film of an unstart that was caused by an internal airflow disturbance are presented in figure IX-7. For this unstart, the 40-60 inlet that was installed with a wing simulator was terminated by a coldpipe and choked plug. The part of the installation that was visible in the schlieren for started inlet operation is outlined by the upper rectangle in figure IX-6. Sketches of the maximum upstream unstarted shock pattern and the unstarted stable shock pattern are also shown. Time in seconds after inlet unstart for the various motion-picture frames is listed on figure IX-7. Frames up to 0.01637 second after unstart show the initial expulsion of the inlet shock system. Figure IX-7(f) shows the maximum upstream position to which the shock system is expelled. The oblique shock wave from a boundary-layer separation on the centerbody oscillates at a frequency of about 130 hertz. Frames which show the downstream-to-upstream movement of the oblique shock for one-half of a cycle of this oscillation are presented in figures IX-7(g) to (i). This inlet also has a large instability, or buzz, which has a frequency of about 12 hertz for the coldpipe termination. The buzz frequency for this inlet terminated by an engine is somewhat higher, about 22 hertz. The boundary-layer separation moves upstream to the

spike tip for the forward extent of the inlet buzz cycle.

The performance during an inlet unstart for a free-stream Mach number of 2.50 is presented in figure IX-8. Variation of the total-pressure recovery measured at the compressor face as a function of time after unstart is presented. A 40-60 inlet unstart from an internal disturbance is illustrated by the dashed trace. The total-pressure recovery drops rather rapidly, from a started level of about 94 percent to a minimum level of about 25 percent. From this minimum level the 40-60 inlet is unstable. A spike and overboard bypass door movement are required to stabilize this inlet at an unstart pressure recovery of 48 percent. The 60-40 inlet unstart from an internal disturbance has the same initial trend as the 40-60 inlet unstart, and drops to a minimum recovery of about 15 percent. The 60-40 inlet, however, recovers rather rapidly to a high recovery and is automatically stable at an unstarted stable recovery of 75 percent. Depending on the cause of unstart, the drop in total-pressure recovery immediately after inlet unstart can be quite different. This is shown by the trace for the 60-40 unstart from an external disturbance, which drops to a minimum level of only 68 percent recovery, and is automatically stable at 75 percent recovery.

A large drop in pressure recovery immediately after unstart may cause the engine to stall and flame out. These data are presented in the paper on effects of engine inlet disturbances. However, if the unstarted inlet has been stabilized, and if the engine is running, a propulsion system with the 60-40 inlet loses about 50 percent of its started thrust. This propulsion system with the 40-60 inlet loses all its thrust and ends up with a drag component. No unstart data are available for the 20-80 inlet. However, this inlet would have a performance penalty at least equal to that of the 40-60.

While the larger internal area contraction inlets have better range characteristics, they also have a larger unstarted performance penalty. Since a typical supersonic cruise aircraft would incorporate multiple propulsion systems, unsymmetrical forces during a single inlet unstart can cause aircraft control problems until the inlet has been restarted.

Angle-of-Attack and Mach Number Tolerance Characteristics

One possible solution to the unstart problem of internal contraction inlets is to design the inlet to accept disturbances without unstarting. First, consider the external disturbances. These disturbances are the result of aircraft maneuvers and atmospheric gusts. The aircraft maneuver is generally slow enough that the inlet's control system can anticipate and compensate for it. But gusts are a sudden occur-

rence and the inlet controls may not be rapid enough to prevent the inlet unstart. Therefore, with its geometry fixed, the inlet must have adequate tolerance to withstand the sudden gusts. Gusts can approach from all directions and affect the angle of attack or yaw and the free-stream Mach number ahead of the inlet (fig. IX-9). Increasing free-stream Mach number has little effect on inlet performance. But when the free-stream Mach number is decreased, the Mach numbers are reduced throughout the supersonic diffuser and in the inlet throat. Large enough reductions in the free-stream Mach number will choke the inlet throat and cause an inlet unstart. This choking can be relieved only by geometry variation.

When the inlet is forced to operate at an angle of attack, the inlet can unstart in two ways. If the terminal shock is in its most forward stable position at 0° angle of attack, a slight increase in the angle of attack is sufficient to force the shock forward into the supersonic diffuser, where it becomes unstable, and the inlet unstarts. Operating the inlet with the terminal shock slightly downstream of the diffuser throat (supercritical operation) allows the inlet to operate at higher angles of attack. But as the angle of attack is increased, additional compression of the internal supersonic flow appears on the top, or leeward, side of the inlet and less compression on the bottom, or windward, side. The lack of compression on the windward side results from expanding the flow around the cowl lip in order to turn the flow axially. The overcompression on the leeward side is the critical region where a local choking condition causes the inlet to unstart. Figure IX-10 illustrates in more detail the local choking that limits the angle of attack for supercritical operation. The top side of the 40-60 inlet with the cowl and centerbody contours is shown in the sketch at the top of the figure. This is the leeward side of the inlet when it operates at a positive angle of attack. The plot shows the cowl static pressure ratioed to free-stream total pressure as it varies along the cowl surface, and identifies the shock reflections on the cowl surface.

The solid lines represent operation at 0° angle of attack and the dashed lines at the angle of attack just before the inlet unstarts. As the angle of attack is increased from 0° to the maximum value of 2.9°, the first shock reflection on the cowl moves forward in the inlet. The second cowl shock reflection moves ahead of the throat region to the forward edge of the porous bleed and compresses the flow to pressures higher than sonic values. This indicates a local choking condition at this point on the cowl. Further increases in the angle of attack would unstart the inlet. This means that this second shock reflection cannot be moved ahead of the cowl bleed region. By moving the porous bleed regions further upstream, a higher angle of attack of 3.0° was reached before an unstart occurred.

Figure IX-11 shows the unstart limits for the 40-60 inlet for both a reduction in free-stream Mach number and an increase in angle of attack. Also, data are

shown for two different bleed configurations. The data indicate that, when the bleed is relocated to an upstream position, larger Mach-number-reduction and angle-of-attack tolerances are realized. Also, as the free-stream Mach number is reduced with fixed inlet geometry, the angle-of-attack tolerance decreases to zero where the maximum reduction in free-stream Mach number occurs. The inlet unstarts beyond these conditions or to the right of these two curves.

For some transport configurations, the accepted minimum tolerances are about 0.05 in free-stream Mach number and 2.5° to 3.0° in angle of attack. However, more tolerance for both these parameters is desirable to increase the inlet safety margin. Also, larger tolerances in these parameters may be desirable for other supersonic dash or cruise aircraft.

The trend in the data presented herein for the 40-60 inlet is typical of the data that were obtained for the other internal contraction inlets of this comparison. All the inlets in this comparison have adequate tolerance to Mach number reductions. However, the angle-of-attack tolerance becomes more of a concern as the inlet's internal supersonic area contraction is increased. This is shown in figure IX-12, which summarizes the angle-of-attack experience for these inlets. The length of the supersonic diffuser, from the cowl lip to the inlet throat for the various inlets, was the parameter examined. This figure presents the unstart angle-of-attack limit as a function of the length from the cowl lip to the geometric throat. This length was nondimensionalized by the cowl lip radius.

The values of this ratio vary from 1.88 for the 20-80 inlet to 1.19 for the 60-40 inlet. The shaded area represents the range of angle-of-attack tolerance for the inlets considered so far with good performing bleed systems. The upper portion of this shaded area is a curve faired through the data points which represent the maximum unstart angle of attack that has been demonstrated so far for each inlet. The curve has been extended to include data of an additional 60-40 inlet that has comparable performance to the previously mentioned 60-40 inlet. Figure IX-13 compares the two 60-40 inlets. The top sketch is the inlet considered previously. This inlet distributed the isentropic compression from the cowl over some length of centerbody. Another way of designing this inlet is to focus this isentropic compression at one point on the centerbody, reducing the length from the cowl lip to the geometric throat. This results in a length ratio of 0.76 for the focused compression inlet. This focused compression inlet has a maximum angle-of-attack tolerance of 9.4°. The tolerance in angle of attack for the inlets varied from about 2.6° for the 20-80 inlet to about 9.4° for the 60-40 focused compression inlet. Therefore, increasing the length of the internal portion of the supersonic diffuser appears to reduce its angle-of-attack tolerance.

Another parameter that must be considered is the distortion at angle-of-attack operation. The distortion is defined as the average total pressure minus the minimum total pressure divided by the average total pressure at the compressor face. For these inlets the distortion was below 0.10 for angles of attack less than 5^{0} and below 0.13 for angles of attack less than 7.5^{0}. Distortion values of 0.06 to 0.07 are normally acceptable for 0^{0}-angle-of-attack operation.

Thus, the inlet's tolerance to external disturbances is limited by choking in the inlet throat. This tolerance can be improved by proper location of the porous bleed. Also the inlets will have less angle-of-attack tolerance as the supersonic diffuser length is increased.

Summary - Effect of Amount of Internal Contraction

The preceding comparisons do not produce an obvious choice. Range is relatively easy to evaluate and clearly favors high-internal-contraction inlets. However, these inlets are more sensitive to gust and maneuver disturbances and also produce a larger disturbance at unstart. It then becomes a problem of choosing the maximum range compatible with acceptable tolerance to gusts and maneuvers and also an acceptable unstart amplitude. The trades have been fairly well defined, but the aircraft designer must be given the difficult choice.

IMPROVED STABILITY OF INTERNAL CONTRACTION INLETS

Inlets with different amounts of internal supersonic contraction have been compared. However, all these inlets are about equally sensitive to internal disturbances. The conventional mixed-compression inlet must operate with the terminal shock near the throat region for peak performance. If this shock inadvertently moves ahead of the throat due to an internal airflow disturbance, unstart will occur. Current inlets have a rather limited stable operating range that is provided by the capacity of the performance bleed system to spill increased airflow as the terminal shock moves upstream. This limited stable range may not be adequate to absorb many of the transient disturbances that are encountered by a supersonic propulsion system. Larger stable margins are currently provided by inlet operation at low performance levels.

These inlets can be designed to prevent unstart for most internal disturbances by utilizing a throat bypass bleed system (refs. 8 and 9). A schematic of this system is presented in figure IX-14. An internal disturbance, such as a momentary

reduction in the amount of airflow that is required by the engine, causes the terminal shock to move upstream. Unstart can be prevented if the excess airflow can be diverted overboard through a large open bleed or bypass in the inlet throat region. The exit area for this bleed region must be controlled to regulate the amount of airflow spillage as the terminal shock moves to a different location. This control prevents prohibitive amounts of airflow from being ducted overboard during normal inlet operation, but allows large amounts of bleed to exhaust in order to prevent unstart as the terminal shock moves upstream over the bleed region. Sixteen fast-acting valves were located in the inlet cowl to provide this exit-area control.

Two types of bleed control valves that were investigated are presented in figure IX-15. The mechanical valve is essentially a free-piston that is positioned by differential pressures. An internal reference pressure, inside the valve chamber, is adjusted to just close the valve during normal inlet operation. Control of this internal reference pressure determines the pressure at which the valve opens. If this reference pressure is exceeded by an increase in bleed plenum pressure that results from a forward movement of the terminal shock over the bleed region, the valve opens and allows bleed flow to occur. This self-acting mechanical valve was a simple design that was investigated to demonstrate the concept of a constant-pressure bleed control.

For the vortex valve, a tangential control airflow creates a vortex inside the valve chamber which shuts off the bleed at the lower pressures that are associated with normal inlet operation. An increase in bleed pressure breaks down this vortex, allowing the bleed airflow to exhaust through the valve exits (top and bottom). The maximum amount of airflow is limited for these valves, since for proper operation the size of the exit must be small when compared to the size of the valve chamber.

Inlet performance for three different types of stability bleed controls at a free-stream Mach number of 2.50 are presented in figure IX-16. Sufficient performance bleed was removed from the centerbody to assure high inlet performance. This bleed was ducted through the centerbody support struts and controlled by fixed exits. In this figure total-pressure recovery is presented as a function of diffuser mass-flow ratio. Inlet performance is shown for fixed-exit bleed controls that are normally used on mixed-compression inlets and for vortex and mechanical valves. The stable margin that each of these stability bleed controls provides can be illustrated if an inlet-engine match condition of about 90-percent recovery is selected. From this condition, the fixed-exit bleed control provides a stable margin of 5.3 percent; that is, the corrected airflow in the inlet diffuser can be reduced by 5.3 percent prior to inlet unstart. The vortex valves provide an increased stable margin to 10.8 percent. Mechanical valves which were a similar physical size to the vortex valves provided a stable margin of 26 percent. These data show that it is possible

to provide an increased tolerance to internal disturbances for mixed-compression inlets by utilizing a throat bypass stability bleed system and a variable exit control.

DISTORTION MEASUREMENT AND CONTROL

One problem that is common to all the inlets is distortion. This is a rather emotional subject, particularly when aircraft and engine designers are attempting to decide the responsibility for propulsion system stability. It is also a very difficult subject because time-varying distortion has recently been recognized.

To define the time-varying distortion at the engine face requires orders of magnitude more data than is required to define the older steady-state or time-averaged distortion. How to process this additional information into an understandable form is not well defined at present.

Distortion Measurement

Distortion measurement is reviewed in figure IX-17. The time-honored method to measure total-pressure distortion has been to install a large number of probes at the compressor face (as shown in the upper right corner of fig. IX-17), each with a long transmission line to a remote sensor. These long lines time-average the data. A pressure contour map constructed from these steady-state pressures would look like the example shown in the lower right. Each contour is a line of constant total-pressure recovery. In this particular example, the inlet was operated at a positive angle of attack, so that the distortion was primarily circumferential, with high pressure in the top portion of the inlet and the low pressure in the bottom portion. There is also a radial component present.

Recently, high-response subminiature pressure sensors have replaced the long transmission lines. With these sensors, it has been found that there is a fluctuating or dynamic component of total pressure superimposed on top of the steady-state value, as shown in the lower left corner of figure IX-17. The instantaneous pressure P_i measured by each sensor is then the sum of the steady-state pressure $\overline{P_i}$ plus the dynamic component ΔP_i. These fluctuations can be the result of one or more flow conditions within the inlet. Terminal shock boundary-layer interactions, transient boundary-layer separations, duct resonances, and engine dynamic feedback are a few of these possible causes. Whatever the cause, these fluctuations do exist, and they combine with the steady-state pressure to produce a different distortion pattern at each instant of time. And since what the engine really sees are

these instantaneous distortions, a complete inlet-engine compatibility effort requires their measurement.

The best way to get a feel for what is actually going on at the compressor face is to make a motion picture from a continuous series of instantaneous pressure contours. The steps which are followed to produce such a motion picture are as follows: First, the instantaneous pressure from each sensor is recorded on analog tape; then, the pressure level on each sensor at a given instant in time is determined by simultaneously digitizing all channels from the analog tape at 8000 points per second per channel; then, for each time slice, a pressure contour map is constructed using a computer program; finally, cartoon methods are used to make the motion picture, wherein each contour is repeated six times and projected at 24 frames per second.

A motion picture was made using this procedure; selected frames from it are shown in figure IX-18. The contour in the upper left is the steady-state pattern and is for the same data point as was shown in figure IX-17. In the representation used in this figure, each shaded area represents a 6-percent recovery range with the lightest area being the highest recovery (94 to 100 percent) and the darkest area the lowest recovery (64 percent and below). The boundary between any two shaded regions is a constant-pressure contour. When viewing the motion picture, the first impression is that there is a great deal of movement in the pressure field. After repeated showings, it becomes apparent that the overall motion is due to the expansion and contraction of the large regions of high and low pressure. The movement of these regions is then the cause of the fluctuations at any one point. By comparing the frames at time instants 1 to 3 in figure IX-18, the variations in size of the different pressure regions can be seen.

From the motion picture, it also appeared as if the amplitude of the fluctuations was not constant across the compressor face. To better determine this, the amplitude of the dynamic component at each sensor can be found. As a measure of the amplitude of the fluctuating component ΔP_i, the root-mean-square (or RMS) level ΔP_{RMS} is used, as indicated in figure IX-17. The RMS level of each sensor was ratioed to the steady-state compressor face pressure and the resulting value was used to construct a dynamic contour map.

Figure IX-19 shows the steady-state and dynamic contours for the same data point as the instantaneous distortions of figure IX-18. These data were recorded in the 10- by 10-Foot Supersonic Wind Tunnel with the 60-40 inlet installed in front of the J85 turbojet engine. (Steady-state interactions between the 40-60 inlet and the J85 turbojet engine are discribed in ref. 10.) The data of figure IX-19 were recorded at Mach 2.6 and 5° angle of attack with the inlet operating somewhat supercritically at a steady-state pressure recovery of about 77 percent and a steady-state distortion of about 18 percent. The steady-state map uses the same representation

as in figure IX-18, except the numerical values of the recovery boundaries are given. Again, notice the combined circumferential and radial pattern. Now, on the dynamic map, each shaded region represents a given range of dynamic activity. Here the darkest region indicates a high dynamic level of between 6 and 7 percent of the steady-state pressure, and the lightest region a very low dynamic level of between 2 and 3 percent. For both the steady-state and the dynamic plots, then, the light areas represent good flow and the dark areas, bad flow. Comparing the two maps shows that in the region of high pressure recovery there is a low RMS level. In the region of low pressure recovery the RMS level is somewhat higher. The region of high dynamics, then, lies in a band located between the high- and low-pressure-recovery regions.

Since the peak-to-peak level of the fluctuations at any one spot is also a measurement of the dynamic level, we should be able to correlate the high dynamic region on the RMS plot to the spatial area in the motion picture which has the greatest number of pressure boundary crossings per unit of time. From the motion picture it was found that in the upper high-pressure region there were very few boundaries crossing a given spot. In the high dynamic band there were at least four different boundaries passing over a given spot rather frequently. In the low-pressure region, it was possible to see two different boundaries crossing a given spot frequently, with two others sneaking in occasionally. It must be remembered while making this comparison that the RMS plot was an average over a long time period, whereas the motion picture covered only 15 milliseconds. (Two seconds of film time equal 1 msec of data time.)

By comparing the information gained from the motion picture to that gained from the RMS plots, it appears that the high dynamic regions are areas where a greater number of pressure boundaries pass per unit of time.

From the same data from which the motion picture was made, it is possible to find the value of a distortion parameter for each instant in time. Figure IX-20 shows such an instantaneous parameter plotted over a 30-millisecond time period just before and during compressor stall. This parameter is a function of average and minimum pressure levels and is discussed in greater detail in the paper on effects of engine inlet disturbances. The steady-state value of the parameter averaged over a much longer period of time is about 0.1. The critical level is the steady-state value of this parameter which would cause engine stall. So it is obvious that the steady-state level is fairly far from critical but that there are transients which do exceed this critical level.

The data from which this plot was obtained were filtered at 1600 hertz. By proper analog filtering or digital averaging, it should be possible to determine the highest frequency content of significance to the engine. Conceptually, with

6

the proper filter and a valid parameter, only the distortion which caused engine stall should exceed the critical level. These methods are being pursued at the present time. However, for the data shown here, the distortion at 10 milliseconds barely exceeded the critical level, but the engine did not stall. The distortion at 18.5 milliseconds exceeded the critical level and did cause an engine stall. The evidence of the stall hammershock is seen at about 27.5 milliseconds. The hammershock is a compression wave which is sent forward due to the stall. The time between 18.5 and 27.5 milliseconds is that needed for the bad pattern to move from the rake station into the compressor and have enough time to cause stall, and then for the stall hammershock to move back through the compressor to the rake station.

Selected motion-picture frames showing the significant occurrences of figure IX-20 are shown in figure IX-21. The times of the frames correspond to the times of figure IX-20. (Frames shown at times of 30.25 and 32.25 milliseconds are beyond the time period shown in fig. IX-20.) The upper left contour is again the steady-state pattern for reference. The frames at times of 18.00 and 18.50 milliseconds show what caused the worst distortion pattern. Just before this worst pattern, the low-pressure region in the bottom of the inlet became lower (time, 18.00 msec) and then the average pressure region increased in extent down around the sides of the inlet (time, 18.50 msec). At 27.50 milliseconds the first evidence of the hammershock can be seen. It appears as a high-pressure region at the top of the compressor face. The high-pressure region then rotates around the inlet in the direction of rotor rotation. At 30.25 millfseconds it is about halfway around the compressor face, and at 32.25 milliseconds it has emcompassed the whole compressor face.

One conclusion that can be drawn from the motion picture is that the high dynamic region is not the only region of importance, as the stall-producing mechanism encompassed regions of both high and low dynamics.

As stated before, an attempt is being made to define the highest frequency of importance to the engine. It is possible to gain a feeling for the highest frequency from figure IX-20. The fastest transient of sufficient amplitude to exceed the critical level occurred in about 1.6 milliseconds. If this is used as the period of a sine wave, the frequency of the wave would be 600 hertz. Thus, it would appear from this limited data that frequencies to at least 600 hertz are of importance for this particular inlet size.

Distortion Control

Now let's examine some possible means of distortion control. Figure IX-22 shows that vortex generators are very effective in reducing both steady-state and

dynamic distortion. The parameters plotted are steady-state and dynamic distortion versus total-pressure recovery. Dynamic distortion is defined as the average RMS pressure level at the compressor face ratioed to the average steady-state pressure at the compressor face. These data were recorded with the 60-40 inlet operating at Mach 2.5 and 0° angle of attack, and were prefiltered to 1 kilohertz. (Similar data for the 40-60 inlet are presented in refs. 11 and 12.) The open symbols in figure IX-22 denote data recorded with a cold-pipe choked plug termination and the solid symbols denote data recorded with the J85 turbojet engine as a termination. The data on the left were recorded without vortex generators and those on the right with vortex generators. First let's consider the data without vortex generators. Point A is a high-pressure-recovery point, with the terminal shock at the geometric throat. Point B is at low recovery, with the shock pulled downstream into the subsonic diffuser. To progress from point A to point B, either the choked plug is retracted or the engine speed is increased. Both steady-state and dynamic distortion increase rapidly as the shock is moved from point A to point B. The 0.1 level of dynamic distortion is quite high, as the peak-to-peak amplitude of the fluctuations would be somewhere between 30 and 60 percent of the average compressor face pressure.

The data on the right were taken with vortex generators installed on both the cowl and centerbody aft of the throat region. The purpose of the generators is to pull high-energy flow from the main duct down into the low-energy boundary layer. Both steady-state and dynamic distortion were reduced over the entire recovery range. Thus, vortex generators are a very effective means of boundary-layer control and, in turn, are an effective means of distortion control. These data also show that the engine had little effect on either steady-state or dynamic distortion. However, it must be remembered that these are time-averaged data. Also, it appears that the dynamic distortion parameter can be used to determine the quality of the dynamic flow at the compressor face, just as the steady-state parameter has been used for years to qualitatively define the steady-state flow.

Figure IX-23 shows the result of a resonant condition which was encountered in an early version of the 40-60 inlet (ref. 11). It was determined that this condition was due to the overboard bypass cavities resonating in an organ-pipe manner. The main duct was then isolated from the bypass cavities by installing a dual-vane cascade at the entrance to each cavity. The data shown were recorded from a single tube at the compressor face without the cascade present. Plotted is the power spectral density versus frequency. The resonance shows up as high-power spikes at 270 hertz and at the second and third harmonic points. This is typical of the data recorded with this inlet; however, these high-power spikes were not always present. When they were present, their relative amplitude depended on the exact position of

the probe at the compressor face. The power content in the spikes adds 130 percent to the RMS level that would be obtained without the spikes present. The cascade virtually eliminated the resonance at the compressor face for most inlet operating conditions. The resonance would tend to reappear, however, if no flow was taken out of the bypass cavity. But typical inlet operating conditions would call for some flow through this region. Thus, the cascade seems to be an effective approach to control of the resonant condition.

Summary - Distortion Measurement and Control

It has been shown that time-varying pressures must be considered in distortion analysis and that the instantaneous analysis technique is a very effective means of qualitatively visualizing the flow dynamics at the compressor face and quantitatively correlating the inlet distortion to engine stall. Unfortunately, the instantaneous distortion data are very time consuming and expensive to obtain. However, some correlation does exist between the instantaneous distortions and the dynamic and steady-state contour plots, which are more easily obtained. Work is continuing on this and other types of correlations.

The dynamic data indicated that dynamic information good to at least 600 hertz is required to describe the major variations in instantaneous distortion at a 16-inch-diameter compressor face. A first guess is that the wavelength of this critical frequency should scale linearly with compressor face diameter; investigations with larger inlets planned for 1971 should help to clarify this critical frequency scaling.

Vortex generators were shown to be an effective method to control distortion. Also, it was demonstrated that a resonance in an inlet duct was suppressed by decoupling the resonant bypass cavity from the energy of the main stream by a cascade. Therefore, it appears that it is possible to control distortion, but more work is required to define optimum configurations.

REFERENCES

1. Anderson, Bernhard H.: Design of Supersonic Inlets by a Computer Program Incorporating the Method of Characteristics. NASA TN D-4960, 1969.

2. Anderson, Bernhard H.: Optimization of Supersonic Inlets Using the Method of Characteristics. Analytical Methods in Aircraft Aerodynamics. NASA SP-228, 1970, pp. 569-581.

3. Anderson, Bernhard H.: Characteristics Study of a Bicone Mixed-Compression Inlet for Mach 1.80 to 2.50. NASA TN D-5084, 1969.

4. Calogeras, James E.; and Meleason, Edward T.: Wind Tunnel Investigation of Techniques for Reducing Cowl Drag of an Axisymmetric External-Compression Inlet at Mach 2.49. NASA TM X-1516, 1968.

5. Cubbison, Robert W.; Meleason, Edward T.; and Johnson, David F.: Performance Characteristics from Mach 2.58 to 1.98 of an Axisymmetric Mixed-Compression Inlet System With 60-Percent Internal Contraction. NASA TM X-1739, 1969.

6. Sorensen, Norman E.; Smeltzer, Donald B.; and Cubbison, Robert W.: Study of a Family of Supersonic Inlet Systems. J. Aircraft, vol. 6, no. 3, May-June 1969, pp. 184-188.

7. Cubbison, Robert W.; Meleason Edward T.; and Johnson, David F.: Effect of Porous Bleed in a High-Performance Axisymmetric, Mixed-Compression Inlet at Mach 2.50. NASA TM X-1692, 1968.

8. Sanders, Bobby W.; and Cubbison, Robert W.: Effect of Bleed-System Back Pressure and Porous Area on the Performance of an Axisymmetric Mixed-Compression Inlet at Mach 2.50. NASA TM X-1710, 1968.

9. Sanders, Bobby W.; and Mitchell, Glenn A.: Increasing the Stable Operating Range of a Mach 2.5 Inlet. Paper 70-686, AIAA, June 1970.

10. Coltrin, Robert E.; and Choby, David A.: Steady-State Interactions from Mach 1.98 to 2.58 Between a Turbojet Engine and an Axisymmetric Inlet with 60-Percent Internal Area Contraction. NASA TM X-1780, 1969.

11. Coltrin, Robert E.; and Calogeras, James E.: Supersonic Wind Tunnel Investigation of Inlet-Engine Compatibility. Paper 69-487, AIAA, June 1969.

12. Calogeras, James E.: Experimental Investigation of Dynamic Distortion in a Mach 2.50 Inlet with 60 Percent Internal Contraction and Its Effect on Turbojet Stall Margin. NASA TM X-1842, 1969.

EFFECT OF INLET CHARACTERISTICS ON SUPERSONIC CRUISE RANGE

SUPERSONIC TRANSPORT - AFTERBURNING TURBOJET

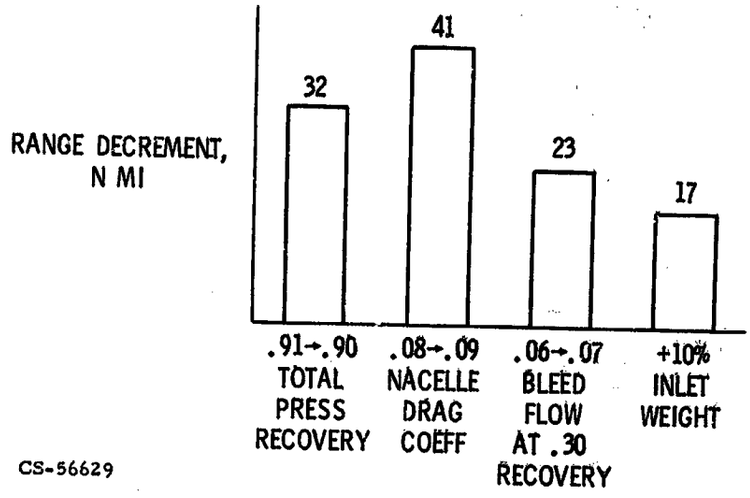

Figure IX-1

SUPERSONIC CRUISE INLETS

100-0 ISENTROPIC COMPRESSION INLET

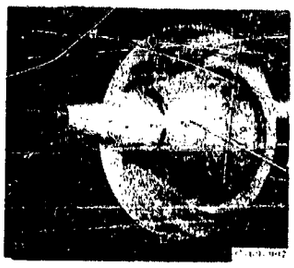

60-40 INLET

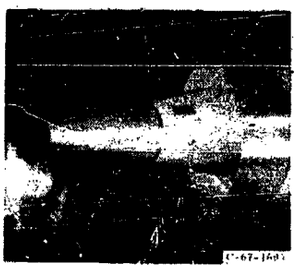

40-60 INLET

20-80 INLET

CS-56633

Figure IX-2

SUPERSONIC CRUISE AXISYMMETRIC INLETS

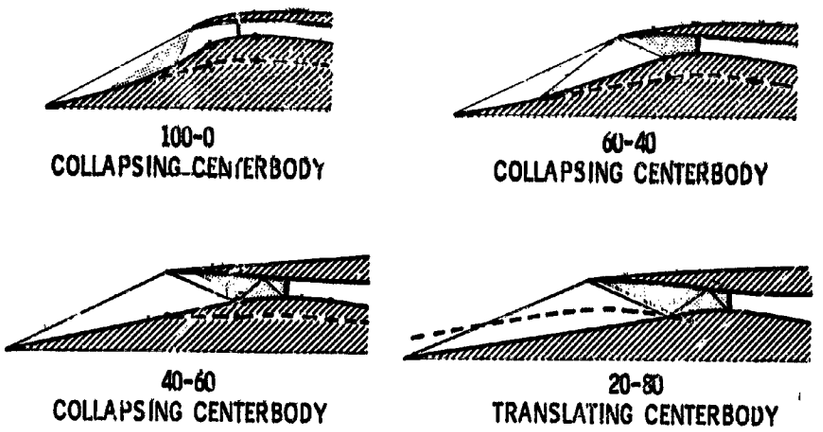

CS-56630

Figure IX-3

INLET SUPERSONIC CRUISE PERFORMANCE

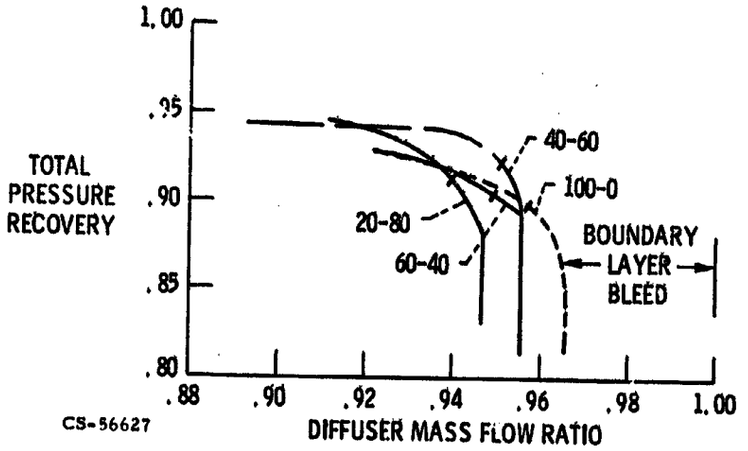

CS-56627

Figure IX-4

EFFECT OF INLET PERFORMANCE ON SUPERSONIC CRUISE VEHICLE RANGE

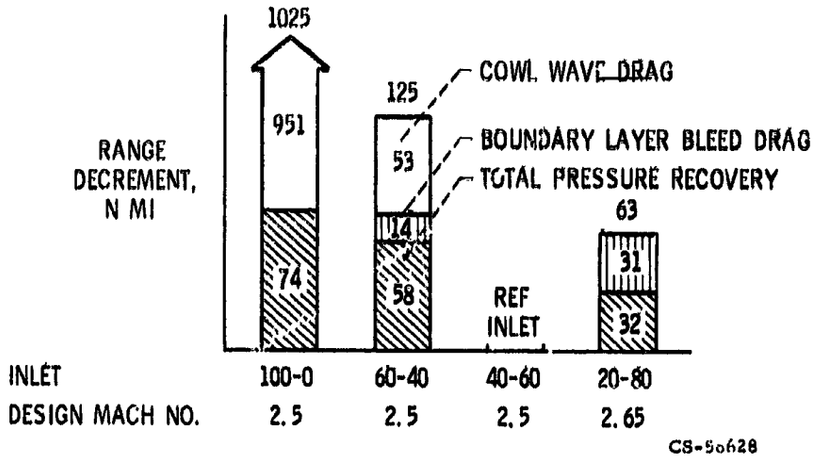

Figure IX-5

40–60 INLET INSTALLED WITH A WING SIMULATOR

$M_0 = 2.50$

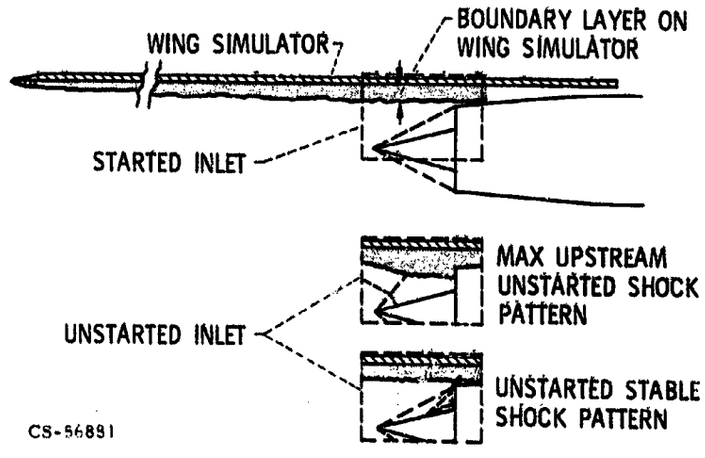

Figure IX-6

SCHLIEREN PHOTOGRAPHS OBTAINED DURING INLET UNSTART RESULTING FROM INTERNAL AIRFLOW DISTURBANCE AT MACH 2.50

(a) TIME, 0 SECOND.

(d) TIME, 0.01059 SECOND.

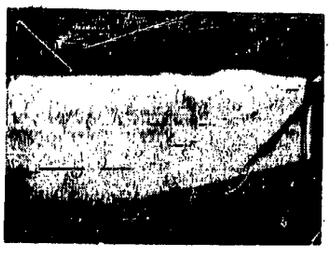

(g) TIME, 0.03627 SECOND.

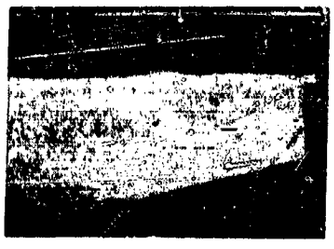

(b) TIME, 0.00096 SECOND.

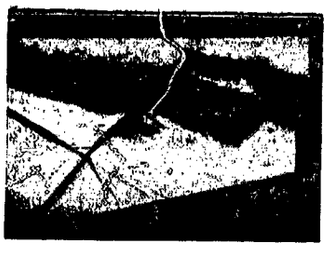

(e) TIME, 0.01444 SECOND.

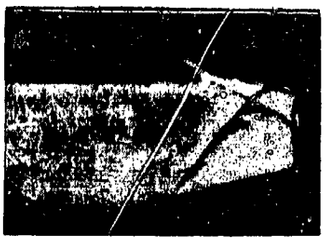

(h) TIME, 0.03852 SECOND.

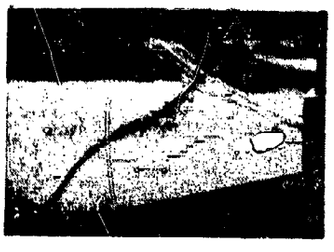

(c) TIME, 0.00482 SECOND.

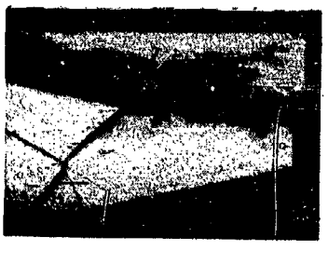

(f) TIME, 0.01637 SECOND.

(i) TIME, 0.04035 SECOND.

Figure IX-7

PERFORMANCE DURING AN INLET UNSTART

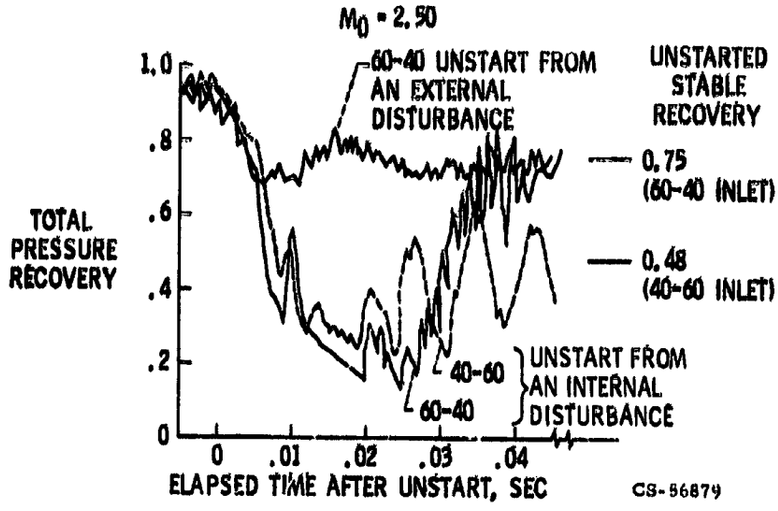

Figure IX-8

EXTERNAL TRANSIENT DISTURBANCE

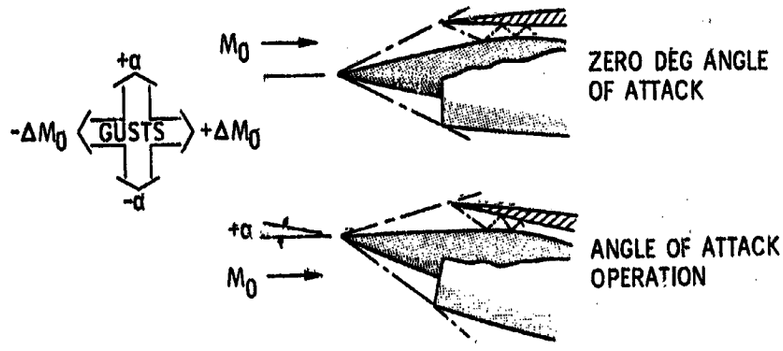

Figure IX-9

CS-56874

UNSTART LIMIT FOR INLET ANGLE OF ATTACK

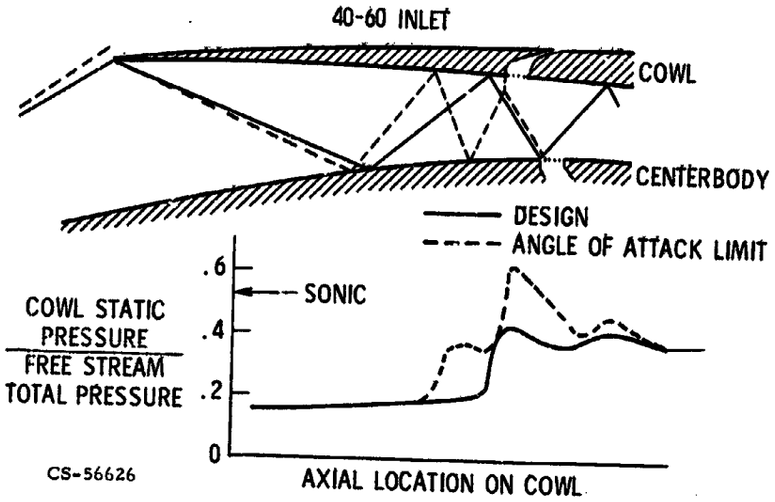

Figure IX-10

UNSTART TOLERANCE OF 40–60 INLET

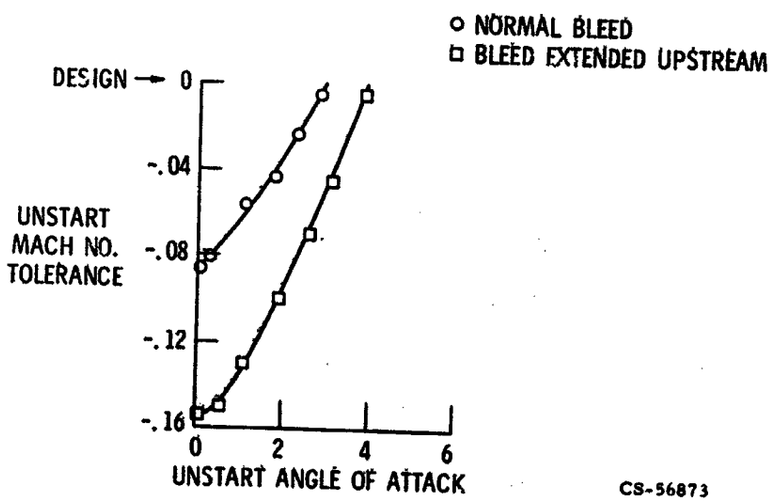

Figure IX-11

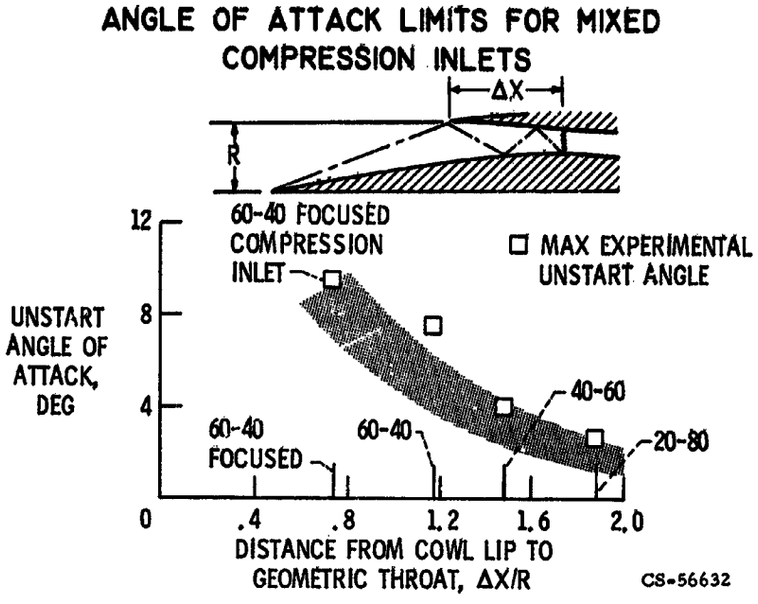

Figure IX-12

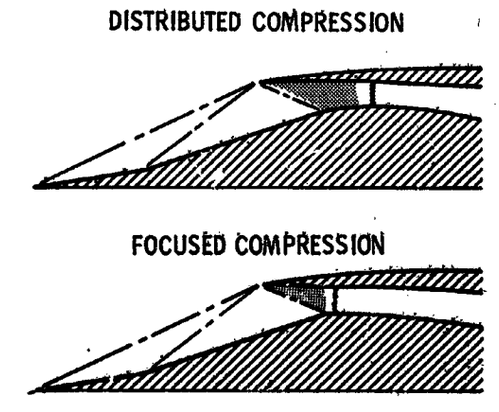

Figure IX-13

CROSS SECTION OF 60-40 STABILITY INLET

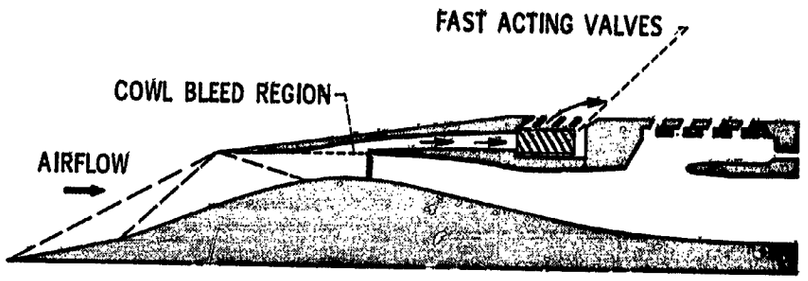

Figure IX-14

FAST ACTING VALVES

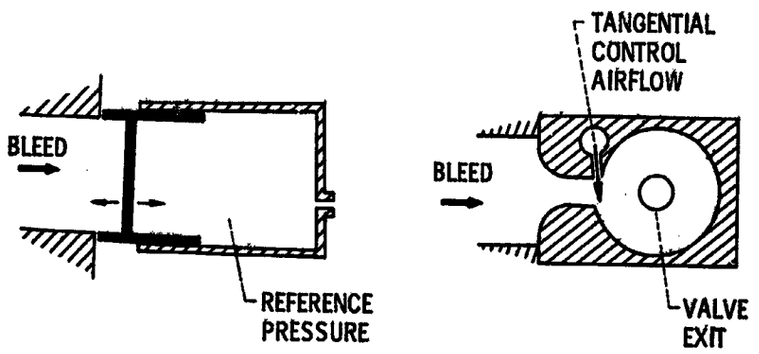

MECHANICAL VALVE

VORTEX VALVE

Figure IX-15

CS-56880

INLET PERFORMANCE
WITH THREE DIFFERENT BLEED CONTROLS

$M_0 = 2.50$

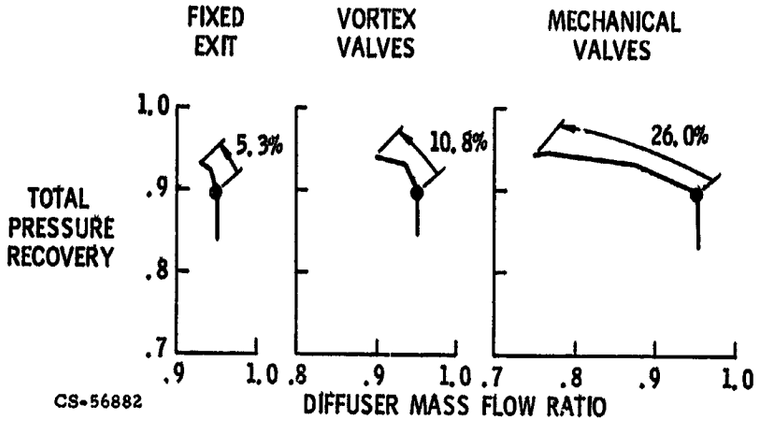

Figure IX-16

INLET DISTORTION

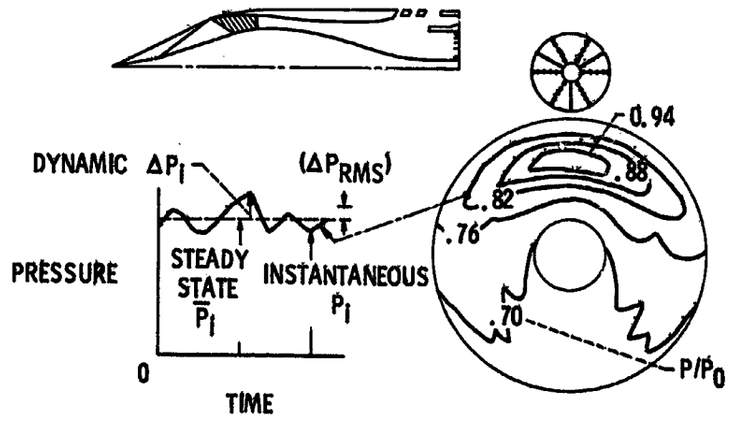

Figure IX-17

CS-56922

INSTANTANEOUS DISTORTION CONTOURS

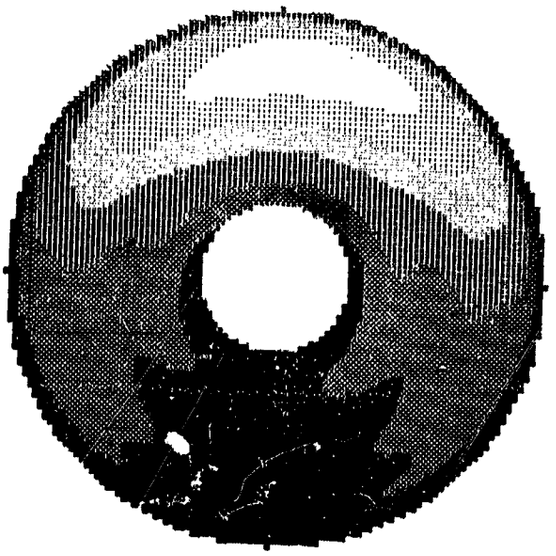

Steady state

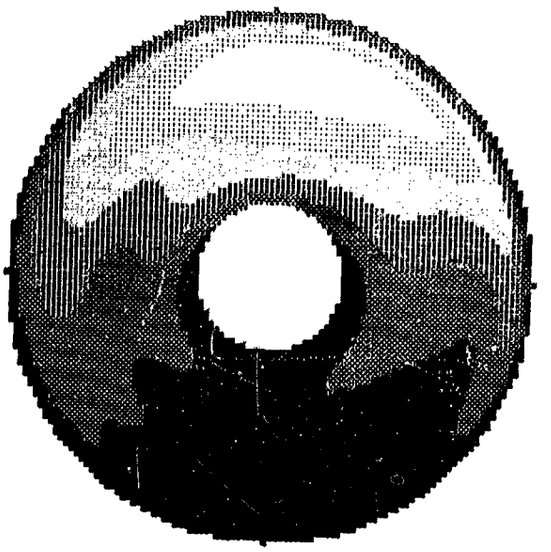

Instant 1

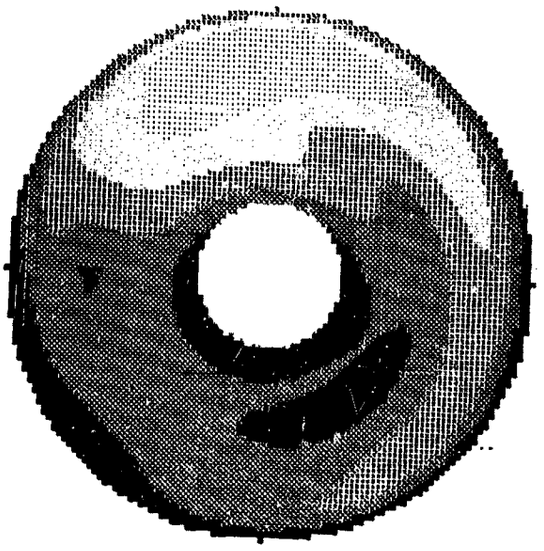

Instant 2

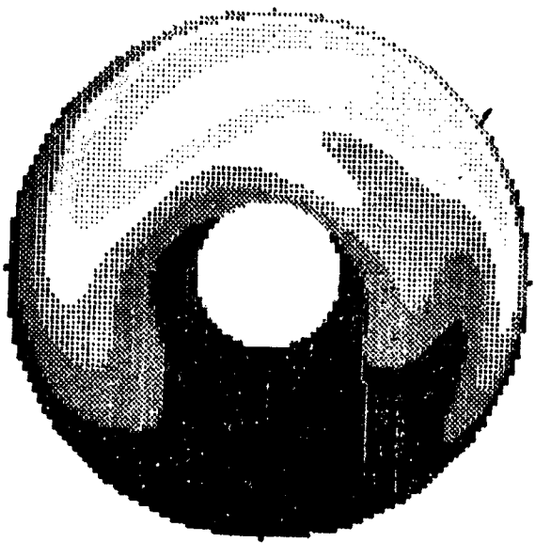

Instant 3

Figure IX-18

DISTORTION CONTOURS

MACH NO., 2.6; ANGLE OF ATTACK, 5^0

STEADY STATE

$P_{AVG}/P_0 = 0.769$; $\Delta P/P_{AVG} = 0.178$

DYNAMIC

$(\Delta P_{RMS})_{AVG}/P_{AVG} = 0.046$

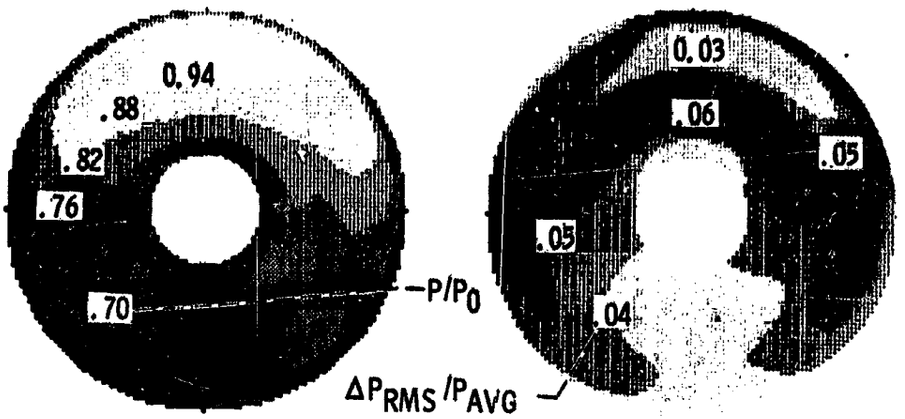

CS-56920

Figure IX-19

INSTANTANEOUS DISTORTION

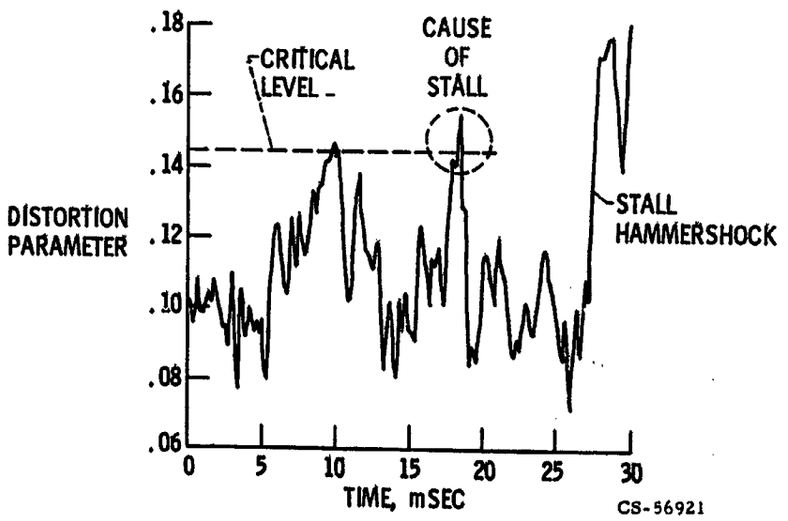

CS-56921

Figure IX-20

INSTANTANEOUS DISTORTION CONTOURS BEFORE AND DURING STALL

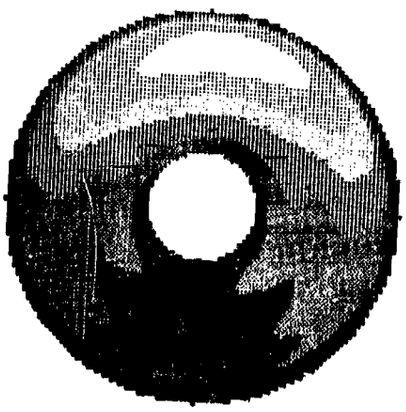

Steady state

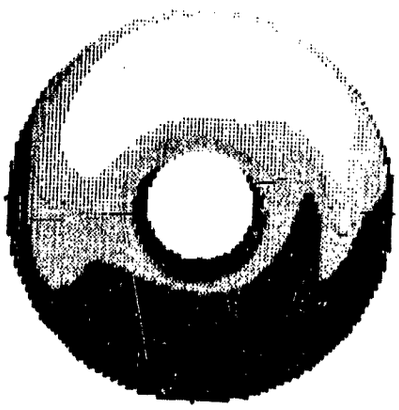

Time, 18.00 milliseconds

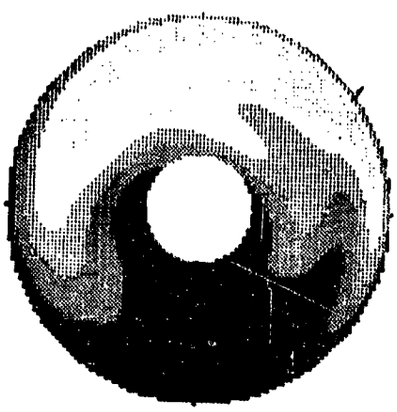

Time, 18.50 milliseconds

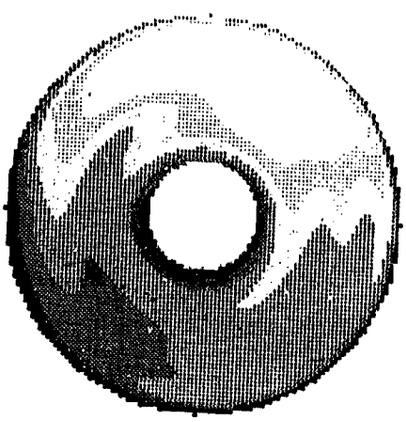

Time, 27.50 milliseconds

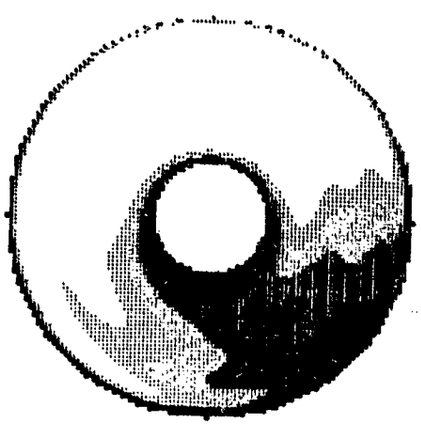

Time, 30.25 milliseconds

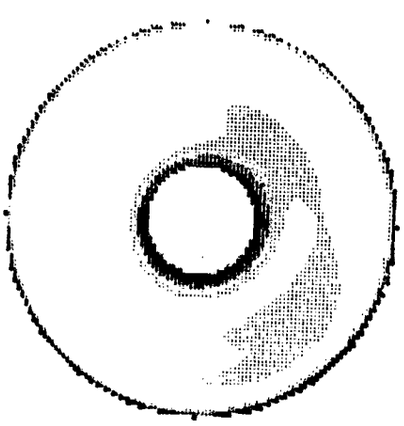

Time, 32.25 milliseconds

Figure IX-21

EFFECT OF VORTEX GENERATORS ON DISTORTION

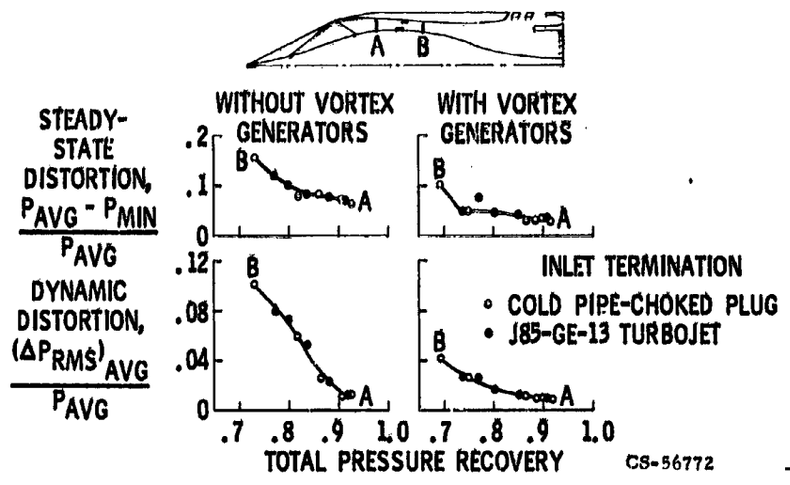

Figure IX-22

RESONANT INLET DYNAMIC DISTORTION

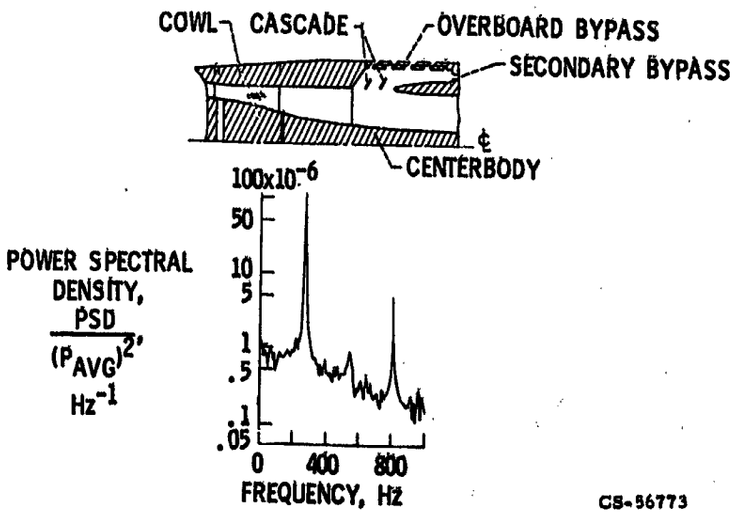

Figure IX-23

X. EFFECTS OF ENGINE INLET DISTURBANCES ON ENGINE STALL PERFORMANCE

John H. Povolny, F. W. Burcham, Jr.,* James E. Calogeras, Carl L. Meyer, and Richard A. Rudey

The operating limits of propulsion systems may restrict the capabilities of both subsonic and supersonic aircraft. One such limit of gas turbine propulsion systems is compressor stall or surge. The performance and operating limits of the engine, especially the compressor system, are influenced by the flow conditions at the engine inlet. This leads to the necessity of adequately matching the inlet and engine so that the capabilities of the aircraft are not compromised by the condition of the flow supplied by the inlet to the engine or the susceptibility of the engine compressor system to this flow. It should be noted that, in addition to the inlet design parameters, the condition of the flow is also determined by external influences such as armament firing, flight maneuvers, thrust reversal, inlet unstart, inlet buzz, etc., some of which cause temperature as well as pressure disturbances. In order to better understand the flight environmental disturbances and their effects on the operating limits of turbine engines, research programs are being conducted at both the NASA Flight and Lewis Research Centers. This paper discusses data obtained from these programs.

FLIGHT ENVIRONMENT

The program at the Flight Research Center includes work with the F-111 airplane shown in figure X-1. Measurements were made at the engine face during the flight of this airplane to show the nature of some of the disturbances that stall the engine. The flight data to be discussed were obtained by the NASA Flight Research Center during tests of an early model F-111A airplane, which was powered by TF30 P-1 engines. Eight total pressure rakes, each with five probes, were installed at the engine compressor face. Four diagonally oriented rakes contained

*NASA Flight Research Center.

miniature transducers for high-response pressure measurements, and the remaining four rakes were for the low-response measurements.

Figure X-2 shows four representative high response compressor-face pressures at 400 samples per second obtained for a compressor stall at a flight Mach number of 2.17 and an altitude of 44 000 feet. Traces A and B are from the 1:30 o'clock rake, which is located in an area of generally high-recovery, and lower traces A' and B' are from the 7:30 o'clock rake which is in a low-recovery region. The difference in pressure levels between the two rakes is an indication of the existence of a steady-state pressure distortion. The rapid pressure fluctuations evident in each trace indicate a variation in distortion that can be either greater or less than the steady-state value depending on the phase relationship between opposite halves of the duct. All four traces show essentially random dynamic pressure variations before stall, with a greater peak-to-peak fluctuation at the 7:30 o'clock rake, which is in the low-recovery region. Note, however, that at the time that the stall was initiated, both 1:30 rake pressures are high and both 7:30 rake pressures are low. The resulting increase in instantaneous distortion over the steady-state distortion was sufficient to stall the engine.

Figure X-3 shows the compressor-face total-pressure recovery maps for this stall. These maps are similar to those presented during the discussion of inlet performance. The low response rake map on the left defines the steady-state distortion and shows a moderately severe 180° distortion pattern with a 10-percent $\Delta p/p$. The compressor-face map on the right was made from the high-response pressures at the time that the stall was initiated, and it defines the instantaneous distortion. No radical difference in pattern is evident, but the spread between the high- and low-recovery areas is greater, and $\Delta p/p$ is increased to 14 percent. This higher value of instantaneous distortion lasted for about one revolution of the fan and is considered to be responsible for initiating the stall.

In the case just discussed, there were no predominant or resonant frequencies present in the inlet flow. Figure X-4 shows a different flight condition, Mach 2.0 and 45 000 feet altitude, where a strong duct resonant mode was present. In this figure power spectral density (PSD) is shown as a function of frequency wherein PSD is defined as

$$\frac{(\Delta P_{rms}/P_{av})^2}{Hz}$$

where ΔP_{rms} is the root mean square value of the fluctuating component of pressure.

Data are presented for all 20 high-response pressures. A predominant peak at 27 hertz is evident in all cases, and a harmonic at 54 hertz can also be seen. Examination of the phase relationships between the corresponding 1:30 and 7:30 o'clock rake pressures showed that these pressures were about 180° out of phase at the 27 hertz resonance and had an essentially random phase relationship at other frequencies. Evidence of this was also seen in the inlet duct, at the cowl lip, and in the engine. Thus there existed a situation wherein each half of the inlet duct was resonating 180° out of phase with the other half.

Basically, then, there are both steady-state and dynamic disturbances to deal with at the engine inlet. Thus, in order to understand what causes the engine to stall, it is necessary to look at the effect of each disturbance individually as well as in combination. This is what is being done at the Lewis Research Center.

ENGINES INVESTIGATED

The work has been primarily with three types of engines (see fig. X-5). The top illustration is a sketch of the General Electric J85 afterburning turbojet engine that was tested. The J85 has a single spool rotor with an eight-stage axial compressor (including inlet guide vanes) driven by a two-stage turbine. The middle illustration is a sketch of the fixed geometry turbofan that was tested; this engine was a Pratt & Whitney TF30. The TF30 has a two-spool rotor with a three-stage fan (including inlet guide vanes) and a six-stage axial compressor driven by a three-stage turbine on the low spool, and a seven-stage axial compressor driven by a single-stage turbine on the high spool. The bottom sketch illustrates the variable geometry turbofan that was tested; this engine was a General Electric 1/10. The 1/10 had a two-spool rotor with a two-stage fan (no inlet guide vanes) driven by a two-stage turbine on the low spool, and a seven-stage axial compressor driven by a two-stage turbine on the high spool. The compressor of this engine was equipped with variable inlet guide vanes and variable first-stage stators. It should be noted that, although all three engines are equipped with afterburners, none of the data presented herein are with afterburning.

STEADY-STATE PRESSURE DISTURBANCES

The first area to be examined will be the effects of various steady-state pressure distortions on the stall performance of these engines. During these discussions it will be shown where the weak link is in the compressor system, particularly for

the more complicated engines. Also shown are some cases of interactions between the fan and the compressor in one of the turbofans and a simplified technique for correlating the effects of circumferential distortions where these are the predominant engine sensitivity. It should be noted that in most cases the stall limit referred to is hard stall rather than rotating stall.

Effect of Type of Distortion

Figure X-6 illustrates the effect of the shape, or the type, of the total-pressure distortion on the stall line of the simple turbojet engine. It shows a standard map of compressor total pressure ratio as a function of corrected airflow rate for the J85-13 engine used in this program. The dashed lines represent the compressor map determined with clean, or undistorted, airflow into the compressor. The solid lines are the stall lines for the distorted inflow cases shown. The total-pressure distortions were produced by placing screens, shown as the shaded regions in each of the patterns, approximately one compressor diameter upstream of the inlet guide vanes. For all of the patterns shown here, the screens were of about the same intensity or porosity. This resulted in about the same distortion amplitude $(P_{av} - P_{min})/P_{av}$ for each of the patterns at a given engine speed.

As can be seen, the hub radial distortion pattern had little effect on the stall line of the compressor, but the tip radial distortion caused a more serious loss in the stall compressor pressure ratio. It was the circumferential distortion pattern shown in the lower right, however, that caused the most loss in compressor pressure ratio at stall. One of the more surprising results occurred when a 120° sector of the hub radial pattern was tested. Although the pure hub radial pattern had little effect on the stall line, the partial radial distortion caused a much more serious stall line degradation. This degradation has been directly attributed to the circumferential component of the distortion pattern.

Inasmuch as circumferential distortion, or the circumferential component of a combined distortion, had the most serious effect on the compressor, the question arose as to the effect of the extent of the circumferential distortion on compressor performance at stall. Data relative to this question are presented in figure X-7. This figure shows the loss in the compressor pressure ratio at stall (the difference between the clean and distorted stall pressure ratios) as a function of screen angle β. Each curve corresponds to a constant corrected engine speed. All the screens used to generate these data were of the same intensity or porosity in order to isolate the effect of circumferential extent. For each of these curves, the loss in stall compressor pressure ratio increased rapidly as the screen angle was

increased from 0^{o} to about 60^{o}. Increasing the screen angle from 60^{o} to 180^{o} had no further effect on the stall line of the compressor. This indicates that 60^{o} is the critical angle of distortion for the J85 compressor. This critical angle is related to the time required by the compressor to respond to a distortion in a quasi-steady-state manner.

Circumferential Distortion Correlation

It would be desirable to have a single curve with which to correlate this loss in stall compressor pressure ratio with a simple circumferential distortion index which accounted for variations in circumferential intensities and extents, as well as engine speed. Several correlation techniques currently in use were tried, and the one which worked best is shown in figure X-8. In this figure, loss in stall compressor pressure ratio is plotted as a function of the ratio of minimum to maximum pressures measured at the compressor inlet station. In order to account for the varying compressor sensitivity to circumferential extents less than 60^{o}, the $P_{min,\,60^{o}}$ used here has been defined as the lowest mean pressure in any 60^{o} sector of the flow field. For example, with the sinusoidal circumferential distortion shown in this figure, the $P_{min,\,60^{o}}$ would be the average pressure of the cross-hatched region.

All of the stall points obtained with pure circumferential distortions are shown in this figure. These include screens of three different porosities, of extents from 30^{o} to 180^{o}, and engine corrected speeds ranging from 87 to 100 percent of the rated engine speed. But, regardless of the extent or intensity of the circumferential distortion, these data correlate quite well with this simple distortion index as long as the critical angle of distortion is taken into account. Of course, the single curve faired through the data can easily be converted to a $(P_{av} - P_{min})/P_{av}$ type of index for more general application, if that is so desired.

Turbofan Weak Link

The foregoing results were for a simple engine with a single compressor. The effect of steady-state pressure distortions on an engine with a more complicated compressor system (the fixed geometry turbofan) will now be examined to see where the weak link compressor component is. This engine was also primarily susceptible to circumferential distortions. Figures X-9 and X-10 together show the operating limits of the fan and low-pressure compressor on maps of pressure ratio as a func-

tion of corrected rotor speed. On both maps, the dashed lines represent the operating line and stall limit without distortion, and the solid lines, the stall limits with two screen-induced fan inlet distortions. Distortion amplitudes, which vary with airflow and therefore rotor speed for a given screen, are shown. Without inlet air distortion, the pressure ratio margin between the operating line and stall limit was greater for the fan than for the low pressure compressor. As a result of the screen induced distortions, the fan stall limits were lowered but remained parallel to the operating line so that pressure ratio margin remained. The low-pressure compressor stall limits, however, were also lowered by the distortions. But they intersected the operating line so that the pressure ratio margin became zero. Therefore, with simple steady-state 180° circumferential distortions at the fan inlet, the weak link component of this fan-compressor system was the low-pressure compressor rather than the fan. The high-pressure compressor was not affected by these fan inlet distortions. They were apparently attenuated before entering that unit.

Reynolds Number and Component Interaction Effects

Effect of Reynolds number index. - It has been observed that both altitude and flight Mach number can influence tolerance for steady-state distortion. This can be seen in figure X-11 which illustrates the effect of Reynolds number on the steady-state distortion tolerance of a TF30-P-3 turbofan operating with its bleeds closed. These results are for simple 180° circumferential distortions. Stall limits are shown in terms of distortion amplitude which resulted in stall as a function of corrected fan rotor speed. Stall-limit curves are shown for various levels of Reynolds number index (ReI). This index is the Reynolds number at the test condition expressed as a fraction of the Reynolds number at standard sea-level static conditions. (The curve for an ReI = 1.0 was estimated.) It can be seen that distortion amplitudes at stall decreased considerably as Reynolds number was reduced by going to higher altitudes. The trend of decreased distortion amplitudes at stall with lowered corrected fan rotor speed indicates that increased flight Mach number would also reduce distortion tolerance. This is because increased flight Mach number results in higher inlet temperature and therefore lowered corrected rotor speed.

It is interesting to note that the weak link on this turbofan engine was not the first component to be hit by the steady-state pressure distortion, but was the second one, that is, the low pressure compressor. It should also be noted that there did not appear to be any interactions between the fan and the compressors although the possibility should be recognized that the large Reynolds number effect could involve such an interaction. Whether this is so remains to be determined for this engine,

but one engine for which it was found to be true is the variable-geometry turbofan that was tested. The next two figures help illustrate this situation.

We encountered the first type of interaction while exploring inlet Reynolds number effects on engine performance with no distortion at the inlet. As you would expect, reducing the engine inlet ReI from 0.41 (nominal test value) to 0.18 resulted in a loss in the operating margin of the fan. This loss, however, was smaller than the loss in margin that was experienced by the high-pressure compressor. This is shown in figure X-12. As before, compressor performance is shown on the conventional pressure ratio-flow rate map. All values are normalized in terms of the rated performance of this component. The stall limit for each ReI was obtained by throttling at the compressor discharge until stall was encountered. As shown, the main effect of the lower engine inlet ReI was to cause a shift in the compressor operating line; very little effect was found in terms of stall pressure ratio. However, the operating line shift caused a significant reduction in the available margin between the stall limit and the operating line.

This operating line shift is attributed to a change in the flow out of the fan which caused a change in the velocity profile going into the compressor. This is shown in figure X-13. Here, the variation in inlet axial velocity with passage height is shown for both engine ReI's of 0.41 and 0.18. The data were obtained at similar engine operating conditions of rotational speed and exhaust nozzle area. The large velocity gradient that was obtained at the ReI = 0.41 is a result of the curving flow path from the fan discharge to the high-pressure compressor inlet. As the engine inlet ReI was reduced, this velocity gradient was effected in two ways. First a steeper variation in velocity from hub to tip was obtained, and second the overall velocity level decreased. The end result of both of these changes is a slight shift in pressure ratio due to the change in incidence angle at the compressor inlet and a reduction in airflow through the compressor due to the overall decrease in velocity. These effects were the principal reasons for the compressor operating line shift. Since the differences in these profiles in figure X-13 are the result of a change in flow conditions out of the fan hub, the loss in compressor stall margin is attributed to the Reynolds number effect on the flow out of the fan and not to the effect on the compressor per se, because the ReI at the compressor inlet was very high in both cases. It should be noted that this type of component interaction can have a significant impact on stall sensitivity of an engine when operating at high altitudes (low ReI). Although the data just presented dealt with Reynolds number effect without distortions being present at the engine inlet, it is anticipated that the effect would be similar with distortion.

Effect of rotating stall. - Another component interaction encountered involved rotating stall in the fan of the variable geometry turbofan. This type of flow insta-

bility was found with both hub and tip radial distortions. Figure X-14 shows the effect of a hub radial distortion on fan performance. Here again, the conventional pressure ratio-flow rate map is used. The dashed lines represent the undistorted performance, and the solid lines the distorted performance. Several values of distortion amplitude are shown as a reference to indicate distortion magnitude.

The main effect of the hub radial distortion was the indicated reduction in fan stall pressure ratio. A slight change in the operating line was also obtained. This indicated reduction in the stall limit was not caused by an abrupt stall in the fan. High response data indicated that the flow was breaking down in the high-pressure compressor and that this flow breakdown was preceded by a rotating stall in the fan. This sequence of events is illustrated in figure X-15 wherein high response pressures at the fan inlet, fan outlet, high-pressure compressor inlet, and high-pressure compressor outlet are shown as they varied with time. (These are only a few of the many pressures recorded during a stall.) A rotating stall cell is indicated by the periodic fluctuation in the fan outlet pressure. As the fan discharge was throttled towards the stall limit, the magnitude of the rotating stall increased, and an abrupt stall occurred in the high-pressure compressor. This is shown by the simultaneous drop in the outlet pressure and rise in the inlet pressure. This stall was then propagated forward through the fan. These results illustrate a component interaction where a small flow instability, such as a rotating stall in one component, caused a serious flow problem, such as abrupt stall in a downstream component. The fan rotating stall did not seriously affect engine operation by itself, but it did cause the high-pressure compressor to stall, thus reducing the stall limit of the engine.

Distortion amplification. - Another type of component interaction that was encountered while testing the variable geometry turbofan engine was related to an amplification of circumferential distortion through the fan. During the initial testing of this engine, the engine stall limit was reduced more than expected by circumferential distortions. The limiting component was again the high-pressure compressor. However, the cause of this lower limit was traced to higher than expected pressure distortions at the high-pressure compressor inlet for a given engine inlet distortion. Since the high-pressure compressor inlet flow conditions are established by the fan hub characteristics, the distorted performance of the fan hub was evaluated, as shown in figure X-16. In this figure is plotted a distortion amplitude ratio as a function of the total to static pressure ratio at the fan hub inlet. This amplitude ratio is defined as the ratio of the fan hub outlet to inlet distortion strength. Values of amplitude ratio greater than one indicate a distortion amplification or increased distortion strength; values less than one indicate an attenuation or decrease in distortion strength. The total to static pressure ratio is an indication of inlet axial velocity. Low values imply low velocity and higher values imply higher velocity. As can

be seen, the distortion amplification was strongly influenced by inlet velocity, varying from 2.5 at low values to about 1.0 at high values. Another way to look at this velocity effect is with the use of a fan equivalent stage characteristic curve as shown in figure X-17. Here, the fan hub performance is plotted in terms of a pressure coefficient as a function of flow coefficient. These coefficients are pressure ratio and inlet axial velocity functions normalized in terms of blade speed. The curve represents the overall performance of both fan stages. The curve can be divided into two performance regions: (1) a region behind an inlet distortion screen, shown by the solid symbols, and (2) a region not behind a distortion screen shown by the open symbols. These two regions can be related to low and high inlet pressure, respectively. In this figure, zero amplification would occur when the pressure coefficients in both regions were equal. If we use the square symbols as a typical example of distorted performance, it can be seen that the pressure coefficient behind the distortion screen is less than that not behind the screen. In other words, less pressure rise was realized in the low inlet pressure region than in the high inlet pressure region. This indicates an increase in distortion amplitude at the fan hub outlet. This agrees with the amplification shown in figure X-16.

In an attempt to change this fan hub characteristic, the engine manufacturer modified the first-stage rotor by increasing the blade chord length by a factor of 4/3 and reducing the number of blades by 3/4. Solidity and blade angles remained constant, and no change in blade loading was made. The second-stage rotor and both stators were not changed. The result of this modification is shown in terms of pressure and flow coefficients in figure X-18. Here, both the modified and the original hub characteristic curves are shown. A significant change in the pressure-flow characteristic is obvious, especially behind the distortion screen as shown by the solid symbols. If the square symbols are again used as an example of distorted performance, we now see that the pressure coefficient behind the distortion screen is larger than that not behind the screen. Therefore, more pressure rise was realized in the low inlet pressure region than in the high inlet pressure region. This indicates a decrease in distortion amplitude at the fan hub outlet. The effect of this change is shown in figure X-19 in terms of amplitude ratio as a function of total to static pressure ratio. Both the modified and original results are shown for comparison. It can be seen that a marked improvement in the fan hub distorted performance was realized. The modified fan attenuated the circumferential distortions, and the original fan amplified these distortions.

These results again illustrate a situation where a flow problem in one component can adversely affect a downstream component. Amplification of distortions through a fan can reduce the engine stall limit because it effects the stall performance of the compressor behind it. Recognizing and understanding interactions like these is

necessary in order to correct the deficient component. The case that was just described, is one example of a correction that was effective in reducing an interaction problem. Two things to be learned from this study are that there can be very significant interactions between compressor components and that what appear to be minor blading changes can have significant effects on the performance. Because the detailed flow processes involved in the foregoing phenomena are not completely understood, the compressor research people have some additional work to do.

DYNAMIC PRESSURE DISTORTIONS

In this section the effects of dynamic disturbances on the stall characteristics of two engines, the simple turbojet and the fixed geometry turbofan, are examined. Before looking at the engine data, however, it would be well to discuss briefly some of the research techniques that were employed.

Research Techniques

Figure X-20 shows a photograph of the simple turbojet (J85) with a flight type inlet installed in the Lewis 10- by 10-foot supersonic tunnel. For the tests to be discussed the tunnel was operated at Mach numbers up to 2.5. The inlet and engine were operated so that inlet unstarts were initiated to determine their effect on the engine, and engine stalls were initiated to determine their effect on the inlet.

The tests on the fixed geometry turbofan (TF30) were conducted in the Lewis propulsion system laboratory altitude test chamber wherein a unique device for creating dynamic disturbances was employed. This device (or technique) is being used to create controllable dynamic or steady-state pressure disturbances at the inlets of engines being tested in the altitude facilities. The technique uses many small air jets upstream of the engine inlet. Figures X-21 and X-22 show the main features of the air jet system. The photograph (fig. X-21) is a view looking toward the engine from the bellmouth entrance of the inlet duct. Primary airflow passes through the bellmouth and inlet duct to the engine. The air-jet system includes an array of small nozzles in the inlet duct. These air-jet nozzles are uniformly distributed in an axial plane and are arranged in a pattern which repeats every 60° of circumferential extent. As indicated in the schematic, secondary airflow is injected from these nozzles and is directed counter to the primary airflow. Flow control of the secondary airflow is provided for each 60° sector of air-jet nozzles by six valves external to the inlet duct. These are high-response valves of NASA design for opera-

tion over an oscillatory frequency range from 0 to about 200 hertz. Separate matched flow lines are provided from each of these valves to each of the air-jet nozzles of a 60° sector. Secondary air is supplied to the valves at pressures up to about 10 atmospheres. Through control with these valves of the secondary-air distribution and the flow rate, a variety of basic dynamic or steady-state inlet pressure disturbances can be created for engine tests.

It has been hoped for some time that the air-jet system could be used to approximately simulate an actual flight environment. Recently, one series of tests to check that potential capability was completed. NASA Flight Research Center cooperated in this and made available engine inlet pressure data from flights of an F111A. Representative pressure data from flight, on analog tape, were used to provide input signals to the high response valves of the air-jet system for engine tests in the Lewis altitude facility. Figure X-23 shows one comparison of the flight environment and the attempted simulation on the basis of power spectral density of inlet pressures over the frequency range from 0 to 200 hertz. This is a favorable comparison. Both sets of data include PSD spikes at 27 and 54 hertz, with the simulation data somewhat attenuated (in these spikes) relative to the flight data. However, the general PSD level of the simulation data is comparable to that of the flight environment. This may or may not be a representative comparison, but is encouraging. Many more comparisons of the data from the flight and simulated environments must be made. Until that is done, conclusions cannot be reached as to the capability of the air jet system to approximate simulation of an actual flight environment.

Inlet-Engine Interactions

Now that the dynamic disturbance testing techniques have been described, some of the results will be examined, starting with the 10 by 10 foot SWT inlet unstart tests on the simple turbojet with a flight inlet. Figure X-24 is a time history of an inlet unstart with the engine operating at 85 percent corrected speed at Mach 2.5 tunnel conditions. (An inlet unstart causes a rapid drop in the compressor inlet pressure.) Shown in this figure as a function of time are the compressor total pressure ratio and the compressor inlet and the exit total pressures, both as ratios of free-stream total pressure. Looking first at the compressor inlet pressure, it can be seen that after inlet unstart this pressure rapidly reaches its minimum in about 0.01 second. On the other hand, there is a significant lag in the pressure drop of the compressor exit total pressure which is associated with the volume effect of the combustor. This lag caused the compressor pressure ratio to rise far above the steady-state stall line for a time equal to about $2\frac{1}{2}$ rotor

revolutions, which time was sufficient to cause compressor stall, as well as combustor blowout.

The effects of this particular unstart transient, as well as some less severe unstart transients, are summarized in figure X-25. This figure shows both the initial and the peak compressor pressure ratios that occurred during the inlet unstarts. The bar on the right represents the Mach 2.5 data just described. The three bars to the left pertain to inlet unstarts at Mach 2.0 with the engine operating from three different initial pressure ratios on the 86-percent corrected speed characteristic. By comparing the relative amplitudes of the bars, you can see that the Mach 2.0 unstart transients were much less severe than the Mach 2.5 transient. But still, depending on the initial compressor operating point, results ranged from no stall to stall and combustor blowout.

Figures X-26 and X-27 show some interstage static pressures during the large-scale transients just discussed. Shown in figure X-26 are time histories of static pressures located at the compressor inlet and at the exits of the first seven stages of the eight-stage compressor. These traces pertain to the inlet unstart that was initiated at Mach 2.5 during engine operation. Almost immediately upon inlet unstart, the pressures at the compressor inlet and all the way through the compressor drop rapidly with time, until that time when all pressures abruptly start to rise. This previously mentioned, this Mach 2.5 unstart transient was severe enough to cause compressor stall as well as combustor blowout. The origin of a stalled zone in a compressor stage causes an abrupt loss in the airflow pumping of that stage. This is analogous to closing a high-response valve. A compression wave is sent forward of the valve, or stalled zone, and an expansion is sent rearward. So the abrupt rise in pressures seen all the way through the seventh stage indicates that stall originated in the eighth, or the last, stage of the compressor. Thus a disturbance at the inlet to the compressor caused a stall which originated at the rear of the compressor.

In contrast, figure X-27 shows what occurs to these same pressures in the compressor when, at the same initial engine and tunnel conditions, the compressor is forced into stall by closing the exhaust nozzle. In this case, the rise in pressure is seen at the compressor inlet and through the first two stages of the compressor, while at the same time the exit of the third stage shows an abrupt drop in pressure, indicative of stall origin in that stage. Thus in this case, a disturbance at the rear of the compressor caused stall which originated in the front stages.

In addition to an inlet unstart, which is initially a single pulse resulting in a rapid decrease in engine inlet pressure, there are other types of rapid pressure disturbances encountered that can also stall the engine. For example, inlet buzz, which can be undistorted cyclic disturbance, and duct resonance, encountered by the F-111, wherein each half of the duct is 180° out of phase with the other.

Effect of Pressure Transients Without Spatial Distortion

The effects of dynamic inlet pressure variations, without distortion, will be considered first. These will include cyclic pressure variations that are analogous to inlet buzz and the pressure-depression pulse which is similar to an inlet unstart.

Figure X-28 illustrates the tolerance of a TF30-P-1 turbofan for dynamic fan-inlet pressure variations induced with the air jet system. Stall limits are shown in terms of pressure amplitude which resulted in stall as a function of disturbance frequency for both cyclic and pulse pressure variations. The particular pulse had a pressure-time response of about 40 to 60 hertz, and is shown at that frequency. Pressure amplitude is schematically defined by the sketches in the figure for both the cyclic and pulse cases. In both cases, pressure amplitude is defined as the ΔP of the pressure depression expressed as a fraction of the pressure level before the disturbance. The pressure amplitude at stall with cyclic variations ranged from about 0.165 to 0.145 in the frequency range from 1 to 20 hertz, and with the pulse was about 0.16. It is apparent, though, that rapid changes in inlet pressure even without distortion can result in stall.

As for the turbojet, rapid changes in inlet pressure also can cause problems in those components of the fan-compressor system of the turbofan which are followed by large volumes. The tolerance of a TF30-P-1 turbofan to cyclic fan-inlet pressure variation without distortion was restricted by the high pressure compressor rather than the fan or low pressure compressor. Figure X-29 shows the time histories of several pressures during the last cycle of a 10-hertz cyclic fan-inlet pressure oscillation which resulted in stall. Variations of total pressures with time are shown at the fan inlet, the fan exit in the tip and hub regions, the middle and exit of the low pressure compressor, and the middle and exit of the high pressure compressor. Stall was found to originate in the high pressure compressor which, of course, is followed by the combustor volume. The sudden reduction in flow associated with stall caused a decrease in pressure aft of the stall (for example, at the high pressure compressor exit) and rapid increases in pressure forward of the stall initiation as stall progressed forward through the low pressure compressor and fan, until a hammershock appeared at the fan inlet.

The time histories of total pressure variations leading to stall were used to obtain time histories of pressure ratios across various stage groups of the fan-compressor system. Figure X-30 shows the time histories of various stage-group pressure ratios that were obtained. Variations of pressure ratios with time are shown for the fan hub and tip regions, the high pressure compressor front and rear stage groups, and the low pressure compressor front and rear stage groups. To the

right of the figure are noted the steady-state pressure ratios which existed for the various stage groups before the 10-hertz cyclic inlet pressure oscillation was induced. It can be seen that the maximum pressure ratio swings were made by the fan and the rear-stage group of the high pressure compressor - both of which are followed by large volumes. Pressure ratios of the fan hub and tip oscillate to values well above the steady-state levels. The fan, however, had sufficient pressure ratio margin and was not the weak link component. In the high pressure compressor, pressure ratios of the front-stage group oscillate but remain below the steady-state level, but those of the rear-stage group oscillate about a mean which is above the steady-state level. Pressure ratio swings of this rear-stage group to values well above the steady-state level, together with the pressure-time traces indicate that it was this stage group in which stall initiated and which was the weak link.

Effects of Pressure Transients With Spatial Distortion

It will be recalled that a duct resonance, which resulted in an oscillating distortion at the engine inlet, was observed from the F111A flight data. The air jet system has been used to induce dynamic inlet distortions of this and other types for engine tests.

Figure X-31 illustrates the tolerance of a TF30-P-1 turbofan for an oscillating 180° circumferential distortion, which is analogous to that duct resonance situation. Stall limits are shown in terms of the distortion amplitude which resulted in stall as a function of frequency of the oscillation. For comparison, distortion amplitudes at stall are noted for a steady-state 180° distortion and for a single pulse pressure depression of a nominal 180° circumferential extent. Distortion amplitude is defined as before. The fan-compressor system was able to tolerate larger distortion amplitudes with oscillating distortion than with steady-state or pulse distortions. The tolerance to oscillating distortions tended to decrease with increasing frequency of oscillation, and approached the steady-state distortion tolerance level at a frequency of about 60 hertz.

Figure X-32 illustrates the tolerance of the same engine for rotating 180° circumferential distortions. Stall limits are shown in terms of distortion amplitudes that resulted in stall as a function of the frequency of rotation for contrarotating and corotating distortion. For comparison, distortion amplitudes at stall are again noted for the steady-state and pulse 180° distortions. It can be seen that the fan-compressor system was able to tolerate larger distortion amplitudes with contrarotating than with corotating distortion. With corotation, tolerance at low rotational frequency was nearly comparable to that with steady-state distortion. There was a

sharp decrease in tolerance to corotating distortion at rotational frequencies above 60 hertz, with the distortion amplitude at stall decreasing to a level somewhat below that associated with the pulse distortion when corotation frequency was about 70 hertz. For the particular engine and its operating conditions, a corotation frequency of about 72 hertz corresponds to half rotor speed. This is approximately the frequency of a single-zone rotating stall.

The results presented in figures X-28 to X-32 indicate that this fan-compressor system had the least tolerance for (1) a corotating distortion at a rotational frequency of about half-rotor speed, and (2) the pulse distortion. The results suggest that distortion tolerance is a function not only of instantaneous distortion level but also rate of change of inlet pressure and dwell time of the fan-compressor blading in the low pressure region of an engine-inlet distortion.

TEMPERATURE DISTURBANCES

Although no intensive investigation of temperature disturbances was conducted, some data have been obtained showing the effects of steady-state temperature distortions and temperature transients on the stall characteristics of the variable geometry turbofan. This work is limited, but the results are sufficiently interesting to be included herein.

Tests were conducted to determine the effect of the extent and magnitude of a spatial temperature distortion and the effect of extent, magnitude, and rate of change for time-variant temperature disturbances. A gaseous hydrogen fueled heater was used to produce both the spatial and time-variant temperature disturbances. A photograph of this heater is shown in figure X-33. This view is looking from the heater inlet, downstream towards where an engine inlet would be located. The heater is divided into four controllable 90° sectors, each containing an array of V-gutter flameholders and swirl can pilot burners. The engine inlet air was heated by burning hydrogen in the V-gutter flameholders.

Effect of Spatial Temperature Distortions

The most sensitive component of the compressor system with either spatial or time-variant distortions was the high pressure compressor. This sensitivity to spatial distortion is shown in figure X-34 which presents a conventional pressure ratio - flow rate map for the high-pressure compressor. For both 180° and 90° circumferential distortions, shown by the symbols, the loss in stall pressure ratio

varied directly with distortion magnitude as indicated by the levels of ΔT shown. These ΔT values are the difference between the temperature of the heated and unheated portions of the engine inlet flow. For temperature differentials in excess of 100° F, compressor stall occurred on the undistorted operating line, thus completely eliminating the operating margin of the engine. These results show that this engine was more sensitive to the magnitude or ΔT of a spatial distortion than it was to the circumferential extent, at least for the 90° and 180° extents tested.

Effect of Temperature Transients

The effect of time variant temperature disturbances on this same engine are shown in figure X-35 which is a plot of the rise in engine inlet temperature during a transient as a function of the rate of change in engine inlet temperature. The symbols specify the three circumferential extents that were imposed at the engine inlet. All of the stalls encountered during these transients were initiated in the high pressure compressor. For all three circumferential extents tested, the minimum rate of change in engine inlet temperature associated with engine stall was approximately 2500° F per second. A rise in inlet temperature of approximately 50° was associated with stall at this rate of change. This value of ΔT is significantly less than the ΔT required to stall the engine on its operating line as shown on the ordinate for the 90° and 180° steady-state spatial distortions. As higher rates of change were imposed at the engine inlet, higher inlet temperature rises were associated with stall. The relationship between the rise and rate of change in engine inlet temperature was a constant for all engine stalls obtained. This constant was equal to 0.02 second.

The results of the transient tests indicate that for this particular engine: (1) the rate of change in engine inlet temperature was a primary factor on the rise in inlet temperature or ΔT at stall; (2) the high pressure compressor was the limiting component; (3) circumferential extent had little effect (for the range investigated) on the engine stall limit; and (4) a constant engine response or time to stall was obtained regardless of the rate of change in engine inlet temperature at stall.

With regard to the effects of combined pressure and temperature effects on engine stability, it can probably be said that a sudden increase in temperature along with a sudden decrease in pressure at the inlet to an engine would have more detrimental effect on engine stall than either of these by themselves. This conclusion is based on these temperature transient results plus the pressure pulse results previously discussed. If a sudden increase in temperature were coupled with a sudden

increase in pressure, the effect would likely be less than a temperature transient by itself.

CONCLUDING REMARKS

Now that the results of some of the NASA programs in the area of inlet engine disturbances and their effects on engine stall performance have been examined, it can be appreciated what a complicated field it is. It can also be appreciated how important it is to determine what is going on inside each type of engine and particularly to determine where stall is originating so that it can be ascertained where the weak link is. Once this is known, then, of course, it is much easier to remedy the situation.

SUMMARY OF RESULTS

The results of the investigation of the effect of inlet environmental factors that disturb engines show that, for steady-state pressure distortions, (1) the circumferential distortion effect was most severe, (2) the weak link is not usually the first stage or first component that sees the disturbance, (3) the distortion tolerance of turbofans is significantly affected by altitude, and (4) interactions between turbofan compressor components have significant effects on stall. Also, for dynamic pressure disturbances (1) rapid pressure changes without distortions can stall an engine, (2) compressor stages adjacent to large volumes go through the greatest pressure ratio excursions, and (3) combined pressure oscillations and distortions can have a greater effect than either individually.

BIBLIOGRAPHY

Baumbick, Robert J.: Device for Producing Dynamic Distortion Patterns at Inlets of Air-Breathing Engines. NASA TM X-2026, 1970.

Bellman, Donald R.; and Hughes, Donald L.: The Flight Investigation of Pressure Phenomena in the Air Intake of an F-111A Airplane. Paper 69-488, AIAA, June 1969.

Braithwaite, Willis M.; Dicus, John H.; and Moss, John E.: Evaluation with a Turbofan Engine of Air Jets as a Steady-State Inlet Flow Distortion Device. NASA TM X-1955, 1970.

Braithwaite, Willis M.; and Vollmar, William R.: Performance and Stall Limits of a YTF30-P-1 Turbofan Engine with Uniform Inlet Flow. NASA TM X-1803, 1969.

Burcham, Frank W., Jr.; and Hughes, Donald L.: Analysis of In-Flight Pressure Fluctuations Leading to Engine Compressor Surge in a F-111A Airplane for Mach Numbers to 2.17. Paper No. 70-624, AIAA, June 1970.

Calvert, Howard F.; Braithwaite, Willis M.; and Medeiros, Arthur A.: Rotating-Stall and Rotor-Blade-Vibration Survey of a 13-Stage Axial-Flow Compressor in a Turbojet Engine. NACA RM E54J18, 1955.

Harry, David P., III; and Lubick, Robert J.: Inlet-Air Distortion Effects of Stall, Surge, and Acceleration Margin of a Turbojet Engine Equipped with Variable Compressor Inlet Guide Vanes. NACA RM E54K26, 1955.

Huntley, S. C.; Sivo, Joseph N.; and Walker, Curtis L.: Effect of Circumferential Total-Pressure Gradients Typical of Single-Inlet Duct Installations on Performance of an Axial-Flow Turbojet Engine. NACA RM E54K26a, 1955.

Kimzey, W. F.: An Investigation of the Effects of Shock-Induced Turbulent Inflow on a YJ93-GE-3 Turbojet Engine. ARO, Inc. (AEDC-TR-66-198, DDC No. AD-377312L), Nov. 1966.

Langston, C. E.: Distortion Tolerance - By Design Instead of by Accident. Paper 69-GT-115, ASME, Mar. 1969.

Lubick, Robert J.; and Wallner, Lewis E.: Stall Prediction in Gas-Turbine Engines. J. Basic Eng., vol. 81, no. 3, Sept. 1959, pp. 401-408.

McAulay, John E.: Effect of Dynamic Variations in Engine-Inlet Pressure on the Compressor System of a Twin-Spool Turbofan Engine. NASA TM X-2081, 1970.

Meyer, Carl L.; McAulay, John E.; and Biesiadny, Thomas J.: Technique for Inducing Controlled Steady-State and Dynamic Inlet Pressure Disturbances for Jet Engine Tests. NASA TM X-1946, 1970.

Povolny, John H.: Stall and Distortion Investigation of a YTF30-P-1 Turbofan Engine. Presented at the USAF Aero Propulsion Lab. Airframe-Propulsion Compatibility Symposium, Miami Beach, Fla., June 24-26, 1969.

Reid, C.: The Response of Axial Flow Compressors to Intake Flow Distortion. Paper 69-GT-29, ASME, Mar. 1969.

Rudey, Richard A.; and Antl, Robert J.: The Effect of Inlet Temperature Distortion on the Performance of a Turbo-Fan Engine Compressor System. Paper No. 70-625, AIAA, June 1970.

Russey, Robert E.; and Lubick, Robert J.: Some Effects of Rapid Inlet Pressure Oscillations on the Operation of a Turbojet Engine. NACA RM E58A03, 1958.

Smith, Ivan D.; Braithwaite, W. M.; and Calvert, Howard F.: Effect of Inlet-Air-Flow Distortions on Steady-State Performance of J65-B-3 Turbojet Engine. NACA RM E55I09, 1956.

Staff of the Lewis Laboratory: Central Automatic Data Processing System. NACA TN 4212, 1958.

Wenzel, Leon M.: Experimental Investigation of the Effects of Pulse Pressure Distortions Imposed on the Inlet of a Turbofan Engine. NASA TM X-1928, 1969.

Werner, Roger A.; Abdelwahab, Mahmood; and Braithwaite, Willis M.: Performance and Stall Limits of an Afterburner-Equipped Turbofan Engine with and Without Inlet Flow Distortion. NASA TM X-1947, 1970.

Winslow, Larry J.; Wendland, Daniel W.; Smith, Brian D.; and Welliver, Albertus D.: Inlet Distortion Investigation - Upstream Engine Influence and Screen Simulation. Boeing Co. (AFAPL-TR-140, DDC No. AD-847095), Jan. 1969.

NASA FRC F-111A AIRPLANE

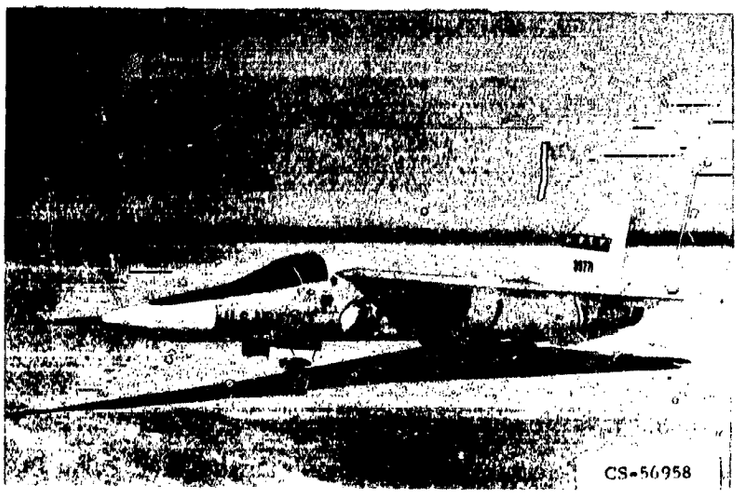

Figure X-1

TIME HISTORY OF ENGINE INLET PRESSURES

F-111A FLIGHT DATA; M = 2.17; 44 000 FT; LEVEL ACCELERATION

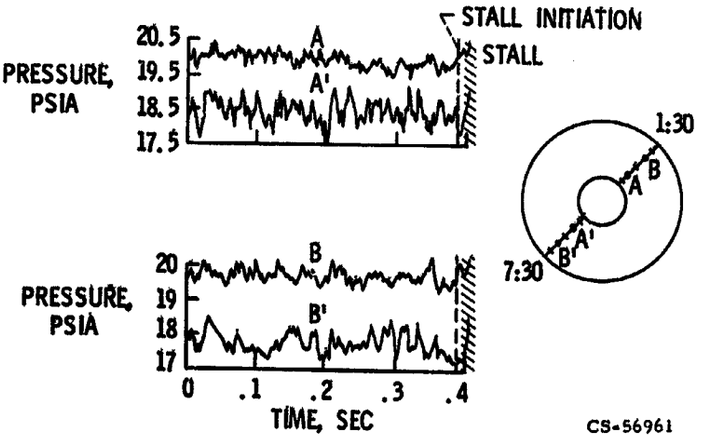

Figure X-2

ENGINE INLET PRESSURE CONTOURS AT STALL

F-111A FLIGHT DATA; M = 2.17; 44 000 FT

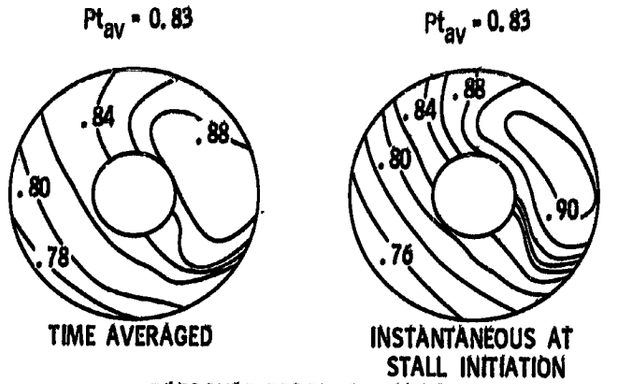

PRESSURE RECOVERY MAPS CS-56960

Figure X-3

PSD FOR ENGINE INLET PRESSURES DURING DUCT RESONANCE

F-111A FLIGHT DATA; M = 2.00; 45 000 FT; STEADY STATE

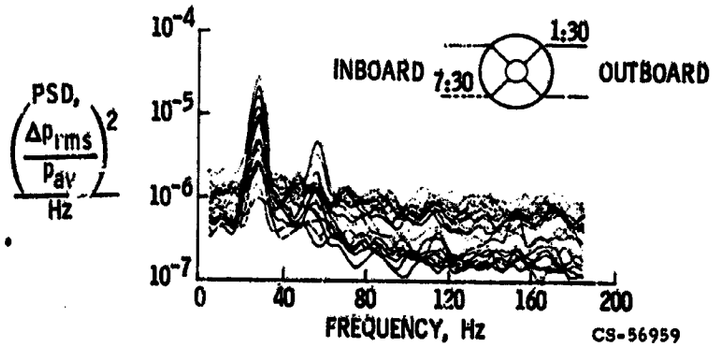

CS-56959

Figure X-4

ENGINES INVESTIGATED

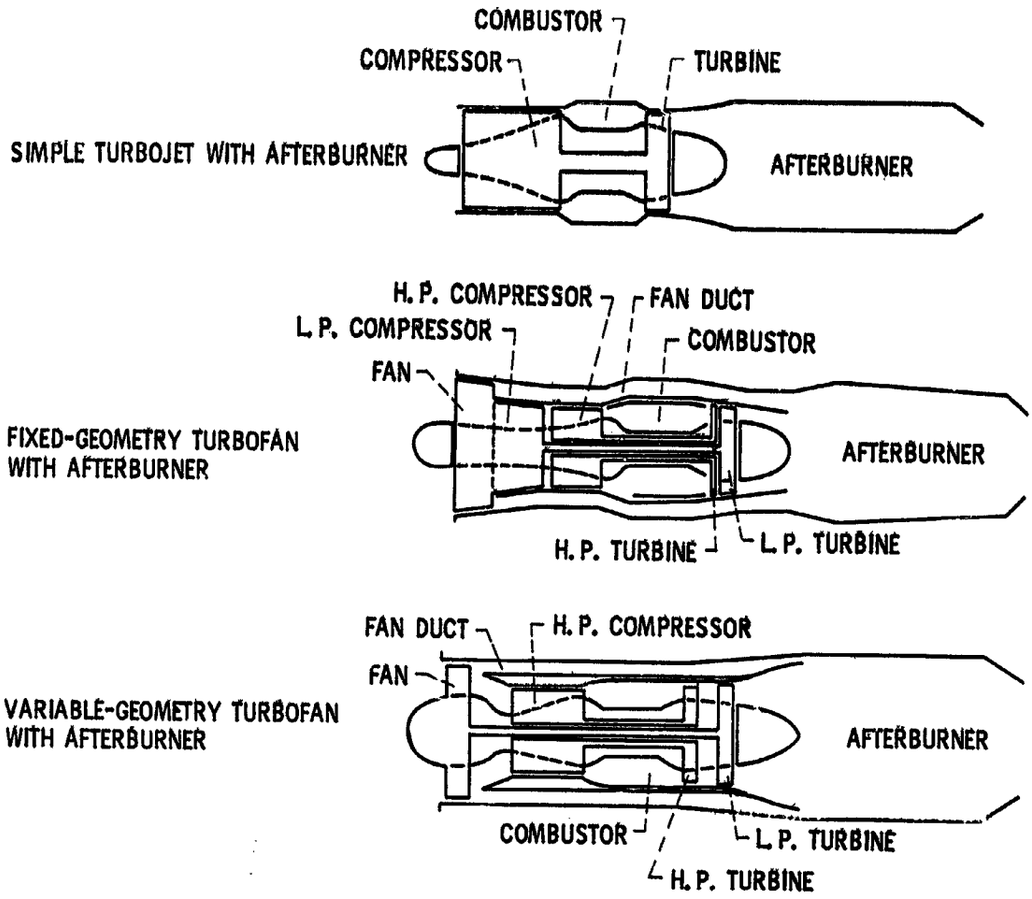

Figure X-5

CS-56991

EFFECT OF STEADY-STATE PRESSURE DISTORTION

SIMPLE TURBOJET

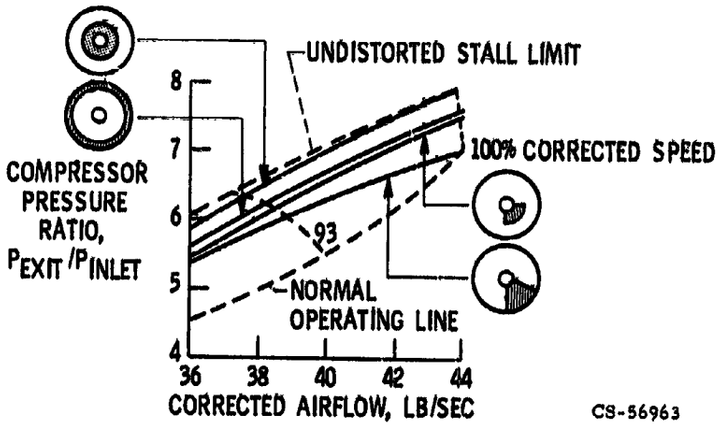

Figure X-6

EFFECT OF EXTENT OF CIRCUMFERENTIAL SPOILING ON COMPRESSOR PERFORMANCE

SIMPLE TURBOJET

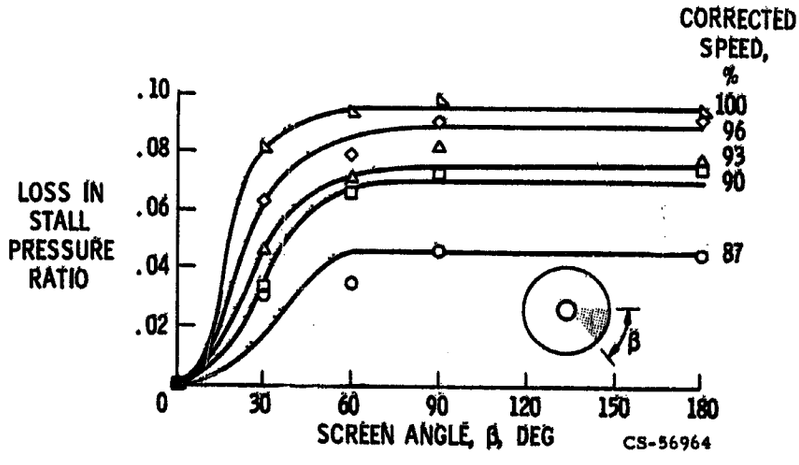

Figure X-7

CIRCUMFERENTIAL DISTORTION CORRELATION

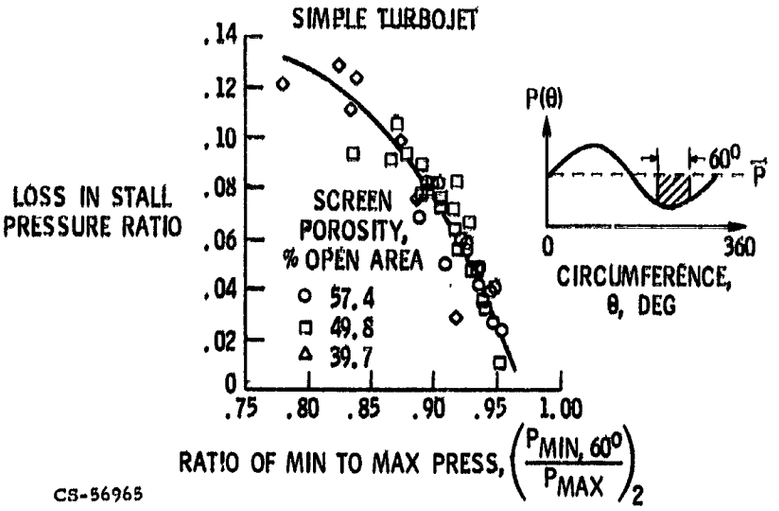

Figure X-8

EFFECT OF 180° CIRCUMFERENTIAL DISTORTION ON FAN

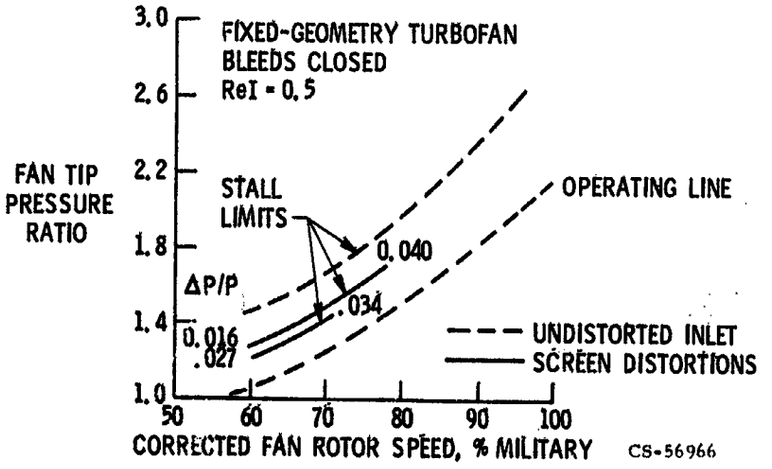

Figure X-9

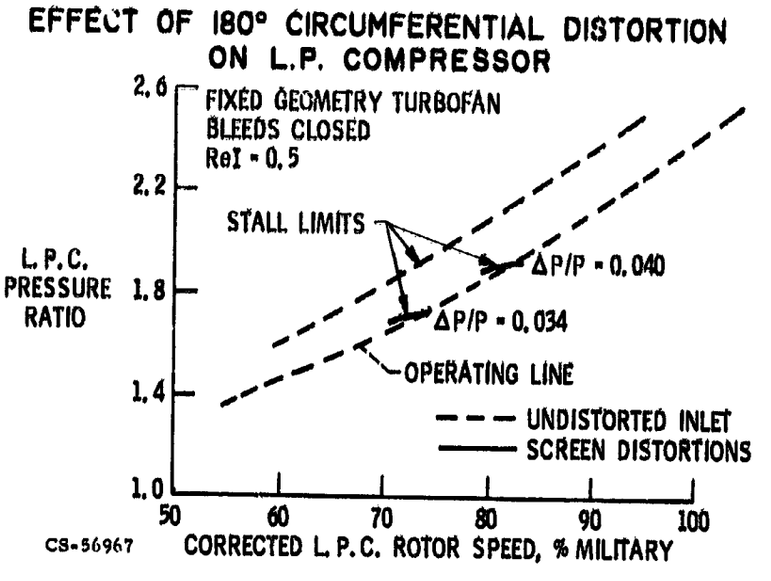

Figure X-10

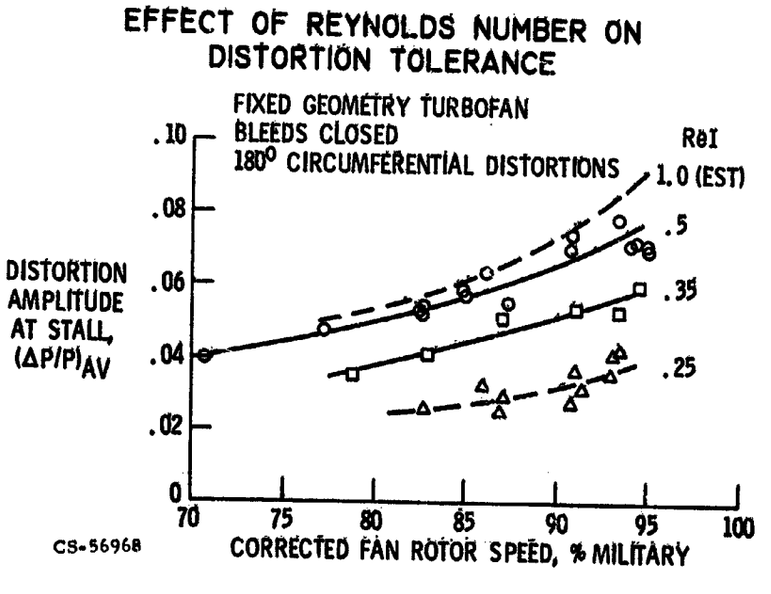

Figure X-11

EFFECT OF ENGINE INLET ReI
H. P. COMPRESSOR PERFORMANCE
VARIABLE GEOMETRY TURBOFAN

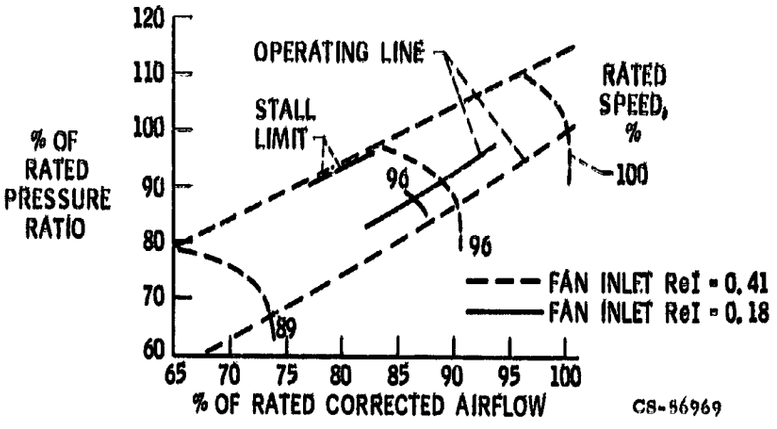

Figure X-12

EFFECT OF ENGINE INLET ReI ON VELOCITY PROFILES
H. P. COMPRESSOR INLET
VARIABLE GEOMETRY TURBOFAN

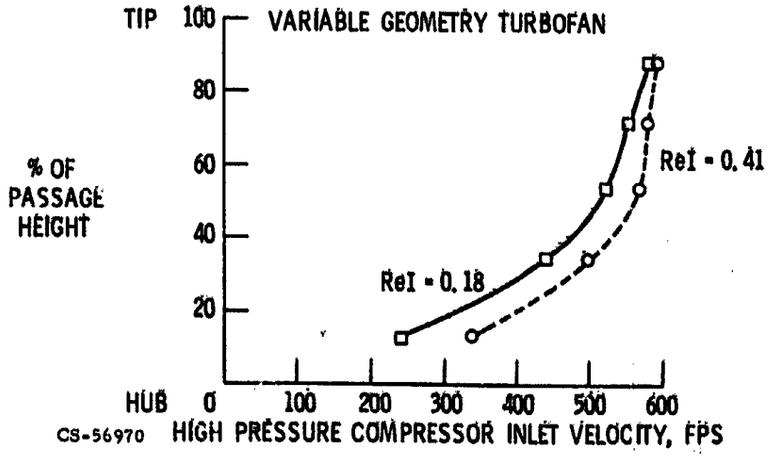

Figure X-13

EFFECT OF HUB RADIAL INLET PRESSURE DISTORTION ON FAN PERFORMANCE

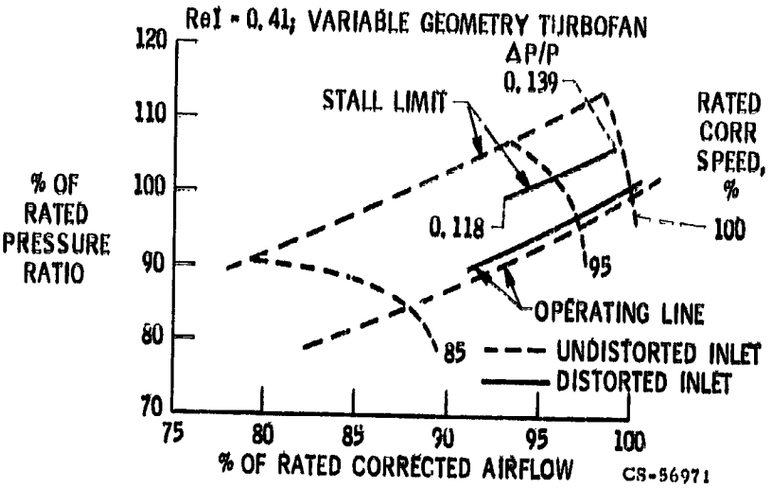

Figure X-14

TYPICAL HIGH RESPONSE PRESSURE TRACES OBTAINED DURING AN ENGINE STALL

VARIABLE GEOMETRY TURBOFAN; HUB RADIAL DISTORTION

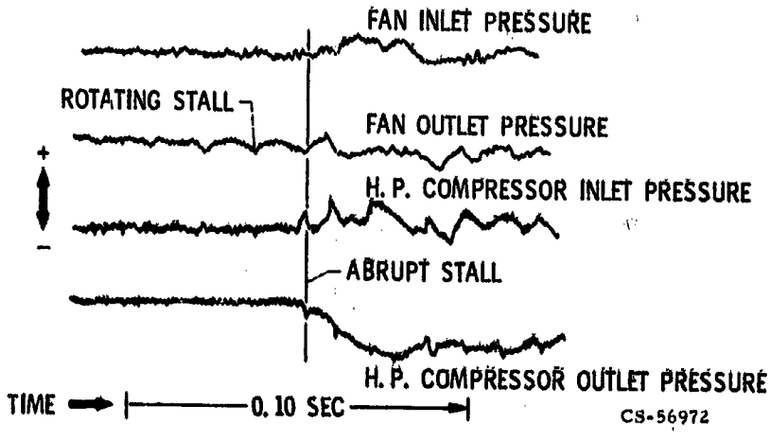

Figure X-15

AMPLIFICATION OF CIRCUMFERENTIAL DISTORTIONS
FAN HUB REGION

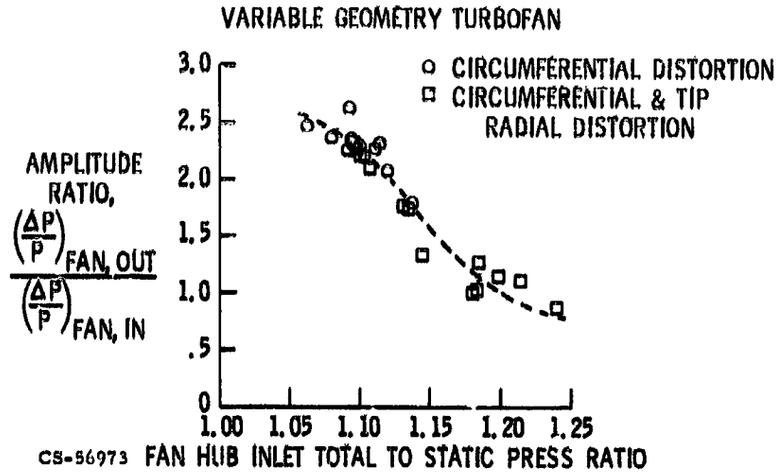

Figure X-16

FAN HUB EQUIVALENT STAGE CHARACTERISTIC CURVE

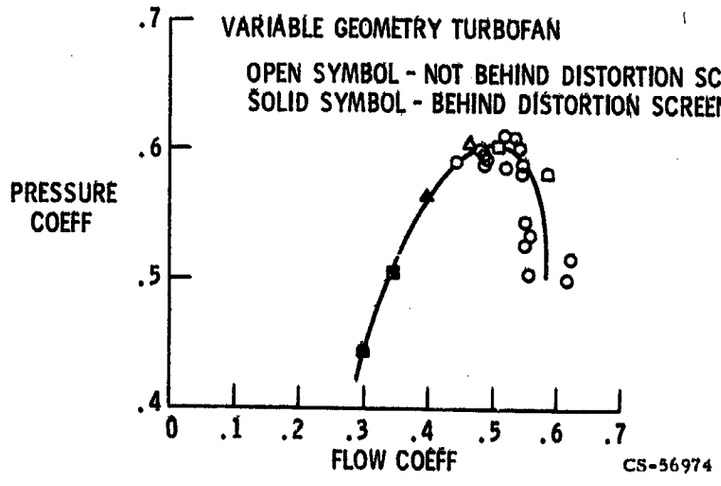

Figure X-17

EFFECT OF FAN MODIFICATION ON THE FAN HUB EQUIVALENT STAGE CHARACTERISTIC CURVES

VARIABLE GEOMETRY TURBOFAN

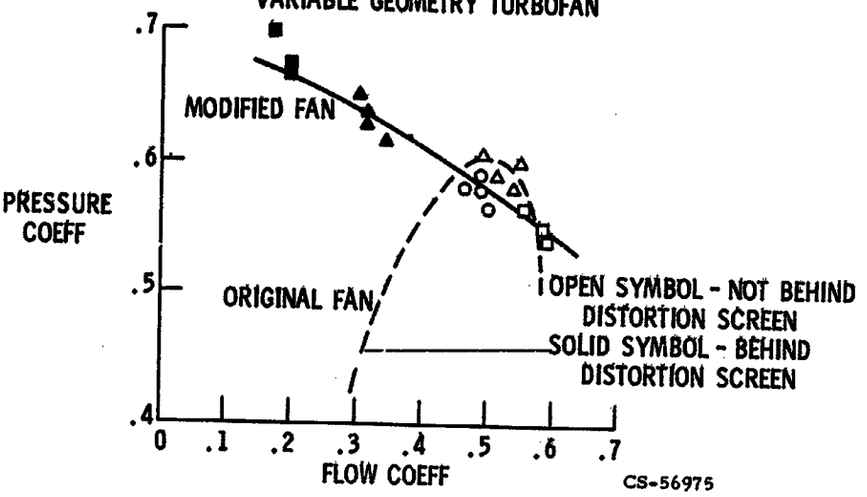

Figure X-18

EFFECT OF FAN MODIFICATION ON AMPLIFICATION OF CIRCUMFERENTIAL DISTORTIONS

FAN HUB REGION

VARIABLE GEOMETRY TURBOFAN

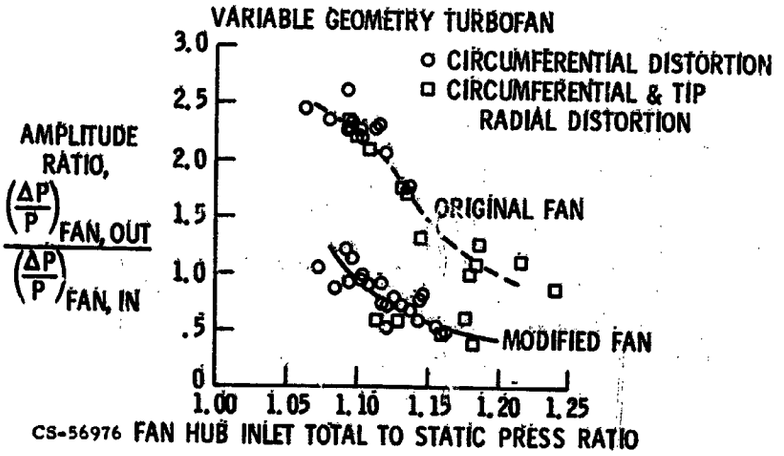

Figure X-19

TYPICAL J-85 NACELLE INSTALLATION
IN 10'×10' SWT

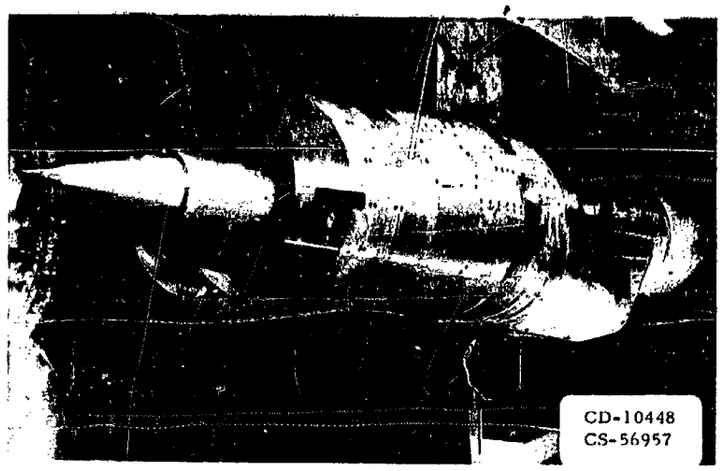

Figure X-20

AIR JETS IN ENGINE-INLET DUCT

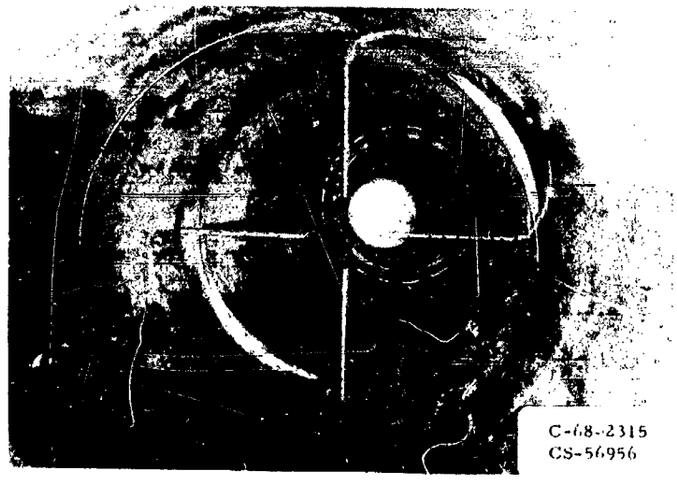

Figure X-21

AIR–JET SYSTEM SCHEMATIC

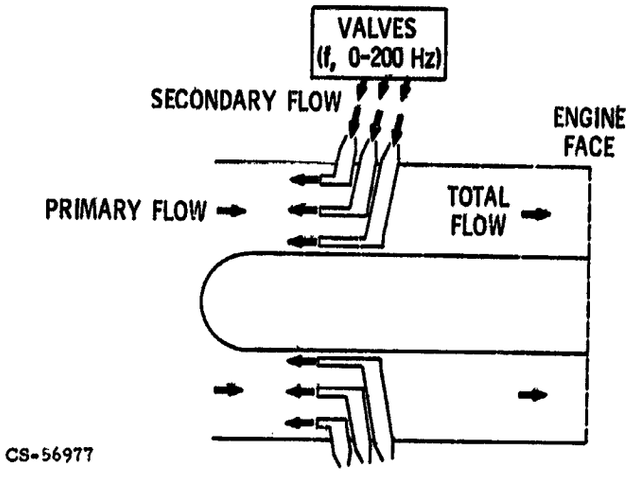

Figure X-22

POWER SPECTRAL DENSITY

FLIGHT ENVIRONMENT (F-111) AND SIMULATION (AIR JETS-PSL)

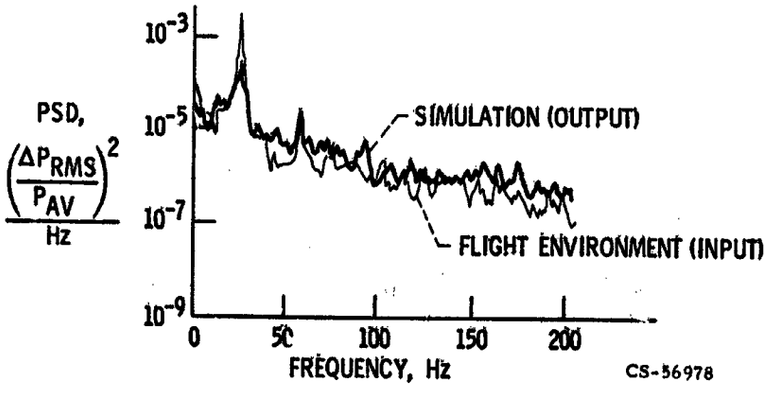

Figure X-23

COMPRESSOR RESPONSE TO INLET UNSTART

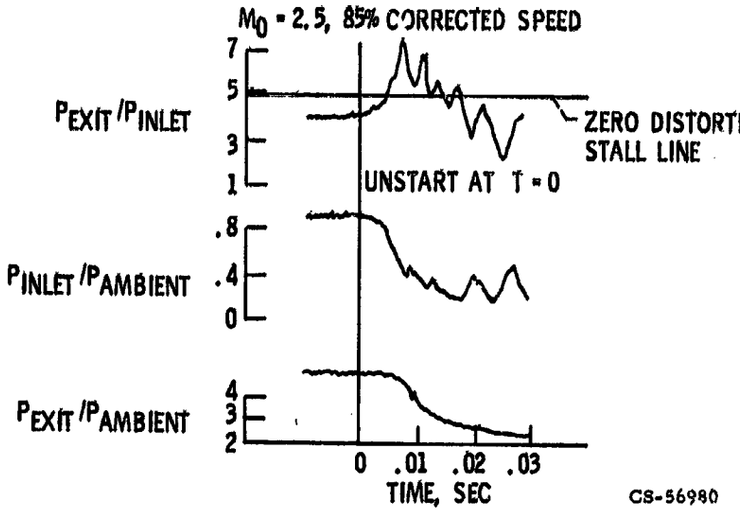

Figure X-24

INLET UNSTART EFFECT ON ENGINE

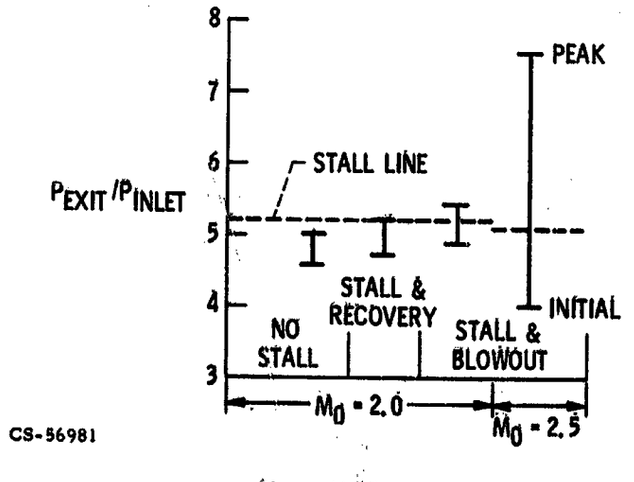

Figure X-25

INTERSTAGE STATIC PRESSURES: INLET UNSTART – COMPRESSOR STALL

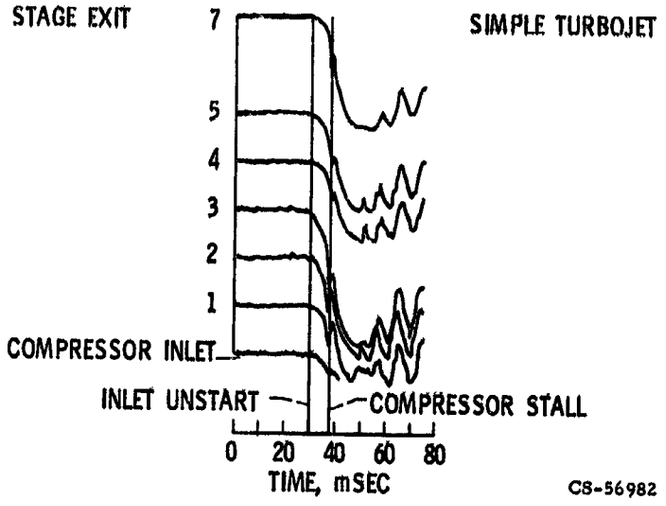

Figure X-26

INTERSTAGE STATIC PRESSURES: COMPRESSOR STALL – INLET UNSTART

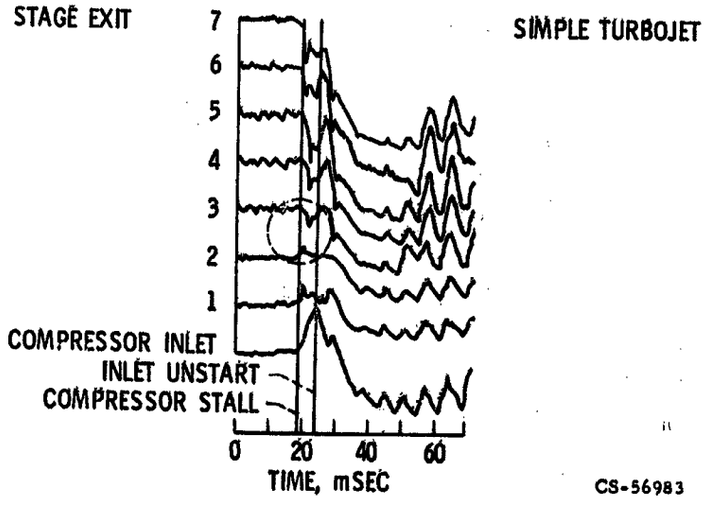

Figure X-27

TOLERANCE TO DYNAMIC INLET PRESSURE WITHOUT DISTORTION

FIXED GEOMETRY TURBOFAN; BLEEDS CLOSED; ReI = 0.5

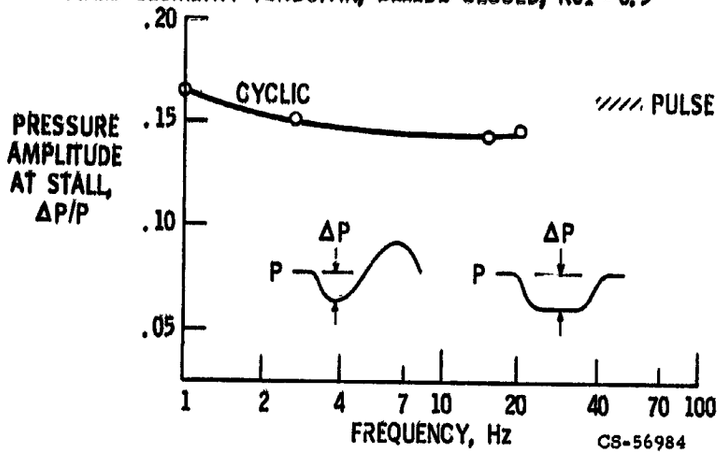

Figure X-28

PRESSURE–TIME HISTORIES

10-Hz CYCLIC WITHOUT DISTORTION; FIXED GEOMETRY TURBOFAN BLEEDS CLOSED; ReI = 0.5

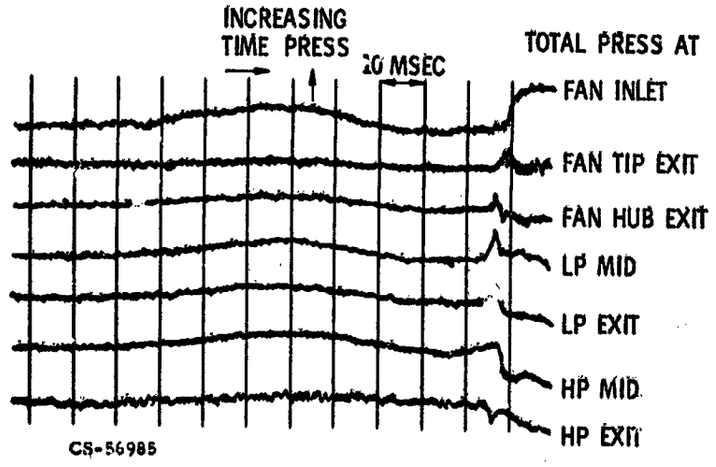

Figure X-29

PRESSURE RATIO HISTORIES

10-Hz CYCLIC WITHOUT DISTORTION; FIXED GEOMETRY TURBOFAN; BLEEDS CLOSED; ReI = 0.5

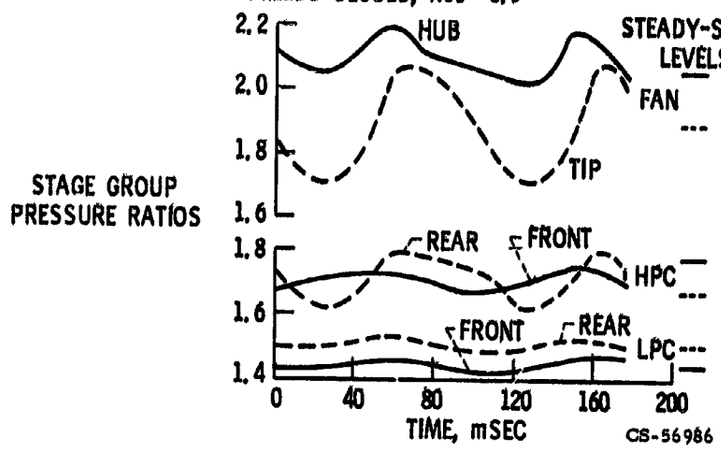

Figure X-30

TOLERANCE TO OSCILLATING 180° CIRCUMFERENTIAL DISTORTION

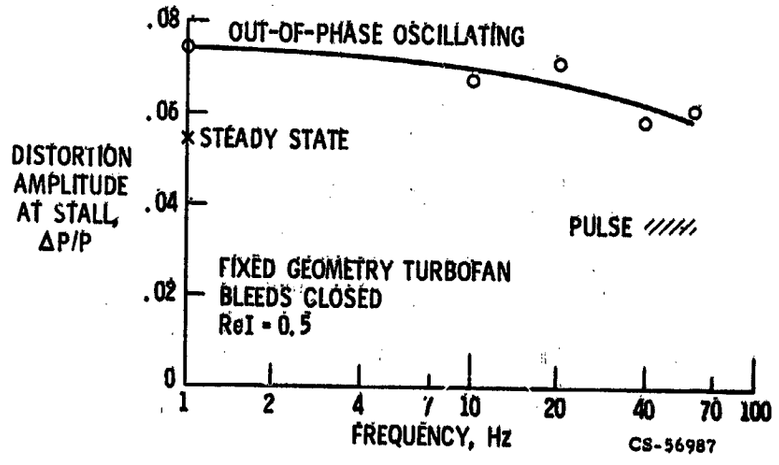

Figure X-31

TOLERANCE TO ROTATING 180° CIRCUMFERENTIAL DISTORTIONS

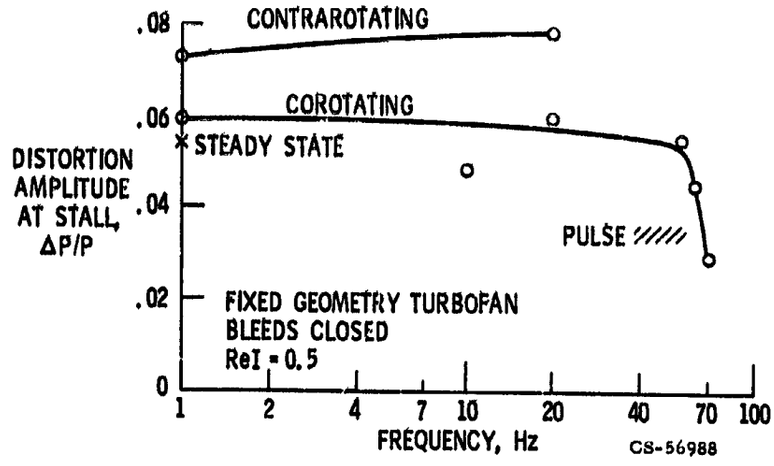

Figure X-32

TEMPERATURE DISTURBANCE DEVICE

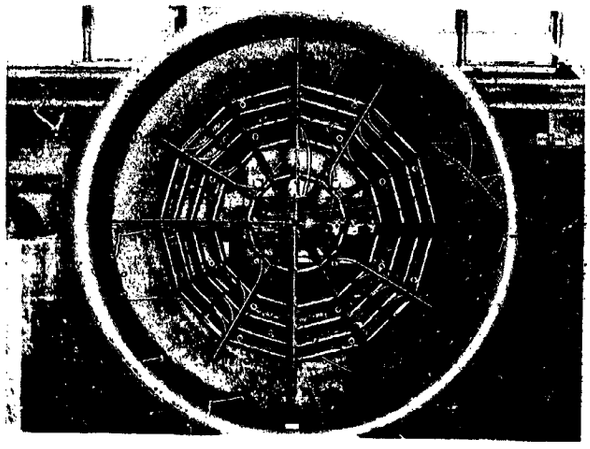

C-69-1384
CS-56955

Figure X-33

EFFECT OF SPATIAL TEMPERATURE DISTORTIONS ON ENGINE STALL

VARIABLE GEOMETRY TURBOFAN; H.P. COMPRESSOR MAP

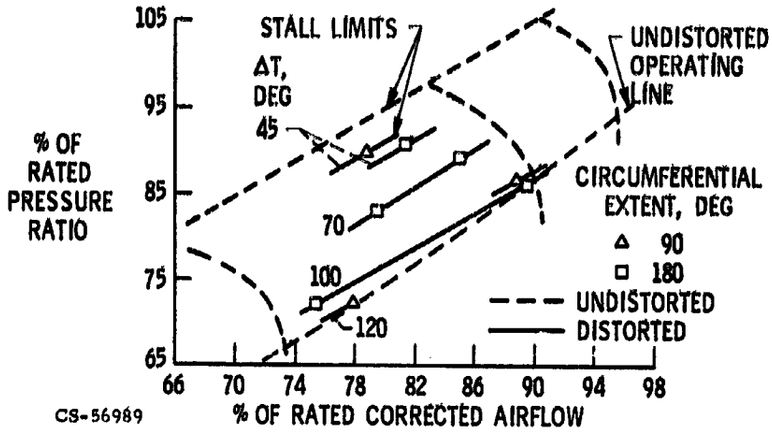

Figure X-34

EFFECT OF INLET TEMPERATURE TRANSIENTS ON ENGINE STALL

VARIABLE GEOMETRY TURBOFAN

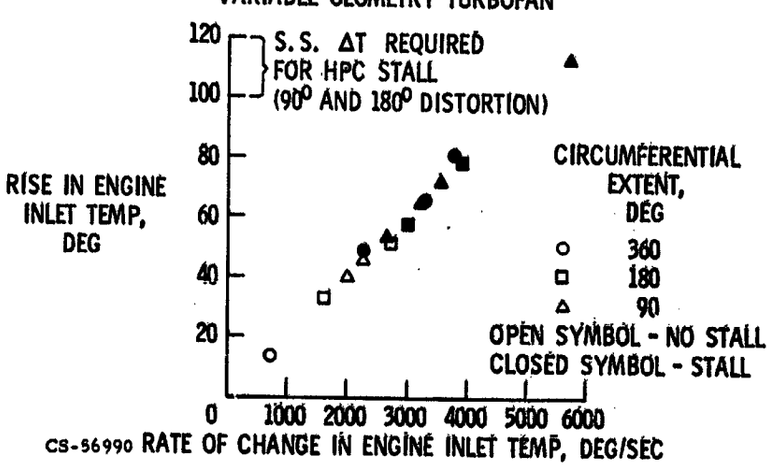

Figure X-35

XI. DYNAMICS AND CONTROL

Aaron S. Boksenbom, Gary L. Cole, Daniel I. Drain, Kirby W. Hiller, Ross G. Willoh, and John R. Zeller

Some of the major problems in dynamics and controls of a supersonic propulsion system are shown in figure XI-1. The job of the control (inlet control, engine control, and coupling signals between the inlet and the engine) shown in the figure is to avoid severe, damaging, or unstable conditions throughout the system. They also maintain system operation at the desired or optimum condition and, when required, move the system from one operating point to another. To design such controls requires an understanding of the dynamic, as well as the static, performance of all system components.

A summary of the subjects presented in this paper is as follows:

(1) For the supersonic inlet, the problem is to maintain high inlet performance, while avoiding inlet unstart and avoiding inlet operation that produces high dynamic distortion at the compressor face.

(2) An inlet unstart would be a very severe experience for a supersonic transport. This unstart might induce combustor flameout and compressor stall. The problem is to recover the system back to normal operation in a short time.

(3)The inlet and engine controls may require coupling to set system operating conditions for best overall performance.

(4) We need an understanding of combustor and compressor dynamics. Compressor performance is especially sensitive to dynamics. The problem is to predict and understand the compressor stall margin available under dynamic and static inlet and compressor conditions.

(5) To conduct significant experimental research, specially developed sensors and servoactuators are needed. These devices should permit more direct measurement of input variables and faster manipulation of outputs.

(6) The complexity of systems and their requirements may require more capable and versatile control computers. The use of digital computers in system control offers a solution to this problem.

(7) Finally, to obtain the utmost improvements in various aspects of measurement, monitoring, and control, the body of mathematical control theory may be applied and incorporated in the control system.

SMALL PERTURBATION DYNAMICS AND CONTROL

For small perturbation dynamics and control, an analytic or computer dynamic model is needed to help us understand inlet behavior and to aid in designing inlet control and stabilization devices.

Inlet Dynamic Analysis

When we started thinking about controls for supersonic propulsion systems, the desired simulation models just were not available. This was especially true for frequencies above 5 or 10 hertz. One of the first things done was to model the various pieces of the propulsion system, beginning with the inlet.

Figure XI-2 shows how the inlet appears to the controls analyst. He thinks of it as a pipe with a variable area section, a normal shock, some disturbance or bypass flow, and an appropriate terminal boundary condition. Physically, a perturbation from equilibrium caused by the engine or bypass doors results in pressure waves moving up and down the duct. Mathematically, it can be described by wave equations. An approximate closed-form frequency response solution was found for the wave equations applied to the subsonic diffuser. Also found were equations relating shock position and velocity to adjacent variables. With this model, it was possible to predict the dynamic behavior of the inlet in response to downstream disturbances, which are the primary disturbances considered in this paper. Experimental data are needed, however, to verify the results.

Experimental frequency response data obtained from an inlet during a wind tunnel test program are presented in figure XI-3. The figure contains amplitude ratio and phase lag characteristics of the inlet normal shock position in response to bypass airflow disturbances. The amplitude ratio has been normalized to unity at a frequency of 1 hertz. Analytical results obtained with the small perturbation model are also plotted for comparison. Agreement between the analytical and experimental data is quite good even out to a frequency of 200 hertz. The termination for this inlet consisted of a choked orifice at the end of a piece of pipe. The pipe length was equivalent to the length of a J-85 engine with an afterburner. Other orifice locations were investigated, and it was found that a choked orifice located at the compressor face station would give results very similar to those obtained with an actual engine. Since the analysis and the data are in agreement, it is felt that a controls design tool for investigating the small one-dimensional disturbance occurring within the inlet has been obtained.

Inlet Control

The requirements for inlet control are now considered. In general, at the diffuser exit of a mixed compression supersonic inlet, total pressure recovery is highest and distortion is lowest when the normal shock is at the inlet throat. Thus, from an engine performance standpoint, it is desirable to fix the normal shock at the throat. Unfortunately, inlet airflow disturbances can occur which might cause the shock to move either upstream or downstream. An upstream displacement of the shock would result in an inlet unstart. A downstream movement increases distortion and decreases pressure recovery. These events are undesirable because of a possible engine upset such as compressor stall and because propulsion system performance can be significantly decreased. Unstart can be avoided in many cases by operating supercritically - that is, with the shock downstream of the throat. If the inlet is supplied with a normal shock control, the degree of supercritical operation can be reduced with the benefit of higher performance.

The control chosen for investigation was a closed loop control that attempted to hold shock position fixed just aft of the throat. To help design such a control, the analytical model of the inlet was used. The model gave open loop amplitude and phase characteristics such as those shown in figure XI-3. A block diagram of the closed loop shock position control system is presented in figure XI-4.

One system that was investigated used a shock position sensor that relied on two static pressures in the inlet to infer shock position. These static pressures were behind the normal shock. When the shock moved forward the pressures increased. The resulting shock position signal was compared to a command value. The difference between the two signals told whether the shock was ahead of or behind its desired location. This difference signal was then amplified by a controller. The controller's gain was frequency sensitive. It had high gain at low frequencies, while at high frequencies its gain was constant. Such control action is called proportional-plus-integral. The output of the controller drives the bypass doors, which were positioned by fast response electrohydraulic actuators.

Figure XI-5 shows the performance obtained from this normal shock control tested on a mixed compression inlet in the 10 by 10 Foot Supersonic Wind Tunnel. The frequency response of shock position to a downstream airflow disturbance is given. Two responses are shown - one for the inlet without control and one for the inlet with control. On the y-axis is the amplitude of shock motion. Both amplitude responses have been normalized by the low frequency amplitude for the uncontrolled inlet. Thus the no control curve starts out with an amplitude ratio of 1.

As frequency increases, the uncontrolled response drops off and then resonates. It is resonant because the inlet was terminated with the long pipe in this experiment.

The solid curve shows the response of the inlet with control. This control is trying to hold the shock position steady. Thus, it acts to hold shock amplitude down to zero. At low disturbance frequencies it does this quite well. For example, at a frequency of 1 hertz the normalized amplitude ratio of shock motion is 0.03 with control. Without control it is unity. Thus, the control has reduced shock motion by about 30 to 1. At higher disturbance frequencies, the attenuation is not as good. This is due to the frequency sensitive gain of the controller. For the faster disturbances, the integral action has less time to work. The controller has to quit in the vicinity of the resonance; otherwise, it would drive the system into oscillation. As can be seen, there was some amplification of the resonance. The only place the control amplified shock motion was near the resonance; at lower frequencies it provided significant attenuation.

Inlet-Engine Control

Until now the discussion has been concerned with an inlet control that manipulates only the inlet's overboard bypass doors to keep the normal shock fixed. Such a control may not always result in the best overall propulsion system performance. For example, an increase in bypass airflow may be required to accommodate a disturbance. This would cause a corresponding increase in spillage drag. Thus, even though the shock is maintained at a high pressure recovery position, there may be a net loss in propulsion system efficiency due to the increase in spillage drag. Since engine speed also affects shock position, there may be some benefit in using both the bypass doors and the engine to control the normal shock. Two methods of coupling normal shock position control and engine speed control were investigated.

The first coupled control approach is shown in figure XI-6. With this approach the inlet normal shock loop is coupled to the engine speed control loop. The items added to the basic inlet control are shown by the heavy lines. The engine speed control loop senses engine speed and compares it with the desired speed as dictated by the throttle setting. The error in speed is input to the controller. The controller modulates engine fuel to decrease the speed error. Coupling is accomplished with the reset device shown in the diagram. The inlet controller output is integrated and the resulting signal is used to trim the speed setting of the engine. With this modified speed setting, the engine speed loop will reset the control bypass doors. This system was evaluated experimentally and showed good results.

Figure XI-7 shows the transient performance of the system when operated experimentally in the supersonic wind tunnel. As the shock controller senses that a

disturbance has occurred, the control doors open quickly to correct for the airflow disturbance. Initially, there is a small upstream excursion of the shock, but this is quickly corrected by the action of the doors. The output of the shock controller to the bypass actuation system is integrated. The output of the integrator is input to the engine speed loop and results in the increase in fuel flow to accelerate the engine to a new speed. The engine responds to this fuel change and finds a new operating speed. As this occurs, the bypass doors are slowly reset to a closed condition, thereby reducing overboard bypass drag. Coupling the controls demonstrated the ability to reset the propulsion system to any arbitrary operating point.

Also investigated was an entirely different coupled control approach (see fig. XI-8) which uses engine speed as the primary control variable. The main features of this system are outlined with the heavy lines shown in the figure. The overboard bypass system in this case is a much simpler design, and therefore lacks the fast response capabilities of previous systems. The engine speed loop has been improved in response by using a fast fuel throttling valve.

In this system, the error in shock position, after it is acted on by the dynamic elements of the inlet controller, is sent directly to the engine speed loop to demand a change in speed. The actual speed is integrated slowly, and the output of the integrator is sent to the bypass actuation system. The performance of this control system, which has been used successfully in the wind tunnel, can best be understood by looking at some of the experimental results.

Figure XI-9 shows a series of transients obtained when the controlled inlet-engine was disturbed in a particular way. A step type or almost instantaneous decrease in the inlet downstream airflow was initiated by a disturbance at the compressor face location. This decrease in overboard airflow caused the shock to move very quickly in an upstream direction or toward the unstarted mode. The resulting error in the shock location is sent to the engine speed loop. As a result, the relatively fast fuel control responds by increasing the engine speed to correct for the upset in inlet downstream airflow. As engine airflow increases, the shock is returned to its desired position. The change in engine speed is integrated slowly. This output is then used as a command to the bypass actuation system. The lower trace shows that the doors open and thereby increase bypass flow. This increased bypass airflow reduces the airflow required to be taken by the engine, thus allowing speed to be reset slowly to some desired operating point.

LARGE PERTURBATION DYNAMICS AND CONTROL

Thus far the discussion has been restricted to small perturbations and normal operation. If the inlet should unstart because of inadequate control, compressor stall, or upstream disturbances, returning the system back to normal operation presents new problems.

Inlet Dynamic Analysis

Considered first is our understanding of the basic mechanisms of inlet unstart. The analysis developed for controls design gave only a small perturbation solution useful for linearized system analysis. The techniques could not be applied directly to inlet unstarts, or any of the other nonlinear phenomena that seem characteristic of supersonic inlets.

An unstart can be caused either by external disturbances (such as a gust or a passing aircraft) or by internal disturbances (such as compressor stall). With an external disturbance a second shock wave can form at the inlet throat, move upstream, and stand in front of the inlet. A downstream disturbance, on the other hand, can cause a pressure wave to form at the compressor face, move up the inlet, join with the normal shock, and then carry it out of the inlet.

In either case, the unstart occurs so rapidly that it is hard to get detailed experimental evidence of what occurs. The decision was made to try to model such inlet behavior analytically.

The method of Lax, one of the finite difference schemes that has been used to study flow field dynamics, was used for the large perturbation problem. Some of the results obtained by applying this technique to the geometry of an inlet are shown in figure XI-10. In this figure inlet pressure profiles are plotted at various times during a transient disturbance. The bottom curve is the initial pressure profile for an operating condition with a high bypass airflow. The initial normal shock location is thus well behind the inlet throat.

The disturbance considered consisted of a ramp in the inlet discharge flow from its nominal value to zero in 3 milliseconds and back in 3 additional milliseconds. As the flow drops, a pressure wave or front begins to propagate back up the duct. The normal shock remains relatively stationary until the pressure front coalesces with it. Then the pressure wave carries the normal shock out of the inlet and an unstart results.

No experimental data resembling inlet pressure profiles during an unstart were available. However, peak pressures were recorded at four inlet stations during an

unstart caused by a compressor stall. These experimental data appear as the curve along the top of the plot and form an upper envelope for the peak pressures. If allowance is made for not knowing how closely the actual compressor stall resembled the 3-millisecond inlet disturbance, the agreement looks good.

Also investigated were the effects of an external disturbance on this same inlet. The results are shown in figure XI-11. Again the bottom trace is the initial static pressure distribution.

The external disturbance was generated by reducing the cowl lip velocity 3 percent in 2.5 milliseconds. In this case, a pressure front forms at the inlet throat and moves out of the inlet. The steepening of the front as it moves toward the cowl lip can be noted. The pressure front will result in a shock wave standing in front of the inlet while a shock still remains in the inlet. Such severe and rapid transients pose special requirements for controls design.

Inlet Restart Control

Unstart transients, like the ones just described, cause a drop in diffuser exit total pressure recovery. Pressure recovery can drop transiently to a value as low as 15 percent. Also, distortion increases. An unstart may also result in a buzz condition where the shock oscillates unstably.

Since unstarted inlet performance is poor, the inlet should be restarted quickly. Figure XI-12 illustrates the functions a restart control should perform. Condition 1 shows the inlet started and with the centerbody at its normal position. The bypass doors are almost closed to position the normal shock just downstream of the inlet throat. This condition results in high total pressure recovery and low distortion at the diffuser exit. If a disturbance causes the inlet to unstart, the inlet goes to condition 2. Initially, the shock may be in a buzz condition. When the bypass doors are opened wide as shown in figure XI-12, the throat becomes choked. Then the inlet is stable, but unstarted, and there is a strong normal or bow shock in front of the cowl lip. This shock is the cause of the large drop in pressure recovery that accompanies unstart. Since the throat is choked, a second normal shock also exists downstream of the inlet throat.

To restart inlets with internal contraction, the ratio of throat area to capture flow area must be increased. This is often done by collapsing or translating the centerbody. For this inlet, the restart cycle begins with a forward translation of the centerbody. A condition just before restart would appear as in condition 3. The centerbody is forward of its normal position, and the two normal shocks still exist.

In general, higher pressure recovery can be achieved as centerbody position changes throughout the restart cycle. The bypass doors must be open enough to pass the inlet airflow not demanded by the engine. If the doors are not open enough, the throat will unchoke and buzz will occur. As usual, if the doors are open too much, pressure recovery will be lower and distortion higher than necessary. For condition 3, it was assumed the doors could be partly closed to give better performance than at 2. This would usually be true, if the engine was not in a stalled or flameout condition.

The centerbody must be translated a little farther than condition 3 to restart the inlet. Then centerbody travel is reversed and brought back to condition 4. The external shock has been swallowed, and as for condition 1, there is a single, normal shock downstream of the throat. The bypass doors are shown to be slightly more closed to give better performance than at 3. However, if the doors are closed too much, the inlet will unstart again.

The restart cycle is completed by retracting the centerbody to its normal position. At the same time, the bypass doors should be positioned to increase inlet performance as the centerbody is retracted.

These, then, are the requirements that must be considered when designing a restart control.

One goal for the restart control system was to make it completely automatic. It was also desired to maintain closed loop control of the normal shock throughout the restart cycle. This would enable the control system to compensate for unexpected disturbances which might occur during the restart cycle. One such disturbance could be an unexpected change in the engine airflow conditions. To accomplish these goals, the restart control system used feedback and some switching and scheduling.

Figure XI-13 is a schematic of the restart control system. This system uses the normal shock feedback control system of figure XI-4. The light lines in figure XI-13 represent the components discussed previously. The heavy lines indicate those components specifically required for restart control.

In this case the normal shock control loop used a single static pressure aft of the normal shock to infer shock position. After the inlet unstarts, its pressure recovery becomes lower, and the level of the sensed static pressure is subsequently reduced. Thus, the command or reference input to the control has to be scheduled. Two schedulers were used. One supplied low values of the command for the conditions where the inlet was unstarted. The other scheduler supplied higher values of the command and was used when the inlet was started. It was found desirable to vary these command values as functions of centerbody position. Therefore, center-

body position was fed back to the schedulers as shown. A relay contact was used to select the output of one of the schedulers. This relay was operated by the output of an unstart detection device. The detector operates in the following way. Two pressures were sensed ahead of the inlet throat. A ratio of these pressures was taken. When the inlet unstarted, the ratio increased. When the ratio exceeded a predetermined reference level, the relay was switched to the unstarted condition. When the inlet restarted, the ratio decreased. When it dropped below the reference level, the relay returned to the started condition.

Another set of contacts on the relay selected one of two commands for the centerbody actuator. A command for the actuator to go to an extended position was used when the inlet was unstarted. The command for the actuator to return to the design position was used after the inlet had restarted. Thus, it was possible to exercise closed loop control of the inlet throughout the restart cycle by switching and scheduling commands.

Figure XI-14 shows the results obtained with this restart control for an inlet connected to a long pipe. A transient is shown consisting of an unstart followed by a controlled restart. The traces are the unstart signal, centerbody position, bypass door area, and throat exit static pressure. The command value of throat exit static pressure is shown where different from the actual value.

The unstart is indicated by a drop in throat exit static pressure and detected by a rise in the unstart pressure ratio. The centerbody is immediately commanded to slew, or translate at maximum velocity, in the forward direction. The static pressure command to the normal shock control is scheduled to a low value. This causes the bypass doors to open to maximum area to suppress buzz. As the static pressure command is increased, the doors come into action controlling static pressure to its command value. When the inlet restart is indicated by the detector the centerbody slews aft. Also, the scheduler commands higher values of static pressure to the shock control loop. The inlet is returned to on-design started conditions in approximately 1.5 seconds. This time depended primarily on the slewing speed of the centerbody servo. The inlet aerodynamics themselves were quite fast, as was the bypass door loop. No centerbody overtravel was permitted, and pressure recoveries were as high as possible without encountering buzz.

Inlet-Engine Restart-Relight Control

This restart control appears to satisfy the inlet restart requirements; however, there are additional problems when the inlet is coupled to an engine instead

of a long pipe. For example, the unstart transient itself is severe and may cause compressor stall and/or combustor flameout. There is concern, then with clearing a possible stall, relighting the combustor, and avoiding a possible turbine overtemperature problem if stall occurs without flameout.

To account for an engine in the system, a relight feature was incorporated into the restart control system of figure XI-13. The igniter was energized automatically upon receiving a signal from the unstart detection device. At the present time no attempt has been made to manipulate any other engine variables such as the throttle setting or exhaust nozzle area.

Figure XI-15 shows an example of the transient that occurred when a restart-relight sequence was attempted in the tunnel. During this particular transient, an engine flameout did occur. In the top trace, unstart is detected by the unstart signal exceeding its reference level. When the inlet restarts, the unstart detection signal drops below the reference level. In the second trace, the action of the translating centerbody is shown. After the inlet unstarts, the centerbody travels at full velocity in the forward direction. At the point where the inlet restarts, the centerbody reverses and returns at full velocity to its on-design condition. The third trace shows the action of the controlled bypass doors. They slowly open to make up for the engine airflow lost by the slowing down of the flamed-out engine. In the next trace, it is noted that there is a rise in the inlet throat exit pressure as the shock moves upstream. When unstart occurs, there is a large decrease in the pressure. As mentioned before, flameout did occur during this transient. This flameout condition is indicated in the bottom trace by the decrease in turbine exit temperature.

The time scale of figure XI-15 shows that the restart transient was completed in about 0.5 second. It should be noted that there is a break in the time along the horizontal axis. Relight of the combustor did not occur for about 5 seconds. Accompanying the relight is an overshoot in the turbine exit temperature. This rise, though, is normal for this engine during a conventional lightoff.

Finally, upon relight, there was a momentary increase in the throat exit pressure. As can be seen, this rise was not appreciable, and it was much smaller than that which occurred when the inlet initially unstarted. This rise is caused by a pressure wave propagating upstream from the engine. The inlet control is presently adequate to handle this pressure rise. However, such rises could be sufficient to reinitiate an inlet unstart. In the future, the dynamics of the relight operation should be carefully investigated to prevent this from becoming a problem area.

The transient of figure XI-15 is only one of many that were taken during this program. Many of the results varied to some extent from that shown in figure XI-15.

In summary, the following observations concerning the results should be noted:

(1) During an inlet unstart, compressor stall did not always occur. When it did occur, however, it was initiated during the unstart portion of the transient and not while restart was being attempted.

(2) Sustained stall never occurred without an accompanying combustor flameout. This, of course, is beneficial in that it eliminates the problem of a turbine overtemperature condition during stall.

(3) In all cases, the restart control system was successful in restoring the inlet to a started condition, even when a compressor stall had occurred. The stall always cleared itself by the time the inlet was restarted.

(4) Following the flameout, the times required to relight varied considerably. This restart-relight system has been evaluated on two J-85-13 engines. On the first J-85, the relight times varied from 2 to 30 seconds. On the second engine, relight times varied from 0.5 to 1.5 seconds. To data, it has not been possible to account for the difference in these relight times on two supposedly identical engines. Such wide variations in relight times cannot be tolerated for a supersonic transport. Therefore, further work on this problem is indicated.

DYNAMICS OF COMBUSTORS AND COMPRESSORS

It has been shown that complete control systems can be built for the inlet and engine which can handle small perturbations, inlet unstart, compressor stall, and combustor flameout. Still, to improve these systems and to further understand the uncontrolled inlet-engine dynamic interactions, more detailed descriptions are needed of dynamic behavior - particularly for combustor dynamics and compressor dynamics.

Combustor Dynamics

In the combustor, the characteristics are generally in the high frequency range from 10 to 100 hertz. Since these dynamics can affect engine system performance, they are of primary concern to the fuel control designer.

Figure XI-16 illustrates the basis of the analysis. This model consists of a primary combustion zone and a secondary mixing zone. The fuel flow, together with a portion of the compressor discharge air, is assumed to be completely vaporized and burned in the combustion zone. The products of combustion are then mixed with additional air in the mixing zone to cool the gas to acceptable turbine inlet conditions.

The mixing process is described with conventional gas dynamic equations. Such analysis results in a lag for the mixing zone gas dynamics. The combustion process is less well understood. For this case, techniques have been borrowed from those developed for rocket engine combustion dynamics. A time delay for fuel vaporization and a second-order lag for the actual combustion process are assumed or calculated empirically. This model for the combustor was then compared with test results.

During some of the supersonic wind tunnel testing, the engine speed control could be switched from the standard engine fuel control to a high response fuel control. It was possible using this control to obtain the frequency response of a number of parameters throughout the engine for a fuel flow disturbance.

The open circles in figure XI-17 indicate the normalized amplitude ratio and phase of combustor pressure to a fuel flow disturbance plotted as functions of frequency. Also shown (as the solid line) are the results of the analytical combustion model. The correlation between the analysis and the data is quite good, even out to 90 hertz. The inclusion of the methods used in rocket engine combustor dynamics properly accounts for the progressively increasing phase shift with frequency. This is an improvement over the mid-1950 combustion models.

Compressor Dynamics

A more difficult matter to handle analytically is the important problem of compressor dynamics. What must be done is to analyze, in detail, the dynamic characteristics of a multistage compressor.

Turbojet compressor dynamics. - When we started modeling the inlet, methods were considered that would let us simulate axial compressors and complete turbojet engine systems. Just as with the inlet analysis, we had to work out our own methods to get the high frequency dynamics.

A dynamic model was patterned after conventional steady-state stage stacking techniques. Simply, each stage is represented by a pressure ratio map and a

temperature rise map, both plotted as functions of airflow. To include gas dynamics, a lumped volume was added with each stage. In the volumes, momentum, continuity, and energy balances were used for the gas dynamics Each of the maps and associated volumes were connected to get an overall compressor model.

Once a working simulation existed, a compressor map was generated to establish the steady-state validity of the model. The agreement was within what could be expected from the available data and an analog simulation. Also, the computer simulation exhibited a stability boundary that looked very much like a compressor stall line. To investigate further, an accurately determined experimental compressor stall line was needed.

Prior to the development of the compressor model, an experimental program had been run in a sea-level test stand where the J-85's compressor performance and stall line were determined. The experimental data were obtained for a J-85 engine having a reduced turbine nozzle area; however, these data could be used for checking the analytical model.

Figure XI-18 indicates the results of the test program plotted in the form of a compressor performance map. Experimental operating points were obtained along constant corrected speed lines. These data provided a method of checking the simulation. The simulation was scheduled to operate with the same schedules used in the test program, and the data obtained were similar to the test data. The solid lines in figure XI-18 are constant speed lines obtained from the simulation; the solid circles indicate the simulation stability boundary. Comparing the solid circles with the test data of the open squares shows that the agreement was good. Therefore, we felt that we had an analytical method that could indicate the compressor stall line provided sufficient stage data were available.

One of the original goals of the simulation program was to model system gas dynamics to 50 hertz or better. Test data were provided to verify the model's frequency response accuracy. Figure XI-19 shows the frequency response of the sixth stage pressure when fuel flow was used as the disturbance signal. The solid line indicates the results obtained by the simulation. The agreement between data and analysis is quite good. Although all of the data obtained during the engine testing did not correlate this well, the agreement was, in general, good.

Thus, we seem to have a suitable analysis method for one-dimensional effects on turbojet engines even out to quite high frequencies.

Turbofan compressor dynamics. - Not all propulsion systems use turbojets. Many use turbofans as shown in figure XI-20. Compared to a turbojet, a turbofan has the added complexity of a fan compressor, and the division of the airflow between the fan bypass duct and the engine core compressors. This additional complexity

poses further analytical difficulties. The flow in the fan bypass duct can exhibit resonances which are transmitted into the core compressors through the discharge conditions they impose on the fan. Analytically, at least, the duct flow poses no problems; the same wave equation methods are used here as were used for the inlet subsonic diffuser flow. The coupling with the fan, however, is another question.

The primary analytical problem posed by the addition of the fan is the division of the fan flow between the fan bypass duct and the core compressors. The flow division is complicated by the different discharge pressures imposed by the duct and core regions. One approach to the problem is to use an average pressure as the fan discharge pressure. The average pressure is used in a momentum balance to determine the total fan flow. The total flow is then divided between the duct and core as a nonlinear function of the duct to core pressure ratio and corrected speed.

Once past the problem of the flow split, the core compressors can be modeled with the techniques applied to the J-85 compressor, and the duct can be modeled as was the inlet subsonic diffuser.

Figure XI-21, which presents analytically predicted frequency responses for the TF-30 engine, shows some of the problems associated with modeling a turbofan engine. Normalized amplitude ratios for various system pressures to a compressor face disturbance are plotted against disturbance frequency.

In particular, the resonant character of the fan duct (dashed curve) can be seen contrasted to the almost constant amplitude ratio of the fan discharge into the core compressor. In addition to the fan, the TF-30 engine has both low and high pressure compressors in the engine core. Frequency response data for the discharge of these compressors are also shown. The low compressor characteristic is quite similar to the fan core characteristic. The high compressor, which discharges into the combustor, however, exhibits a characteristic similar to the data for the J-85 engine. It would appear from these analytical results that the effects of fan duct resonance are negligible. Unfortunately, our experimental results are somewhat different from our analytical results. To investigate turbofan dynamics experimentally, uniform sinusoidal pressure was imposed at the engine inlet and the frequency response characteristics were determined at various stations throughout the engine. This program was done with the airjet system, described in paper X.

The test results (see fig. XI-22) do exhibit shapes similar to the analytical results up to frequencies of 20 hertz. Above that frequency, the duct pressure resonances appear to be interacting with the core pressures. This effect is ob-

viously not indicated by the analytical model. It would seem that a high frequency characteristic is missing, possibly in the fan simulation procedure.

In an attempt to match these data, the shape of the nonlinear map used to establish the flow split was changed. However, to get reasonable agreement between analytical and experimental results, the map had to be changed beyond physical reality. Thus, work must still be done on the problem.

To conclude, there are resonances that occur in turbofan engines which as yet cannot be predicted analytically. When modeling the turbofan, the basically one-dimensional techniques considered for axial compressors do not give good agreement with experimental data. Our present one-dimensional methods allow for time varying spatially uniform compressor face conditions. We have started a two-dimensional model for an axial compressor to try to include the effects of spatial distortion. This effort, however, is still in progress.

Summary

The other components in the propulsion system, such as the turbine, afterburner, and exhaust nozzle may have important dynamical effects. For a turbojet engine, where the turbine nozzle is usually choked, such dynamics do not couple back into the rest of the system. For other configurations, such as a turbofan engine or an engine used as a gas generator, the dynamic coupling may be important. These problems are not discussed in this paper.

DEVELOPMENT OF SENSORS, SERVOACTUATORS AND TESTING TECHNIQUES

The earlier portion of the paper has emphasized results of some propulsion dynamics and controls investigations. The kinds of experimental results obtained imply the use of sensors and servos with rather uncommon capabilities. This portion of the paper is concerned with explanations of some of these research tools.

Shock Position Sensor

Considerable work has been done in the area of directly sensing an inlet's normal shock position. Potentially, such a device can facilitate safe operation

of an inlet while reducing the margin of supercritical operation.

In most cases, our primary indicator of shock position has been a static pressure. This pressure (shown in fig. XI-23) is located aft of the normal shock operating range and is referred to as the throat exit static pressure. This signal gave an adequate indication of shock position for the condition at which the inlet was operated. However, a more direct measure of shock position is desirable because shock position measured with respect to the inlet throat is directly related to inlet performance and stability.

A common way to determine shock position is to observe the static pressure profile in the vicinity of the shock. The shock location is identified by a jump in static pressure. Ideally, this occurs as shown in figure XI-23. The flow at the inlet throat has a Mach number greater than one. Downstream of the throat, the inlet area increases. In supersonic flow, Mach number increases as area increases, and thus static pressure decreases ahead of the shock. At the normal shock there is a discontinuous jump in pressure. Also, the flow Mach number jumps from supersonic ahead to subsonic aft of the shock. Since the area is still increasing aft of the shock, Mach number decreases and static pressure increases.

In a real inlet, the pressure profile can be measured with a series of closely spaced static taps. Figure XI-24 shows two typical static pressure profiles that were measured simultaneously in a real inlet. These profiles were measured with the inlet at an angle of attack. The upper profile was measured by taps in the upper half of the inlet. The upper profile indicates the shock to be between taps 5 and 6 because of the steep pressure rise between those taps. The lower profile was measured by taps in the lower half of the inlet. The profile indicates the shock to be between taps 3' and 4'. This is about two taps forward of the position indicated by the upper taps. Thus, the shock does not lie in a plane normal to the inlet's longitudinal axis. Nonplanar conditions, although not as severe, were discovered even when the inlet was at a 0° angle of attack. Also, the pressure profile ahead of the shock does not exhibit a continuous decrease in pressure as does the ideal profile - for example, the rise between 2 and 3 on the upper, and the rise between 1' and 2' on the lower. Such irregularities were also found in profiles measured at 0° angle of attack.

These problems and others make it difficult to apply simple logic schemes to the profiles to determine shock position. Despite these problems, some progress has been made here in shock sensing schemes. Two different logic schemes have been tried to date. The simplest logic determined the shock to be between the first tap having a higher pressure than tap 1 and its adjacent upstream tap. For example, in the upper profile the shock would be between 5 and 6 (6 being the first tap with a higher pressure than 1, and 5 its adjacent upstream tap). On the lower profile the

shock would be determined to be between 1' and 2'. Although it is not shown in figure XI-24, the lower taps always indicated the shock to be between 1' and 2'. This is because the pressures at taps 2' to 8' were always greater than that at 1' regardless of shock position. For the 0° angle of attack condition at which tests were conducted, this problem did not exist.

The scheme just described, as well as the other one tried, were both implemented in two ways: one using electronic pressure transducers and logic elements, and one using fluoric elements. We have been most successful with the electronic sensors, although the fluoric sensors did give promising results. The electronic sensors are being used in the wind tunnel control room as shock position indicators, and they have been used in some of the normal shock control investigations. These sensors have followed shock position very well for frequencies up to 65 hertz with a maximum phase lag of 20°. However, in some cases the sensor had to be adjusted for the conditions under which a test was conducted. And it has been shown that operating the inlet at an angle of attack causes problems. These shortcomings are obviously not desirable for a flight application.

Another scheme which appears could work over a wide range of inlet conditions is being considered. This scheme would use the same logic as described before, except that instead of 1 or 1' being used as the reference pressure the reference pressure would be based on a total pressure just ahead of the static tap region. This reference is indicated on the profiles in figure XI-24. Based on the upper profile, the shock would be indicated between 5 and 6, which is correct. Based on the lower profile, the shock would be indicated between 5' and 6', which is two taps aft of the actual location. Although there is some error, it may not be unacceptable. In addition, this scheme can be implemented very simply by using differential pressure switches. The static tap pressures would be compared to the reference pressure directly, rather than using expensive transducers and electronic comparators. The outputs of the switches could be summed to give an electronic signal proportional to shock position.

Certainly, further investigation is called for in this area.

Fast Response Servos

Another area of development of controls hardware has been that of fast response actuators. These have permitted manipulation of the experimental models to frequencies in the 100-hertz range. A benefit has been that of getting better experimental verification of the analytical models. It has also permitted controls investi-

gations that were limited not by the actuation devices, but by the basic dynamics of the propulsion systems themselves.

Applications for which fast response actuation equipment has been designed and developed are as follows (also included are the areas in which these have been used):

(1) Fuel throttling valve - Used for compressor dynamics evaluations as well as a control element in propulsion controls research

(2) Air distortion valve - Used to determine compressor stall margins under various dynamic distortion patterns

(3) Inlet bypass valve - Used for determining inlet dynamics as well as a control element for high performance inlet shock control systems

All of the fast response actuation has been accomplished with the servosystem shown in figure XI-25. Basically this system uses a high performance two-stage electrohydraulic servovalve driving a piston-in-cylinder actuator to which the load is attached. The servovalve is driven by a specially designed servoamplifier which, through the position feedback device, provides the closed loop operation of the actuation system. To aid in the design of the systems for the various applications, a complete nonlinear simulation of the system of figure XI-25 was implemented.

One of the first systems developed was the fuel throttling valve. Figure XI-26 shows its response for various levels of desired output motion. The curves of figure XI-26 show that the response exceeds 100 hertz for the smaller amplitude inputs. As the input amplitude increases, the system does not respond quite as well.

During the various design programs and with the aid of the nonlinear simulation, it was found that the dynamic performance for these particular electrohydraulic servos could encounter response limitations in unexpected regions. An analysis of these limitations resulted in a new design criteria for maximizing the range of fast response capability. The details of this criteria are well documented in several of the publications listed in the bibliography (p. 375).

The actuation system for the air distortion valve was designed using the new more optimum criteria. The normalized frequency response curve of figure XI-27 shows its experimental performance. As can be seen, its response is flat to beyond 150 hertz. Also shown is one of the fuel valve responses of figure XI-26. It can be seen that the new more optimum design criteria provides some significant improvement in response. Moreover this improvement is obtained even though the distortion valve moves an output whose weight is three times that of the fuel valve servo.

Other Techniques

In addition to these special types of hardware, special techniques have been developed for experimentally obtaining dynamic data in our large facilities. These techniques are explained in several publications listed in the bibliography (p. 375).

FUTURE TRENDS IN AIRBREATHING PROPULSION CONTROL

Future trends in an airbreathing propulsion control will follow future system configurations and requirements. The low cost engine with its low cost and simple control was discussed in paper VII. Control problems in the use of cryogenic fuels are discussed in paper XII. The propulsion control problems for VTOL-STOL airplanes are of vital importance for these systems. Studies in this area have just begun.

Systems are becoming more complex. The capabilities of hydromechanical control, always limited, may be inadequate for the future. We are also seeing the development of fast, large capacity, flight worthy, digital computers.

Some of the advantages and new problems that will result from the application of digital control to propulsion systems are now considered.

Digital Control of Complex Systems

The advantages of computer control will be felt throughout the aircraft control system. As regards the overall aircraft flight objectives, a more complex control will be able to take into account information concerning air traffic control, and weather as well as flight range and speed. The flight computer can then determine an optimum arrangement of the aircraft control commands. Part of this information will be concerned with the operating condition of the propulsion system. In this way then, the propulsion system and aircraft will be totally integrated through the use of digital computer control.

A possible configuration for the propulsion control system is shown in figure XI-28. The propulsion control computer is required to operate the engine satisfactorily and safely in response to the demands of the overall flight objectives of the aircraft. The propulsion control may have its own separate digital computer, or it may be part of a more complex central computer. This is a matter not dealt with in this paper.

With the computer, the propulsion system control can be separated into more distinct levels of operation. Each level will be assigned its area of responsibility or control supervision. In general, these areas of supervision can be separated as shown in figure XI-28. Of most overall concern will be the optimum scheduling of propulsion system inputs according to some desired performance criteria. Propulsion system performance is measured in terms of such items as thrust, specific fuel consumption, and reliability. The aircraft and external disturbances will determine tradeoffs between these measures of performance.

A second and more direct role of the propulsion control computer pertains to system constraints such as stall, unstart, turbine overtemperature, and engine overspeed. Sequences for restoring normal operation following the violation of a constraint can be greatly improved over what exists today. Improvement at this level again can come by the controller taking into account both aircraft and external environment information.

There is, then, the most direct level that the computer control will be required to operate. This is concerned with the normal dynamic or transient conditions of the propulsion system process. Here the controller must be capable of maintaining the propulsion system in a stable and responsive mode of operation. Aircraft propulsion systems are highly nonlinear devices in which the steady-state and dynamic characteristics change drastically over the operating range. Present controls crudely schedule various control elements as a function of operating point to counteract these anticipated changes. The computational capabilities of the digital computer can greatly improve this situation and provide for a tighter control under all conditions.

To implement some of the concepts just presented, the J-85 engine control is currently being replaced with a digital computer. The shock position of an inlet has already been controlled by a digital computer. For this test, the inlet was terminated by a choked orifice and not by an engine. Ultimately we intend to control an inlet-engine propulsion system.

For these tests, the digital computer is a process control type of computer. The computer and its peripherals were selected so that we can control a real time process. Special attention was given to enhancing the speed with which the computer can execute a control concept or detect and account for any abnormality. The control sophistication possible by having a digital computer in the system does not come without some associated problems. Some of these problems are caused by the hardware, some by software, and some by both.

These problems are as follows:

(1) Computation speed. As the process is sampled and commands are made at

discrete intervals of time, one no longer has a continuous control device. Obviously, inadequate computer speed will cause problems.

(2) Quantization error. The input data are quantized by the number of sample levels being used for the range of each variable. This will set the ultimate accuracy of the system.

(3) Sample rate requirements. For real time operation, care must be used in the selection of the sample rate of the analog to digital converter. To be consistent with sampled data theory, the sample rate must be twice that of the highest frequency contained in the input data. This problem is illustrated in figure XI-29 where 1 second of random input data is presented. It has been frequency limited to 10 hertz. For this case, 20 samples per second are the minimum number of points from which the original data may be theoretically reconstructed from the sample points. For convenience, the same data are shown with three different sample rates. At 10 samples per second the high frequency content in the data is obviously missed. A less oscillatory curve can also fit these sample points. This ambiguity will cause errors, because the sample points resulting from the high frequencies in the data will be interpreted as a lower frequency oscillation which is not in the data. This effect is called frequency folding, and it will occur when the sampled data theory rule is violated. Obviously, 40 samples per second will give pretty good results and cause no problems.

(4) Round-off errors. In addition to the previous input data errors, there are other more well known digital computer problems, such as round-off errors, within the computer's computation processes.

(5) Numerical stability. Finite word size also limits the setting accuracy of the coefficients of the control law or control algorithm (as it is more properly called). This problem can have an effect on numerical stability. Thus, it is possible for the control algorithm to be stable in theory, yet be numerically unstable when inserted into the experimental system.

With careful controller design, these problems can be minimized. This has been demonstrated by our digital control program with the inlet in the supersonic wind tunnel. A computer control law appropriate for controlling inlet shock position has been devised. Figure XI-30 is a block diagram of the system.

The error between the commanded shock position and the actual sensed shock position was periodically sampled and fed into the digital controller.

The computer implements the control law and calculates the command necessary to correct for the error in the shock position. This command is output to the bypass doors. It is held constant until new information is sampled, taken into the computer, and operated on. Only then is the bypass actuation system updated with a new command.

Figure XI-31 shows the experimental results obtained with an inlet under digital and under analog computer control. The frequency response of normal shock position for a downstream airflow disturbance is shown. The solid curve shows the response under analog computer control. This is a continuous control similar to the ones that produced the control results shown before. The analog response as indicated before, increases with frequency at the low frequencies because of the integral action of the controller. The dashed curve shows the response under digital control with a sampling rate of 1000 times per second. The digital control response is very close to that of the analog control. At the high disturbance frequencies it coincides with the solid analog curve. Thus, in spite of the difficulties just mentioned, it performed very much like the analog control. The broken curve is for the digital control with a slower sampling rate of 100 times per second. This curve also corresponds closely with the other two curves over most of the frequency range. At disturbance frequencies above 50 hertz, however, the solid curve is not intended to also represent the slower digital. If input frequencies above 50 hertz had been used, the sampling theorem, as explained previously, would have been violated, and significant excursions in shock position above the solid line would have resulted. Thus, it is noted that a fast updated digital control behaved much like an analog control. A slow updated digital did about as well at low frequencies, but it could produce undesirable effects at frequencies above half its sampling rate.

Applications of Modern Control Theory

With such digital computer control capability and our understanding of system dynamic behavior, we might hope to make significant improvements in system operation. This presents the challenge of fully exploiting these capabilities. As a result we have been forced to take a careful look at control theory, or the way to design control systems. When designing control systems, we are really interested in how they perform dynamically or as a function of time. Modern high speed computers permit the solution of control design problems directly in the time domain. In the past, controllers were designed somewhat artificially through the use of frequency domain techniques. The capability of solving control problems directly now enables the designer to optimize the control system to certain realistic measures of performance.

We have been working at applying these new techniques to propulsion system control problems. Our first application was designing a control to minimize the expected frequency of unstarts of a supersonic inlet to a random airflow disturbance.

The significance of this application is illustrated in figure XI-32. When the inlet control was discussed before, it was specified that the normal shock, when influenced by disturbances, should be held as close as possible to some desired position downstream of the throat. The distance of this desired steady-state shock setting has been designated as α. Unstart occurs when the disturbance is sufficient to cause the shock to move forward greater than this distance α. The expected frequency of inlet unstarts to a random disturbance with known statistical properties, then, is a function of the magnitude of the setting α. It is also a function of the mean square value of the shock movement around the steady-state setting. The control designed to minimize unstarts will accomplish this by manipulating the bypass doors. Thus, the extent to which the frequency of unstarts can be minimized will be dependent on the capacity of the bypass system provided.

The results shown in figure XI-33 were obtained with an analytical model of a mixed compression inlet. The lower curve, which represents the smallest of the three steady-state shock settings α, shows how the time between unstarts increases as more capability is provided in the control bypass system. Likewise, as α increases for a fixed amount of control effort, the mean time between unstarts gets longer.

The larger values of α mean that the steady-state shock is located further downstream from the throat, thus reducing inlet pressure recovery or efficiency. With this type of information, the designer, assuming how frequently an unstart can be tolerated, can decide between the penalty in efficiency related to larger values of α and the design penalties associated with larger bypass doors.

In summary, then, these data are the predicted performance for a family of optimal inlet control systems. Since the inlet modeled was available for an experimental program, one of the optimal control systems was tried.

Figure XI-34 shows one of the results from the experimental program set up to do frequency response testing of an inlet. The figure presents an optimal control and a more classical control compared on a frequency response basis. The dashed curve shows the performance of the classical control designed with frequency domain techniques. This control, which is similar to the ones discussed earlier, produced significant low frequency reduction of shock motion due to its integral action. The solid curve shows the performance of the optimal inlet control. The design of the optimal control was based on the assumption that the random disturbances had most of their energy at low frequencies, but that some energy did exist in the midfrequencies.

Compared to the classical control, the optimal control, is seen to produce less attenuation of low frequency disturbances; in the midfrequencies it produces greater

attenuation of shock motion. Thus, compared on a frequency response basis, one might conclude that the classical control is better.

When these controllers were evaluated on an unstart basis, however, the better low frequency attenuation of the classical control did not indicate that it had certain merits over the optimal design. The results of this evaluation are shown in figure XI-35. The mean time between unstarts for each control was calculated using the experimental frequency response data. Also calculated was the RMS value of the control bypass airflow each would expend. The random airflow disturbance assumed for both controls had a frequency spectrum identical to that for which the optimal control was designed. The two data points on the figure show that the optimal control gives considerably longer mean time between unstarts. In fact, for this disturbance, it is better than the classical control by 30 to 1. Also, it accomplishes this with about the same amount of RMS control bypass flow. From this example it can be seen how the use of optimal control theory can give considerable improvement when a real criterion of performance is used in the design.

In conclusion, then, these results encourage the investigation of even more extensive applications of this type of theory in future control designs.

SUMMARY

Adequate inlet control can be provided and inlet-engine coupling can be mechanized and used to advantage.

In the event of inlet unstart, restart controls have proved successful where the relight of the combustor may still be a problem.

Our understanding of combustion dynamics is good. However, our understanding of compressor system dynamics still has unknown effects.

The development of special sensors and servoactuators has permitted wide range experimental programs.

Future uses of digital computer control are clearly indicated. Applications of control theory will point the way to the full utilization of this equipment to realize the maximum effectiveness of propulsion systems.

BIBLIOGRAPHY

Arpasi, Dale J.; Zeller, John R.; and Batterton, Peter G.: General Purpose Digital System for On-Line Control of Airbreathing Propulsion Plants. NASA TM X-2168, 1970.

Batterton, Peter G.; and Zeller, John R.: Dynamic Performance Analysis of a Fuel-Control Valve For Use in Airbreathing Engine Research. NASA TN D-5331, 1969.

Batterton, Peter G; Zeller, John R.: Performance Characteristics of Improved Servoamplifier for Electrohydraulic Control Systems. NASA TM X-2167, 1970.

Baumbick, Robert J.: Device For Producing Dynamic Distortion Patterns at Inlets of Air-Breathing Engines. NASA TM X-2026, 1970.

Cole, Gary L.; Neiner, George H.; and Crosby, Michael J.: An Automatic Restart Control System For an Axisymmetric Mixed-Compression Inlet. NASA TN D-5590, 1969.

Cole, Gary L.; Neiner, George H.; and Crosby, Michael J.: Design and Performance of a Digital Electronic Normal Shock Position Sensor For Mixed-Compression Inlets. NASA TN D-5606, 1969.

Coltrin, Robert E.; and Calogeras, James E.: Supersonic Wind Tunnel Investigation of Inlet-Engine Compatability. Paper 69-487, AIAA, June 1969.

Coltrin, Robert E.; and Mitchell, Glenn A.: Preliminary Investigation of Distortion Dynamics in a Mach 3 Mixed Compression Inlet. NASA TM X-1706, 1968.

Cole, Gary L.; Neiner, George H.; and Wallhagen, Robert E.: Coupled Supersonic Inlet-Engine Control Using Overboard Bypass Doors and Engine Speed to Control Normal Shock. NASA TN D-5619, 1970.

Crosby, Michael J.; Neiner, George H.; and Cole, Gary L.: Restart and High Response Terminal Shock Control For an Axisymmetric Mixed-Compression Inlet With 60-Percent Internal Contraction. NASA TM X-1792, 1969.

Drain, Daniel I.; Bruton, William M.; and Paulovich, Francis J.: Airbreathing Propulsion System Testing Using Sweep Frequency Techniques. NASA TN D-5485, 1969.

Griffin, William S.: Design and Performance of Flueric Shock Position Sensor for a Mixed-Compression Supersonic Inlet. NASA TM X-1733, 1969.

Lorenzo, Carl F.: Variable-Sweep-Rate Testing: A Technique to Improve the Quality and Acquisition of Frequency Response and Vibration Data. NASA TN D-7022, 1970.

Mitchell, Glenn A.; and Cubbison, Robert W.: An Experimental Investigation of the Restart Area Ratio of a Mach 3.0 Axisymmetric Mixed Compression Inlet. NASA TM X-1647, 1968.

Neiner, George H.: Servosystem Design of a High-Response Slotted-Plate Overboard Bypass Valve for a Supersonic Inlet. NASA TN D-6081, 1970.

Paulovich, Francis J.; Neiner, George H.; and Hagedorn, Ralph E.: A Supersonic Inlet-Engine Control Using Engine Speed as a Primary Variable for Controlling Normal Shock Position. NASA TN D-6021, 1970.

Seldner, Kurt; and Gold, Harold: Computer and Engine Performance Study of a Generalized Parameter Fuel Control for Jet Engines. NASA TN D-5871, 1970.

Szuch, John R.; Paulovich, Francis J.; Bruton, William M.: Study of Turbojet Combustor Dynamics Using Sweep-Frequency Data. NASA TN D-6084, 1970.

Wasserbauer, Joseph F.; and Whipple, Daniel L.: Experimental Investigation of the Dynamic Response of a Supersonic Inlet to External and Internal Disturbances. NASA TM X-1648, 1968.

Wasserbauer, Joseph F.: Dynamic Response of a Mach 2.5 Axisymmetric Inlet With Engine or Cold Pipe and Utilizing 60 Percent Supersonic Internal Area Contraction. NASA TN D-5338, 1969.

Wenzel, Leon M.: Experimental Investigation of the Effects of Pulse Pressure Distortion Imposed on the Inlet of a Turbofan Engine. NASA TM X-1928, 1969.

Wilhelm, Walter E.: Investigation of Tubing Effects on Amplitude Frequency Response of Pressure Sensing Systems Using Nonresonant Terminations. NASA TM X-1988, 1970.

Willoh, Ross G.: A Mathematical Analysis of Supersonic Inlet Dynamics. NASA TN D-4969, 1968.

Willoh, Ross G.; and Seldner, Kurt: Multistage Compressor Simulation Applied to the Prediction of Axial Flow Instabilities. NASA TM X-1880, 1969.

Zeller, John R.: Design and Analysis of a Modular Servoamplifier for Fast-Response Electrohydraulic Control Systems. NASA TN D-4898, 1968.

Zeller, John R.: Analysis of Dynamic Performance Limitations of Fast Response (150 to 200 Hz) Electrohydraulic Servos. NASA TN D-5388, 1969.

PROPULSION SYSTEM

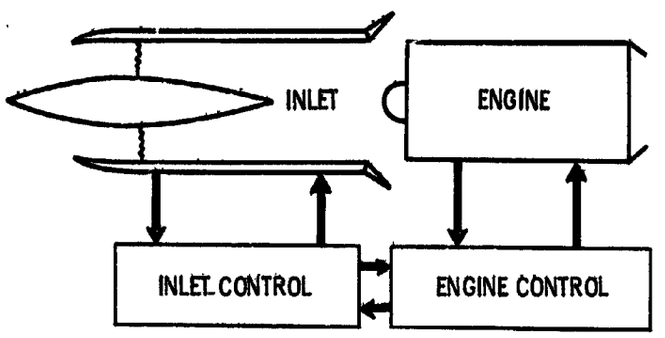

CS-56909

Figure XI-1

IDEALIZED INLET WITH TERMINATION

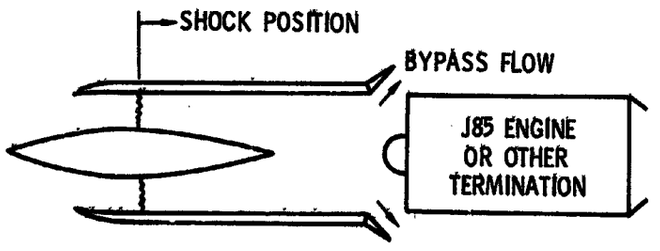

CS-56902

Figure XI-2

FREQUENCY RESPONSE OF SHOCK POSITION

COMPARISON OF ANALYTICAL AND EXPERIMENTAL RESULTS

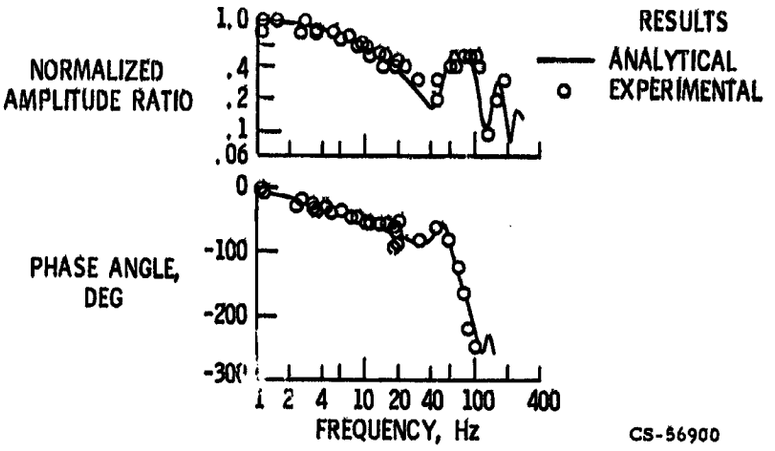

Figure XI-3

SHOCK POSITION CONTROL SYSTEM

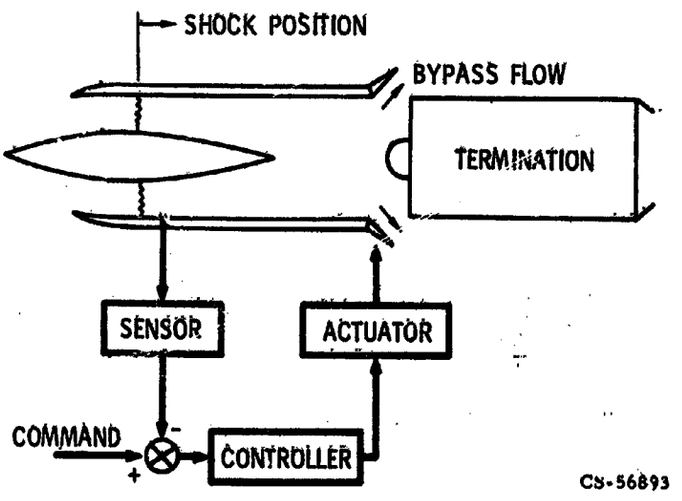

Figure XI-4

FREQUENCY RESPONSE OF SHOCK POSITION

COMPARISON WITH AND WITHOUT CONTROL

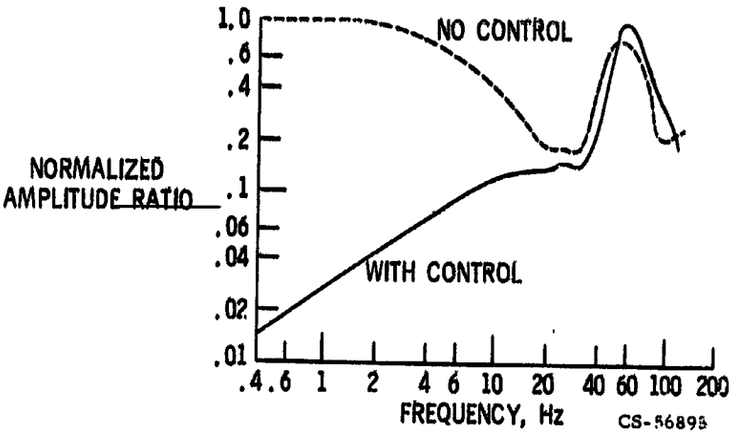

Figure XI-5

COUPLED CONTROL SYSTEM

BYPASS DOORS CONTROL SHOCK POSITION

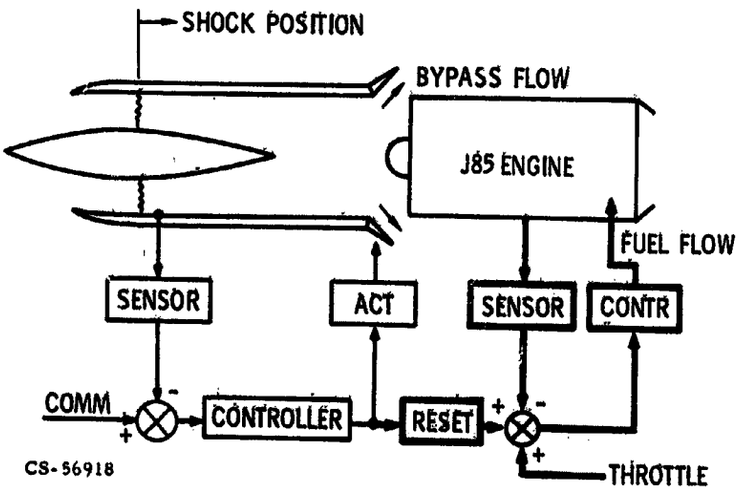

Figure XI-6

TRANSIENT RESPONSE OF COUPLED SYSTEM

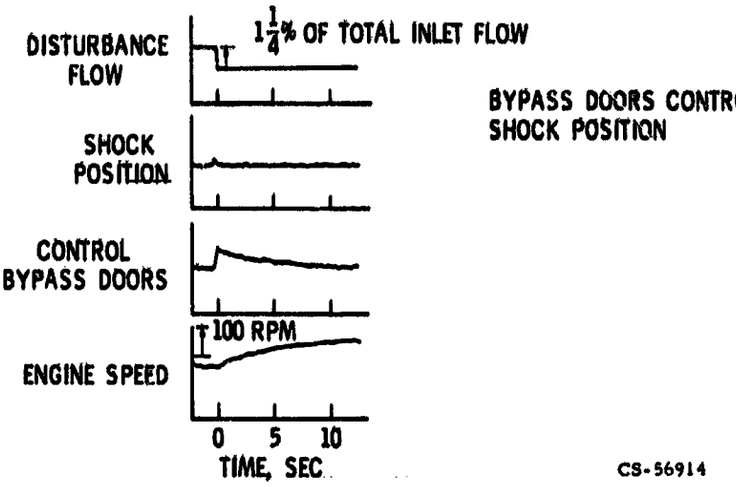

Figure XI-7

COUPLED CONTROL SYSTEM

ENGINE SPEED CONTROLS SHOCK POSITION

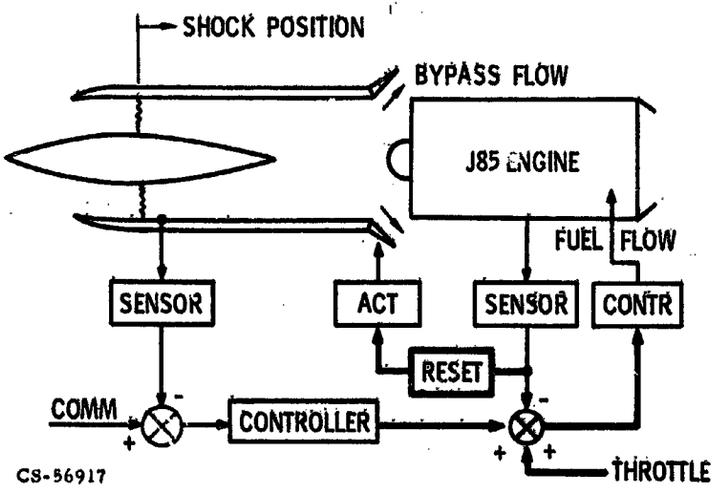

Figure XI-8

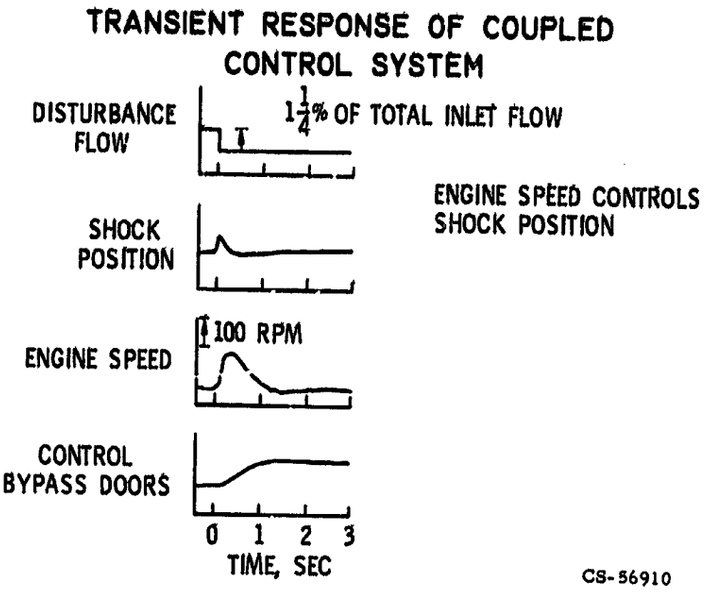

Figure XI-9

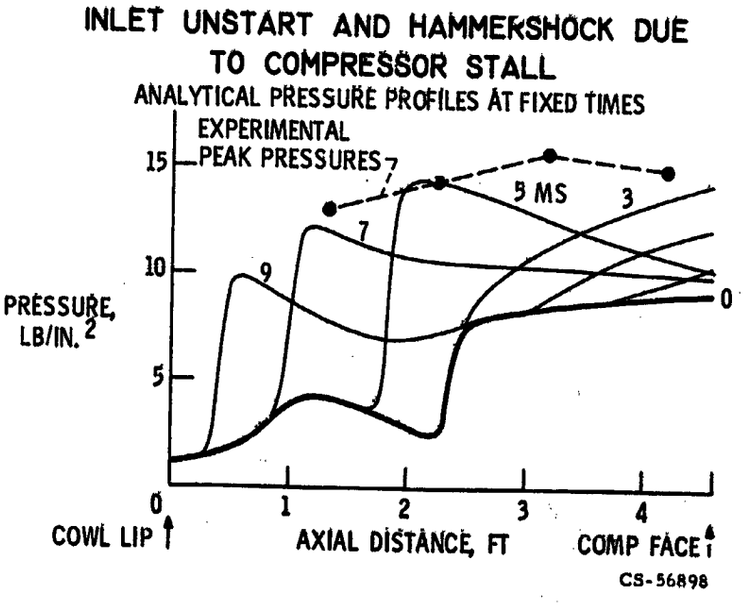

Figure XI-10

INLET UNSTART DUE TO EXTERNAL GUST

ANALYTICAL PRESSURE PROFILES AT FIXED TIMES

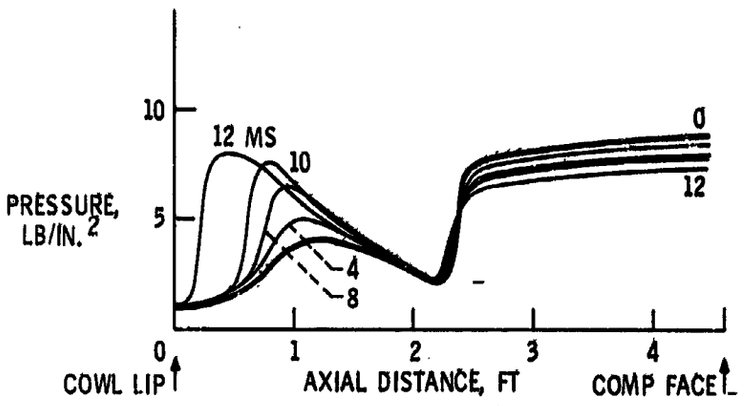

CS-56897

Figure XI-11

INLET RESTART REQUIREMENTS

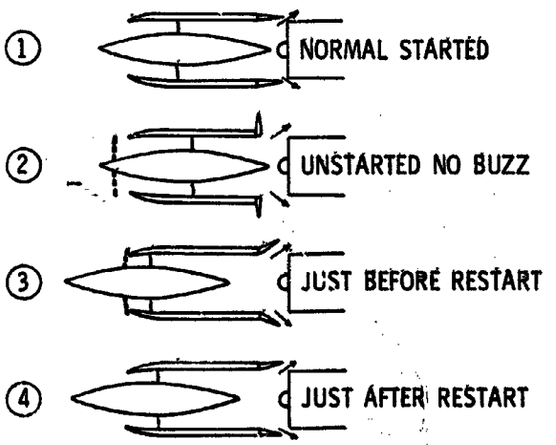

Figure XI-12

CS-56904

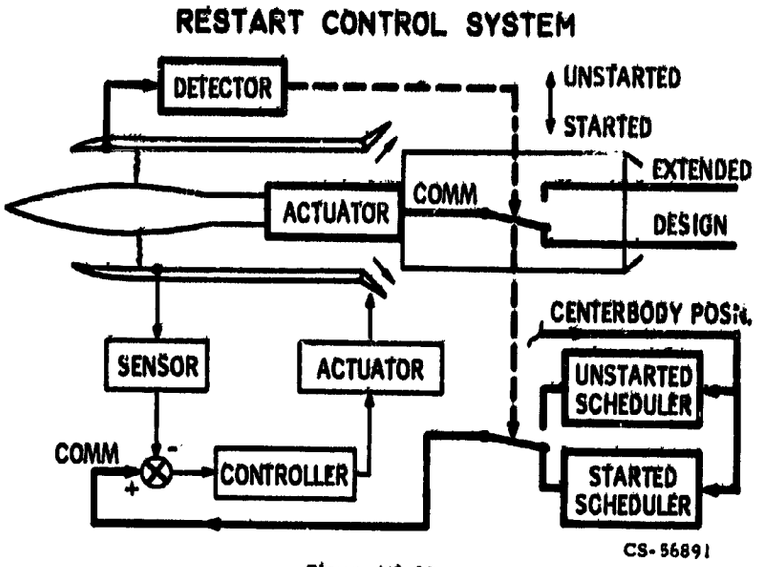

Figure XI-13

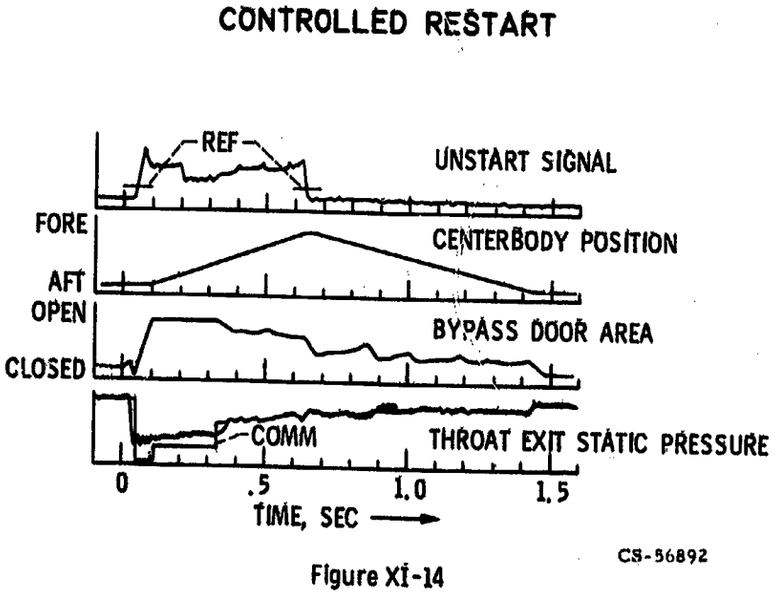

Figure XI-14

CONTROLLED RESTART

COMBUSTOR RELIGHT

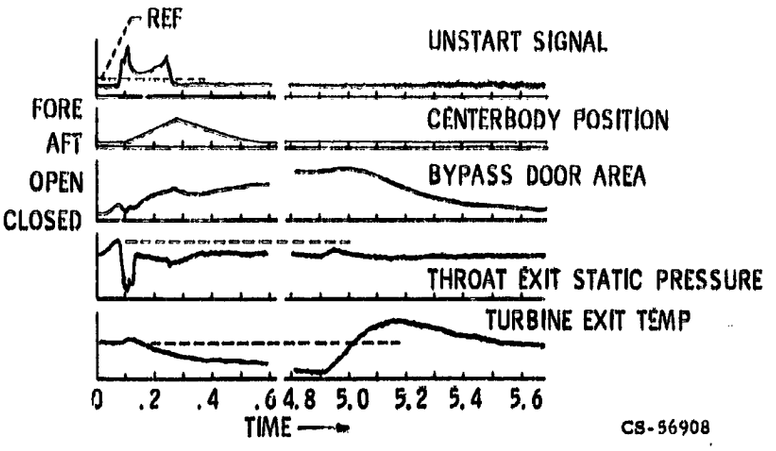

Figure XI-15

IDEALIZED COMBUSTOR

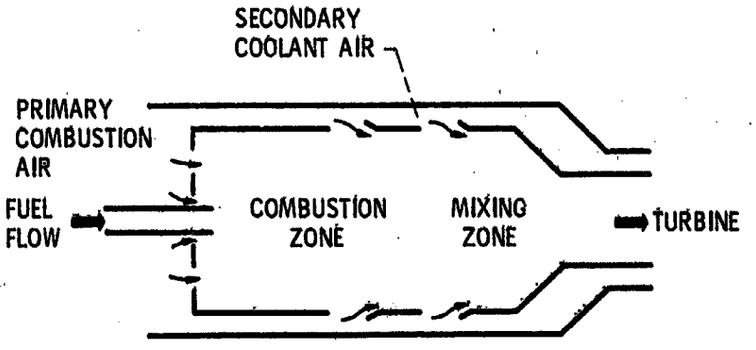

Figure XI-16

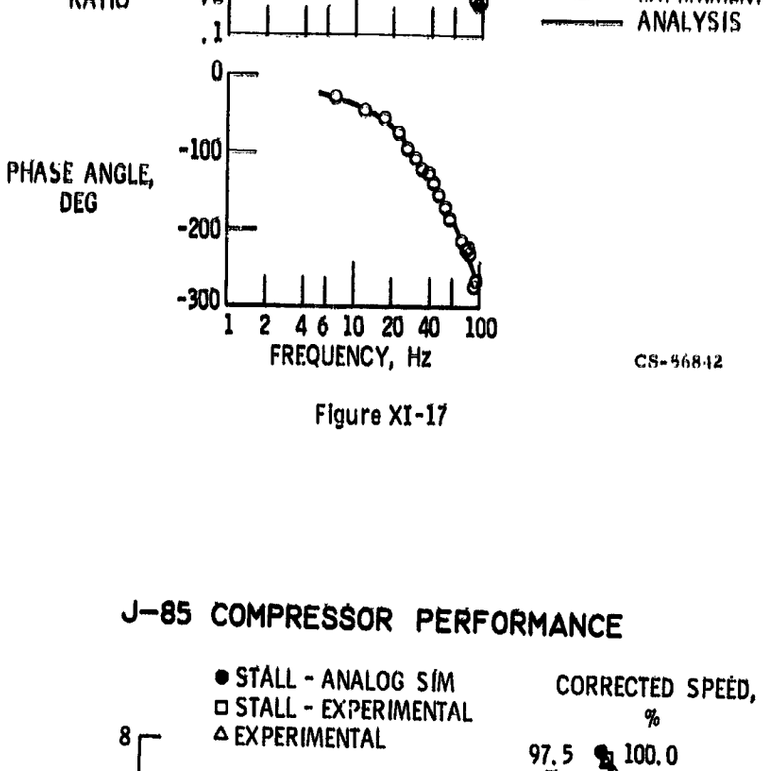

Figure XI-17

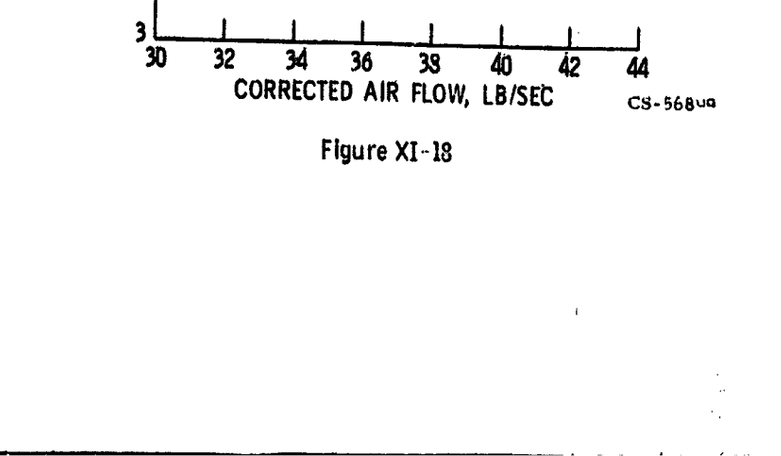

Figure XI-18

FREQUENCY RESPONSE OF SIXTH STAGE PRESSURE
FUEL FLOW DISTURBANCE; J85

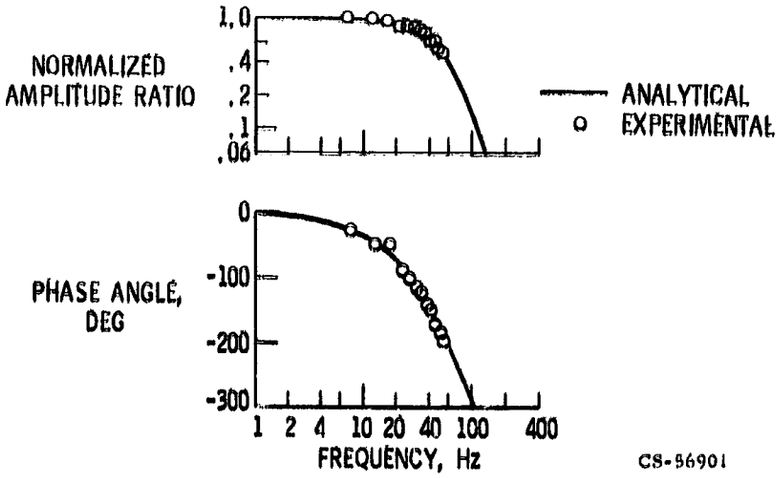

Figure XI-19

TF-30 TURBOFAN SCHEMATIC

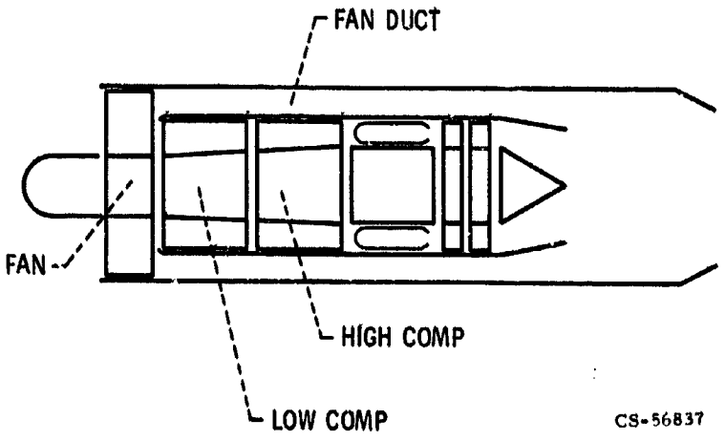

Figure XI-20

RESPONSE OF TURBOFAN ANALYSIS

INLET PRESSURE DISTURBANCE; TF-30

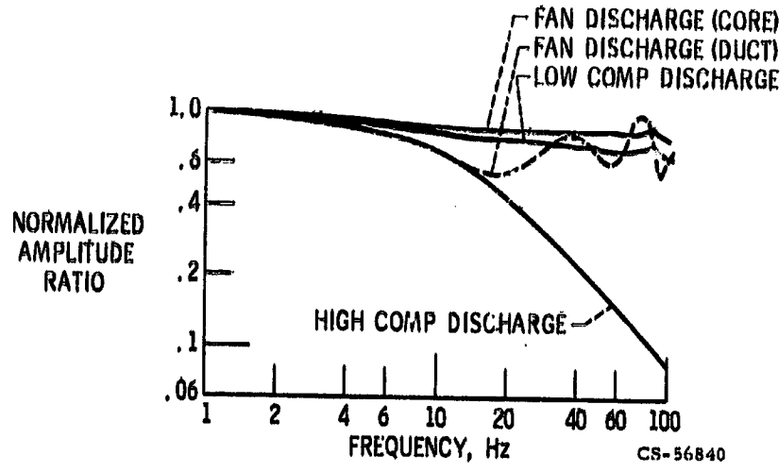

Figure XI-21

RESPONSE OF TURBOFAN EXPERIMENTAL

INLET PRESSURE DISTURBANCE; TF-30

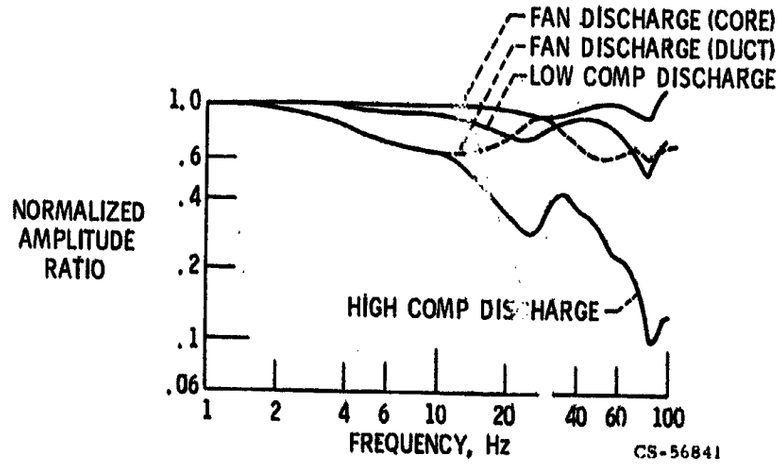

Figure XI-22

IDEAL INLET STATIC PRESSURE PROFILE

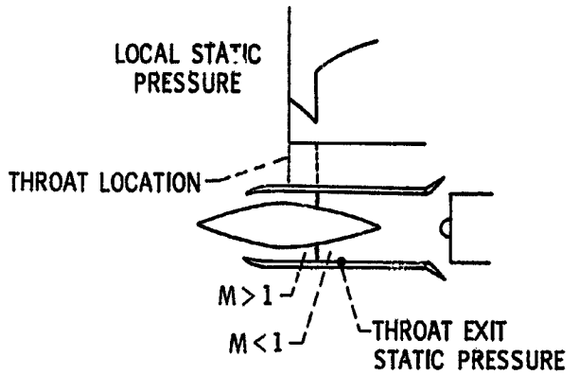

Figure XI-23 CS-56906

TYPICAL REAL INLET STATIC PRESSURE PROFILES

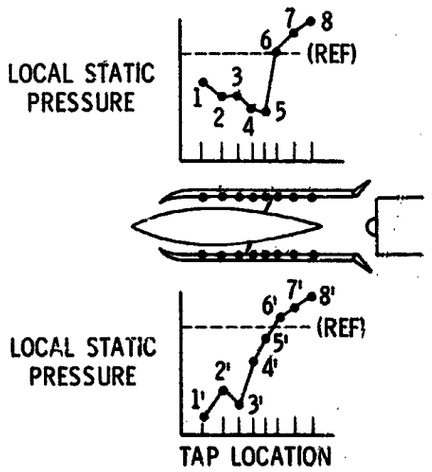

CS-56905

Figure XI-24

ELECTROHYDRAULIC SERVOSYSTEM

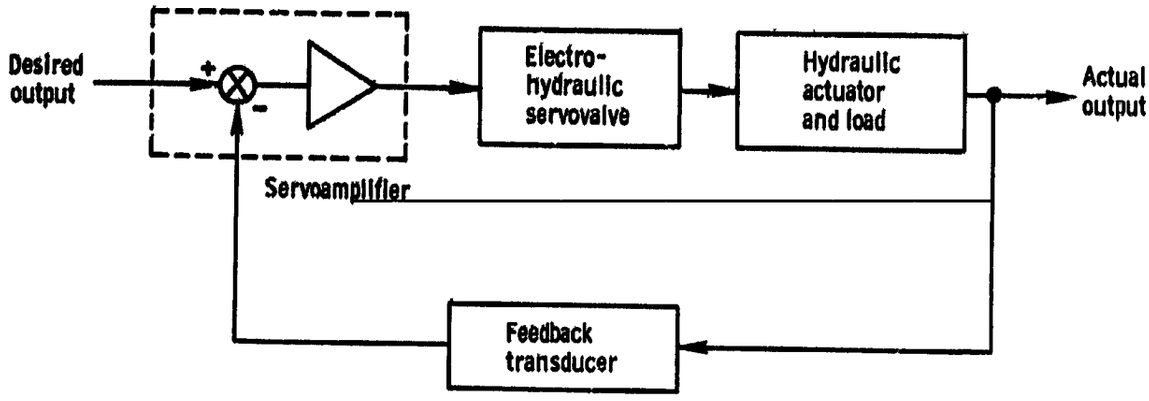

Figure XI-25

FREQUENCY RESPONSE OF FAST RESPONSE SERVO

FUEL THROTTLING VALVE

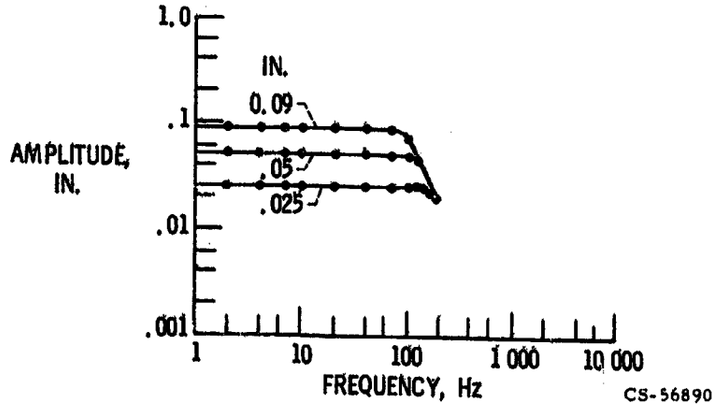

Figure XI-26

FREQUENCY RESPONSE OF RESEARCH SERVOS

COMPARISON OF TWO SERVOS OPERATING AT 40% AMPLITUDE

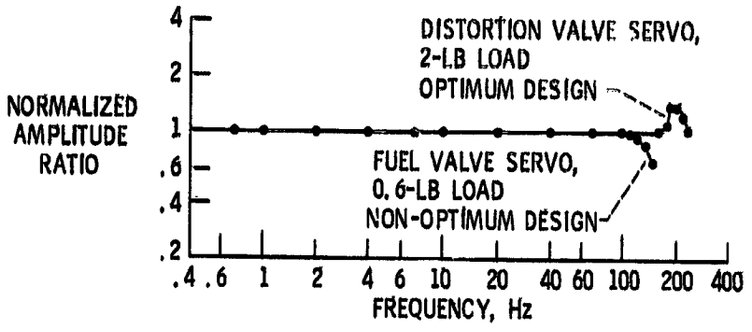

CS-56889

Figure XI-27

DIGITAL COMPUTER CONTROL SYSTEM

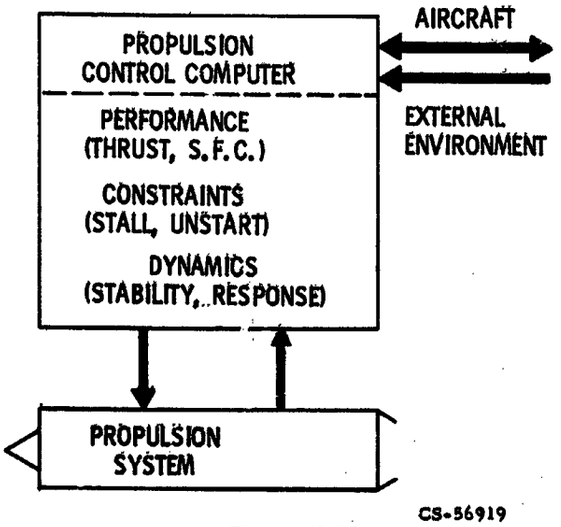

CS-56919

Figure XI-28

SAMPLE RATE REQUIREMENTS

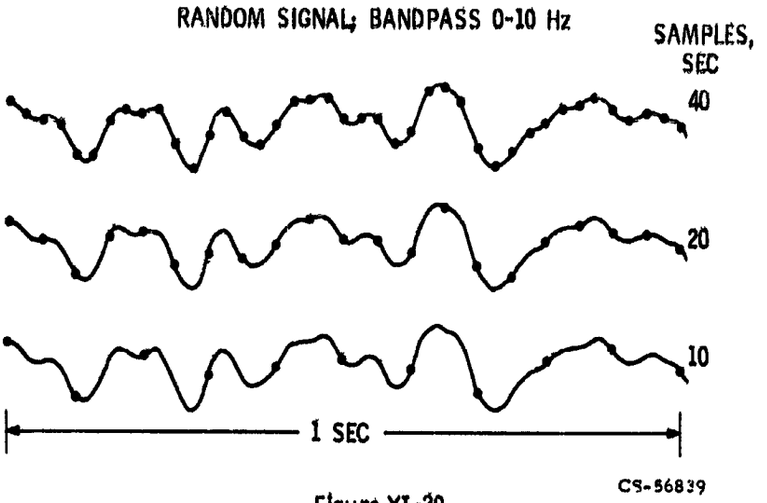

Figure XI-29

SHOCK POSITION CONTROL SYSTEM

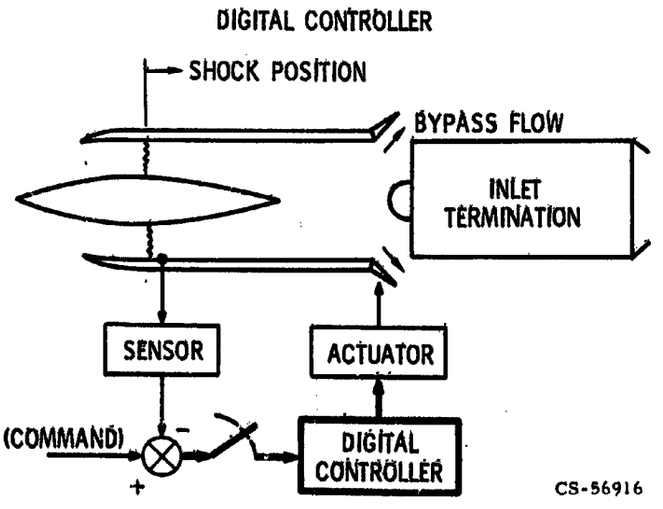

Figure XI-30

FREQUENCY RESPONSE OF SHOCK POSITION

COMPARISON OF ANALOG AND DIGITAL CONTROLS

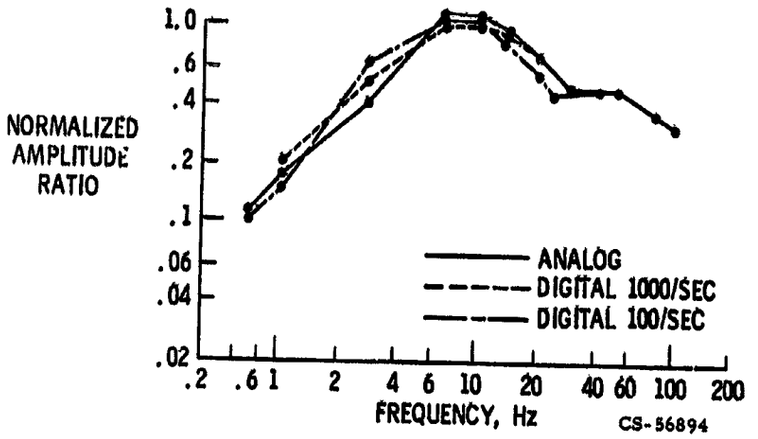

Figure XI-31

IDEALIZED INLET WITH TERMINATION

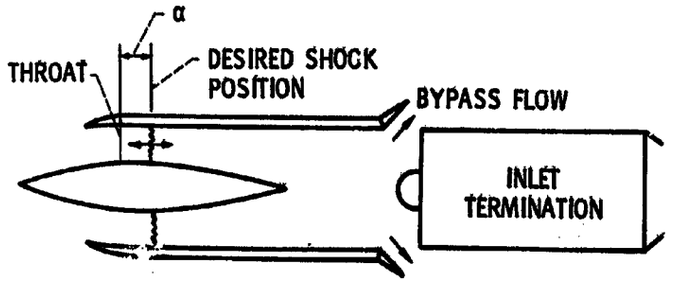

Figure XI-32

CS-56915

APPLICATION OF CONTROL THEORY TO A SUPERSONIC INLET

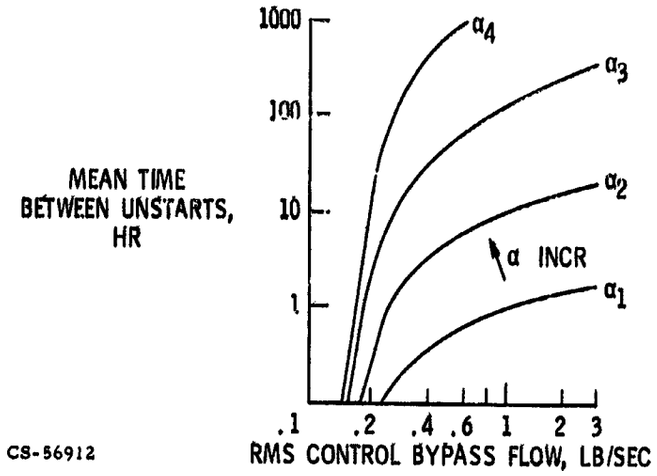

Figure XI-33

FREQUENCY RESPONSE OF SHOCK POSITION

COMPARISON OF CLASSICAL AND OPTIMAL CONTROL

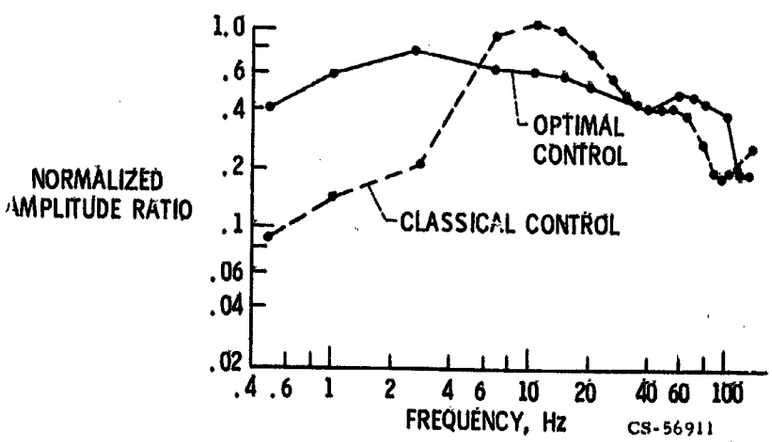

Figure XI-34

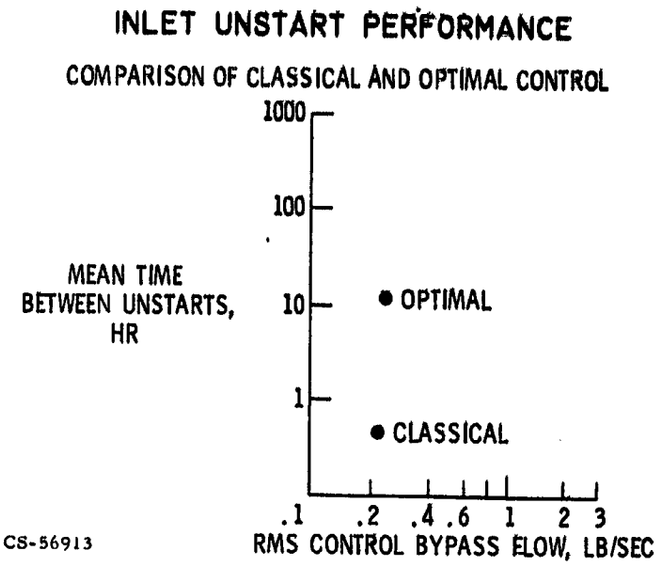
INLET UNSTART PERFORMANCE
COMPARISON OF CLASSICAL AND OPTIMAL CONTROL
1000
100
10
1
MEAN TIME BETWEEN UNSTARTS, HR
OPTIMAL
CLASSICAL
.1
.2
.4
.6
1
2
3
RMS CONTROL BYPASS FLOW, LB/SEC
CS-56913

Figure XI-35

XII. CRYOGENIC FUELS FOR AIRCRAFT

Jack B. Esgar

This discussion concerns some exploratory research being done by NASA on the use of cryogenic fuels for airbreathing gas turbine engines. Some of the results of this research may not find immediate application, but a portion of NASA's (and its predecessor NACA) research has historically been devoted to advanced concepts. For example, NACA began research on turbine cooling almost 15 years before it was embraced by industry.

Both NASA and industry have developed a significant background in the use and handling of cryogenic fuels for space vehicle boosters. This background information serves as an aid in the exploration of payoffs that might be obtained if cryogenic fuels are to be used in aircraft engines. This paper discusses the possible application of liquid methane to a supersonic transport type aircraft and the application of liquid hydrogen to the airbreathing engines for recoverable boosters and orbiters for the space shuttle.

ADVANTAGES AND PROBLEMS

Fuel Properties

The two prime reasons for the interest in cryogenic fuels for advanced aircraft are the higher heating value per pound of fuel (relative to Jet A) and the heat sink capacity that is available in this fuel for cooling hot components in the engine or the aircraft. These advantages are at least partially offset by the complications involved by having to store this fuel at a very low temperature and by the fact that the fuel has a lower density. A larger storage volume and insulated tanks are required.

Comparative fuel property trends are shown in figure XII-1 and table XII-1. In the figure the various fuel properties are plotted as functions of the hydrogen-carbon ratio H/C. The vertical dash-dot lines indicate the hydrogen-carbon ratios for Jet A, propane, methane, and hydrogen fuels. These trend curves indicate that the heating value, the heat sink, and the maximum use temperature (based on coking or fuel cracking) all increase with increasing values of the hydrogen-carbon ratio.

Conversely, the boiling temperature and the density decrease with an increasing hydrogen-carbon ratio. The cost of some of these fuels, such as propane and methane, are not accurately known for large supply quantities at an airport. But the information that is available indicates that Jet A, propane, and methane would cost approximately the same on a Btu basis. The cost of hydrogen is about six times that of the other fuels. Figure XII-1 also shows the flammable fuel-air ratio range for the four fuels. The flammable range initially decreases with an increasing hydrogen-carbon ratio to the minimum value corresponding to that for methane. Hydrogen, with an infinite hydrogen-carbon ratio, is a very reactive fuel and has a wide flammability range.

The low flammable fuel-air ratio range for methane can be both an advantage and a disadvantage. It is an advantage from the point of view of safety, because ignition can only occur within a narrow range of fuel-air ratios. It is somewhat of a disadvantage for the combustor. Having a narrow flammable range of fuel-air ratios can cause problems in the combustor, particularly in blowout limits and more difficult lightoff.

The ignition and burning characteristics of large pools of liquid methane were investigated at Lake Charles, Louisiana in 1961 by Conch Methane Services Limited. These tests were conducted on open pools of methane enclosed within a dike. The largest pool tested was 20 by 20 feet and contained liquid methane to a depth of 1 foot. The following conclusions (ref. 1) were drawn from these tests:

"(1) The flammable zone of vapors was confined well within the visible vapor (condensed moisture) cloud emanating from the pool.

(2) Although the vapor cloud remains visible for a distance of several pool diameters downwind, the flammable zone of vapors was confined to a few inches directly above the pool and to less than one-half the pool diameter in the horizontal downwind direction near ground level.

(3) The radiation flux level from the burning LNG pool was sufficient to cause ignition of wood under low wind conditions within a distance of about 1.25 pool diameters from the edge of the pool."

The relative safety of having "spills" or open pools of liquid methane was illustrated in a movie of these tests which showed a man walking up to the edge of a large pool of liquid methane holding a lighted torch in his hand. He lowered the torch down to within a few inches of the pool level. At this point, the pool slowly ignited and the man walked away unharmed.

The data for figure XII-1 are given in table XII-1. This table gives the more specific values of the heating value, limiting temperatures, heat sink, boiling temperature, density, flammable limits, and costs of Jet A, propane, methane, and hydrogen fuels. Although propane appears to have many desirable properties as illus-

trated in table XII-1, it has not been considered seriously as a fuel for aircraft. One reason is that at present propane is a byproduct of petroleum processing plants, and large scale production of propane would require major plant changes or construction of new plants. Probably more important is the fact that propane vapor is heavier than air; therefore, when a spill occurs the vapor hangs at ground level and provides a safety hazard. In the cases of methane and hydrogen, the vapor densities are less than that of air, and the vapor soon disperses into the atmosphere after a spill. The hazard is thereby decreased.

Liquid Methane for Supersonic Transport

Mission analyses, as reported in references 2 to 4, have shown that the payload or direct operating cost of a supersonic transport could be appreciably improved by using liquid methane as fuel in place of the more conventional Jet A fuel. The gains that can be obtained depend on the type of engine used in the aircraft, the mission, and the noise constraints. If there were no noise constraints, the direct operating cost or payload could be improved by more than 30 percent by switching from Jet A to liquid methane as a fuel. With noise constraints, which must be considered for commercial aircraft, the improvement in payload or direct operating cost is reduced; but the benefits are enough superior to those for Jet A fuel that it is worthwhile to continue research on the problems relating to the application of methane fuel to supersonic cruise aircraft. The gains in aircraft performance are due to primarily two factors. First, liquid methane has approximately 13 percent more energy per pound of fuel than Jet A fuel. Second, the heat sink of methane can be up to $7\frac{1}{2}$ times that of the Jet A fuel. This high heat sink capacity is very useful for high speed aircraft for cooling the engine components such as the turbine, cooling the lubricating oil and hydraulic fluid, and for controlling temperatures in the passenger cabin. Using the methane heat sink for reducing turbine cooling air temperature can substantially reduce the amount of compressor air that must be bled from the engine for turbine cooling. This reduction in compressor air bleed can significantly improve the engine performance.

There are also a number of problems involved with using liquid methane as an aircraft fuel. The most significant problems requiring research are the following:

(1) Fuel storage in aircraft

(2) Combustor development

(3) Engine fuel control and pumping system

(4) Ground handling and storage in large quantities

(5) Impact on aircraft size, drag, and design

(6) Future methane cost and worldwide availability

Research is presently underway at NASA Lewis Research Center on the first three items. Results of this research are discussed later in this paper. Investigations of the remaining three items are expected to be conducted in the future. Some discussion of these remaining three items is required, however. There is considerable experience with the ground handling of liquid methane gas. Liquid natural gas (about 93 percent methane), which is produced in significant quantities in North Africa, is transported by ship to various parts of the world. At the unloading areas, it is stored in various types of facilities, primarily in above-ground insulated tanks. The handling and storage problems of liquid methane (or liquid natural gas) for aircraft could be somewhat different. For some airport locations in the world, the methane would probably be stored as a cryogenic liquid and could be piped to and pumped into the waiting aircraft. For other locations, it may be desirable to pipe the methane in the form of natural gas to the airport. At the airport a liquification plant could produce the liquid methane which would be supplied to the aircraft. Investigations are required to determine the technological and financial effects that the use of cryogenic fuels would have on airport fuel handling problems.

The use of liquid methane fuel will have a significant effect on the aircraft design. Liquid methane has a density about one-half that of conventional Jet A fuels. As a result, the storage of liquid methane in the aircraft would require increased tank volume; therefore, aircraft size would probably increase. This increased size could affect the aircraft drag characteristics and could diminish some of the gains resulting from switching to liquid methane as a fuel. An investigation is also required on the structural problems that would be involved by storing a cryogenic fuel with a temperature of approximately -260° F in an aircraft where the outside structure of the aircraft would be heated to temperatures between 400° and 750° F (depending on the flight Mach number) by aerodynamic heating. The thermal distortion problems that result from these large temperature differences require a detailed design study.

Preliminary investigations have been made on the projected cost and worldwide availability of liquid methane if it were to be used for a supersonic transport fleet. These preliminary investigations indicated the cost to be competitive or probably lower than that for Jet A fuel in most of the world's airports. This preliminary investigation was conducted prior to the current concern over the possible shortage of fossil fuels for both household and industrial needs. As a result, a further investigation is required on the feasibility of using liquid methane for a worldwide fleet of supersonic transport aircraft.

Supersonic transport aircraft show the greatest advantages from switching from

Jet A fuel to liquid methane, primarily because of the need for a large heat sink capacity resulting from both turbine cooling requirements and aerodynamic heat input. In addition, the number of airports in the world that would have to supply liquid methane would be more limited than if the fuel were to be used for other aircraft. There are some advantages, however, to using liquid methane in subsonic aircraft and in helicopters. The engine trend for these aircraft is toward higher turbine inlet temperatures. With the higher inlet temperatures the heat sink capacity of liquid methane can be used very advantageously to lower turbine cooling air temperature and thus reduce the quantity of air required. The smaller cooling air quantities improve engine performance. The higher heating value of liquid methane, compared to Jet A fuel, is also an advantage. Although this discussion on liquid methane refers most specifically to supersonic transport aircraft, most of the research being conducted is equally applicable to subsonic aircraft and helicopter use.

Liquid Hydrogen for Space Shuttle

For conventional subsonic and supersonic aircraft with gas turbine engines, liquid hydrogen probably would not be considered as a suitable fuel. The primary reason is that it has an extremely low density, less than one-tenth that of conventional Jet A fuel. This low density creates a very difficult storage problem in conventional aircraft. A second reason is that hydrogen has very wide flammability limits. The danger of ignition and explosion would be significant in normal everyday use. The space shuttle presents a unique application for liquid hydrogen as a fuel for airbreathing engines. The space shuttle will use liquid hydrogen as a fuel for the propulsion rockets. Therefore, hydrogen will already be available in the vehicle. The plans for the space shuttle call for airbreathing propulsion in the recoverable booster and recoverable orbital vehicles. These engines would be used to obtain the required cross range and to have the capability for go-around at the airport upon landing. Using hydrogen that is already in the aircraft eliminates the necessity of providing separate tanks and fuels for these engines. Another advantage of hydrogen is that it has more than $2\frac{1}{2}$ times as much energy per pound of fuel as conventional Jet A fuel. These combined effects could result in either a vehicle with reduced weight or increased payload if the return airbreathing propulsion is required.

Because of the limited locations where liquid hydrogen will be used for space shuttles, and the fact that provisions will already require supplying liquid hydrogen into the vehicle, there are fewer problems that require investigation in the application of liquid hydrogen to the airbreathing engines than there are for liquid methane. The only problems that appear to require investigation are

(1) Combustor development

(2) Engine fuel control and pumping system

The combustor development is expected to be a minor problem because hydrogen is an extremely reactive fuel and burns easily. NACA conducted tests on gas turbine engines burning hydrogen in the late 1950's. These tests were conducted both in ground test engines and flight test engines. These tests did not thoroughly investigate the liquid hydrogen pumping problems nor engine transient operation. As a result, additional research is required on engine fuel control and the liquid hydrogen pumping systems. This research is presently underway at NASA Lewis Research Center.

HEAT SINK UTILIZATION

Two methods of using the heat sink of cryogenic fuels are shown in figures XII-2 and XII-3. Figure XII-2 is a result of an analytical study on the heat exchangers required to reduce the cooling air temperature for an engine that can be used in a Mach 3 transport aircraft. This engine would have a takeoff airflow of 475 pounds per second. Two heat exchangers would be used for reducing cooling air temperatures. These heat exchangers would be annular in shape and wrapped around the inner and outer diameters of the combustors. The dimensions of the heat exchangers are shown in figure XII-2. The heat exchangers are quite small and would have very little effect on the overall engine dimensions. The combined weight of the two heat exchangers is less than 1 percent of the engine weight. With heat exchangers of this size the cooling air temperature could be reduced more than 400° F. This reduction results in a significant reduction in cooling airflow. The amount of cooling airflow reduction is dependent on the turbine inlet temperature level and the method of cooling used in the turbine. Reductions of at least 50 percent in the coolant flow requirements are easily possible with a 400° F temperature reduction of the cooling air.

Figure XII-3 illustrates a direct cooling application using cryogenic fuels. Paper VIII by Beheim et al. discusses the research conducted on air cooling an exhaust plug nozzle. Approximately 3.5 percent of the compressor airflow is required to air cool the exhaust nozzle under afterburning conditions.

Calculations have been made on direct cooling a plug nozzle using Jet A fuel. In this case, the fuel would be circulated through small tubes brazed to the internal surface of the plug nozzle. The temperature rise of the Jet A fuel is approximately 560° F using this method of cooling. A temperature rise of this magnitude could result in fuel coking, which could create some problems in long-term operation. It

may be feasible, however, to periodically remove the carbon that has formed in a manner similar to that used in self-cleaning ovens. The plug nozzle would be operated at a temperature of approximately 1200° F with air passing through the fuel tubes. At this temperature the carbon would oxidize and the tubes would be cleaned. This operation could be performed by running the engine without afterburning.

Research was conducted with AiResearch Manufacturing Company (contract NAS1-5002) under the sponsorship of the NASA Langley Research Center (ref. 5) to investigate the direct cooling of surfaces of hypersonic cruise vehicles with methane and with hydrogen. The results of this investigation showed that a configuration (see inset in fig. XII-3) could be successfully used for cooling panels with methane or hydrogen at heat fluxes equivalent to those in the exhaust nozzle of an airbreathing engine under afterburning conditions. The methane temperature rise for direct cooling, using the quantity of fuel that would be burned in the afterburner, would be 650° F. The resulting final fuel temperature would be sufficiently low that no coking would be expected. If hydrogen were used as a coolant, the temperature rise would be only 310° F. There are no coking problems at any temperature level with hydrogen. Under some conditions, however, material problems could develop from hydrogen diffusion and embrittlement, and from surface decarburization.

An analytical investigation was also conducted (ref. 6) to investigate the feasibility of direct cooling stator vanes of the turbine using either hydrogen or methane as the coolant. This stator vane cooling method results in a somewhat complex construction problem in order to keep from overcooling the vane outer surfaces. Internal coolant tubes were separated from the vane shell by means of low thermal conductivity metal fibers that provided adequate, but not excessive, conduction between the fuel tubes and the outer shell. The results of the investigation show that the cooling would be feasible if the vane did not have a long thin trailing edge. The trailing edge region was the only region which was difficult to cool. The problem in the trailing edge is in providing adequate coolant passages into the thin cross section.

CRYOGENIC FUEL SYSTEM

A research program is underway to investigate the fuel systems for liquid methane and liquid hydrogen fueled engines under realistic operating conditions. The fuel systems are being designed and fabricated under contract (NAS3-14319) with the General Electric Company. These fuel systems will then be installed on an experimental engine and tested in the altitude test facility at the NASA Lewis Research Center. Figure XII-4 presents a schematic illustration of the cryogenic fuel systems that will be investigated. The four heavy boxes in figure XII-4 illustrate the

components that are similar for conventional fuel systems and for cryogenic fuel systems. These common (in principle) elements include boost pump, heat exchangers for the hydraulic fluid and the engine oil, and engine combustor. For the cryogenic fuel systems, particularly a methane system for a supersonic cruise aircraft, additional heat exchangers would be utilized. A heat exchanger would probably be used for controlling the air temperature in the passenger cabin. (A secondary heat exchange medium would probably be used between the methane and cabin air to ensure against methane leakage into the cabin in the event of a heat exchanger leak.) Two additional heat exchangers would be utilized for reducing the cooling air temperature for the turbine. These heat exchangers would be similar to those shown in figure XII-2.

One of the most significant changes in the fuel system would be in the fuel pump. Conventional Jet A fuel systems use a pump that bypasses excess fuel back to the pump inlet. Such an arrangement is not feasible with cryogenic fuels, because part of the fuel would vaporize and the pump would become vapor locked.

For the experimental fuel system that is to be used in the NASA investigation, a variable speed vane pump will be used. Such a pump has been constructed, and pumping tests with liquid hydrogen have been started. The pump operation is satisfactory, but not enough experience has been gained to establish pump durability. Past experience in cryogenic fuel pumps for flight applications have been limited to a few hours of use. Most of these applications have been for space vehicle boosters, and long life has not been a requirement. For aircraft use, pump life would have to be in excess of 1000 hours. It is expected that considerable development will be required before such pump life can be obtained.

The fuel control system is also more complicated than it is for a Jet A fueled engine. The cryogenic fuel would be metered in the vapor state into the combustor. Metering in this location would be required to obtain adequate engine response time. The fuel control must also control the amount of liquid fuel that is pumped so the quantity of fuel pumped matches the quantity of fuel metered to the combustor. The fuel system to be investigated in the NASA investigation is still in the design stage; consequently, no experimental results are available.

FUEL STORAGE IN THE AIRCRAFT

Saturated Methane Fuel

Liquid methane can be stored in either the saturated or subcooled state. The saturated fuel state is that which occurs when the fuel is at its boiling temperature.

This is the equilibrium state of liquid methane fuel and is therefore the state in which the fuel can be more easily handled. It would be desirable if the fuel could be used in this state in the aircraft from the standpoint of ground handling problems. A disadvantage of using saturated fuel is that heat addition or reduced vent pressure (such as occurs with increased altitude) causes fuel boiloff.

The amount of boiloff that could occur is shown in figure XII-5. This figure shows boiloff as a function of altitude for two tank vent pressures. If the tank were vented to ambient pressure, the figure shows that by the time the aircraft had climbed to 70 000 feet, which would be a likely cruise altitude for a Mach 3 aircraft, the boiloff would be approximately 12 percent of the initial fuel weight in the tank.

Conventional tanks can withstand some pressurization. If these tanks could be pressurized to 4 pounds per square inch above the ambient pressure, the boiloff at the end of the climb to 70 000 feet would be 8 percent. This boiloff is still excessive and would eliminate much of the gain that could be obtained by switching from conventional Jet A fuel to liquid methane.

The boiloff resulting from change in altitude could be eliminated if the tanks were designed to withstand an internal pressure of 1 atmosphere, but boiloff could still occur due to aerodynamic heating. Figure XII-6 illustrates the tank weights that would be obtained for a number of different types of tanks designs capable of withstanding an internal pressure of 15 pounds per square inch gage (psig). These results were obtained from references 7 to 9 for wing and fuselage tanks. The ordinate in figure XII-6 is the tank weight as a fraction of the fuel weight contained within the tank. The abscissa is the tank volume as a fraction of the total available volume within the cavity in the fuselage or the wing where the tank would be located. Each data point is the result of a design study of a particular configuration. It is desirable to have the ratio of tank volume to available volume as high as possible since methane fuel density is low. All available volume in spaces allocated to fuel tanks would be required for fuel storage. The results shown in figure XII-6 indicate that with reasonable ratios of tank volume to available volume the fuselage tank weights, including the weight of the insulation, would be of the order of 3 percent of the fuel weight contained. The wing tanks will be heavier because they have a less favorable surface to volume ratio. The wing tank weight can be of the order of 5 to 6 percent of the fuel contained within the wing tanks. The insulation accounts for approximately one-third of the weights shown for both fuselage and wing tanks. These tank weights are consistent with the values assumed in the mission analyses that showed the gains to be obtained by switching to methane fuel from conventional Jet A fuel.

There is an advantage to designing the tanks to withstand pressures greater than 15 psig. These greater pressures would reduce fuel boiloff due to aerodynamic heat-

ing. The results presented in references 7 and 8 show that for some tank construction methods the weight penalty for tanks designed for 30 psig is only slightly greater than those designed for tank pressures of 15 psig because the minimum gage requirements for tank walls established the weight of the tanks rather than wall stresses.

Subcooled Methane

A liquid is subcooled if its temperature is below the boiling temperature. The heat sink is increased by using subcooled methane instead of saturated methane. If the methane were subcooled approximately 25° F at 1 atmosphere pressure, its vapor pressure would be lower than that which would occur at the high altitude cruise point with tanks vented to 4 psi above ambient pressure. As a result, the problem of boil-off due to increasing altitude could be eliminated by using subcooled fuel and only moderate tank pressurization. Subcooled fuel introduces new problems, however. Ground handling is complicated by the need for added refrigeration equipment to keep the fuel cooled to a temperature lower than the boiling temperature. A more serious problem, however, is the reduced vapor pressure of the fuel when it is subcooled. Storing the fuel in a tank, where the fuel vapor pressure is less than ambient atmospheric pressure, leads to the risk of tank collapse unless the tank is pressurized to keep the pressure inside the tank at least equal to the pressure external to the tank. There is a problem finding a suitable pressurant for liquid methane that is insoluble and noncondensible at liquid methane temperature. Helium would be a suitable pressurant, but if liquid methane were to be used as a fuel for a worldwide fleet of supersonic transports, the world's supply of helium may be inadequate. Nitrogen would seem to be a suitable pressurant, but nitrogen goes into solution in liquid methane in excess of 11 weight percent at 25° F subcooling (ref. 10). A possible method of using liquid nitrogen as a pressurant will be presented later.

Another problem involved in the use of subcooled methane is to get the methane into the aircraft tanks in a subcooled state. The tanks will normally be warm as the result of aerodynamic heating. These tanks must then be cooled by the fuel loaded into the tanks. If the fuel is in a subcooled state when it is loaded in the tanks, some or all of this subcooling will be eliminated by cooling the tanks. This problem has been investigated under a NASA contract (NAS3-12411) with Martin Marietta Corporation in Denver. The results of part of this investigation are shown in figure XII-7. This figure shows the quantity of subcooled fuel to be loaded into a tank (tank initially at room temperature) to obtain a fuel bulk temperature approaching the supply temperature. The tank used in the experiments was one that represented a wing tank for a supersonic cruise vehicle, including the insulation system. It can be seen in figure

XII-7 that when the tank became initially filled the amount of subcooling of the bulk fuel in the tank was only one-half the subcooling of the supply fuel. The fuel supplied to the tank was continued with the excess fuel being flowed out of the tank vent and into other tanks. Figure XII-7 shows that somewhat in excess of two volumes of tank fuel were required before the bulk temperature of the fuel approached that of the supply temperature. Having to supply twice as much fuel to an aircraft and recirculate it in order to cool all the fuel to the required temperature would be a problem in ground handling that should be avoided if at all possible.

Gelled and Slush Methane

Possible solutions to the problems of nitrogen solubility in subcooled methane and the tank cooling problem can be obtained by first gelling the methane to decrease the convection currents and then partially freezing the methane to make a mixture that provides a larger heat sink. Aerojet Liquid Rocket Company is presently investigating (NASA contract NAS3-14305) methods of gelling liquid methane. The results obtained to date have indicated that adding $1\frac{1}{4}$ weight percent of water to the liquid methane in the form of extremely fine ice crystals results in a gelled solution. Tests conducted with subcooled gelled methane have shown that nitrogen solubility is almost completely eliminated under both static and sloshing conditions for time periods consistent with aircraft storage.

Figure XII-8 shows approximately 500 cubic centimeters of gelled methane in a glass Dewar. It is observed that gelled methane is milky in appearance, whereas normal liquid methane is as clear as unpolluted water. Figure XII-8 shows gas bubbles suspended in the gelled methane, which indicates there is a lack of mobility. This lack of mobility undoubtedly explains why nitrogen solubility is low. The nitrogen probably still goes into solution at the methane surface, but due to the mixing currents being essentially eliminated in the gelled methane, only the surface becomes saturated and solubility does not occur in the rest of the methane within the time periods expected for supersonic transport flight.

Experiments have not as yet been conducted on partially freezing gelled methane to provide gelled slush. It would be expected, however, that gelling will stabilize the slush so that a homogeneous mixture will occur. In loading slush methane into a tank, the tank will be cooled by melting the slush. If 50 weight percent of the methane were frozen to form slush, the heat sink of the slush would be equivalent to about 12° F of subcooling. This much of a heat sink is likely to be enough to cool the tanks during filling. The methane will then be left in a subcooled state, and the loading problem will be simplified.

Methane Tank Insulation

Insulation systems for methane tanks are being investigated under NASA contract NAS3-12425 with the Martin Marietta Corporation in Denver for both internal and external insulation systems. Figure XII-9 illustrates the internal insulation system under investigation. In this system the insulation is placed inside the tank. A unique feature of this insulation is that there are no pressure forces on the insulation. This elimination of pressure forces results from perforations in the Kapton film covering the insulation. These perforations permit the methane contained in the tank to permeate the insulation system. The methane that permeates into the interior is quickly vaporized. The surface tension of methane provides a liquid-vapor interface at the film perforation. The minimum thermal conductivity of this type of insulation system is that of the methane vapor. This conductivity is low enough to be satisfactory for storage of liquid methane in an aircraft. It is also satisfactory for storage of other cryogenics, such as liquid hydrogen in space boosters.

The components of the insulation system shown in figure XII-9 include a polyimide flexcore filled with fiber glass. The fiber glass essentially eliminates methane vapor convection currents, which would increase the heat flux through the insulation. The fiber glass is also opacified to radiation by either coating the fiber glass filaments with aluminum or mixing small aluminum particles in with the fiber glass. This opacification to radiation is required to obtain an effective insulation system when the external surface is heated to temperatures of the order of 400° to 700° F by aerodyanmic heating.

Also shown in figure XII-9 is a scrim cloth, which is used as a bonding aid between the polyimide flexcore and the tank wall.

This internal insulation system is still under development and only preliminary results have been obtained. The results obtained thus far have been encouraging, and it appears that the system can be used in the future after development is complete.

Calculations have been made of the boiloff that would be obtained from insulated methane tanks (refs. 11 and 12). It is expected that these results would be applicable to the insulation system shown in figure XII-9. The bargraphs in figure XII-10 show methane boiloff as a fraction of the initial fuel weight contained in fuselage tanks for various insulation thicknesses, tank vent pressures, and initial methane temperatures. It is shown that with a tank pressurized to 15 psia, an insulation thickness of 1 inch will result in a boiloff of approximately 2.5 percent of the initial fuel weight. As would be expected, the boiloff is approximately inversely proportional to the insulation thickness. The figure also shows that if the tank could with-

stand a pressurization of 30 psia, boiloff could be essentially eliminated with 1 inch of insulation.

Figure XII-10 also illustrates the boiloff encountered with two different amounts of subcooling using 1 inch of insulation and the tank at a vent pressure of 4 psi greater than ambient pressure. This portion of the figure shows that if 25° of initial subcooling could be obtained, the boiloff would be less than would occur if saturated methane were stored in a tank pressurized to 15 psia. The figure shows, however, that the amount of subcooling obtained is very critical. If only 20° of subcooling were obtained, the boiloff would be greater than for the pressurized tanks. As illustrated in figure XII-7, it may be difficult to get the amount of subcooling that is desired. As a result, considerable research is still required to determine if adequate subcooling could be utilized in aircraft tanks.

Figure XII-10 shows boiloff results for fuselage tanks. The boiloff for wing tanks is slightly less than that for fuselage tanks because the pilot would probably expend fuel from the wing tanks first. These tanks would therefore be emptied during the first half of the mission. Boiloff stops when the tanks become dry. The total boiloff for both fuselage and wing tanks for a typical Mach 2.7 supersonic transport mission amounts to less than 2 percent of the total fuel contained in the aircraft. Calculations in reference 12 indicate that if the flight Mach number were increased to 3.5 for the identical insulation system, the total fuel boiloff would increase to only 2.25 percent of the initial fuel contained in the aircraft.

METHANE COMBUSTORS

Research has been conducted using swirl can combustors with methane as a fuel at NASA Lewis Research Center. The swirl can combustors, illustrated in figures XII-11 and XII-12, are similar to those discussed in paper IV by Grobman et al. and in references 13 and 14. Combustion efficiency data are presented in figure XII-13, which shows that combustion efficiencies of approximately 100 percent can be obtained at reference velocities of the order of 80 to 90 feet per second. Reference velocities of this magnitude are consistent with low pressure losses in aircraft combustors. Combustion efficiencies exceeding 100 percent, shown in figure XII-13, result from uncertainties in temperature rise measurements.

The figure also shows that the combustion efficiency is influenced by the temperature of the methane entering the combustor. During supersonic cruise, the methane will be heated to temperatures between 600° and 1200° F; therefore, high combustion efficiencies can be expected. During the limited operation of engine startup, idle, and letdown at subsonic speeds, the methane entering the combustor could be at a

lower temperature. For these conditions some penalty in combustion efficiency is likely to occur. It appears, however, that combustion efficiency in a properly designed methane combustor need not be a problem.

Figure XII-14 shows blowout limits for two types of combustors using Jet A and methane as fuels. The blowout limits are not satisfactory for either combustor, but the primary conclusion drawn from figure XII-14 is that the blowout limits for methane are inferior to those for Jet A. It is indicated, therefore, that research will have to continue on obtaining combustors with adequate blowout limits for methane. The actual fuel used to obtain the data in figures XII-13 and XII-14 was natural gas. Natural gas contains approximately 93 percent methane. The results are expected to be the same as if pure methane were used.

CONCLUSIONS

It can be concluded from the investigations that there are no insurmountable problems for utilizing either liquid methane or liquid hydrogen as fuels for aircraft gas turbine engines. Additional combustion research is required for liquid methane primarily to improve the blowout limits at high altitude.

Engines have been run at NASA and at aircraft engine plants with both methane and hydrogen as fuels during the last 15 years. There is no question that engines can run on these fuels. More research is required, however, on the fuel control and pumping systems where the liquid methane or hydrogen is pumped in the liquid state, vaporized and superheated in heat exchangers, and them metered in the vapor state to the combustor. Cryogenic pumps that will have adequate life for long time aircraft operation will undoubtedly be a development problem.

Investigations have not been made of overall aircraft problems resulting from using liquid methane as a fuel. This low density, cryogenic fuel will affect aircraft size, drag, and the structural design requirements to accommodate the large temperature differences between aircraft structure adjacent to the liquid methane and the outside aircraft surfaces which are subject to aerodynamic heating.

Methane fuel availability and cost are thought to be satisfactory for aircraft use, but recent forecasts of possible shortages of fossil fuels make it necessary to investigate further the availability and cost.

The ground handling of liquid methane fuel at airports would be far different from the present ground handling methods used for Jet A fuel. As a result, there would be significant changes to the airport fuel supply systems, and nearby liquid methane liquefaction plants might be required.

There is no assurance at this time that liquid methane fuel will be used in future supersonic transports. It appears, however, that there are no great problems inhibiting its use. It is quite possible that the advantages gained due to its higher heating value, reasonable cost, and greater heat sink might make future supersonic transports more attractive than those using conventional Jet A fuels.

REFERENCES

1. Welker, J. R.; Wesson, H. R.; and Sliepcevich, C. M.: LNG Spills: To Burn or Not to Burn. Preprint 69-D-23, Distribution Conference of A. G. A., Operating Section, Philadelphia, Pa., May 12-15, 1969.

2. Whitlow, John B., Jr.; Eisenberg, Joseph D.; and Shovlin, Michael D.: Potential of Liquid-Methane Fuel for Mach-3 Commercial Supersonic Transports. NASA TN D-3471, 1966.

3. Koenig, Robert W.; and Kraft, Gerald A.: Influence of High-Turbine-Inlet-Temperature Engines in a Methane-Fueled SST When Takeoff Jet Noise Limits are Considered. NASA TN D-4965, 1968.

4. Weber, Richard J.: A Review of the Potential of Liquid-Methane Fuel for Supersonic Transports. Presented at the National Academy of Sciences Cryogenic Engineering Conference, Cleveland, Ohio, Aug. 19-21, 1968.

5. Walters, F. M.; and Buchmann, O. A.: Heat Transfer and Fluid Flow Analysis of Hydrogen-Cooled Panels and Manifold Systems. AiResearch Mfg. Co. (NASA CR-66925), 1970.

6. Colladay, Raymond S.: Thermal Feasibility of Using Methane or Hydrogen Fuel for Direct Cooling of a First-Stage Turbine Stator. NASA TN D-6042, 1970.

7. Chambellan, Rene E.; Lubomski, Joseph F.; and Bevevino, William A.: Structural Feasibility Study of Pressurized Tanks for Liquid-Methane Fueled Supersonic Aircraft. NASA TN D-4295, 1967.

8. Chambellan, Rene E.; and Bevevino, William A.: Comparative Study of Fuselage Tanks for Liquid-Methane-Fueled Supersonic Aircraft. NASA TN D-4837, 1968.

9. Eisenberg, Joseph D.; and Chambellan, René E.: Tankage Systems for a Methane-Fueled Supersonic Transport. NASA TM X-1591, 1968.

10. Hibbard, Robert R.; and Evans, Albert, Jr.: On the Solubilities and Rates of Solution of Gases in Liquid Methane. NASA TN D-4701, 1968.

11. Pleban, Eugene J.: Analytical Heat Transfer Investigation of Insulated Liquid Methane Wing Tanks for Supersonic Cruise Aircraft. NASA TN D-5641, 1970.

12. Pleban, Eugene J.: Analytical Heat Transfer Investigation of Insulated Liquid Methane Fuselage Tanks for Supersonic Cruise Aircraft. NASA TN D-6157, 1970.

13. Marchionna, Nicholas R.; and Trout, Arthur M.: Turbojet Combustor Performance with Natural Gas Fuel. NASA TN D-5571, 1970.

14. Schultz, Donald F.; Perkins, Porter J.; and Wear, Jerrold D.: Comparison of ASTM-A1 and Natural Gas Fuels in an Annular Turbojet Combustor. NASA TM X-52700, 1969.

TABLE XII-I. - COMPA ISON OF FUEL PROPERTIES

	Jet A	Propane	Methane	Hydrogen
Hydrogen-carbon ratio	0.16	0.22	0.33	∞
Heating value, Btu/lb	18 600	19 700	21 100	49 900
Limiting use temperature, ^{o}F	400	850	1250	∞
Heat sink, Btu/lb				
To limiting use temperature	175	705	1320	7000
To 1000^{o} F	700	820	1085	4950
Boiling temperature, ^{o}F	350	-44	-259	-423
Density, lb/ft^3	50.5	36.2	26.6	4.4
Flammable limits, percent stoichiometric	52 to 400	51 to 280	46 to 164	14 to 250
Relative cost per Btu	1.0	[a]0.8 to 1.0	[a]0.8 to 1.0	6

[a]Estimates based on available information.

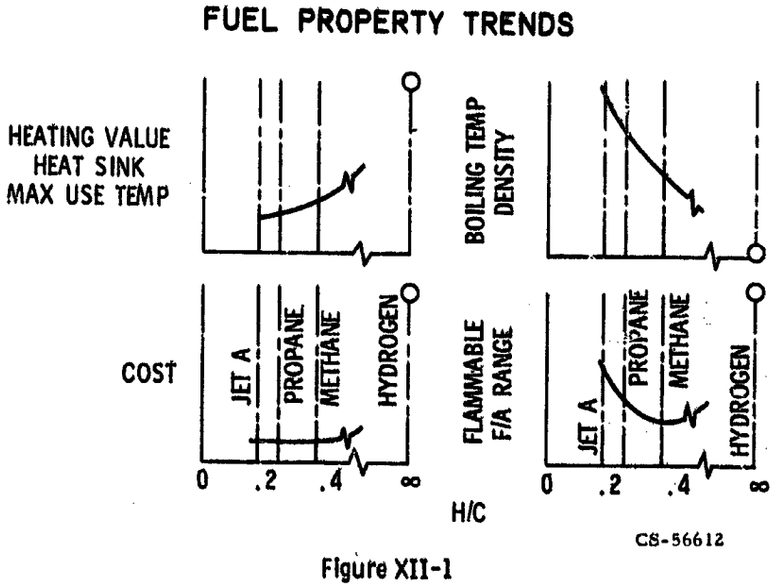

Figure XII-1

POSSIBLE METHANE HEAT EXCHANGER INSTALLATION

COMPRESSOR DISCHARGE = 1652° R

COOLING AIR TEMPERATURE = 1236° R

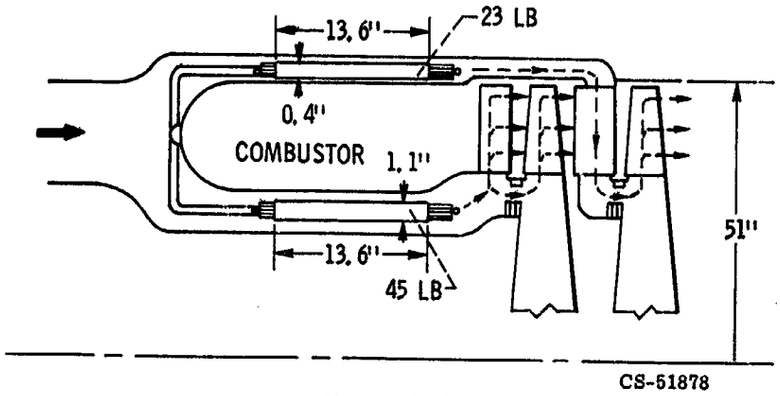

Figure XII-2

EXHAUST NOZZLE COOLING

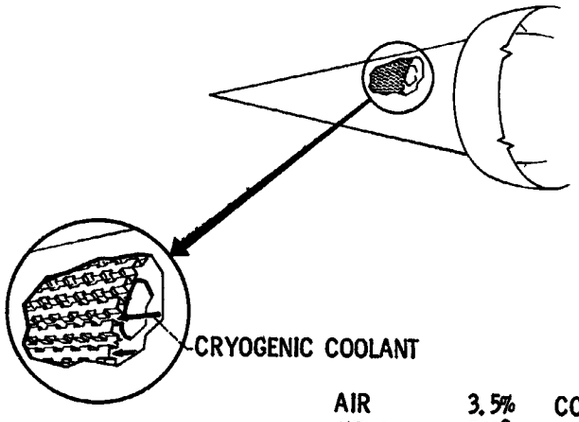

AIR	3.5%	COMPRESSOR FLOW
JET A	560° F	TEMP RISE
METHANE	650° F	TEMP RISE
HYDROGEN	310° F	TEMP RISE

Figure XII-3

SCHEMATIC OF A CRYOGENIC FUEL SYSTEM

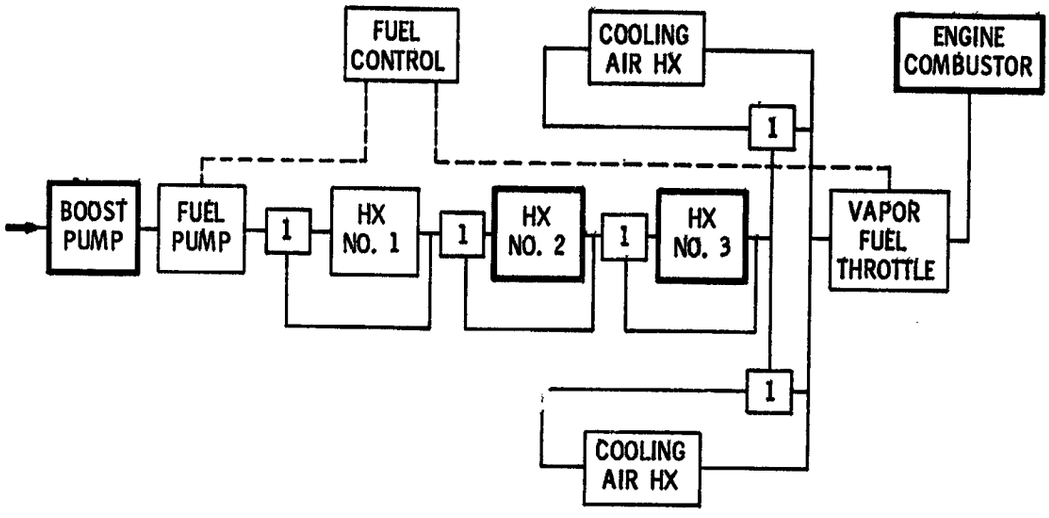

1 HEAT EXCHANGER BYPASS CONTROL
HX NO. 1 ENVIRONMENTAL COOLING
HX NO. 2 HYDRAULIC OIL
HX NO. 3 ENGINE OIL

CS-56604

Figure XII-4

METHANE BOILOFF FROM REDUCED TANK PRESSURE

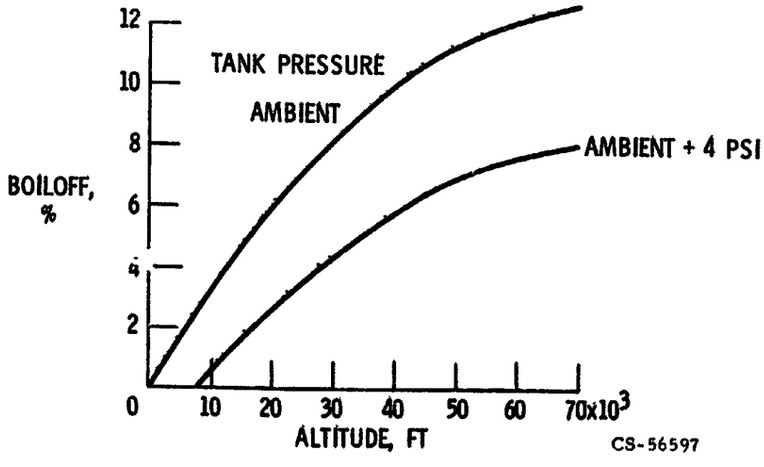

CS-56597

Figure XII-5

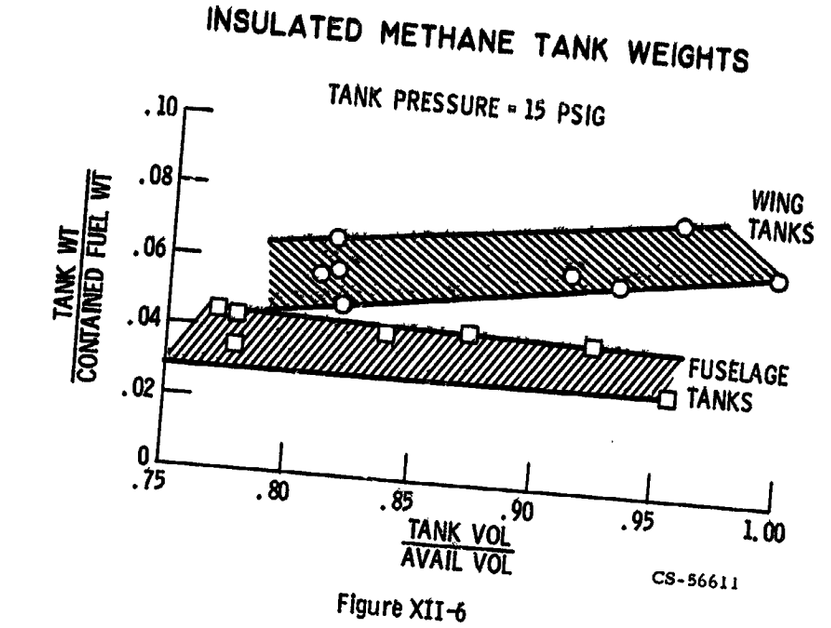

Figure XII-6

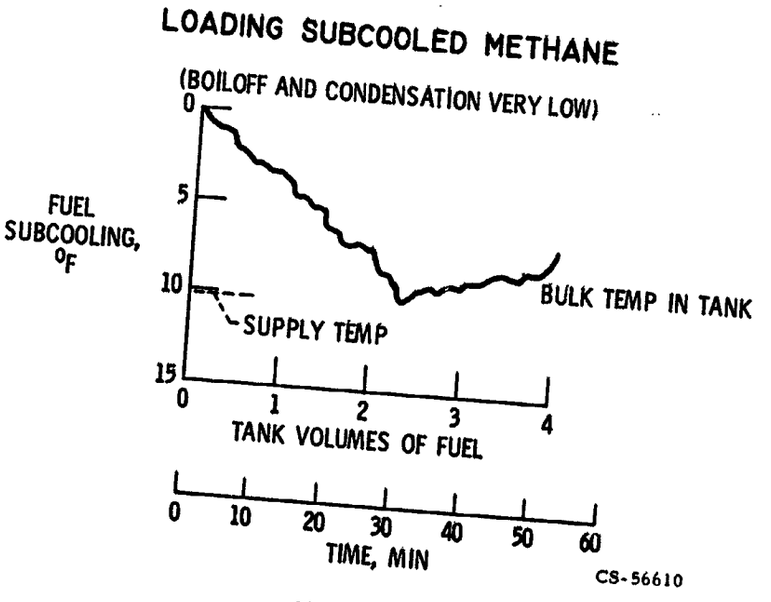

Figure XII-7

GELLED METHANE

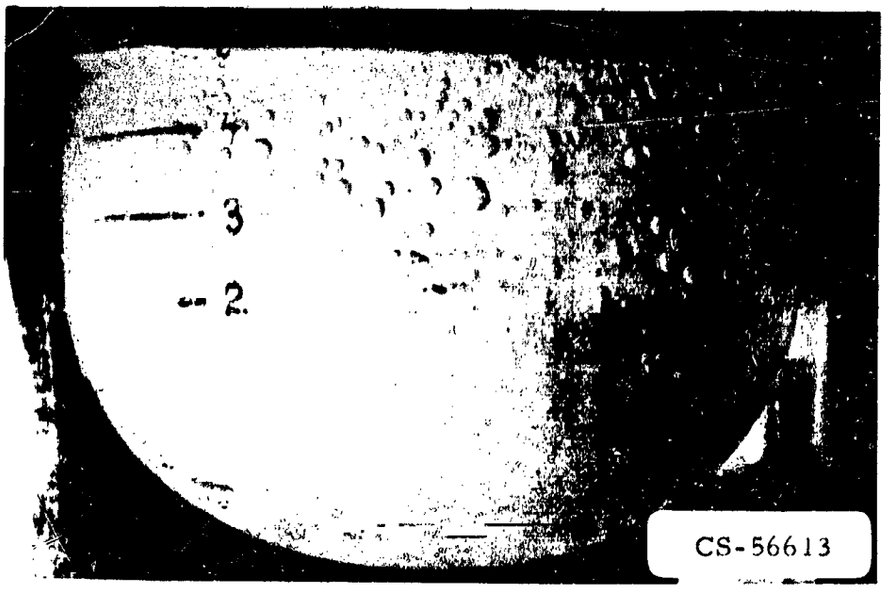

Figure XII-8

INTERNAL INSULATION SYSTEM

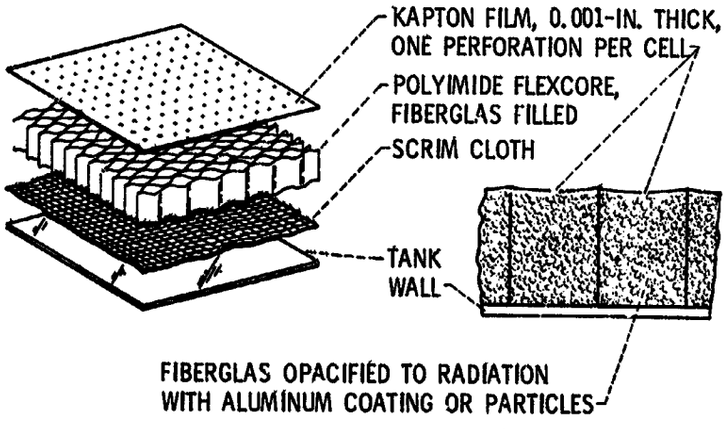

Figure XII-9

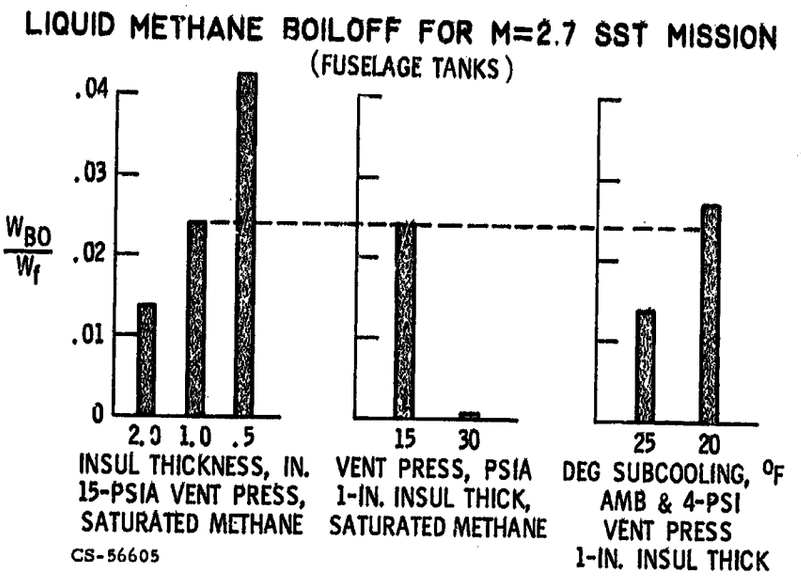

Figure XII-10

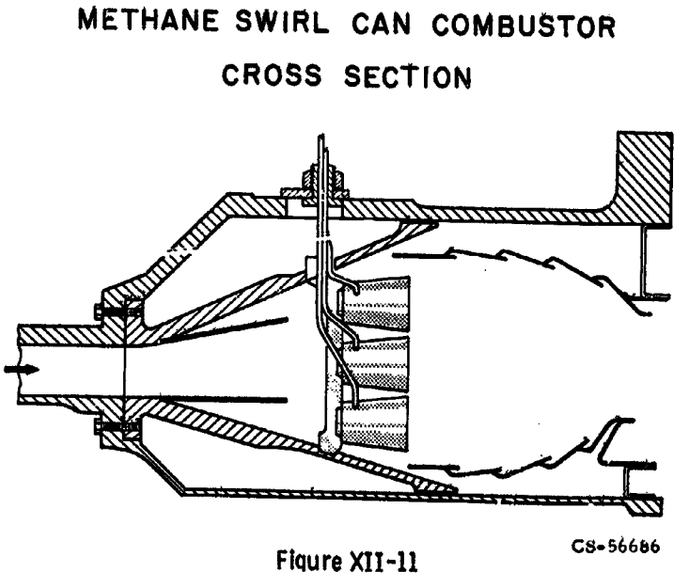

Figure XII-11

EXPERIMENTAL METHANE SWIRL CAN COMBUSTOR

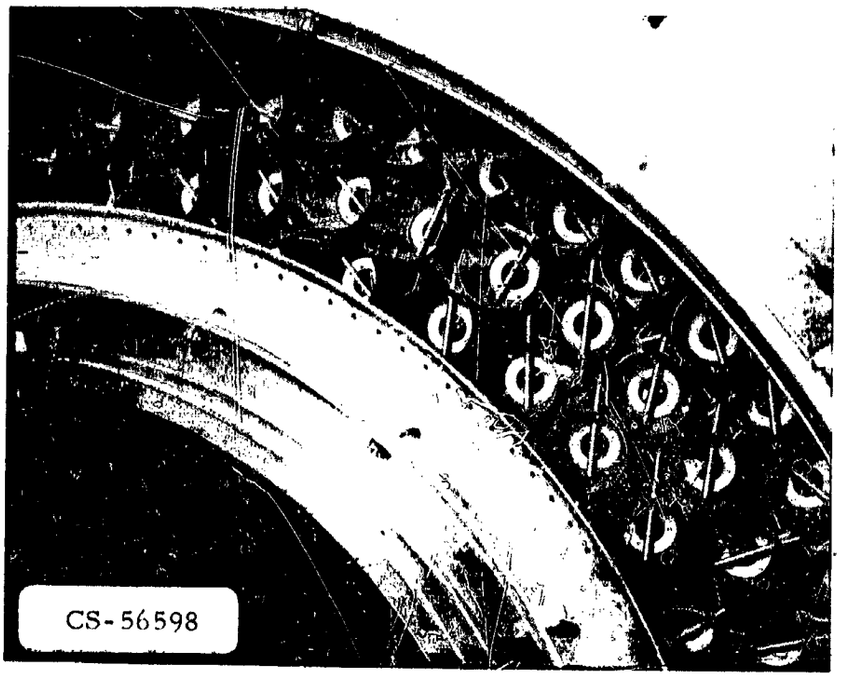

Figure XII-12

METHANE COMBUSTOR EFFICIENCY

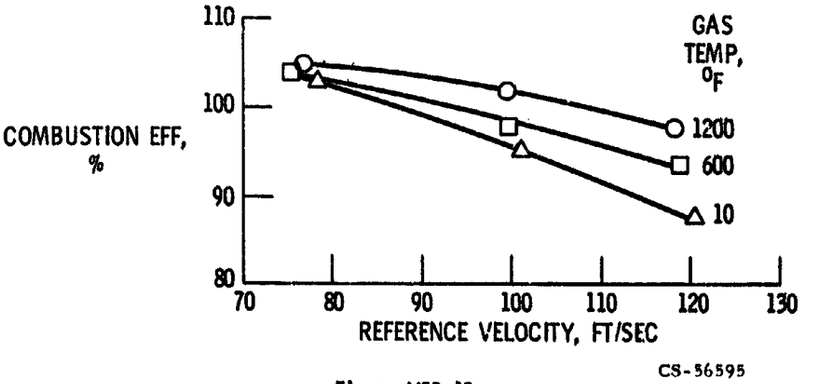

Figure XII-13

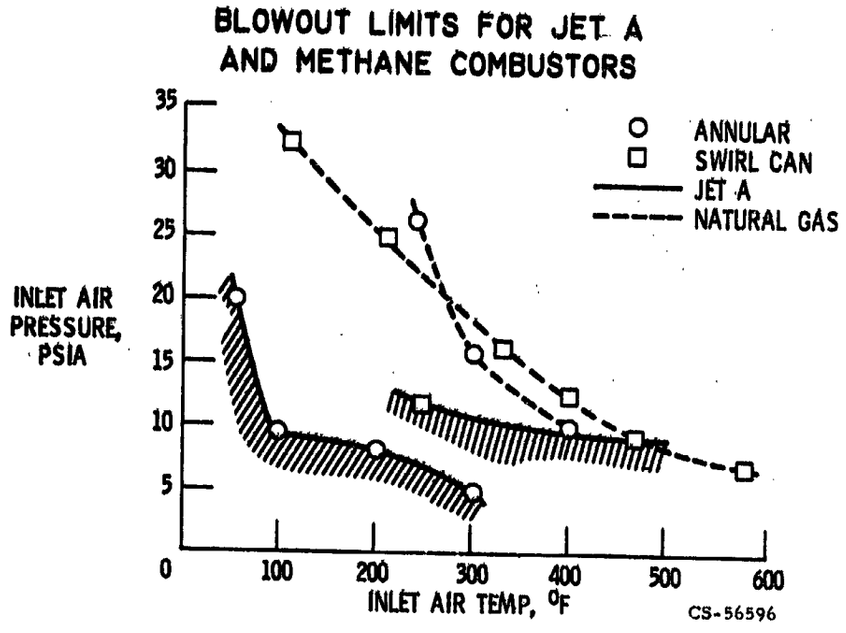

Figure XII-14

XIII. ADVANCEMENTS IN BEARINGS, SEALS, AND LUBRICANTS

Erwin V. Zaretsky and Lawrence P. Ludwig

Advances in airbreathing turbojet engines have dictated that bearing materials and lubricants operate at higher temperatures, higher speeds, and higher loads. The first generation supersonic transport (SST) turbine engine main-shaft bearings will operate at a bearing temperature of 425° F and a maximum speed of 1.3 million DN. It is anticipated that more advanced engine designs may require bearings to operate at temperatures between 500° and 550° F and speeds of approximately 2 million DN. Projection of these trends would predict bearing temperatures to 600° F and bearing speeds of 3 to 4 million DN, which would produce higher bearing operating stresses (fig. XIII-1).

Aircraft gas turbine engines have main-shaft seals to restrict gas leakage into the bearing compartments (sumps). Various types of shaft seals are used; some engines use labyrinth seals exclusively; others use face and/or circumferential type contact seals. Labyrinth seals have the disadvantages of high leakage rates and associated debris passage; long operating life and reliability are the chief advantages as compared to rubbing contact type seals. The contact seals have low leakage capability but are limited in pressure differential and speed because of rubbing contact. For conventional contact seals, current limits are sealed pressure differential near 125 psi, sliding speed of 350 feet per second, and sealed gas temperature of 800° F (ref. 1).

Main-shaft seal conditions are shown in figure XIII-2. In 1970 the requirements are sliding speeds of approximately 400 feet per second with air pressures of approximately 250 psi and gas temperatures of approximately 1000° F. It is predicted that future requirements will be sliding speeds in the range of 500 to 600 feet per second, air pressures of 400 to 500 psi, and air temperatures near 1400° F.

The work reported herein is a summary of the rolling-element bearing and seal state of the art with emphasis on NASA contributions to solving problems encountered in advanced airbreathing turbojet engines.

ROLLING-ELEMENT BEARINGS

In order to assure proper bearing operation at elevated temperatures, a lubricant film is required to separate the contacting components. This is illustrated in figure XIII-3. A ball or roller is in contact with a surface. The ball deforms because of the force which is placed on it and the elastic properties of the material. Under dynamic conditions and with the introduction of a lubricant, a film, which is referred to as an elastohydrodynamic (EHD) film (due to the elastic deformation of the material and the hydrodynamic action of the lubricant), is formed between the two surfaces (ref. 2). This film, which is generally dependent on lubricant base stock and viscosity, is of the order of 5 to 10 millionths of an inch thick at elevated temperatures (ref. 3).

A commonly accepted minimum tolerable hardness for bearing components is Rockwell C 58. At a hardness below this value, brinelling of the bearing races can occur. Since hardness decreases with temperature, conventional bearing materials such as SAE 52100 can be used only to temperatures of about 350° F. Much effort has gone into developing steel alloys suitable for nigher temperatures. The addition of elements such as molybdenum, tungsten, chromium, and vanadium promotes the retention of hardness at elevated temperatures. Other materials which promote hardness retention are aluminum and silicon (ref. 4).

Several bearing alloys are available for operation between 350° and 750° F. The most common of these is AISI M-50. In most turbojet applications, this material is used exclusively. The material has the capability of maintaining a hardness above Rockwell C 58 to temperatures of approximately 600° F (ref. 4).

Retainers (cages) are a much more severe problem in small-bore bearings than in larger ones. In extreme-speed applications of small-bore bearings, it is frequently necessary to use a silver-plated, semihard, tool steel retainer rather than a bronze and oil-mist lubrication rather than recirculating oil to reduce churning losses. In large-bore bearings, retainer failure is much less common than in small-bore bearings (ref. 4).

HIGH-TEMPERATURE LUBRICANT SELECTION

Groups of 7205-size (25-mm bore) angular-contact ball bearings made from consumable-electrode vacuum-melted AISI M-1 steel were tested with the 11 lubricants (table XIII-1) in a low-oxygen environment (less than 1 percent by volume). These lubricants varied with respect to base stock, additive content, or

TABLE XIII-1. - TEST LUBRICANT PROPERTIES

Lubricant type	Lubricant designation	Base stock	Additive content	Representative viscosity, cS[a]		
				100° F	210° F	[b]500° F
Modified polyphenyl ether	A	Blend of three-ring and four-ring components	Not available	20	4.3	0.82
	B	Blend of three-ring and four-ring components	Not available	60	6.9	.85
Polyphenyl ether	C	5P4E	None	366	13.1	1.07
	D	5P4E	(c)	365	13.1	1.07
	E	6P5E	None	1831	24.7	1.20
Ester	F	Mixed polyester-diester	Not available	40	8.4	1.70
	G	Diester	(c), (d), (e)	37	7.8	1.60
Hydrocarbon	H	Synthetic paraffinic oil	None	314	32	2.9
	I	Synthetic paraffinic oil	(d)	314	32	2.9
	J	Superrefined naphthenic mineral oil	(c), (d), (e)	79	8.4	1.1
	K	Superrefined paraffinic mineral oil	None	480	28	2.1

[a]Manufacturers' data.
[b]Estimated.
[c]Oxidation inhibitor.
[d]Antiwear additive.
[e]Antifoam agent.

viscosity at room temperature. Test conditions included speeds from 20 000 to 46 000 rpm and bearing thrust loads from 150 to 918 pounds, which produced maximum Hertz stresses ranging from 189 000 to 347 000 psi on the bearing inner race. The test conditions included outer-race temperatures of 400° to 600° F (ref. 6).

Types of high-temperature failure modes are discussed in references 6 and 7. These modes can be categorized as fatigue pitting, surface glazing and pitting, and surface smearing or deformation. The fatigue failures reported in this paper were associated with more surface distress (glazing and superficial pitting) than classical fatigue spalls normally experienced under more conventional temperature environments. An example of this fatigue failure is given in figure XIII-4. A normal appearing race run under good elastohydrodynamic (EHD) conditions is shown in figure XIII-5(a) for comparison.

Surface glazing, which can be present without spalling occurring, is illustrated in figure XIII-5(b). Continued operation results in superficial pitting, as shown in figure XIII-5(c) and/or wear of the rolling-element surfaces. This condition was present in all bearings run with the various lubricants except lubricant I. The glazing was more severe with the bearings tested with the polyphenyl ethers, which were short lived. If operation of the bearing is continued under the condition shown in figure XIII-5(c), spalling of the rolling-element surface will occur as illustrated in figure XIII-4. References 6 and 7 attribute the glazing phenomenon to marginal elastohydrodynamic film thicknesses. Under marginal elastrohydrodynamic lubrication, high tangential forces can be induced which will tend to relocate the maximum shearing stresses closer to the surface (ref. 8). Under these conditions, more shallow fatigue spalls would be expected than normally occur under complete elastohydrodynamic conditions.

It is interesting to note that, with lubricant I (the synthetic paraffinic oil with the antiwear additive), no glazing, superficial pitting, fatigue spalling, or wear occurred for all 10 bearings tested. Each of these bearings was run for at least 180 hours. For the same lubricant without the additive (lubricant H) under the same conditions (i.e., temperatures between 550° and 600° F) some glazing was observed. It is conceivable that antiwear additives will reduce the tangential forces under marginal elastohydrodynamic conditions and thus increase bearing life.

Another mode of failure at elevated temperature is that of "smearing." This mode is illustrated in figure XIII-5(d). Smearing manifests itself by gross metal transfer, deformation, and/or galling of the rolling-element surfaces. It is believed that smearing occurs when the condition is primarily that of boundary lu-

brication accompanied by a high degree of sliding in the ball-race contact. This mode of failure was dominant for those bearings which failed other than by fatigue spalling.

Cage wear can be another failure mode in high-temperature bearing operation. Based upon work reported in references 9 and 10, cages were manufactured from AISI M-1 material having a nominal hardness of Rockwell C 58. To further assure minimal wear, the cages were silver plated. In all bearing tests in this investigation, cage wear was not a mode of failure.

Lubricant oxidation can be another mode of failure (ref. 11). When a lubricant starts to fail through oxidation, the result is usually formation of both soluble and insoluble compounds that may appear as resins, sludges, or acidic compounds. The resulting effects are the following:

(1) A gradual rise in viscosity of the lubricant

(2) The formation of adherent surface deposits that may interfere in small clearance spaces in the bearing

(3) Corrosion or deterioration of the metal parts

(4) General dirtying of the system by sludges or other insoluble compounds

Lubricant viscosity changes were not a problem in the tests reported in this paper inasmuch as fresh lubricant was periodically added to the test rig to replenish that lost because of evaporation or leakage and because of the low-oxygen environment in most of the tests. Consequently, bulk viscosity change was not apparent for the lubricants tested. In addition, corrosion or deterioration of the bearing elements did not occur or manifest itself with the various test lubricants. This may have been due to the relatively short testing times.

Formation of sludge appeared to be a minor problem with lubricant C, the 5P4E polyphenyl ether. However, this problem could be reduced either by the insertion of a copper screen in the lubricant test sump or by the addition of an oxidation inhibitor as in lubricant D. The experience with the other polyphenyl ether lubricants was similar. Sludging was not increased by exposing lubricant D to an air environment at elevated temperature. No deposit formations appeared on the bearings with the polyphenyl ethers.

The esters had a tendency to form hard coke deposits on the bearings at 500° F under the low-oxygen environment. The hydrocarbons exhibited no noticeably hard coke formations under the low-oxygen environment, although the fluid became blackened and some sludge deposits were evident after extended running at 600° F.

Based upon the failure modes discussed in this paper, the lubricant temperature, stress, and life limits were estimated and are summarized in table XIII-2.

TABLE XIII-2. - ESTIMATE OF LUBRICANT TEMPERATURE, STRESS, AND LIFE LIMITS BASED ON OPERATION OF 7205-SIZE ANGULAR-CONTACT BEARINGS IN A LOW-OXYGEN ENVIRONMENT

Lubricant type	Lubricant designation	Estimated maximum bearing operating temperature, °F	Estimated maximum Hertz stress, psi	Estimated life potential at maximum temperature and stress, (a)	Apparent minimum viscosity for avoidance of ball-race contact surface damage, cS
Polyphenyl ether	A	>500	$>233\times10^6$	Fair	0.7 to 1.0
	B	>550	>250	Fair	↓
	C	>600	>302	Poor	
	D	>600	>250	Fair[b]	
	E	>600	>233	Fair	
Ester	F	>500	$>233\times10^6$	Good	1.5 to 1.7
	G	>500	>250	Good	1.5 to 1.7
Hydrocarbon	H	>550	$>250\times10^6$	Good	0.9 to 2.5
	I	↓	>250	Excellent	↓
	J		>268	Good	
	K		>250	Good	

[a]Comparison based on performance of lubricant I.
[b]Air environment.

The estimated bearing life potential was based upon the appearance and performance with the lubricant relative to the appearance and performance of those bearings run with lubricant I, the snythetic paraffinic oil with the antiwear additive.

Damage to the bearings in the form of surface distress and pitting of the race surfaces occurred in relatively short time periods with the polyphenyl ether lubricants. Consequently, the life potential with this family of lubricants was estimated to be only fair relative to the performance of lubricant I under the respec-

tive temperature and stress conditions listed. However, the bearings operated with lubricant C, the 5P4E polyphenyl ether without an oxidation inhibitor, exhibited a poor life potential in the low-oxygen environment even at lower stresses than that listed. The ester and hydrocarbon based lubricants showed good life potential relative to lubricant I with minimal surface distress at temperatures of the order of 500° and 550° F, respectively, under the low-oxygen environment.

BEARING LIFE AT ELEVATED TEMPERATURE

Tests were conducted with ABEC-5 grade, split-inner-race 120-millimeter-bore angular-contact ball bearings having a nominal contact angle of 20°. The inner and outer races were manufactured from one heat of consumable-electrode vacuum-melted (CVM) AISI M-50 steel, and the balls were manufactured from a second heat. The nominal Rockwell C hardness of the balls and races was 63 at room temperature. Each bearing contained 15 balls of 13/16-inch diameter. The cage was a one-piece outer-land-riding type made of a nickel-base alloy (AMS 4892) having a nominal Rockwell C hardness of 33. The retained austenite content of the ball and race material was measured at less than 3 percent. The inner- and outer-race curvatures were 54 and 52 percent, respectively. All components with the exception of the cage were matched within ±0.5 Rockwell C point. This matching assured a nominal differential hardness in all bearings (i.e., the ball hardness minus the race hardness, commonly called ΔH) of zero (refs. 3, 12, and 13).

Test conditions were a thrust load of 5800 pounds, which produced a maximum Hertz stress on the inner race of 323 000 psi, an outer-race temperature of 425° F, and a speed of 12 000 rpm with an advanced ester lubricant and a synthetic paraffinic oil in an air environment. The results of these tests are shown in figure XIII-6. The ester fluid produced lives approximately 6 times the Anti-Friction Bearing Manufacturers Association (AFBMA) predicted (catalog) life, while the synthetic paraffinic oil produced lives over 10 times the AFBMA lives. Current-state-of-the-art bearings and lubricants at 350° F in flying aircraft produced lives approximately 5 times the AFBMA prediction.

At temperatures above 425° F the viscosity of an ester fluid is such that it is questionable whether the fluid can produce an adequate EHD film. On the other hand, the viscosity of a synthetic paraffinic lubricant is adequate to support an EHD film but the lubricant oxidizes rapidly. As a result, at temperatures much above 425° F, a relatively low-oxygen environment must be provided.

Bearing tests were conducted at outer-race temperatures of 400° , 500° , and 600° F with the synthetic paraffinic fluid under a low-oxygen environment (less than 0.1 percent oxygen by volume). There were no statistical differences between these low-oxygen environment tests nor any statistical difference between those tests run in air with the same fluid. As a result derating in bearing life is not necessary at temperatures between 400° and 600° F, nor when running under a low-oxygen environment.

Typical fatigue spalls occurring on the balls of a bearing run with the synthetic paraffinic oil can be seen in figure XIII-7. Metallurgical examination of the bearings indicated that failure was by classical rolling-element fatigue. The fatigue spalls were of subsurface origin, initiating in the zone of resolved maximum shearing stresses. An unfailed bearing run to suspension (500 hr of operation) is shown in figure XIII-8.

Tests were conducted with the 5P4E polyphenyl ether at an outer-race temperature of 600° F in an air environment. At a maximum Hertz stress of 323 000 psi, mixed lubrication existed with boundary lubrication being the predominant mode. As a result, the thrust load was lowered to 4365 pounds, which produced a maximum Hertz stress on the inner race of 295 000 psi. A series of 26 bearings was tested in an air environment. Despite this apparently less hostile environment and the reduced load, most of the tests with the polyphenyl ether had to be suspended because of a large amount of ball wear. In tests running from 2 to 65 hours, the average reduction in ball diameter was approximately 0.001 inch. After a relatively short running time, a stable suspension of wear particles manifested itself in the polyphenyl ether fluid. These particles can act as an abrasive which may accelerate the wear processes. However, 10 bearings ran for over 450 hours (325×10^6 inner-race revolutions) with minimal wear. The ball diameters on these bearings were reduced by not more than 0.0003 inch. On all the bearings tested, glazing of the contacting surfaces was present. However, with the long-lived bearings, no micropitting of the surface accompanied the glazing.

Of the 26 bearings tested, only 2 failed by fatigue. This is an insufficient number of failures to permit an accurate life estimate. However, a rough estimate of life with this fluid was made on the basis of the fatigue data. The life estimate is presented in figure XIII-9 and is compared with the lives obtained with synthetic paraffinic oil under similar test conditions.

With the polyphenyl ether, oil consumption was quite high. It was estimated that at least 30 percent of the oil was lost by evaporation during a 24-hour oper-

ating period. Because of this evaporation, fluid had to be periodically added to the sump.

Tests were performed with a fluorocarbon fluid which was not investigated with the 25-millimeter bearings previously discussed. Preliminary tests with this fluid at 600° F and a thrust load of 5800 pounds under a low-oxygen environment (less than 0.1 percent by volume) produced considerable ball wear and/or surface distress. These tests indicated that, at a maximum Hertz stress of 323 000 psi, mixed lubrication existed with boundary lubrication being the predominant mode. As with the polyphenyl ether the thrust load was lowered to 4365 pounds, which produced a maximum Hertz stress on the inner race of 295 000 psi. The fatigue results with this lubricant are summarized in figure XIII-9 and are compared with those for the other two fluids tested.

While the fatigue life with the fluorocarbon was approximately three times that predicted by the AFBMA, the performance of the fluid was not consistent. The predominant lubrication mode ranged from boundary to elastohydrodynamic at the maximum Hertz stress of 295 000 psi. Some ball wear was apparent, as evidenced by a decrease in ball diameter of 0.005 to 0.002 inch within 500 hours of operation. However, there were tests which had to be aborted because of rather extensive wear. Conversely, there were some tests, which were terminated at 500 hours, exhibiting extremely good surfaces with no evidence of incipient fatigue failure or measurable wear. It is speculated that this fluid may be very sensitive to minute variations in bearing geometry and/or very minor changes in the test conditions.

Based upon its chemical makeup, the fluorocarbon fluid has the greatest potential as an extremely high-temperature lubricant. It exhibits a number of properties which make it extremely attractive to engine designers, chief among which is its inherent fire-safe operation. Conversely, the corrosive aspect might tend to make it difficult to apply in existing lubricating systems, although this should not be a major problem in advanced engines, where the lubricating system can be designed with materials which will accommodate this undesirable characteristic. However, as noted previously, the fluid did not exhibit the severe corrosive effects which had been anticipated and, in fact, the overall damage to either the test facilities or the test bearings themselves was within acceptable limits.

The most serious drawbacks of the fluorocarbon fluid appear to be its high density and its low thermal conductivity. As a result, the fluorocarbon-lubricated bearings, for identical operating conditions, tended to stabilize at a temperature approximately 100° to 125° F above that observed for the bearings lubricated with the other fluids. Additional lubricant cooling was provided to

overcome this problem. Hence, in order to accommodate this fluid in a turbine engine, it will be necessary to reevaluate the engine cooling system and/or to make changes in the basic bearing design to decrease heat generation.

BEARING MATERIAL AND SELECTION

Bearing Retainers (Cages)

At temperatures above 500° F, tests have indicated that bearing cage wear can be a limiting factor in the operation of bearings under the severe lubrication conditions encountered at these elevated temperatures. Therefore, in addition to the race and the rolling-element material, careful consideration must be given to the choice of cage (retainer) material.

In conventional rolling-element bearings, both metallic and nonmetallic cages have found widespread use. Under normal temperatures, for nonaerospace applications, practically all the roller bearings and a large percentage of the ball bearings in use have been equipped either with stamped cages of low-carbon steel or with machined cages of iron-silicon bronze or lead brass. Precision bearings, such as those used for aerospace applications, are usually equipped with cages machined from copper alloys or nonmetallic phenolic materials. In some applications, where marginal lubrication exists during operation, such as at high temperatures, silver plating on the bronze has been used. Phenolic materials are limited to temperatures of approximately 250° F, while copper-base alloys are suitable for operation to approximately 600° F. Above 600° F, some success has been obtained with low-carbon steel or cast-iron cages, but, generally, the most successful high-temperature cages have been nickel-base alloys. One of the nickel-base alloys used is AMS-4892 (ref. 11).

Other materials which have shown promise are high-temperature plastics which exhibit low friction and wear characteristics, high-alloy steels capable of maintaining their hot hardness at elevated temperatures, and stainless steels.

Results of 30-minute tests at a test temperature of 500° F with a naphthenic mineral oil as the lubricant for six materials are shown in figure XIII-10. At this set of conditions, four materials show promise of operating for extended periods of time: M-1, AMS-4892, modified 440C stainless steel, and a basic polyimide polymer. Tests were also conducted at 700° F with the same materials but with the 5P4E polyphenyl ether as the lubricant. The results of these tests are shown in figure XIII-11. At this condition, the M-1, AMS-4892, and

440C stainless steel materials show the greatest promise. The high wear with the polyimide is not totally unexpected inasmuch as thermal degradation of this polymer begins at 700° F (ref. 14). The addition of 15 percent by weight graphite to the basic polyimide polymer had no effect on the wear results at 500° F.

In both the 500° and the 700° F tests, the M-1 and AMS-4892 materials exhibited the least amount of wear relative to the other materials. It, thus, can be concluded that for elevated-temperature bearing applications M-1 and AMS-4892 of Rockwell A hardnesses 81 and 67, respectively, have potential bearing cage application.

Additional tests indicate that for the M-1 and AMS-4892 materials, cage wear decreases with increasing hardness. However, for small differences in hardness of the modified 440C stainless steel materials, there was no significant difference in wear. Operating temperature will, of course, decrease material hot hardness. The effect of increasing temperature from 500° to 700° F with M-1 and AMS-4892 cage materials run with the naphthenic mineral oil as the lubricant shows that wear will increase two to five times, depending on the material and its heat treatment. However, the Rockwell A hardness for M-1 and AMS-4892 decreases approximately 1 and 0.5 point, respectively, because of the increase in temperature from 500° to 700° F. These differences in hardness are not sufficient to account for the marked increases in wear. It can therefore be concluded that, with these materials, temperature affects the amount of wear through its effect on the lubrication process.

From these results it can also be concluded that, in general, potential high-temperature cage materials of the types reported herein should be heat-treated to their maximum room-temperature hardness, while sufficient ductility to prevent cracking is maintained. In application, however, the rolling-element material should be somewhat harder than the cage material to prevent damage to the rolling elements. Wear-resistant platings or coatings may also be used to reduce cage wear.

Bearing Steels

Three bearing materials were investigated at 600° F (ref. 15). These were AISI M-50, WB-49, and AISI M-1. AISI M-50 is a martensitic high-speed tool steel which has been used in critical bearing applications for the past decade. The steel was developed primarily for use as a high-strength, highly wear-resistant tool steel. It has inherently high hardness and good compressive

strength. Its operational temperature capability is in excess of 600° F.

The material as presently available is produced by the consumable-electrode vacuum-remelting process, utilizing either an air-melted or an induction-vacuum-melted electrode. The M-50 is characterized by a fine-grained martensitic matrix (with relatively uniform, small and well dispersed alloy carbides) compared to the other two materials evaluated. The material has good through hardenability. For the test bearings, the material hardness was controlled at room temperature to Rockwell C 63±1 for the rings and Rockwell C 63±0.5 for the balls. This material was used for all the lubricant tests previously mentioned in this paper. The results with bearings made from this material are shown in figures XIII-6, XIII-9, and XIII-12.

AISI M-1 is also a high-speed tool steel which has been under investigation as a potential high-temperature bearing material for a number of years. This material tends to have rather large carbides which agglomerate or band. Since these massive carbides will act as nuclei for fatigue failure, assuming they are located in the critical stress region, they may tend to reduce the rolling-element fatigue life. The material hardness for the test bearings was controlled to Rockwell C 63±1 for the rings and Rockwell C 63±0.5 for the balls. The bearings were of the same design as the AISI M-50 bearings. The fatigue results obtained with this material are shown in figure XIII-12 and compared with the M-50 bearings under the same operating conditions.

WB-49 is a material developed specifically for high-temperature bearing applications (ref. 16). It contains considerably more alloying elements than either the M-50 or the M-1 material. The inherent difficulty with this material is the tendency toward rather massive carbide segregation which, at least in the present case, could not be sufficiently broken up during forging to eliminate its effect as a stress raiser.

The WB-49 rings were heat-treated to a room-temperature hardness of Rockwell C 64±0.5. The WB-49 bearings utilized M-1 tool-steel balls from the same heat as that for the AISI M-1 bearings. Previous experience (ref. 9) has shown that WB-49 balls could not be manufactured without producing incipient microcracking. As a result, balls made from WB-49 had extremely short fatigue lives.

Fatigue results with the WB-49 bearings are compared with those of the AISI M-50 and AISI M-1 bearings in figure XIII-12.

From these data, the fatigue-life difference between the M-50 and M-1 steels can be considered statistically insignificant at 600° F. However, the difference between the WB-49 and both the M-50 and M-1 materials is statistically signifi-

significant. For the M-50 and M-1 bearings run with the synthetic paraffinic oil, the experimental bearing 10-percent life exceeds the AFBMA-predicted (catalog) life by factors in excess of 13 and 6, respectively. As a result, for these two materials no derating of bearing life is required. However, the life of WB 49 was less than half the AFBMA-predicted (catalog) life. Hence, this material would have to be derated.

SPEED EFFECTS ON BEARING LIFE

Effect of Reduced Ball Mass

When ball bearings are operated at DN values above 1.5 million, centrifugal forces produced by the balls can become significant. The resulting increase in Hertz stresses at the outer-race ball contacts can seriously shorten bearing fatigue life. There are several possible approaches to solving this problem.

The first and most obvious approach is to optimize the bearing internal geometry for maximum life using a high-speed, ball-bearing-dynamics computer program (ref. 17). This will yield the optimum ball diameter and number, race curvatures, and contact angle. However, this approach will not yield more than a small, incremental improvement in life over that of bearings now in use. As a result, less conservative approaches must be considered.

Another approach is to reduce the mass of the ball. A 50-percent reduction in ball weight, while maintaining the ball diameter constant, can theoretically result in a significant increase in life at DN values greater than 3 million. The effects of decreasing ball weight in a 150-millimeter-bore ball bearing are illustrated in figure XIII-13. For the 5000- and 1000-pound loads, the life can be increased more than three times at the higher DN values simply by reducing the ball mass 50 percent.

Spherically Hollow Balls

One means of reducing the ball mass is to manufacture hollow balls. Spherically hollow balls are fabricated by forging two hemispherical shells by electron-beam welding, and finishing and heat treating the hollow balls by methods normally used in the manufacture of conventional solid balls.

Hollow balls of 11/16-inch diameter with 0.060-inch wall thickness were fabricated in this manner and fitted to 75-millimeter-bore ball bearings. The bearings were operated at 500- and 1000-pound thrust loads at speeds up to 18 000 rpm (1.35 million DN). A superrefined naphthenic mineral oil was used as the lubricant in an air-oil mist with flow rates ranging from 0.01 to 0.07 pound per minute (refs. 18 and 19).

Post-test inspection of the bearings after a few hours running showed extensive damage to the hollow balls with many spalls on the outer surface. Several balls from one bearing were sectioned through the weld and polished to determine the extent and source of the failures. A cross section of a hollow ball is shown in figure XIII-14. A bead on the inner diameter is formed by the electron-beam weld. It is speculated that this bead acted as a notch or stress raiser in the ball wall and initiated flexure fatigue failures after the bearing was operated for only 13 hours. A typical flexure fatigue failure is shown in figure XIII-15. The upper photograph shows two cracks eminating from the weld bead toward the outer surface of the ball. The crack shown in the lower photograph has also originated at the weld bead but has propagated into a crack network and a fatigue spall at the ball outer surface. Balls from other bearings that were run under similar conditions were examined. Some showed spalls on the outer surface; some showed no apparent damage. All these balls were sectioned and polished, and all revealed cracks originating in the vicinity of the weld bead at the inner surface. From the examination of all run hollow balls, it was concluded that they all had failed in flexure because of a stress concentration in the region of the weld at the inner ball surface.

The use of hollow balls can still be advantageous at higher bearing DN values, provided the following steps can be taken: (1) use a wall thickness such that flexure is minimized and yet mass reduction is appreciable, (2) control the weld penetration around the periphery of the ball, and (3) maintain a uniform wall thickness. Unless these steps are taken, hollow balls will have an unbalance and a different stiffness at the weld. Under dynamic conditions, these factors adversely affect the lives of the balls.

Drilled Balls

Another method of reducing ball mass is to machine a concentric hole through the ball (fig. XIII-16). The amount of mass reduction equal to that of a thin wall spherically hollow ball can be achieved with several advantages. Using drilled

balls alleviates possible problems of ball unbalance, because the hole concentricity can be maintained very accurately. Additionally, a very smooth surface finish can be achieved, without the irregularities present in the area of the weld (ref. 20).

Tests were conducted with 75-millimeter-bore ball bearings using 11/16-inch-diameter drilled balls. The bearings were operated at a thrust load of 500 pounds at speeds to 28 000 rpm (2.1 million DN) with air-oil-mist or oil-jet lubrication. The drilled balls were made by electric discharge machining (EDM) a 0.42-inch-diameter hole through the center of a solid ball to effect a 50-percent weight reduction. A finished ball is illustrated in figure XIII-16. Pins through the center of each ball pocket at the pitch diameter of the bearing (fig. XIII-16) were used to restrain the edge of the hole from contacting the race groove prior to operation. During operation the balls position themselves where no significant contact occurs between the edge of the holes and the pins.

Two 75-millimeter ball bearings operated successfully over a range of conditions without damage or excessive wear. One bearing was still operating satisfactorily after 107 hours of accumulated running time, with 65 hours above 1.5 million DN.

In another study, four 125-millimeter-bore ball bearings using drilled balls providing a weight reduction of over 50 percent were operated under a 2500-pound thrust load at speeds from 8000 to 24 000 rpm (1.0 to 3.0 million DN) in two separate tests. Special modifications were made to the bearings that provided for adequate lubrication and sufficient cooling with a type II ester oil. All four bearings operated satisfactorily at these extreme conditions for several hours running time without damage or significant wear. One of these drilled ball bearings is shown in figure XIII-17. It can be seen that the components of this bearing are in very good condition after 4.7 hours of operation. The results of these experimental programs indicate that the drilled ball bearing concept shows a great deal of promise for high-speed bearing applications.

Series Hybrid Bearing

Another means of achieving high-speed bearing operation and long life is through the series hybrid bearing (fig. XIII-18). In essence the series hybrid bearing comprises an angular contact ball bearing in series with a fluid film bearing. Both bearings handle the same thrust load of the main shaft; however, as speed is increased, the fluid film bearing lifts off at its pad because of the in-

creased pressure caused by the centrifugal force of the lubricant fed through the main shaft. As the bearing lifts off, there is a differential in speed between the portion attached rigidly to the shaft and that attached to the angular contact bearing resulting in a lower speed of the angular contact bearing relative to the shaft. The test results with this bearing are shown in figure XIII-19, which is a plot of the inner race speed of the ball bearing as a function of the shaft speed. In normal operation the shaft speed is always equal to the inner-race speed. As the speed of the shaft is increased and the pressure is built up in the fluid film bearing, there is a fluid film formed and a decrease in speed between the fluid film bearing rigidly attached to the shaft and that attached to the ball bearing. This results in a decrease in the inner-race speed of the ball bearing. In this case (fig. XIII-19) a fluid film is formed in the fluid film bearing at a speed of approximately 1 million DN. The decrease is approximately 30 percent at the elevated speed of approximately 2 million DN. The decrease in speed means a decrease in centrifugal force and as a result an increase in life. A comparison of the drilled ball bearing and the series hybrid bearing on bearing life at the elevated speeds is shown in figure XIII-20. For comparison purposes data for a solid ball bearing are given. In comparing the drilled ball with the solid ball at 4 million DN, the life ratio with the drilled ball is of the order of 5 to 1. With a series hybrid bearing with a 30-percent speed reduction, the life ratio is approximately 6 to 1.

The drilled ball concept can be combined with the series hybrid bearing. With this combination the life ratio at 4 million DN is approximately 10 to 1 over the conventional solid ball bearing. What is also important is that there is only a small decrease in life with speed.

SEAL FUNCTIONS AND DESIGN CONSIDERATIONS

Seal Systems

As previously stated, main-shaft seals are used in gas turbine engines to restrict gas leakage into the bearing compartments (sumps). The seals at the front of the compressor (fig. XIII-21) usually present no problem since the sump can be surrounded by compressor bleed air of moderate pressure and temperature. Bleed air leaks through the seal and, thus, pressurizes the front sump. For moderate bleed air pressures and temperatures a single shaft seal of many types is adequate. As an example, ring seals have been used at 54 psi and

330° F; circumferential seals are more than adequate for this location, and in the present state of development, have been used to 85 psi and 700° F with a sliding speed of 240 feet per second. Face seals are also adequate, as some are operating at 125 psi, 800° F, and a sliding speed of 300 feet per second. The final selection of the seal type for the front compressor location depends on the many design and system considerations, including preference.

At the middle of the engine (fig. XIII-21) and at the turbine bearing sump, the seal operational requirements become more severe. The bearing(s) and seal(s) tend to be large because of shaft size and because the thrust bearing must be large enough to carry the net thrust load on the rotating parts. In addition, the sump is usually surrounded by higher pressure gas (and corresponding higher temperature) than the front of the engine.

Figures XIII-22 to XIII-24 show some shaft seal arrangements for the turbine bearing sump location. Here the basic problem is protection of the bearing sump from the turbine cooling gas. In early engines the cooling gas pressure and temperature were relatively low and a single labyrinth seal, which restricted turbine cooling gas leakage into the sump, was adequate (fig. XIII-22). (Some engines use a once-through lubrication system in which the sump is pressurized by relatively cool bleed air, and this air and the oil lubricant are allowed to vent overboard.) At these pressures, the efficiency loss due to seal leakage was not significant. However, a disadvantage of the labyrinth seal, as compared to the close-clearance seals (ring, circumferential, and face), is high leakage with corresponding larger ducting requirements and easier passage of airborne water and dirt into the sump. In addition, for labyrinth seals, reverse pressure drops must be avoided to preclude high oil loss. Furthermore, ram air temperature (minimum-temperature sump-pressurizing air available) increases with increasing flight speed. Therefore, a flight speed limit exists beyond which the low-leakage close-clearance seals are desirable in order to preclude sump fires.

The required pressure of the turbine cooling gas is determined by the turbine inlet pressures. As turbine cooling gas pressure requirements increased with engine development, the single labyrinth seal of figure XIII-22 was no longer suitable, and some of the seal systems such as illustrated in figures XIII-23 and XIII-24 were used. A conventional face seal (fig. XIII-23) has satisfactory performance to pressures of 125 psi, temperatures of 800° F, and sliding speeds of 350 feet per second. Recent seal studies (ref. 1) showed that operation at higher pressures, temperatures, or sliding speeds was unsatisfactory from a wear and leakage standpoint; subsequent analysis revealed that the seal limitations were primarily due to thermal deformations that induced seal imbalance,

which, in turn, caused high wear and leakage. See reference 21 for a discussion of the imbalance problem that limits the capability of the conventional face seal.

When the pressure, speed, and temperatures exceed the capability of conventional contact seals (such as that of fig. XIII-23), a pressure staging seal system is used. Such a system of multilabyrinths is shown in figure XIII-24. In this seal system a labyrinth seal restricts the leakage of relatively high pressure (P_1), high-temperature turbine cooling gas to an overboard vent (P_0') (or to a low-pressure region). Low-pressure compressor bleed (P_1') surrounds the sump and, hence, provides thermal protection, and leakage (through the labyrinth) into the sump provides required sump pressurization. It should be noted that, as the turbine cooling gas pressure (P_1) increases, the leakage has a significant effect on efficiency.

In some engines, combinations of labyrinth and face seal are used to form the seal system. In these systems the labyrinth seal next to the sump (see fig. XIII-24) would be replaced with a face or shaft riding contact seal. Such a system provides low air leakage into the sump and is used when the seal pressurizing air (P_1') is too hot (supersonic flight) to allow high leakage into the sump.

Advanced Seal Requirements

As previously noted, figure XIII-2 shows how the main-shaft seal environment has become increasingly severe. Projected future requirements are shown. These are based on past history of engine development and on presently desired operating goals. During the past 20 years seal sliding speeds have doubled and sealed air pressures and temperatures have had corresponding increases.

It is anticipated that advanced engines will have compressor discharge pressures in the range of 400 to 500 psi and seal temperatures of approximately 1400° F. The seals for these engines will have sliding speeds of 500 to 600 feet per second. Engines for supersonic aircraft may generally have lower compressor discharge pressures, but the turbine cooling gas temperatures will be near 1200° F. The high sliding speeds in these advanced engines dictate that the sealing surfaces should not be in rubbing contact. Thus, the self-acting seals, since they operate without rubbing contact, are potentially useful in the advanced engines.

FACE SEAL WITH SELF-ACTING GEOMETRY FOR LIFT AUGMENTATION

Figure XIII-25 is a cross section of a face seal with self-acting lift geometry. As with a conventional face seal, it consists of a rotating seat that is attached to the shaft (all rotating parts are shaded) and a nonrotating seal head assembly that is free to move in an axial direction and thus accommodate engine thermal expansion (axial). The secondary ring (piston ring) is subjected only to the axial motion (no rotation) of the head assembly, and several springs provided mechanical force to maintain contact at start and stop. In operation, the sealing faces are separated a slight amount (in the range of 0.0005 in.) by action of the self-acting lift geometry, and gas leakage is from the high-pressure side (inside diameter of carbon primary ring) across the sealing dam into the bearing sump. This gas leakage pressurizes the sump and assures proper scavenging of the bearing lubricant. It should be noted that, although the sealed gas temperature is high, tests have shown that considerable gas temperature drop occurs in the leakage flow so that the leakage into the sump does not pose a fire hazard when the seal is operating properly. Operation to 40 standard cubic feet per minute and 1200° F sealed air temperature has been obtained without a sump fire.

A more detailed schematic of the seal is shown in figure XIII-26. The seat is thermally and partially structurally isolated from the shaft by the following means:

(1) The radial spacer between the seat and the shaft serves as a spring that mitigates the effect of nonuniform shaft thermal growth (radial) due to the axial thermal gradient. The effect of thermal movement is further attenuated by piloting the seat over its centroid.

(2) The bellows clamping spacer applies a predetermined clamping force (approximately 2000 lbf), which is probably an order of magnitude less than clamping forces produced by the usual bearing lock nut assembly technique. Therefore, the deformation during assembly is minimized. The seat thermal design is tailored to minimize the axial thermal gradient. Use of a molybdenum alloy, instead of the conventional SAE 8740 or heat-resistant alloy, provides a relatively low deformation criterion which is defined as the ratio of thermal expansion to thermal conductivity (ref. 22). The cooling oil flow path (see fig. XIII-26) is also tailored to minimize the axial thermal gradient. By passing the cooling oil under the radial spacer, the first contact of the cooling oil with the seat is near the hotter face (face mated with nosepiece) of the seat. Analysis

had shown that this oil route minimizes the thermal gradient. Centrifugal pumping action due to rotation and the 45 radial exit holes near the hot face assure even distribution of the cooling oil. (See ref. 23 for description of the self-acting seal components.)

The self-acting lift pads consist of a series of shallow recesses arranged circumferentially around the seal under the sealing dam as shown in figures XIII-27 and XIII-28. An important point is that the lift pads are bounded at the inside diameter and outside diameter by the sealed pressure, P_1. (This is accomplished by feed slots that communicate with the annular groove directly under the sealing dam.) Therefore, a pressure gradient due to gas leakage occurs only across the seal dam. Thus the effects of force changes due to seal face deformation are minimized (ref. 24).

The effect of the self-acting pads on face seal operation is illustrated in figure XIII-28, which shows parallel sealing faces operating without rubbing contact because of a balance between the closing force and the opening force (lift pad forces plus the pressure acting between the sealing faces). For this parallel case, if the seal tends to close, the average pressure in the gap does not change but the gas bearing force increases. Thus, a condition of no rubbing contact can prevail except at startup and shutdown. (See refs. 24 and 25 for a detailed discussion on self-acting pad forces and sealing gap forces.)

The self-acting lift pads develop high forces at operating speeds to prevent rubbing contact (ref. 24). For instance, calculations of lift pad force (fig. XIII-29) indicate an 80-pound lift force at a 0.0002-inch gap height with 315-psi air and a 500-foot-per-second sliding speed. However, if the gap opens (e.g., to 0.001 in.), the lift force drops markedly to 4 pounds. Thus, there is little tendency for the lift pads to hold the seal open at large gaps where leakage will be high. The lift pads, therefore, have a force-against-gap-height characteristic (high-gas film stiffness) which makes lift pad incorporation inherently suited to seal operation. Thus the lift pads provide the following important features generally missing in conventional face seals: (1) high-gas film stiffness that allows the head to dynamically track the seal face motions without rubbing contact and (2) the ability to operate with divergent face deformation.

It is important to note that, because of the axial thermal gradient of the engine, divergent sealing faces are a natural tendency. If the parallel faces of figure XIII-28 become divergent (with respect to gas leakage direction), the average gap pressure will decrease and an unbalance force will tend to close the gap. However, as the gap decreases, the lift-pad force increases rapidly and acts to prevent rubbing contact. There is a limit, however, to the amount of divergence

that can occur before rubbing contact is established at the inside diameter of the lift pads.

Self-Acting Seal Performance

A 120-hour endurance run was made at 400-foot-per-second sliding speed, 200-psi sealed pressure differential, and 1000° F sealed gas temperature. The gas leakage during the 120 hours (fig. XIII-30) averaged about 11.7 standard cubic feet per minute and this is about one-tenth that of a well designed labyrinth seal. The sharp increase in leakage at 116 hours was found to be caused by failure of the thrust bearing. (Bearing spall produced severe rig vibrations which the seal accomodated without rubbing contact.) The surface profile trace taken after the 120-hour endurance run is shown in figure XIII-31. Inspection revealed that the dam had circumferential scratches that were probably from airborne debris passing across the sealing dam. Thus, the amount, particle size, and type of airborne debris may be a significant factor in degradation of the seal dam. The deepest scratch was 0.0002 inch. The pad wear was 0.0005 inch; original polishing scracthes were still visible on the pad surfaces.

Figures XIII-32 and XIII-33 show the condition of the primary seal ring after the 338 hours of running. Figure XIII-33 shows a closeup of the portion circled in figure XIII-32. The original polishing scratches are still visible on the land areas of the pads. Thus, the seal was operating without rubbing contact (except at start and stop).

In order to check the effect of starting and stopping, the seal was subjected to 40 starts and stops. The runs were conducted with room temperature air at 115 psia. The seal was then allowed to coast to a stop (required about 25 sec). A comparison of surface profile traces before and after the 40 starts and stops revealed carbon wear was less than 0.00005 inch.

Leakage and Wear Comparison

A leakage and wear comparison for conventional face seals, labyrinth, and self-acting seals is shown in figure XIII-34. In tests under simulated engine conditions a conventional face seal had 400 times the wear of a self-acting seal. The operating conditions were similar except that the conventional face seal was

run for 9.7 hours and the self-acting seal for 338 hours. A labyrinth seal, however, can be expected to operate without wear.

In leakage comparison the labyrinth seal has about 10 times that of the self-acting seal, and this is the principal disadvantage of the labyringh seal. The leakage of the rubbing-contact seal was greater than that of the self-acting seal. The greater leakage is caused by the high wear rate (wear debris causes sealing face separation) and seal vibration associated with rubbing contact.

CONCLUDING REMARKS

Based upon technology which has been advanced by NASA, bearings can be operated at 600° F in inert environments with reliability equal to or in excess of that experienced in flying engines today. Technological advancements also allow high-speed bearing operation with long life. Drilled ball and series hybrid bearing concepts were developed to increase allowable bearing speeds. Tests to 3 million DN confirm that these bearing concepts have the predicted speed potential. Finally, tests on the self-acting seal showed higher speed and pressure capability than conventional face seals, and gas leakages were one-tenth those of commonly used labyrinth seals. Additional work on these high-speed bearings and seals is needed to explore their full potential and to establish their endurance life.

REFERENCES

1. Parks, A. J.; McKibben, A. H.; and Ng, C. C. W.: Development of Main Shaft Seals for Advanced Air Breathing Propulsion Systems. Rep. PWA-3161, Pratt & Whitney Aircraft (NASA CR-72338), Aug. 14, 1967.
2. Zaretsky, E. V.; and Anderson, W. J.: EHD Lubrication. Machine Design, vol. 40, no. 26, Nov. 7, 1968, pp. 167-173.
3. Zaretsky, Erwin V.; Anderson, William J.; and Bamberger, Eric N.: Rolling-Element Bearing Life From 400° to 600° F. NASA TN D-5002, 1969.
4. Anderson, W. J.; and Zaretsky, E. V.: Rolling-Element Bearings. Machine Design, vol. 42, no. 15, June 18, 1970, pp. 20-37.
5. Zaretsky, Erwin V.; and Anderson, William J.: Preliminary Determinations of Temperature Limitations of Ester, Ether, and Hydrocarbon Base Lubricants in 25-mm Bore Ball Bearings. NASA TN D-4146, 1967.

6. Sibley, L. B.: Elastohydrodynamic Lubrication. Machine Design, vol. 38, no. 24, Oct. 13, 1966, pp. 220-221.

7. Given, P. S.: Lubricant Film Effects on Rolling-Contact Fatigue. Paper presented at Dartmouth College Bearings Conference, Hanover, N. H., Sept. 1966.

8. Smith, J. O.; and Liu, Chang K.: Stresses Due to Tangential and Normal Loads on An Elastic Solid With Application to Some Contact Stress Problems. J. Appl. Mech., vol. 20, no. 2, June 1953, pp. 157-166.

9. Wachendorfer, C. J.; and Sibley, L. B.: Bearing-Lubricant Endurance Characteristics at High Speeds and High Temperatures. Rep. AL65T088, SKF Industries, Inc. (NASA CR-74097), 1965.

10. Zaretsky, Erwin V.; and Anderson, William J.: Evaluation of High-Temperature Bearing Cage Materials. NASA TN D-3821, 1967.

11. Bisson, Edmond E.; and Anderson, William J.: Advanced Bearing Technology. NASA SP-38, 1964, pp. 175-202, 328-329.

12. Bamberger, E. N.: Bearing Fatigue Investigation. Rep. R67FPD209, General Electric Co. (NASA CR-72290), Sept. 15, 1967.

13. Bamberger, Eric N.; Zaretsky, Erwin V.; and Anderson, William J.: Fatigue Life of 120-mm Bore Ball Bearings at 600° F With Fluorocarbon, Polyphenyl Ether, and Synthetic Paraffinic Base Lubricants. NASA TN D-4850, 1968.

14. Buckley, D. H.; and Johnson, R. L.: Degradation of Polymeric Compositions in Vacuum to 10^{-9} mm Hg in Evaporation and Sliding Friction Experiments. SPE Trans., vol. 4, no. 4, Oct. 1964, pp. 306-314.

15. Bamberger, E. N.; and Zaretsky, E. V.: Fatigue Lives at 600° F of 120-Millimeter-Bore Ball Bearings of AISI M-50, AISI M-1, and WB-49 Steels. NASA TN D-6156, 1971.

16. Philip, T. V.; Nehrenberg, A. E.; and Steven, G.: A Study of the Metallurgical Properties That Are Necessary for Satisfactory Bearing Performance and the Development of Improved Bearing Alloys for Service up to 1000° F. Crucible Steel Co. of America (WADC TR-57-343, pt. 2) Oct. 1958.

17. Harris, T. A.: An Analytical Method to Predict Skidding in Thrust-Loaded, Angular-Contact Ball Bearings. Paper 70-LubS-7, ASME, May 1970.

18. Coe, Harold H.; Parker, Richard J.; and Scibbe, Herbert W.: Evaluation of Electron-Beam Welded Hollow Balls for High-Speed Ball Bearings. Paper 70-LubS-17, ASME, May 1970.

19. Coe, Harold H.; Scibbe, Herbert W.; and Parker, Richard J.: Performance of 75-Millimeter-Bore Bearings to 1.8 Million DN With Electron-Beam-Welded Hollow Balls. NASA TN D-5800, 1970.

20. Coe, H. H.; Scibbe, H. W.; and Anderson, W. J.: Evaluation of Cylindrically Hollow (Drilled) Balls in Ball Bearings at DN Values to 2.1 Million. NASA TN D-7007, 1971.

21. Johnson, Robert L.; and Ludwig, Lawrence P.: Shaft Face Seal With Self-Acting Lift Augmentation for Advanced Gas Turbine Engines. NASA TN D-5170, 1969.

22. Ludwig, Lawrence P.; Strom, Thomas N.; Allen, Gordon P.; and Johnson, Robert L.: Improving Performance of Face Contact Seal in Liquid Sodium (400 to 1000° F) by Incorporation of Spinal-Groove Geometry. NASA TN D-3942, 1967.

23. Ludwig, L. P.; and Johnson, R. L.: Design Study of Shaft Face Seal With Self-Acting Lift Augmentation, III - Mechanical Design. NASA TN D-6164, 1971.

24. Zuk, John; Ludwig, Lawrence P.; and Johnson, Robert L.: Design Study of Shaft Face Seal With Self-Acting Lift Augmentation. I - Self-Acting Pad Geometry. NASA TN D-5744, 1970.

25. Zuk, John; Ludwig, Lawrence P.; and Johnson, Robert L.: Design Study of Shaft Face Seal With Self-Acting Lift Augmentation. II - Sealing Dam. NASA TN D-7006, 1970.

ADVANCED ENGINE BEARING REQUIREMENTS

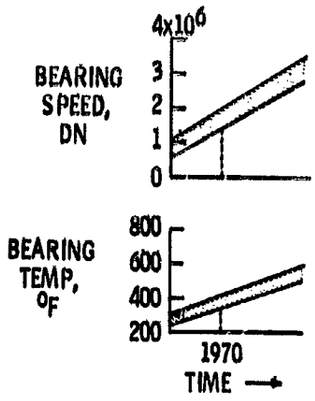

CS-56858

Figure XIII-1

MAINSHAFT SEAL ENVIRONMENT

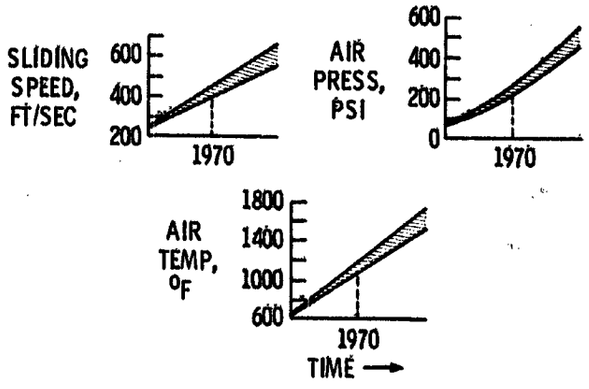

Figure XIII-2

CS-56859

ELASTOHYDRODYNAMIC LUBRICATION

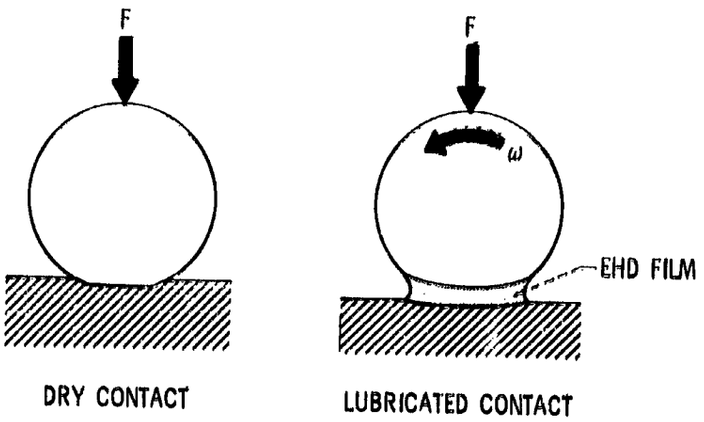

Figure XIII-3 CS-56856

TYPICAL FATIGUE SPALL

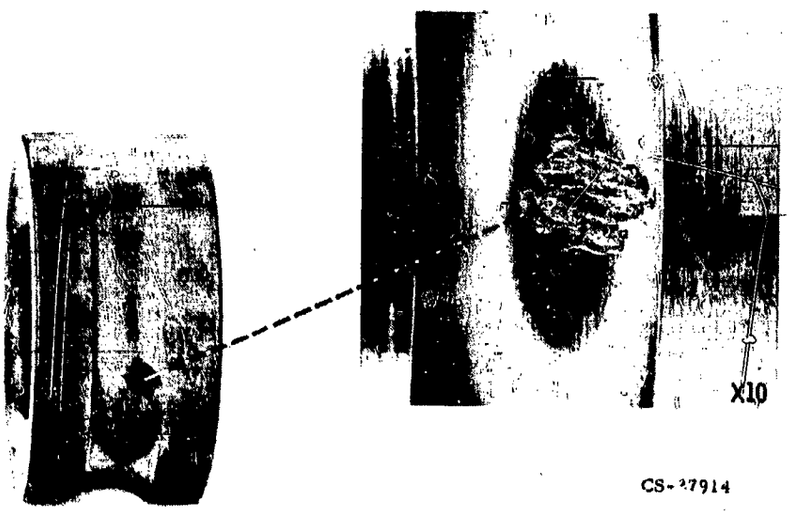

CS-27914

Figure XIII-4

EFFECT OF EHD LUBRICATION ON SURFACE DAMAGE TO BEARING RACES

(A) NORMAL RACE APPEARANCE RESULTING FROM FULL EHD FILM
(B) RACE GLAZING RESULTING FROM MARGINAL EHD FILM
(C) GLAZING AND SUPERFICIAL PITTING
(D) GROSS PLASTIC DEFORMATION OR SMEARING

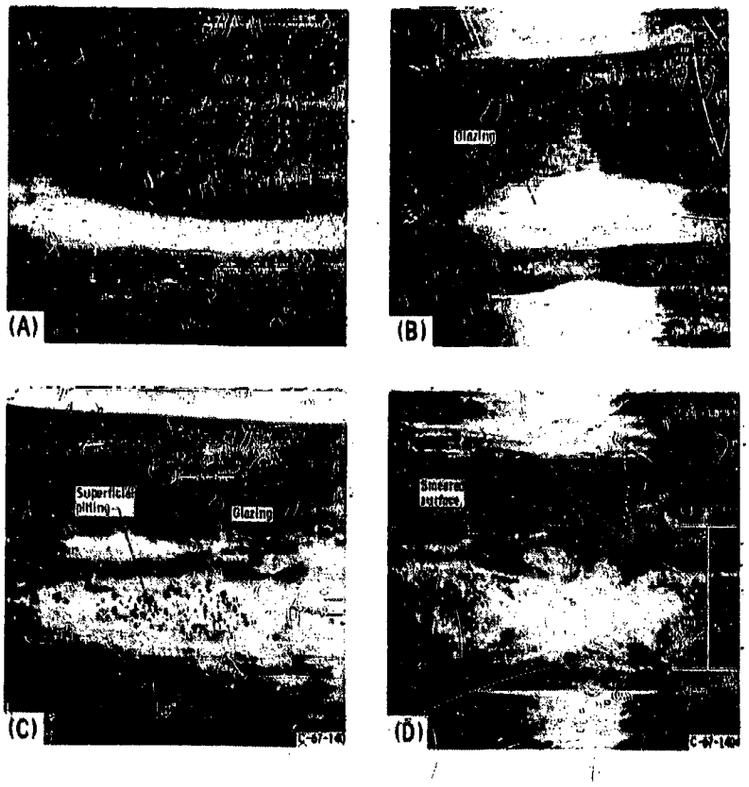

Figure XIII-5

BEARING FATIGUE LIFE AT 425°F IN AIR

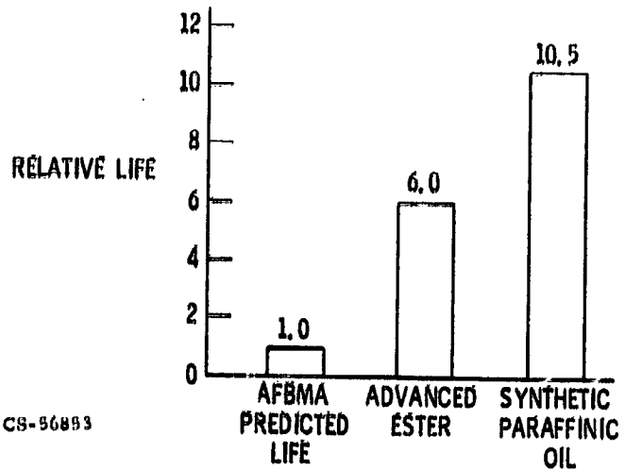

Figure XIII-6

TYPICAL FATIGUE SPALLS ON BEARING BALLS WITH SYNTHETIC PARAFFINIC OIL

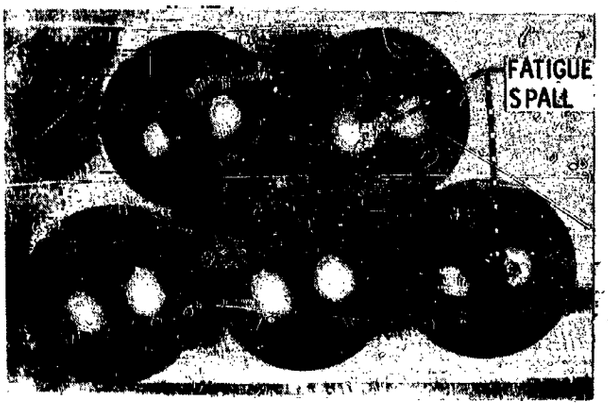

Figure XIII-7

UNFAILED BEARING RUN WITH
SYNTHETIC PARAFFINIC OIL

500 HR AT 600° F; INERT ENVIRONMENT

Figure XIII-8

BEARING FATIGUE LIFE AT 600°F

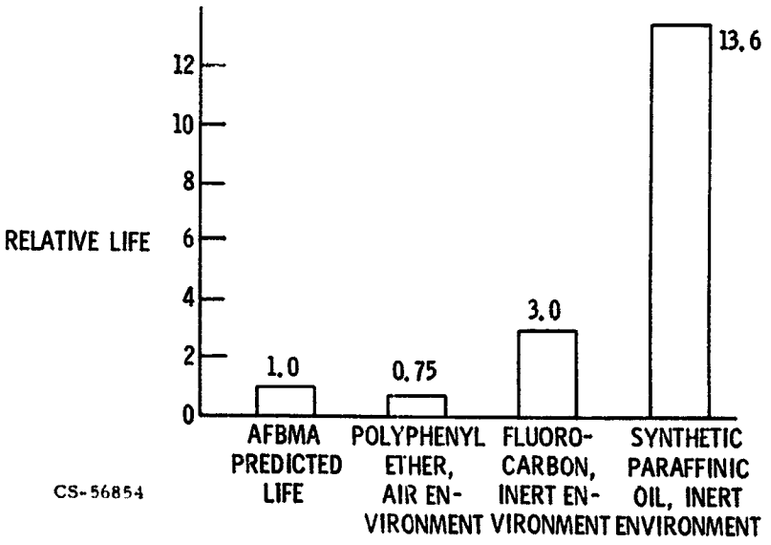

Figure XIII-9

EFFECT OF VARIOUS MATERIALS ON CAGE WEAR
IN AN INERT ENVIRONMENT

AT AMBIENT TEMPERATURE OF 500° F WITH SUPERREFINED NAPHTHENIC MINERAL OIL

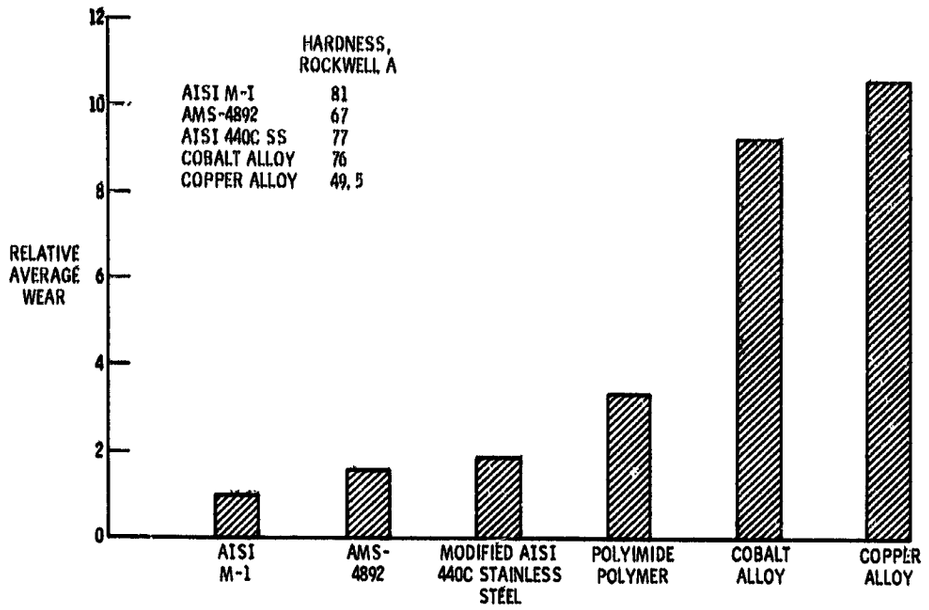

Figure XIII-10

EFFECT OF VARIOUS MATERIALS ON CAGE WEAR
IN AN INERT ENVIRONMENT

AT AMBIENT TEMPERATURE OF 700° F WITH 5P4E POLYPHENYL ETHER

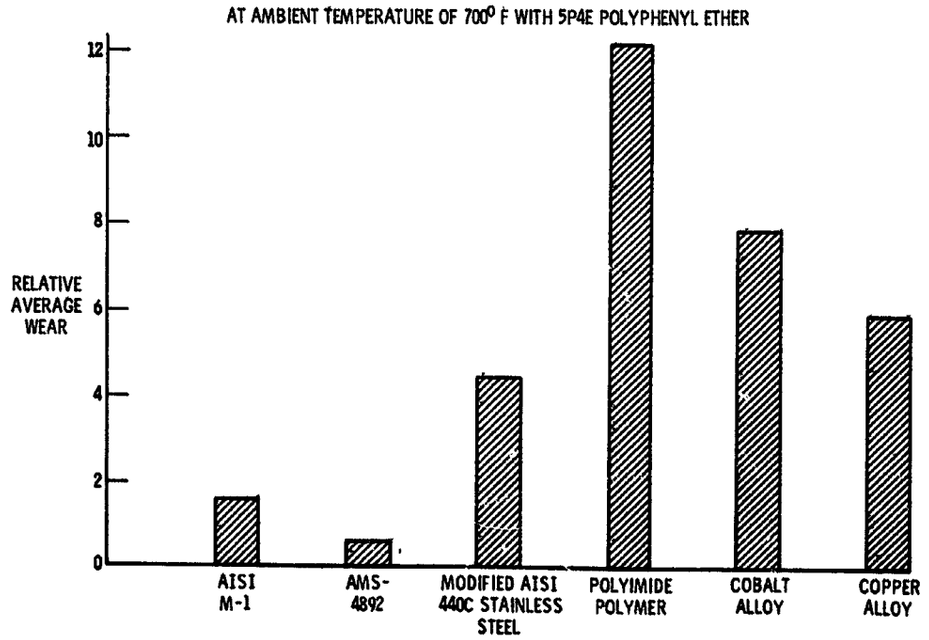

Figure XIII-11

BEARING LIFE WITH THREE STEELS AT 600° F
WITH SYNTHETIC PARAFFINIC LUBRICANT, INERT ENVIRONMENT

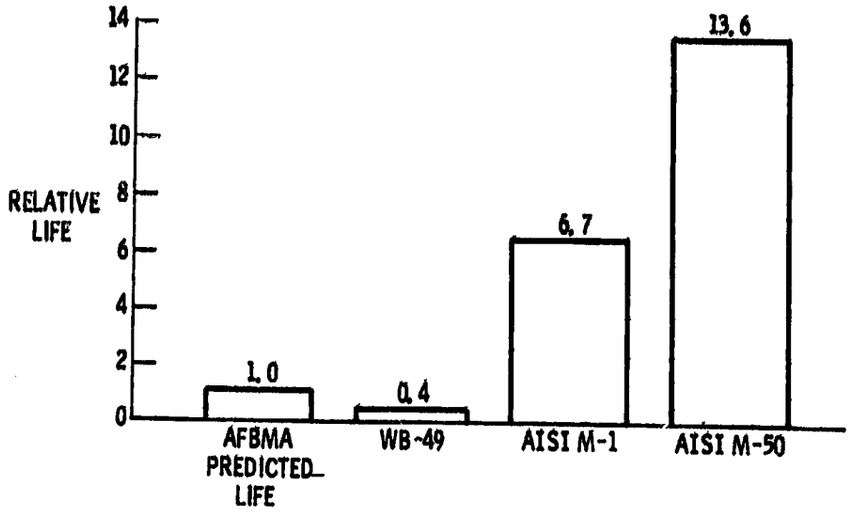

Figure XIII-12

EFFECT OF SPEED ON LIFE

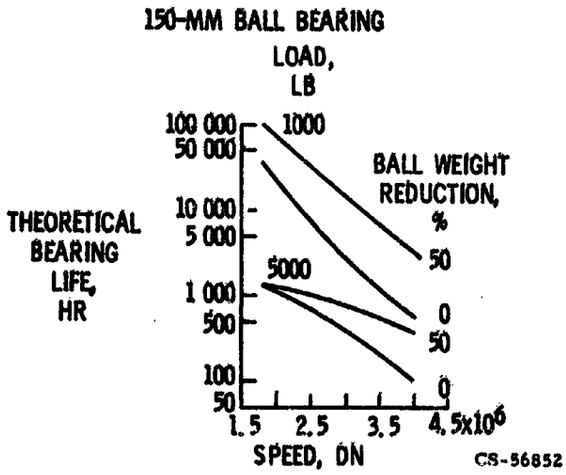

Figure XIII-13

CROSS SECTION OF HOLLOW BALL

CS-56868

Figure XIII-14

HOLLOW BALL FAILURE

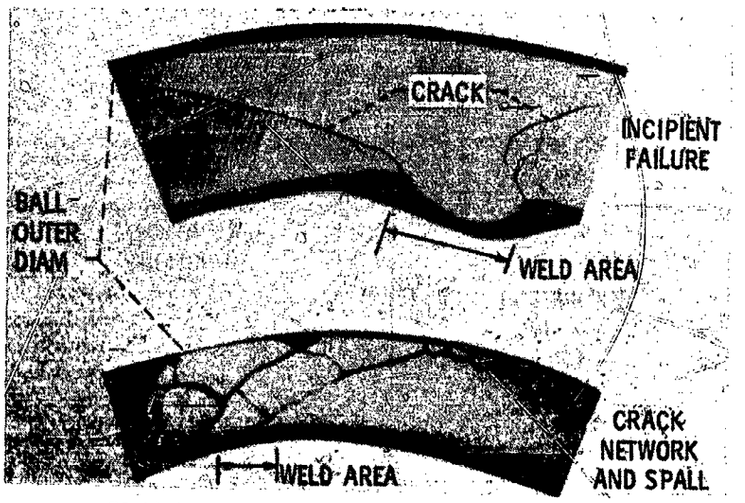

CS-56864

Figure XIII-15

DRILLED BALL BEARING

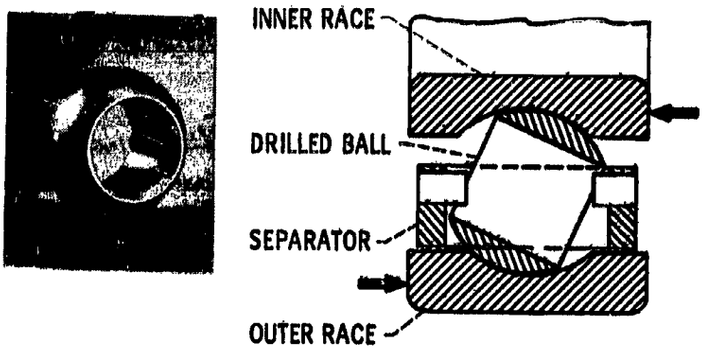

Figure XIII-16

CS-56860

DRILLED BALL BEARING
4.7 HR OF OPERATION

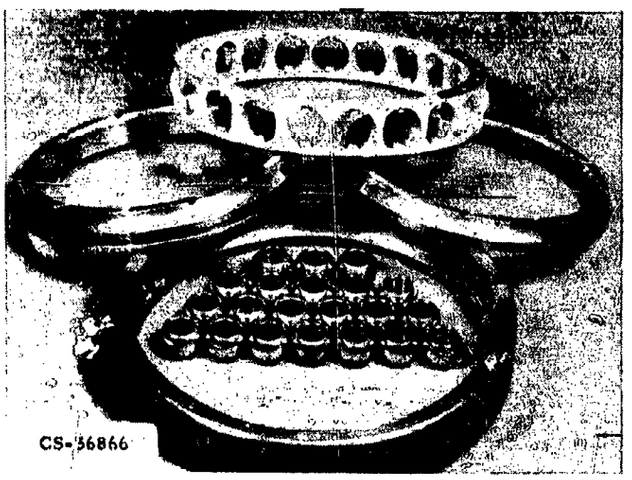

Figure XIII-17

SERIES HYBRID BEARING

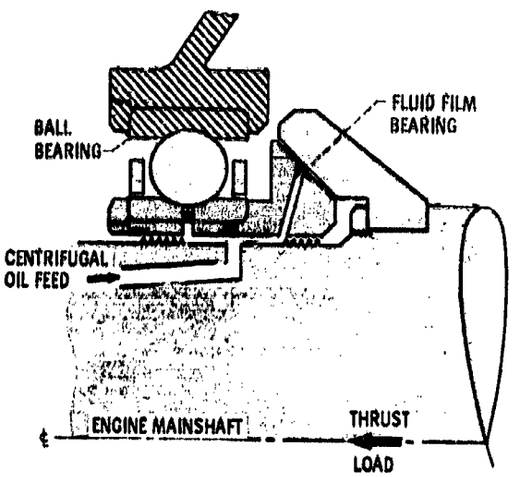

Figure XIII-18

SERIES HYBRID BEARING

TEST RESULTS

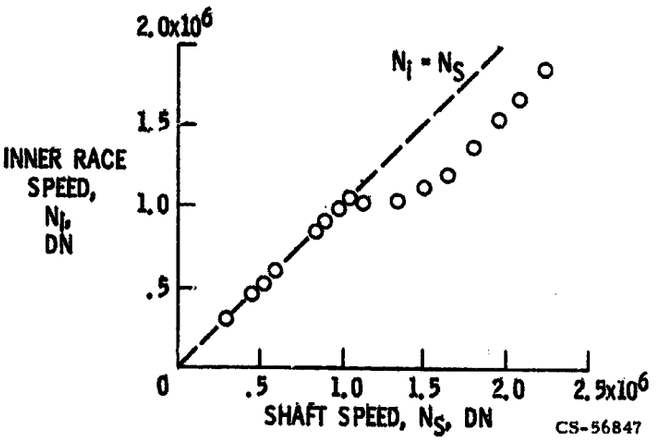

Figure XIII-19

EFFECT OF SPEED

150-MM BALL BEARING WITH 5000-LB LOAD

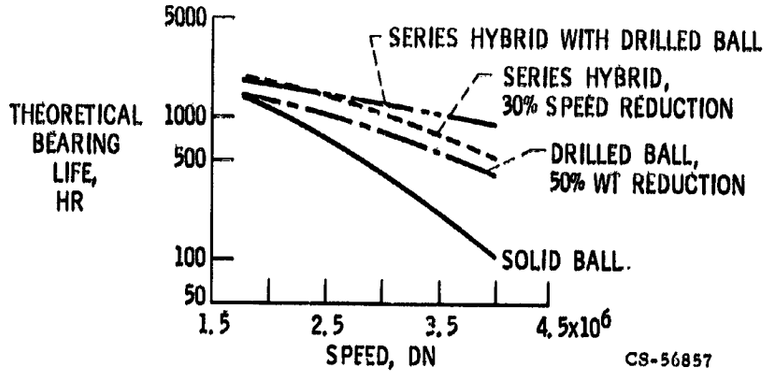

Figure XIII-20

ENGINE SCHEMATIC

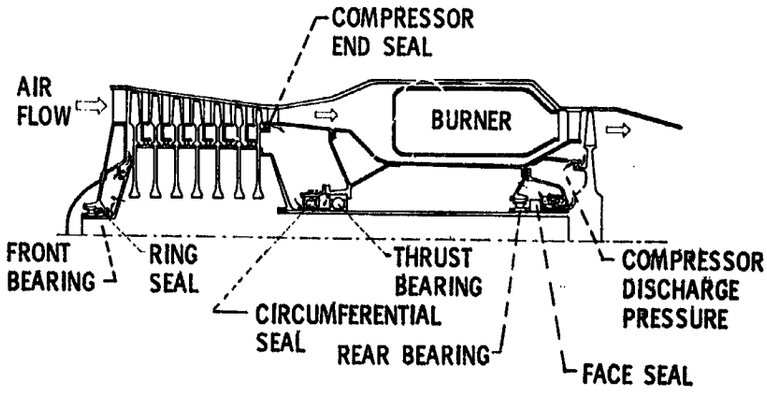

Figure XIII-21

LABYRINTH SEAL

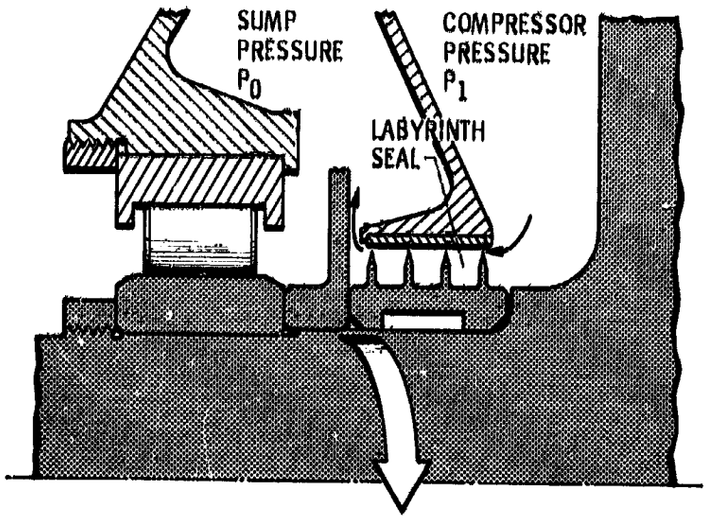

Figure XIII-22

CONVENTIONAL FACE SEAL

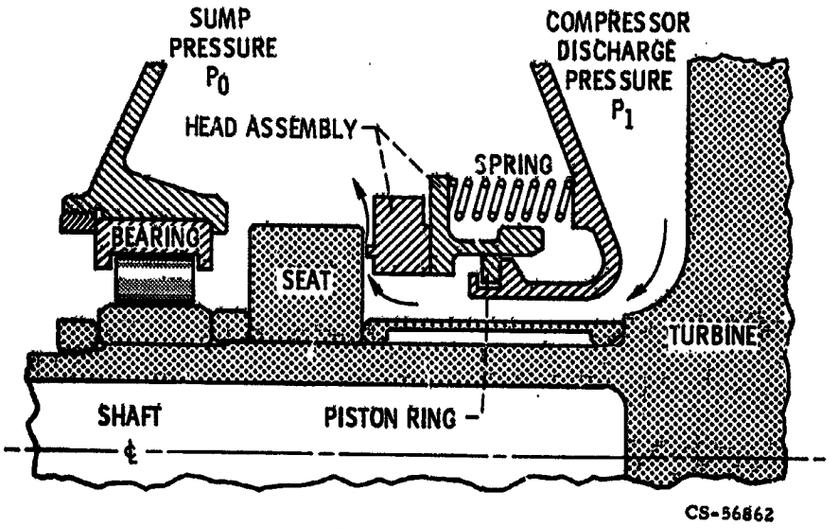

Figure XIII-23

LABYRINTH SEAL SYSTEM SCHEMATIC

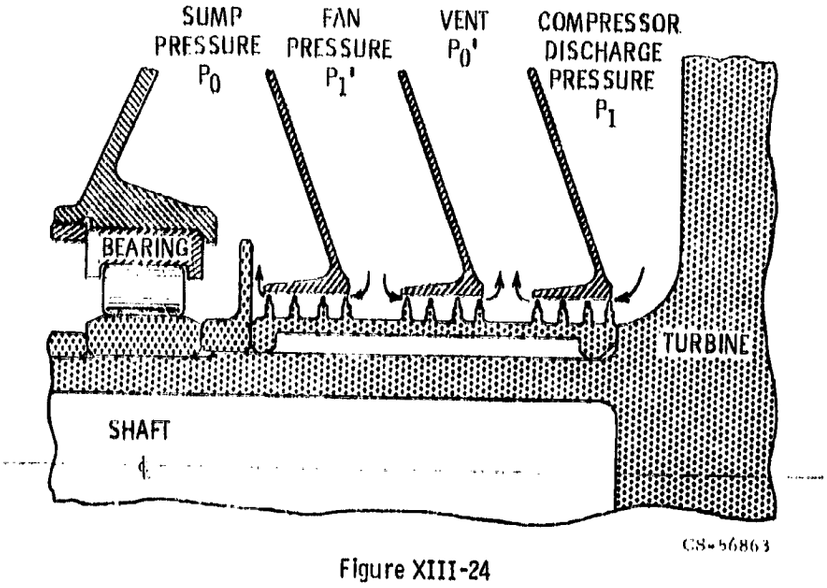

Figure XIII-24

SELF-ACTING FACE SEAL

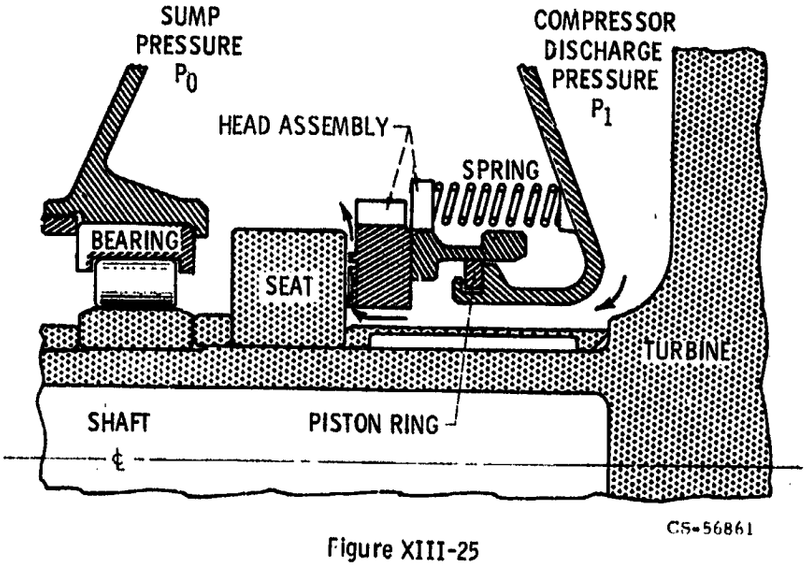

Figure XIII-25

SHAFT FACE SEAL WITH SELF-ACTING LIFT GEOMETRY

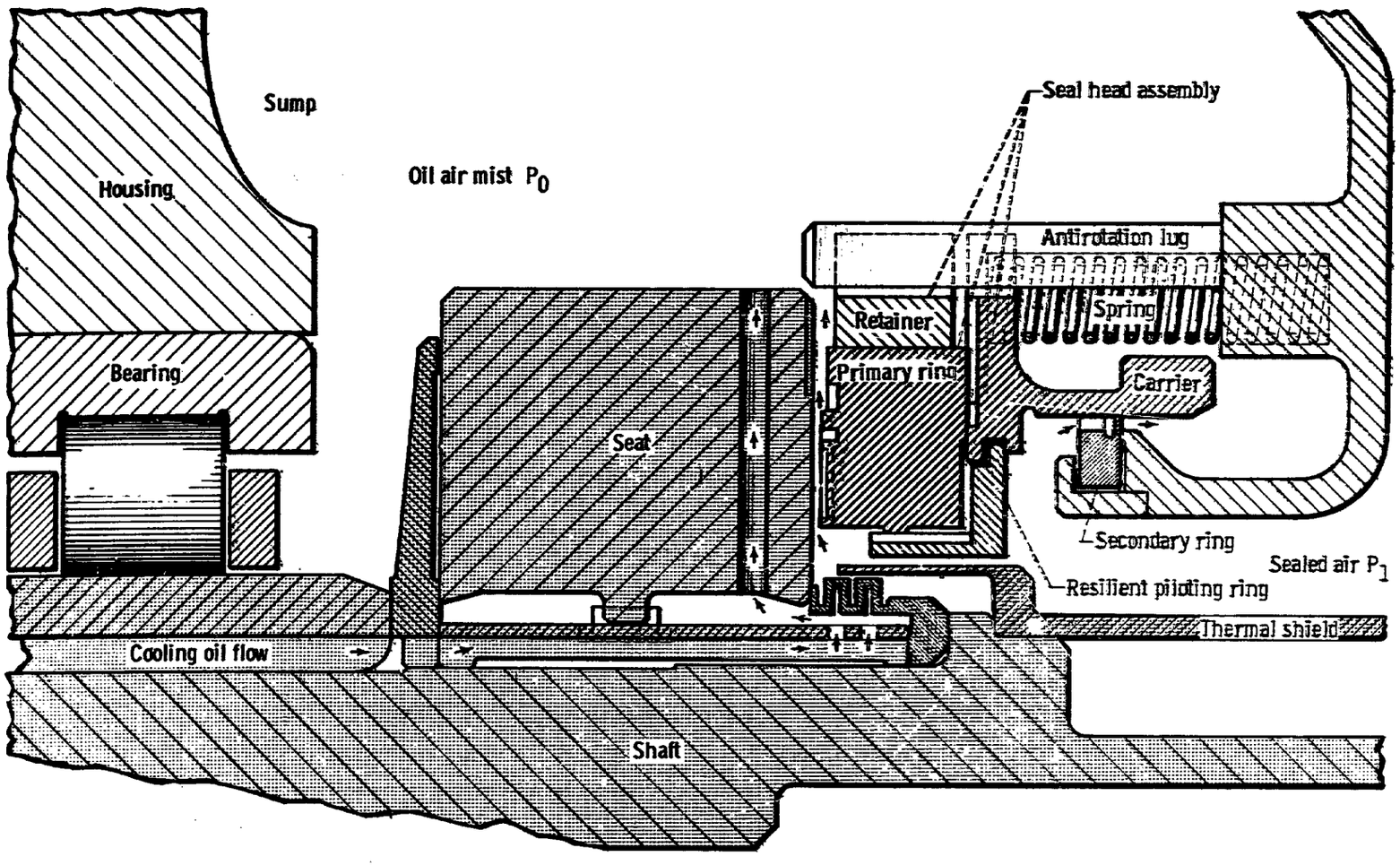

Figure XIII-26

SELF-ACTING SEAL WITH PADS ON PRIMARY RING

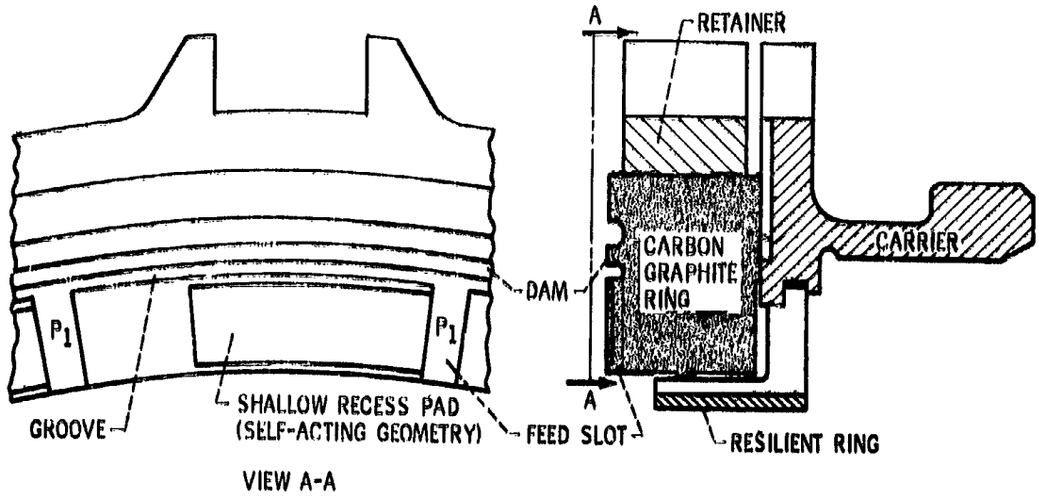

Figure XIII-27

SELF-ACTING SEAL WITH MECHANICAL, PNEUMATIC, AND SELF-ACTING FORCES ACTING ON PRIMARY RING

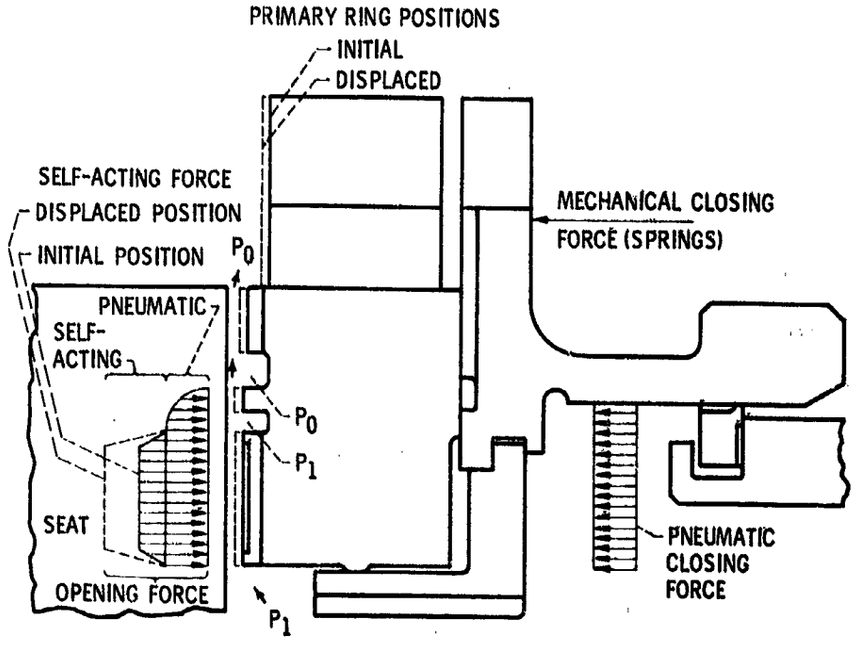

Figure XIII-28

CALCULATED LOAD CAPACITY OF LIFT PAD PORTION OF SEAL

NUMBER OF STEP PADS, 20; ABSOLUTE PRESSURE, 315 PSI; GAS TEMPERATURE, 1300° F; SLIDING SPEED, 500 FEET PER SECOND; PARALLEL SEALING FACES

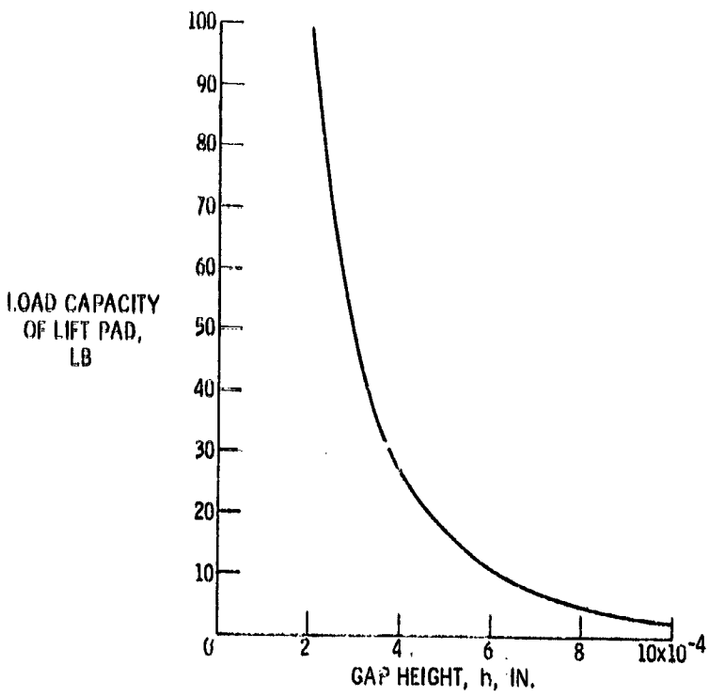

Figure XIII-29

AIR LEAKAGE FOR 120-HOUR ENDURANCE RUN

SLIDING SPEED, 400 FEET PER SECOND; SEALED PRESSURE, 215 PSIA; SEALED TEMPERATURE, 1030° F

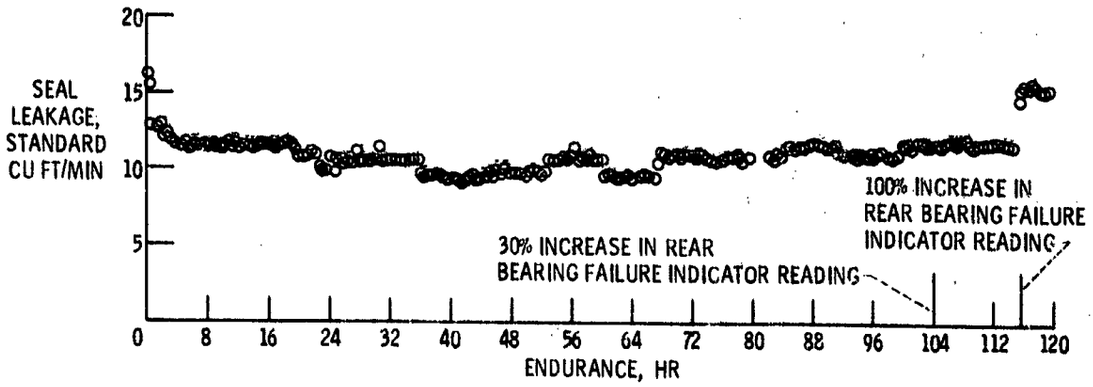

Figure XIII-30

SURFACE PROFILE TRACE RADIALLY ACROSS LIFT PAD AND SEALING DAM AFTER 120 HOURS

SLIDING SPEED, 400 FEET PER SECOND; SEALED PRESSURE DIFFERENTIAL, 215 PSIA; SEALED GAS TEMPERATURE, 1000° F

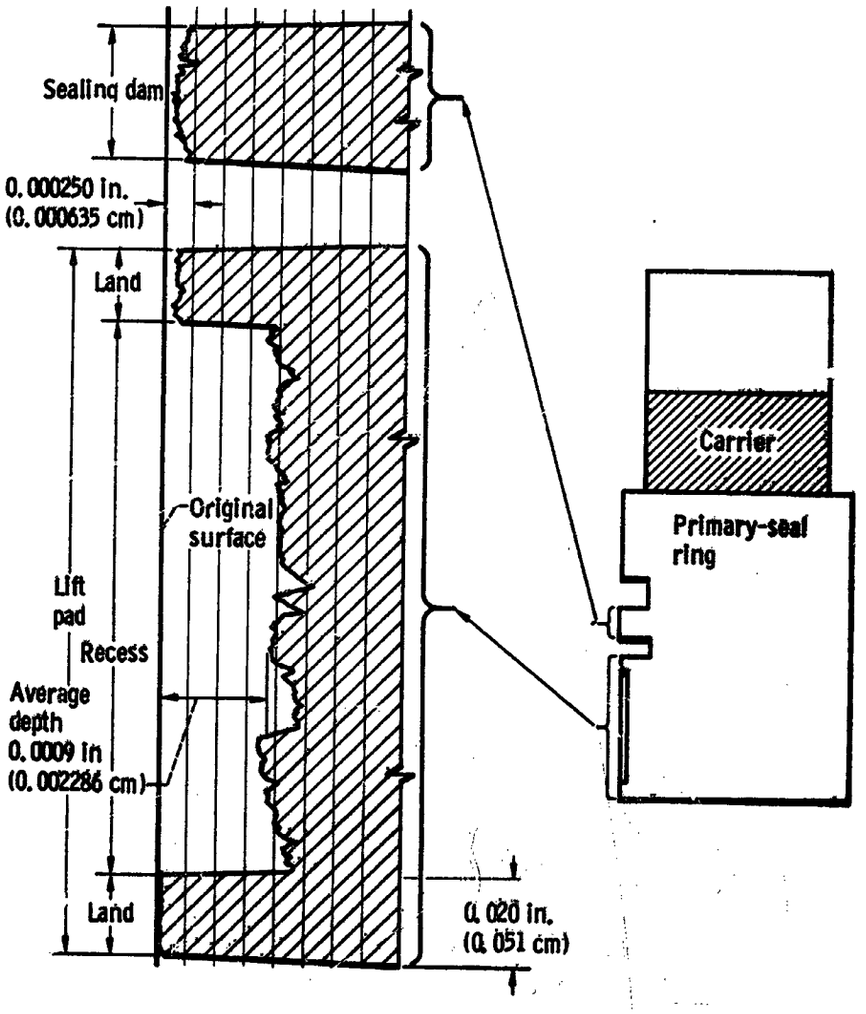

Figure XIII-31

PRIMARY RING ASSEMBLY

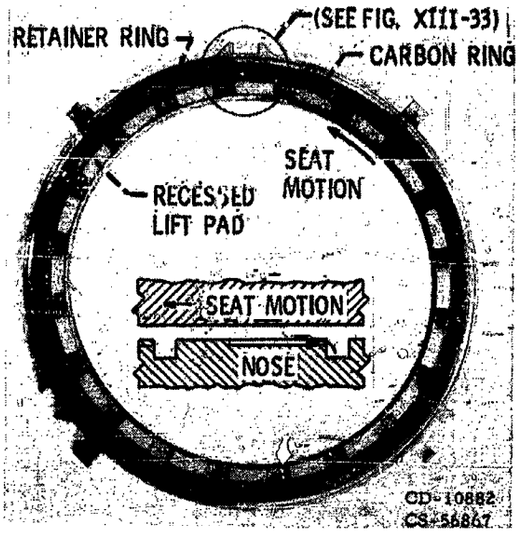

Figure XIII-32

SECTION OF PRIMARY RING ASSEMBLY

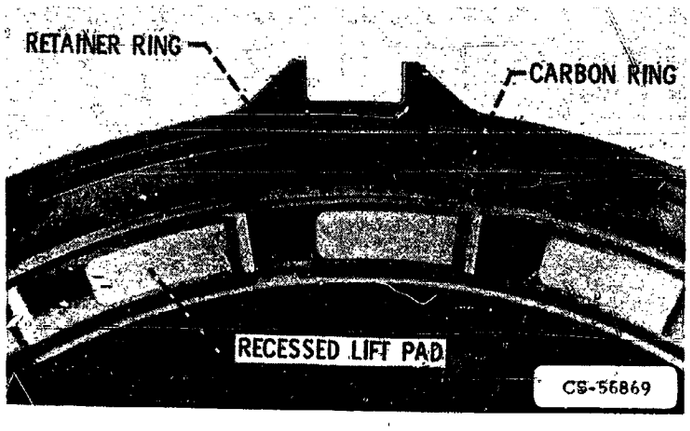

Figure XIII-33

SEAL PERFORMANCE COMPARISON

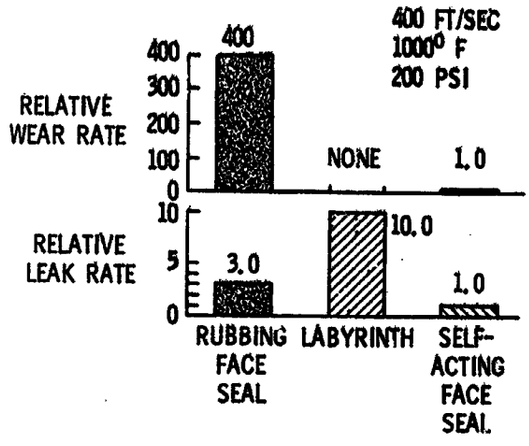

CS-56850

Figure XIII-34

RESEARCH AND DEVELOPMENT CONTRACTORS AND GRANTEES

These contractors and grantees efforts are supplementing NASA in-house programs in aircraft propulsion research and technology:

Companies:

Aerojet General Corporation
AiResearch Manufacturing Co.
Bendix Corporation
Boeing Company
Bolt, Beranek, and Newman, Inc.
de Havilland Aircraft of Canada Ltd.
E. I. du Pont de Nemours & Co., Inc.
Fairchild-Hiller Corporation
Garrett Corporation
General Electric Company
General Motors Company
Gruman Aerospace Corp.
Industrial Tectonics, Inc.
Koppers Company, Inc.
Marlin-Rockwell Co.
Martin-Marietta Corporation
Mechanical Technology, Inc.
Mobil Research & Development Corporation
Monsanto Research Corporation
North American Rockwell Corporation
Northern Research & Engineering
Shell Development Company
SKF Industries, Inc.
United Aircraft Corporation
Union Carbide Corporation

Educational and Research Institutions:

University of Arizona
Battelle Memorial Institute
California Institute of Technology
Case Western Reserve University
Chico State College
University of Cincinnati
Clemson University
Georgia Institute of Technology
University of Illinois
Johns Hopkins University
Massachusetts Institute of Technology
University of Minnesota
Newark College of Engineering
Northwestern University
University of Oklahoma
Princeton University
Rensselaer Polytechnic Institute
Stanford University
University of Southampton, England
University of Tennessee

NASA-Langley, 1971 —— 18 E-6071